NANOPOROUS GAN BY CHEMICAL VAPOR DEPOSITION: CRYSTAL GROWTH, CHARACTERIZATION AND APPLICATIONS.

Oleksandr Bilousov

Dipòsit Legal: T 1557-2014

Nanoporous GaN by Chemical Vapor Deposition: crystal growth, characterization and applications

Oleksandr Bilousov

Doctoral Thesis

Supervised by:

Dr. Joan Josep Carvajal
Prof. Dr. Magdalena Aguiló

Departament de Química Física i Inorgánica

Física i Cristal·lografia de Materials i Nanomaterials (FiCMA-FiCNA)

UNIVERSITAT ROVIRA I VIRGILI

Tarragona
2014

Nanoporous GaN by Chemical Vapor Deposition: crystal growth, characterization and applications

Oleksandr Bilousov

Física i Cristal·lografia de Materials i Nanomaterials (FiCMA-FiCNA)
Departament de Química Física i Inorgánica
Universitat Rovira i Virgili
C/ Marcel·li Domingo, s/n
E-43007, Tarragona (Spain)

UNIVERSITAT ROVIRA I VIRGILI
NANOPOROUS GAN BY CHEMICAL VAPOR DEPOSITION: CRYSTAL GROWTH, CHARACTERIZATION AND APPLICATIONS.
Oleksandr Bilousov
Dipòsit Legal: T 1557-2014

UNIVERSITAT ROVIRA I VIRGILI
DEPARTAMENT DE QUÍMICA FÍSICA I INORGÀNICA
Campus Sescelades
Marcel·lí Domingo, s/n
43007 Tarragona
Tel. +34 977 55 81 37
Fax +34 977 55 95 63
www.quimica.urv.es

We STATE that the present study, entitled **"Nanoporous GaN by Chemical Vapor Deposition: crystal growth, characterization and applications"**, presented by Oleksandr Bilousov for the award of the degree Doctor, has been carried out under our supervision at the Department of Physical and Inorganic Chemistry of this university, and that it fulfils all the requirements to be eligible for the European Doctorate Award.

Tarragona, 21 May 2014

Doctoral Thesis Supervisors

Dr. Joan Josep Carvajal

Prof. Dr. Magdalena Aguiló

UNIVERSITAT ROVIRA I VIRGILI
NANOPOROUS GAN BY CHEMICAL VAPOR DEPOSITION: CRYSTAL GROWTH, CHARACTERIZATION AND APPLICATIONS.
Oleksandr Bilousov
Dipòsit Legal: T 1557-2014

Abstract

Nanoporous GaN by Chemical Vapor Deposition: crystal growth, characterization and applications

Modern society is experiencing a constantly increasing demand for energy. A significative amount of the energy consumed is used for lighting purposes. Gallium nitride (GaN) is a wide band gap semiconductor with important applications in white-light LEDs, which are an attractive alternative to conventional light sources with many benefits that include long operating life, compact size, vibration resistance, low-voltage operation, minimal maintenance cost and minimal environmental impact. The savings of replacing conventional light sources by LEDs would represent a reduction of around 20% in the total electricity consumed. High-efficiency and high power LEDs are now commercially available. However, the overall efficiency requires further improvement. GaN, in its porous form, is expected to enhance the light extraction and internal quantum efficiencies of these LEDs. The main objective of this thesis is focused on fabrication of fully porous *p*-*n* junctions for future LED applications. Nanoporous GaN particles and epitaxial layers were synthesized by chemical vapor deposition (CVD) through the direct reaction between Ga and NH_3, using different doping elements such as Mg and Si to generate the *p*- and *n*-type required semiconductors. The advantage of our technique is that it does not require any secondary treatment after growth to generate the pores. In this way, porous GaN *p*-*n* junctions were obtained showing promising properties for potential application in high brightness GaN-based light emitting diodes and sensor devices with improved sensitivity.

Keywords: porous GaN, chemical vapor deposition, semiconductor, light-emitting diode, graphene.

Preface

The research contained in this doctoral thesis was conducted in the laboratories of the *Física i Cristal·lografia de Materials i Nanomaterials (FiCMA-FiCNA) group* of the *Departament de Química Física i Inorganica* of the *Universitat Rovira i Virgili* in Tarragona, and was supervised by Dr. Joan Josep Carvajal and Prof. Dr. Magdalena Aguiló.

This research was financed by

Agencia de Gestió d´Ajuts Universitaris i de Recerca, AGAUR, de la Generalitat de Catalunya through the fellowships 2013FI_B2 00108, 2012FI_B1 00139 and 2011FI_B 00975.

The EU Framework 7 under Project No. FP7-SPA-2010-263044

The Spanish Government under Projects No. MAT2011-29255-C02-02, TEC2010-21574-C02-02, PI09/90527.

Catalan Authority under Project No. 2009SGR235.

Oleksandr Bilousov
Tarragona, 2014

Acknowledgements

The realization of this thesis would not be possible without the support and encouragement of many people. Foremost, I would like to express my sincere gratitude to my advisors Dr. Joan Josep Carvajal and Prof. Dr. Magdalena Aguiló, as well as to Prof. Dr. Francesc Diaz, for giving me the opportunity to perform my Ph.D. I would like to thank Dr. Joan Josep Carvajal for transmitting to me all his enthusiasm and motivation in the research world, and his immense knowledge, which he was always ready to share.

This thesis would also not have been possible without the help of the technicians of this group. I would like to thank Agustí Montero, Nicolette Bakker and Laura Escorihuela for her great help in the laboratory.

I would like to thank all my colleagues Venkatesan Jambunathan, Martha Segura, Jaume Cugat, Western Bolaños, Mina Moeini, William Barrera, Muhammad Usman Qadri, Oleksandr Savchuk, Ali Butt, Carla Jose Berrospe, Josue Mena, Marc Medina, Josep Maria Serres, Xavier Martinez and Eric Pedrol, as well as to Cinta Pujol, Jaume Massons, Xavier Mateos, Rosa Sole and Airan Rodenas. Thanks to for the continuous support of my Ph.D study and research, for the motivation and enthusiasm.

I give my thanks to the technicians of the Servei de Recursos Científico-Tècnics of the University Rovira i Virgili (Mariana, Francesc, Rita, Merce, Nuria and Lucas), who helped me a lot in my research.

Outside of FiCMA-FiCNA, I owe my deepest gratitude to Dr. Colm O'Dwyer, Dr. Hugh Geaney and Dr. Vitaly Zubialevich for their advices and discussion during my stay in University College Cork.

Also, I would like to thank all people I met in Tarragona and for a great experience that I had here.

Specially I would like to thank my family for their great support.

UNIVERSITAT ROVIRA I VIRGILI
NANOPOROUS GAN BY CHEMICAL VAPOR DEPOSITION: CRYSTAL GROWTH, CHARACTERIZATION AND APPLICATIONS.
Oleksandr Bilousov
Dipòsit Legal: T 1557-2014

To my family...

List of publications

This doctoral thesis is partially based on the work contained in the following papers, referred to by roman numerals in the text:

Paper I: Mena, J.; Carvajal, J.J.; Bilousov, O.V.; Díaz, F. and M. Aguiló. *Optimization of the growth conditions of nanoporous GaN particles by Chemical Vapor Deposition.* Submitted to CrystEngComm.

Paper II: Bilousov, O.V.; Carvajal, J.J.; Drouin, D.; Mateos, X.; Díaz, F.; Aguiló, M. and O'Dwyer, C. *Reduced workfunction intermetallic seed layers allow growth of porous n-GaN and low resistivity, ohmic electron transport* **(2012)** ACS Applied Materials and Interfaces, 4 (12), pp. 6927-6934.

Paper III: Bilousov, O.V.; Carvajal, J.J.; O'Dwyer, C.; Mateos, X.; Díaz, F. and Aguiló, M. *Low resistivity electrical contacting of porous n-type GaN layers due to reduced workfunction intermetallic seed layers* **(2013)** Proceedings of SPIE - The International Society for Optical Engineering, 8625.

Paper IV: Carvajal, J.J.; Bilousov, O.V.; Drouin, D.; Aguiló, M.; Díaz, F. and Rojo, J.C. *Chemical vapor deposition of porous GaN particles on silicon* **(2012)** Microscopy and Microanalysis, 18 (4), pp. 905-911.

Paper V: Bilousov, O.V.; Geaney, H.; Carvajal, J.J.; Zubialevich, V.Z.; Parbrook, P.J.; Giguère, A.; Drouin, D.; Díaz, F.; Aguiló, M. and O'Dwyer, C. *Fabrication of p-type porous GaN on silicon and epitaxial GaN* **(2013)** Applied Physics Letters, 103 (11), art. no. 112103.

Paper VI: Bilousov, O.V.; Carvajal, J.J.; Vilalta-Clemente, A.; Ruterana, P.; Diaz, F.; Aguilo, M. and O'Dwyer, C. *Porous GaN and high-k MgO-GaN MOS diode layers grown in a single step on silicon*. **(2014)** Chemistry of Materials, *26* (2), pp 1243–1249.

Paper VII: Bilousov, O.V.; Carvajal, J.J.; Drouin, D.; Vilalta, A.; Ruterana, P.; Pujol, M.C.; Mateos, X.; Díaz, F., Aguiló, M. and O'Dwyer, C. *Metal catalyzed porous N-type GaN layers: Low resistivity ohmic contacting and single-step MgO/GaN diode formation* **(2013)** ECS Transactions, 53 (2), pp. 17-27.

Paper VIII: Bilousov, O.V.; Carvajal, J.J.; Martínez, O.; Jiménez, J.; Geaney, H.; Díaz, F.; Aguiló, M. and O'Dwyer, C. *Epitaxially grown (0001) oriented porous GaN p-n junctions by chemical vapour deposition*. Submitted to Advanced Functional Materials.

Paper IX: Bilousov, O.V.; Carvajal, J.J.; Geaney, V. H.; Zubialevich, V.Z.; Parbrook, P.J.; Martínez, O.; Jiménez, J.; Díaz, F.; Aguiló, M. and O'Dwyer, C. *Fully porous GaN p-n junctions fabricated by chemical vapor deposition*. Submitted to Advanced Materials.

UNIVERSITAT ROVIRA I VIRGILI
NANOPOROUS GAN BY CHEMICAL VAPOR DEPOSITION: CRYSTAL GROWTH, CHARACTERIZATION AND APPLICATIONS.
Oleksandr Bilousov
Dipòsit Legal: T 1557-2014

Contents

UNIVERSITAT ROVIRA I VIRGILI
NANOPOROUS GAN BY CHEMICAL VAPOR DEPOSITION: CRYSTAL GROWTH, CHARACTERIZATION AND APPLICATIONS.
Oleksandr Bilousov
Dipòsit Legal: T 1557-2014

Chapter 1

Introduction

Gallium Nitride (GaN) is considered one of the most important semiconductors for a number of applications in electronics. GaN-based laser diodes (LD) are used to read Blue-ray discs; GaN high-electron-mobility transistors (HEMTs) are used in various wireless infrastructures; GaN-based metal-oxide-semiconductor field-effect transistors (MOSFET) and metal-semiconductor field-effect transistors (MESFET) offer many advantages in high power electronics for automotive applications. However, one of the most important applications of GaN is found in light emitting diodes (LEDs) as the active light emitting element of various optical components, ranging from traffic lights to large area displays. In its porous form, GaN has received particular interest in the last decade due to interesting optical and electronic properties that allowed, for instance, the demonstration of gas sensors with enhanced sensitivity and also LEDs with improved light extraction efficiency, of crucial importance for the modern society, since a significant amount of the energy consumed is used for lighting. Replacing conventional light sources by LEDs would save up to 85% of the electricity consumed. Taking into account that around 20% of the electricity worldwide is consumed in lighting, LEDs in general, but porous LEDs in particular, can make a big impact on worlds energy savings.

This chapter will start by highlighting the properties and characteristics of GaN. Also, we will put GaN into perspective with other wide-bandgap semiconductors and their applications. After this, we will discuss the interest, advantages, fabrication, characterization and applications of porous GaN. Finally, we will present the objectives of this thesis.

1.1 GaN, an important semiconductor in electronics and optoelectronics

GaN is an important semiconductor for a wide range of applications, principally due to its wide direct band gap (3.39 eV at room temperature) and is the most used material for solid state lighting, both as LEDs and diode lasers, with emissions in the UV and visible (including the production of white light) [1], replacing other semiconductors developed earlier for the same purposes. Using a direct band gap material allows the fabrication of more efficient LEDs, compared to materials with an indirect band gap [2]. It has also excellent prospects in high temperature electronics because of its large band gap, high thermal stability and excellent physical properties [3].

GaN crystallizes in the hexagonal system with the space group $P6_3mc$ (wurzite structure), although a metastable cubic phase (zinc blende structure) has also been described in the literature [4, 5]. Wurtzite is the most commonly utilized one in optoelectronics. In wurtzite GaN, the Ga and N atoms are tetrahedrally bonded to their neighbors, as illustrated in Figure 1.1.

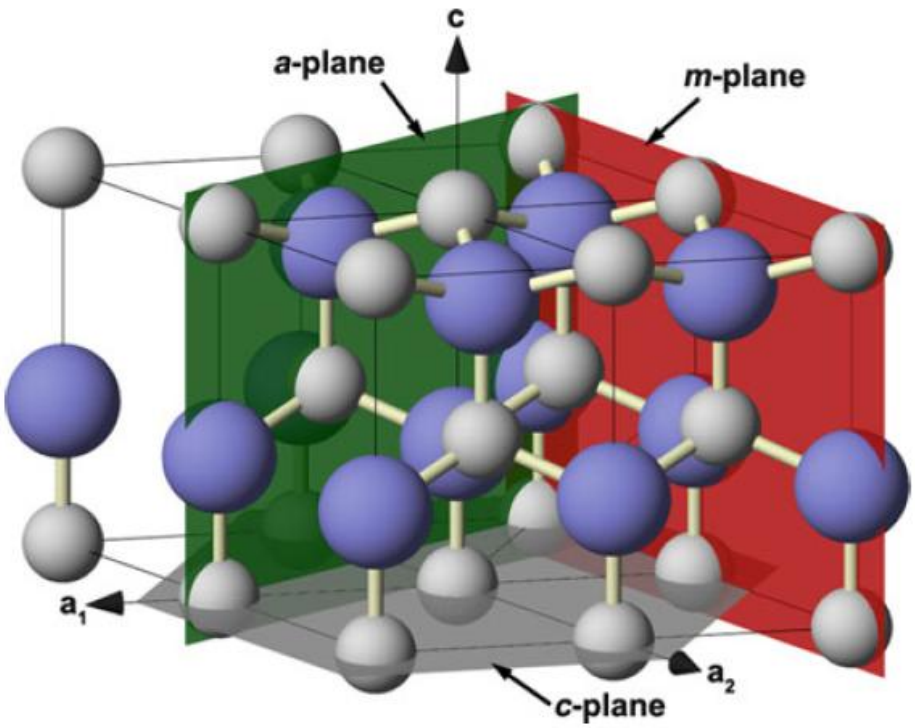

Figure 1.1. Schematic representation of the wurtzite structure of GaN [6].

GaN is a very hard and mechanically stable material. Its appearance can be colourless, white, grey, and yellow, depending on the N vacancies present in the structure [6]. GaN is steady in boiling water, practically insoluble in acids, or bases at room temperature, but it dissolves in hot alkali solutions at a slow rate [4]. GaN also has a high heat capacity and thermal conductivity [7- 9] making it suitable for high power and high frequency applications.

GaN can withstand ionizing radiations better than other semiconductor materials, what makes GaN a good option for space, betavoltaics and photovoltaics use [10, 11].

GaN can be doped to obtain *p*- or *n*-type semiconductors. This is essential for the fabrication of functional semiconductor devices. Magnesium is the most important dopant to form *p*-type GaN [12]. Silicon is most commonly used element as the *n*-type dopant [13]. However, when hydrogen-containing precursors are used in the growth process, it has been difficult to obtain the *p*-type semiconductor. Hydrogen plays a crucial role in passivating the Mg acceptors, and creates electrically inactive complexes Mg-H that prevents the formation of holes as charge carriers in GaN [14]. Therefore, it was shown that *p*-type conductivity could be activated by breaking the Mg-H complexes using low-energy electron irradiation [15] or thermal annealing at ~973 K [16]. However, Mg-doped GaN grown by Molecular Beam Epitaxy (MBE) can be an as-grown *p*-type semiconductor without any thermal activation process, since there are no hydrogen or H-N radicals produced during the growth process [17]. Also, *p*-type GaN was achieved by implantation of Mg into GaN, followed by high-temperature annealing (~1373 K) [18]. The possibility of obtaining *p*-type GaN allowed the realization of GaN based *p*-*n* junctions, the base of LEDs, that were developed first in 1991 [19].

Table 1.1 shows a comparison of some of the fundamental physical properties of GaN, SiC and ZnO, which are the most used wide band-gap semiconductors in electronics [20-22]. Semiconductors with wide band gaps can operate at high temperatures, when compared to narrow band gap semiconductors [23]. In addition, they present high electric breakdown fields, which results in power devices with high breakdown voltages. However, GaN, similar to ZnO, has a significantly lower thermal conductivity compared to SiC [20]. This property is especially important in high power and high temperature operation since the heat generated inside the device needs to be driven out as fast as possible to improve reliability and prevent premature failure. Also, a low thermal conductivity leads to degradation of the device operation at elevated temperatures [24]. The values of dielectric permittivity ε_r, for the wide band gap semiconductors are considerably lower than those for the narrow band gap semiconductors. This allows, for example, a GaN device to be larger in area for a given impedance. Thus, this increased area enables the generation of larger currents. GaN has an advantage compared with SiC in the enhanced mobility of electrons in a two-dimensional electron gas (2DEG) that is generated at a single heterojunction (interface between two different materials) or in doped heterostructures that form superlattices (periodic arrays of interfaces). The room temperature mobility for the 2DEG generated in a AlGaN/GaN heterointerface is in the range of 1000–1500 $cm^2/V \cdot s$ [25, 26], and the saturation velocities, which are significantly better than those for SiC, are very suitable for fabricating functional devices, such as LEDs and FETs.

Table 1.1. Physical characteristics of the main wide bandgap semiconductors.

Property	**GaN (wurtzite)**	**6H-SiC**	**ZnO (wurtzite)**
Bandgap, E_g (eV)	3.44	3.03	3.37
Dielectric permittivity, ε_r	9	9.66	8.66
Electric breakdown field, E_c (MV/cm)	3	2.5	-
Electron mobility, μ_n ($cm^2/V \cdot s$)	1250	500	200
Hole mobility, μ_p ($cm^2/V \cdot s$)	850	101	5-50
Thermal conductivity, κ (W/cm·K)	1.3	4.9	1-1.2

GaN belongs to the group of III-V semiconductors, in particular to the III-nitrides group. GaN and its related alloys, such as InN and AlN, have received much attention in the realization of new devices for electronics, microwave, and optoelectronics/photonics applications. The good emission properties of III-nitride semiconductors are mainly determined by their direct band gap which makes the radiative recombination of electron-hole pairs much more efficient as compared with bulk Si, for instance, which is an indirect semiconductor. Figure 1.2 shows a plot of the band gap energy versus lattice constant for various semiconductors including III-nitride semiconductor materials — (Al, In, Ga)N. It can be seen that the combination of III-nitride semiconductor alloys cover band gap energies from 0.8 eV to 6.2 eV, which correspond to wavelengths ranging from infrared to deep UV. In Figure 1.2 the visible optical spectrum has been included for better visualizing this property of III-nitrides. This makes the nitride system attractive for the development of optoelectronic device applications, such as LEDs [27], LDs [28] and photodetectors [29]. An additional advantage of III-nitride semiconductors in comparison to other semiconductors belonging to III-V and II-VI groups, like GaAs, InAs, ZnSe, etc., is that III-nitride semiconductors are not toxic for the environment [30-32].

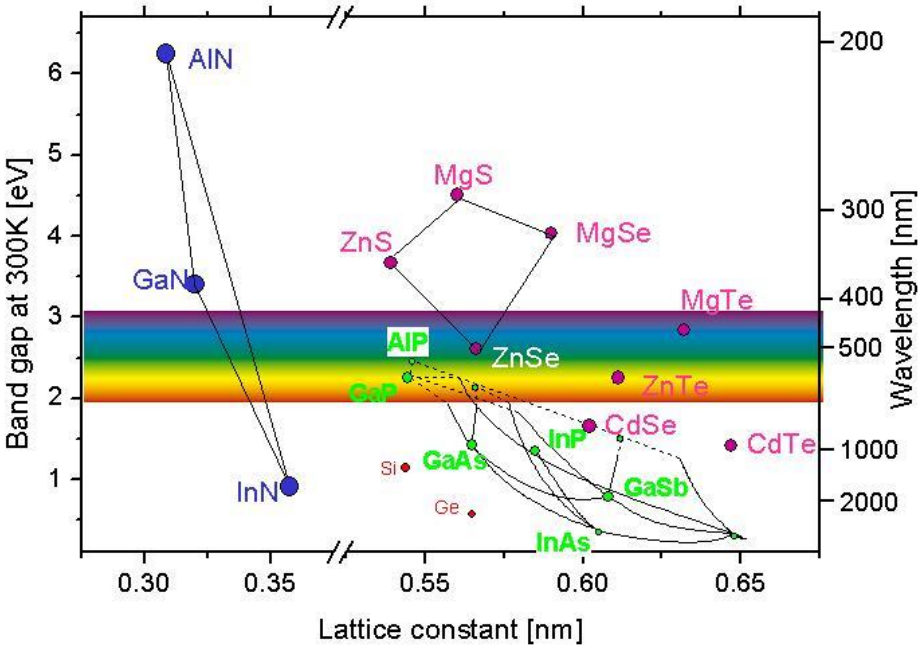

Figure 1.2. Bandgap energy versus lattice constant for various semiconductors [33].

1.2 Crystal growth techniques for the production of wurtzite GaN

GaN single crystals cannot be grown by melt standard techniques (like Czochralski or Bridgman techniques), since it has a high melting temperature and a very high decomposition pressure. At high temperatures and conventional pressures, nitrogen evaporates out of the crystal as it grows and the gallium and nitrogen atoms would not bond. To keep the nitrogen in, very high pressures are needed (more than 1000 MPa), which are difficult to achieve in a commercial process. One of the techniques so far available has been based on solution growth of GaN from molten gallium at temperatures in the range 1673 – 1773 K, using nitrogen over-pressures of typically 10 kbar [34]. Another approach to bulk GaN growth is a process using Na flux [35]. It consists on the thermal decomposition of sodium azide (NaN_3) and the reaction between nitrogen created this way with gallium in the Na-Ga melt. The process takes place at temperatures in the range 573 – 1073 K and pressures ranging from atmospheric to few MPa. The ammonothermal method enables growth of truly bulk GaN [36]. The scheme of the crystal growth process in the ammonothermal method is as follows: GaN containing feedstock is dissolved in one zone of the high pressure autoclave, then transported by convection as a result of the temperature gradient to the second zone, where GaN is crystallized on native seeds due to the supersaturation of solution (see Figure 1.3a). The typical temperatures and pressures applied are 773 – 873 K and 0.2–0.5 GPa, respectively. Figure 1.3b shows the photograph of a 1 inch thick GaN crystal grown by this technique.

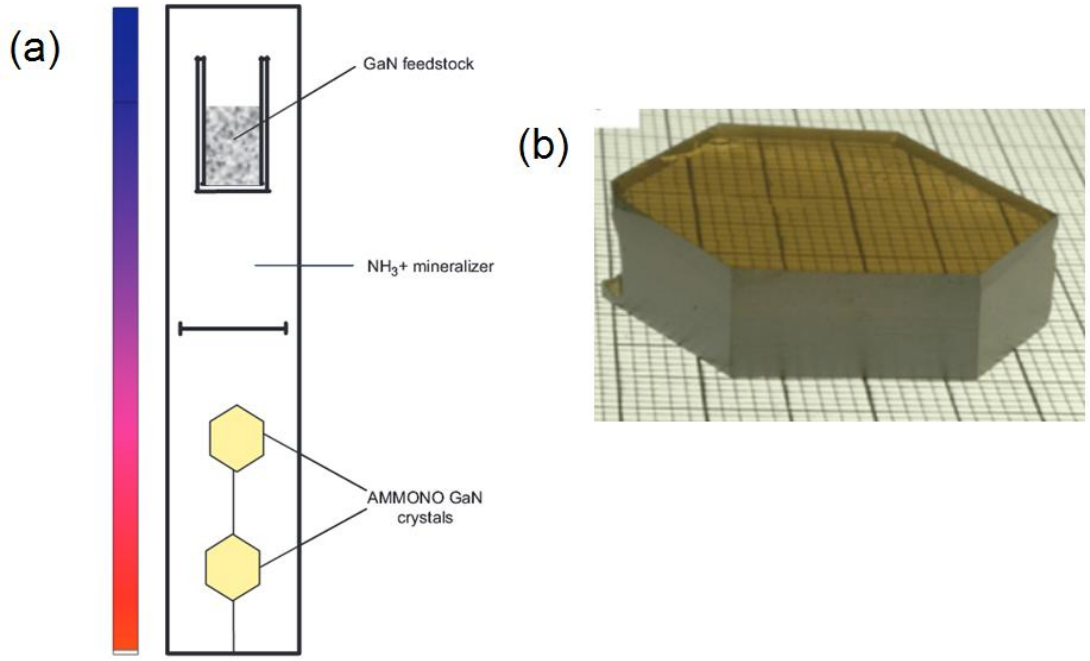

Figure 1.3. (a) Schematic representation of the crystal growth system used in the ammonothermal method for the production of GaN crystals [37]. The colored bar in the left represents the temperature gradient: Red — highest temperature, Blue — lowest temperature. (b) 1 inch thick GaN crystal produced by the ammonothermal method [38].

Aside from the methods mentioned above, GaN is grown epitaxially on foreign substrate materials and these constitute the main crystal growth method for obtaining crystalline GaN [39]. The substrate is placed in a growth environment with the necessary source materials, temperature and pressure. When the conditions are favorable, GaN begins to crystallize on the substrate, inheriting the crystalline structure of the template material. However, the substrate used and the overgrown GaN typically have different lattice parameters, resulting in tensions in the growing film [40]. Suitable substrate materials for the production of GaN should have a low thermal expansion coefficient and lattice mismatch with GaN. Also, they should be resistive to the growth reactants (such as NH_3 or H_2) at high growth temperatures (in excess of 1273 K in some cases). Taking into account these facts, sapphire (Al_2O_3) and SiC are the most popular substrate materials used currently [41]. Other materials with a close lattice mismatch with GaN, such as $LiGaO_2$, have been also used for epitaxial growth of GaN [42]. However, the GaN layers grown on these substrates lacked the desired electronic properties due to either a rough growth or unintentional contamination from the substrates.

The most commonly used methods for epitaxial growth of GaN include hydride vapor phase epitaxy, metal-organic vapor phase epitaxy and molecular beam epitaxy:

- *Hydride vapor phase epitaxy (HVPE).* HVPE is one of the primary means of growing thick GaN films. The first HVPE of GaN was reported by Maruska et al. in 1969, using a sapphire substrate [43]. The GaN epitaxial layer obtained allowed measuring the band-edge absorption and lattice constant of the material for the first time,

although the epitaxial layers obtained did not exhibit a high quality. Figure 1.4 illustrates the basic principle of the method. For GaN growth, source materials are gallium chloride ($GaCl_3$) and ammonia (NH_3) gases. $GaCl_3$ is formed inside the growth system by the reaction of gaseous HCl and metallic Ga. Formed $GaCl_3$ is transported into the growth zone of the system where it reacts with NH_3 forming GaN. Substrates are located in the growth zone and, if growth conditions, including substrate parameters, are suitable, a GaN epitaxial layer is formed on the substrate. The method provides deposition rates of several microns per minute making it possible to grow hundreds of microns thick layers [44, 45].

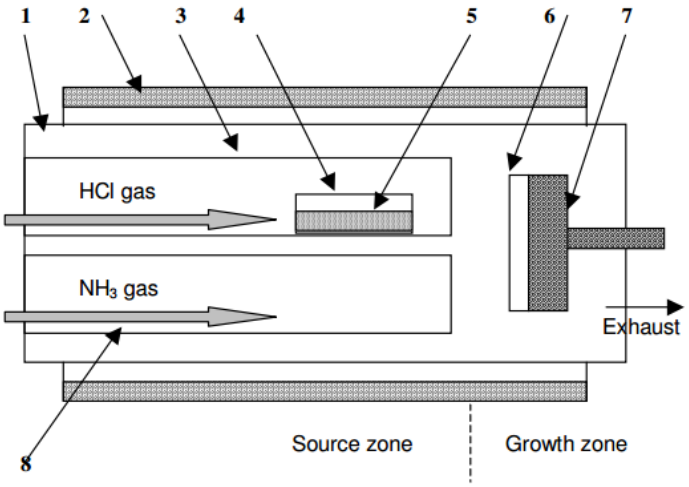

Figure 1.4. Schematic illustration of the GaN HVPE growth system: 1 — main reactor tube, 2 —heating elements, 3 — Ga source gas channel, 4 — boat with melted Ga, 5 — Ga melt, 6 — substrate, 7 — substrate holder, and 8 — ammonia source tube [44].

- *Metal Organic Chemical Vapor Deposition (MOCVD)*. MOCVD is the most commonly process used to grow GaN thin films. This method is based on a thermally induced reaction of gas-phase precursor molecules on a heated substrate surface. MOCVD growth of GaN involves the use of the metalorganic compound trimethylgallium ($Ga(CH_3)_3$ or TMGa) and ammonia (NH_3) as precursors for GaN growth, with nitrogen as carrier gas. The basic MOCVD describing the GaN deposition process can be described by the following reaction:

$$Ga(CH_3)_3 + NH_3 \rightarrow GaN + 3CH_4$$

The more likely reaction cascade leading to GaN growth is the stepwise homogenous decomposition of $Ga(CH_3)_3$ as shown below:

$$Ga(CH_3)_3 \rightarrow Ga(CH_3)_2 + CH_3$$

$$Ga(CH_3)_2 \rightarrow GaCH_3 + CH_3$$

$$GaCH_3 \rightarrow Ga + CH_3$$

Ammonia decomposes heterogeneously to yield atomic nitrogen or nitrogen containing radical at high temperatures:

$$NH_3 \rightarrow \dot{N}H_{3-x} + x\dot{H}$$

Therefore, the possible mechanism of GaN formation that occurs can be expressed as:

$$Ga\dot{C}H_3 + \dot{N}H \rightarrow GaN + CH_4$$

The possible processes involved in the MOCVD growth process are shown in Figure 1.5. A mixture of precursor gases flows through the system in one direction. After entering the high temperature reaction zone, molecules of $Ga(CH_3)_3$ and NH_3 are adsorbed, thermally dissociated and chemical reactions occur at the gas–solid interface and near the hot surfaces of the substrate followed by deposition of the epitaxial layer of GaN. The gaseous by-products of the reactions are desorbed, and together with unreacted precursor gases, exhausted from the reactor. Compositional variations in the deposited GaN film can be achieved by varying the gas flow ratio. Using MOCVD high purity and high structural quality GaN thin films can be produced [46-48].

.

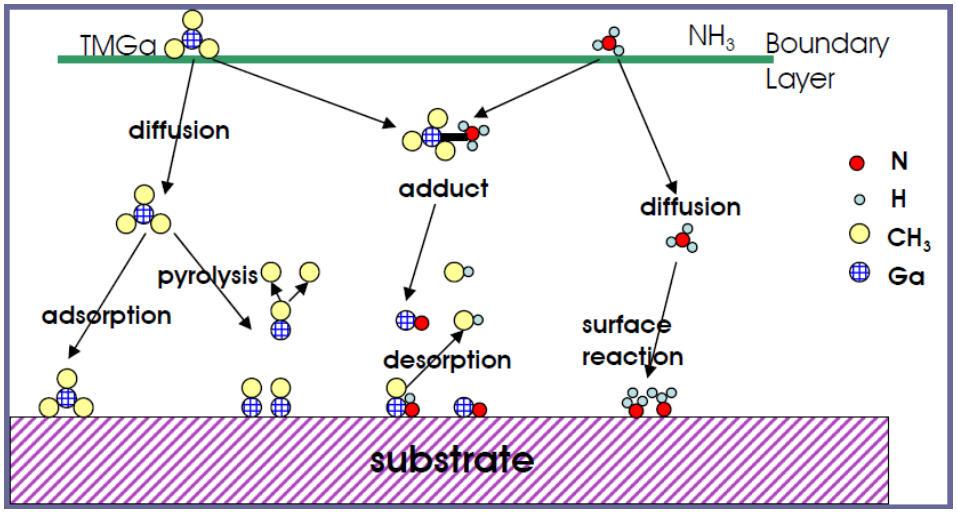

Figure 1.5. Possible processes involved in the MOCVD growth process [49].

- *Molecular Beam Epitaxy (MBE).* This is a method of epitaxial growth that appeared in the late sixties and early seventies after work on epitaxial films by Davey and Pankey [50], Shelton and Cho [51], and Arthur [52]. MBE growth is characterized by the interaction of molecular or atomic beams at the surface of a heated crystalline substrate. This interaction occurs in an ultra-high vacuum chamber (~10^{-9} torr). At this pressure the mean free path of a gas particle is approximately 40 km, what allows the

gas molecules to collide with the chamber walls many times before colliding with each other. The ultra-high vacuum also provides the best available purity, because the rates of contaminants are significantly lower than typical chemical vapor deposition conditions. Figure 1.6 shows a schematic of MBE system for GaN growth. GaN MBE growth is a non-equilibrium process where a Ga vapor beam and an nitrogen beam from a nitrogen RF plasma source, where purified N_2 is converted into a more active atomic and molecular species, are directed towards a heated substrate. Under suitable conditions, layer-by-layer deposition of Ga and N atomic planes is possible. The chamber is cryogenically cooled with liquid nitrogen. In addition to Ga, the MBE chamber can be equipped with Si and Mg sources for *n*- and *p*-type doping, as well as In for InGaN growth. The Ga metal source and dopant materials are introduced through an effusion cell, where a solid material is placed in a crucible, (typically pyrolytic boron nitride) and heated until the material sublimates or evaporates [53, 54].

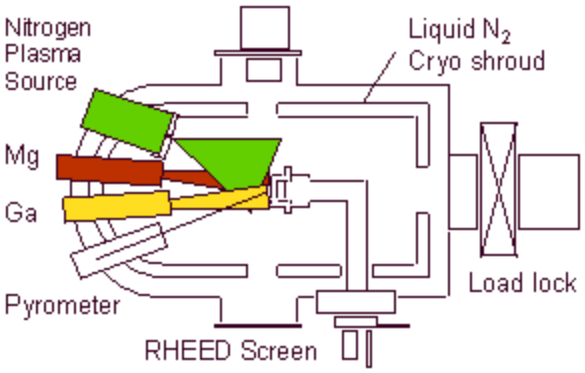

Figure 1.6. Schematic illustration for GaN MBE growth [55].

Also, there are many derivatives of these methods, such as Plasma-Enhanced CVD (PECVD) that utilizes plasma to enhance chemical reaction rates of the precursors. In this way, GaN nanowires with high crystal quality were fabricated [56]. Another example is hot-wire CVD (HWCVD) that uses a hot filament to chemically decompose the source gases. By this technique cubic GaN on GaAs(100) was otained [57].

1.3 GaN and LEDs

LEDs are an attractive alternative to conventional light sources according to their high efficiency and long lifetime. A typical III-nitride LED consist of a multi-quantum well (MQW) stack of InGaN, AlGaN and GaN sandwiched between the *p*- and *n*-type GaN layers (see Figure 1.7). The electrically injected free carriers diffuse to the junction area where they are confined in the quantum well. Therefore, the recombination process of injected free holes and free electrons occurs with subsequent emission of photons [58, 59].

Another benefit of the InGaN and AlGaN heterostructures arises from the negligible reabsorption of the emitted light by the device. When the band gap of the surrounding

material is equal to the band gap of the active region, the emitted photons have a significant probability to be reabsorbed before leaving the material, limiting the efficiency of the device [60]. In heterostructures, the potential well area of MQW emits photons with energy smaller than that of the band gap of the surrounding areas. Thus, these photons leaving the active region are not easily reabsorbed by the rest of the structure of the LED.

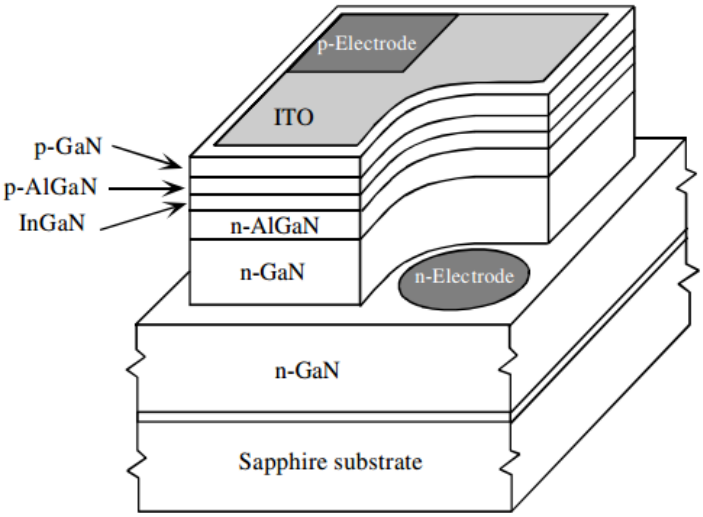

Figure 1.7. Typical structure of GaN-based LED [60].

An important role in GaN-based LED technology is played by electrical contacts to *n*-type and *p*-type GaN. A good Ohmic semiconductor-metal contact exhibits a symmetric, linear and temperature-independent I-V characteristic. The main rule is to use a metal whose work function is as low as possible for the *n*-type semiconductor and as high as possible for the *p*-type semiconductor. Thus, titanium or aluminum and Ti/Al bi-layers are traditionally used to form an electric contact on the *n*-type GaN, taking advantage of the good adhesive properties of Ti and good electrical conductivity of Al. Usually titanium and aluminum are covered by gold to avoid oxidation. Also, it is necessary to deposit a barrier to avoid the diffusion of gold. Then, the contact layers are typically Ti/Al as adhesion and contact layers and Ti/Au, Pt/Au or Ni/Au as protection layers. Beyond the metal deposition, thermal annealing is also used, which leads to the Ohmic contact desired and also reduces the contact resistance [61]. The *p*-type contact on GaN is a complex challenge. Ideally, the metal used for the contact on *p*-type GaN should exhibit a work function about 6.5-7.5 eV. However, high work function metals, such as Pt, Ni, Pd and Au exhibit work function values of 5.65, 5.15, 5.12 and 5.1 eV, respectively. Thus, it seems not possible to realize a real Ohmic contact based only on the thermionic effect, and tunneling effect has to be promoted [62]. Most of the *p*-type contacts used are stacks of Ni/Au, Ni/Pt/Au, Ti/Pt/Au or Pd/Au [63]. Again, the characteristics of the contact are closely related to the thermal annealing process applied to the contact. Only the annealing under an oxygen atmosphere leads to an Ohmic contact to *p*-type GaN [64], by enabling the diffusion of Ni atoms into the upper GaN layer and promoting its oxidation to NiO that behaves as a wide-band gap semitransparent semiconductor that allows high transparency at visible wavelengths [65]. In order to further improve the

performance, conductive oxides like indium tin oxide (ITO) are used to obtain a good optical transmittance [66]. The deposition of an ITO with a thin Ni layer between GaN and ITO provides an Ohmic contact with low resistivity [64]. For LEDs in advanced configuration, the contact for *p*-type GaN is buried and also has a light reflection function. For this purpose silver-based metallic layers are used, in which Ni layers allow obtaining the ohmicity while keeping a high reflectivity [67]. Also, novel structures based on graphene, material with outstanding electrical conductivity and high transparency over a wide range of the optical spectrum, were fabricated, such as Au/Cr/graphene electrode structures in which Cr penetrates into graphene and leads to a low-resistance contact with *p*-type GaN that can be used in high-power GaN LEDs [68-69], for example.

Progress in the fabrication of GaN-based compound semiconductors enabled the practical breakthrough of LEDs [70]. The improvement in the quality of InGaN with its compositionally dependent tunable band gap, blue (430 nm), green (530 nm), and later white LEDs become available. Now, GaN-based LEDs cover the entire visible spectrum, enabling their entry into additional power signaling applications, such as traffic lights, since LEDs based on these materials are considered energy-saving and environmental-friendly light sources [71-73]. However, overall efficiency requires further improvement. More efficient light-generating and light-extracting structures at reduced price and power consumption are searched to develop applications for these LEDs in fields such as general lighting, automotive lighting, backlights of liquid-crystal displays, etc [74]. The overall efficiency of LEDs is mainly determined by the internal quantum efficiency and the light-extraction efficiency. The internal quantum efficiency is the number of photons generated from an electron-hole pair injected into the quantum wells. For a conventional LED, the light-extraction efficiency is limited by the total internal reflection at the interface of the semiconductor and the outer medium. Due to the large difference in refractive indices between the GaN film (~ 2.5) and air (~ 1), light can only travel from GaN to air within a critical angle of total internal reflection of 23º [75]. The photons emitted outside the critical angle are reflected from the interface, absorbed by the electrodes and semiconductors, and confined internally, reducing the efficiency of the LED.

High-efficiency and high-power III-nitride LEDs have been demonstrated partly due to improvements in the internal quantum efficiency of these compounds [76], and progress in the light extraction and operating power density of these LEDs [77]. The light extraction efficiency of these devices can be improved up to ~ 65 % in air and up to ~ 80 % in an encapsulated device [78]. However, encapsulation comes along with severe drawbacks. First, all encapsulators presently used are organic-polymer-based compounds, so they turn opaque because of the thermal overstress on the polymer at high flux densities [79]. Second, the encapsulator increases the optical size of the source by a factor of approximately two [80], decreasing the surface brightness of the source. Hence, a high-extraction-efficiency unencapsulated device is desirable for high-power and high-brightness applications.

One of the approaches that have been used to enhance the light extraction efficiency in III-nitride based LEDs is the use of graded-refractive-index oxide films with disordered porous structures [81], achieving a luminance intensity 1.31 times higher than that obtained on uncoated LEDs (see Figure 1.8). The improvement in the light extraction of this kind of

LEDs compared to that of an uncoated LED is ascribed to the reduction in optical losses due to Snell and Fresnel transmission. Another approach to increase the light extraction efficiency of LEDs consisted in coating the textured surface of a III-nitride LED with transparent Al_2O_3 powders (see Figure 1.9), resulting in an improvement of the light extraction efficiency steamming from both a decrease in the total internal reflection and angular randomization of the photons because the transparent Al_2O_3 powders have an intermediate refractive index between GaN film and air [82], as can be seen in Figure 1.9b.

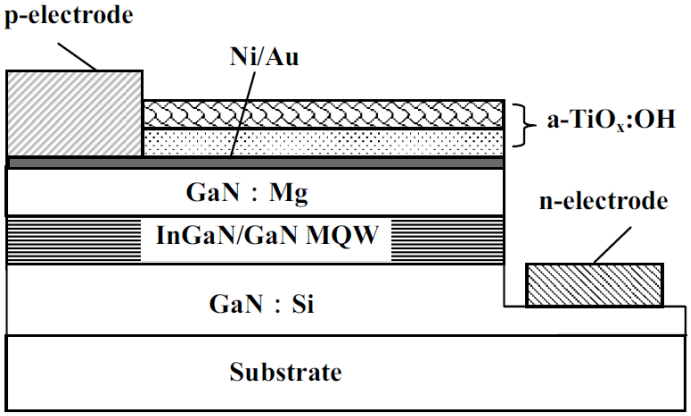

Figure 1.8. Schematic cross section of a GaN-based LED with a graded-refractive-index oxide *a*-TiO*x*:OH structure [81].

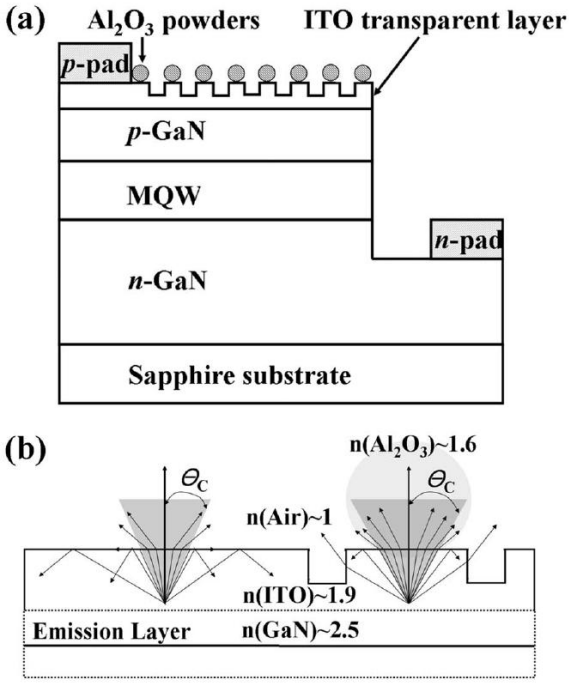

Figure 1.9. (a) Schematic diagram of a surface-textured GaN-based LED coated with Al_2O_3 powder and (b) possible photon paths for a flat surface and a surface textured structure coated with Al_2O_3 powder [82].

Also, emission intensity of InGaN/GaN MQWs has been enhanced by surface plasmon coupling [83-85], getting up to 200% increase of the emitted power in green LEDs. However, one of the main problems of using this technology is that the metal nanoparticles have to be located near the quantum wells in the LED to benefit from the surface plasmons (see Figure 1.10). In a conventional LED, the effect of surface plasmon coupling becomes limited, since this process relies on the range of its evanescent field, which is in the order of a few tens of nanometers in GaN, so the thickness of the *p*-type GaN layer must be reduced to a few tens of nanometers. Such a thin *p*-type GaN layer, compared to the conventionally layers used, with a thickness of 120-200 nm, leads to degradation of the current spreading and hence the LED electrical properties.

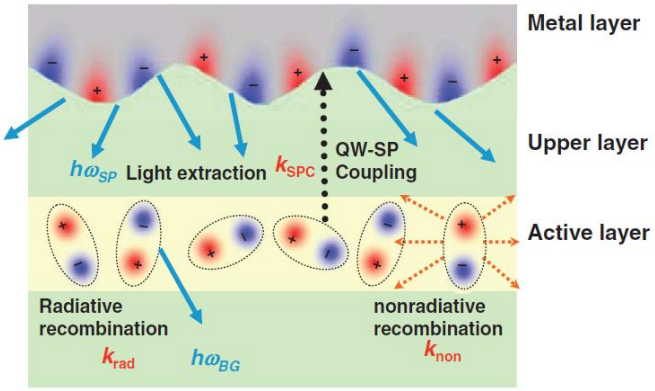

Figure 1.10. Schematic diagram of the electron–hole recombination and QW – surface plasmon coupling [86].

Other approaches have been developed using different types of diode configurations. In the conventional chip (CC) configuration, the cathode is fabricated by locally etching the *p*-type GaN layer to deposit a contact on the *n*-type GaN layer (see Figure 1.11a). In the flip chip (FC) configuration a reflective metal layer ensures a good *p*-contact on a large area of the diode and enhances the light extraction (see Figure 1.11b). In this case, the light is emitted through the substrate [87, 88]. For the vertical thin film (VTF) configuration, the *p*-contact is deposited on the whole diode area (see Figure 1.11c). Then the substrate is removed by the laser lift-off (LLO) technique to reveal the *n*-type GaN layer for *n*-contact deposition. The *n*-type contact is deposited in the center of the top surface of the device. The surface roughening of the sample can be performed after the LLO step and thus the light extraction coefficient can be increased [89].

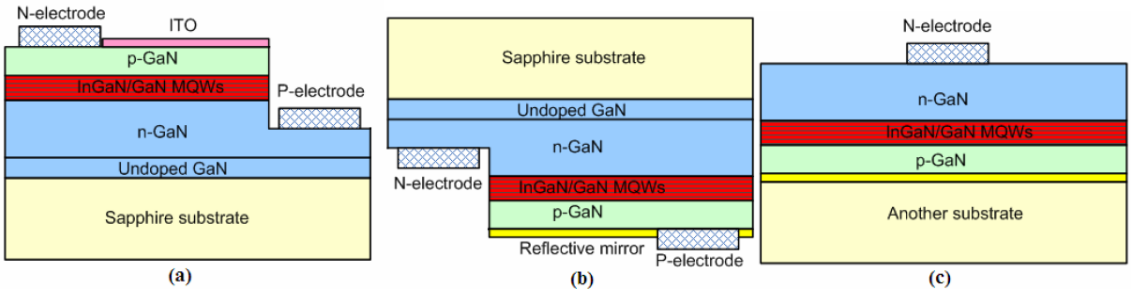

Figure 1.11. Schematic structures of (a) conventional chip (CC), (b) flip chip (FC) and (c) vertical chip thin film (VTF) LEDs [90].

Finally, another of the approaches explored to develop unencapsulated LEDs is the use of photonic crystals in one of the layers that constitute the LED since these structures contribute to increase the light extraction efficiency and enhance the internal quantum efficiency of the LEDs [91]. Photonic crystals are materials in which the refractive index is modulated periodically on a wavelength scale, offering control of the way in which light propagates through the medium [92]. When applied to LEDs, these photonic crystal structures might inhibit light emission into guided modes or might increase light extraction efficiency if the photonic band gap is tuned near the emission wavelength of the LED and the photonic crystal penetrates through the entire device. However, realization of such structures in functional devices is very challenging. Thus, up to now, scientific efforts have focused only on using photonic crystals as diffraction gratings in any of the parts of the LED (top or bottom layer, electrodes, etc.) (see Figure 1.12). In this scheme, spontaneous emission into guided modes is allowed but these modes are subsequently outcoupled by the diffractive properties of the photonic crystal, increasing the light extraction efficiency of the device [93-96]. For instance, Wierer et al. demonstrated a high-performance unencapsulated III-nitride thin film photonic-crystal LED with a light extraction efficiency around 73 % when the photonic crystal was implemented at the top layer of a LED based on GaN (see Figure 1.13) [97]. If the photonic crystal is implemented on the bottom of the III-nitride LED via insertion of nanometer-sized air holes in the underlying *n*-type GaN layer the internal quantum efficiency and the light-extraction efficiency are improved by 12 and 7%, respectively, resulting in an enhancement of 23 % on the performance of the fabricated LED (see Figure 1.14) [98].

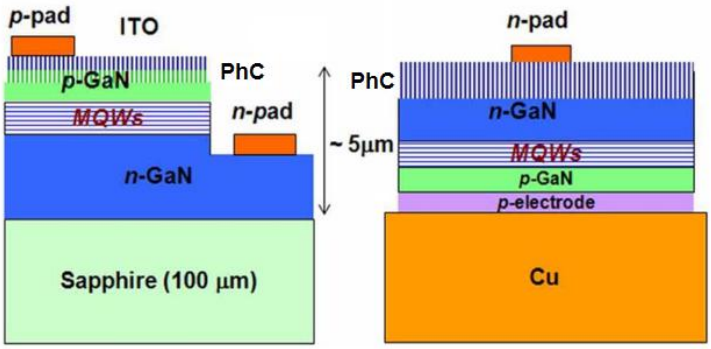

Figure 1.12. Schematic cross section of GaN-based LEDs with photonic crystal structures implemented in the electrode and at the top of the *n*-type GaN layer [95].

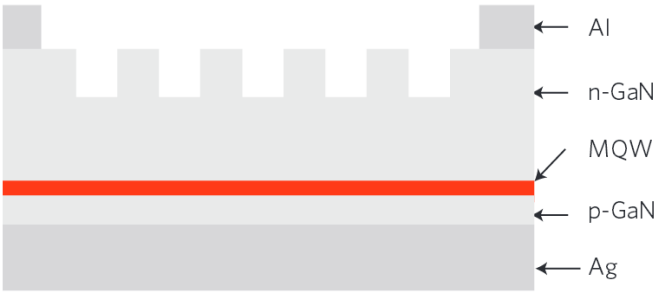

Figure 1.13. Schematic cross section of a GaN-based LED with a photonic crystal structure implemented at the top *n*-type GaN layer of LED [97].

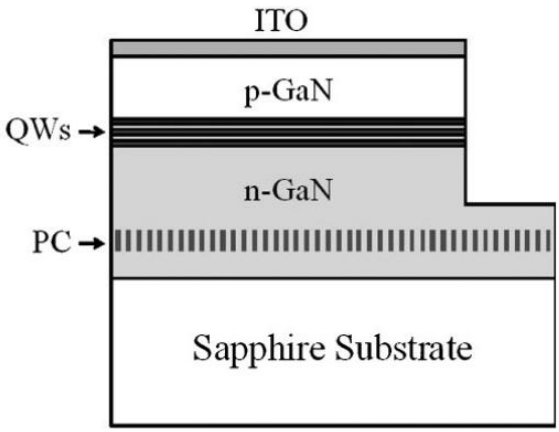

Figure 1.14. Schematic cross section of a GaN-based LED with a photonic crystal structure implemented on the bottom *n*-type layer of the LED [98].

However, such structures have been fabricated by etching techniques, e-beam lithography and nanoimprinting that are not cost effective. Furthermore, these techniques might generate problems when applying these structures to commercial products, since they require the removal of the etching mask after surface texturing, which make them not applicable for low-cost large scale production. Also, due to the extreme chemical stability of group III nitrides, etching has to be carried out with corrosive etching methods like electrochemical etching o metal-assisted electroless etching [99, 100], for example, as will be explained in the next section. This might generate damages while smooth sidewalls required in many optoelectronic devices are difficult to obtain, resulting in degradation of the device performance.

1.4 Porous GaN: interest, advantages, fabrication and applications

The discovery of light-emitting porous Si [101] propelled investigations of porosity formation in III-V and IV groups semiconductors [102-104]. Porous semiconductors have received a considerable interest, primarily due to their unusual optical and electrical properties, that sometimes can be radically different from those of the bulk material. Here we should consider not only basic semiconductor parameters like conductivity, band gap energy and absorption/emission of light, which might be quite different, but also internal symmetries/anisotropies, high-order effects and even basic chemistry. Some of the novel properties discovered for porous semiconductors are:

- Fast chemical reactions practically not previosly observed in bulk materials, including violent explosions due to the large surface to volume ratio and optimal diffusion conditions [105].
- Novel absorption characteristics (e.g., transparent for UV while blocking larger wavelength [106].
- Optical anisotropy [107] and new types of optical anisotropy not encountered in natural materials if two or more sets of pores are present simultaneously [108].

- Strongly decreased thermal conductivity (and concomitantly changed phonon spectra) [109].
- Strongly changed conductivity, sensitive to the presence of gases or humidity [110].

The recent advances in the production technologies of porous semiconductor materials together with the unique properties that these materials exhibit have promoted the utilization of them in the fabrication of devices for advanced nanoelectronics, sensors with enhanced sensitivity, interfacial structures and catalysis, among others [111]. The actual applications of these materials, however, depend on the development of processing methods able to precisely control the optical and electrical properties of the resulting porous materials. Among these semiconductor materials, the wide band gap semiconductors such as porous GaN, play an important role in developing new technologies for applications in optoelectronics, magnetism, catalysis and biotechnology.

Porous GaN, in particular, exhibits some specific properties:

- A strong photoresponse was observed in epitaxial GaN layers grown on 6H-SiC substrates and anodized in aqueous solutions of HF. The photoconductivity (PC) spectra of porous GaN showed a steady increase of the photoresponse as the photon energy was increased from 2.5 to 3 eV. The formation of a potential barrier was also observed at the GaN/SiC interface after anodization [112].
- It has been proven that porous GaN exhibited lesser stress compared to its bulk counterpart [113].
- Porous GaN has the property to shift its band edge emission further into the ultraviolet (UV) due to quantum confinement, that appears due to wire-like structures in porous GaN [114].
- Photoluminescence (PL) intensity in porous GaN shows an intensity enhancement at room temperature and a much higher intensity enhancement at low temperature [115].

Porous GaN has been typically fabricated by (photo)electrochemical and chemical etching methods. The (electro)chemical reaction is sensitive to many parameters, such as the electrolyte chemistry, applied potential or current density, temperature, flow conditions of the electrolyte, doping type and doping concentration of the semiconductor, illumination state of the semiconductor, and surface conditions (polished, rough, masked). These limitations, together with the complex equipment required to control each parameter, and the fact that many electrolytes are highly toxic and/or corrosive, makes challenging the production process from a technical point of view.

However, here it is important to summarize the techniques used up to now to produce porous GaN:

- *Anodic etching of GaN*: In anodic etching, the semiconductor and an inert electrode are attached to the positive and negative terminals of a direct voltage source, respectively. Both electrodes are put inside an electrolyte (aqueous sodium hydroxide

(NaOH) solution, for example). The semiconductor is oxidized by removal of bonding electrons from the surface bonds via an external voltage source, that injects holes in the semiconductor. The resulting oxides subsequently dissolve into the electrolyte. A drawback of anodic etching is the extra infrastructure and complexity of applying an electrical bias to a thin wafer submerged in an etchant [116]. GaN was etched using 0.1 M NaOH solution with 0.2 M NaCl. A GaN electrode was used as anode. A Pt electrode was used as cathode. Using a DC voltage supply, a constant current was supplied between these electrodes through the NaOH electrolyte. The whole area of the GaN film was covered by pores after the etching process (see Figure 1.15) [117].

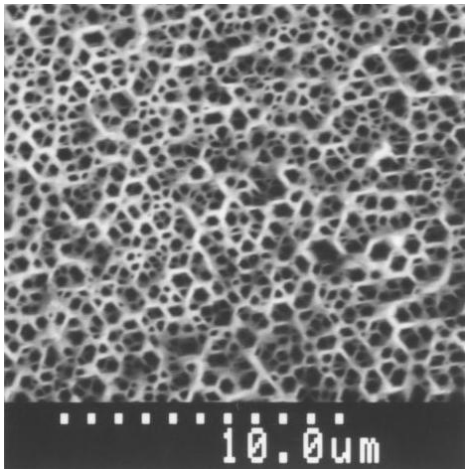

Figure 1.15. SEM image of the surface of the GaN samples after anodic etching, showing the pores formed [117].

- *Metal-assisted electroless etching technique:* This technology introduces a thin, noble metal catalyst film (a few nanometers in thickness) onto the semiconductor wafer surface, prior to immersion in an aqueous, oxidizing solution of hydrofluoric acid and hydrogen peroxide. For electroless etching, neither an external voltage nor electrical contact to the samples are required. The oxidation of the semiconductor is driven by the potential of an oxidizing agent in the electrolyte, which depletes valence band electrons in the semiconductor, and thus, supplies holes. The noble metal acts as a microscopic cathode on which the reduction of the oxidant occurs. The semiconductor atoms under the noble metal are oxidized due to the hole injection and dissolved by aqueous solution of hydrofluoric acid. Electroless etching is thermodynamically possible only if the redox potential is higher than the potential of the solid semiconductor in equilibrium with its ions in the solution. Besides etching in the dark, electroless etching of semiconductors can be enhanced by UV ilumination. Electron-hole pairs are generated by photons from an illumination source. The photogenerated holes assist in the oxidation of the semiconductor surface and the excess electrons are consumed by the reduction of the oxidizing agent in the electrolyte. This process results in the simple and effective production of a porous semiconductor. The simplicity and patterning capability of this method enables large-scale production of a variety of semiconductors. Selective deposition or patterning of the noble metal

catalyst allows controlled creation of etch variations in substrates below and adjacent to the metal. This method can also create selected areas with unique emission properties. However, the electrochemical reaction in the metal-assisted electroless etching technique is sensitive to many parameters, what complicates to obtain reproducible structures of porous materials [116]. This method has been tested for the generation of porous GaN obtained from various sources and growth conditions. Porous GaN was prepared via Pt-assisted electroless etching by placing the GaN substrate in a solution of CH_3OH, HF and H_2O_2 in a 1:2:1 CH_3OH:HF:H_2O_2 volume ratio. The Pt-coated GaN surface was immersed in the etchant and illuminated with a mercury lamp. The morphology of resulting GaN is dominated by the formation of ridge structures that evolve over time, and of a deep porous network between and under the ridges. The ridges appear to originate through the coalescence of the pores, forming craters and exposing larger areas of the surface to the etchant, improving the wetting inside the porous network, and causing the ridges to grow deeper. Figure 1.16 shows the evolution of the morphology of porous GaN produced by the metal-assisted electroless etching technique at different etching times [118].

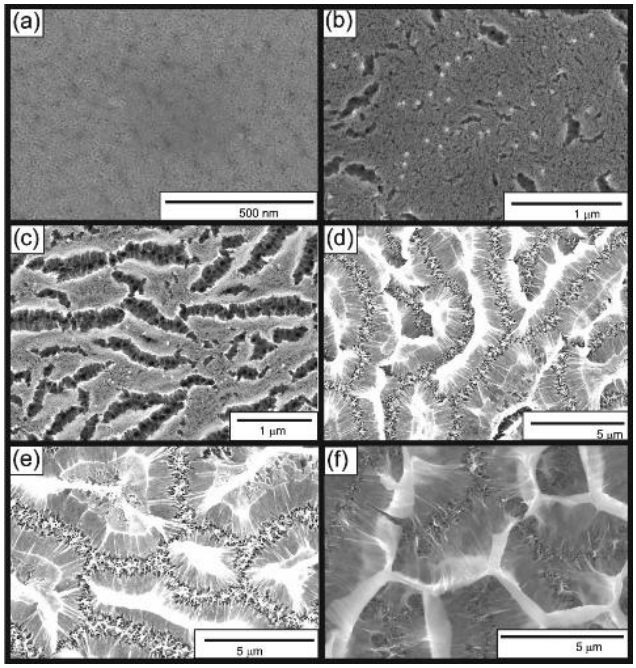

Figure 1.16. SEM images of unintentionally doped HVPE GaN on sapphire etched in 1:2:1 CH_3OH:HF:H_2O_2 volume ratio solution for (a) 15, (b) 25, (c) 30, (d) 35, (e) 40, and (f) 60 min, using the metal-assisted electroless etching technique [118].

- *Photoelectrochemical (PEC) wet etching method:* If the excess of electrons in anodic etching are consumed by the reduction reaction on the counter electrode instead of reducing the oxidizing agents, the etching process uses an illumination source and is called PEC. In PEC experiments the semiconductor sample is immersed in an electrolyte in a cell which contains an optical window for UV illumination, which is used to generate electron–hole pairs that are indispensable for etching to occur. An

electrical contact and counter electrode(s) are required in PEC, unlike electroless etching. A potential is applied between the semiconductor electrode (anode) and a counter electrode (cathode, e.g., platinum) immersed in the same electrolyte. The potential of the semiconductor is measured versus a reference cathode (saturated calomel electrode). In this way, the current flowing between the semiconductor and the counter electrode can be recorded as a function of the potential versus the reference electrode. Also, this method is quite complex, which influences reproducibility [119]. Figure 1.17 shows a scheme of a typical PEC etching system. Porous GaN was produced by UV assisted PEC using buffered HF aqueous solution ($HF:H_2O$ = 2:1, volume ratio) as an electrolyte. A Pt electrode was used as cathode during the etching process. The anodization current was varied from 20 mA/cm^2 – 50mA/cm^2 for different samples with a constant etch time of 60 min. Figure 1.18 shows the top view SEM image of the porous GaN surface prepared using a buffered HF aqueous solution ($HF:H_2O$ = 2:1, volume ratio) with an anodization current density of 50 mA/cm^2 [120].

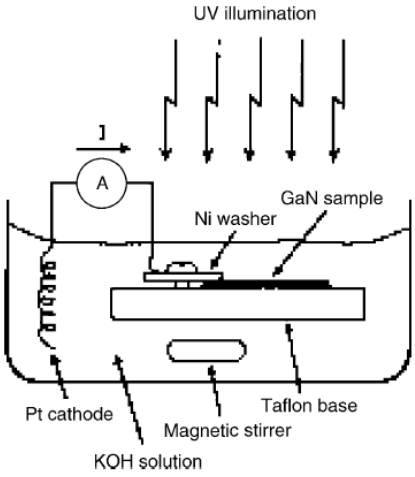

Figure 1.17. Schematic representation of a typical PEC etching apparatus SEM images [121].

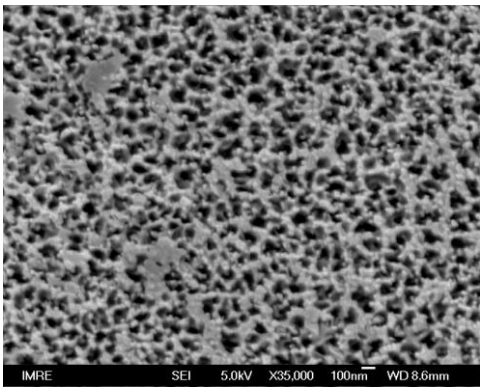

Figure 1.18. SEM image of a porous GaN layer obtained by PEC etching using a buffered HF aqueous solution ($HF:H_2O$ = 2:1, volume ratio) with an anodization current density of 50 mA/cm^2 [120].

- *Alternating current photo-assisted electrochemical etching (ACPEC):* The idea of this technique is to apply, instead of the common direct current used in an electrochemical

process, an alternating current with a given frequency and peak voltage. The formation of the porous semiconductor is performed in the same electrolyte used in the common direct current constant electrochemical etching process. UV illumination is used to assist in the generation of electron-hole pairs, where etching proceeds through the oxidation and consequently, dissolution of the semiconductor surface. The supply of holes available at the surface to participate in the oxidation reaction is greatly enhanced by the absorption of incident radiation, resulting in significantly enhanced etch rate. During the ACPEC process, the holes that are required for the process are supplied during the positive half cycle of the alternating current. A typical electrochemical cell for the generation of porous GaN is schematically shown in Figure 1.19. The etching process is produced using a sine-wave AC (50 Hz) with a current density of 25 mA/cm^2 in a 4 wt % concentration of KOH electrolyte under illumination with a 500 W UV lamp. Pt and GaN acted as cathode and anode, respectively. This technique allowed obtaining well-defined layers of hexagonal like pores of GaN (see Figure 1.20). The average pore size for 45 min and 90 min etched samples was about 35-40 nm and 55-60 nm, respectively. The average pore size varied significantly based on the quality of the starting GaN epilayers [122].

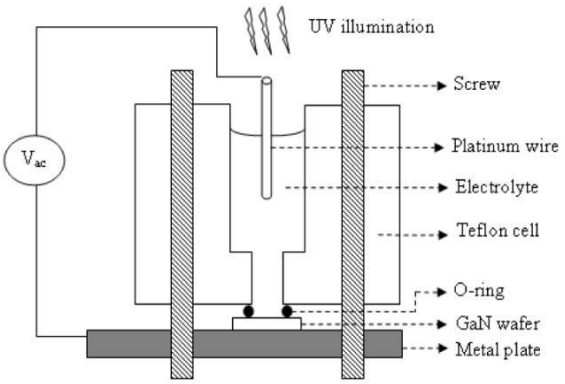

Figure 1.19. Typical electrochemical cell for the generation of porous GaN in the ACPEC process [122].

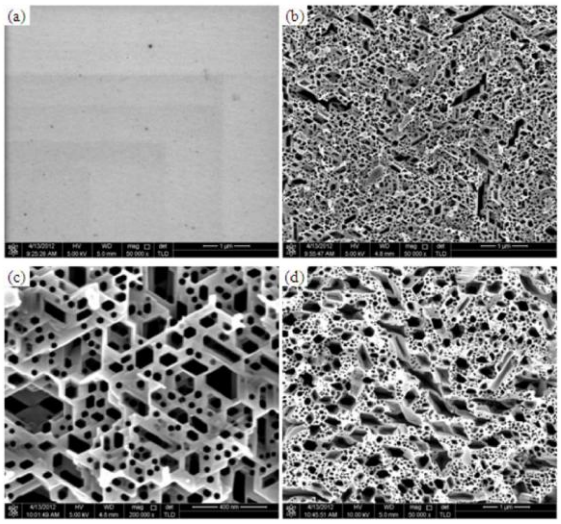

Figure 1.20. SEM images of the as grown and porous GaN formed at different etching times by the ACPEC technique. (a) As grown, (b) 45 minutes, (c) 45 minutes at high magnification, and (d) 90 minutes etching times [122].

Porous GaN found a wide range of applications. Porous GaN thin films have been used as buffer layers in growing epitaxial GaN layers with a low level of defects. The reduction in the threading dislocations density in the overgrown thick GaN layers was demonstrated, as dislocations annihilate at the interface between the buffer layer and the overgrown GaN layer. Some of these dislocations undergo bending back to the underlying porous GaN layer while others branched together to give a single propagating dislocation (see Figure 1.21) [123].

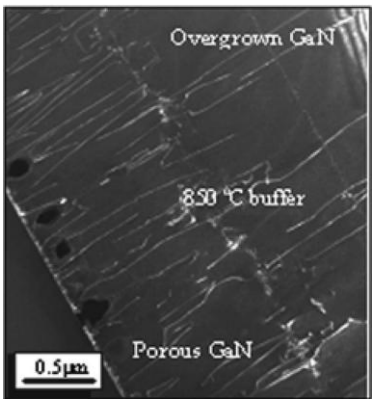

Figure 1.21. Dark field cross-section TEM image showing that threading dislocations in overgrown GaN were significantly reduced with annihilation at the interface of the buffer layer with the porous GaN template [123].

Nanoporous GaN was also used in a lift-off process of GaN layers and devices through nanoporous transformation. In this way, GaN layers for vertical LEDs were sliced and separated through a electrochemical anodization process to create nanoporous GaN of designed porosity profiles. It is shown that this voided region decreased the lateral fracture resistance and enabled large-area separation of the LED structures after appropriate wafer bonding. Figure 1.22 shows an schematic conceptual representation of the process for epitaxial lift-off [124].

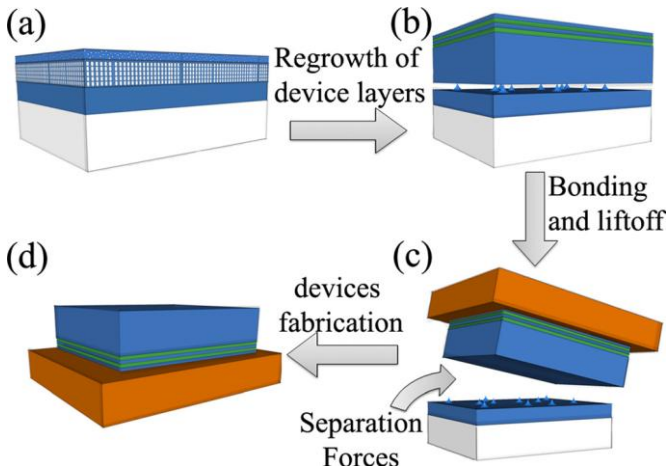

Figure 1.22. Conceptual lift-off process: (a) preparation of a porous GaN with a designed porosity profile; (b) MOCVD overgrowth of GaN and transformation of nanoporous GaN into a voided region; (c) wafer bonding after GaN growth and separation; and layer transfer for thin-film vertical LED devices fabrication [124].

Porous GaN has also been used to fabricate gas sensors with high sensitivity [125, 126]. As an example, Pd/GaN, and Pd/porous GaN Schottky diode gas sensors for hydrogen gas detection were fabricated [125]. The Pd/porous GaN Schottky diode exhibited a more pronounced change of current upon exposure to H_2 as compared to the Pd/as-grown GaN Schottky diode (see Figure 1.23), attributed to the microstructure at the porous Pd/porous GaN interface which allowed higher accumulation of hydrogen, subsequently producing a larger electrical polarization that drives to the lowering in the effective Schottky barrier height.

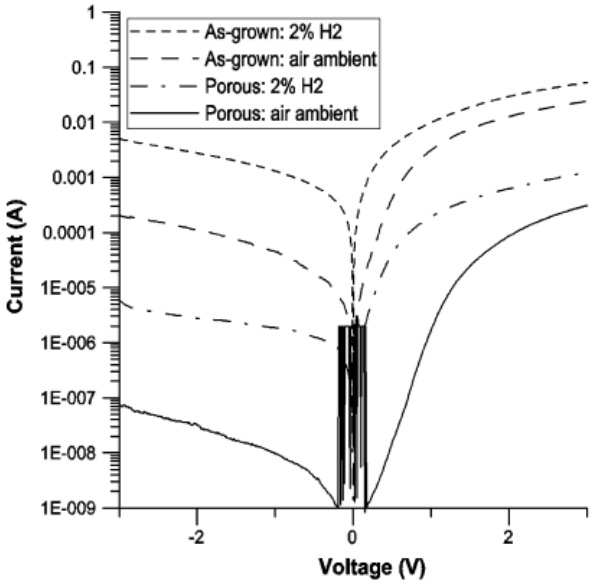

Figure 1.23. I–V characteristics of Pd/GaN and Pd/porous GaN gas sensors operating in air ambient and 2% H_2 gas [125].

Porosification of GaN has also been used to enhance the light extraction and internal quantum efficiencies of GaN-based LEDs. Pores increase the internal quantum efficiency due to the geometrical quantum wire effect associated with the thin walls remaining between the pores. This quantum confinement effect results in an increased band gap energy [127]. Also, the light emitted from the active layer of the LED is deflected by the porous layer, and thus, the porous surface might minimize the total internal reflection and increase the transmission at the interface to air, increasing the light extraction efficiency. Another way of explaining the same effect would be by considering the effective refractive index for the porous layer, that will be smaller than that of a non-porous layer. Thus, the light extraction cone will be larger, due to the lower contrast between the effective refractive index of porous GaN and the refractive index of air.

The light extraction of LEDs, for instance, can be enhanced by producing porous structures in one of the semiconductors that form the LED structure [128]. So far, most of the studies based on enhancing the light extraction properties of GaN-based LEDs deal only with the formation of partially porous diodes, where only a *p*-type or an *n*-type porous semiconductor is formed. In this way, porous *p*-type GaN was fabricated by metal-assisted electroless etching in a mixture of HF and $H_2S_2O_8$ under UV illumination to improve the light

extraction efficiency of GaN-based LEDs. The PL ratio enhancement was 2.8 and 4 and the light-output power improved to 32.7 % and 18.6% for the LEDs etched for 10 min and 20 min, respectively (see Figure 1.24) [129].

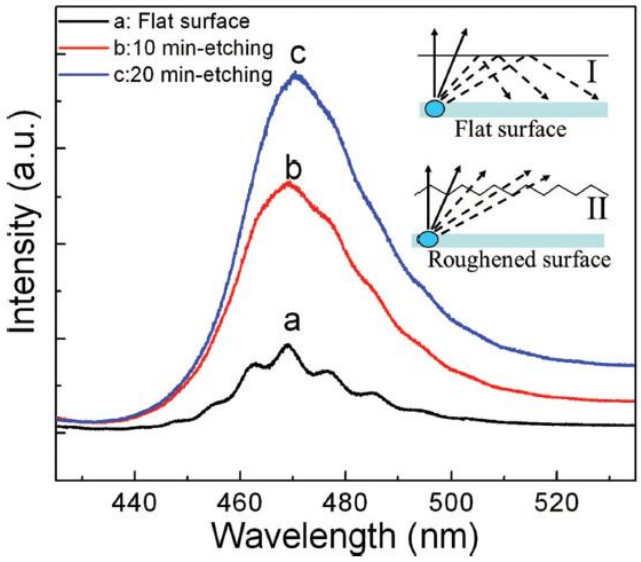

Figure 1.24. Room temperature PL spectra of the conventional LED wafer and nanoporous LED wafers after etching for 10 min and 20 min by metal-assisted electroless etching. The inset shows the light traces for the planar (I) and roughened (II) surfaces [129].

Also, nanopores were formed on *p*-type GaN surfaces of InGaN/GaN MQW LEDs by nanopatterning with an anodic-aluminum-oxide (AAO) template in an inductively coupled plasma dry etching process. The LED formed shows enhanced light extraction at a wavelength of 450 nm (see Figure 1.25). The significant enhancement of light extraction has been correlated with the nanoscaled roughness of a randomly distributed and nanoporous *p*-type GaN surface [130].

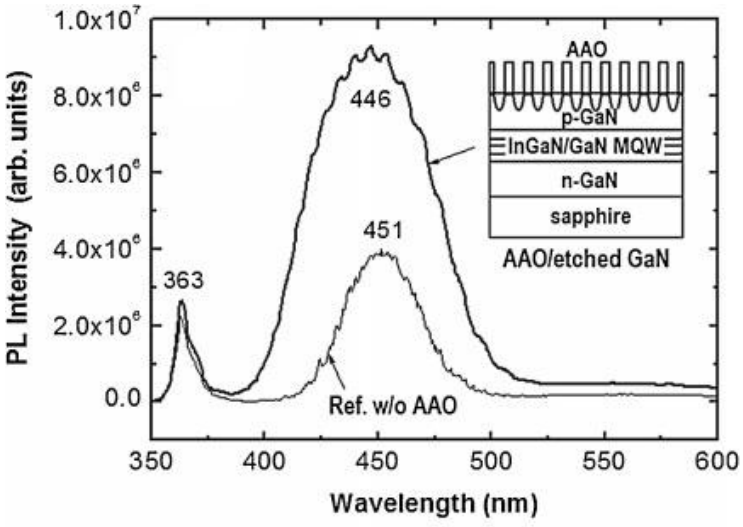

Figure 1.25. Room temperature PL spectra of LED with nanopores formed on *p*-type GaN [130].

Another example is the fabrication of photonic crystals structures on the GaN-based LED chip. An important fabrication of a high-performance GaN-based LED with photonic-crystal structure produced by dry etching and implemented at the top layer of *n*-type GaN was shown by Wierer [97]. This photonic-crystal LED has a very high light extraction efficiency of 73% without using any encapsulants, as can be seen in Figure 1.26.

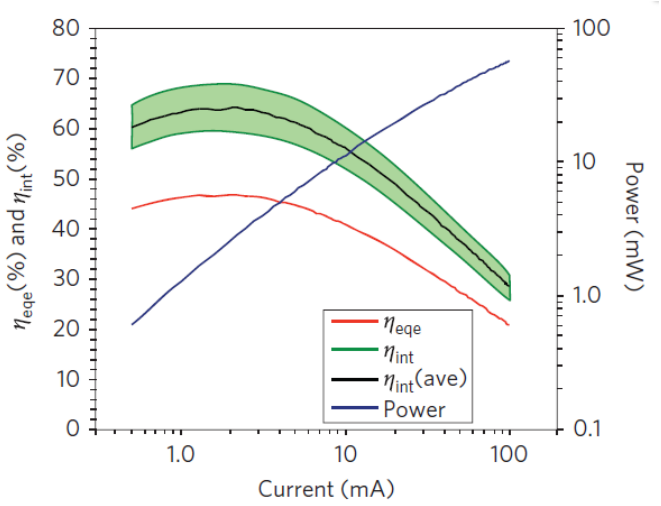

Figure 1.26. External quantum efficiency (red line), total light output power (blue line), estimated bounds for the internal quantum efficiency (green area), and average internal quantum efficiency (black line) versus current of a tuned high-performance photonic-crystal LED emitting into air [97].

A bottom photonic crystal GaN-based LED composed of nanometer-sized air holes, that were formed by AAO nanopatterns, was also fabricated. From temperature-dependent photoluminescence measurements, the enhancement of internal quantum efficiency was estimated to be 12%. Moreover, the fabricated bottom photonic crystal LED showed a 23 % higher optical power than a reference LED (see Figure 1.27) [131].

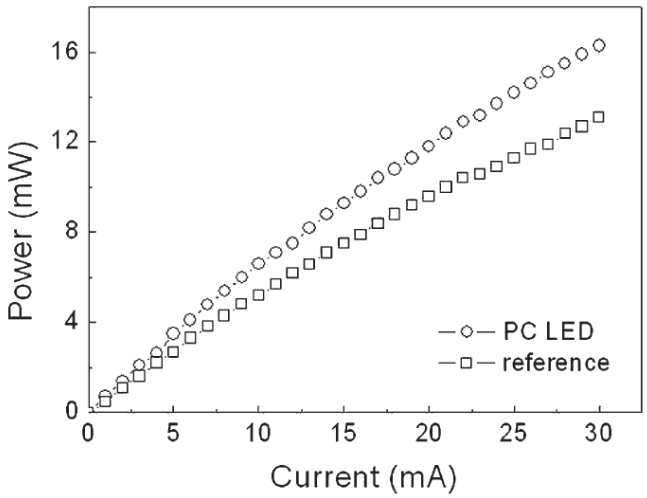

Figure 1.27. Light–current characteristics of the bottom photonic crystal GaN-based LED compared with the reference LED [131].

An increase of the light output power of LED with photonic crystal structure selectively grown on *p*-GaN was shown to be by 70% [132] and using self-organized nanoscale patterning of *p*-type GaN was 46% higher than refernce LED [133].

Also, a highly-ordered porous AAO mask, with a pitch on the wavelength scale, was adopted as the selective dry etching mask. Photonic crystals structures with different pore depths were simultaneously formed on the entire surfaces of the GaN-based LED chip, including ITO, GaN, surrounding contacts and the sidewalls of the mesa structure by one-step reactive ion etching (RIE) (see Figure 1.28) [134]. An improvement on light output power up to 94% was achieved (see Figure 1.29).

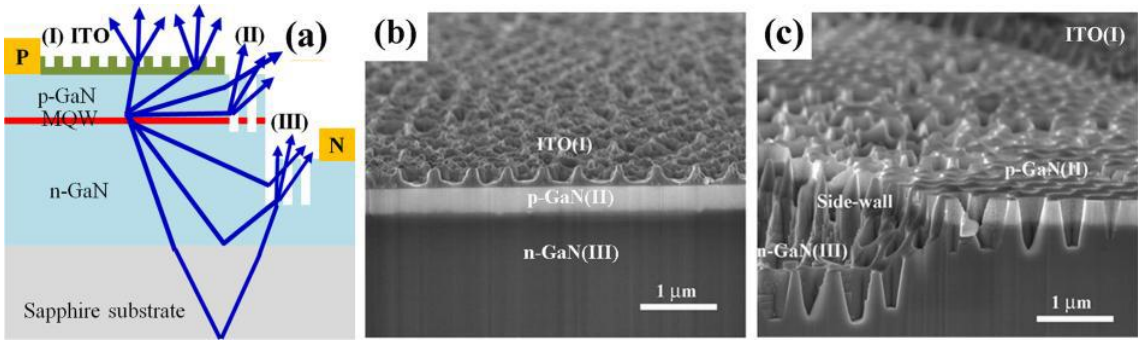

Figure 1.28. Photonic crystal structures fabricated on the surfaces of a GaN-based LED. (a) Schematic diagram of light traces emitted from the photonic crystal-based LED. (b) Side view SEM image of the photonic crystal structure generated on the ITO surface of the GaN-based LED. (c) Side view SEM image of the photonic crystal structure generated on the surfaces of the *p*-type GaN and *n*-type GaN layers [134].

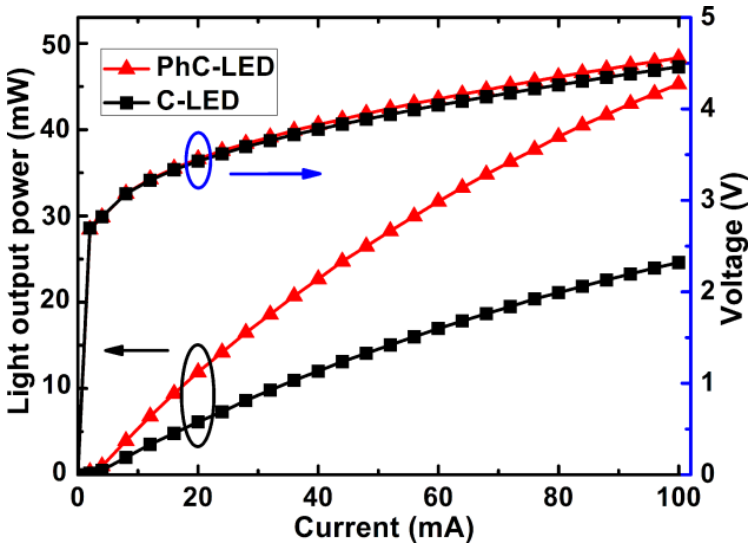

Figure 1.29. Typical light output power-current-voltage curves of the conventional GaN-based LED and the surface-patterned GaN-based LED with photonic crystal structures fabricated by using an AAO template as a selective dry etching mask [134].

1.5 Aims of the thesis

The research described in this thesis is focused on the synthesis and characterization of porous GaN particles and layers with the final goal to fabricate fully porous *p*-*n* junctions for future LED applications.

In this thesis, porous GaN is synthesized by the chemical vapour deposition (CVD) technique through the direct reaction between Ga and NH_3 [135], using different doping elements such as Mg and Si to generate the *p*- and *n*-type required semiconductors, as conventional techniques to produce porous GaN do. The advantage of the technique we developed is that it does not require any secondary treatment after growth to generate the pores.

We also used luminescent nanoparticles in order to explore the possibilities of converting the UV emission from GaN into visible light. We tried to synthesize them directly inside the pores of the GaN particles by using sol-gel techniques.

Finally, we worked on graphene deposition by electrospray with the final aim to use graphene layers as transparent electrodes for the future LEDs based on porous GaN.

Chapter 3 is focused on the optimization of the growth conditions of porous GaN particles by CVD, in order to get an homogenous porous GaN layer with a high degree of porosity. For this, different reaction parameters, such as the temperature, the III/V precursors ratio, the pressure at which the system is kept while the growth process develops, the deposition time, the shape of the crucible or Ga holder used, and the catalyst with which the Si substrates are coated, are studied. Therefore, the porous GaN particles obtained are characterized by X-ray diffraction, their shapes are observed by electron microscopy and their luminescence and electrical properties are measured, in order to know the quality and type of conductivity of porous GaN. Here, the mechanism of growth of porous GaN is also discussed.

Chapter 4 describes the doping procedures of porous GaN with Mg, in order to obtain *p*-type GaN and with Si, in order to have *n*-type GaN with a higher charge carrier concentration. Also, a metal-oxide semiconductor (MOS) porous GaN/MgO diode is presented, formed in a single step when high concentrations of Mg-precursor are used.

In Chapter 5, different substrates were tested to ascertain if they might play a role in the crystallographic orientation of the GaN particles. For this purpose we used as substrates amorphous quartz, pyrolitic boron nitride (p-BN), tungsten wire (W), sapphire (Al_2O_3), SiC, as well as, AlN and GaN thin films grown on sapphire (0001). The results show that the lattice mismatch between the substrate and the porous GaN layer plays an important role in achieving a continuous and oriented layer formed by discrete porous microparticles. Also, the structural, electrical and luminiscence properties of partially and fully porous GaN *p*-*n* junctions formed only by CVD means are shown.

The possibilities of tuning the emission of the potential LEDs based on porous GaN by fabricating luminescent nanoparticles/porous GaN composites is described in Chapter 6.

Chapter 7 presents the synthesis of graphene flakes, together with their deposition on silicon and quartz substrates by the electrospray method, since graphene is considered a promising transparent conductive electrode for GaN-based LEDs.

Finally, the main conclusions of this thesis are presented.

Chapter 2

Experimental techniques

This chapter describes the experimental techniques used in this thesis. At the beginning of the chapter, the crystal growth of porous GaN structures by Chemical Vapor Deposition (CVD) is presented. The second part is focused on microscopy techniques, which are essential for the observation and characterization of porous GaN structures. They include Scanning Electron Microscopy (SEM), Transmission Electron Microscopy (TEM), High-resolution Transmission Electron Microscopy (HRTEM), Atomic Forced Microscopy (AFM) and Focused Ion Beam (FIB) tomography. The techniques for structural characterization, such as X-ray diffraction and Raman scattering, are discussed in the third part of this chapter. The fourth part presents some clean room facilities, which were used for the preparation of ordered porous GaN microstructures. Electrical characterization techniques of porous GaN structures consisting in two-probe, four-probe, Van de Pauw geometry and capacitance-voltage measurements are discussed in fifth part of this chapter. The chapter ends by presenting photoluminescence and cathodoluminescence techniques used for the characterization of the optical quality of the porous GaN structures obtained.

2.1 Synthesis techniques

2.1.1 Crystal growth by chemical vapor deposition (CVD)

Chemical vapor deposition (CVD) is a chemical process for the deposition of a solid film on a substrate from vapor phase reactions of chemical reagents. CVD is used in many applications, especially in the microelectronics industry in order to prepare thin films serving as semiconductors, dielectrics, conductors, oxidation barriers, etc. By controlling the experimental conditions, such as the composition of the reaction gases, the gas flow rate, the substrate material, the substrate temperature and the total pressure gas flow, materials with different properties can be grown.

Typically, a conventional CVD process consists on the following steps, as shown in Figure 2.1:

1. A defined and stable mix of gases, together with inert carrier gases if needed, are introduced at a specified flow rate into the reaction chamber with one or more heated substrates to be coated.

2. The gases are transported by the carrier gases towards the substrate.

3. Gaseous reactants are adsorbed onto the heated surface of the substrate and heterogeneous chemical reactions occur at the gas–solid interface and near the hot surfaces of the substrate, which produces the deposit of the material desired and by-product species.

4. The deposits will diffuse along the heated surface of the substrate, forming the crystallization centres from which the growth of a thin film will evolve.

5. The gaseous by-products of the reactions, together with unreacted precursor gases are exhausted from the reaction chamber.

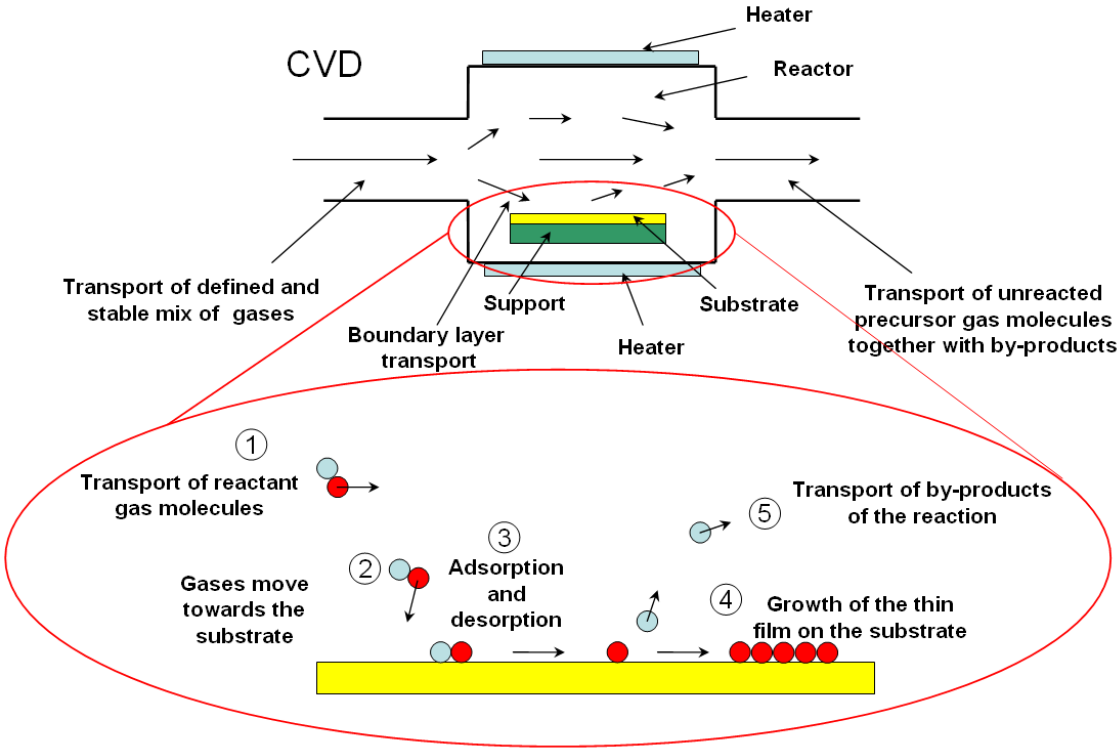

Figure 2.1. Scheme of processes that typically occur during CVD.

In general, the CVD equipment consists of three main components including the precursor gases supply system, a CVD reactor, and a gas handling system. At the same time, the CVD equipment is individually tailored for specific conditions of reaction, materials, etc. Since there is a large variety of deposited materials, there are many variants of CVD. It can be performed at sub-atmospheric total pressures, as well as at above-atmospheric pressures. There is also a variety of CVD-assisted/activated techniques by the use of plasmas, ions, photons, lasers, hot filaments, etc. CVD can be done in hot-wall reactors and cold-wall reactors, depending if the chemical reaction is activated by a thermal process or not [136].

In comparison to other deposition techniques CVD, has the distinctive advantages:

- A wide range of materials, including metals, carbides, nitrides, oxides, sulphides, III–V and II–VI materials, can be deposited by CVD with very high purity; CVD produces uniform films with good reproducibility and adhesion at high deposition rates.
- CVD can be applied for covering pieces with elaborated shapes, including the insides and undersides of them, since CVD films are generally quite conformal.
- Controlling the CVD process parameters it is possible to control the crystal structure, the surface morphology, the thickness and the crystallographic orientation of the products deposited.

However, there are some disadvantages of CVD:

- The process often requires the use of toxic, corrosive, flammable and/or explosive precursor gases, some of the reagents have a high cost.
- Sometimes it is difficult to deposit multicomponent materials with well controlled stoichiometry because different precursors have different vaporization rates.
- Use of high temperatures for deposition of CVD films, that can result in stresses in the deposited films, if substrate and film have different thermal expansion coefficients, and can lead to mechanical damages of the deposited materials [49].

In this thesis the synthesis of porous GaN was performed by a conventional CVD method using the direct reaction of metallic Ga (Alfa Aesar 99.999%) and NH_3 (Carburos Metalicos >99.98%) as gallium and nitrogen sources, respectively. The formation of GaN is based on the following reaction:

$$2Ga + 2NH_3 \rightarrow 2GaN + 3H_2$$

At the temperature of reaction, metallic Ga evaporates and reacts with NH_3 on the surface of the substrate. Heterogeneous decomposition of NH_3 at the growing surface is probably the dominant reaction path to create N atoms for GaN growth. A molecule of NH_3 is polar and is preferentially adsorbed by an electron acceptor. The surface Ga atom plays the role of acceptor of electrons during the crystal growth process, therefore, it chemically adsorbs NH_3 which decomposes and allows the formation of GaN [137].

The CVD reaction was performed in a horizontal single zone tubular furnace Thermolyne 79300, Thermo Fisher Scientific Inc., USA with a built-in temperature controller. The

chemical reaction undergoes inside an amorphous tube. The inlet of the tube is connected to an automatic Sierra INC. Smart-Trak flowmeter, through which NH_3 gas is introduced. The outlet of the tube is connected to a digital pressure controller CMOVE 1250 from Oerlikon Leybold Vacuum, with the possibility to control pressure manually or automatically, together with a vacuum pump from Oerlikon Leybold Vacuum that allows to get the desired pressure inside the furnace and exhausts the gaseous by-products of the reactions and unreacted NH_3 from the reaction zone as it can be seen in Figure 2.2.

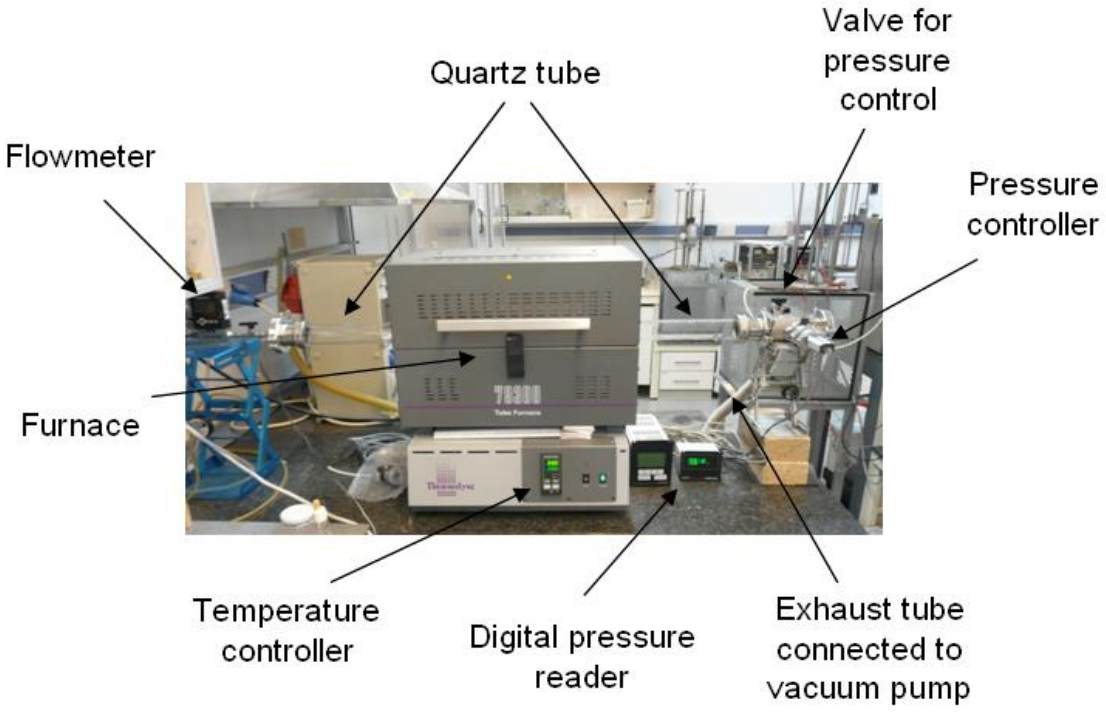

Figure 2.2. CVD set up used in the synthesis of GaN nanostructures.

In order to know the distribution of temperature along the tube, the thermal characterization of the furnace was performed. A representation of the thermal characterization made at 1073 K and 1173 K temperatures, as read in the temperature controller of the furnace, is shown in Figure 2.3. The temperature in different places of the quartz tube was monitored by a Pt-Rh thermocouple. The difference between the measured temperature in the center of the tube and the temperature read in the controller is less than 3 K. In the range from 0 mm (center of the tube) to 50 mm far from this center the variation of the temperature is less than 5 K. This region was considered for positioning the substrate during the synthesis of porous GaN structures, since the thermal stability is very good. Since we suppose that the thermal behavior of the furnace is symmetrical, we would have 10 cm in which the variation of the temperature is less than 5 K.

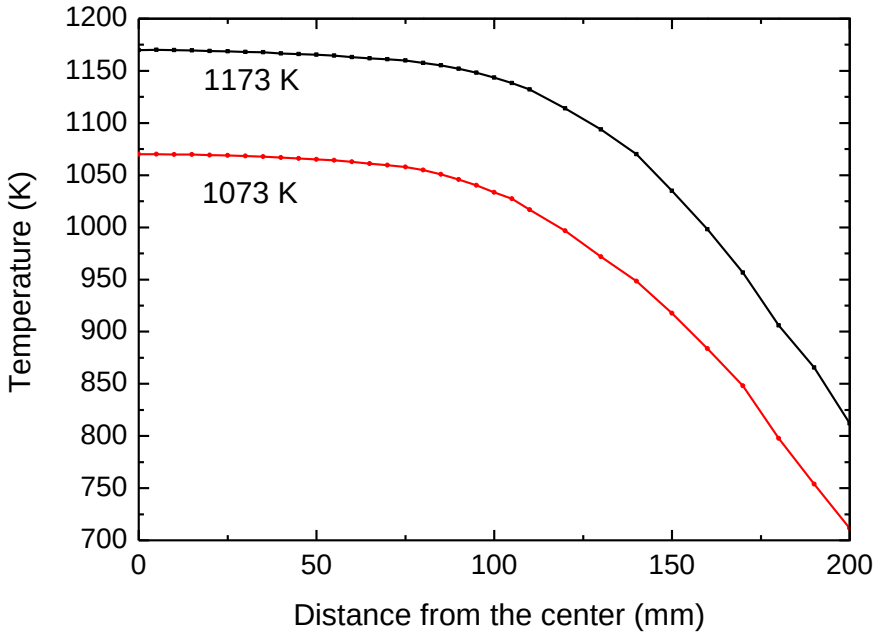

Figure 2.3. Distribution of the temperature along the amorphous quartz tube at two different temperatures.

A liner made of amorphous quartz was used to easily introduce and position the substrate and source of Ga and protect the quartz tube from contamination. Pure metallic Ga was placed into the liner in the form of a droplet onto an amorphous quartz crucible. Since metallic Ga tends to oxidize on air and form a thin layer of gallium oxide, all manipulations with Ga were made inside a Precise Controlled Atmosphere Glove Box 5220120 CA from Labconco filled with nitrogen. The substrate was placed above the Ga source standing at a vertical distance of ~ 2 cm onto a BN plate. BN was used as support for the substrate, since it has a very high thermal conductivity, allowing an homogeneous distribution of the temperature on the substrate and at the same time it allows keeping the substrate at the desired distance from the Ga source for the deposition of GaN. Moreover, it is quite easy to machine BN, giving to it the required shape and size, and also BN is a chemically stable material at high temperatures and in corrosive atmospheres. A scheme of the experimental system used for the synthesis of porous GaN is shown in Figure 2.4.

In a typical experiment, prior to the start of the chemical reaction, the quartz tube was degassed to a vacuum pressure of 1×10^{-2} Torr. After that, pure ammonia gas was introduced into the quartz tube through the mass-flow controller. No additional carrier gas was used. The furnace was heated up to the reaction temperature with a rate of 60 K/min from room temperature. Then, the furnace was kept at the reaction temperature during the reaction time, under a constant flow of NH_3, keeping the pressure of the system constant during the time of the chemical reaction, that we changed depending on the experiment, as it will be described in Chapter 3. When the reaction was finished, we cooled down the furnace to room temperature while we stopped the ammonia flow. The resulting porous GaN structures were deposited on the surface of the substrate facing to the Ga source.

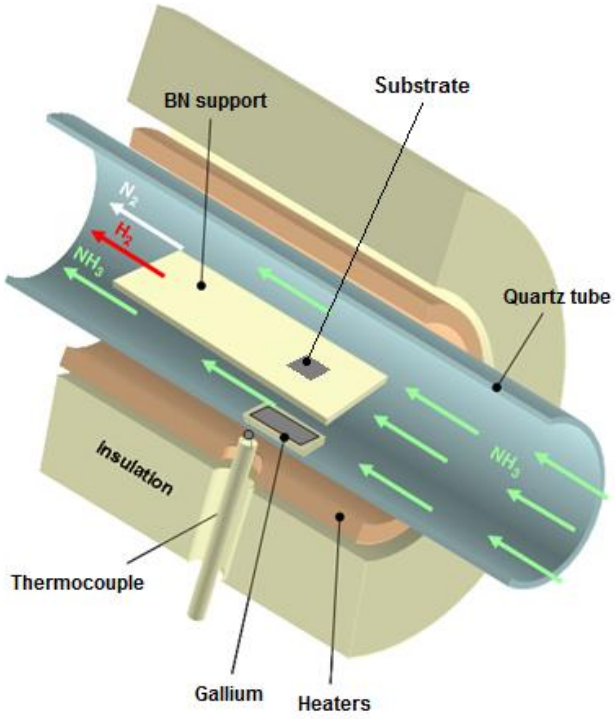

Figure 2.4. Schematic representation of the CVD system used for the synthesis of porous GaN (reproduction of Figure 1 from Paper I).

2.1.2 Synthesis of the luminescent nanoparticles by the sol-gel modified Pechini method

Sol-gel technology plays a principal role in the development of modern nanotechnology for the preparation of new materials [138]. Stoichiometric amounts of the oxides of the elements contained in the nanoparticles were first converted to their nitrate forms by dissolution in concentrated HNO_3. Later the excess of HNO_3 was evaporated to obtain nitrate precipitates by slow heating. In the next step, an aqueous solution of ethylenediaminetetraacetic acid (EDTA), used as the chelating agent in a specific molar ratio (C_M) to prepare metal-EDTA complexes, were mixed and added to to the nitrate precipitates. The molar ratio C_M was defined as:

$$C_M = [EDTA]/[METAL] \quad \text{(Eq. 2.1)}$$

which describes the degree of the chelation process of the metal in the organic product. Afterwards, ethylene glycol (EG), the sterification agent was added in molar ratio (CE), which describes the degree of sterification between the chelating agent and the ethyleneglycol

$$C_E = [EDTA]/[EG] \quad \text{(Eq. 2.2)}$$

In this process, the molar ratios of C_M and C_E used are in the ratio of 2:1, respectively. The resulting solution was heated slowly to obtain the precursor resin, which is a rigid polyster net

that reduces any segregation of metals. The following stage is the two step calcinations procedure. The first step is the calcination at 573 K for 3 hours, during which the precursor resin decomposes to provide the precursor powder and in the second step, the calcinations procedure depends on the nanocrystals to be obtained, since each material was calcined at a certain temperature and for a particular time to obtain the desired crystalline phase.

2.1.3 Deposition of graphene by the electrospray method

Electrospray is a quite simple and controllable method that allows spraying substances in the form of an aerosol by creating a thin layer of material on a substrate [139]. It consists on a cylinder connected to a rotating motor that holds the substrates and a capillary that provides the prepared dispersion of graphene (see Figure 2.5). The dispersion flows through the capillary at a fixed velocity. A positive high voltage is applied to the capillary forming a Taylor cone on the tip of the capillary, where forms the aerosol from the dispersion of graphene. The aerosol particles are positively charged. The back electrode, that has the same potential than the capillary, creates a uniform electric field between the back electrode and the ion field. When the spray reaches the substrates, the deposition of the graphene layers occurs. The substrate gets positively charged from the positively charged graphene sheets, what would generate repulsion for the next graphene layer deposition. In order to overcome this problem, a negative ionic field is introduced in the back part of the cylinder to neutralize the positive charge on the sample. The negative ionic field is generated by a needle connected to a negative power supply.

Experiments on deposition of graphene by the electrospray method were performed in Droplets, intErfaces and floWs (DEW) group, Universitat Rovira i Virgili, Tarragona.

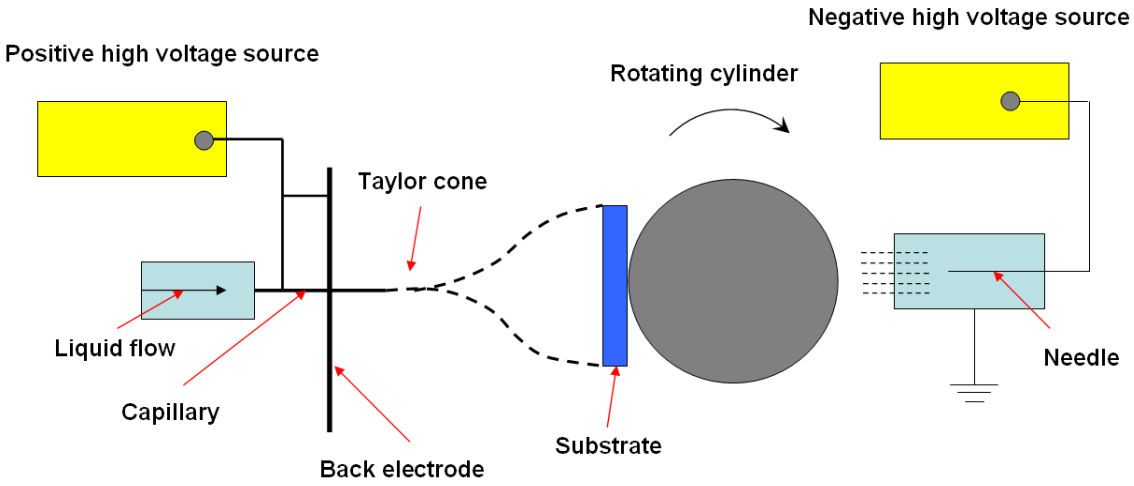

Figure 2.5. Set-up for deposition of graphene flakes by electrospray.

2.2 Microscopy techniques

2.2.1 Scanning Electron Microscopy (SEM)

Scanning electron microscopy (SEM) is a method for high-resolution imaging that provides detailed morphological and compositional information of surfaces. In SEM a focused beam of high-energy electrons generates a variety of signals, produced by electron-sample interactions. These signals include secondary electrons, backscattered electrons, characteristic X-rays, visible light photons (cathodoluminescence), Auger electrons and diffracted electrons (see Figure 2.6). Using SEM, the images with magnification up to 300,000× can be obtained and, at the same time, it allows excellent depth of the field [140].

The incident electrons in SEM are generated by an electron gun using an emission from tungsten filaments. A positive electrical potential is applied to the anode and the filament (cathode) is heated by the beam of electrons produced. The positive potential accelerates electrons down the SEM column. Depending on the studied objects the energy of the incident electrons can vary from 100 eV to 35 keV. Inside the SEM column the electrons are focused by a series of lenses and coils and directed onto the desired point of the surface of the sample to visualize. To get the final image, the electron beam scans the region of interest on the surface of the sample and the electrons of different kind emitted from the sample are detected for each position by an electron detector. The SEM column and sample chamber require high vacuum conditions in order to allow the electrons to travel freely without scattering with gas molecules. A schematic diagram of a scanning electron microscope is shown in Figure 2.7.

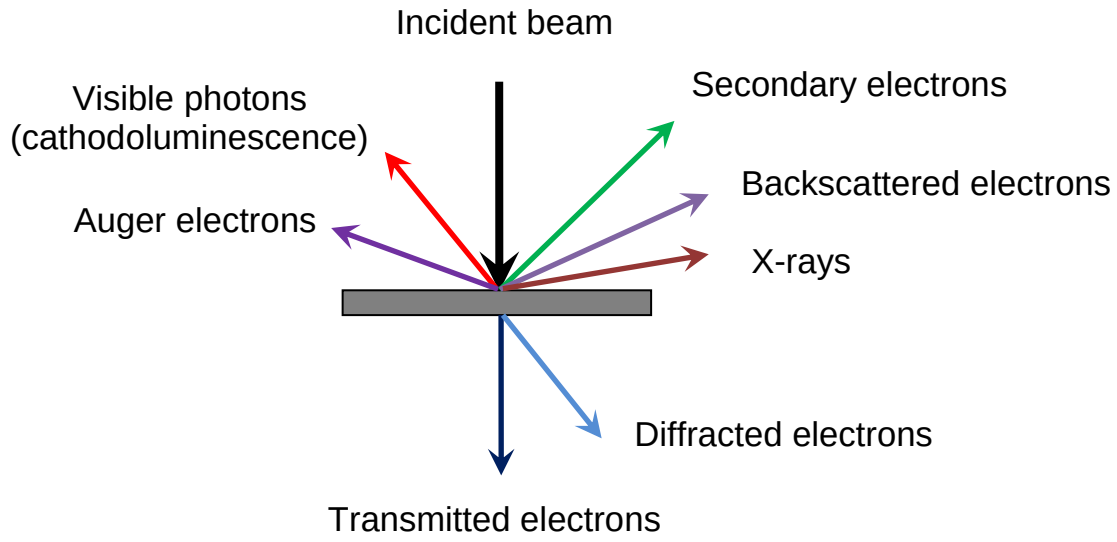

Figure 2.6. The interactions of an electron beam with the sample.

The interaction of the electron beam with the atoms in a sample results in elastic and inelastic scattering. High-energy or backscattered electrons are originated by elastic scattering of incident electrons with atoms of the sample. The intensity of backscattered electrons depends on the atomic number of the material, what results in changes of the image contrast in relation to the composition of the sample. Thus, brighter areas in the image are associated with elements with a higher atomic number. Lower-energy or secondary electrons are

produced from inelastic scattering when an incident electron excites an electron in the sample. Secondary electrons have typically energies lower than 50 eV and they are most suitable for visualization of morphology and topography on samples. In addition to those signals, other signals, such as characteristic X-rays, Auger electrons and cathodoluminescence, provide important information about the sample. Characteristic X-rays are used for elemental analysis. The energy of an Auger electron is characteristic of the type of element from which it was released, thus, Auger Electron Spectroscopy can provide information about elements present on the sample surface. Cathodoluminescence provides an emission spectrum or an image of the distribution of UV, visible and IR photons emitted by the specimen, depending on the detector used for this purpose [140].

SEM analysis needs electrically conductive samples to allow incident electrons to be conducted away from the sample surface and to avoid charging effects that can degrade the quality of the image. Nonconductive samples can be coated with a thin layer of a conductive metal such as gold. Gold has a high atomic number, and sputter coating of the samples with gold allows obtaining high topographic contrast and resolution images.

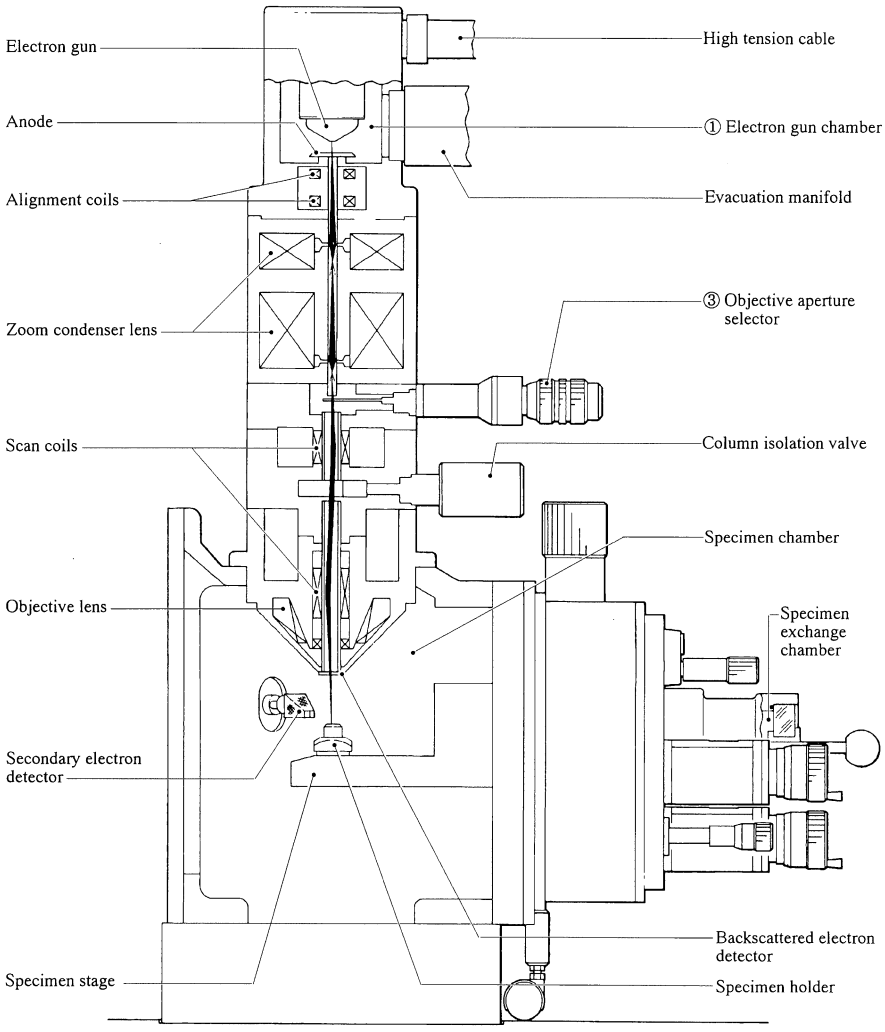

Figure 2.7. Schematic diagram of a scanning electron microscope taken from the user's manual of Jeol JSM 6400.

Environmental scanning electron microscopy (ESEM) works under the same principle as SEM. However, an advantage of using ESEM is the possibility to work without coating non-conductive samples with a conductor media such as gold, thus, their original characteristics can be observed. The ESEM uses multiple Pressure Limiting Apertures (PLAs) that separate the sample chamber from the column. The sample chamber contains gas at low pressure, while the column is at high vacuum. The incident electrons travel across the gas environment and interact with the gas molecules producing positive ions and additional electrons, which amplify the original secondary electron signal. In a non-conductive sample, the positive ions created are attracted to the sample surface, and effectively suppress charging effects.

In this thesis a Jeol JSM 6400 SEM was used. Before observation samples were coated with gold with a Bal-Tec SCD004 sputterer. Also a FEI Quanta 600 ESEM coupled to an Oxford Inca 3.0 microanalysis was used. The microscopes and the sputterer are available at the Servei de Recursors Científics i Técnics of the Universitat Rovira i Virgili. In addition, SEM analysis was performed on a FEI Quanta 650 FEG high-resolution SEM equipped with an Oxford Instruments X-MAX 20 large area Si diffused EDX detector, available at Tyndall National Institute, Cork (Ireland).

2.2.2 Transmission Electron Microscopy (TEM) and High-resolution Transmission Electron Microscopy (HRTEM)

The transmission electron microscope (TEM) uses a high energy beam of electrons that is transmitted through a very thin sample. The resulting interactions between the electrons and the atoms are used to observe and analyze the structure of materials with atomic scale resolution (in the case of HRTEM). TEM is also useful for the analysis of crystal structure, chemical composition and defects such as dislocations and grain boundaries [141].

The electron gun in TEM consists of an electron source that uses emission from tungsten filaments to generate electrons. The acceleration energies are typically of 40–100 keV. The beam of electrons from the electron gun is focused by a series of condenser lenses. In order to remove electrons that are scattered to high angles, the beam is restricted by the condenser aperture. Later the beam passes the sample and a magnified image is formed by a set of lenses. This image is projected onto a fluorescent screen or a CCD camera (see Figure 2.8).

The darker areas in the resulting TEM image mean that fewer electrons are transmitted through the sample. Thus, these darker areas are related to denser areas and areas containing heavier elements, while low-density areas and areas containing light elements appear bright. This imaging mode is called bright field mode. In case of crystalline materials, diffraction of electrons will occur on the sample. This diffraction can be easily seen by projecting the resulting diffraction pattern of the sample onto the screen, when the objective aperture is displaced from the optic axis to intercept the transmitted beam. This allows an analysis of the crystal structure and crystallographic orientation of the sample. This mode is known as dark field mode.

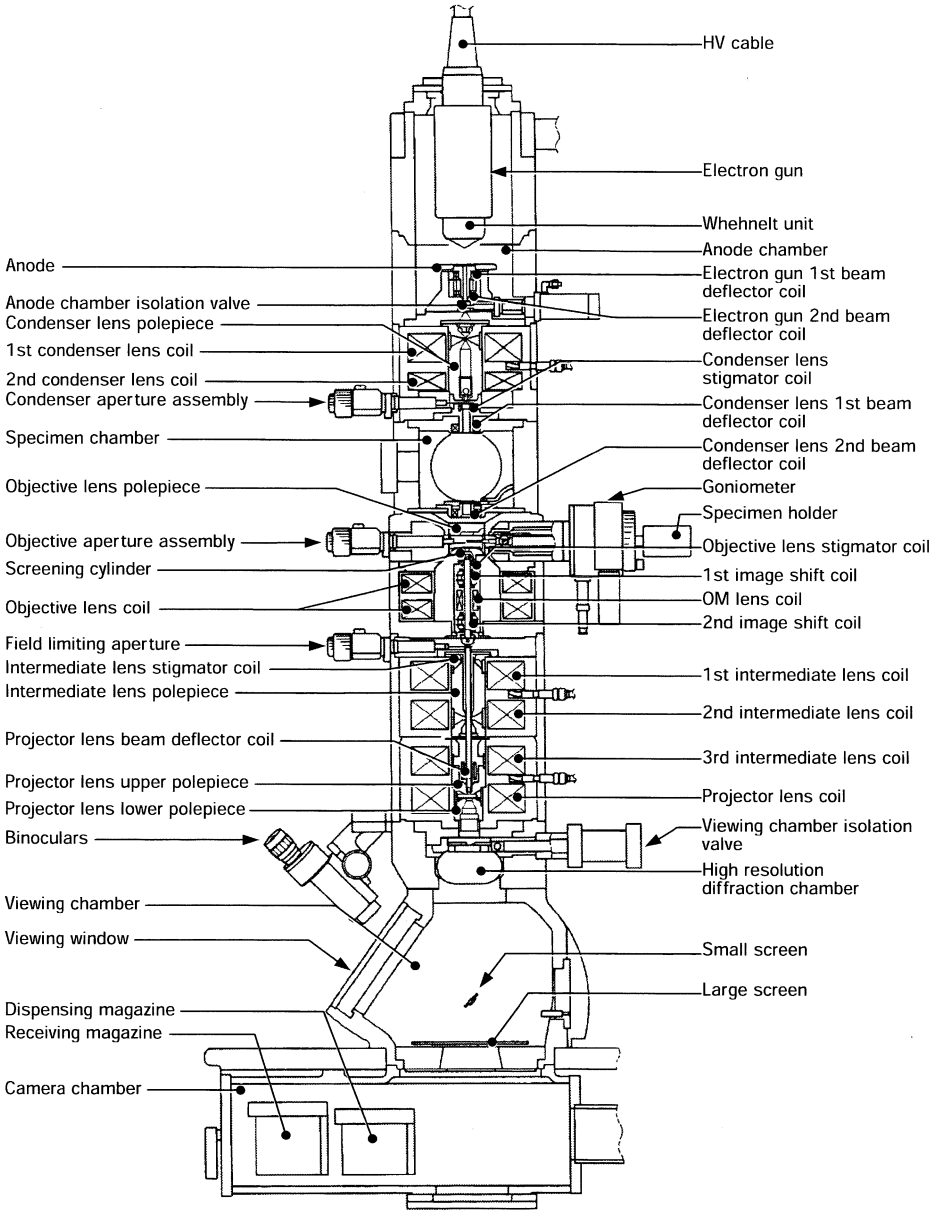

Figure 2.8. Schematic diagram of a transmission electron microscope taken from the user's manual of JEOL JEM-1011.

The selected area diaphragm is used to select only one part of the sample. This mode is called selected area electron diffraction (SAED). It allows obtaining important quantitative structural and crystallographic information about crystalline materials such as symmetry of the crystal lattice and calculating interplanar distances. In SAED a parallel beam of incident electrons is used. When the incident beam of electrons is converted into a cone, it is possible to perform a diffraction experiment on several angles at the same time. This technique is called Convergent Beam Electron Diffraction (CBED) and can provide the full three dimensional symmetry of the crystal.

Another mode of TEM is related to the differences in the phases of the electrons scattered through the sample. Unlike conventional bright-field and dark-field TEM that normally use only the central electron beam or a single diffracted beam, the phase contrast method is based

on the interference among at least two beams and commonly many electron beams. The electrons going from the bottom surface of a thin sample have small phase differences, arising from scattering in the sample. Phase contrast imaging is called high-resolution TEM (HRTEM). In HRTEM the voltage at which electrons are accelerated is higher than in TEM. HRTEM in general refers to imaging in which atomic resolution is achieved. HRTEM provides significant information about the sample, such as analyzing crystalline defects and interfaces at the atomic scale, and observing and verifying devices, nanoscrystals and nanostructures [141].

In this thesis, the TEM analysis was performed with a JEOL JEM-1011 microscope, which is available at the Servei de Recursors Científics i Técnics of the Universitat Rovira i Vigili. HRTEM and CBED measurements were conducted on a JEOL 2100F FEGTEM operating at 200 kV and on a JEOL FEM3000F TEM available at Tyndall National Institute, Cork (Ireland). Also, TEM observations were made with a JEOL-2010FEG TEM instrument operating at 200 keV, coupled to an energy dispersive X-ray spectroscopy (EDS) system has been used to determine the local composition in Mg-doped GaN, available at CIMAP, Caen (France).

2.2.3 Focused Ion Beam (FIB) tomography

Focused ion beam (FIB) tomography is a technique used in material science that combines high resolution imaging with localized milling and etching by an ion-beam at the microscopic/submicroscopic level. The FIB instrument is similar to a SEM. The main difference is that ions are used, instead of electrons. Also, FIB is usually combined with SEM, what allows manipulation using either one of the beams.

The FIB generally uses a liquid Ga metal ion source that is focused onto the sample by electrostatic lenses. Typical accelerating voltages in FIB are in the range from 1 to 30 keV. Interactions of the ions with the sample produces the ejection of secondary electrons, neutral atoms and ions [142].

FIB has several applications, including imaging, local removal (milling/etching) and local deposition of materials. The high-resolution imaging of the material is possible using secondary electrons and secondary ions, what allows obtaining different contrast properties. When the high-energy Ga ions strike the sample, they can cut trenches in the sample surface with submicrometer precision. Varying the current of the ion beam allows removing material at a desired location with the desired dimensions. The etching rate can be increased by injecting certain gases to the sample. Also, by means of FIB, metals and insulating materials can be deposited on the sample surface, when the ion beam interacts with the molecules of gases carrying the desired precursor material for deposition [142].

Here, shapes, lengths, and propagation directions of the pores in the GaN particles were analyzed by FIB tomography, i.e., time-resolved serial slicing and imaging with a Zeiss 1540 Cross Beam microscope. This dual beam system is equipped with a FIB column with a Ga source and a high-resolution field emission electron column. The FIB column stands at 52° to the electron column, and the sample surface is perpendicular to the ion column. The ion

milling was performed using a 5 pA beam current to minimize surface damage and material redeposition. The FIB tomography system we used is available at Université de Sherbrooke, Sherbrooke (Canada).

2.2.4 Atomic Force Microscopy (AFM)

Atomic Force Microscopy (AFM) is a form of scanning probe microscopy (SPM) with high resolution, which is used for surface characterization of a wide range of materials. The AFM technique provides a 3D profile of the surface with a nanometric scale resolution and can map mechanical, adhesive, magnetic and electrical properties of the surface, if the suitable additional detectors are present in the equipment.

The AFM principle is based on the interaction between the sample surface and a small tip of nanometer scale sharpness (<10 nm) that scannes across a selected area of the sample surface. The tip is fixed at the end of a small cantilever and this probe is connected to a piezoelectric scanner. The tip and the cantilever are typically made of Silicon or Silicon Nitride. As the tip scans the sample, interatomic forces between the probe tip and the sample surface cause a displacement of the tip and the corresponding bending of the cantilever. A laser light is pointed on the back of the cantilever and reflected to the photodetector. The position of the reflected laser light changes depending on the cantilever movements. The photodetector converts this change in an electrical signal and sends it to a computer, where a map of topography and/or other properties of interest are generated (see Figure 2.9) [143]. AFM imaging areas are in the range of 100 × 100 μm in the x- and y-directions as maximum. Also, areas less than 100 × 100 nm can be imaged. From the above description, it can be seen that no optical processes take place in scanning the sample, except the reflection of the laser from the cantilever. Thus, limitations that exist in optical microscopes are eliminated.

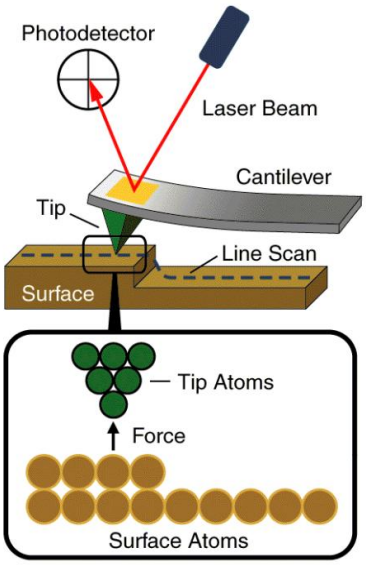

Figure 2.9. Principle of operation of an Atomic Force Microscope (image taken from the user's manual of Agilent 5500 microscope).

The dominant interactions in AFM are van der Waals interactions. During contact with the sample, the probe is predominately influenced by repulsive van der Waals forces. It results in the deflection of the tip. As the tip moves away from the sample surface, attractive van der Waals forces become dominant. Thus, three primary modes in AFM imaging exist depending on the tip-surface separation: contact, tapping and non-contact mode (see Figure 2.10).

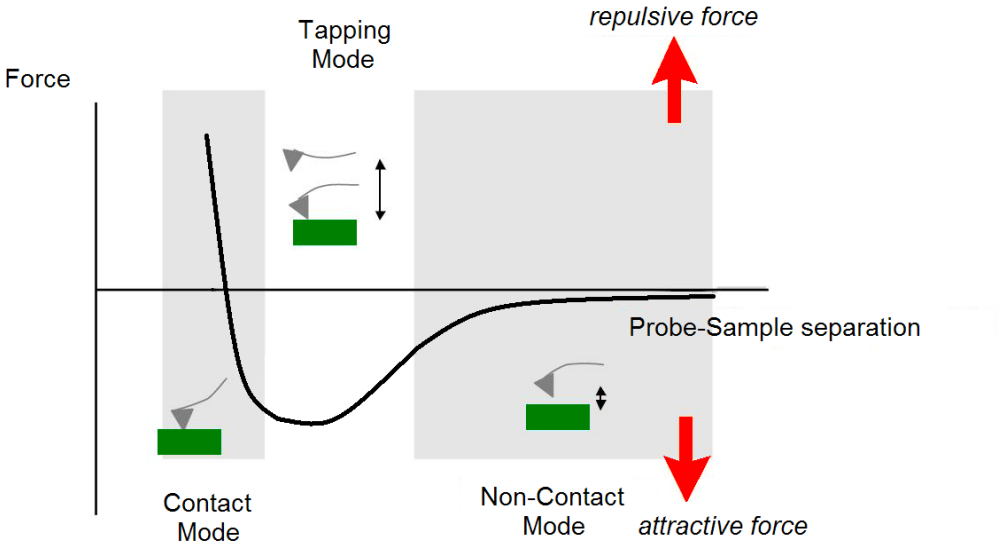

Figure 2.10. Plot of force as a function of probe-sample separation [144].

In the simplest measurement method, the contact mode, the probe cantilever is deflected by topographical changes and the scanner adjusts the probe position to restore the original cantilever deflection. The scanner position information is used to obtain a topographical map. This mode provides a fast scanning, but can damage or deform soft samples. In the tapping mode the probe cantilever is oscillated at its resonant frequency. While maintaining constant oscillation amplitude, the oscillating probe tip is scanned at a height where it barely touches the sample surface. The system monitors the probe position to get topographical information. This mode is less destructive than the contact mode and it allows visualizing the sample surface with high resolution. However, slower scan speeds are required. In non-contact mode the probe tip does not contact the sample surface, but oscillates above the surface during scanning. This mode extends probe lifetime applying very low forces on the sample surface, but generally has a lower resolution [145].

In our studies, the surface of porous GaN films were visualized by an Agilent 5500 microscope in the tapping mode with Si tips with a diameter of 10 nm and oscillating at a resonance frequency of 75 kHz. This equipment is available at the Servei de Recursors Científics i Técnics of the Universitat Rovira i Vigili.

2.3 Structural characterization techniques

2.3.1 X-ray diffraction (XRD)

X-ray diffraction (XRD) is a non-destructive technique that provides detailed information about the atomic structure of crystalline substances. X-ray diffractometers typically consist of an X-ray source, a goniometer, containing the sample holder, and an X-ray detector. X-rays are generated when high energy electrons collide with a metal target (Cu in our case) and knock out core electrons. An electron from a higher energy orbit will replace the lost electron, thus emitting X-rays. These X-rays are filtered to produce monochromatic radiation, collimated and directed towards the sample.

The structure of crystalline materials is defined by ordered planes of atoms that form a crystal lattice. When a focused X-ray beam interacts with these planes of atoms, part of the beam is transmitted, absorbed by the sample and scattered, and part is diffracted. When the X-ray beam after interaction with the sample produces constructive interference (diffraction), the conditions of Bragg´s law will be satisfied (see Figure 2.11), that takes the form of the following expression:

$$n\lambda = 2d \sin\theta \qquad \text{(Eq. 2.3)}$$

In this equation n is the order of the diffracted beam, λ is the wavelength of the incident X-ray beam, d is the distance between crystalline planes of atoms (the d-spacings), and θ is the angle of incidence of the X-ray beam. From Bragg´s law we can easily calculate the d-spacings, since we know λ (1.54056 Å in our case, corresponding to the K_α of Cu) and θ can be measured. When the intensity of the X-rays detected is plotted as a function of θ, an X-ray diffraction pattern is obtained, which is unique and characteristic for each structure. The peak intensities correspond to the diffraction of various d spacings in the crystal lattice, depending on the structure and the crystal system. Comparing the positions and intensities of the peaks with reference XRD patterns, we can identify the structure or crystalline phase of the material. Also, it may be possible to quantify each phase, the crystallinity of a sample, the crystal structures and their lattice parameters, the crystallite size and the structural strain [146].

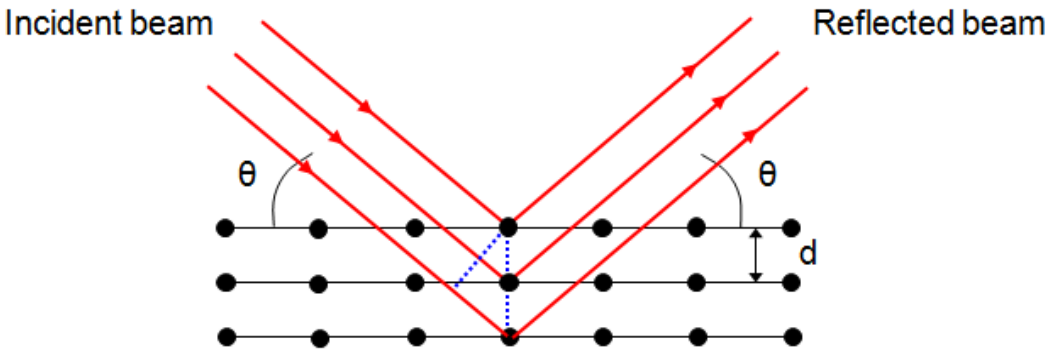

Figure 2.11. Schematic representation of Bragg´s law, the fundamental law for diffraction of X-rays in a crystalline material.

In this thesis, XRD patterns of the as-grown porous GaN samples were recorded using Cu Kα radiation in a Bruker-AXS D8-Discover diffractometer equipped with a parallel incident beam (Göbel mirror), a vertical θ−θ goniometer, an XYZ motorized stage, and a General Area Diffraction Detection System (GADDS) HI-STAR detector with a multiwire proportional counter of 30 × 30 cm^2 area and 1024 × 1024 pixel density. Samples were placed directly on the sample holder, and the area of interest was selected with the aid of a video-laser focusing system. An X-ray collimator system allows the analysis of an area of 500 μm^2. The X-ray diffractometer was operated at 40 kV and 40 mA. We collected 2D XRD patterns covering a range of 2θ between 20 and 85° corresponding to 3 frames of the GADDS detector, located at a distance of 15 cm from the sample. The exposure time was 120 s per frame. Identification of the crystalline phases was achieved by comparing the XRD diffractogram with the JCPDC database using the Diffracplus Evaluation software from Bruker.

Additionally, rocking curves (ω-scan) of the (0004) reflection of the porous GaN films were recorded using the same system. The rocking curves covered an omega angle of 6º corresponding to 120 frames from GADDS detector with a step size of 0.05^o and 15 s of exposition time per frame.

XRD powder diffraction of luminescent nanoparticles was performed on a Siemens D5000 X-ray diffractometer. This system works with the Bragg-Brentano parafocusing geometry and a θ−θ configuration, where the source, the detector and the sample are oriented in the same direction and occupy three consecutive positions on a focusing circle. The source and the detector maintain a symmetrical position and move on a circle that is centred on the sample. This allows obtaining a discrete pattern of the reflections for the families of planes parallel to the sample surface. All these equipments are available at the Servei de Recursors Científics i Técnics of the Universitat Rovira i Vigili.

2.3.2 Raman scattering

Raman scattering is a technique based on the inelastic scattering of monochromatic light, usually from a laser source, when it interacts with a sample. Photons of the laser light are absorbed and then reemitted. There is a shift in frequency of the reemitted photons in comparison with the original monochromatic frequency, which is basically in which consists the Raman effect. The scattered light produced by the Raman effect provides information about the energies of molecular vibrations and rotations. Using Raman scattering, solid, liquid and gaseous samples can be analyzed. A Raman system typically consists on the excitation source (a laser), the sample illumination system, the light collection optics, the wavelength selector and the detector. The scattered light is collected with a lens and is sent through an interference filter or an spectrophotometer to the detector to obtain the Raman spectrum [147].

When monochromatic laser light strikes the sample, it excites molecules and transforms them into oscillating dipoles. These dipoles emit light of three different frequencies:

1. Elastic Rayleigh scattering occurs when a molecule without Raman-active modes absorbs a photon and emits light with the same frequency of the incident photon. The excited molecule returns back to the basic vibrational state.

2. When a Raman-active molecule absorbs the photon, it is promoted from the ground to a virtual state and then it relaxes to a higher energy vibrational state. Thus, the scattered photon has less energy than the incident photon, and therefore a longer wavelength. This is called Stokes scattering.

3. Another possibility is that, when a photon is absorbed by a Raman-active molecule, which, at the time of interaction, is already in an excited vibrational state, then, the excessive energy of the excited Raman active mode is transferred to the scattered photon and the molecule relaxes to the ground vibrational state. Therefore the emitted photon has a shorter wavelength than the incident photon. This is called Anti-Stokes scattering.

For a better understanding of the mentioned above processes, they are represented in an energy level diagram in Figure 2.12.

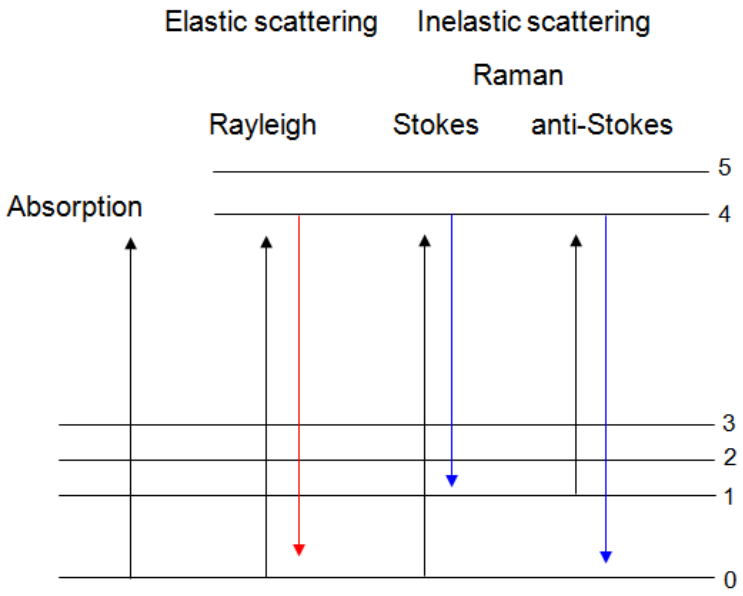

Figure 2.12. Schematic representation of an energy diagram of Rayleigh and Raman (Stokes and anti-Stokes) scattering.

The vast majority of all incident photons suffer from elastic Rayleigh scattering. This type of signal has no use for practical molecular characterization. Only about 0.001% of the photons produce inelastic Raman signal with Stockes and anti-Stockes frequencies. Since spontaneous Raman scattering is very weak, special measures should be taken to eliminate the predominant Rayleigh scattering. Also, at room temperature most of the molecules are in the ground vibrational state ($\nu = 0$) with very low population in the first vibrational excited state ($\nu = 1$). Thus, the Stokes lines in the Raman spectrum are much more intense than the anti-Stokes lines, because there is a much higher probability to excite a molecule from its ground vibrational state, than from the first vibrational excited state.

Here, Raman scattering measurements were carried out using a micro-Raman system Renishaw-InVia spectrometer equipped with a confocal microscope Leica 2500 and a CCD

camera as detector. Radiation of an Ar laser (λ = 514 nm) was focused by microscope objectives on the surface of the sample. This micro-Raman equipment is available at the Servei de Recursos Científics i Técnics, Universitat Rovira i Virgili, Tarragona.

2.4 Clean room facilities

2.4.1 Sputtering

Sputtering is a technique used to deposit thin films of materials on the surface of a substrate. In sputtering, the substrate is placed in a vacuum chamber together with the source material (named target). A voltage is applied between them so that the target is the cathode and the substrate is attached to the anode. An inert gas (typically Ar) in the form of plasma is used to bombard the target and erode the material to be deposited. The ions of gas are accelerated by the electric field created between the target and the anode to which the substrate is attached. The material to be deposited is in the form of neutral particles with a small fraction of ions. These particles ballistically travel from the target in straight lines and impact on the substrate. In this way the substrate is coated by a thin film of the source material (see Figure 2.13).

When an Ar ion strikes the target, an electron is ejected from the surface and combines with the Ar ion to neutralise it, bringing it to the vacuum as an Ar atom. An energy source (Radio frequency (RF) or direct current (DC)) is required to maintain the plasma state while the plasma is losing energy. If the target material is dielectric, this process rapidly results in charging at its surface, since Ar ions are no longer attracted and electrons are no longer released. It makes the plasma quench. Thus, to sputter non-conducting materials, it is needed to apply a pulsed power (RF, for example) to the target. In this way the ion charge, that was collected on the surface, is driven out during the positive phase. However, the deposition rates for RF sputtering are lower than those for DC sputtering. Also, sputtering sources often include magnetrons that confine charged plasma particles next to the surface of the sputter target using strong electric and magnetic fields [148].

In this thesis, RF sputtering was utilized to cover Si wafers with thin films of metals, such as Au, Ti, Pt and Ni that were used as catalysts in the crystal growth process of porous GaN. Magnetron sputtering was performed by an ATC Orion 8-HV AJA International system, which is available in the clean room of the Servei de Recursos Científics i Técnics, Universitat Rovira i Virgili, Tarragona. In order to deposit 20 nm thick films of Au, Pt and Ni on Si substrate the RF sputtering was used at a power of 150 W, a flow rate of Ar of 20 sccm and a pressure of 3 mTorr. In order to deposit a Ti layer 20 nm thick on Si DC sputtering was used at a power of 200 W, a flow rate of Ar of 20 sccm and a pressure of 3 mTorr.

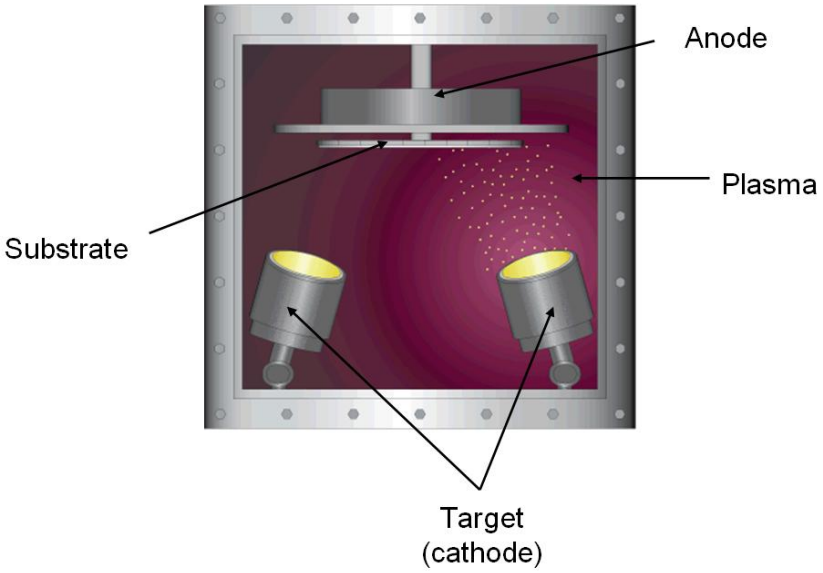

Figure 2.13. Scheme of the sputtering set-up taken from the user's manual for ATC Orion 8-HV on AJA International webpage.

2.4.2 Spin-coating

Spin-coating is a fast and simple method to generate thin and homogeneous films on flat substrates. The process of spin-coating involves the deposition of the coating fluid (solution) onto the center of a wafer or a flat substrate. Afterwards, the substrate is accelerated up to the desired rotation speed until it is spinned at a high speed constant rate for the required time. Centrifugal forces cause the fluid to spread to and off the edges of the substrate, leaving a thin film of the fluid material on the surface of the substrate. Together with the spreading and thinning of the fluid, the solvent evaporates, while the substrate is still spinning at a constant rate. When the solvent evaporation dominates, the solid film starts to generate. An additional drying step can be added after the high speed rotation step to further dry the film without substantially thinning it. This is typically used for thick films, since long drying times may be necessary to increase the physical stability of the film [149].

The combination of selected rotation speed and time defines the final thickness of the film. In general, higher rotation speeds and longer rotation times create thinner films. Also, the final film thickness and its properties depend on the nature of the fluid (viscosity, drying rate, concentration of solvent, surface tension, etc.). Spin-coating is widely used in microfabrication to create thin films with the desired thicknesses and in photolithography to deposit layers of photoresist [149].

In one of the steps of the fabrication of ordered microstructures of porous GaN a APT SPIN150 spin-coater was used. The Si wafer was covered with ~700 nm thick layer of AZ 1505 photoresist (Microchemicals) by spin coating at 500 rpm for 30 s. Additionally, after the spin-coating, softbake was performed at 373 K for 30 s. The spin-coater is available in the clean room facility of the Servei de Recursos Científics i Técnics, Universitat Rovira i Virgili, Tarragona.

2.4.3 Laser lithography

Lithography is the transfer of geometric shapes on a mask to a smooth surface. In modern semiconductor manufacturing, optical lithography or photolithography is widely used for device microfabrication. Photolithography uses optical radiation to transfer a geometric pattern from a photomask to a light-sensitive photoresist on the substrate. The photolithography system generally consists of an illumination system, a photomask, an optical system, and the photoresist applied by spin-coating on top of the substrate. The operation principle of a standard photolithography process is based on the ability of the photoresist to store an image of the desired pattern. The mask, that already has this pattern, is exposed to the light and the optical system images the pattern of the mask onto the photoresist. The photoresist is a photosensitive material that changes its chemical composition during light exposure. A special solution, called developer, is then applied to the photoresist, which remains or dissolves depending on if it has been exposed or not to the light, depending on its polarity. Afterwards, chemical etching is used, when a chemical agent removes the layer of the substrate in the areas that are not protected by the photoresist. Finally, the photoresist is removed from the substrate. After the completion of the photolithography process, a replica of the mask pattern is left on the substrate surface [150].

Laser lithography or direct laser writing is a form of maskless lithography. It is similar to the standard photolithography technique with the fundamental difference of the avoidance of a photomask. Instead, the radiation of a narrow laser beam is used to directly write the image onto the photoresist. The laser light induces a dramatic change in the solubility of the photoresist for appropriate developers. In this case the chemical properties of the photoresist change due to a multi-photon absorption process, in most of the cases a two-photon absorption process.

In order to produce a patterned SiO_2 layer on a Si substrate for ordered growth of porous GaN, in this thesis a DWL66FS laser lithography system from HEIDELBERG INSTRUMENTS was used, that is available in the clean room facility of the Servei de Recursos Científics i Técnics, Universitat Rovira i Virgili, Tarragona. The diode laser of this system operates at 405 nm with a maximum power of 50 mW. A wafer of SiO_2-coated Si (100) was covered with ~700 nm thick layer of AZ 1505 photoresist (Microchemicals) by spin coating (500 rpm, 30 s). The pattern of holes with 1.5 μm in diameter and an area of 1 cm^2 was fabricated using this system. The photoresist was removed by the AZ 726 MIF developer with 2.38 % tetramethylammonium hydroxide (TMAH) with surfactants added for fast and homogeneous substrate wetting.

2.5 Electrical characterization

Electrical characterization includes the use of electrical measurement techniques that are used to define various electrical parameters of a system. Electrical measurements often are related to either measuring current or voltage. The relationship between the

direct current through the semiconductor or an electronic device and the voltage across its terminals is called the current–voltage characteristics or I-V curves. I-V curves are generally used as a tool to determine and understand the basic parameters of the semiconductor or device, the charge transport behavior, and can also be used to model their behavior in an electrical circuit. The simplest I-V curve belongs to a resistor, which according to Ohm's law, has a linear relationship between the applied voltage and the resulting current. However, a non-linear I-V curve of the resistor can be obtained depending on the material characteristics. When we have semiconductor devices such as diodes and transistors, they are built using semiconductor *p-n* junctions. Here, the shape of the I-V curve is determined by the transport of charge carriers through the so-called depletion region that appears at the *p-n* junction.

In order to analyze the porous GaN layers and devices we developed, in this thesis we used two- and four-probe electrical measurements, capacitance-voltage measurements and the van der Pauw technique for resistivity determination.

2.5.1 Two-probe measurements

I-V curves are often recorded using the two-probe electrical measurement technique. This technique uses two probes aligned linearly or in a square pattern that contact the surface of the sample under test. Two probes are connected at a fixed spacing distance on the sample surface. Current is sent through one probe and exits through the second one. The voltage between the two probes is measured by either a potentiometer or a voltmeter. Each contact serves as a current and as a voltage probe. Using the voltage and current measurements in the two-probe technique, it is possible to calculate the material resistance between the two probes. Using the Ohm’s law the total resistance is given by

$$R_{total} = V/I = 2R_w + 2R_c + R_s \qquad \text{(Eq. 2.4)}$$

where R_w is the wire or probe resistance, R_c is the contact resistance, and R_s is the resistance of the sample under test (see Figure 2.14).

A known current flows through the unknown resistance. The voltage across the resistance is measured and then the resistance is determined by dividing the measured voltage by the source current. A problem that occurs when using a two-probe technique is that the voltage measured across the resistance also includes the resistance of the probes and contacts. When the resistances of the probes and contacts are negligibly small, it is possible to obtain the value of resistance of the material with a good accuracy. However, when measuring low resistances on nanoscale materials, for instance, obtaining accurate results with a two-probe measurement may be a problem [151].

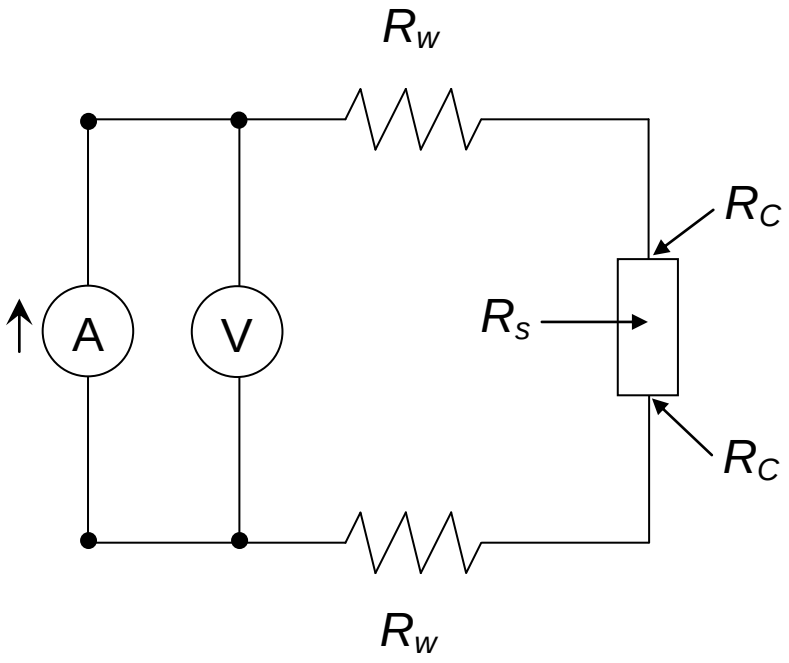

Figure 2.14. Scheme of the principle of work of the two-probe mesuraments.

In this thesis two-probe electrical measurements of porous GaN films were conducted using a dc voltage and an Agilent 34401A Digital Multimeter in a Peltier cell, thermostated to 295 K in a Faraday cage. Liquid metal contacts were made using In−Ga eutectic blown into a sphere from a gold metalized short borosilicate capillary tube, ensuring good wetting (several μm^2) to the rough top-surface morphology of the porous GaN and avoiding electrical shorting to the underlying metallized silicon. Also, two-probe electrical measurements of the various Mg-doped GaN samples were conducted using In/Ga liquid eutectic contacts and a Biologic SP-50 potentiostat. An In/Ga eutectic droplet was placed on top of the GaN material with the other contact placed either directly on the Si or epitaxial GaN substrate (depending on the substrate under investigation). The In/Ga eutectic droplets were used as Ohmic contacts. Linear voltage sweeps were obtained in the range of -3 V and 3 V with a 50 mV/s sweep rate. The measurements were repeated with contacts on various points of each sample to ensure repeatability. These measurements were performed in the Applied Nanoscience Group, University College Cork, Cork (Ireland).

2.5.2 Four-probe measurements

The four-probe electrical measurement is a commonly used technique to measure the semiconductor resistivity. It is also known as Kelvin measurements, named after William Thomson, Lord Kelvin. This technique uses two separate sets of probes. One set of probes serves for carrying current. The second set of probes is used for voltage sensing. Each of those probes has a probe resistance R_w, a probe contact resistance R_c and a spreading resistance associated with it (see Figure 2.15). However, these unwanted resistances don't

have to be taken in consideration for the voltage probes, since the voltage is measured with a high impedance voltmeter and there is negligible current. Thus, the voltage drops across these unwanted resistances are extremely small. Therefore, only the voltage drop across the sample is measured.

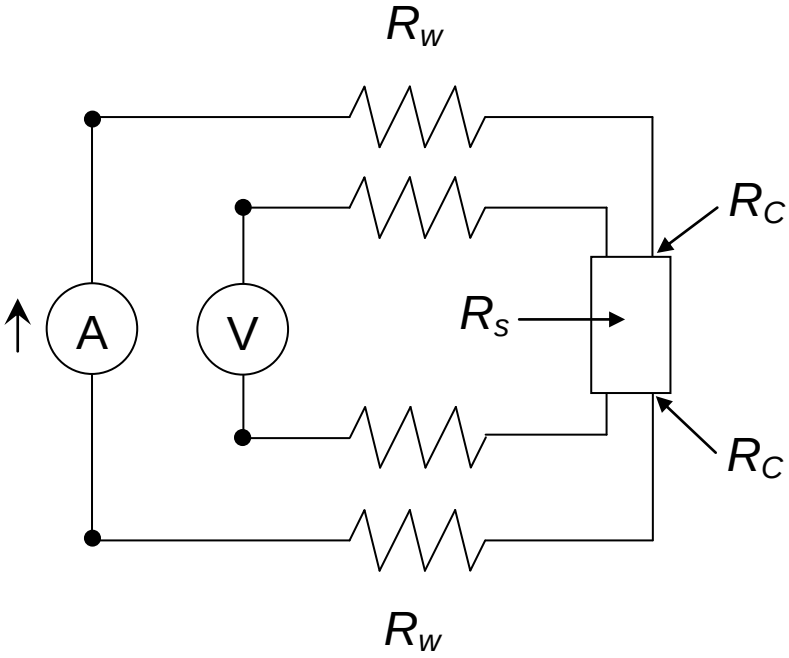

Figure 2.15. Scheme of the principle of work of the four-probe mesuraments.

The four-point probe method provides more accurate measurements of the resistance or the I-V curve than the traditional two-probe method, since the effects introduced by the probe resistance, probe contact resistance and spreading resistance are eliminated. While the four-probe technique is quite simple in principle, there are experimental issues that must be taken in consideration. In particular, the application of a metal to a semiconductor often forms a Schottky diode rather than an Ohmic contact. The samples with very high or very low resistivity need adjustment of the drive current to get reliable results [151].

In this study, the four-probe measurements were conducted on the porous GaN films using a DC voltage and an Agilent 34401A Digital Multimeter in a Peltier cell, thermostated to 295 K in a Faraday cage. As in the two-probe measurements, liquid metal contacts were made using In−Ga eutectic blown into a sphere from a gold metalized short borosilicate capillary tube. Resistivity values were extracted from the I−V curves obtained. These measurements were performed in the Applied Nanoscience Group, University College Cork, Cork (Ireland).

2.5.3 van der Pauw resistivity measurements

The van der Pauw resistivity measurements technique is very popular in the semiconductor industry. Frequently it is difficult to determine accurately the geometry of the sample, what results in unknown current distribution and limits the accuracy of the measured

resistivity. The advantage of the van der Pauw technique is that it allows avoiding problems when the sample geometry is irregular. A typical geometry for Van der Pauw resistivity measurements consist of 4 electrical contacts at the four corners of a roughly square sample (see Figure 2.16). For the samples with arbitrary shape this technique is also applicable. The theoretical foundation of measurements of samples with irregular shapes was developed by L.J. van der Pauw [152]. He demonstrated that the resistivity of a flat sample material of arbitrary shape can be determined without knowing the current pattern. However, the following conditions have to be satisfied:

- the contacts should be located at the edges of the sample.
- the contacts should be sufficiently small.
- the sample is uniformly thick.
- the surface of the sample is simply connected, i.e., the sample does not have isolated holes.

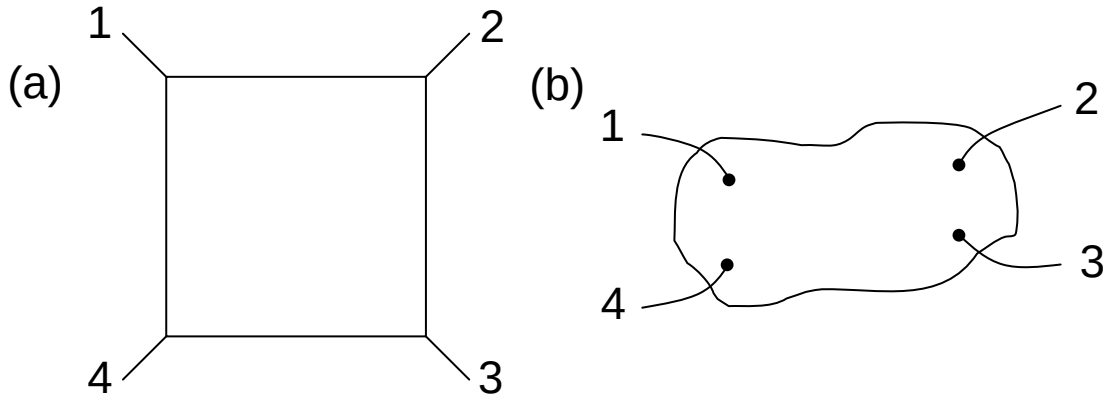

Figure 2.16. Geometry for van der Pauw measurements of 4 electrical contacts at (a) the four corners of a roughly square sample and (b) an arbitrarily shaped sample.

When the aforementioned conditions are fulfilled, the resistivity is calculated through the van der Pauw equation:

$$\exp\left(-\frac{\pi d R_{12,34}}{\rho}\right)+\exp\left(-\frac{\pi d R_{23,41}}{\rho}\right)=1 \qquad \text{(Eq. 2.5)}$$

where d is the thickness of the sample, ρ is the resistivity, $R_{12,34}$ is the resistance defined by dividing the potential difference $V_4 - V_3$ by the current going from contact 1 to 2, and $R_{23,41}$ is the resistance defined by dividing the potential difference $V_4 - V_1$ by the current going from contact 2 to 3.

In general, an explicit expression for the resistivity cannot be obtained from equation 2.5, unless the sample has a symmetrical shape, such as a circle or a square (see Figure 2.16). In this case from equation 2.5 we get:

$$\rho = \frac{\pi d}{\ln 2} R_{12,34} \qquad \text{(Eq. 2.6)}$$

In other cases, the resistivity is given in the form:

$$\rho = \frac{\pi d}{\ln 2} \frac{\left(R_{12,34} + R_{23,41}\right)}{2} f\left(\frac{R_{12,34}}{R_{23,41}}\right) \qquad \text{(Eq. 2.7)}$$

Where *f* is the "correction function" that satisfies the relation:

$$\frac{R_{12,34} - R_{23,41}}{R_{12,34} + R_{23,41}} = \frac{f}{\ln 2} \operatorname{arccosh}\left(\frac{\exp(\ln 2 / f)}{2}\right) \qquad \text{(Eq. 2.8)}$$

The "correction function" *f* is a function only of the resistance ratio $R_{12,34}/R_{23,41}$ and is tabulated for each value.

In this thesis, the resistivity measurements on porous GaN were also made with the van der Pauw technique using liquid metal contacts made of In−Ga eutectic, as explained before. These measurements were performed in the Applied Nanoscience Group, University College Cork, Cork (Ireland).

2.5.4 Capacitance-voltage measurements (C-V)

Capacitance-voltage (C-V) measurements are widely used to determine semiconductor parameters. Using C-V measurements, semiconductor devices, such as field-effect transistors (FETs), III-V compound devices, thin-film-transistor (TFT) displays, photovoltaic cells, photodiodes and other devices can be characterized [153-155]. The C-V technique is based on the fact that the width of the reverse-biased space-charge region depends on the applied voltage. Most often in C-V measurements a metal–semiconductor junction or *p-n* junction is used to create a depletion region, which behaves like a capacitor. The relation between the depletion width and the applied voltage provides quantitative information about the semiconductor parameters, such as its doping profile, the mobile concentrations of majority carriers and the diffusion potential. The C-V measurements can be made at very low frequencies (few mHz) and at high frequencies (either 100 kHz or 1 MHz).

While performing a typical C-V measurement, three regions in the C-V curve can be pointed out (see Figure 2.17): the accumulation region, when the majority of carriers accumulate near the semiconductor surface; the depletion region, when the device starts to deplete and the majority of charge carriers are pushed away from the semiconductor surface; and the inversion region, when minority carriers are generated and dominate near the

semiconductor surface. The minority carriers do not respond to high frequency stimulus and their generation is relatively slow.

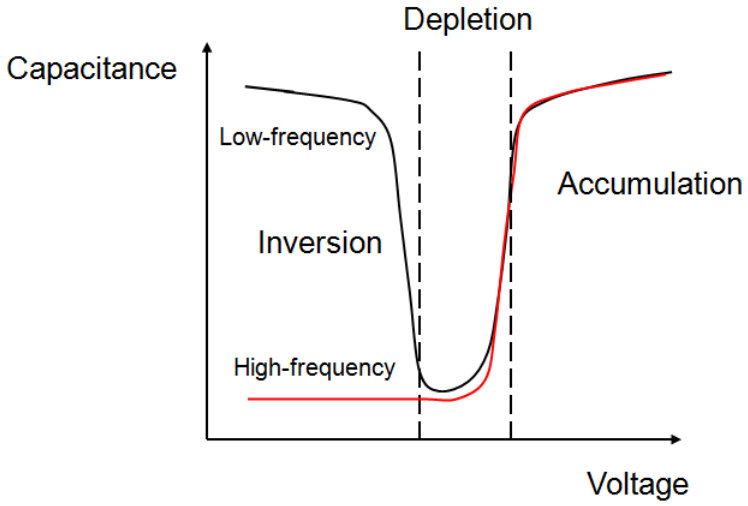

Figure 2.17. A typical curve in C-V measurements.

In this thesis, C-V analysis was performed by scanning the applied potential at a rate of 10 mV s^{-1} with a superimposed AC signal with amplitude of 15 mV at a frequency of 1 MHz using a Agilent 34401A Digital Multimeter to determine the capacitance of porous GaN under depletion conditions and define its donor concentration. Gold contacts were deposited onto porous GaN, that formed a Schottky contact for the measurement. The $1/C^2$ vs. V analysis was made to confirm the type of conductivity and donor concentration of porous GaN. The donor concentration was defined by the slope:

$$N_D = 2C^2V / q\varepsilon\varepsilon_0 \qquad \text{(Eq. 2.9)}$$

where ε = 8.9 is the dielectric constant for GaN and q is the charge of the electron [156].

The Schottky barrier height was determined from the following equation:

$$\varphi^0_{B,n} = eV_{bi} + eV_n + kT \qquad \text{(Eq. 2.10)}$$

where eV_{bi} is the built-in voltage and eV_n is the difference between the Fermi level and the conduction band minimum for a neutral semiconductor.

The C-V measurements were performed in the Applied Nanoscience Group, University College Cork, Cork (Ireland).

2.6 Luminescence characterization

Luminescence is the spontaneous emission of light from exited electronic states of the material. Prior to the emission of light the process of excitation occurs, which may be

produced by a variety of stimulations. When the excitation is achieved by the absorption of light it is called photoluminescence (PL), and when it is achieved by stimulation with an electron beam it is called cathodoluminescence (CL). Both techniques have been used in this thesis.

2.6.1 Photoluminescence (PL)

Photoluminescence (PL) spectroscopy is a non-contact and nondestructive method of analysis of the electronic structure and properties of materials. In PL, light is directed onto the sample where it is absorbed and where a process of excitation can occur. After relaxation, the emitted luminescence is collected by a lens and passed through an optical monochromator or spectrometer onto a photodetector. Absorption of photons by a molecule excites it from the electronic ground state to a higher energy electronic state. Photoluminescence occurs when the molecule returns from the excited state to the electronic ground state by emission of a photon. In a semiconductor, the electron after excitation passes from the valence band to the conduction band, leaving a hole in the valence band. The excited electron and hole will relax very rapidly to the lowest energy states within their bands by emitting phonons. When the electron finally arrives at the bottom of the conduction band, the electron-hole pair can recombine radiatively [157].

In this study, the PL measurements of luminescent nanoparticles introduced into porous GaN were carried out by using a fluorescence spectrophotometer from Photon Technology International Inc. with a 150 W Xenon lamp used as the excitation light source at room temperature. Both excitation and emission spectra were recorded in a 90º geometry and taking measurements every 1 nm at a scanning rate of 1 $nm \cdot s^{-1}$. Figure 2.18 shows an scheme of the fluorescence spectrophotometer which is available in the laboratories of the Nephos group of the University Rovira i Virgili.

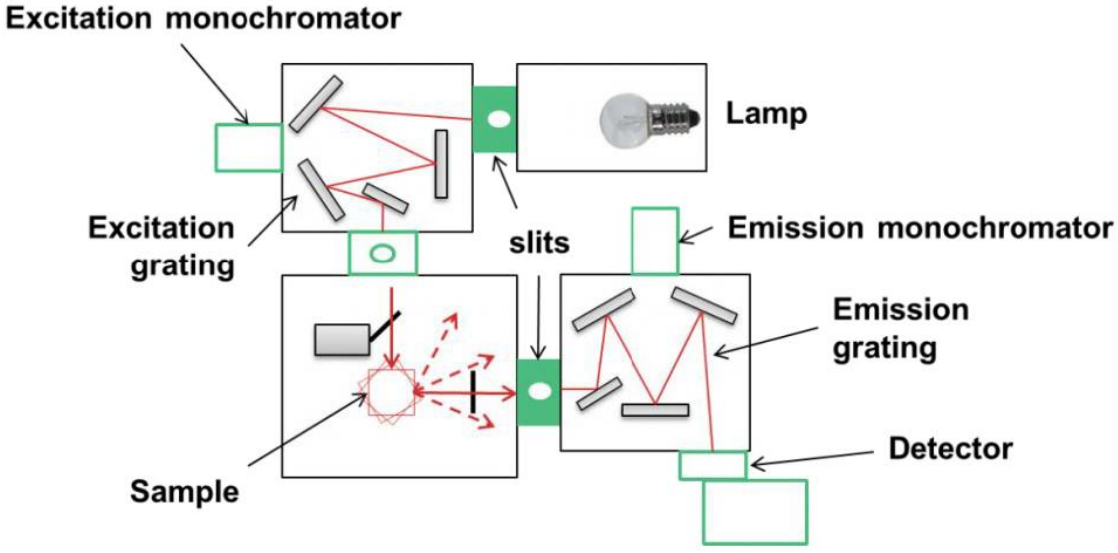

Figure 2.18. Schematic view of the fluorescence spectrophotometer from Photon Technology International Inc used to record the PL from luminescent nanoparticles embedded in porous GaN.

The PL of porous GaN was obtained after excitation at 244 nm using a doubled cw Ar-ion laser with a power density of 2 W/cm^2. The PL spectra were acquired using a Horiba iHR320 spectrometer equipped with a Synapse CCD matrix. Samples were placed in the evacuated chamber of a Janis closed-cycle helium cryostat for PL measurements at different temperatures (see Figure 2.19). This PL setup is available at Tyndall National Institute, Cork (Ireland).

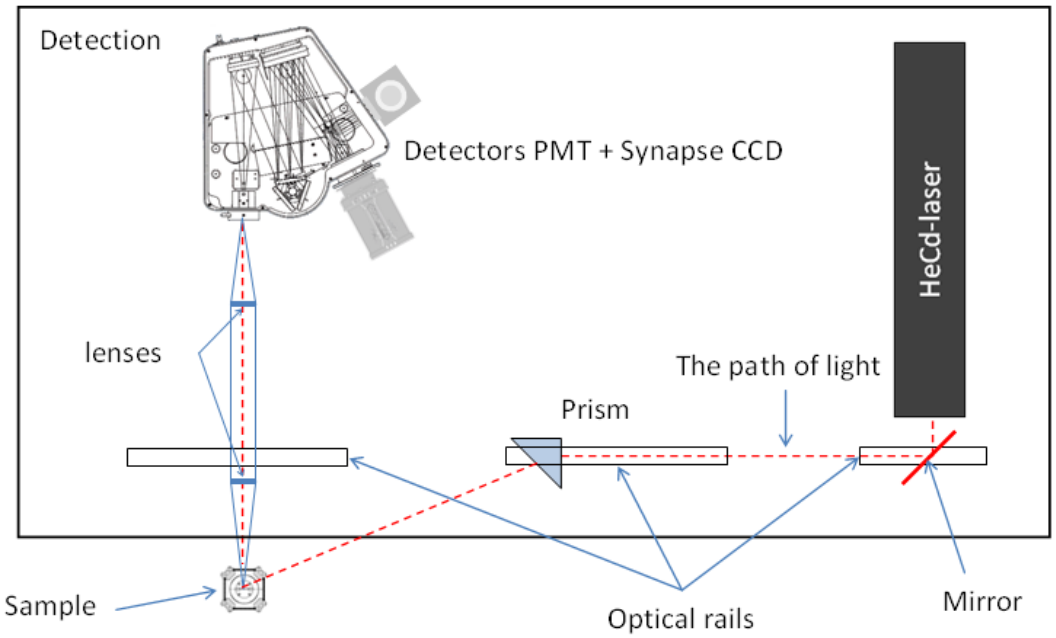

Figure 2.19. Schematic view of the experimental PL set-up used in this study to record the PL of porous GaN.

2.6.2 Cathodoluminescence (CL)

Cathodoluminescence (CL) is the light emission phenomena based on electron beam excitation of a luminescent material. CL is one of the various processes that are created during irradiation of the material with an electron beam. This technique is similar to photoluminescence, but instead of photons, electrons are used to excite the sample. Thus, CL occurs when a high energy electron beam strikes the sample and it results in the promotion of electrons from the electronic ground state to a higher electronic state. When the sample is a semiconductor, the electron can be promoted from the valence band into the conduction band, leaving a hole in the valence band. When the electron returns to the valence band, it is possible the emission of a photon. The energy of those emitted photons is typically in the range from 0.3 to 6 eV, covering wavelengths from the UV to the near-infrared, depending on the detection system. The energy (color) and the probability of emission of the photon depend on the material and its purity.

CL is a powerful method for investigations in geology, mineralogy and material science. CL is used to study internal structures of semiconductors, rocks, ceramics, glass, etc., in order

to get information on the composition, growth and quality of the material. A great advantage of the CL technique is that it can be used coupled to a scanning electron microscope (SEM), what enables the correlation of the optical properties (via CL) with the surface morphology (via secondary electrons) from a localized area of the sample at the nanometer scale [158].

Here, room temperature cathodoluminescence (CL) imaging and spectroscopy of porous GaN microparticles were performed in a field emission scanning electron microscope (Zeiss Supra 55) operating at 4 keV and 200 pA using a Gatan (Pleasanton, CA, USA) MonoCL 2 system and a Hamamatsu (Hamamatsu City, Japan) photomultiplier tube (R2228) over a scanned area of 4,000 μm^2. All spectra were corrected for the monochromator and detector response and normalized to maximum intensity. These CL measurements were performed in Université de Sherbrooke, Sherbrooke, Québec (Canada). We also used a field emission scanning electron microscope (Carl Zeiss-LEO 1500) operating at 10 kV coupled to a XiCLOne mono-CL2 system from Gatan with detection being done with a charge-coupled device camera, available in the Departamento de Física de la Materia Condensada, Universidad de Valladolid, Valladolid (Spain).

Chapter 3

Deposition of porous GaN on Si

Silicon is prevailing as the semiconductor of reference in electronics, because it has superior physical and technological properties compared to many other semiconductor materials. Also Si can be obtained at low costs, thus, current microelectronic technology fabrication techniques are totally dependent and adapted to Si. Deposition of high quality porous GaN on Si with controlled parameters, such as degree of porosity, crystallographic orientation, type of conductivity, etc., is highly desired and the possibility of using the existing silicon-device integration base for light-emitting diodes (LED) and also other optoelectronic development is very attractive.

This chapter presents the results obtained on the study of the deposition of porous GaN on Si by CVD through the direct chemical reaction of metallic Ga and NH_3 gas and the properties of the obtained porous GaN structures. The first part of the chapter presents the study of the growth conditions of porous GaN particles on Si substrates by CVD. The second part of the chapter discusses the mechanism of growth and the structure of porous GaN. The third part describes the electrical characterization of porous GaN. The fourth part of this chapter shows the CL characterization of porous GaN. And finally, the last part presents experiments of growth of porous GaN guided by electric fields and the growth of porous GaN on an orderly patterned SiO_2 layer thermally grown on Si(100) substrate with the aim of crystallographically orienting the GaN porous particles.

3.1 Crystal growth by chemical vapor deposition: influence of the chemical reaction parameters on the morphology and porosity of GaN

The chemical reaction between Ga and NH_3 described in Chapter 2 depends on several parameters, including the temperature at which the reaction is performed, the III/V precursors ratio, the pressure at which the system is kept while the growth process develops, the time at which the chemical reaction is maintained to produce porous GaN, the shape of the crucible or Ga holder used and the catalyst with which the Si substrates are coated. In this section we analyzed in detail the effect of all these parameters on the morphology and porosity degree of the GaN particles obtained.

The effect of each parameter of the chemical reaction on the size and morphology of porous GaN particles is studied by maintaining the rest of the parameters affecting this reaction constant. Firstly, we analyzed the effect of the temperature in the range from 1183 K to 1213 K. The effect of the III/V precursors ratio was analyzed by changing the NH_3 gas flow rate and the quantity of the Ga metal precursor. A series of experiments were performed at 10, 15 and 20 Torr total pressures and at the reaction times of 30, 45, 60 and 120 min. Quartz crucibles or Ga holders with three different shapes were investigated: a flat plate, half of a cylindrical tube and a concave crucible. As substrates we used silicon wafers with (100) and (111) crystallographic orientations. As catalysts, $Ni(NO_3)_2$ was used, where the catalyst was deposited on the surface of the Si substrates by spreading several drops of a solution of $Ni(NO_3)_2$ 0.01 M in ethanol, as well as films, 20 nm thick, of Au, Pt, Ti, Ni and W deposited on the substrates by RF sputtering. Thus, we found the optimum conditions for porous GaN fabrication on Si substrates with a high degree of porosity and a uniform coverage of the substrate.

3.1.1 Effect of temperature

Porous GaN was synthesized on Si(100) at temperatures ranging from 1183 K to 1213 K, keeping constant the flow rate of NH_3 at 75 sccm, the time of reaction at 60 min and the pressure of the system at 15 Torr. In all experiments the solution of $Ni(NO_3)_2$ in ethanol was used as catalyst. SEM pictures, shown in Figure 3.1, show that the obtained particles at 1203 K and 1213 K are quite homogeneous in morphology, consisting on a pyramidal shape similar to a hexagonal pyramid with smooth lateral faces. The pores are only observed on the basal plane of the micron-size particles. This agrees with porous GaN particles obtained on BN [135]. The dimensions of these particles along the *c*-crystallographic direction ranged between 1 and 2 μm. The micron-size particles obtained at 1183 K and 1193 K (see Figure 3.1a and 3.1b) do not present the same homogeneity in morphology and have a lower quantity of pores. The particles with the highest porosity were obtained at 1203 K, as can be seen in Figure 3.1c. The pores have diameters smaller than 50 nm. Thus, the temperature that we choose for the experiments of growth of porous GaN is 1203 K.

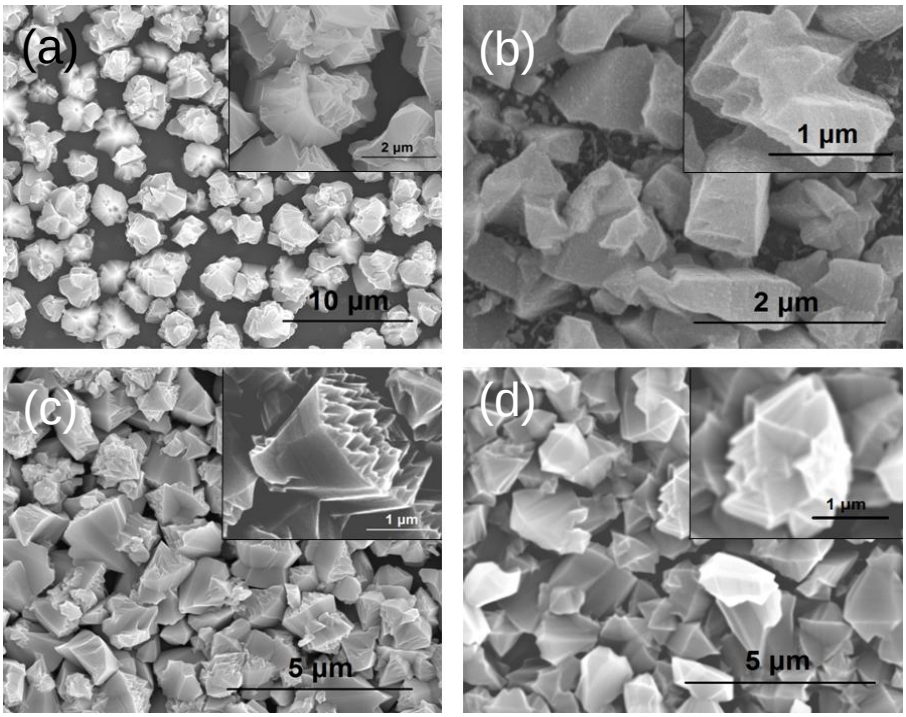

Figure 3.1. SEM micrographs of porous GaN grown on Si(100) using $Ni(NO_3)_2$ as catalyst at: (a) 1183 K, (b) 1193 K, (c) 1203 K and (d) 1213 K.

3.1.2 Effect of III/V precursors ratio

We studied the effect of the III/V precursors ratio on morphology and porosity of the samples by varying the NH_3 flow rate, while keeping constant the quantity of Ga. After choosing the optimum NH_3 flow rate for the CVD reaction, we performed a series of experiments with different quantities of Ga, while keeping the NH_3 flow rate constant.

Experiments at ammonia flow rates of 65, 75, and 85 sccm with 0.5 g of Ga were performed, corresponding to 0.0412, 0.0357 and 0.0315 III/V precursor mol ratios, respectively. The temperature of the reaction was kept at 1203 K and the total pressure of the system was kept at 15 Torr during the time of the reaction. As catalyst, $Ni(NO_3)_2$ was used. At a NH_3 flow rate of 65 sccm, we obtained porous GaN particles with diameters ranging between 2 and 3 µm and a low number of nanopores with sizes ~100 nm, as it can be seen in Figure 3.2a. At the flow rate of 75 sccm the particles have smaller diameters, ranging between 1 and 2 µm, but the density of the nanopores is much higher, with diameters smaller than 50 nm (Figure 3.2b). Figure 3.2c shows the particles synthesized at a flow rate of 85 sccm. These particles have a similar size to the particles synthesized at 65 sccm, but the density of nanopores is lower. In all cases we obtained a high and homogeneous coverage of the substrate. Therefore, the optimum NH_3 flow rate for the future experiments is 75 sccm with 0.5 g of Ga, that corresponds to a III/V precursors mol ratio of 0.0357.

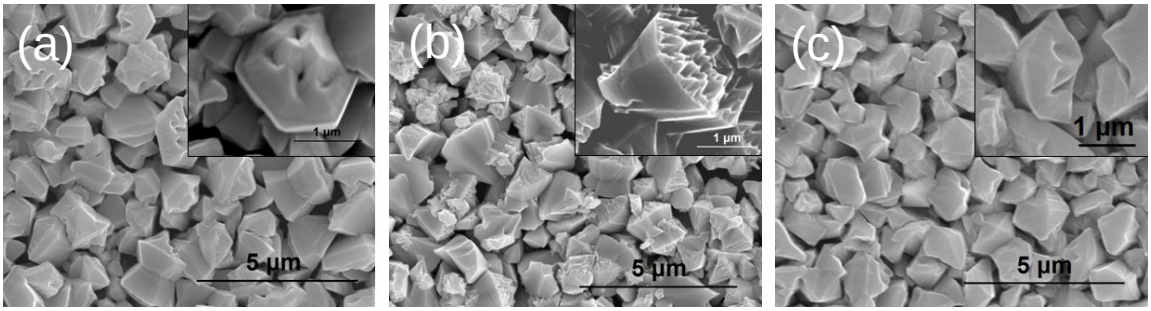

Figure 3.2. SEM micrographs of porous GaN grown on Si (100) at NH_3 flow rates of: (a) 65 sccm, (b) 75 sccm and (c) 85 sccm.

Experiments with different amounts of Ga were carried out to analyze its effect on the morphology and the coverage of the substrate with porous GaN particles, as described in Paper I. Three sets of experiments were carried out using 0.2 g, 0.4 g and 0.6 g of Ga while keeping constant the other reaction parameters, which represented 0.0143, 0.0286 and 0.0428 III/V mol ratios, respectively. Figure 3.3 shows SEM pictures of the GaN particles grown using different amounts of Ga. When 0.2 g of Ga were used (see Figure 3.3a) a low degree of coverage of the substrate was observed. This was attributed to the low concentration of Ga evaporated and deposited on the substrate forming a small number of nucleus along the substrate. This is confirmed by the fact that particles are bigger in diameter, around 5-6 µm. A higher coverage of nanoporous GaN particles could be seen when 0.4 g of Ga were used (see Figure 3.3b), and the particle diameter is lower, of around 2 µm. This was attributed to the evaporation of a higher quantity of Ga and the formation of a higher number of Ga-metallic catalyst nucleus which lead to a higher coverage of the substrate with smaller nanoporous GaN particles. Finally, in Figure 3.3c we can see a SEM image of GaN particles grown using 0.6 g of Ga. A similar particles density and size was observed when compared to the experiment using 0.4 g of Ga. This would indicate that it exists a quantity of Ga above which no more GaN particles are formed, probably related to the III/V ratio used. Interferometric microscope measurements of the thickness of the porous GaN layer of the sample grown using 0.2 g of Ga confirmed the presence of isolated nucleuses of porous GaN particles with heights around 4 µm, similar to the size of the particles observed by the SEM images. A quite uniform layer is seen when 0.4 g of Ga were used with a mean thickness of the porous film of 1.10 ± 0.15 µm. Finally, in the sample grown using 0.6 g of Ga, we observed a tendency to have higher heights of the porous film towards the center of the sample. The mean thickness value is similar to that obtained with 0.4 g of Ga, 1.19 ± 0.35 µm. This would confirm that, above 0.4 g of Ga the deposition of GaN is limited. Table 3.1 summarizes the results obtained in those experiments. Thus, for the future growth of porous GaN layers on Si optimum conditions are 75 sccm of NH_3 flow rate and 0.4-0.5 g of Ga metal precursor, which corresponds to III/V precursor mol ratios in the range 0.0286-0.0357.

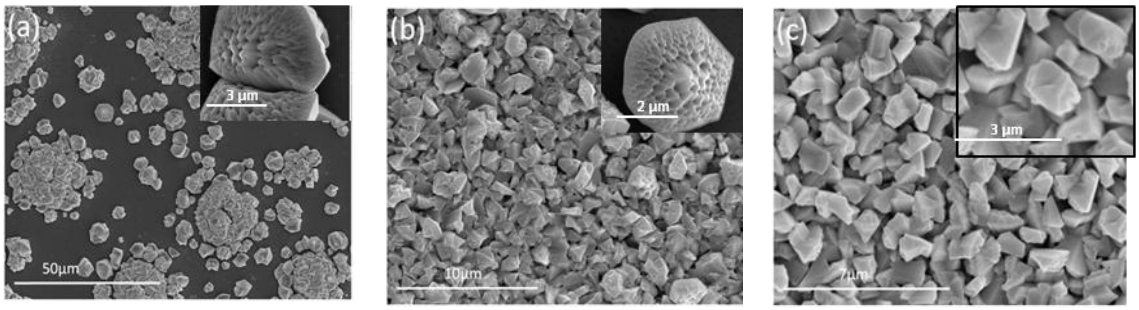

Figure 3.3. SEM pictures of the nanoporous particles obtained using different Ga quantities (a) 0.2 g, (b) 0.4 g and (c) 0.6 g (reproduction of Figure 4 in Paper I).

Table 3.1. Effect of III/V precursor ratio on porosity and morphology of porous GaN particles.

III/V ratio	Particles morphology	Particles size (µm)	Pores size (nm)	Number of pores
0.0143	hexagonal	5-6	~ 50	high
0.0286	hexagonal	2	~ 50	high
0.0315	irregular	2-3	~ 100	low
0.0357	hexagonal	1-2	~ 50	high
0.0412	hexagonal	2-3	~ 100	low
0.0428	mostly hexagonal	1-2	~ 50-100	average

3.1.3 Effect of the pressure of the CVD reactor

Three experiments were performed at total pressures of the system of 10, 15 and 20 Torr, while the temperature of the reaction and the flow rate of ammonia were kept at 1203 K and 75 sccm, respectively, to analyze the effect of the pressure on the morphology, sizes and porosity of the GaN particles. The size of the obtained particles is similar in all experiments and ranging between 1.5 and 2 µm (see Figure 3.4). The highest degree of porosity was observed for the particles synthesized at 15 Torr. The particles synthesized at 10 and 20 Torr show a markedly reduced number of pores. Thus, the rest of the experiments will be performed at a total pressure of the CVD reactor of 15 Torr.

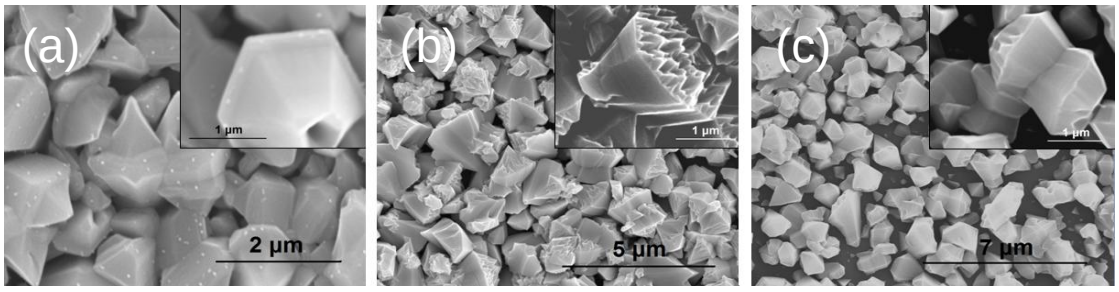

Figure 3.4. SEM micrographs of porous GaN grown on Si(100) substrates at total pressures of the CVD reactor of: (a) 10 Torr, (b) 15 Torr and (c) 20 Torr.

3.1.4 Effect of the reaction time

Experiments to analyze the influence of the reaction time on the shape and porosity of the GaN particles were performed, as described in Paper I. The reaction times selected were 30, 45, 60 and 120 min. The first time duration for the chemical reaction chosen is related to a particular moment in the reaction, when the leaning of the crucible using a half cylindrical tube crucible occurred, as can be seen in Figure 2 in Paper I, due to the wetting of both, the crucible and the liner because of the spreading of Ga at 30 min after the reactor reached 1203K. The second one is the time when we observed the scalation of the material covering the crucible, identified later as GaN by X-ray diffraction, 45 min after the reactor reached 1203K, as can also be seen in Figure 2 in Paper I. We also have explored one additional reaction time above 60 min, which is the time used up to now to produce these nanoporous GaN particles [135], to analyze if the chemical reaction continued after we observed the scalation of GaN on the crucible.

We observed that the reaction time has an important effect on the coverage of the substrate with porous GaN particles, as can be seen in Figure 3.5. We observed that the density of particles increases with time until 60 min, above which no additional particles nucleated and the particles density remained constant. Hexagonal pyramidal porous particles were obtained in all cases; however, as we increased the total reaction time the morphology of the particles seems to fade away. Also, at long times, smaller particles can be seen covering the substrate, which might form by decomposition and further nucleation at expenses of the big particles, which would explain the deformation observed. It seems that the particles obtained after 30 min reaction time (Figure 3.5a and 3.5b) have a bigger amount of pores, and those seem to be more superficial. These particles seem also to show a smaller number of ridges, formed by the coalescence of the neighbouring pores. These ridges are more apparent at the central part of the particles as the reaction time is extended. Also, the bigger contrast observed in the pores, seem to indicate that those pores are deeper. When the reaction time of the GaN synthesis is 120 min the porosity is less evident (see Figure 3.6g and 3.6h), which would corroborate the evaporation of the material to form the smaller particles observed in the background.

The deposition time has an important effect on the coverage of the substrate with nanoporous GaN particles, as can be seen in Figure 3.5k, while the particle size is more or less constant. Figure 3.5k shows the evolution of the thickness of the nanoporous GaN film with deposition time. Even though the sample grown during 30 min shows an average thickness value of 1.61 ± 0.11 μm it is mainly due to isolated nucleuses that are encountered along the substrate. A similar fact occurs with the sample grown at 45 min, which shows a mean thickness of 2.08 ± 0.28 μm but the layer is not covering totally the substrate. When the deposition time is set for 60 min we have a uniform layer 1.1 ± 0.14 μm thick. Finally, the interferometric measurements of the sample grown at 120 min show a decrease of the layer thickness. In order to get a uniform and dense coverage by a layer of porous GaN microparticles on Si, we will use 60 min of the reaction time for the future experiments.

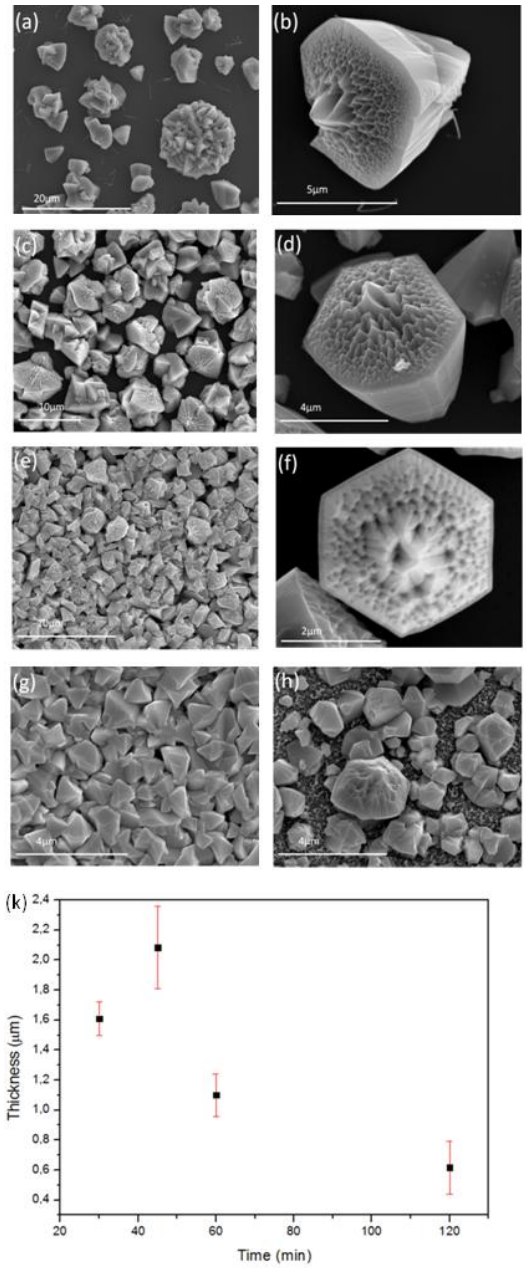

Figure 3.5. SEM pictures of the particles obtained at (a,b) 30 min, (c,d) 45,(e,f) 60, and (g,h) 120 min reaction times (k). Evolution of the thickness of the porous GaN layers with deposition time (reproduction from Figure 5 in Paper I).

3.1.5 Effect of the shape of the gallium holder

A set of experiments with several holders for Ga with different shapes were performed to analyze how the shape of the crucible affected the spreading of the Ga droplet introduced at the beginning of the experiment, and how this affected to the final shape and porosity of the particles obtained, as it is described in Paper I. Three different Ga holders were used: (a) a quartz flat plate, which does not limit the spreading of the Ga dropet, (b) half of a quartz cylindrical tube, which limits the spreading of the Ga droplet along two directions and (c) a

quartz concave crucible, which limits the spreading of the Ga droplet along all directions in the plate.

SEM pictures of the GaN samples synthesized, using a flat plate, half of a cylindrical tube and a concave crucibles on Si(100) substrates covered with Ni catalyst are shown in Figure 3.6. In all cases, the reaction temperature allowed to ensure the total spreading of the Ga droplet, generating the maximum extension of the surface of metallic Ga to favour the evaporation of this precursor. Similar particles were obtained when using a flat plate or a half cylindrical tube as Ga holders, with sizes between 1-3 μm, and a similar degree of porosity (see Figures 3.6a and 3.6b). The particles obtained using the concave crucible (see Figure 3.6c) are bigger in size (around 4 μm), and the pores seem to be smaller in diameter and do not form ridges, giving a more rough aspect to the surface of the particles.

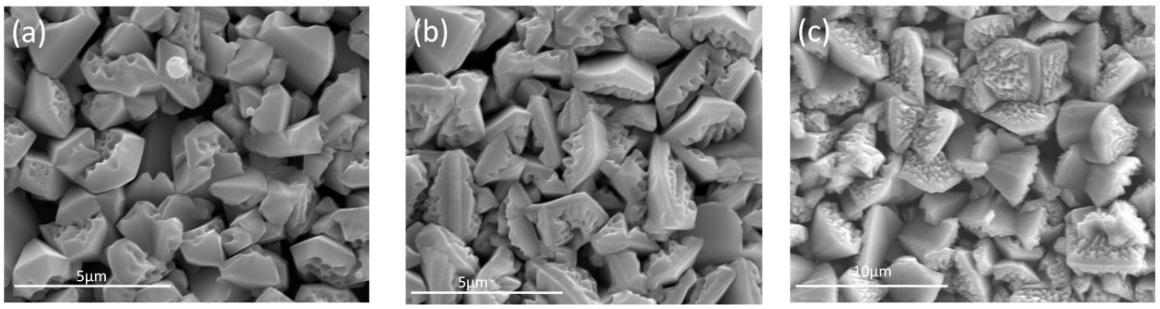

Figure 3.6. SEM pictures of the porous particles obtained using different Ga holders: (a) flat plate, (b) half cylindrical tube, and (c) concave crucible (reproduction from Figure 3 in Paper I).

Depending on the shape of the Ga holder used, the thickness of the layer seems not to be uniform along the substrate. The sample grown using a flat plate had the maximum ununiformity in thickness with an average value of 2.53 ±1.73 μm. The sample grown using a half cylindrical tube has the smallest thickness, 1.1 ±0.14 μm, but with a higher uniformity. Finally, the highest thickness value was obtained in the sample grown using the concave crucible, with a mean value of 3.61 ± 0.87 μm. According to these measurements, despite the thickness of the layer obtained using a half cylindrical tube was the smallest, it was very uniform, what is a necessary condition for the fabrication of functional devices based on these nanoporous GaN particles. Thus, in the rest of the experiments, we used this kind of Ga holder.

3.1.6 Effect of catalyst

Different catalysts with which we coated Si(100) and Si(111) substrates were tested to evaluate their effect on the final morphology and degree of porosity of the GaN particles produced on them: Ni, introduced as $Ni(NO_3)_2$ dissolved in ethanol, and 20 nm thick films of Ni, Au, Pt, and Ti deposited by RF sputtering, as discussed in Paper I. We tested also Si(111) substrates since it has been reported that (0001) oriented GaN films can be deposited on these substrates [159]. Since this is also the direction along which the pores are aligned, if we can

obtain a way to orient the porous GaN particles, the pores will be oriented at the same time, being perpendicular to the surface.

SEM pictures of as-grown GaN on Si(100) substrates demonstrate that by using all catalysts (except Ti) GaN appears in the form of microsized nanoporous particles (see Figure 3.7). The biggest particles were obtained using $Ni(NO_3)_2$, while using Pt and Au we obtain smaller particles very homogenous in size. The highest level of porosity was obtained, however, in the GaN particles synthesized using $Ni(NO_3)_2$.

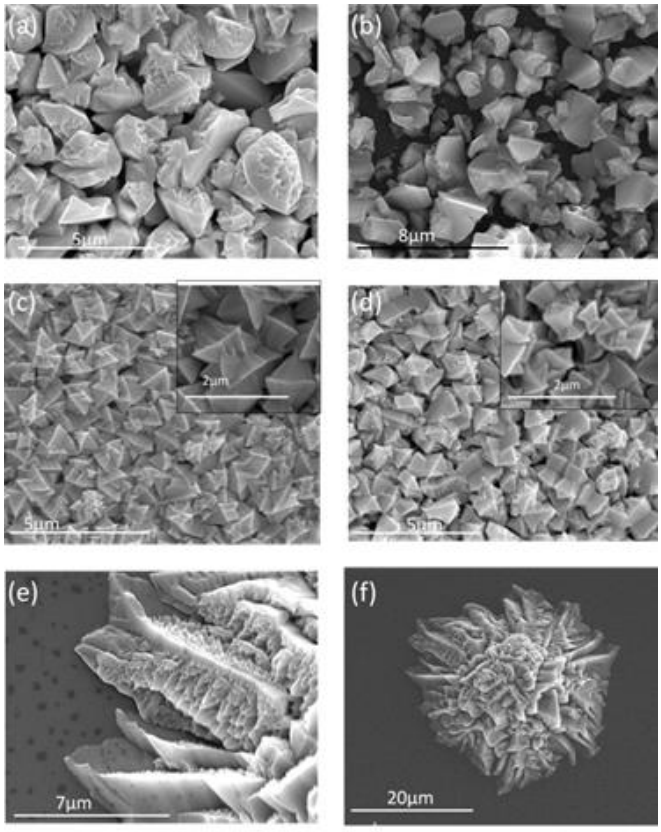

Figure 3.7. SEM pictures of nanoporous GaN grown on Si(100) with the use of different catalysts: (a) $Ni(NO_3)_2$, (b) Ni, (c) Au, (d) Pt, (e) and (f) Ti (partial reproduction from Figure 6 in Paper I).

It is curious to notice that Ni, introduced as $Ni(NO_3)_2$ or directly as metallic Ni has a different effect on the morphology and porosity degree of the particles, despite $Ni(NO_3)_2$ is reduced to Ni under the reaction conditions. The different effect observed might be attributed to the distribution of the catalyst on the surface of the substrate. Agglomeration of big particles with high porosity were obtained using $Ni(NO_3)_2$ as can be seen in Figure 3.7a. As can be seen in Figure 3.7b particles grown on a continuous Ni film have an irregular shape and a low degree of porosity. Porous GaN grown using Pt and Au as catalysts shows a uniform coverage of the substrate with GaN particles (Figure 3.7c and 3.7d). These polycrystalline films show an interesting dual porosity since they present interparticle and intraparticle pororosity, as can be seen in the scheme shown in Figure 1 in Paper II. However, the level of intraparticle porosity is higher when Pt is used. Porous GaN grown on Ti thin films have the shape of a sea star with a high level of porosity. In this case it seems that GaN

starts growing as an epitaxial layer on the substrate with a later growth of nanoporous GaN particles on the top of it (see Figure 3.7e and 3.7f).

GaN grown on Si(111) substrates coated with different catalyst appears in the form of micronsized nanoporous particles with a mean particle size of 2-5 μm (see Figure 3.8) The lowest degree of porosity was obtained when tungsten was used as catalyst (see Figure 3.8d). Also, some nanowires were observed together with the porous GaN particles. They are more evident, when Au and Pt were used as catalyst (see insets of Figures 3.8a and 3.8b). When Ti and W were used as catalyst, nanowires are observed at the edges of the area of the sample where porous GaN is deposited, but they disappear as we shift to the centre of the sample (see insets of Figures 3.8 (c-d). If we compare the particles obtained on Si(100) and Si(111) substrates coated with the same catalyst, we observe that the GaN particles obtained on Si(111) substrates tend to be more irregular in shape. According to these images, it seems that the combination of the substrate and the catalyst play a big role in the morphology of the particles.

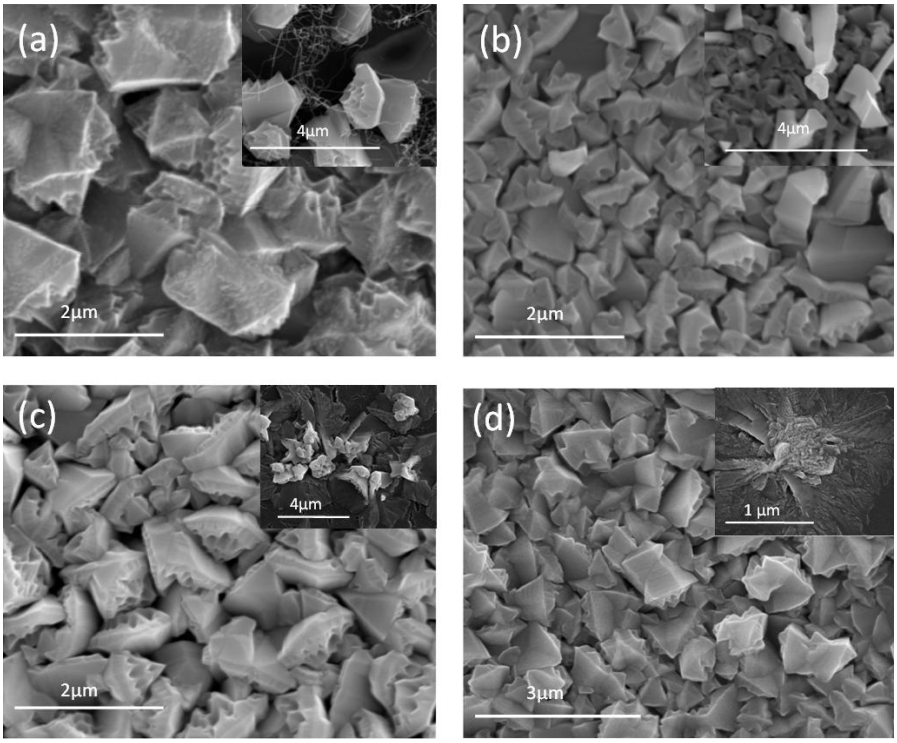

Figure 3.8. SEM images of the porous GaN particles grown on Si(111) coated with different catalysts: (a) Au, (b) Pt, (c) Ti, and (d) W (partial reproduction from Figure 8 in Paper I).

Optimized CVD conditions

After studying the conditions of the chemical reaction, it can be concluded that the optimum conditions for the synthesis of porous GaN on Si substrates are shown in Table 3.2.

Table 3.2. Optimized CVD conditions

Temperature of the reaction	1203 K
NH_3 flow rate	75 sccm
Quantity of Ga	0.4-0.5g
III/V precursor mol ratio	0.0286-0.0357
Total pressure of the CVD chamber	15 Torr
Time of the reaction	60 min
Shape of Ga holder	Half of a cylindrical tube
Catalyst	It can be selected depending on future application

3.1.7 Effect of thermal annealing

The porous GaN we grew on Si(100) substrates using the optimized conditions was later annealed at a temperature higher than the temperature of synthesis (1273 K) in vacuum in order to analyze its thermal stability and possible morphological evolution. Figure 3.9 shows SEM images of the resulting porous GaN particles after annealing. The porous structure on the basal plane of GaN microparticles is degraded due to the thermal decomposition of GaN. A similar degradation was also observed on the smooth lateral faces of the microparticles, although not as intense as in the case of the basal planes, indicating that the porous basal face is more reactive than the rest of the particle.

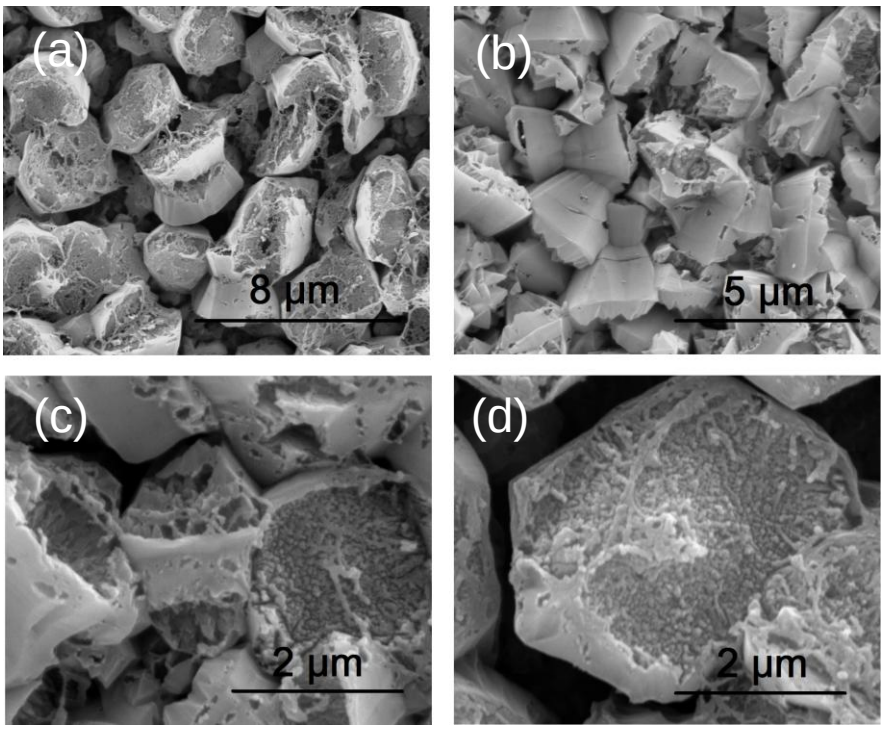

Figure 3.9. SEM images of porous GaN microparticles annealed at 1273 K in vacuum.

3.2 Structural characterization: mechanism of growth

To know the crystal structure of porous GaN, XRD analysis of the samples deposited on Si(100) substrates coated with different catalysts was performed. XRD patterns for the nanoporous GaN synthesized using $Ni(NO_3)_2$ dissolved in ethanol and a Ni continuous film are shown in Figure 3.10. For the nanoporous particles prepared with $Ni(NO_3)_2$ all peaks on the XRD pattern matched the hexagonal wurtzite GaN structure (JCPDS database, pattern (00-0052-0792)). The sharp diffraction peaks also reveal that the nanoporous GaN have a good-crystalline quality. When a Ni continuous film was used, the hexagonal wurtzite GaN structure was also formed, but also another crystalline structure was detected, which corresponds to α-silicon nitride (JCPDS database, pattern (01-0071-0570)). The formation of the silicon nitride on the surface of the substrate was possible due to the reaction between ammonia and the silicon substrate, accelerated by the metallic catalyst. Also, we observed that the (0002), $(10\bar{1}2)$ and $(10\bar{1}3)$ peaks show much less intensity than expected. However, the Debye rings show a quite homogenous distribution of intensity (see Figure 3.10d). Thus, no apparent texturation seems to be present. In both cases the peaks from the substrate were not observed, since we worked under conditions to avoid their appearance, to avoid damages in the X-ray detector.

Porous GaN grown on Si substrates coated with Ti thin films seems to be textured. This texturation of the film, induced by the catalyst, is confirmed by the XRD pattern recorded for this sample and shown in Figure 3.11. The anisotropic distribution of intensity in the Debye rings observed with the GADDS detector (Figure 3.11b) and the different ratio of the intensity of the diffraction peaks when compared to the reference XRD pattern for GaN (00-050-0792) (see Figure 3.11a), reveal a texturation of the sample, although it is not easy to establish which is the preferential orientation of the particles, from the data obtained. This is more evident when we compare this XRD pattern with that recorded for the porous particles obtained on $Ni(NO_3)_2$ (see Figure 3.10a).

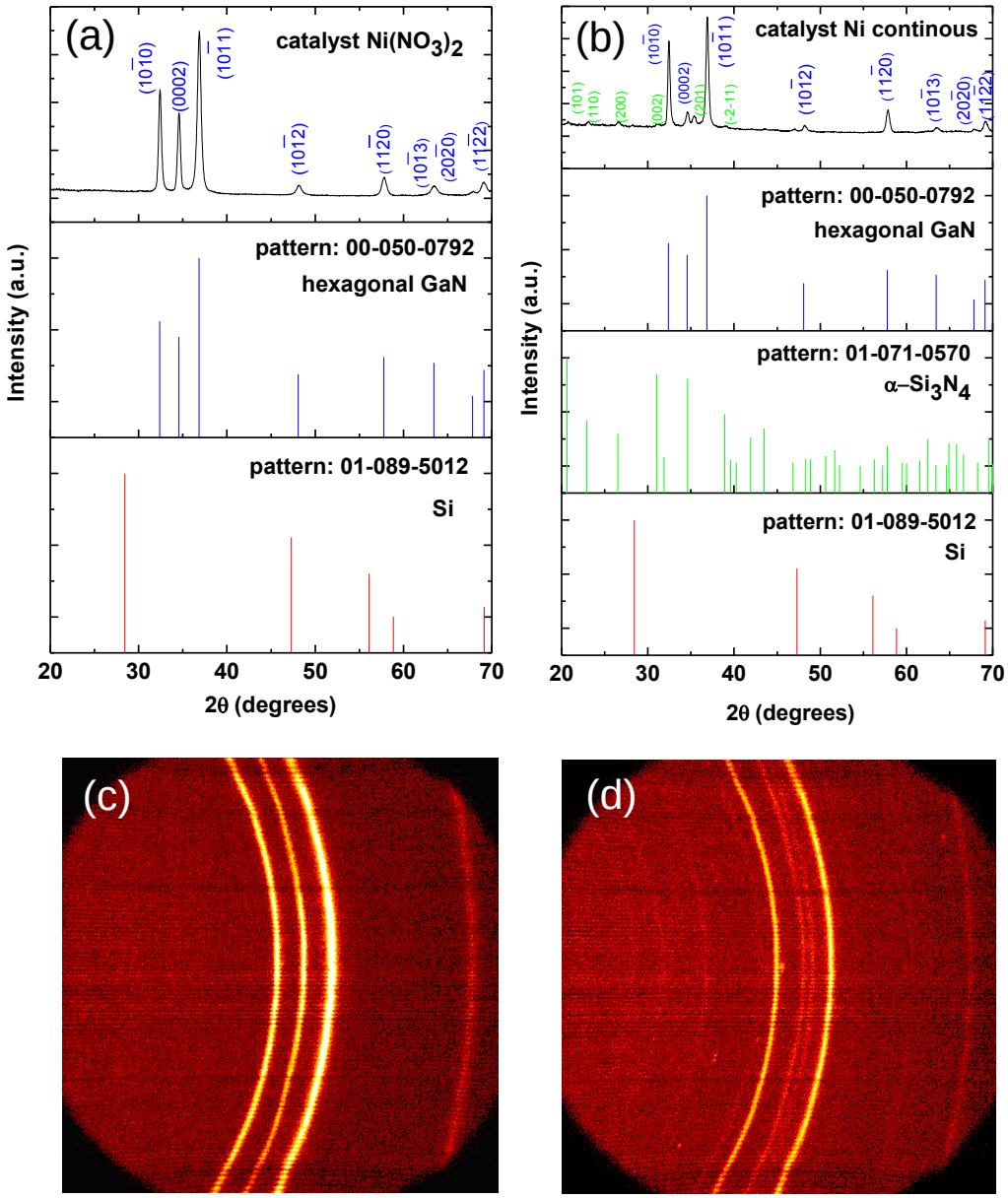

Figure 3.10. XRD patterns for nanoporous GaN on Si(100) substrates synthesized using (a) $Ni(NO_3)_2$ dissolved in ethanol and (b) Ni as catalysts and corresponding Debye rings (c) and (d). Reference patterns for hexagonal GaN (00-050-0792), Si (01-089-5012) and α-Si_3N_4 (01-0071-0570) are included for a better interpretation of XRD patterns presented.

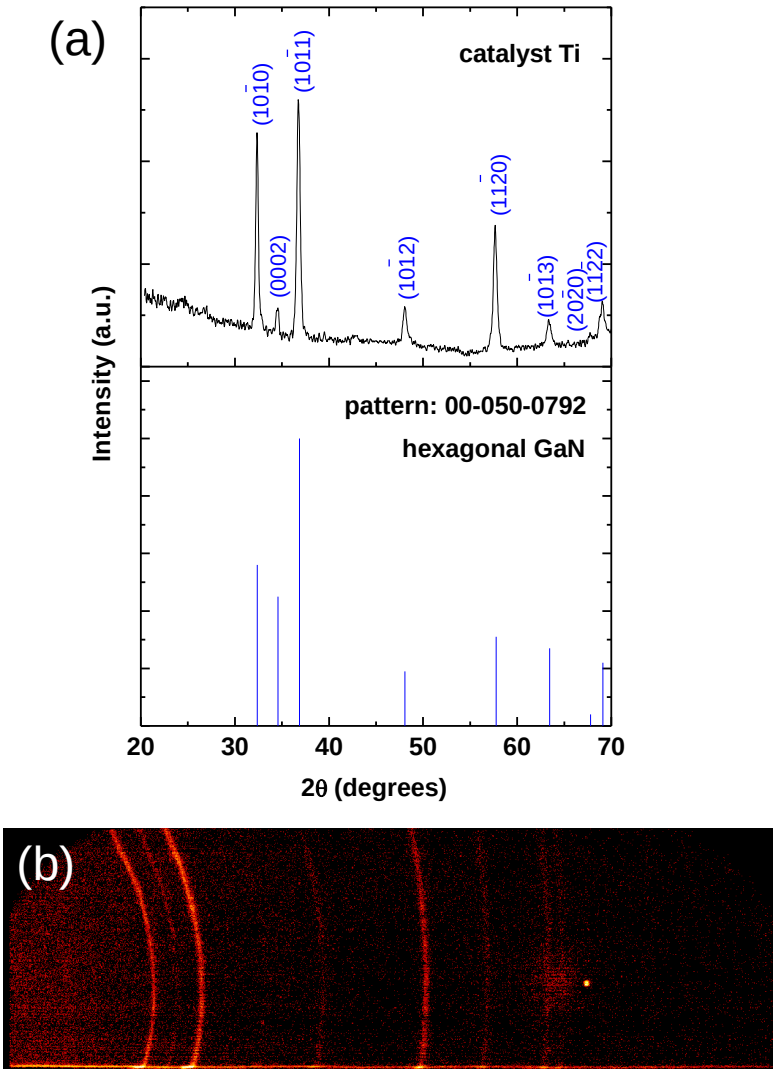

Figure 3.11. X-ray diffraction pattern of porous GaN obtained on Si(100) substrates coated with Ti. (a) Diffraction pattern and (b) Debye rings recorded for the sample. The reference pattern for hexagonal GaN (00-050-0792) is included for comparison.

The XRD patterns of the crystalline structure of the porous GaN particles deposited on Si substrates coated with Au and Pt are shown in Figure 3.12a and 3.12c. As described in Paper II and III, for GaN grown on Au-coated Si substrates, the XRD pattern confirms the crystalline wurtzite GaN structure with a predominant diffraction intensity from low-index crystal facets. Also, lower intensity reflections, attributed to Si_3N_4 and an Au-Ga intermetallic alloy (Ga_2Au) are observed. The uniform intensity of the Debye rings collected for porous GaN on Au-coated substrates confirms that there is no texturing in the porous layer (see Figure 3.12b). For porous GaN grown on Pt-coated substrates, similar results were obtained, although we could not identify the formation of any specific crystalline Pt-Ga alloy, as can be seen in Figures 3.12c and 3.12d.

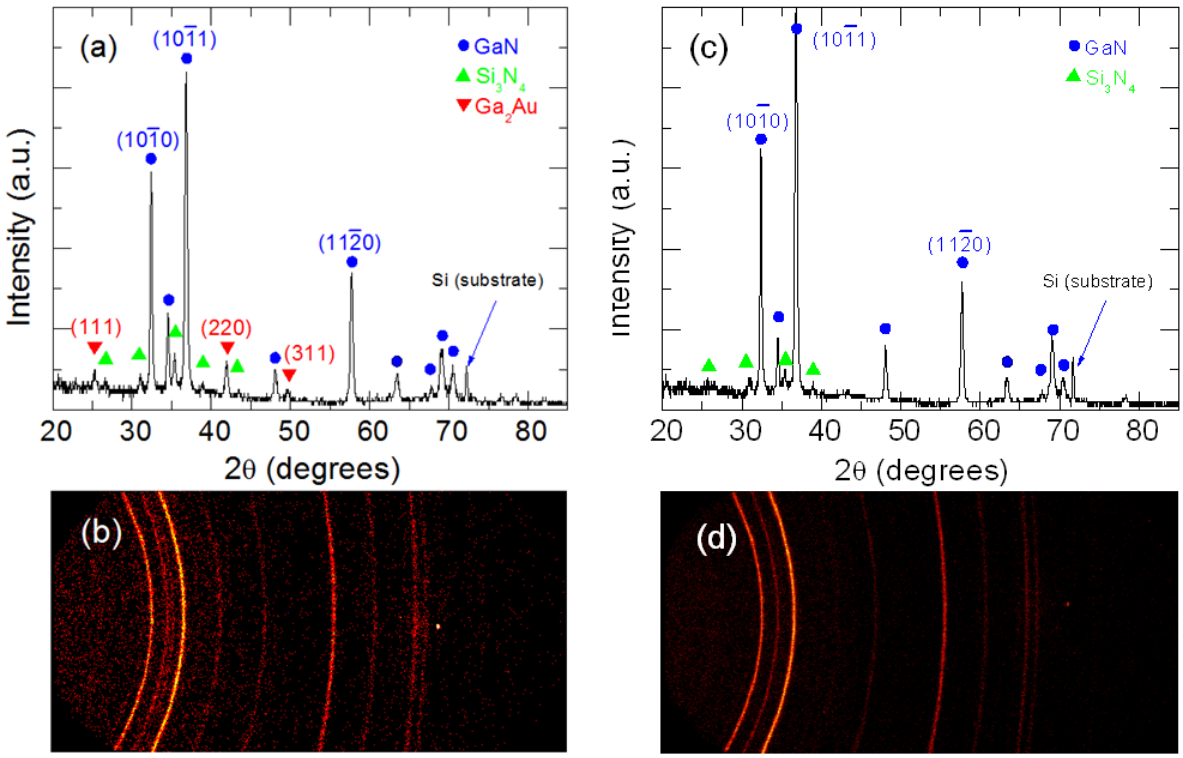

Figure 3.12. (a) XRD pattern for porous GaN deposited on Au-coated Si(100) showing the formation of crystalline GaN (00-0052-0792), Si_3N_4 (01-0071-0570) and Ga_2Au alloy (03-065-8613). (b) Debye rings recorded with the GADDS detector indicating no texturation of the porous GaN layer. (c) XRD pattern for porous GaN deposited on Pt-coated Si(100) showing the formation of crystalline GaN (00-0052-0792) and Si_3N_4 (01-0071-0570). (d) Debye rings recorded with the GADDS detector indicating no texturation of the porous GaN layer (reproduction of Figure 3 from Paper III).

Raman spectra of porous GaN obtained by using $Ni(NO_3)_2$, Au and Ni catalysts on Si (100) substrates were recorded at room temperature after excitation at 514.5 nm. The frequencies and assignments of the common phonon modes observed in the GaN Raman spectrum are listed in Table 3.2. Figure 3.13a shows the Raman spectrum of nanoporous GaN obtained with the use of $Ni(NO_3)_2$ catalyst. It exhibits only the A_1(LO), E_1(TO) and E_2 modes [160]. The peaks are broad, asymmetric, and with a small red shift in their position when compared to the tabulated values for GaN, which can be explained by size confinement effects due to the porosity. Also we observe a strong peak at 520 cm^{-1}, which belongs to the Si substrate. There is also one peak located at 421 cm^{-1}, which does not belong to the spectrum of the hexagonal GaN. Different possibilities can be regarded to analyze the origin of this peak, such as metallic alloys formed between Ga and the metallic catalyst, although no contribution was found in the literature, due to the scarce information about these alloys.

Table 3.2. Phonon modes observed in the Raman spectrum of GaN at room temperature, with their corresponding symmetry assignments [160].

Symmetry assignment	Raman shift, (cm^{-1})
E_2(low)	145
A_1(TO)	533
E_1(TO)	561
E_2(high)	571
A_1(LO)	737
E_1(LO)	743

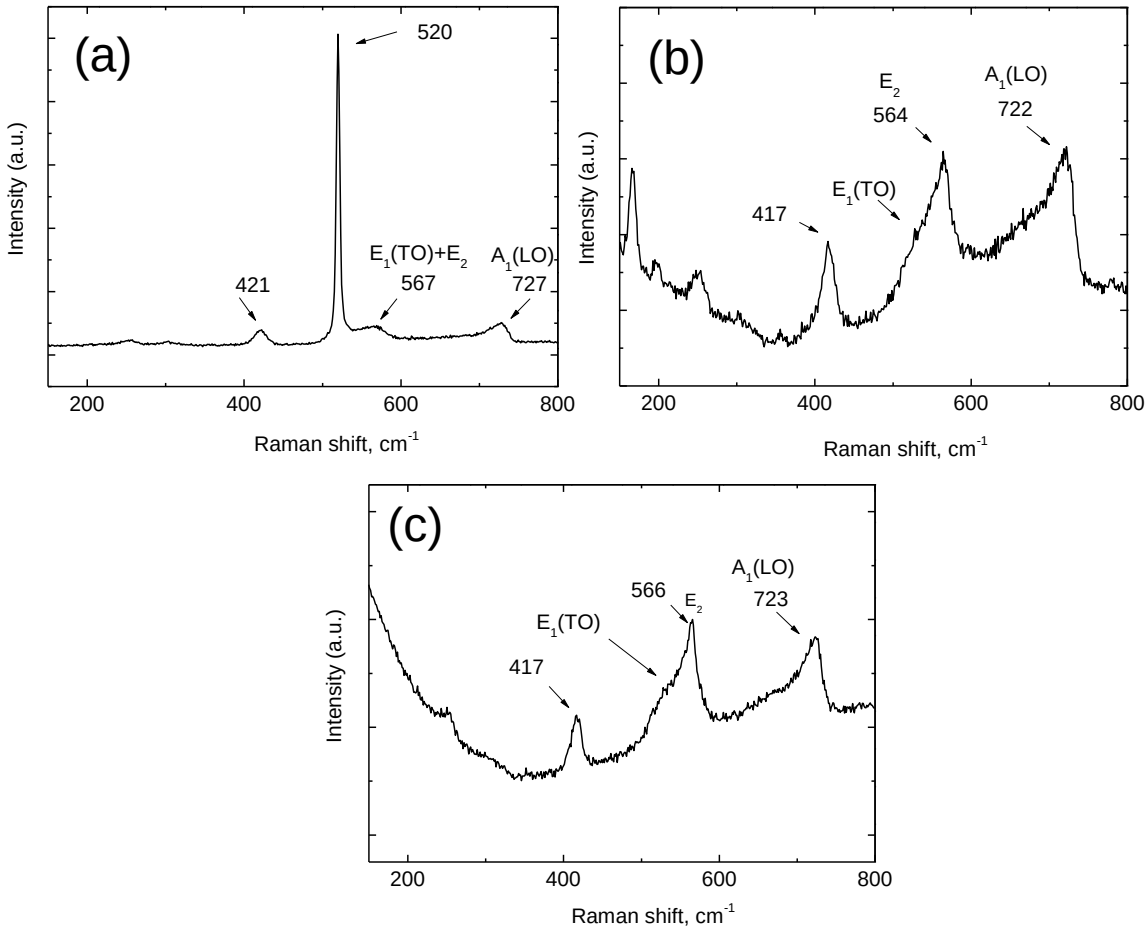

Figure 3.13. Raman spectra recorded for porous GaN samples synthesized by using (a) $Ni(NO_3)_2$, (b) Ni and (c) Au films as catalysts.

Figure 3.13b and Figure 3.13c show the Raman spectra of porous GaN obtained by using Ni and Au catalysts, respectively. Here the same peaks, observed in the previous case appear, except the peak which corresponds to the Si(100) substrate, which can be due to the better coverage of the surface of the substrate by GaN. In all spectra some additional low intensity peaks appeared in the low energy region that could not be assigned to a unique substance.

They could correspond to any additional phases identified by X-ray diffraction on these substrates such as α-Si_3N_4, and metallic alloys.

HRTEM measurements were carried out to confirm the crystalinity of the porous GaN microparticles, as described in Paper II. Figure 3.14a shows different TEM images of a typical porous GaN particle. Because of the thickness of the particle, the pores contained on the basal plane could not be observed. In the higher magnification image shown in this figure, and recorded in a thin part of the particle, the two-dimensional atomic structure can be clearly observed with *d*-spacings of 0.52 and 0.28 nm which corresponds to the (0001) and $(10\bar{1}0)$ planes of hexagonal wurtzite GaN, respectively. Figure 3.14b shows a selected area electron diffraction (SAED) pattern taken from the corner of the particle. The diffraction peaks correspond to the wurtzite structure of GaN, thus, the nanoporous GaN particle in the measured region is single crystalline. Also some defects as stacking faults are presented in the crystal structure, as can be observed in Figure 3.14c, confirmed by the observation of diffraction streaks in the SAED pattern. We marked some of the streaks with a circle in Figure 3.14d.

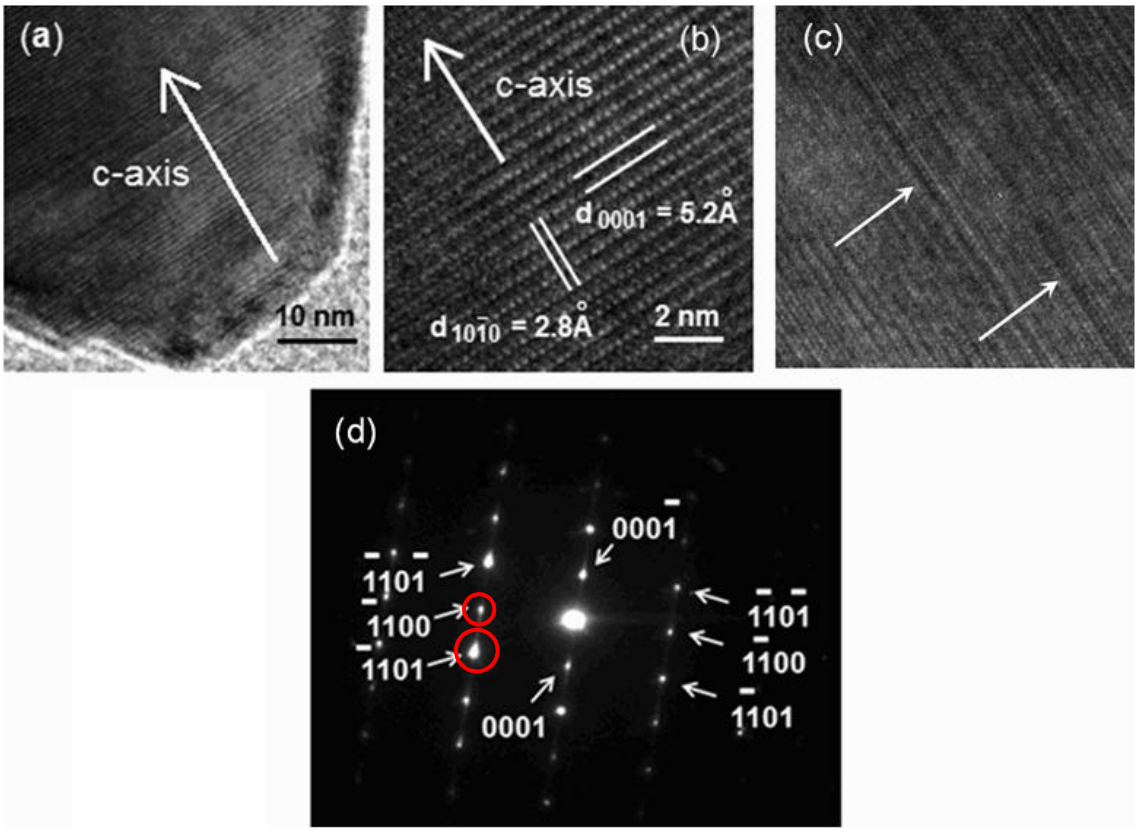

Figure 3.14. (a) HRTEM image of a porous GaN particle, showing its crystallinity by the two-dimensional atomic structure with *d*-spacings for the (0001) and $(10\bar{1}0)$ planes of wurtzite GaN shown in (b); (c) stacking faults observed in GaN particles; (d) SAED zone $[11\bar{2}0]$ axis pattern of the same particle (partial reproduction of Figure 3 from Paper II).

For Pt seeded porous GaN, we examined the surface of the silicon substrate directly underneath the GaN crystals, as described in Paper II. Figure 3.15a shows a bright field TEM image of a portion of the silicon substrate where Pt-Ga seed crystals (dark regions) are found.

EDX analysis in Figure 3.15b confirms the presence of both Pt and Ga, and while the intensity of Pt is greater as would be expected, the atomic concentration of Ga follows that of Pt, where the variation stems from increasing seed crystal volume along the line scan. Corresponding mapping of the intermetallic Pt-Ga seeds in Figure 3.15 shows that not all of the Pt particles contain Ga.

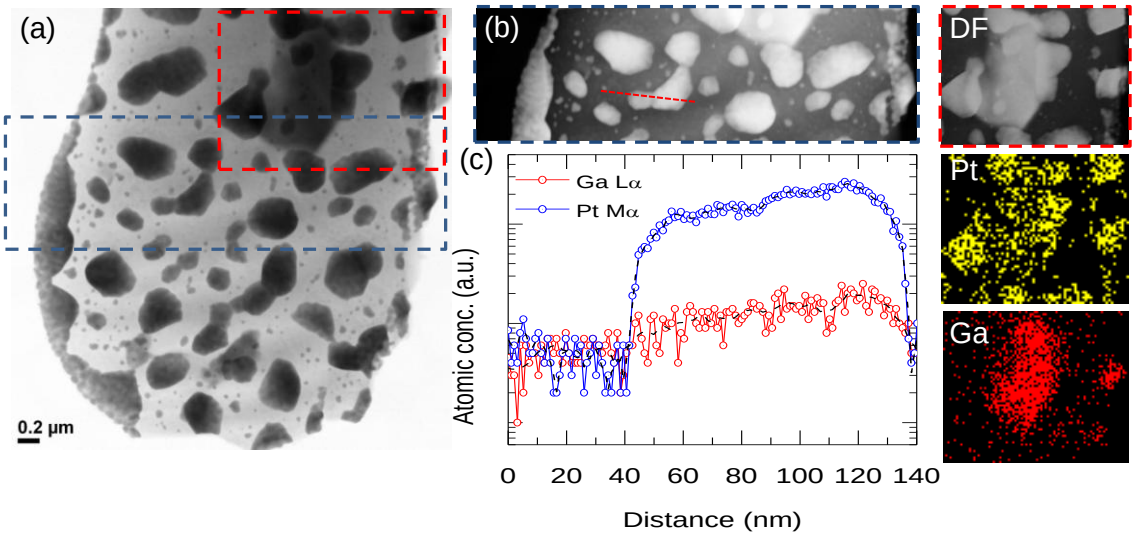

Figure 3.15. (a) Bright field TEM image of the Pt-Ga intermetallic islands formed at the GaN interface and (b) corresponding dark field STEM image with (c) corresponding line profiles of atomic concentration for the Ga Lα and Pt Mα X-rays. (Right) EDX maps confirming the presence of Pt and Ga in most metallic islands on the silicon surface (reproduction of Figure 4 from Paper II).

The metal catalyst-assisted crystal growth through either a vapor−liquid−solid (VLS) [161] or vapor−solid−solid (VSS) [162] mechanism by chemical vapor deposition (CVD), where the catalyst can influence the growth process, are the most probable mechanism for the formation of porous GaN by CVD. In the VLS mechanism the catalyst melts forming a liquid that absorbs precursors that arrive to it as gases, and when the liquid is saturated, GaN starts to precipitate as solid. In the VSS process, the metal catalyst seed remains at solid state during the growth process, with the precursors dissolving in the solid seed and forming the alloy, what finally results in the nucleation and growth of the crystals. Thus, the VSS growth mechanism is a solid-phase diffusion mechanism, in which a solid catalyst acts as the energetically favoured site for absorption of gas-phase reactants.

GaN in the form of porous microparticles was deposited on Si substrate using metal catalysts, such as Au and Pt. The formation of the Au−Ga crystalline intermetallic alloy of cubic Ga_2Au, detected by XRD, which occurs here above the solid-solution formation temperature, confirms intermetallic seeding to form GaN by reaction with NH_3 through a VSS process. As with the Ga_2Au seeds, the Pt-Ga seeds, detected by TEM underneath the GaN crystals, are where GaN growth starts, but a crystalline diffraction pattern is not found for this phase as readily as for Au-seeded GaN. Thus, taking into accout these evidences we consider metal catalyst-assisted crystal growth of porous GaN undergoes through VSS mechanism, the main stages of which are: the Ga incorporation into the metallic solid phase eutectic, the

formation of a Ga-Au or Ga-Pt alloy, the solubilisation of nitrogen on the Ga-Au(Pt) alloy, and finally the nucleation and growth of GaN (see Figure 3.16). The alloy was not found on the top of the grown porous GaN particles, what usually occurs when growth mechanism is VLS in GaN nanowires, for example [163], thus confirming again that the growth process proceeds through the VSS mechnism.

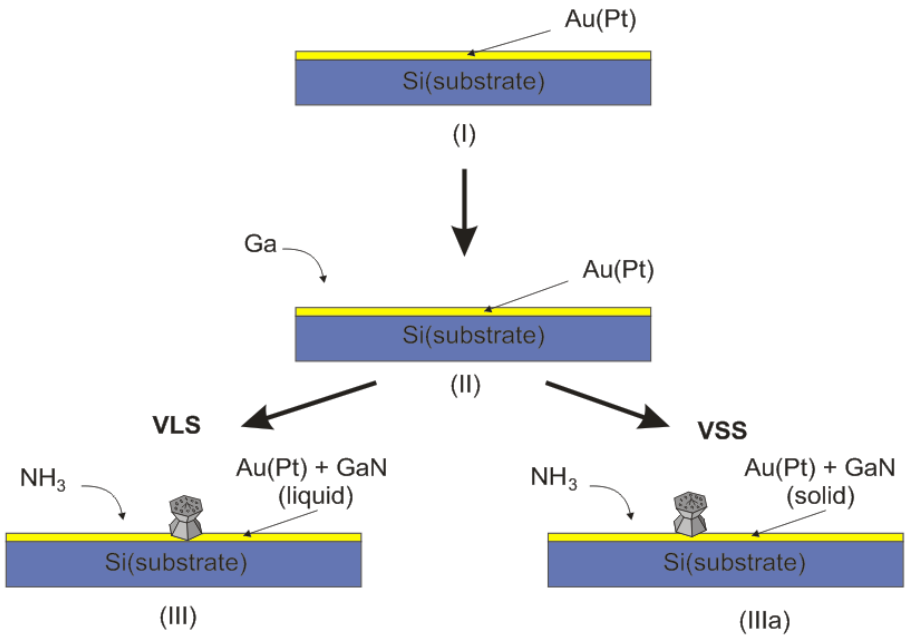

Figure 3.16. Mechanism of growth of the GaN nanoporous particles through the VLS and VSS process.

3.3 Porosity characterization

We also undertook FIB tomography to perform a cross-section analysis of a discrete porous GaN particle, as described in Paper IV. In this way we analyzed the shape and the length of the pores, as well as their direction of propagation inside of the GaN particles by removing layer by layer the material closer to the lateral surfaces of the GaN nanoporous particles. Nanopores were always observed on the (0002) faces of these GaN particles. The images recorded with the SEM connected to FIB revealed straight pores with lengths as long as 3 μm, similar to the sizes of the GaN particles, not interconnected among them, and not branched. The diameters of the pores ranged from 50 to 100 nm, with almost no variations in diameter with length. Figure 3.17 shows different images taken at different times on two different GaN nanoporous particles, showing different steps of the FIB milling and revealing different nanopores in the particles. A schematic sketch of the morphology of these particles drawn with the Shape software has been included for a better understanding of their crystallographic orientation. As can be seen in Figure 3.17a, the nanopores in the central part of the GaN particles seem to follow an orientation parallel to the [0001] crystallographic

direction. However, the nanopores found in the most external parts of the GaN particles (Figure 3.17b, 3.17e) seem to be parallel to the lateral faces of these particles.

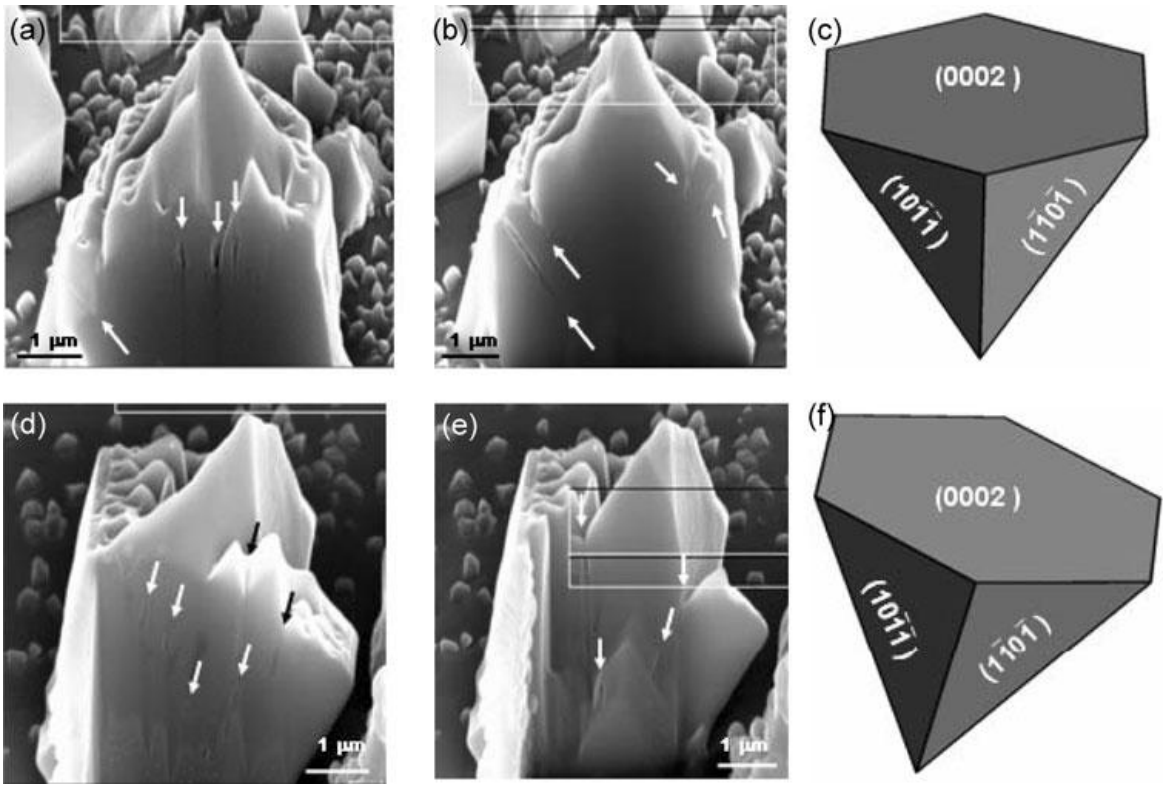

Figure 3.17. Tomography images of two different GaN nanoporous particles obtained by FIB tomography (a, b, d, e), and schematic sketches of the morphology for a better understanding of the crystallographic orientation of the nanopores (c, f). Arrows indicate the position of the pores observed on the samples.

From the SEM images extracted from the time-resolved FIB tomography. A three dimensional (3D) model of the porous GaN particle was developed using the Avizo Fire software, version 7.0 trial. Figure 3.18 shows the reconstructed images of pores at different angles. As can be seen in Figure 3.18a, 3.18b and 3.18e, straight pores beginning from the rough basal plane and following through the length of the particle have been observed. These pores are parallel to each other and do not interconnect among them nor branch, as can be seen from the views perpendicular to the basal plane (see Figure 3.18c and 3.18d). From Figure 3.18 we can conclude that at least the nanopores in the central part of the GaN particles follow an orientation parallel to the [0001] crystallographic direction.

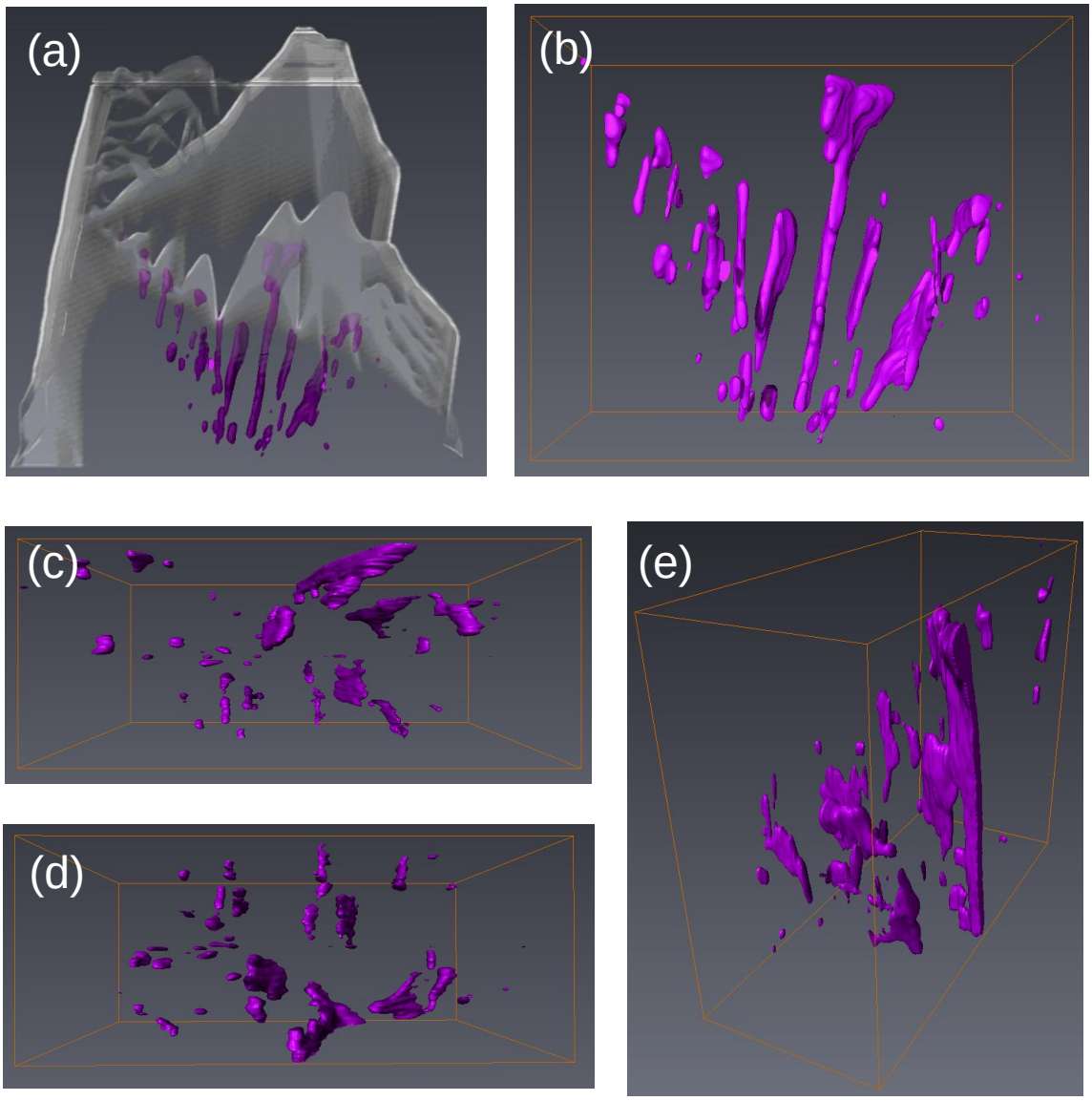

Figure 3.18. Three dimensional (3D) model of the porous GaN particle reconstructed using the SEM images taken from the video sequence recorded in the time-resolved FIB: (a) Pores shown on a semitransparent SEM image of porous GaN particles, (b) view of the pores perpendicular to the [0001] crystallographic direction, (c), (d) view of pores parallel to the [0001] crystallographic direction, (e) view of the pores perpendicular to the [0001] crystallographic direction at a different rotational angle in relation to the initial position of image (b).

3.4 Electrical characterization

Prior to electrical characterization porous GaN was deposited on Si(100) and catalyzed by Pt or Au films that at the same time acted as electrodes for electrical characterization. Another electrode was a liquid eutectic alloy of In-Ga.

Figure 3.19 shows the *I-V* curves recorded for the porous GaN samples catalyzed by Pt (Figure 3.19a), and by Au (Figure 3.19b), as reported in Paper II. The ln(*I*)-*V* curves show only slight asymmetry indicative of near Ohmic, weak Schottky barriers of Pt and Au. The conductivity of porous GaN grown from Pt is higher than that grown from Au. The *I-V* curve of porous Pt-seeded GaN in Figure 3.19c shows the low-bias non-linearity consistent with a weak Schottky barrier. Both contacts can be described by the thermionic emission theory, acknowledging a high ideality factor for weak barriers. The Schottky barrier height (SBH) can be estimated from:

$$I = I_0\left[\exp\left(\frac{qV - IR_S}{kT}\right) - 1\right] \qquad \text{(Eq. 3.1)}$$

where $I_0 = AA^{**}T^2\exp(-q\varphi^{o}_{B,n}/kT)$ [164] with A^{**} as the effective Richardson constant. The estimated SBHs for Pt and Au contacted porous GaN are 0.66 eV and 0.53 eV, respectively.

In spite of higher porosity, low contact resistivities between 2.2 – 4.1 × 10^{-4} Ω cm^2 were found for Pt-catalyzed GaN, while those of Au-catalyzed GaN were 5.9 – 8.8 × 10^{-4} Ω cm^2. From these results it seems that the interface between porous GaN and the metallic contact dominated the transport more than the crystallinity or morphology of the porous microstructure, and effective Ohmic contacts can form with GaN.

Two terminal transport measurements acquired between the In-Ga alloy contact and porous GaN showed perfect Ohmicity, from which low contact resistivities were determined with variable intercontact separation using the TLM approach and found to be in the range 1.7 – 4.4 × 10^{-4} Ω cm^2, in spite of the multifaceted, porous morphology.

The corresponding 4-probe analysis gives sheet resistances for porous GaN films in the range 4.3-4.9 kΩ/□. The van der Pauw measurements confirm these values independent of contact area and effective geometry on rough surfaces. The values match those of MBE grown GaN thin films with Ti/Au alloy contacts after annealing to 973 K [165] and this indicates the efficient interface between the metal and the growing porous GaN.

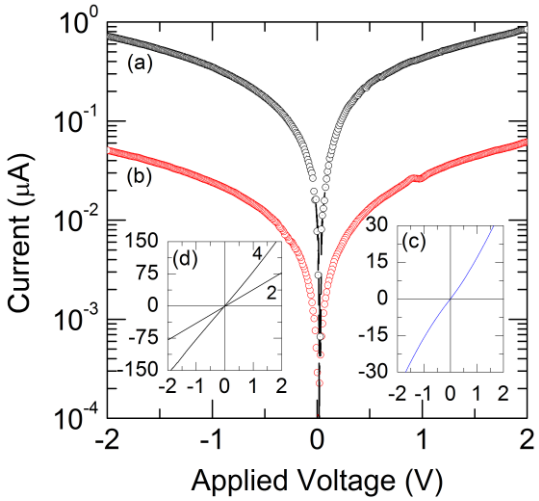

Figure 3.19. (a) ln(*I*)-*V* curves for porous GaN grown on Pt and (b) Au-coated Si(100) substrates. (c) *I-V* curve for the porous GaN grown directly from Pt and (d) *I-V* curves from 2- and 4-probe measurements using In-Ga Ohmic contacts to porous GaN (partial reproduction of Figure 5 from Paper II).

Capacitance-voltage (C-V) analysis was performed by scanning the applied potential at a rate of 10 mV s^{-1} with a superimposed AC signal with an amplitude of 15 mV at a frequency of 1 MHz to determine the capacitance of the porous GaN under depletion conditions, as reported in Paper II. Gold contacts deposited on porous GaN after growth and different from those used as catalysts, formed a Schottky contact for the measurement. The $1/C^2$-V analysis in the framework of the Mott-Schottky [151] model, shown in Figure 3.20, confirms an unintentional *n*-type GaN with a donor concentration N_D, given by the slope $N_D=2C^2V/q\varepsilon\varepsilon_0$, of n = 1.6 × 10^{16} cm^3 using a dielectric constant ε = 8.9 for GaN. These low values for unintentionally doped *n*-type GaN give a corresponding SBH that can be calculated by the following equation:

$$\varphi^0{}_{B,n} = eV_{bi} + eV_n + kT \qquad \text{(Eq. 3.2)}$$

where eV_{bi} is the barrier height from the voltage intercept and $eV_n = E_{C,n} - E_F$, where $E_{C,n}$ is the conduction band minimum and E_F is the Fermi level. According to this, SBH are 0.78 ± 0.1 eV and 0.62 ± 0.1 eV for Pt-seeded GaN and Au-seeded GaN, respectively.

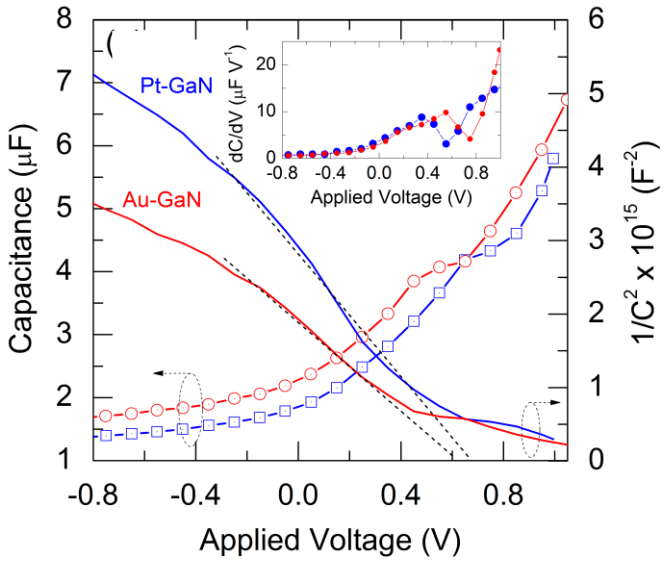

Figure 3.20. Interface capacitance and Mott-Schottky ($1/C^2$ – V) profile for Pt and Au catalyzed porous GaN layers. Inset: plot of differential capacitance vs. voltage (partial reproduction of Figure 7 in Paper II).

Minima in differential capacitance indicating transition beyond depletion conditions are also found close to the respective values for the built-in potential of these Schottky junctions (see inset of Figure 3.20). These values are lower than those encountred for standard epi-layer of *n*-type GaN (0.87 eV for Au/n-GaN and 1.01 eV for Pt/*n*-type GaN [166]), even when accounting for image force lowering of the barrier height in this case. The Fermi level energy with respect to the Pt and Au workfunction is markedly reduced compared to standard values owing to the interfacial alloy [167], whose work function is less than that of the respective noble metal, giving lower Schottky barriers to carrier transport through the high grain-boundary density GaN layer.

This is also reflected in the carrier mobilities from which, for a doping density of effectively ~10^{16} cm^{-3} calculated in the C-V analysis, an average electronic mobility of ~208 cm^2 V^{-1} s^{-1} is determined.

A plausible band structure for the interfacial intermetallic contact is shown in Figure 3.21, which shows the presence of the Ga_2Au interface, with its lower workfunction, between the Au and GaN. A similar situation can be drawn when using Pt rather than Au. With forward bias, electrons can easily overcome the significantly reduced barriers, by thermionic-field emission to inject into the Au or Pt from the intermetallic. When the bias becomes negative, holes can tunnel through the Au/intermetallic interface barrier and inject into the notch to recombine with electrons. The contact resistance is markedly reduced as it provides a recombination center for carriers giving a linear *I-V* response.

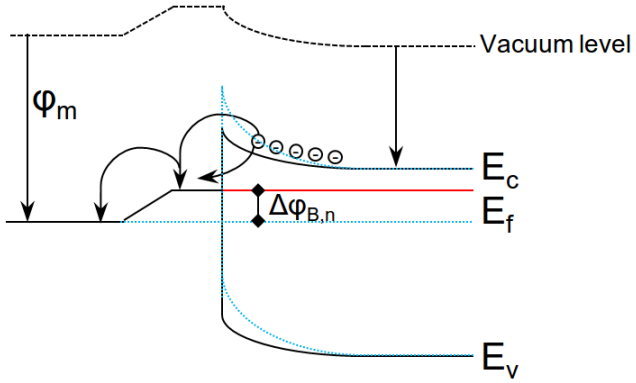

Figure 3.21. Proposed band structure model for intermetallic interface phase formation acting as the effective Ohmic contact. The barrier with (solid line) and without (dashed line) the presence of the intermetallic is shown (partial reproduction of Figure 7 in Paper II).

On Au, we confirmed the formation of an intermetallic Ga_2Au phase, which suggests a band structure that promotes transport by lowering the Schottky barrier by acting as a low barrier, Ohmic contact to the GaN, rather than forming a definitive tunnel contact which would show ohmicity over a small potential range. Thus, the intermetallic formation at the interface that allows the growth of the GaN effectively acts as an intermetallic Ohmic contact at the semiconductor interface.

3.5 Catodoluminescence characterization

Cathodoluminescence (CL) is a powerful tool to study nitride semiconductors. GaN show luminescence bands in the range 3.0-3.5 eV, due to excitons and donor-acceptor recombinations [168].

Room temperature CL spectra shown in Figure 3.22 corresponds to nanoporous GaN particles obtained on Si(111), as described in Paper IV. Near band-edge emission was observed at room temperature at around 365 nm (3.4 eV). CL studies revealed, a sharp and

well defined band-gap emission, with a FWHM of 0.16 eV. This near band-edge emission was located at a similar position to those observed in nonporous GaN, and the bandwidth measured at FWHM was also similar [169], what confirms that the porosity in GaN microparticles does not affect the near band-edge emission of GaN. Other possible emissions at lower energies like the blue luminescence (BL) [170] or the yellow luminescence (YL) [171] due to defects, vacancies or impurities [172] are not observed.

Figure 3.22b shows the monochromatic CL image recorded at λ = 364 nm, corresponding to the near band-edge emission region in the ultraviolet range of the spectrum. The bright spots in the image represent high emission intensity regions, while dark spots represent low emission intensity regions. The smallest features observed in these images are of the order of 50 nm in diameter. Since these samples are not flat they are not limited by diffusion length and interaction volume (50 nm at 4 keV for GaN), and topography should be the major factor modulating the CL intensity. Cathodoluminescence images revealed that luminescence is not spatially homogeneous. A higher intensity of light from the edges of the rough basal planes that contains the nanopores in the particles in comparison to the smooth lateral surfaces is observed. The SEM image together with the CL image recorded in the same region (Figures 3.22c and 3.22d), where the porous structure of the basal plane of one of the nanoporous GaN particles can be clearly seen, show that the strong UV emission comes from areas surrounding the pores of the structure, while the pores coincide with dark spots in the images. The observed CL contrast might be related to the presence of dislocations in the structure, that have been shown to act as non-radiative centers around the pores.

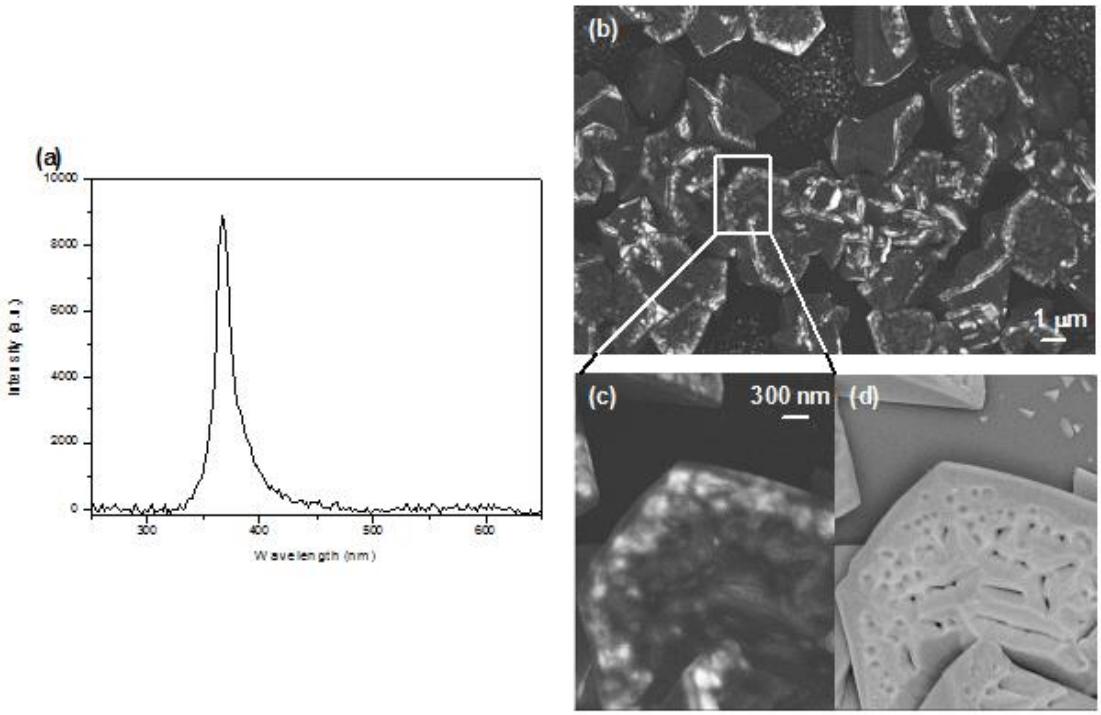

Figure 3.22. (a) Room temperature cathodoluminescence spectra and (b) monochromatic image (λ = 364 nm) of nanoporous GaN particles recorded at 4 keV and 200 pA. An enlarged image of the selected region in (b) can be seen in (c). The same region under secondary electrons can be seen in (d) (partial reproduction of Figure 6 in Paper IV).

3.6 Oriented growth of GaN on Si

The orientation of the pores of GaN is of interest, because it might increase the brightness of potential LEDs, fabricated with these porous particles, since light extraction is higher around the pores, as observed by cathodoluminescence (see Paper IV and Figure 3.22). This is due to the multiple reflections of the photons on pores walls. Porosification increases the reflection probabilities of emitted photons, and provides additional surfaces through which photons can escape (see Figure 3.23) [97]. Thus, the porous surface can minimize the total internal reflection and increase the transmission at the interface to air, increasing the light extraction efficiency. Also, porosification increases internal quantum efficiency due to geometrical quantum well or wire effect associated with the thin walls remaining between the pores. This quantum confinement leads to an increase in the effective band-gap energy, and therefore the energy for electrons to enter the region between the pores. These regions may be considered as quantum wires or quantum wells.

To align those pores, we should orient crystallographically the porous GaN microparticles obtained on Si(100) substrates by CVD in such a way that the (0001) faces of porous GaN, that are the faces that contain the pores, should be perpendicular to the surface of the Si substrates. For this purpose, we used two different approaches: a) crystal growth under the influence of electric fields and b) structuration of Si substrates coated with a SiO_2 layer.

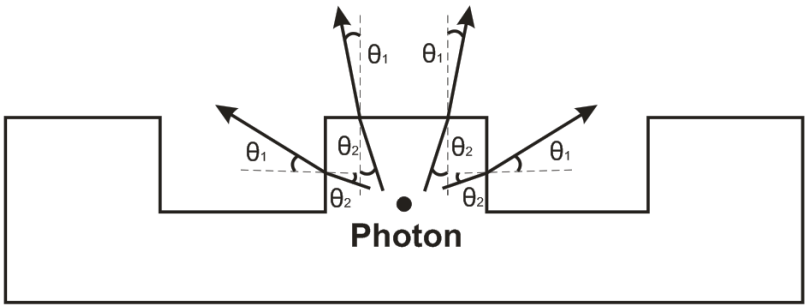

Figure 3.23. Increase of the light extraction efficiency in a porous structure.

3.6.1 Crystal growth on electrical fields

Applying an electric field during the crystal growth process can influence the direction and orientation of crystals of polar structures [173]. Since GaN along the *c* crystallographic axis is a polar structure, one of the possibilities to align GaN microparticles along this direction, is to grow GaN porous microparticles under the influence of an electric field. Figure 3.24 shows the scheme of the set up we used to generate an electrical field to influence the crystal growth process, that acts as a capacitor. One of the electrodes is the silicon substrate coated with a thin layer of Pt, the other one is a platinum grid. An electric field is generated between these two electrodes connected to a potential source. The source of Ga is placed

under the Pt grid, thus vapours of Ga generated during the growth process can penetrate through the holes of the grid, react with ammonia and form crystals of GaN that can deposit on the surface of the Si substrate facing the Pt grid.

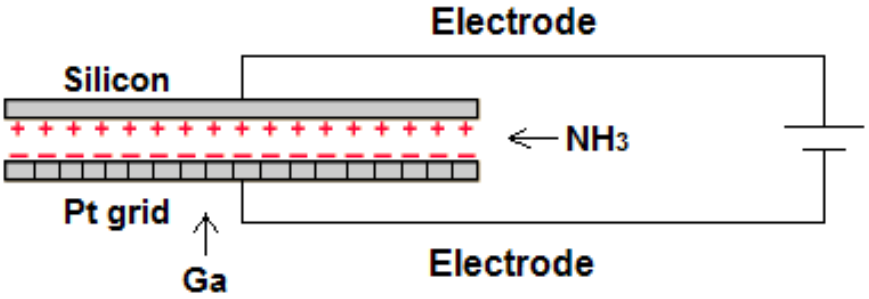

Figure 3.24. Scheme of the capacitor used to study the influence of an electric field during the growth process of porous GaN.

Two types of platinum grids with different mesh (2 × 2 mm and 0.5 × 0.5 mm) were fabricated and fixed to a BN support (see Figure 3.25). 12 V were applied to generate the electric field between the Pt mesh and the Pt-coated Si electrodes. The distance between the Pt grid and the Si substrate was kept constant at 1.5 mm.

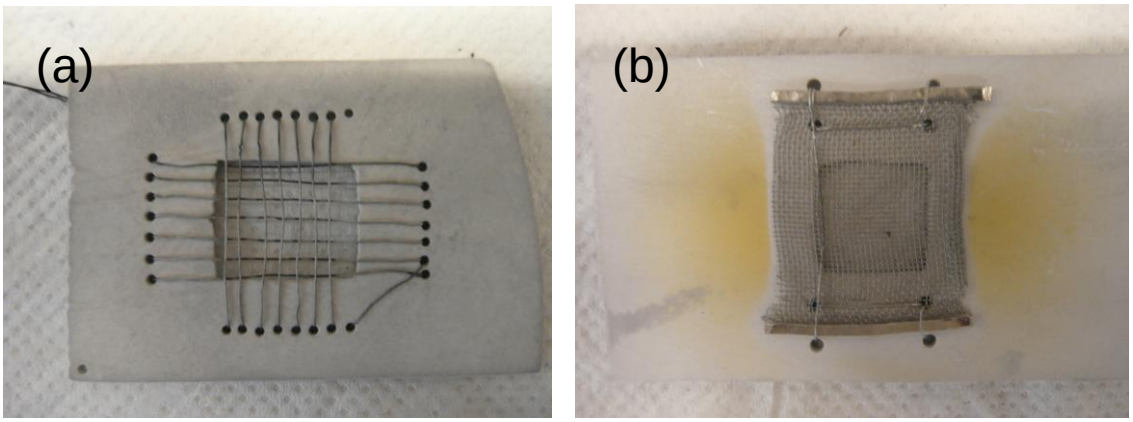

Figure 3.25. Photographs of the two types of Pt grids with different meshes fixed to a BN support: (a) 2 × 2 mm mesh and (b) 0.5 × 0.5 mm mesh.

Figure 3.26 shows the SEM images of the GaN microparticles obtained using the Pt grid with a low density mesh. Particles are deposited as separated islands, with a low coverage of the Si substrate. A high-magnification image of the microparticles obtained show that despite they are porous, they are not crystallographically aligned, and their pores point towards random directions (see Figure 3.26c).

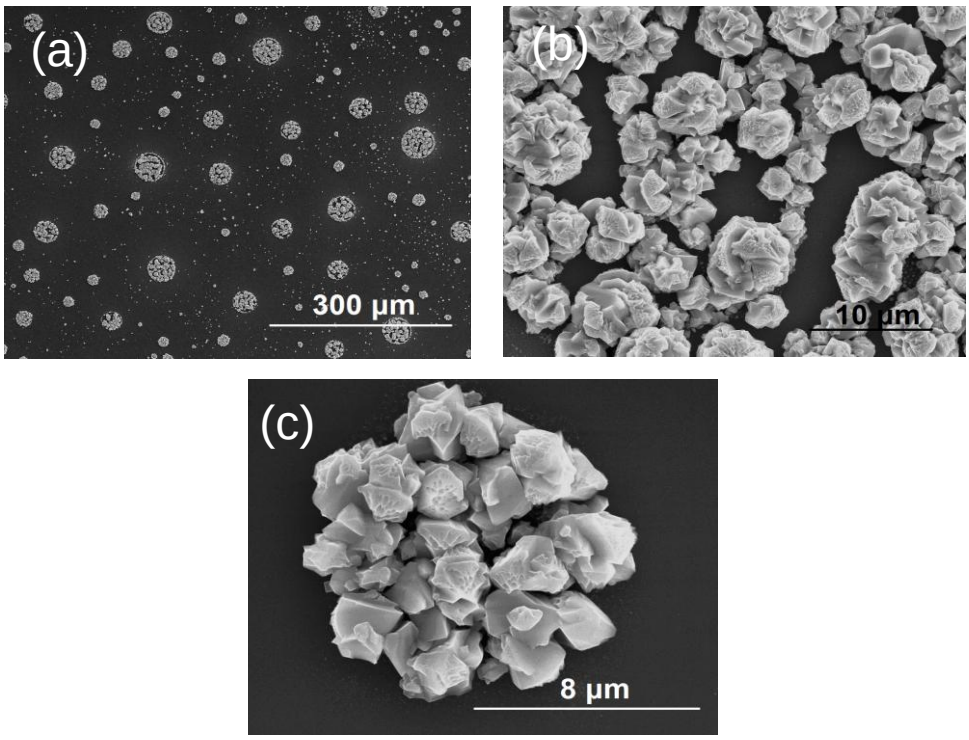

Figure 3.26. SEM images with different magnification of porous GaN microparticles grown on Si(100) using a Pt grid with a low density mesh and under the influence of an electric field generated after connecting the capacitor to a 12 V source.

The strength and the density of electric field lines in this case might not be sufficient to influence the process of growth, due to low mesh density of the Pt grid.

When a higher voltage 25 V was applied, in order to increase the intensity of the electric field in the capacitor with a Pt grid with a low density mesh, no significant changes in the morphology and porosity of the GaN particles were observed (see Figure 3.27). Again, it seems that this voltage is not sufficient to induce the oriented growth of GaN microparticles along the *c* crystallographic direction and higher voltages would be required to prove the influence of the electric field on the growth of porous GaN crystals.

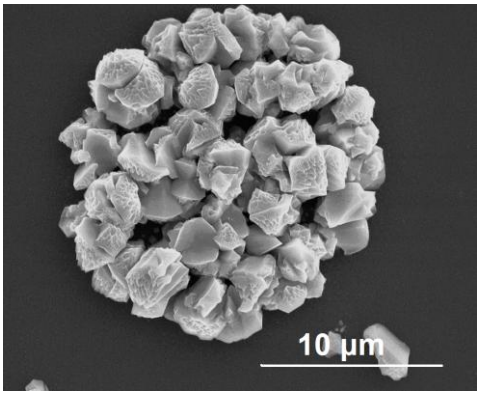

Figure 3.27. SEM image of porous GaN microparticles grown on Si(100) using a Pt grid with a low density mesh under the influence of an electric field generated after connecting the capacitor to a 25 V source.

When a Pt grid with a higher density mesh was used, the coverage of the Si substrate was even lower than in the previous case. The obtained particles are irregular in shape and they are not porous (see Figure 3.28). In that case, maybe the free space left by the Pt grid is not enough for Ga vapors to flow inside the capacitor.

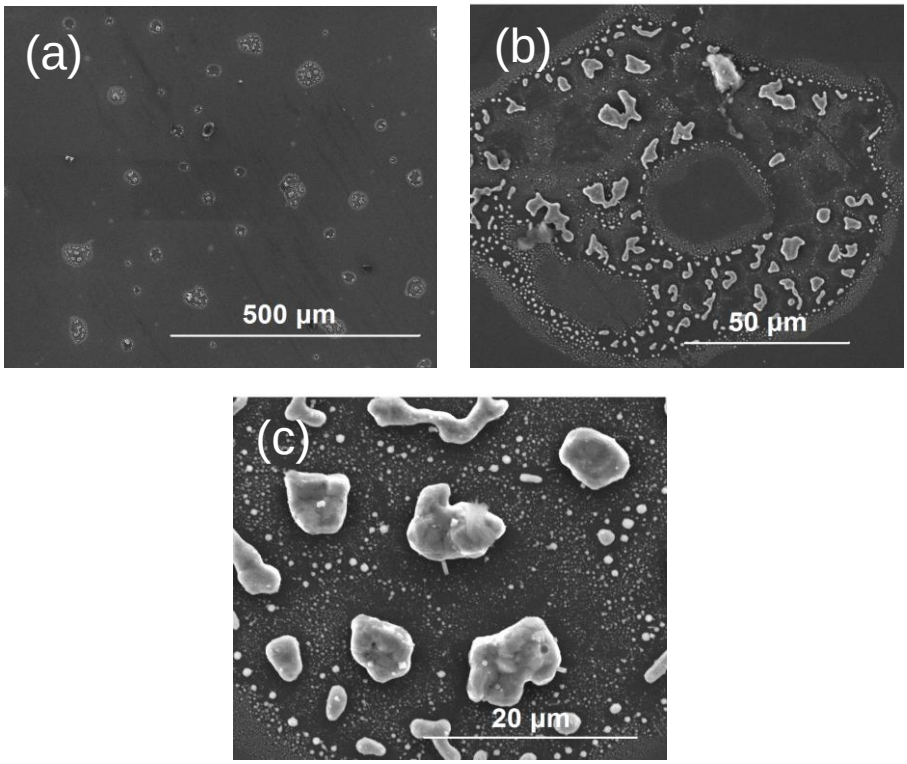

Figure 3.28. SEM images with different magnification of porous GaN microparticles grown on Si(100) using a Pt grid with a high density mesh under the influence of an electric field generated after connecting the capacitor to a 12 V source.

3.6.2 Structuration of Si substrates coated with a SiO_2 layer

Another approach we explored to orient crystallographically the porous GaN particles consisted in using a Si(100) substrate coated with a SiO_2 thin layer, with further patterning of SiO_2 in order to limit the growth of porous GaN microparticles [174]. A commercial Si(100) wafer with already thermally grown SiO_2 (50 nm thick) was used. The design for the patterned substrate is shown in Figure 3.29. The patterned structure of a 2D array of micron-sized holes on SiO_2 with a diameter of 1.5 µm was fabricated using laser lithography and etching techniques. Metallic Ti was deposited inside the holes by a sputtering technique.

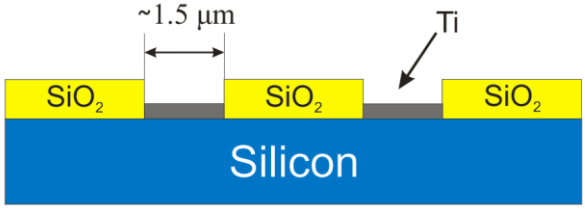

Figure 3.29. Micron-size hole design for the SiO_2 patterned structure on a Si(100) wafer.

To create the microhole structure on SiO_2 the following procedure was applied (see Figure 3.30):

(i) *Preparation of the substrate:* The wafer was initially heated to a temperature sufficient to drive off any moisture that may be present on the wafer surface. (473 K, 10 min)

(ii) *Photoresist coating:* The wafer was covered with ~ 700 nm layer of AZ 1505 photoresist (Microchemicals) by spin coating (500 rpm, 30 s). Softbake was performed afterwards at 373 K during 30 s.

(iii) *Exposure and development:* The photoresist was illuminated with a 405 nm laser to create a pattern of holes, 1.5 μm in diameter, in an area of 1 cm^2 using the laser lithography system. The exposure to the laser light causes a chemical change in the photoresist that can then be removed by the developer (AZ 726 MIF, 2.38 % TMAH with surfactants added for fast and homogeneous substrate wetting). In this way the areas of SiO_2, in which the photoresist has been removed, are exposed.

(iv) *Etching:* A buffered HF solution (7 vol. of H_2O to 1 vol. of 50 % HF, Aldrich) solution was used as the chemical agent to remove the SiO_2 layer of the substrate in the areas that are not protected by the photoresist, exposing the surface of Si in these areas.

(v) *Deposition of Ti:* Before the remaining photoresist was removed we coated the surface of the substrate with a 20 nm thick Ti layer by sputtering. In this way we coated the exposed surface of Si with a Ti layer that will act as the metallic catalyst for the growth process of porous GaN. Using Ti we expect porous GaN microparticles to grow oriented along the *c*-crystallographic direction, since Ti and GaN belong to the hexagonal system and there is a small lattice mismatch between Ti and GaN [174].

(vi) *Photoresist removal:* Finally, since the photoresist is no longer needed, it must be removed from the substrate. To do that, a resist stripper solution was used, which chemically alters the photoresist so that it no longer adheres to the substrate. Together with the photoresist the Ti layer deposited on the top of the photoresist was removed, while that covering the bottom of the holes and deposited on Si, remained.

The obtained patterned substrate was characterized by AFM and SEM techniques, as can be seen in Figure 3.31. Figure 3.31a shows that the patterning is quite homogenous in form and with equal sizes of holes (~ 1.5 μm in diameter). A profile of the surface of the sample corresponding to the green line indicated in Figure 3.31a is shown in Figure 3.31b. This profile evidences that the depth of our holes is around 30 nm, that corresponds to the thickness of the SiO_2 layer in the commercial Si wafer. SEM images of the patterned substrate (see Figure 3.31c) confirm the homogeneity of the prepared structure. Analysis by SEM in the

back-scattered electrons mode (BSE) also shows that the parts corresponding to the places of the holes are coated with a heavier element, which is the Ti catalyst (see Figure 3.31d).

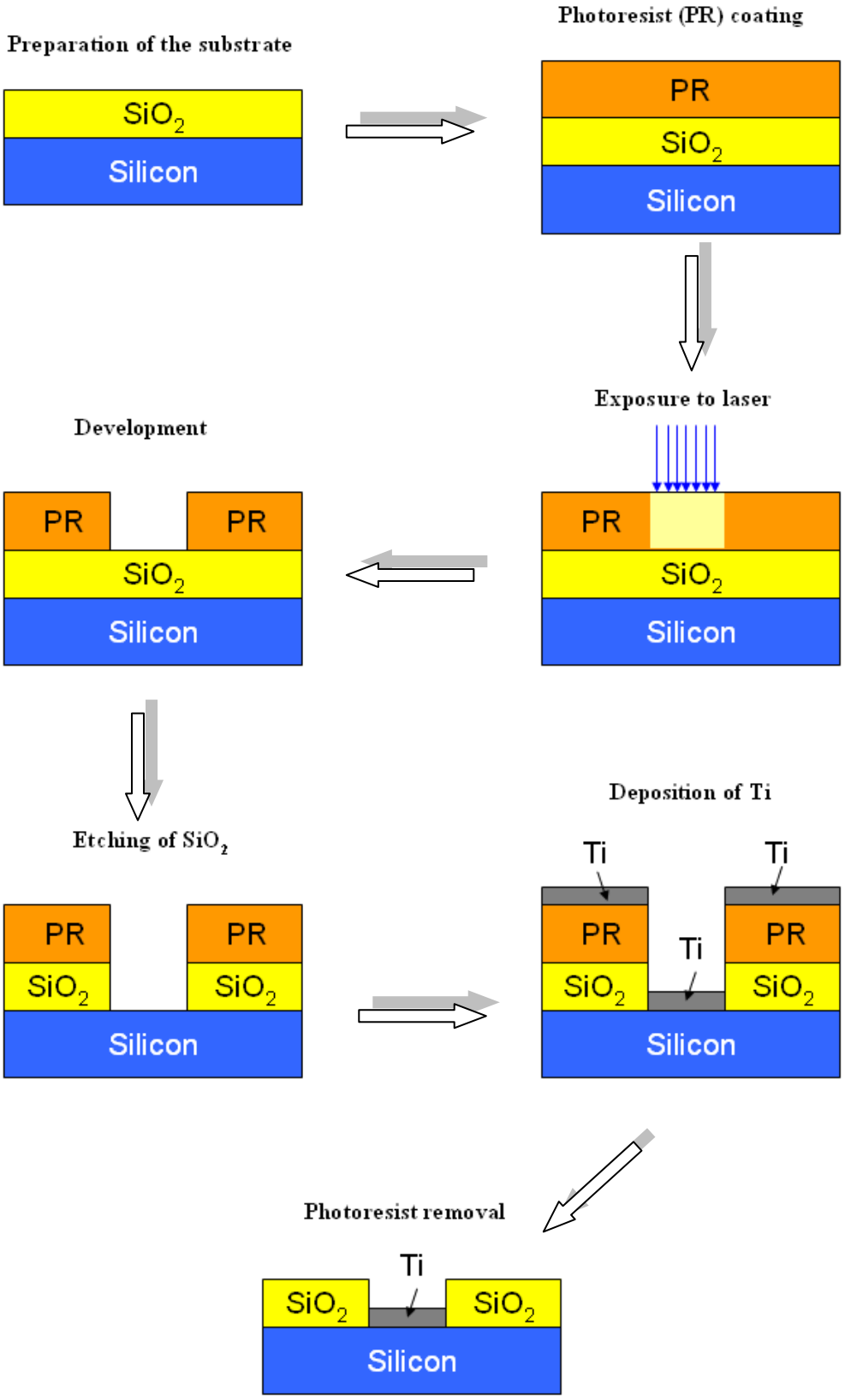

Figure 3.30. Scheme of the process of patterning of Si (100) substrates coated with SiO_2.

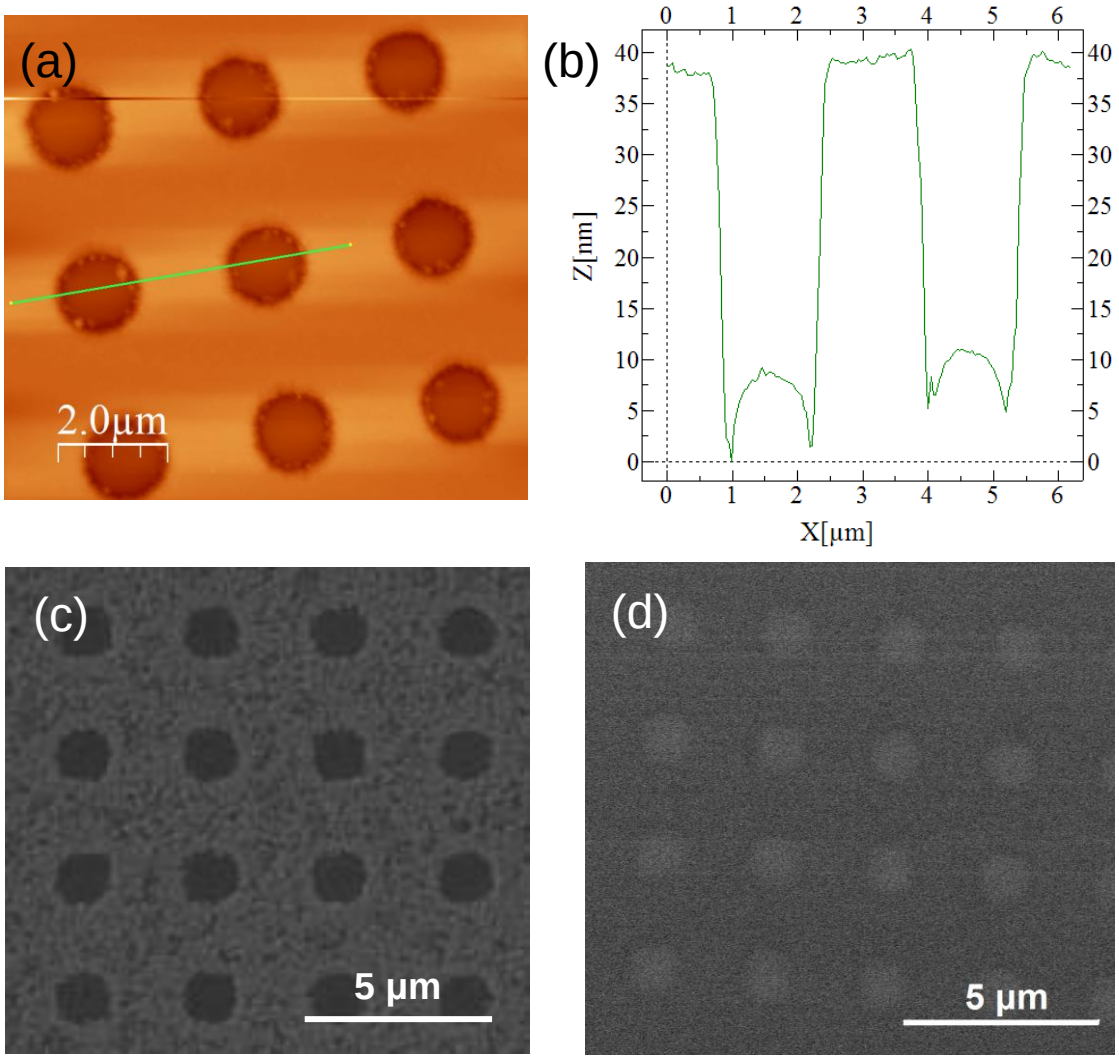

Figure 3.31. (a) AFM image of the patterned SiO_2-coated Si(100) substrates. (b) Depth profile of the patterned substrate, corresponding to the green line shown in panel (a). SEM images of the patterned SiO_2-coated Si(100) substrates recorded using (c) secondary electrons and (d) back-scattered electrons.

These patterned substrates were used on the synthesis of nanoporous GaN microparticles. In those experiments, different quantities of Ga (0.5 g, 0.25 g and 0.1 g) were used to limit the number of GaN particles formed and favor the orientation process. Figure 3.32 shows SEM images taken when 0.5g of Ga were used. GaN particles completely covered the surface of the substrate (see Figure 3.32a). When the quantity of Ga was reduced to 0.25 g, the growth of GaN particles was restricted to the holes of the substrate (see Figure 3.32b).When the quantity of Ga was decreased even more, to 0.1 g, the density of deposited GaN particles decreased drastically, and most of the surface of the substrate remains empty (see Figure 3.32c).

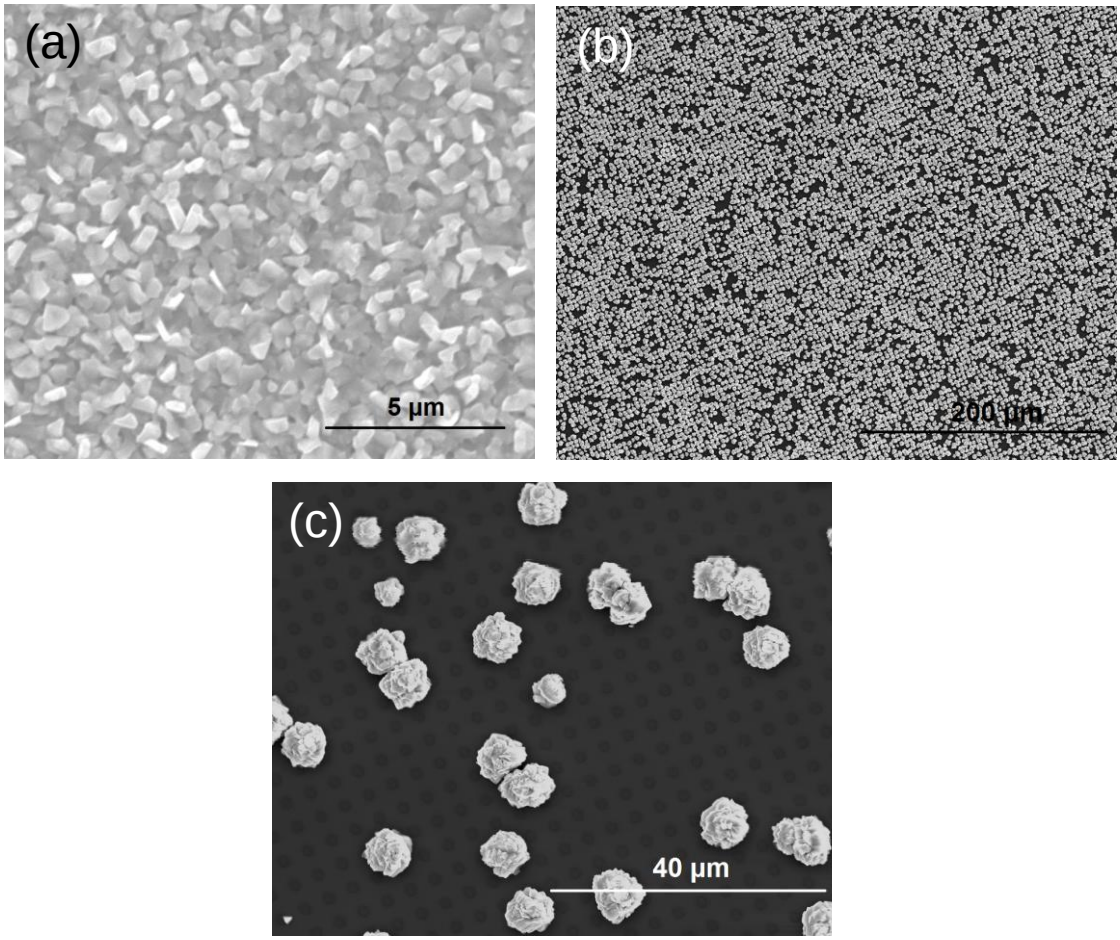

Figure 3.32. SEM images of porous GaN grown on patterned SiO_2-coated Si(100) substrates using different quantities of Ga: (a) 0.5 g, (b) 0.25 g and (c) 0.1 g.

Using 0.25 g of Ga and decreasing the time of the reaction to 15 min in order to avoid overgrowth of porous GaN microparticles, a good-ordered structure was obtained, covering the whole area of the patterned substrate, as can be seen in Figure 3.33. The growth is restricted to the patterned area (see Figure 3.33a and 3.33b), that coincides with the Ti-seeded regions. However, porous GaN was grown in the form of aggregated micron-sized nanoporous GaN particles without any preferential crystallographic orientation XRD, as can be seen in Figure 3.33c.

The same experiment was repeated coating the patterned substrate with a Au layer, 20 nm thick. The result obtained, however, was similar to that obtained when Ti was used as catalyst (see Figure 3.34a). From the XRD analysis we observe that the $(10\bar{1}0)$ peak show less intensity that expected. However, the Debye rings show a quite homogenous distribution of intensity (see Figure 3.34c). Also, crystalline Au was detected in the XRD analysis, as indicated in Figure 3.34b.

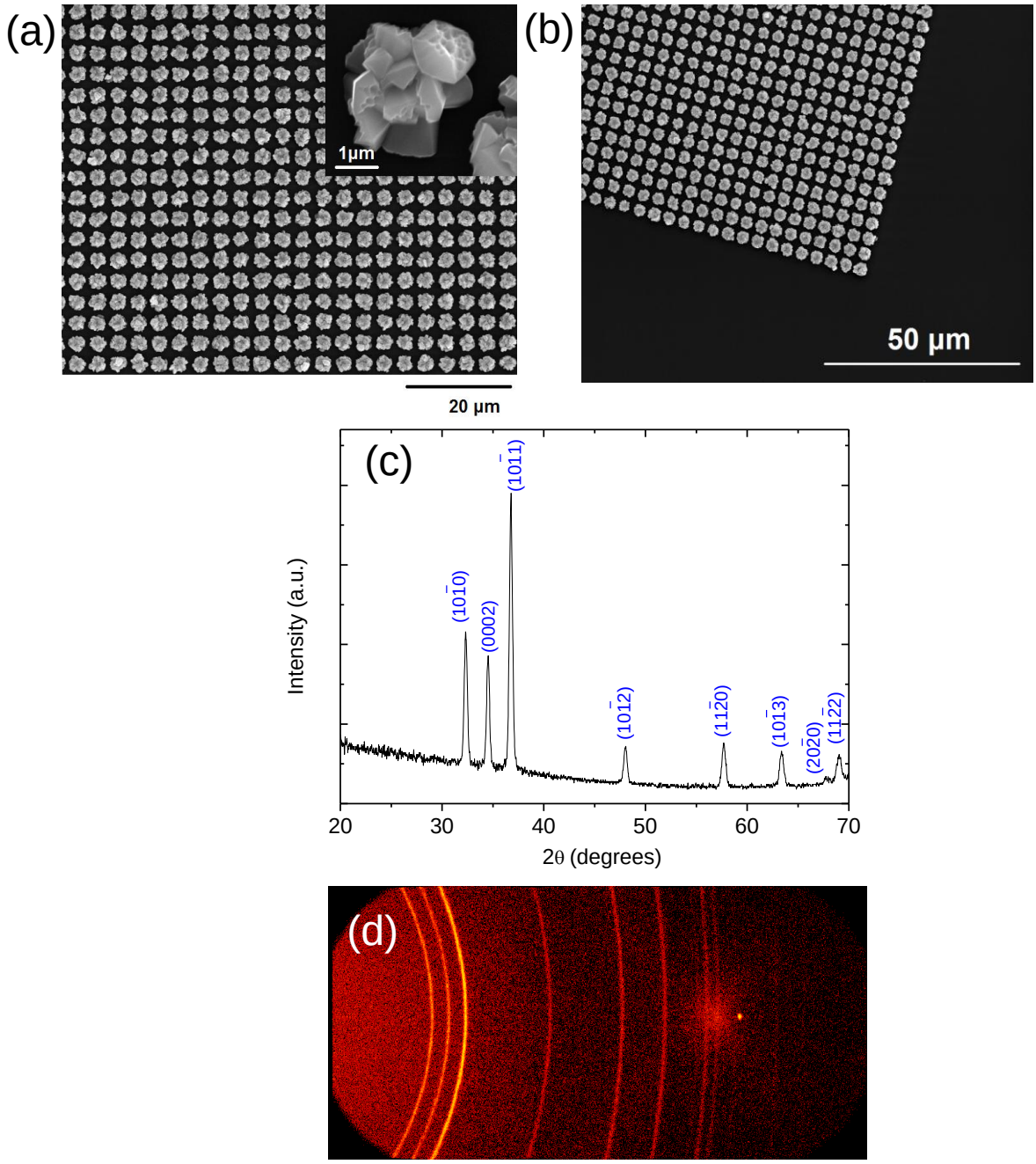

Figure 3.33. (a), (b) SEM images of the ordered porous GaN structure grown by CVD using Ti metal seeds on the patterned SiO_2-coated Si(100) substrates (Inset: magnified image of the porous GaN particles obtained in one of the holes of the patterned substrate). (c) XRD pattern recorded for this structure with the corresponding Debye rings (d).

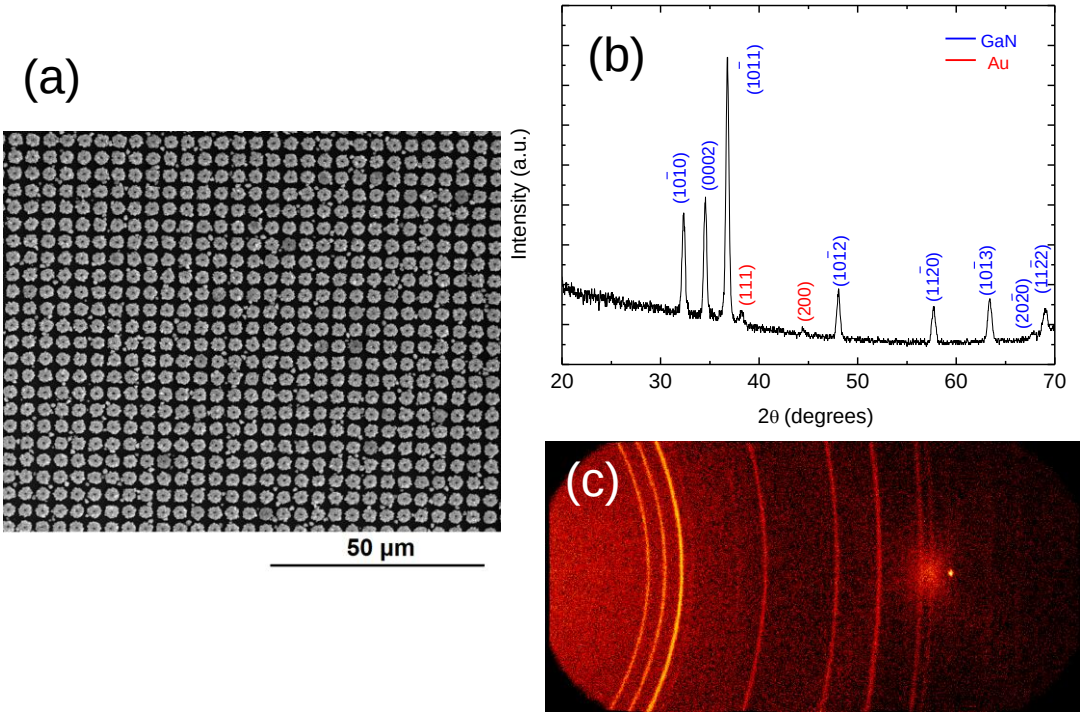

Figure 3.34. (a) SEM image of the ordered porous GaN structure grown by CVD using Au metal seeds on the patterned SiO_2-coated Si (100) substrate. (b) XRD pattern recorded for this structure with the corresponding Debye rings (c).

Figure 3.35 shows SEM images of the sample grown using the Au metal catalyst recorded in different places of the patterned substrate. The substrate was placed in such a way, that the distance between the Ga source and the different places of the substrate was different, so that crystal growth occured with different rates. As can be seen from the images, at early stages, the crystal growth process starts from the edges of the microholes and progress towards the center of the microhole. Thus, the crystallographic orientation of the GaN particles, expected through an orientational effect of the metallic catalyst, is missed due to the nucleation of the GaN particles on the SiO_2 walls of the holes, that do not have the required crystallographic orientation.

A possible solution for this problem might be the replacement of Si(100) by Si(111) as subtrate, which may induce the growth of porous GaN along the *c* crystallographic direction [159], although this approach was not tested yet.

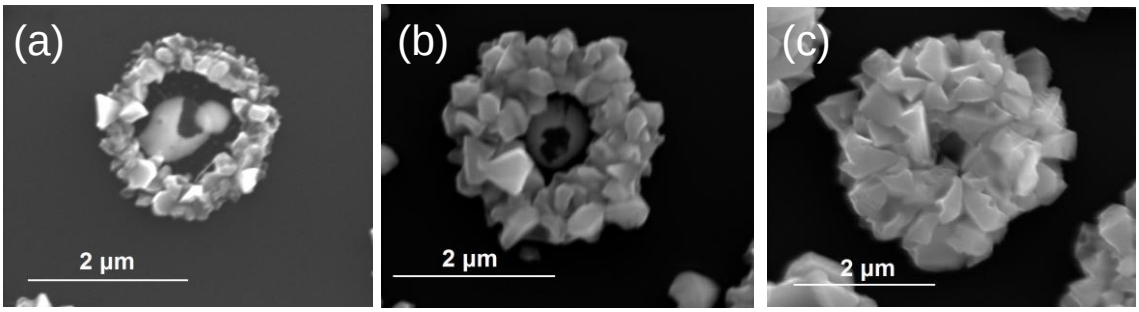

Figure 3.35. SEM images of porous GaN on patterned SiO_2-coated Si(100) substrate using Au as metallic catalyst grown at different growth stages.

Chapter 4

Doping porous GaN

The production of *p*-type and *n*-type GaN has a critical importance for the development of GaN-based optoelectronic devices, such as LEDs, for example. Thus, introducing by CVD a suitable dopant using a suitable precursor into porous GaN plays an important role in the fabrication of good-quality and reproducible *p*-type and *n*-type porous GaN.

The aim of this chapter is to explore the effect of magnesium doping on the production of porous *p*-type GaN and also to show preliminary studies on doping porous GaN with silicon. Thus, here the crystal growth and characterization of *p*-type GaN by Mg-doping on Si and epitaxial GaN substrates through the CVD process using magnesium nitride and magnesium acetylacetonate as initial reagents for magnesium precursors is presented. Evidences of the *p*-type GaN formation were obtained from the electrical characterization of the layers and devices formed and also from PL and CL data. Additionally, when we increased the magnesium concentration we observed the formation of a polycrystalline high-κ oxide layer consisting of MgO located between the Ohmic alloy interlayer contact and the Mg-doped porous GaN layer. Electrical measurements show how a MOS-type porous GaN diode can be formed under these conditions. Finally, the crystal growth and morphological characterization of porous GaN doped with silicon using silicon tetraiodide as precursor is also presented.

4.1 Doping porous GaN with Mg

4.1.1 Crystal growth by CVD: Mg precursors and location of the Mg source

Magnesium (Mg) is a dopant typically used to generate *p*-type conductivity in GaN, since Mg is the shallowest acceptor which can be introduced in sufficient concentrations to obtain reproducible *p*-type GaN [175, 176]. Although Mg is a shallow acceptor [177, 178], for a long time it was not possible to obtain *p*-type GaN. This was due basically to two reasons: (i) hydrogen, which is always present in the CVD growth chamber due to the thermal decomposition of NH_3, passivates Mg by forming electrically inactive complexes [179, 180] and (ii) heavily Mg-doped GaN suffers from self-compensation due to donor-like defects, which includes compensation of Mg acceptors by Mg donors and results in low *p*-type doping efficiency [181]. However, postgrowth treatments, like thermal annealing and electron-beam irradiation, allow the conversion of the high-resistivity as-grown Mg-doped GaN into GaN with *p*-type conductivity. Hydrogenated Mg can be activated by annealing at temperatures above 600 °C in vacuum or in a nitrogen atmosphere [182, 183] or by electron-beam irradiation [184], unlike self-compensated Mg-doped GaN, which cannot be modified by annealing procedures.

Porous GaN doped with Mg was grown through the direct reaction of metallic Ga with NH_3 gas utilizing a Mg precursor in the CVD system. In order to dope GaN with Mg two different precursors were used: magnesium nitride (Mg_3N_2, 99.95 %) and magnesium acetylacetonate dehydrate ($Mg[CH_3COCHC(O)CH_3]_2 \cdot 2H_2O$, 98 %). Mg_3N_2 is in the form of a crystalline powder at room temperature and pressure. Mg_3N_2 starts to decompose at 1073 K [185]. The metalorganic compound $Mg[CH_3COCHC(O)CH_3]_2 \cdot 2H_2O$ (MgA) is also a crystalline powder at room temperature and pressure and starts to decompose at 538 K [186]. Since both precursors are in the form of a crystalline powder, they can be easily manipulated compared to liquid and gaseous precursors. Mg_3N_2 was chosen as a precursor for Mg doping because the by-product of its chemical decomposition is the inert gas nitrogen, that does not produce any problem on doping porous GaN. In the CVD chamber, Mg_3N_2 decomposes thermally to form Mg and nitrogen, according to the following chemical reaction [187]:

$$Mg_3N_2(solid) \rightarrow 3Mg(gas) + N_2(gas)$$

MgA was chosen as precursor for Mg doping because of its low decomposition temperature and gaseous by-products of the decomposition reaction that can be easily exhausted from the CVD reaction chamber. When MgA decomposes thermally, acetone, carbon dioxide, methane, water, etc. can be formed [188]:

$$Mg[CH_3COCHC(O)CH_3]_2 \cdot 2H_2O(solid) \rightarrow Mg(gas) + CH_3COCH_3(gas) + CO_2(gas) + CH_4(gas) + H_2O(gas) + ...$$

To introduce effectively Mg into porous GaN as a dopant, the precursor was located upstream of the Ga source, as it is indicated in Figure 4.1. The position of the precursor was chosen based on the thermal profile of the furnace (see Figure 2.3), choosing a suitable

temperature in the location of the Mg precursor to produce its decomposition while porous GaN is being grown. Since the decomposition temperature of MgA is lower than Mg_3N_2, MgA was located at a further distance from the center of the furnace, where the Ga source is located. Thus, the location of the precursor inside the CVD chamber influences its sublimation and decomposition rate and, as we will show in this chapter, the dopant incorporation into porous GaN depends on the separation distance between the Ga source and the Mg source.

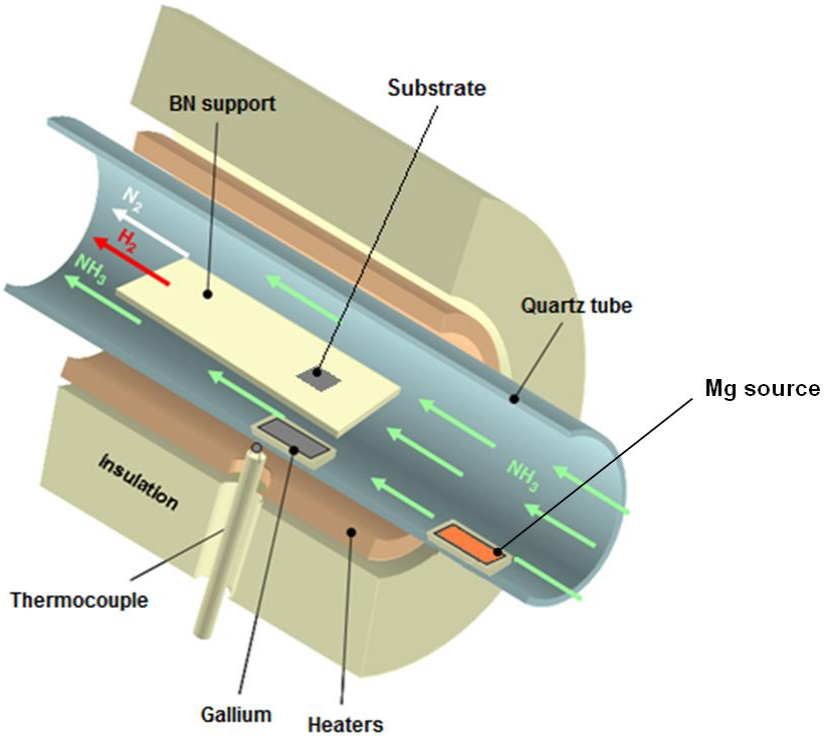

Figure 4.1. Schematic representation of the location of the substrate, the Ga source and the Mg source inside the CVD chamber to produce Mg-doped porous GaN.

For the crystal growth of Mg-doped porous GaN, Si(100) and epitaxial GaN(0001) films on sapphire were used as substrates. As catalysts, a 0.01 M solution of $Ni(NO_3)_2$ in ethanol and 20 nm thick films of Au or Pt deposited by sputtering on Si(100) substrates were utilized. In the case of the epitaxial GaN substrates no catalyst was needed for the deposition of porous GaN. The porous GaN layer was deposited on substrates with an area of ~1 cm^2. After the growth process the as-grown samples were annealed in an atmosphere of N_2 for 20 min at 973 K in order to break the Mg-H complexes and activate the *p*-type conductivity of porous GaN.

4.1.2 Use of Mg_3N_2 as precursor

4.1.2.1 Effect of the distance and Mg_3N_2 quantity

We investigated the introduction of Mg into GaN as a dopant by designing a set of experiments in which we changed the quantity of the Mg_3N_2 precursor powder and the distance between the Ga and the Mg sources. Mg_3N_2 was placed at distances of 15 cm, 10 cm and 5 cm between the Ga and Mg sources that correspond to temperatures of ~1050 K, ~1150 K and ~1175 K, respectively. The distances were chosen based on the thermal profile of the furnace described in Chapter 2 and the decomposition temperature of Mg_3N_2, which is 1073 K [185]. As substrate, silicon (100) and as catalyst, a 0.01 M solution of $Ni(NO_3)_2$ in ethanol were used. The quantities of precursor introduced in the furnace were 0.0075 g, 0.0125 g, 0.0250 g and 0.0500 g, which corresponds to Mg vs. Ga molar ratios 0.031, 0.052, 0.104 and 0.207, respectively. The samples and the conditions under which they were prepared are listed in Table 4.1.

Table 4.1. The Mg-doped porous GaN samples prepared by using Mg_3N_2 as Mg precursor.

Sample ID	Distance between the Ga and Mg sources (cm)	Quantity of Mg_3N_2 (g)	Mg vs. Ga molar ratio
A	15	0.0075	0.031
B	10	0.0075	0.031
C	5	0.0075	0.031
D	5	0.0125	0.052
E	5	0.0250	0.104
F	4	0.0075	0.031
G	4	0.0125	0.052
H	4	0.0500	0.207
K	4	0.0750	0.311

The SEM images shown in Figure 4.2a, 4.2b and 4.2c, which correspond to separation distances between the Ga and Mg sources of 15 cm, 10 cm and 5 cm, respectively, while keeping the quantity of precursor constant at 0.0075 g, indicate a slight decrease of porosity of GaN when the separation distance decreased.

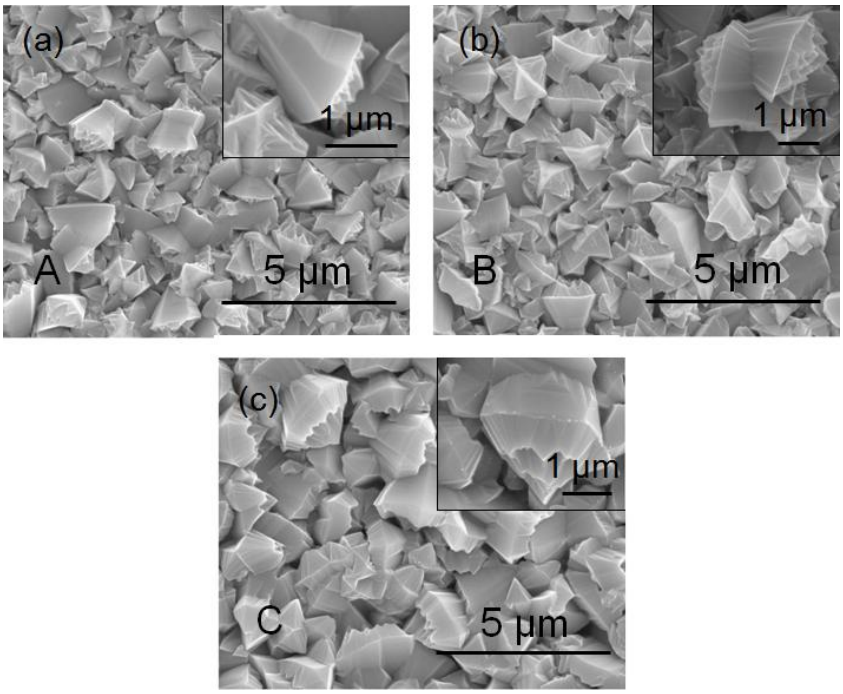

Figure 4.2. SEM images of porous Mg-doped GaN using 0.0075 g of Mg_3N_2 at (a) 15 cm, (b) 10 cm and (c) 5 cm separation distance between the Ga and the Mg sources. The samples ID are indicated in each picture.

The same effect is observed when the separation distance was kept at 5 cm and the quantity of precursor was increased from 0.0075 g to 0.025 g, as can be seen in Figures 4.3a-4.3c.

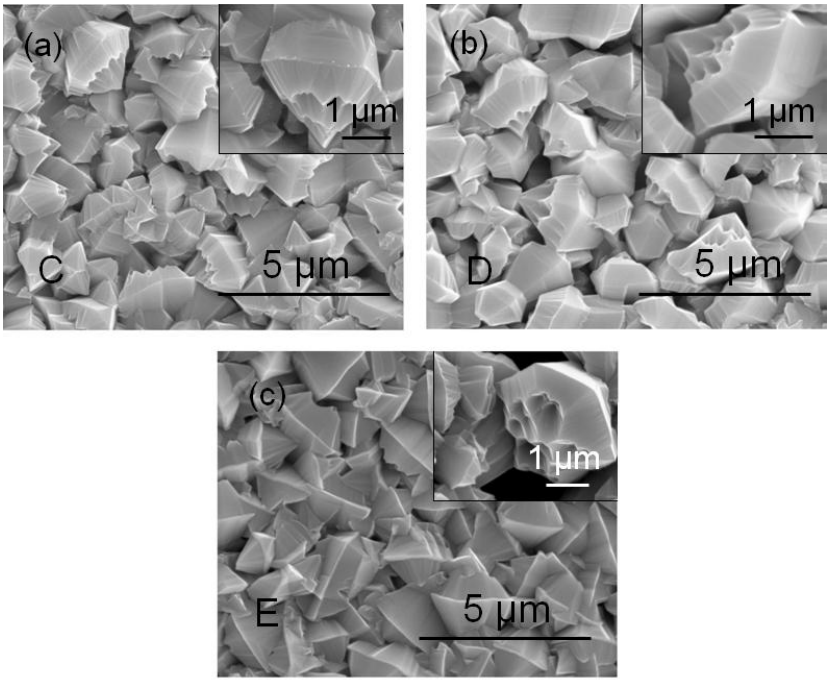

Figure 4.3. SEM images of porous Mg-doped GaN using (a) 0.0075 g, (b) 0.0125 g and (c) 0.025 g of Mg_3N_2 located at 5 cm from the Ga sources. The samples ID are indicated in each picture.

Another set of experiments were undertaken by placing Mg_3N_2 closer to the Ga source (4 cm, what corresponds to ~ 1200 K). The experiments were performed with 0.0075 g, 0.0125 g, 0.0500 g and 0.0750 g of Mg_3N_2, corresponding to samples F, G, H and K (see Figure 4.4). Here, the decrease of porosity in GaN microcroparticles is more evident, and in samples grown using 0.0500 g and 0.0750 g of Mg_3N_2 pores are practically absent.

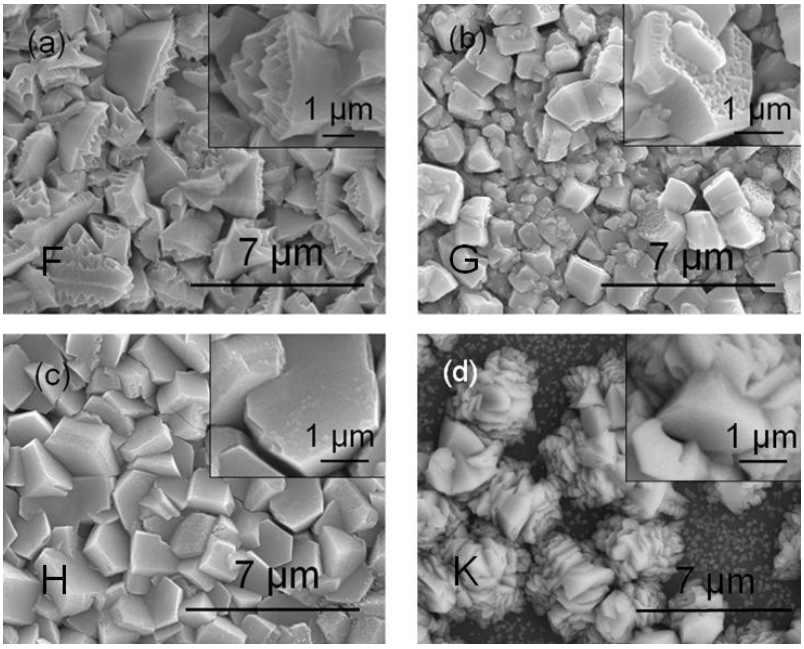

Figure 4.4. SEM images of porous GaN doped with Mg using Mg_3N_2 as precursor located 4 cm away from the Ga source and with Mg_3N_2 quantities: (a) 0.0075 g, (b) 0.0125 g, (c) 0.05 g and (d) 0.075 g. The samples ID are indicated in each picture.

After studying the conditions of the chemical reaction, it can be concluded that the optimum conditions for growing Mg-doped porous GaN with a high degree of porosity using Mg_3N_2 as precursor are 4 cm distance between the Ga and Mg sources and 0.0075 g of Mg_3N_2.

4.1.2.2 Effect of the catalyst

In order to study the effect of the catalyst used to deposit Mg-doped porous GaN, we grew porous particles using 0.0075 g of Mg_3N_2 located at a separation distance of 4 cm from the Ga source on Si(100) substrates coated with 20 nm thick films of Au and Pt, similarly to what we did with undoped porous GaN (see Chapter 3). Figure 4.5a shows a schematic presentation of the Mg-doped porous GaN on Si with Ga_2Au and Pt-Ga intermetallic layers formed between the Si substrate and the Mg-doped porous GaN layer. Figures 4.5b, 4.5c and 4.6d show the SEM images of Mg-doped porous GaN particles grown using $Ni(NO_3)_2$, Au and Pt catalysts, respectively. Porous GaN particles have a morphology similar to that observed in undoped samples. However, the degree of porosity is higher in the case of $Ni(NO_3)_2$ catalyst, while those grown on Pt seem to show the lowest degree of porosity.

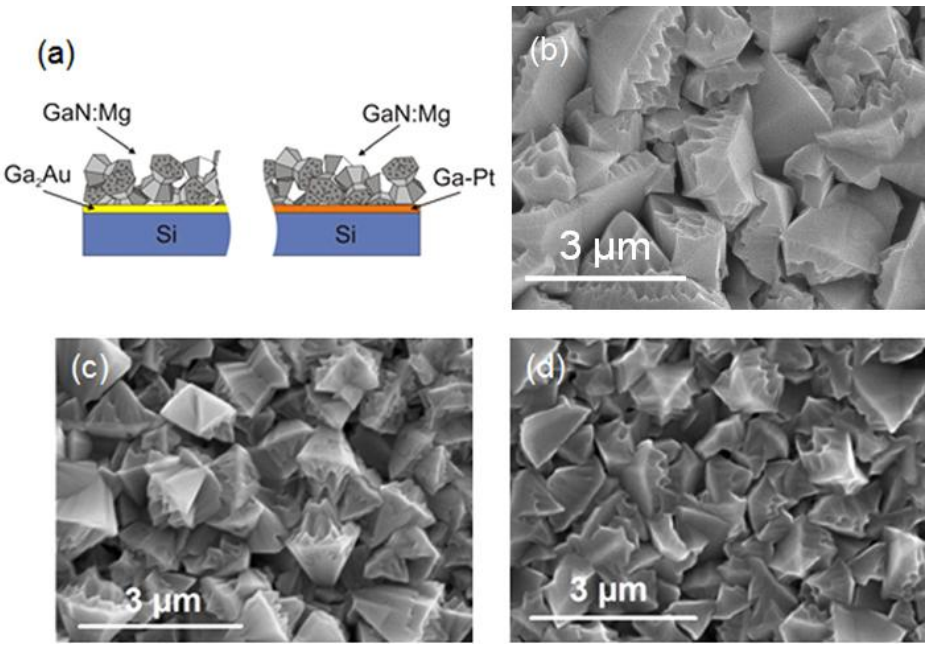

Figure 4.5. (a) Schematic presentation of porous Mg-doped GaN particles grown on Si with Ga_2Au and Pt-Ga intermetallic layers. SEM images of porous Mg-doped GaN particles grown on Si substrates coated with (b) $Ni(NO_3)_2$, (c) Au and (d) Pt (partial reproduction of Figure 1 from Paper V).

4.1.2.3 Structural characterization

The structural XRD characterization of the Mg-doped porous GaN particles confirms the crystalline wurtzite structure (see Figure 4.6). The sharp diffraction peaks reveal that the GaN nanoporous particles have a good-crystalline quality. Also, no additional crystalline phases were detected.

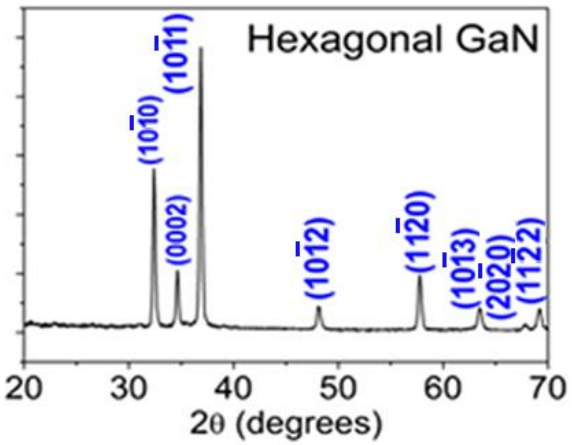

Figure 4.6. X-ray diffraction pattern of porous Mg-doped GaN particles on Si (100) (partial reproduction of Figure 1 from Paper V).

4.1.2.4 Compositional analysis

Figure 4.7 shows a cross-section TEM image of the porous GaN layer grown using 0.0075 g of Mg_3N_2 located at a separation distance of 4 cm. Here, two regions have been observed. Region I corresponds to the Si substrate. Region II, totally detached of the substrate in the picture, corresponds to Mg-doped GaN, with a thickness of ~ 4.5 μm. EDX analyses corresponding to 10 separate locations of this sample, listed in Table 4.2, indicate that the concentration of Mg increases for points located far away from the substrate. Thus, the doping process of GaN is not homogeneous and the quantity of Mg incorporated in the porous particles is higher at the last stages of the growth process.

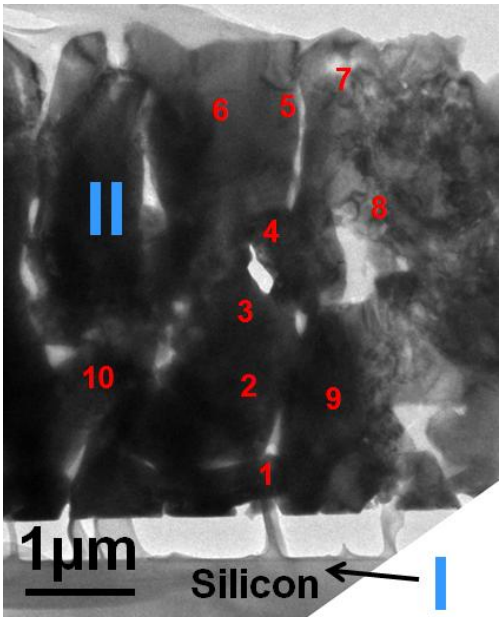

Figure 4.7. Cross-section TEM image of the porous GaN layer grown using using 0.0075 g of Mg_3N_2 located at a separation distance of 4 cm (partial reproduction of Figure 3 from Paper VI).

Table 4.2. EDX content of Mg and Ga in the Mg-doped GaN. The measurement points (#) relate to those numbered in Figure 4.7.

Position #	**Mg %**	**Ga %**	**Position #**	**Mg %**	**Ga %**
1	1.3	98.7	6	2.2	97.8
2	1.5	98.5	7	2.5	97.6
3	1.9	98.1	8	1.8	98.2
4	3.9	96.1	9	1.8	98.2
5	2.6	97.4	10	1.4	98.6

4.1.2.5 Electrical characterization

After crystal growth and prior to perform electrical characterization, a thermal annealing at 973 K in a N_2 atmosphere for 20 min was performed in order to break the Mg-H complexes and activate Mg acceptors and *p*-type conductivity in Mg doped porous GaN. Figure 4.8 shows the SEM images of Mg-doped porous GaN particles grown using Pt catalyst before (see Figure 4.8a) and after (see Figure 4.8b) the annealing process. We can observe that thermal annealing does not change the morphology of Mg-doped porous GaN particles.

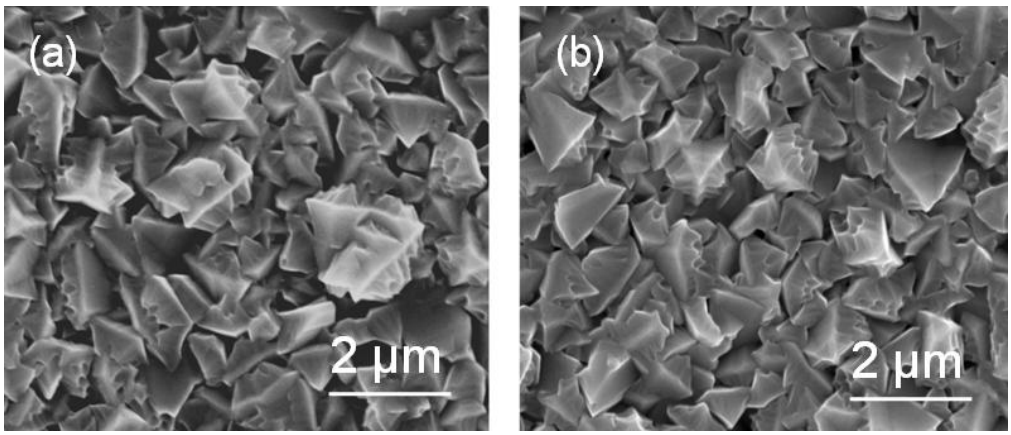

Figure 4.8. SEM images of the Mg-doped porous GaN particles grown using Pt catalyst (a) before and (b) after annealing process at 973 K in a N_2 atmosphere for 20 min.

As it was reported in Paper V, two-probe electrical measurements of Mg-doped GaN samples were conducted using In/Ga liquid eutectic drops as Ohmic contacts. Linear voltage sweeps were obtained in the range from -3V to 3V with a 50 mV/s sweep rate. Figures 4.9a and 4.9b show the I-V curves recorded for the Mg-doped porous GaN particles grown on Au and Pt-coated Si (100) substrates, respectively. For samples grown using a Au catalyst, a near Ohmic contact behavior was repeatedly observed which is consistent with the formation of a Ga_2Au intermetallic between the underlying substrate and the GaN layer in a similar way observed for undoped porous GaN particles (see Chapter 3). However, for the GaN samples grown using Pt as catalyst, the response was markedly different with the profile indicating the formation of a Schottky contact. For porous GaN specifically, the thickness is determined by the size of the crystals and their assembly on the surface, which results in a "rough" topology, with a high density of grain boundary scattering centers. For electrical measurements, particle distributions confirm that the formation of a percolating conduction layer beneath the GaN layer is prevented; thus, the electrical characterization corresponds to the porous GaN polycrystalline layer. At room temperature, the effective linearity of the I−V response measured for porous GaN to high work function metals, with an intermetallic seed layer between the metal and GaN, is maintained at high bias. As stated earlier, the Pt-Ga alloy results in a Schottky contact to the porous *p*-type GaN. The Schottky barrier height $\varphi^{o}_{B,p}$ (SBH) can be estimated from equation 3.1. The estimated SBHs for Pt contacted porous *p*-type GaN is 0.57 eV. While a small in-built potential also exists for the Au-contacted sample, the symmetry in the response at negative bias confirms that the presence of the intermetallic

Ga_2Au at the GaN-Si interface prevents a rectifying barrier. Also, as with unintentionally *n*-type GaN we investigated previously (see Chapter 3), the Pt-Ga contact to the GaN at the silicon interface results in an order of magnitude higher current, but in the case of *p*-type GaN, the transport mechanism gives a non-linear, Schottky-type response.

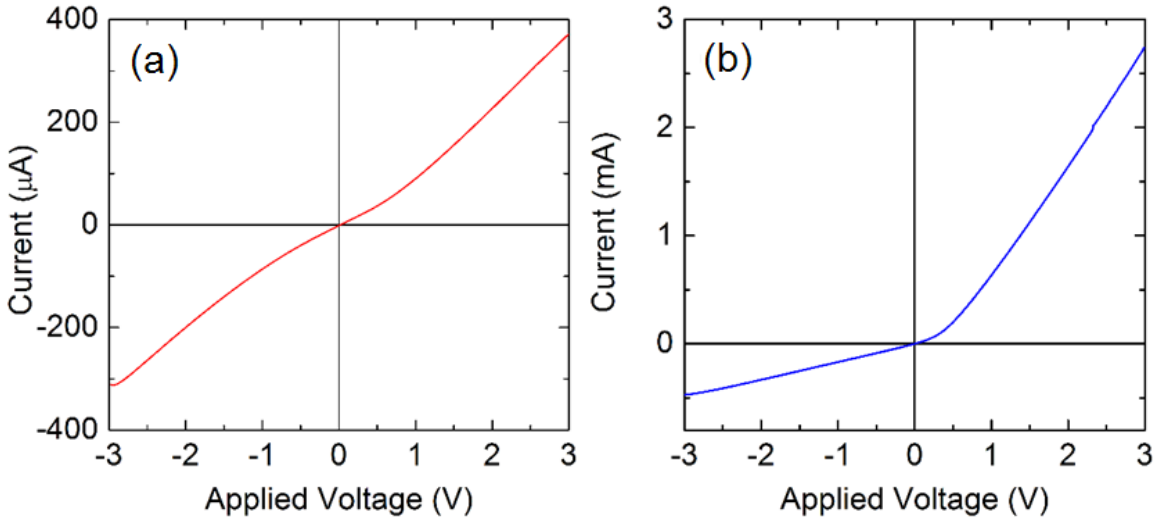

Figure 4.9. I-V curves of porous Mg-doped GaN particles grown on Si substrates coated with (a) Au and (b) Pt catalysts (partial reproduction of Figure 1 in Paper 5).

From these data it is not possible to determine if Mg-doped GaN has a *p*-type conductivity. This will be demonstrated in the next chapter, from the epitaxial porous GaN layers grown on non-porous GaN substrates, for which clear *p*-*n* junction responses could be determined. Thus, we suppose that the Mg-doped porous GaN particles characterized in this chapter, and grown under similar doping conditions than the epitaxial layer, also exhibit *p*-type conductivity.

4.1.2.6 Cathodoluminescence

CL investigations of the porous GaN samples G, K and undoped porous GaN for comparison were performed, as described in Paper V. Figure 4.10a and 4.10b show the SEM and the panchromatic CL corresponding images of porous undoped GaN and Mg-doped porous GaN particles. Higher intensity of luminescence is observed in the areas around the pores. Typically, epitaxial or MBE grown GaN films suffer from low intensities due to electron-hole pair formation at low voltages, which increases non-radiative surface recombinations. In this case of porous GaN, the emission is enhanced at the high density of sharp edge surfaces found on the crystal and thus throughout the porous film. Figure 4.10c shows the CL spectra recorded for porous GaN samples at room temperature. In the spectra acquired at an accelerating voltage V_{acc}=10 kV, a shift of the CL peak is found for Mg-doped samples in comparison to undoped GaN, which would indicate the effective incorporation of

Mg in the GaN structure [189]. The yellow luminescence (YL) seen from CL shows two contributions, typically ascribed to pair recombination and deep level emission characteristics of doped *p*-type GaN. The near-band edge emission is similar in doped samples and not found in undoped GaN, but lower in energy (397 nm) than the bandgap emission from GaN (the monochromator edge was 368 nm for Mg-doped CL).

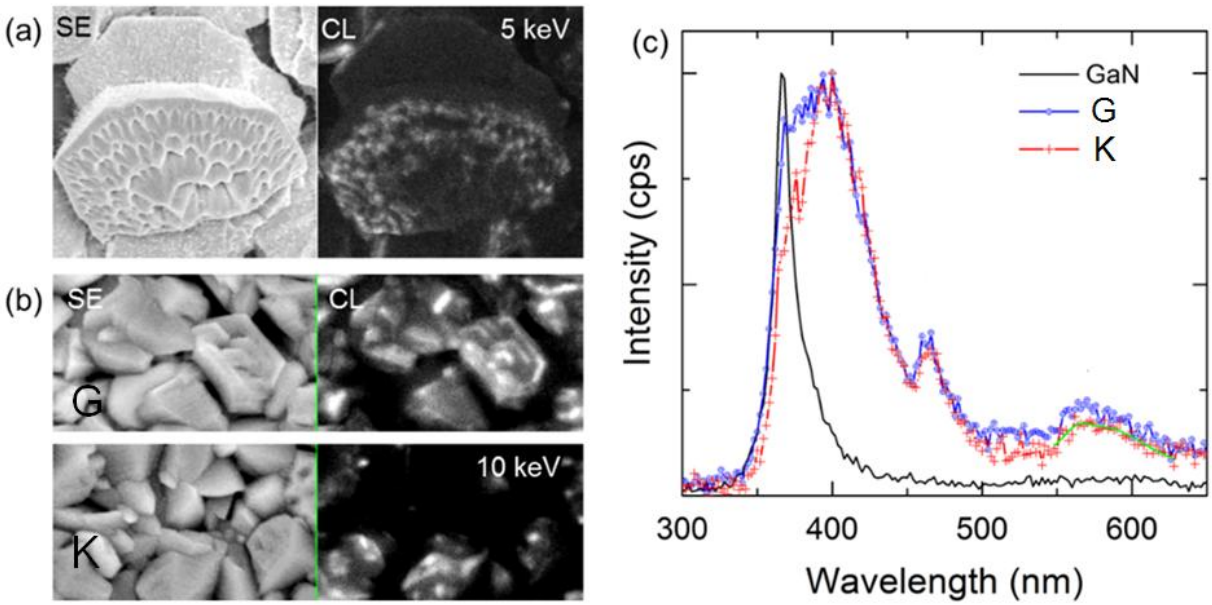

Figure 4.10. (a) SEM and panchromatic CL images of undoped *n*-type GaN crystals at 5 kV. (b) SEM and CL images of the porous GaN G and K samples at 10 kV. (c) CL spectra from undoped and Mg-doped porous GaN (partial reproduction from of Figure 3 in Paper V).

4.1.3 Use of magnesium acetylacetonate as precursor

We investigated also the introduction of Mg into GaN as a dopant through a different precursor, magnesium acetylacetonate. We designed a set of experiments in which we changed the quantity of the MgA precursor powder and the distance between the Ga and Mg sources, as in the previous case. The MgA precursor powder was placed up-stream of the Ga source at distances of 15 cm, 20 cm, 21 cm, 23 cm, 24 cm, 26 cm and 30 cm, where temperatures of ~1050 K, ~830 K, ~770 K, ~700 K, ~650 K, ~530 K and ~380 K can be found corresponding to the thermal characterization of the furnace (see Figure 2.3), while the decomposition temperature of MgA is 538 K [186]. As substrate silicon (100) and as catalyst a 0.01 M solution of $Ni(NO_3)_2$ in ethanol were used. The samples we prepared and the conditions under which they have been prepared are listed in Table 4.3.

Table 4.3. Mg-doped porous GaN samples prepared with the MgA precursor.

Sample ID	Distance between the Ga and Mg sources (cm)	Quantity of MgA (g)	Mg vs. Ga molar ratio
A	15	0.0507	0.0273
B	15	0.0844	0.0455
C	15	0.1688	0.0910
D	20	0.0507	0.0273
E	20	0.0844	0.0455
F	23	0.0507	0.0273
G	24	0.0507	0.0273
H	26	0.0507	0.0273
K	30	0.0507	0.0273
L	20	0.1688	0.0910
M	21	0.1688	0.0910
N	23	0.1688	0.0910
O	24	0.1688	0.0910

SEM images of the A, B and C samples can be seen in Figure 4.11. They reveal a similar and high degree of porosity in the GaN particles obtained.

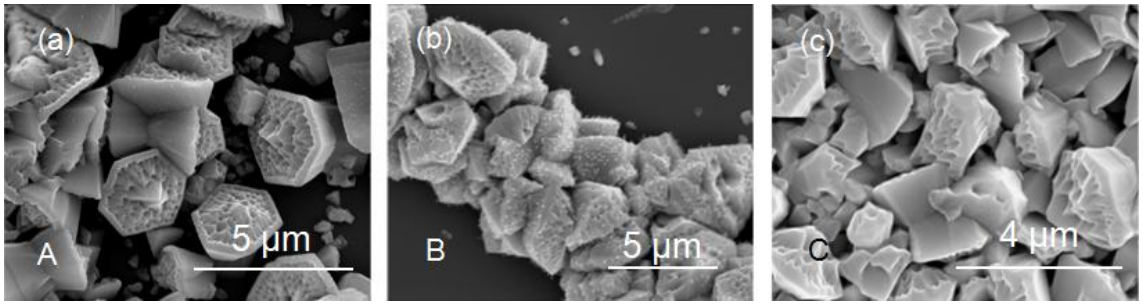

Figure 4.11. SEM images of Mg-doped porous GaN samples prepared with different quantities of the MgA precursor and at a distance of 15 cm between the Ga and Mg sources (a) 0.0507 g (sample A), (b) 0.0844 (sample B) and (c) 0.1688 g (sample C). The samples ID are indicated in each picture.

CL investigation of the Mg-doped porous GaN particles was performed on samples grown using the MgA dopant at room temperature, using accelerating voltages of 5 kV and 20 kV to excite parts of the particles located at different depths. Accelerating voltage of 5 kV excites only the most superficial parts of the particles, while an accelerating voltage of 20 kV excites more internal parts of the particles where Mg-H complexes could not be formed. The SEM and the corresponding panchromatic CL pictures recorded for the A, B and C samples, as well as their CL spectra are shown in Figure 4.12. The CL images demonstrate that the luminescence is not distributed homogeneously in the sample. High intensity luminescence regions corresponds to the edges of the rough basal planes of the GaN particles, where pores are located, as in the previous cases, while weak luminescence can be seen on the smooth

lateral faces of the porous GaN particles. The peak emission observed in the spectra at ~370 nm in all samples corresponds to the GaN band-gap energy. In the spectrum acquired for sample C at an accelerating voltage of 20 kV we observe an additional peak, marked with an arrow on the CL spectrum in Figure 4.12c, when compared to the spectra recorded at 5 kV. This would indicate that Mg has been introduced in the bulk material, since excitation at 20 kV allows recording the luminescence generated from deeper regions of the particles, avoiding surface effects like those observed when excited at 5 kV.

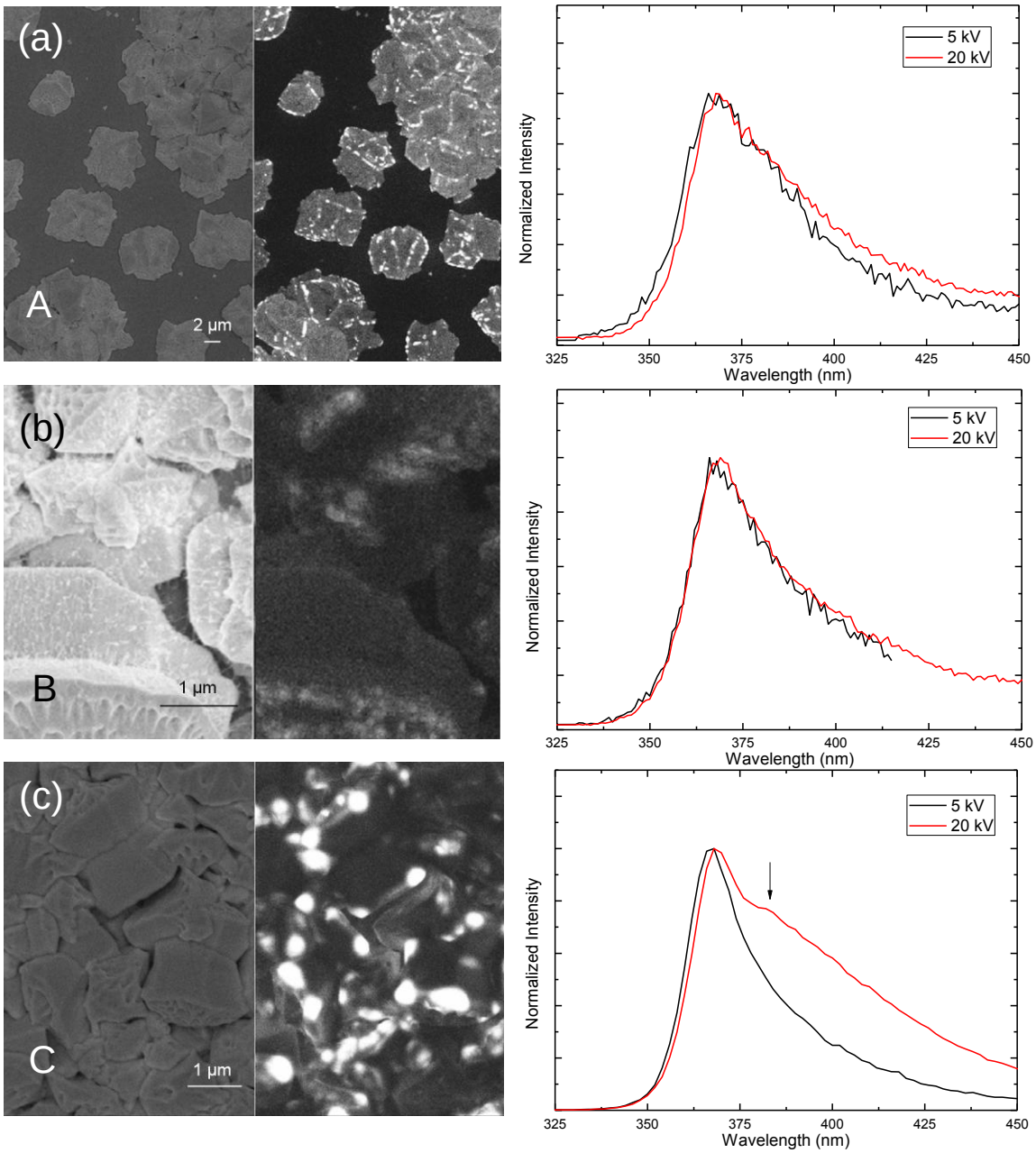

Figure 4.12. SEM and panchromatic CL images, and corresponding CL spectra of Mg-doped porous GaN samples prepared with different quantities of the MgA precursor located at a distance of 15 cm between the Ga and Mg sources (a) 0.0507 g (sample A), (b) 0.0844 (sample B) and (c) 0.1688 g (sample C).

Sample C was analyzed more in detail. The CL spectra collected at different accelerating voltages is presented in Figure 4.13. We used different voltages to activate deeper regions in the GaN particles, to determine if the distribution of Mg in the samples is homogenous. At an accelerating voltage of 10 kV the band related to Mg acceptors in Mg-doped porous GaN becomes evident. The intensity of this band is higher at 10 and 15 kV. Also, its position for these voltages is the most red-shifted from all the voltages analyzed. This would mean that the distribution of Mg in the porous particles is not homogeneous, being higher in the outer regions.

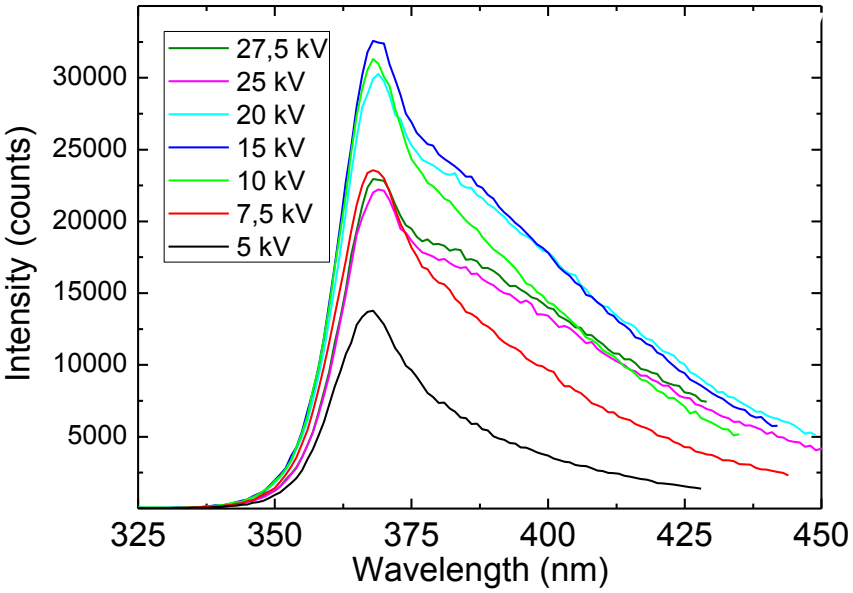

Figure 4.13. CL spectra collected at different acceleration voltages for sample C.

Then, the separation distance between the Ga and the Mg source was increased to 20 cm to reduce the temperature applied to MgA, using of 0.0507 g and 0.0844 g of the precursor, that corresponds to samples D and E (see Figure 4.14). It seems that the porosity is slightly reduced when the quantity of precursor is reduced, as can be seen in Figure 4.14b.

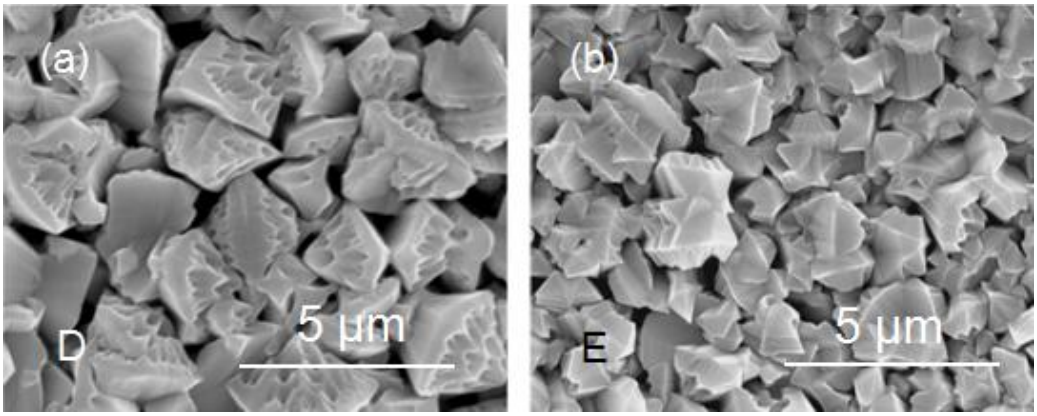

Figure 4.14. SEM images of samples (a) D and (b) E samples synthesized using 0.0507 g and 0.0844 g, respectively, of MgA, placed at 20 cm from the Ga source.

The SEM and panchromatic CL pictures recorded for D and E samples, as well as the corresponding CL spectra are shown in Figure 4.15. In the spectra in Figure 4.15 recorded at an accelerating voltage of 20 kV we observe a shift of the band-edge emission peak, that would indicate the effective doping of porous GaN with Mg. For sample E the shift in the position of the emission peak is larger, this can be related to a higher doping level of porous GaN in that case. We also observe additional peaks marked with arrows in the blue and UV regions that can be attributed to DAP recombinations.

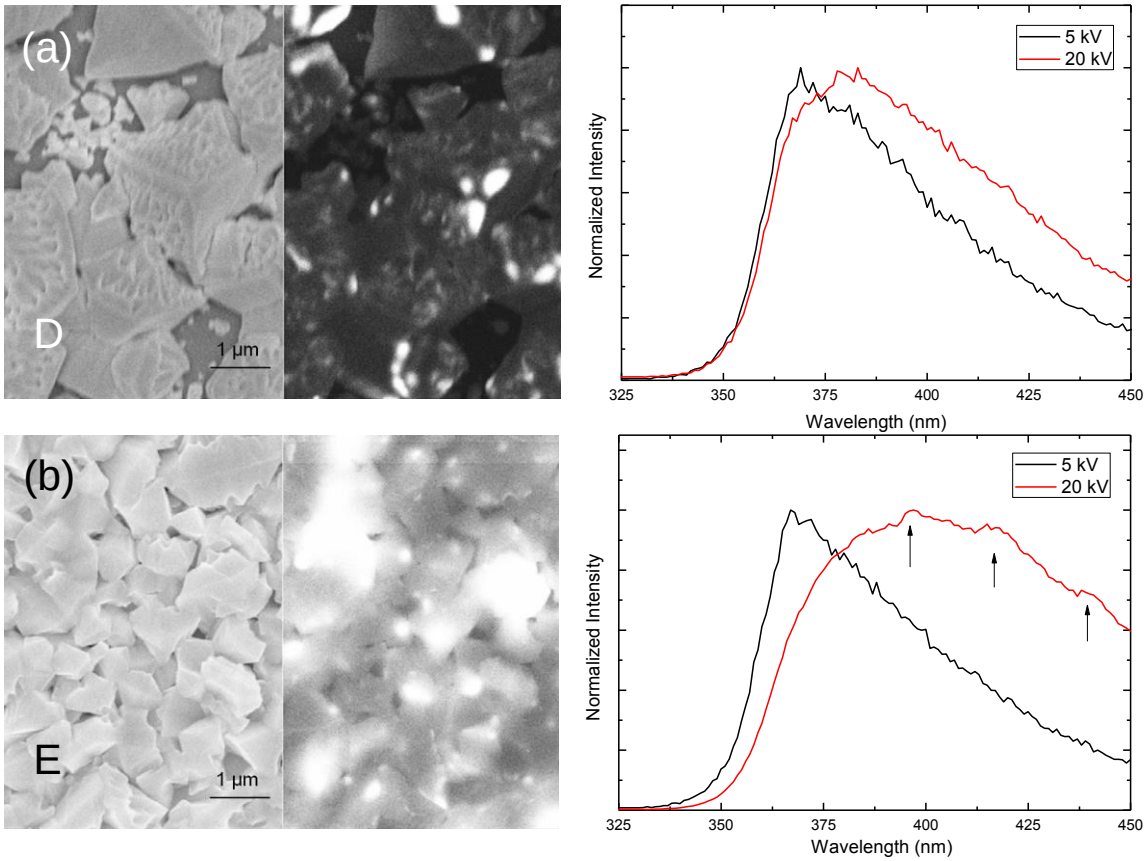

Figure 4.15. SEM and panchromatic CL images and corresponding CL spectra of samples D and E, synthesized using (a) 0.0507 g and (b) 0.0844 g of MgA located at 20 cm from the Ga source.

In order to study if the irradiation with an electron beam could activate the *p*-type conductivity on the surface of the material, an experiment was designed in which sample E was irradiated in the same area successively with 5kV, 20 kV and again 5 kV accelerating voltages. We used two different voltages, because at higher accelerating voltages the electron beam can penetrate and excite deeper areas of the material. The corresponding CL spectra shown in Figure 4.16 evidence that irradiation with an electron beam has no effect on the CL collected at a low acceleration voltage. Thus, Mg acceptors were not activated on the surface of porous GaN by the electron beam, and an additional annealing process would be necessary for this purpose. The fact that we do not see emission in UV and blue region of the spectrum at low accelerating voltages, might be related to the presence of Mg-H complexes on the surface of porous GaN that deactivate the Mg acceptor [190]. At high accelerating voltages

the electron beam is able to penetrate and excite deeper areas of the material with active Mg acceptors, not passivated by hydrogen.

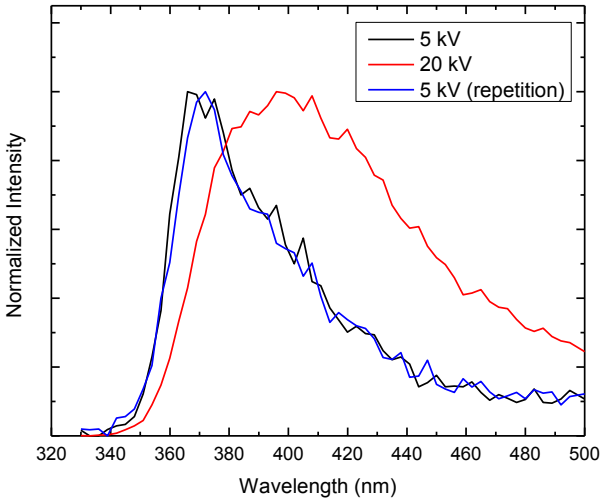

Figure 4.16. CL spectra of sample E synthesized using 0.08440 g of MgA located at 20 cm from the Ga source, collected successively at 5 kV, 20 kV and 5 kV of acceleration voltages.

We wanted to analyze if placing the Mg precursor at colder places of the furnace, we would still be able to incorporate Mg to porous GaN. For this, we kept constant the MgA concentration, using 0.0507 g of this compound, while the distance between the Ga and the Mg sources was increased to 15 cm, 20 cm, 23 cm, 24 cm, 26 cm and 30 cm. In all cases the porosity of the GaN particles was maintained (see Figure 4.17), for distances < 30 cm.

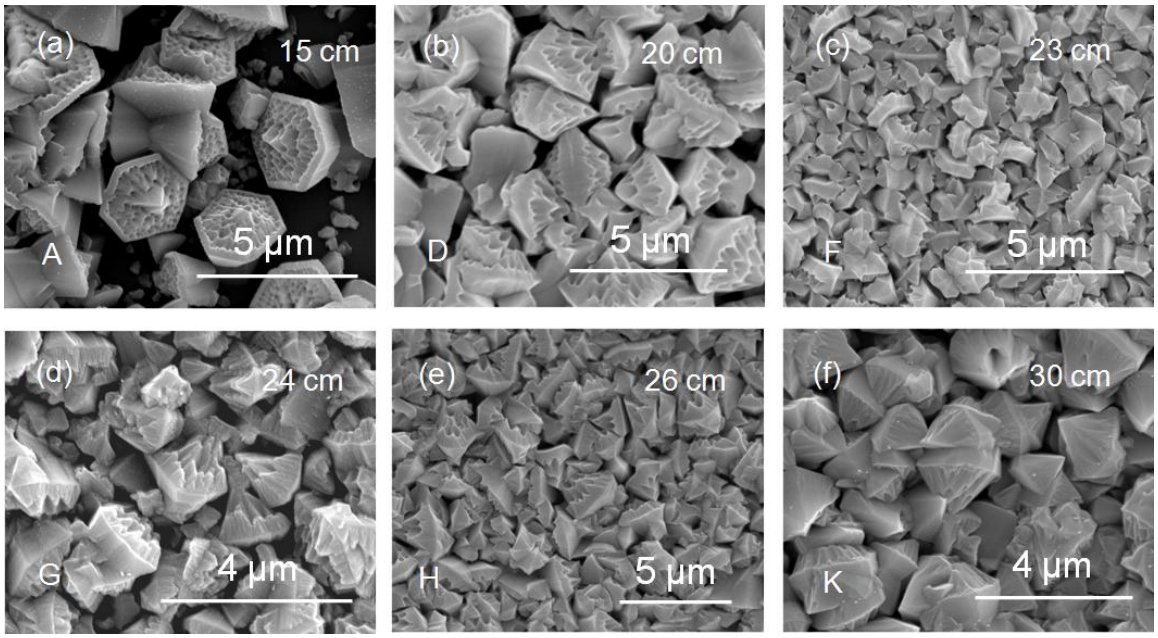

Figure 4.17. SEM images of Mg-doped porous GaN samples synthesized using 0.0507 g of MgA, while the distance between the Ga and the Mg sources was increased, as indicated in the pictures. Also, samples ID are indicated in each picture.

The SEM and panchromatic CL pictures and the corresponding CL spectra recorded for these samples are shown in Figure 4.18 In the cases where an effective incorporation of Mg is produced, we should observe a red-shift of the emission peak in the spectra collected at 20 kV to respect that collected at 5 kV. The largest shift is observed in samples D and F for which MgA was located at 20 cm and 23 cm, respectively, to respect the Ga source. Thus, it can be concluded that the optimum distance between the Ga and the Mg sources for a successful doping porous GaN produced by the CVD process and using MgA as precursor is around 20-23 cm.

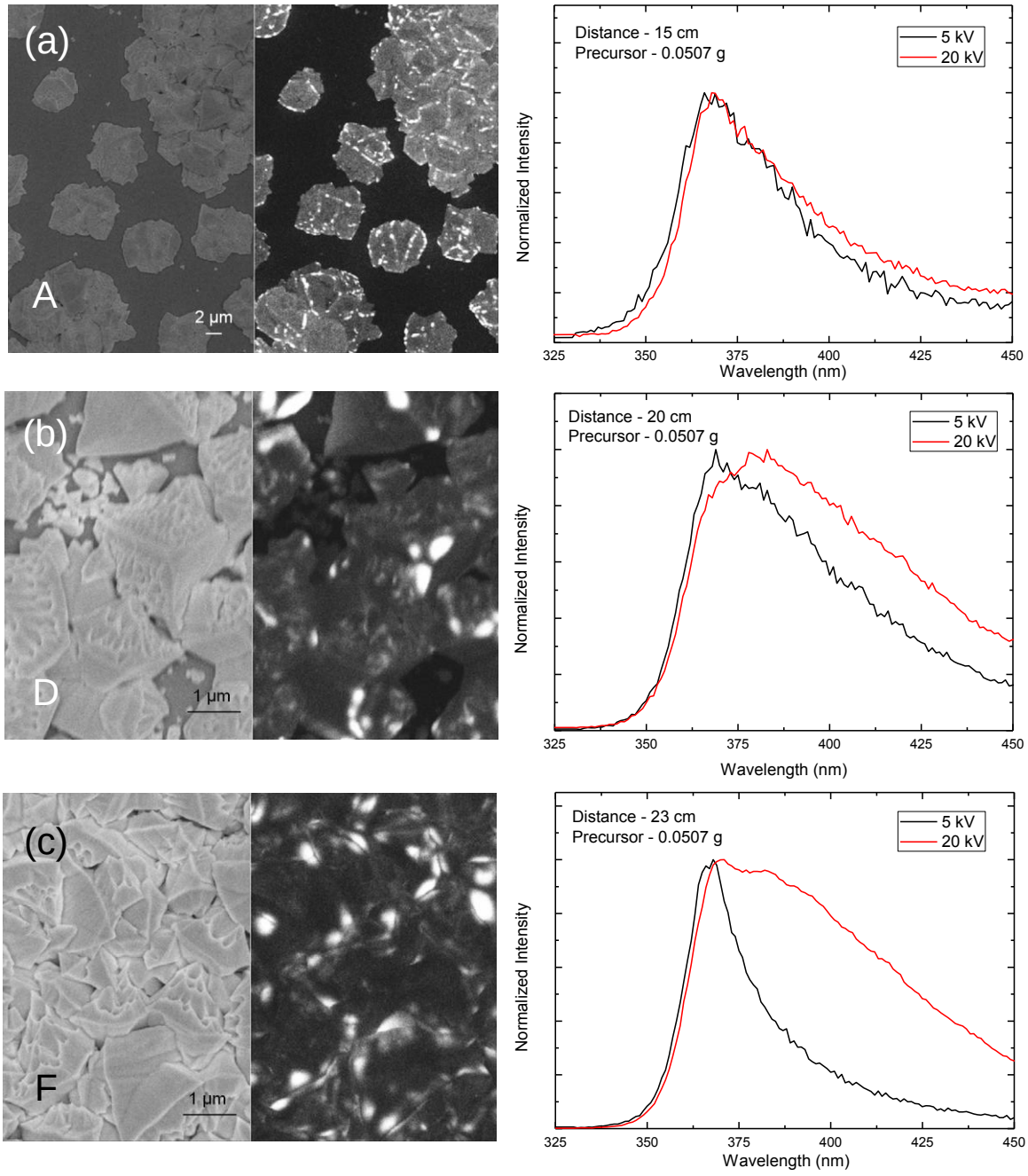

Figure 4.18. SEM, panchromatic CL images and corresponding CL spectra of Mg-doped porous GaN samples synthesized using 0.0507 g of MgA. The distances between the Ga and the Mg sources and the samples ID are indicated in each picture (continuation next page).

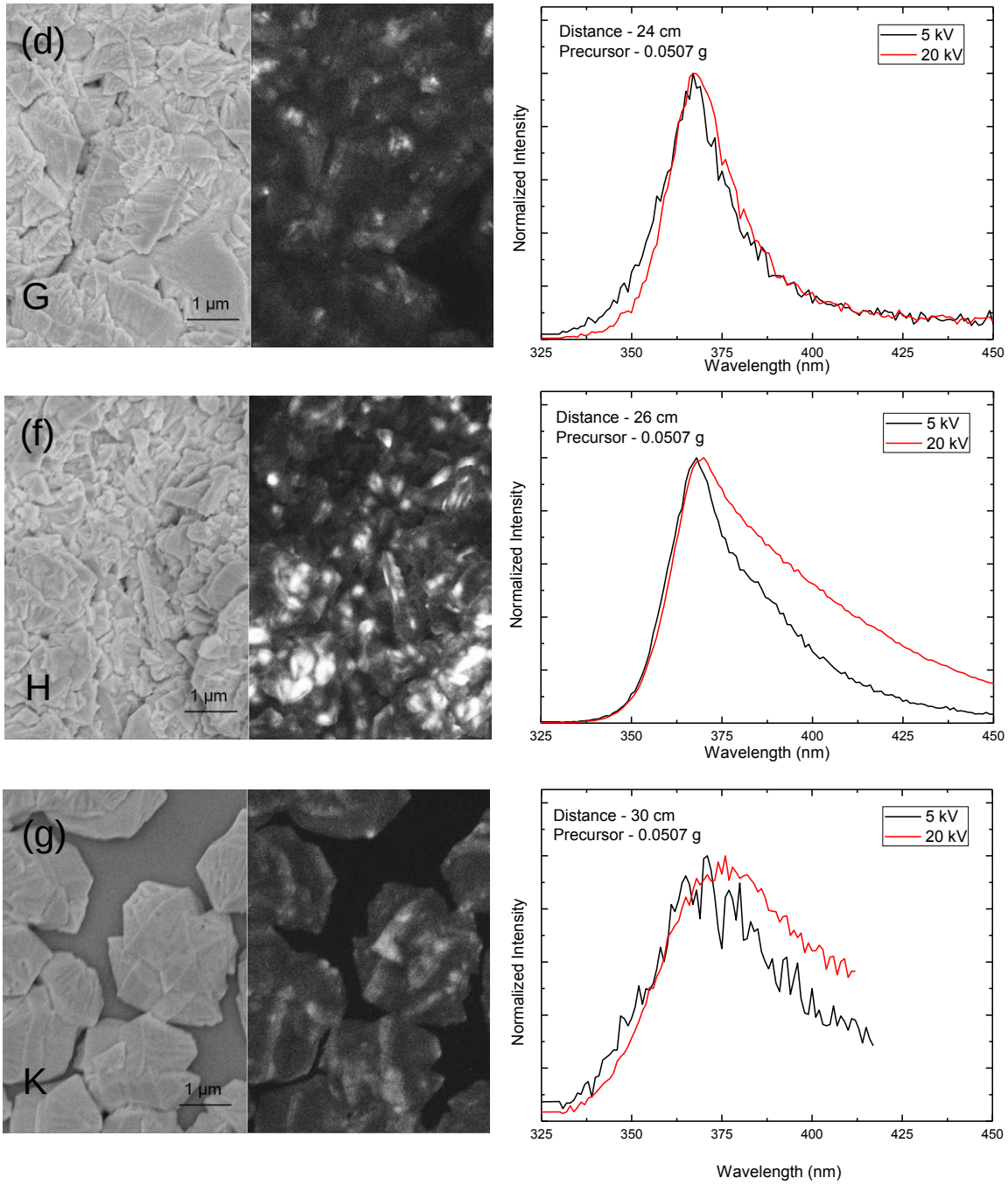

Figure 4.18. SEM, panchromatic CL images and corresponding CL spectra of Mg-doped porous GaN samples synthesized using 0.0507 g of MgA. The distances between the Ga and the Mg sources and the samples ID are indicated in each picture.

Finally, to optimize the distance at which the MgA precursor should be placed, four additional experiments were performed at separation distances of 20 cm, 21 cm, 23 cm and 24 cm with a higher quantity of precursor (0.1688 g), corresponding to samples L, M, N and O in Table 4.3. In Figure 4.19 the porosity of the particles decreased dramatically at distances above 21 cm. However, the level of Mg incorporation and the type of conductivity of porous GaN has to be proven by cathodoluminescence and electrical characterization techniques.

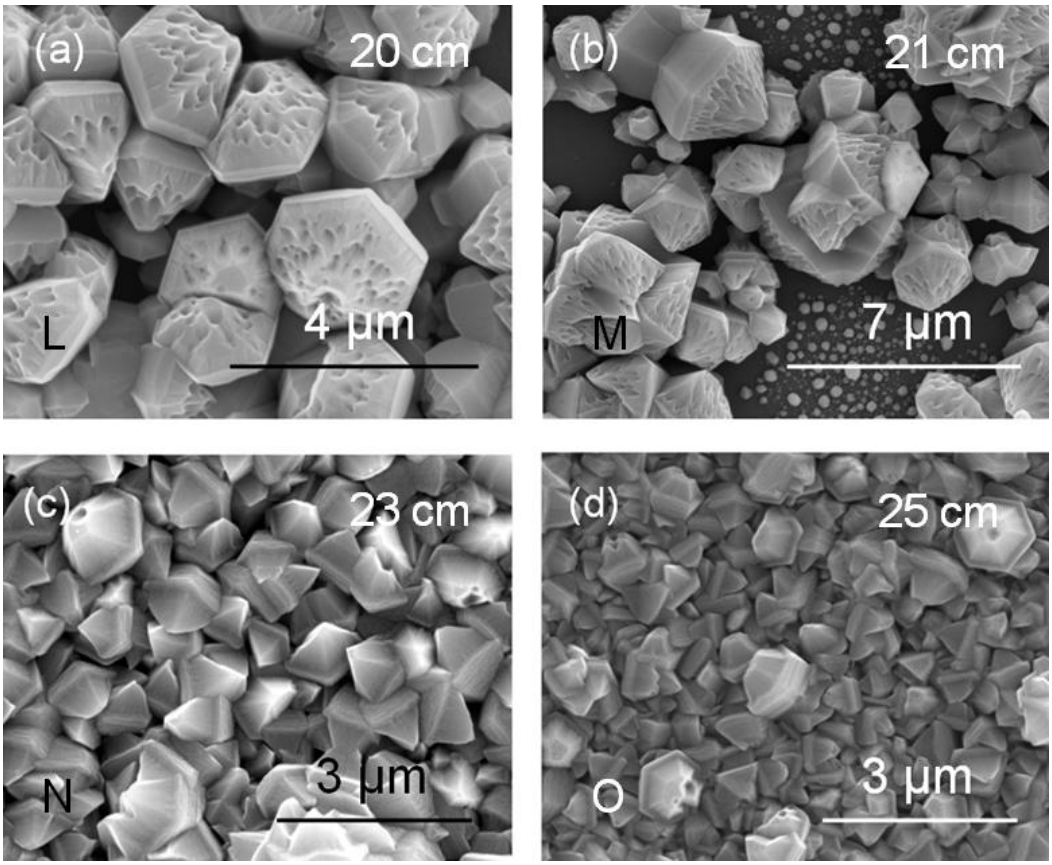

Figure 4.19. SEM images of porous GaN doped with Mg using 0.1688 g of MgA as precursor located at various distances between the Ga and the Mg sources, as indicated in the pictures together with sample ID.

4.2 Porous MgO-GaN metal-oxide semiconductor (MOS) diode

By increasing the concentration of Mg_3N_2 in the synthesis of porous GaN we have discovered the possibility of fabricating MgO-GaN metal-oxide semiconductor diodes in one single synthesis step. The synthesis consisted in using a 0.052 Mg to Ga molar ratio, locating Mg_3N_2 4 cm upstream of the Ga source. Under these conditions a layer of crystalline MgO was formed underneath Mg-doped GaN layer, as reported in Paper VI and Paper VII. As catalysts, we used 20 nm thick film of Au and Pt deposited on Si(100). The growth of the porous GaN particles was assisted by a solid particle through the vapor-solid-solid (VSS) mechanism, described in Chapter 3.

4.2.1 Morphological and structural characterization of MOS

Figures 4.20a and 4.20b confirm that the porous GaN particles, corresponding to the MOS structure, have a characteristic morphology consisting of faceted hourglass crystals with a mean size of ~1.5 μm.

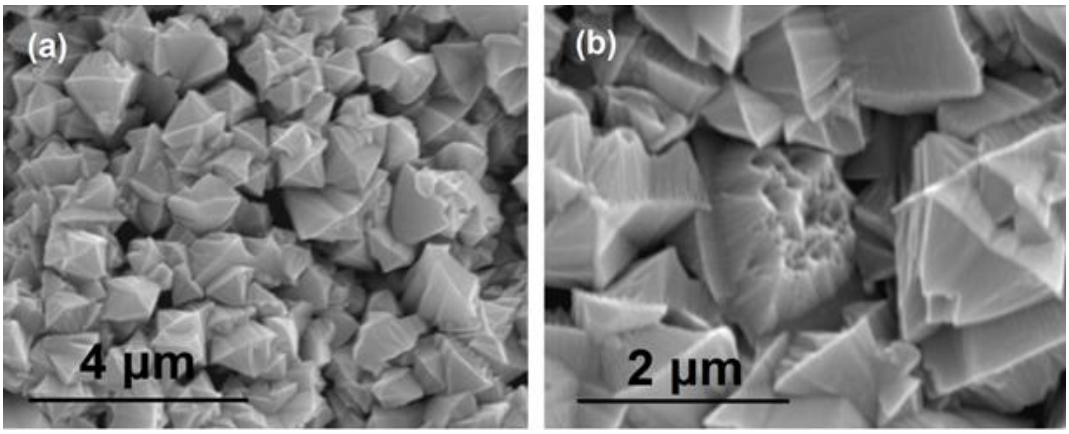

Figure 4.20. SEM image of porous GaN particles corresponding to the MOS structure grown on Si (100) substrates coated with (a) a 20 nm thick film of Au and (b) a 20 nm thick film of Pt (partial reproduction of Figure 1 from Paper VI).

Figure 4.21 shows the XRD pattern for MOS diode. The XRD pattern for the MgO/GaN layer grown on Au-coated Si substrates confirms crystalline wurtzite GaN growth. The uniform intensity of the Debye rings confirms that there is no texturation of the layer of porous crystals. We can see that the deposit formed with 0.052 Mg vs. Ga molar ratio contains crystalline MgO. The porous GaN single crystals formed are similar to those grown in the absence of the Mg precursor, and they also retain their unintentionally *n*-doped conduction because we did not anneal this sample to activate the *p*-type conduction.

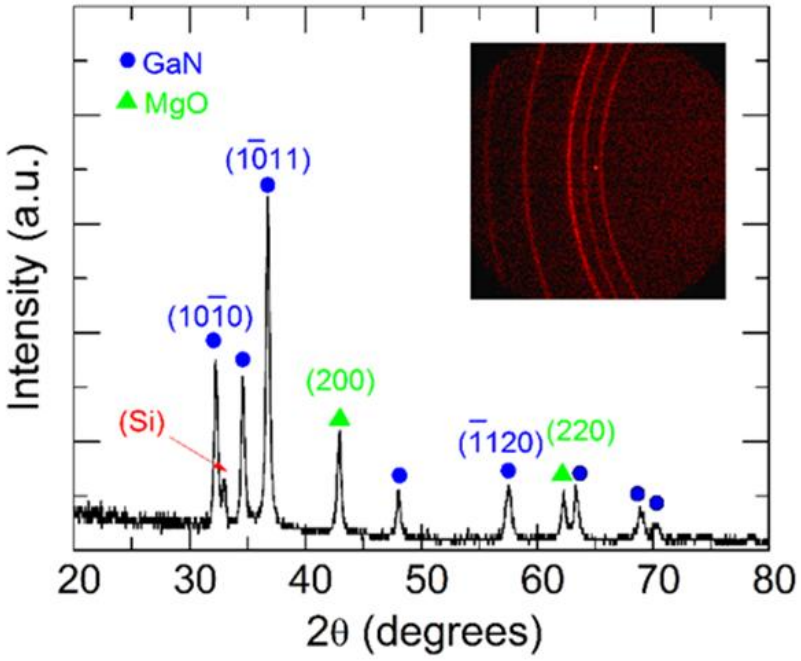

Figure 4.21. XRD pattern of the porous MgO-GaN MOS structure grown on a Si (100) substrate, with inset of Debye rings. The Si (400) diffraction peak has been excluded to avoid intensity saturation (partial reproduction of Figure 2 from Paper VI).

TEM analysis confirms that the polycrystalline MgO is located under the porous GaN. The high quantities of the Mg-containing precursors preferentially forms this layer rather than doping the GaN lattice. This is in contrast with what has been observed when a smaller amount of Mg_3N_2 is used, in which case, only the polycrystalline layer of porous GaN is observed (see Figure 4.7).

Figure 4.22 shows a cross-section TEM image of the porous MgO-GaN MOS diode on a Si(100) substrate using 0.052 Mg to Ga molar ratio. The image shows different regions with a variation in contrast related to the variable Mg content (and thus scattering) in each of the marked regions. Energy dispersive X-ray spectrometry (EDX) analysis was used to quantify the Mg spatial density from 12 separate locations as indicated in Figure 4.22 and Table 4.4. Four different regions were defined in this sample. Region I corresponds to the Si substrate. Region II, around point 1, is characterized by a dark contrast, with a Ga content of 26.7 % and Mg content of 73.3 %. The phase formed in this region does not exhibit diffraction as an intermetallic crystal, and likely corresponds to a Mg-Ga alloy. In region III (points 2 to 4), the Ga content is low (~1.5-3 %), while the Mg content is ~97-98%, indicating that a new phase rich in Mg is formed, corresponding to MgO. The thickness of this layer is ~1 μm. Finally, in region IV (points 5-12) we find a phase reach in Ga (90.5-97.8 %), while the Mg content remains ~7.9-11.7%. This region corresponds to Mg-doped GaN with a mean thickness of ~0.5 μm. TEM energy dispersive X-ray analysis confirms the interfacial location of the MgO between the silicon substrate/intermetallic seed layer, and the porous GaN.

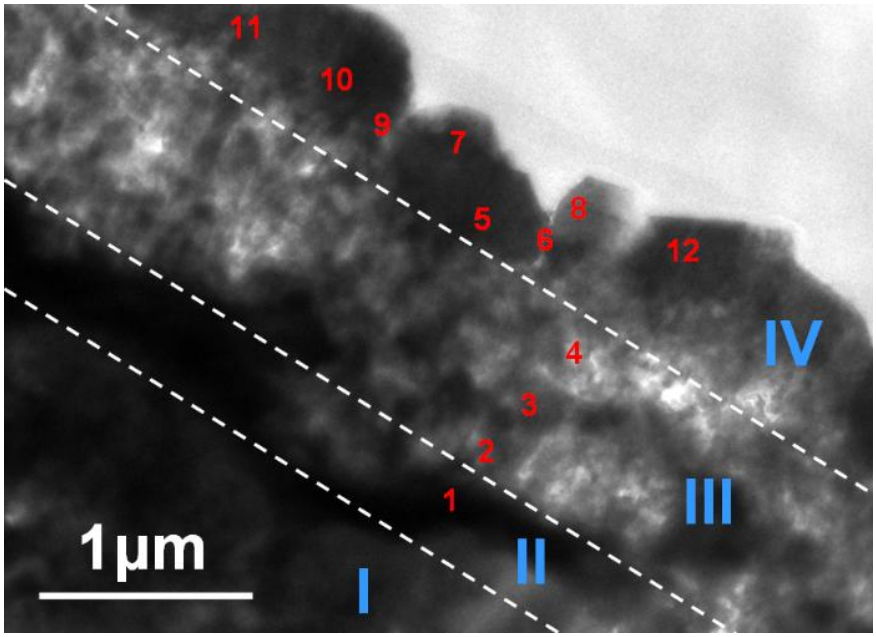

Figure 4.22. Cross-sectional TEM image of the porous MgO-GaN MOS diode fabricate by CVD in a single step on a Si(100) substrate (partial reproduction of Figure 3 from Paper VI).

Table 4.4. EDX content of Mg and Ga in the final MOS diode layers. The measurement points (#) relate to those numbered in Figure 4.22.

Position #	Mg %	Ga %	Position #	Mg %	Ga %
1	73.3	26.7	7	11.7	97.8
2	98.5	1.5	8	7.9	92.1
3	97.0	3	9	9.5	90.5
4	97.3	2.7	10	8.9	91.1
5	7.9	92.1	11	7.9	92.1
6	11	89	12	8.1	91.9

4.2.2 Mechanism of formation of the porous MgO-GaN MOS diode

The following mechanism is proposed for the uninterrupted CVD growth of the interfacial high-κ MgO layer on an Ohmic intermetallic with catalytic growth of GaN as a MOS diode, as reported in Paper VI (see Figure 4.23). Firstly, a intermetallic layer of Ga, Mg and the metallic catalyst (Au or Pt) used for a solid eutectic phase forms layer II. At higher temperatures a second layer, formed almost entirely by Mg, is deposited on the intermetallic layer. This layer quickly oxidizes to polycrystalline MgO, probably when we opened the furnace, forming layer III. Finally, the growth of nanoporous GaN particles doped with Mg (layer IV) should proceed on the top of this Mg layer, acting Mg as a catalyst for the formation of this porous layer, since it appears not to be in contact with the catalyst with which we coated the substrate. Since no residual Mg, or MgO is found on the unintentionally *n*-doped GaN after heating and exposure to oxygen when the furnace was opened, the growth of the porous GaN particles proceeds through the Vapor-Solid-Solid (VSS) mechanism.

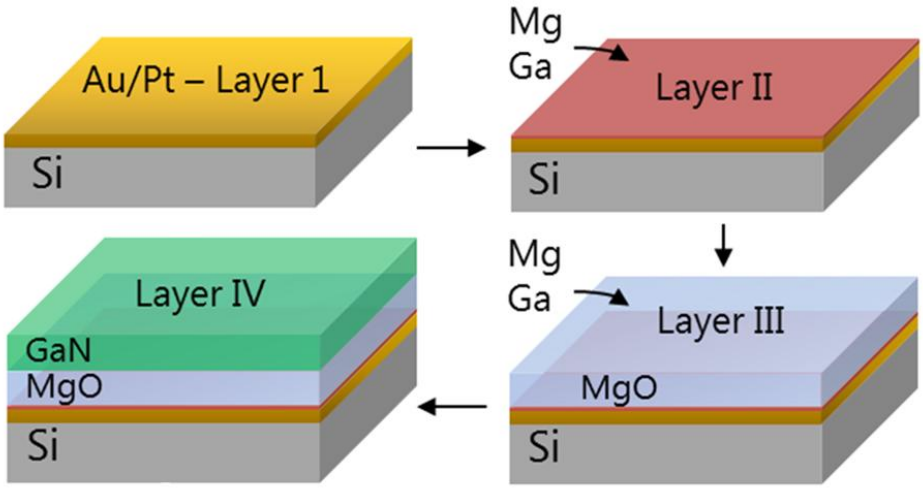

Figure 4.23. Mechanism of formation of the porous MgO-GaN MOS diode by subsequent catalytic VSS growth during CVD (partial reproduction of Figure 1 from Paper VI).

4.2.3 Electrical characterization

The MgO-GaN porous layers formed on silicon exhibit diode behavior consistent with a MOS system, as reported in Paper VI and Paper VII. Figure 4.24 shows the *I-V* curves recorded across the device using an In-Ga euctectic to Ohmically contact both the silicon substrate and the porous GaN. A rectifying diode response is found in the presence of the MgO, compared to Ohmic response between the intermetallic termination porous *n*-type GaN and the substrate. We assumed that the net current is due to thermionic emission current since the metal-semiconductor-metal contact now contains a dielectric at one interface, mimicking a Schottky contact with series resistance and an interfacial layer. Additionally, this is confirmed by forward bias voltages of $V > 3kT/q$, which is the case for this MOS diode. The downturn to linearity in the current after ~0.25 V confirms a series resistance, R_S most likely originated from the MgO and porous *n*-type GaN, as opposed to either of the metal contacts which are confirmed to be Ohmic in nature. At higher bias (> 0.25 V), the R_S dominates, as can be seen from the differential conductance d*I*/d*V* curve in Figure 4.24b.

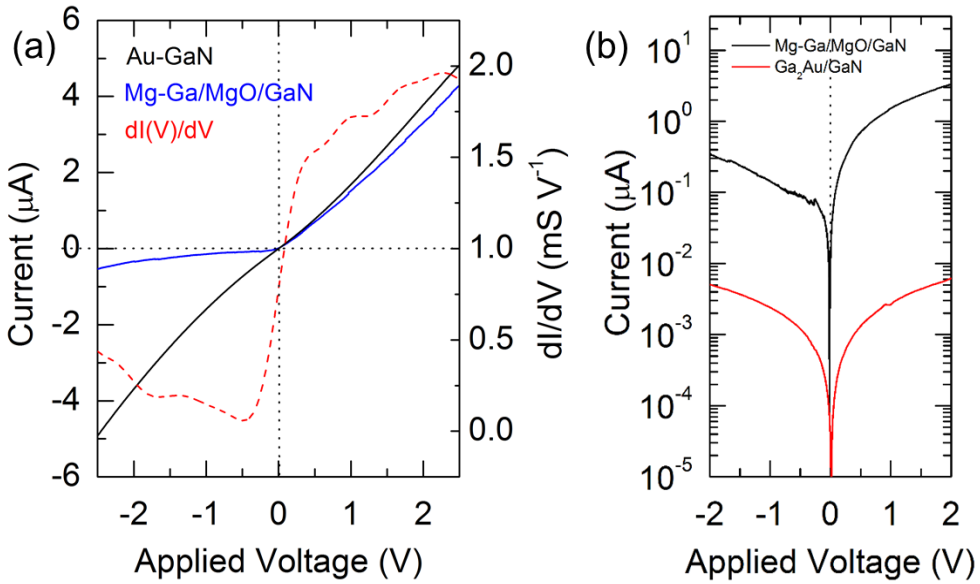

Figure 4.24. (a) *I-V* and d*I*/d*V* curves for porous *n*-type GaN with a MgO dielectric layer, and from a Au-seeded porous GaN layer on silicon. (b) ln(*I*)-*V* curve for the Ohmic Au-seeded GaN contact and the MgO-GaN diode (reproduction of Figure 4 from Paper VI).

Figure 4.24 shows also for comparison the *I-V* curves recorded for the porous GaN catalyzed by Au (forming Ga_2Au) that are different from those presented in Figure 4.9, since in that case we did not activate *p*-type GaN by thermal annealing. The *I-V* curves show only slight asymmetry indicative of near Ohmic, weak Schottky barriers. The intermetallic layer contacts are described using the thermionic emission theory, taking into account a high ideality factor for weak barriers. The estimated SBHs for Au-catalysed porous *n*-type GaN is 0.66 eV. It is worth noting that the *n*-type contacts were effectively Ohmic as deposited and did not need any post-deposition annealing to induce this effective ohmicity. For porous GaN, and also for GaN grown on Mg-based films, the effect of an interfacial oxide was considered.

The barrier height of an untreated metal/GaN diode can be altered by (photo)electrochemical etching treatment that leave defective GaN surface and interfaces, and described according to

$$\varphi_{B,n} = \varphi^{o}_{B,n} + \Delta\varphi \qquad \text{(Eq. 4.1)}$$

where $\varphi^{0}_{B,n}$ represents the barrier height without the interfacial layer and $\Delta\varphi$ is the additional barrier due to the oxide. The parameter $\Delta\varphi$ is considered like a tunneling barrier of the form

$$\Delta\varphi = \frac{2kT}{\hbar}(2m\chi)^{\frac{1}{2}\delta} \qquad \text{(Eq. 4.2)}$$

where *h* is Plank's constant, *m* is the tunneling effective mass, χ is the mean tunneling barrier and δ is the thickness of the interfacial oxide. $\Delta\varphi$ was found to be in the range 0.18 – 0.25 eV for Pt and Au based intermetallic contacts to *n*-type GaN. This corresponds to a maximum native oxide thickness of ~ 2.7 nm on untreated GaN and would increase the overall effective barrier height. Microscopy and transport measurements thus confirm the porous catalyzed GaN growth is mostly free of influential surface contaminants.

Effective Ohmic contacts can form with *n*-type GaN suggesting that the resistivity dominates transport through an alloyed interface that promotes Ohmic transport. When a high-κ MgO layer is introduced, the series resistance markedly increases at much lower voltages. The MgO/*n*-type GaN sandwich effectively has an altered electron affinity with respect to the In-Ga top contact. The overall series resistance, R_S, to which the sheet and contact resistivities contribute can also be determined from diffusion and thermionic emission theory summarised for a barrier-dominated diode. The current system behaves as a diode but utilizing an Ohmic contact formed by the intermetallic under the MgO layer, biased by the underlying silicon substrate. In the presence of the intermetallic bottom contact, the transport is effectively Ohmic at the MgO interface. As the top contact to *n*-type GaN is also Ohmic, the diodic response is dominated from affinity differences between the MgO and the *n*-type GaN. The series resistance can also be obtained from the differential resistance through its proportionality to the current according to

$$\frac{dV}{dI} = \left(R_s + \frac{kT}{q}\left[\frac{1/I_0}{I/I_0 - 1}\right]\right) \approx R_s + \frac{nkT}{qI} \qquad \text{(Eq. 4.3)}$$

Figure 4.25 shows the differential resistance d*V*/d*I* as a function of the inverse of the current, plotted according to Eq. 4.3. Although it does not allow deconvolution of the specific grain boundary resistance contribution to current flow through the porous layers, the series resistance is estimated to be in the range 5-6 kΩ for the MgO/porous GaN sandwich; d*V*/d*I* approaches R_S at the higher currents, but as seen in Figure 4.25b, the series resistance also includes likely tunnelling effects as the ideality factor is strongly voltage dependent and quite high in the higher current and higher bias regions. Further work is needed to identify the mechanism contributing to such high ideality factors, which are indicative of several mechanisms including tunnelling current through multiple heterojunctions. Porosity

complicates the transport mechanism, increasing shunt and series resistances [191]. Different possibilities are a strong contribution by Poole–Frenkel (P-F) tunneling and surface leakage. In the former, electron-hole transport processes are accommodated by lowering the barrier when the carriers interact with the trap states in the MgO layer. These recombinative states are likely to have a high density in a thick MgO film with a graded MgO composition at the interface with GaN and also with the silicon, as determined by elemental concentrations within the MgO layer at either interface. Variations in the interfacial composition is known to strongly affect Schottky and P-F leakage current in MOS diode structures [192].

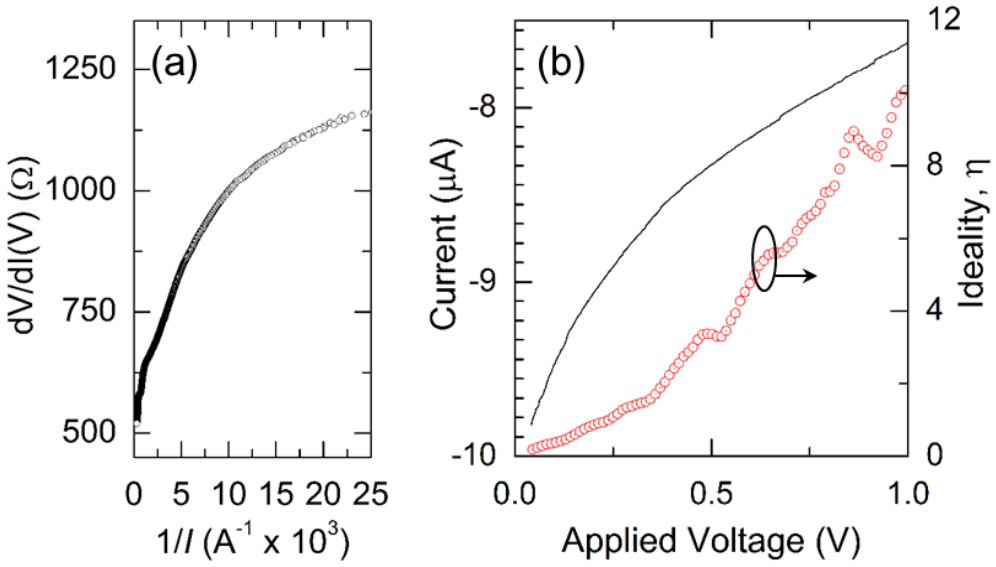

Figure 4.25. (a) Differential resistance (d*V*/d*I*) as a function of current for the MgO/porous GaN MOS diode. (b) ln(*I*)-*V* curve and the voltage dependence of the ideality factor for the diode (reproduction of Figure 5 from Paper VI).

We believe this method of fabrication of MOS diodes in a single synthesis step may be extended to growing nanoscale III-N materials and alloys using metals that are not typically employed for contacting, to give Ohmic response and MOS-based systems for chemically inert, high surface area transistors for (bio)sensing.

4.3 Doping porous GaN with Si

Undoped porous GaN exhibits *n*-type conductivity with a carrier concentration ~10^{16} cm^{-3}, as reported in Chapter 3. However, the concentration is too low compared to that of Mg-doped porous GaN (~10^{18} cm^{-3}) to fabricate functional LEDs. In order to increase the carrier concentration, porous GaN was doped with Si through the direct reaction of metallic Ga with NH_3 gas in the CVD system. To dope GaN with Si, silicon tetraiodide (SiI_4, 99.9 %) was used as precursor. SiI_4 is in the form of a crystalline powder at room temperature and pressure. SiI_4 melts at 393.5 K and boils at 560.4 K [193].

We performed preliminary investigation on the incorporation of Si into GaN as a dopant by designing a set of experiments in which we changed the distance between the Ga and the Si sources. Like in the case of Mg-doped porous GaN, in the synthesis of Si-doped porous GaN the SiI_4 precursor was also placed up-stream of the Ga source. The studied distances between the Ga and the Si sources were 15 cm, 20 cm and 25 cm that corresponds to temperatures of ~1050 K, ~830 K and ~600 K. As substrate silicon (100) and as catalyst a 0.01 M solution of $Ni(NO_3)_2$ in ethanol were used. The quantities of SiI_4 we analyzed were 0.105 g (0.0273 Si vs. Ga molar ratio) and 0.120 g (0.0312 Si vs. Ga molar ratio). The resulting Si-doped porous GaN particles reveal a high degree of porosity and no significant differences in morphology can be observed in the samples analyzed (see Figure 4.26). Future investigations are needed to prove the doping level and electrical properties of Si-doped porous GaN. However, during the crystal growth process vapors of SiI_4 were deposited on the pressure meter, which generated problems to control the pressure in the system. Thus, for future experiments on Si doping, a more careful choice of the Si precursor is needed to avoid this problem.

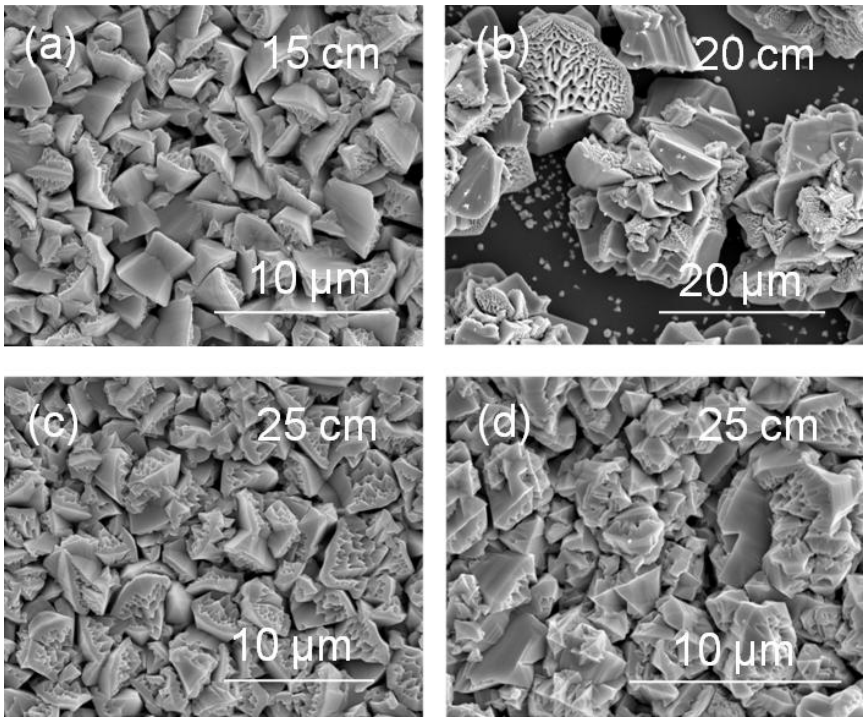

Figure 4.26. SEM images of porous GaN doped with Si using (a), (b), (c) 0.105 g and (d) 0.120 g of SiI_4 as precursor, located at various distances between the Ga and the Mg sources indicated on the SEM images.

Chapter 5

Epitaxial growth of porous GaN: towards porous *p*-*n* junctions and LEDs

Significant improvements in the crystal quality of GaN enabled the fabrication and good conductivity control of *p*- and *n*-type GaN. This led to the production of the GaN-based *p*-*n* junction blue LED. However, there is still a problem with the efficiency and the brightness of current GaN-based LEDs because of the high refractive index contrast between GaN and air that confines light inside the material. One of the efficient solutions to overcome this problem is porosification of GaN, what allows drastically improving the light extraction from LED as explained in the Introduction. Thus, cheap and simple fabrication method of porous GaN-based LEDs will allow getting high-brightness LEDs at a commercial level and with a low price.

This chapter describes the epitaxial growth of *p*-type and *n*-type oriented (0001) porous GaN layers by CVD. Based on those layers, the fabrication and characterization of partially and fully porous rectifying *p*-*n* junctions is presented.

5.1 Influence of the substrate on the orientation of the porous GaN layer

Different substrates were investigated to ascertain if they might play a role in the crystallographic orientation of the porous GaN particles. For this purpose we used amorphous quartz, tungsten wire (W), pyrolitic boron nitride (p-BN),sapphire (Al_2O_3), SiC, AlN and GaN thin films grown on sapphire (0001) as substrates, as described in Paper I and Paper VIII. These substrates were chosen with the criteria of using an amorphous substrate (quartz), a cubic substrate different than Si and without a particular crystallographic orientation (W wire), a substrate with hexagonal structure and quasi-oriented crystallographically (p-BN), and hexagonal substrates with the same or similar structure than GaN, crystallographically oriented, with different lattice mismatches in relation to GaN, such as sapphire on which GaN is typically grown [39], SiC(0001), AlN(0001) and GaN(0001) thin films grown on sapphire(0001) substrates. An ethanolic solution of $Ni(NO_3)_2$ was sprayed on the surface of the substrates to facilitate the nucleation of GaN, except on sapphire, SiC, AlN and GaN substrates.

SEM pictures of the porous GaN particles grown on amorphous quartz, W wire and p-BN substrates reveal in all cases that GaN appears in the form of hexagonal micron-sized porous particles (see Figure 5.1). When using quartz, the level of porosity in the particles is lower, with the pores located at the central part of the particles, and with an elongated shape towards the external parts of the particles, instead of exhibiting the round shapes observed up to now (see Figure 5.1a). On the W wire, the density of particles is very high, which might induce to think that GaN particles grow with a plate shape instead of the pyramids observed before (see Figure 5.1b). In the case of p-BN, a certain degree of alignment of the GaN particles can be observed since a bigger number of pores perpendicular to the surface can be seen (see Figure 5.1c), however, and due to the misalignment of the BN flakes, there are also particles with different crystallographic orientations. Also the porosity degree in these particles is lower.

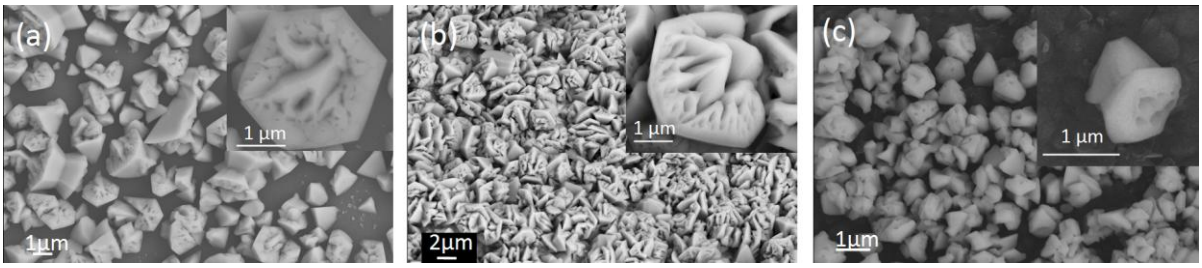

Figure 5.1. SEM images of the porous GaN particles grown on different substrates: (a) amorphous quartz, (b) W wire and (c) pyrolitic BN, using $Ni(NO_3)_2$ as catalyst (partial reproduction of Figure 8 in Paper I).

Figure 5.2 shows the SEM top view images of the porous GaN films obtained on the Al_2O_3(0001), SiC(0001), AlN(0001) and GaN(0001) substrates. Prior to the experiments, we expected porous GaN layers to grow oriented along the *c*-crystallographic direction, since all our substrates belong to the hexagonal system and are oriented perpendicular to the [0001] direction. However, the morphology, grain structure and the crystallographic orientation of the obtained films depend strongly on the lattice mismatch between the substrate and GaN.

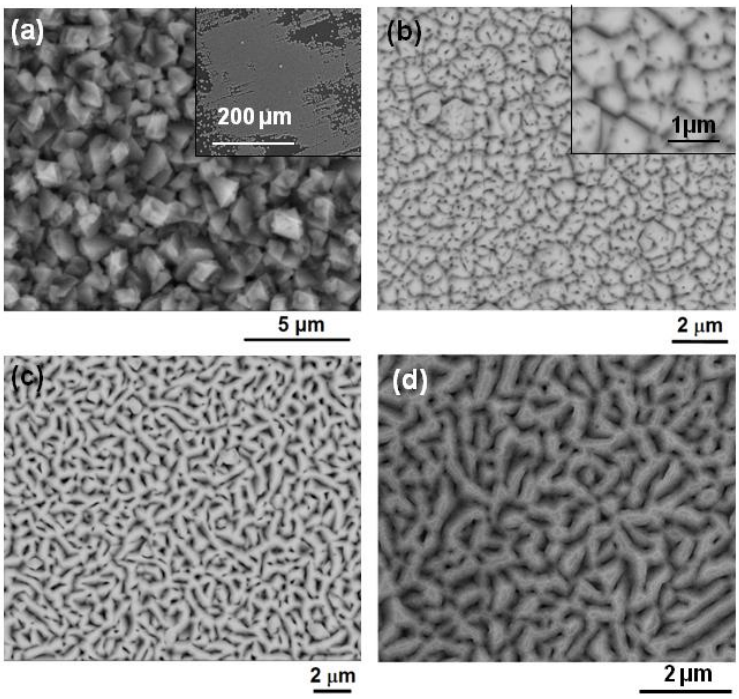

Figure 5.2. SEM images of porous GaN films obtained by CVD on (a) Al_2O_3(0001), (b) SiC(0001), (c) AlN(0001) and (d) GaN(0001) thin films on sapphire without the use of any catalyst (reproduction of Figure 1 from Paper VIII).

We calculated the two-dimensional lattice mismatch from the expression:

$$f_{(hkil)} = [(S^{L}_{(hkil)} - S^{S}_{(hkil)})/S^{S}_{(hkil)}] \times 100 \qquad \text{(Eq. 5.1)}$$

where $S^{S}_{(hkil)}$ and $S^{L}_{(hkil)}$ are the areas calculated from the periodicity vectors of the substrate and the layer, respectively, for the (0001) plane. Table 5.1 summarizes the lattice parameters used to calculate the lattice mismatch and the obtained values for the different substrates. The sign of the lattice mismatch indicates if the as-grown films might be under compressive or tensile strain after growth on a particular substrate. A negative lattice mismatch means that the plane of the substrate is larger than that of GaN, in this case the porous layer should be under tensile strain. A positive lattice mismatch means that the surface area of the (0001) plane of the substrate is smaller than that of GaN, thus the porous films suffer from compressive stress.

As it can be seen in Table 5.1, sapphire offers a negative lattice mismatch with GaN, while SiC and AlN result in positive lattice mismatches. The lattice mismatch calculated for the films grown on GaN is obviously zero. Thus, the porous GaN layer grown on sapphire should be stretched, whereas those layers obtained on SiC and AlN should be compressed. Furthermore, the absolute value of the lattice mismatch calculated for GaN/Al_2O_3 is larger than for GaN/SiC and GaN/AlN, and can be arranged in the following order from bigger to smaller: $f^{Al_2O_3}_{(0001)} > f^{SiC}_{(0001)} > f^{AlN}_{(0001)} > f^{GaN}_{(0001)}$.

The lattice mismatch between GaN and the substrate can be also estimated by the difference between the ***c***-axis parameters of the substrates and the thin film, according to the following equation:

$$f'_{[0001]} = \left[\frac{c^L - c^S}{c^S} \right] \times 100 \qquad \text{(Eq. 5.2)}$$

where c^S and c^L are the ***c*** cell parameters of the substrate and the layer, respectively. If this methodology is used, the lattice mismatch between sapphire and GaN is reduced to -11%, while the rest of the calculated lattice mismatches do not change substantially.

Table 5.1. Theoretical lattice mismatch, calculated for the (0001) plane, between GaN and the different substrates analyzed.

	Lattice parameters		**Lattice mismatch (%)**	
Substrate	***a* (Å)**	***c* (Å)**	$f_{(hkil)}$	$f'_{[0001]}$
Sapphire (Al_2O_3) [194]	4.75	12.99	-55.1	-11.16
6H-SiC[195]	3.07	10.05	7.7	7.7
AlN[196]	3.11	4.98	5.1	5.1
GaN[197]	3.19	5.18	0	0

Porous GaN obtained on Al_2O_3 appears in the form of a continuous layer of randomly oriented GaN particles, with porosity present on the (0001) face (see Figure 5.2a), as observed previously on Si and BN substrates. However, an ordered coverage of the surface of the substrate is apparent at low magnifications (see inset in Figure 5.2a).

In the case of SiC(0001), the smaller lattice mismatch and the similar thermal expansion coefficients with GaN [198], results in porous GaN growing as a quasi-continuous layer with porous GaN particles aligned along the [0001] crystallographic direction and pores on the (0001) face (see Figure 5.2b). However, crystal grains do not tend to coalesce during growth, and individual particles are still evident in the image.

On AlN, a ***c***-oriented continuous porous GaN layer similar to that on SiC is obtained, but with a different morphology. Individual particles are not evident; however, we observe pores with larger diameters and a large dispersion of shapes (see Figure 5.2c). It looks like interparticle porosity in this case is favoured, while negligible intraparticle porosity (within each crystal) is found, as is the case in other growth regimes.

Similar results to those obtained on AlN were obtained on GaN(0001) thin films on sapphire (see Figure 5.2d).

The porous GaN epitaxial layers obtained on GaN(0001) coated sapphire(0001) substrates were further investigated to follow the evolution of the morphology of the pores and the growth rate with reaction times between 15 and 60 min. Figures 5.3a-5.3c show the top-down SEM images of the porous GaN layers obtained. These micrographs show that by increasing the reaction time the diameter of the pores increases. The sample obtained at 15

min showed the highest degree of porosity, while the sample obtained after 60 min of reaction showed the lowest degree of porosity but with pores larger in size . This evolution of the porosity with time seems to suggest that a coarsening of the pores is happening as the reaction time increases. Especially in the case of the porous GaN obtained at 15 and 30 min, they have the appearance of a perfectly ***c***-oriented continuous porous GaN layer, and the aspect of a true epitaxial porous layer. These results obtained on GaN(0001) coated sapphire(0001) substrates suggest that by decreasing the reaction time on the epitaxial growth of porous GaN on AlN, also porous epitaxial layers would be obtained.

To know the thickness of the porous GaN epitaxial layers obtained on GaN(0001) coated sapphire(0001) substrates, cross sectional-images of the samples were recorded by SEM, as shown in Figures 5.3d-5.3f, corresponding to 15, 30 and 60 min of growth, respectively. These cross-sectional micrographs clearly show the sapphire substrate, the non-porous GaN film with a thickness of ~ 5 μm, and the porous GaN layer. The interface between the non-porous GaN film, and the porous GaN layer is well defined and abrupt, which is the consequence of the change in density (material quantity) of the two layers. The thickness of the porous GaN layer increases with growth time, from ~ 0.5 μm at 15 min to 1.7 μm at 60 min.

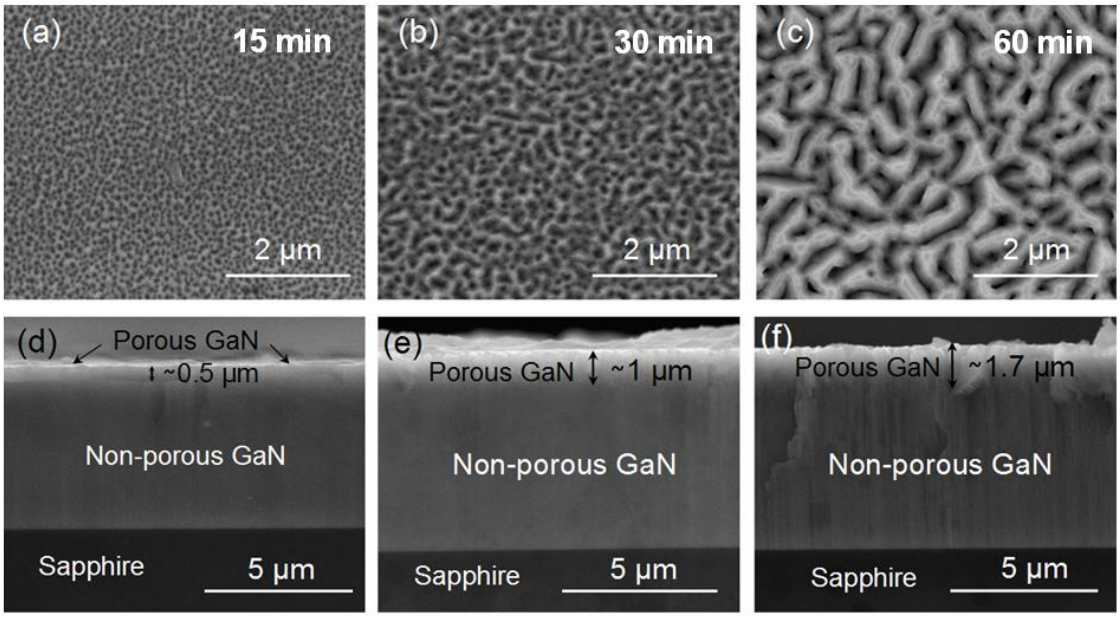

Figure 5.3. Top views and cross-sectional SEM images of the porous GaN epitaxial layers obtained on GaN(0001) thin films coated sapphire(0001) substrates obtained after (a), (d) 15 min, (b), (e) 30 min, and (c), (f) 60 min growth time (reproduction of Figure 2 from Paper VIII).

Figure 5.4 shows SEM images of the porous GaN epitaxial layer grown during 30 min taken at an inclination angle of 70º. Here, the rough porous surface of the epitaxial layer with pores of different diameters can be clearly observed.

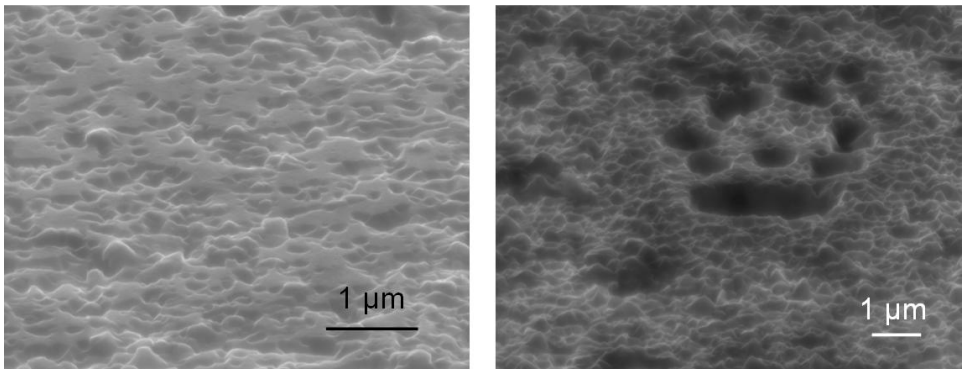

Figure 5.4. SEM images of the porous GaN epitaxial layer grown during 30 min obtained at an inclination angle of 70º.

AFM in tapping mode was also used to visualize more in detail the porous GaN layers gown for 30 min (see Figure 5.5a). The porosity is evident in the image, and pores with different diameters are observed. Two profiles of the surface of the sample, corresponding to the lines indicated in Figure 5.5a, are shown in Figure 5.5b to describe the typical diameters of the pores, ranging between 200 and 300 nm.

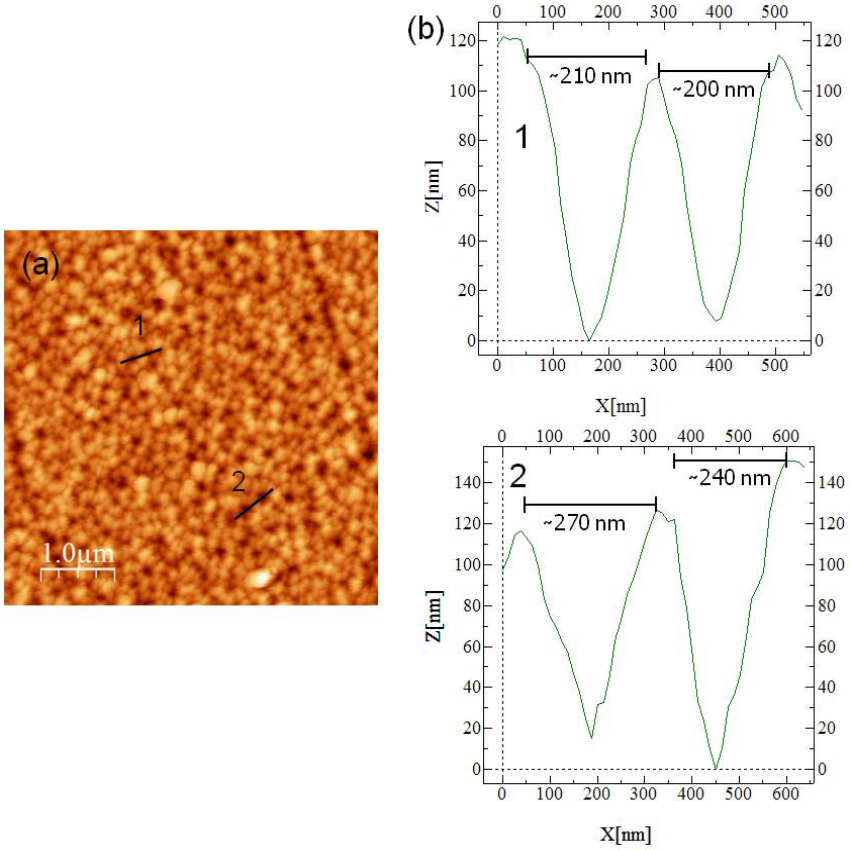

Figure 5.5. (a) AFM image and (b) profiles of the porous GaN epitaxial layer grown on non-porous GaN film coated sapphire (0001) substrates for a growth time of 30 min, taken at the locations highlighted in (a), showing the typical diameters of the pores (reproduction of Figure 3 from Paper VIII).

5.2 Fabrication of partially and fully porous p-n junction

To further demonstrate the potential of porous GaN layers to form *p-n* junctions, we have grown them on non-porous GaN film (~5 μm thick) on sapphire with *n*-type or *p*-type conductivity, depending on the experiment and the *p-n* junction to be formed, as described in Paper IX. The reaction was undertaken for 30 min. Mg-doped samples were grown to produce *p*-type nanoporous GaN films as described in Chapter 4. Three types of porous GaN diodes were prepared (see Figure 5.6). Undoped *n*-type porous GaN was grown on non-porous *p*-type GaN(0001) thin films (porous *n-p* diode, hereafter). A second type of diode was formed by a Mg-doped porous *p*-type GaN layer grown on non-porous *n*-type GaN(0001) thin films (porous *p-n* diode, hereafter). Finally, a third type of diode was fabricated, formed by a Mg-doped porous GaN layer, grown on an undoped porous *n*-type GaN layer that was previously grown on a non-porous *n*-type GaN(0001) thin film (fully porous *p-n* diode, hereafter). These fully porous *p-n* junctions were fabricated in a two crystal growth step process. First, an undoped *n*-type porous GaN layer was grown on non-porous GaN(0001). Second, another porous Mg-doped *p*-type GaN layer was grown on the top of the porous *n*-type GaN layer, as we represented in Figure 5.6, following the same reaction conditions.

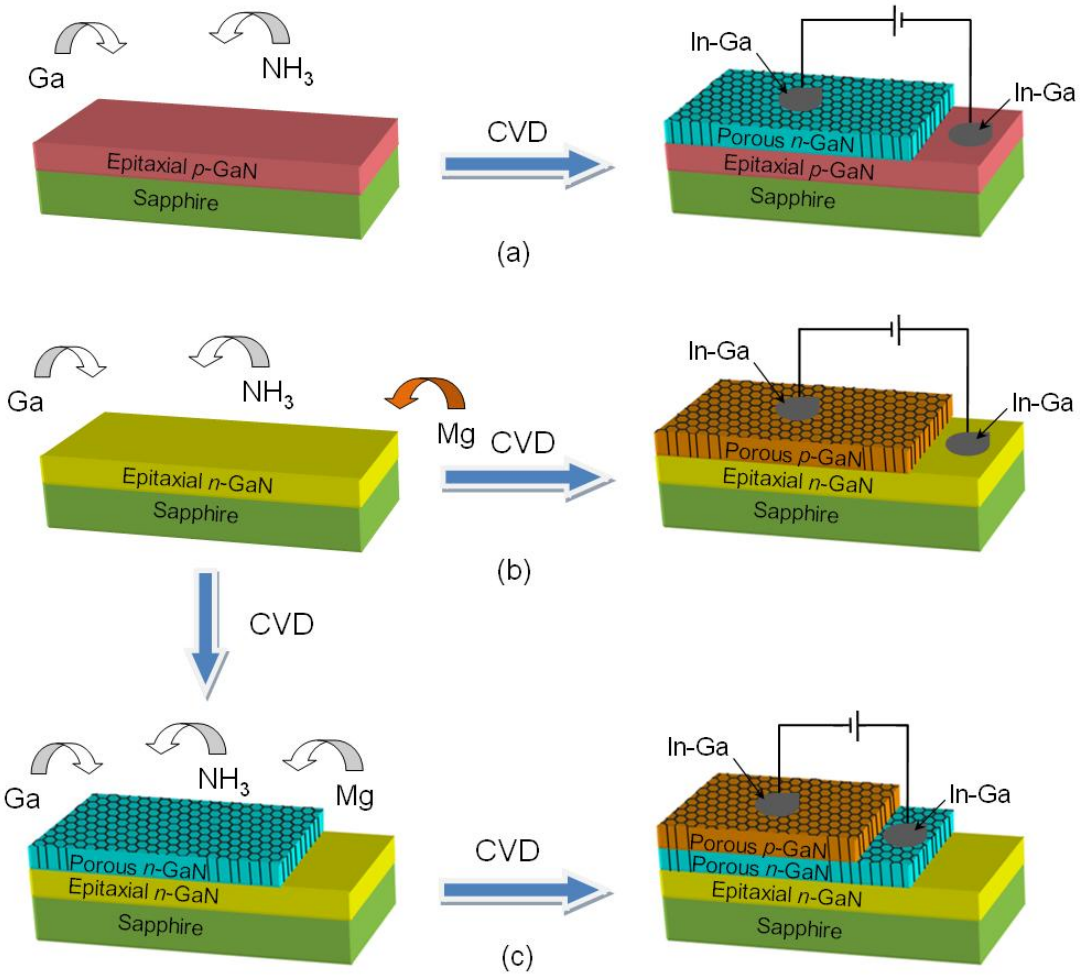

Figure 5.6. Schematic representation of the process of formation of partially and fully porous GaN *p-n* junctions by CVD (reproduction of Figure 1 from Paper IX).

Figures 5.7 and 5.8 show top-view SEM images of the porous layers obtained. All the porous GaN layers reveal a high degree of porosity with a large number of pores. Despite being grown under the same conditions, the porous *p*-type layers tend to show pores larger in diameter when compared to those observed on the *n*-type porous layers. This is especially significative on the fully porous *p*-*n* diode. In that case the pores observed in the *p*-type layer are significantly wider than those observed on the *n*-type layer prior to the second growth step. The reason for this different apparent porosity might be related to the time of exposure at high temperature of the porous *n*-type layer during the second growth step to deposit the porous *p*-type layer. This would affect the porous substrate in terms of widening its pores by thermal etching [199], thus inducing the growth of the second porous layer also with wider pores. In fact, in porous layers grown for a longer time (60 min), this effect of widening of the pore diameters has also been observed (see Figure 5.3). Another reason for this different porosity in *n*-type and *p*-type layers might be related to the corrugation of pores during the second growth step due to a lower decomposition temperature of Mg-doped GaN [200], which would be accentuated by the presence of the pores.

In all cases, however, the porous Ga layers grew oriented along the ***c***-crystallographic direction, which matches the crystallographic orientation of the non-porous epitaxial GaN thin-films used as substrates. Pores are always parallel to this direction.

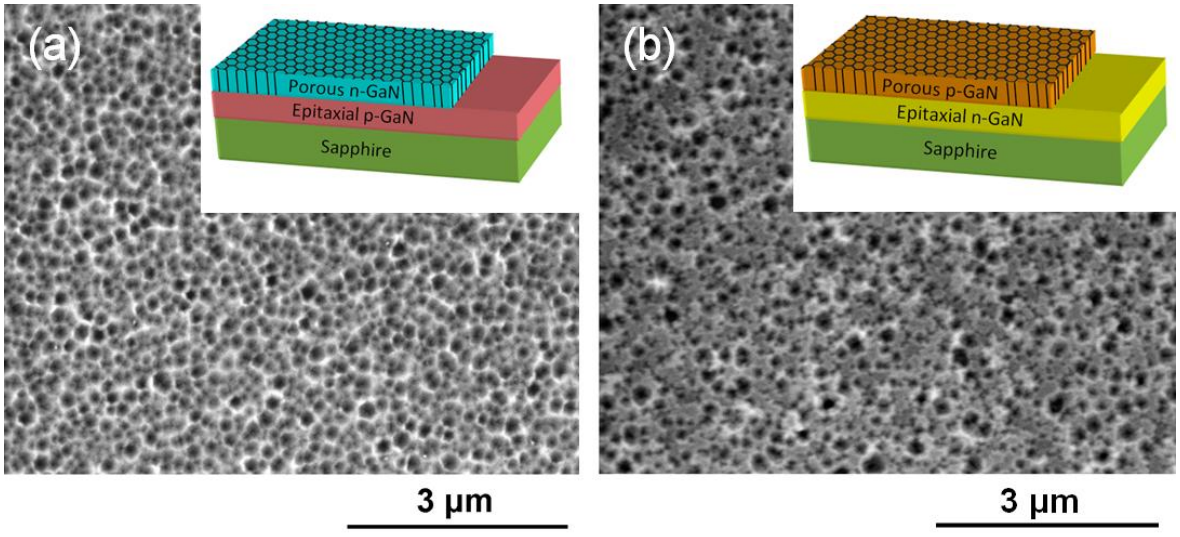

Figure 5.7. SEM top-view images of (a) porous *n*-type GaN grown on non-porous *p*-type GaN coated sapphire and (b) porous *p*-type GaN grown on non-porous *n*-type GaN coated sapphire. Insets show schemes of the corresponding porous GaN diodes fabricated (partial reproduction of Figure 2 from Paper IX).

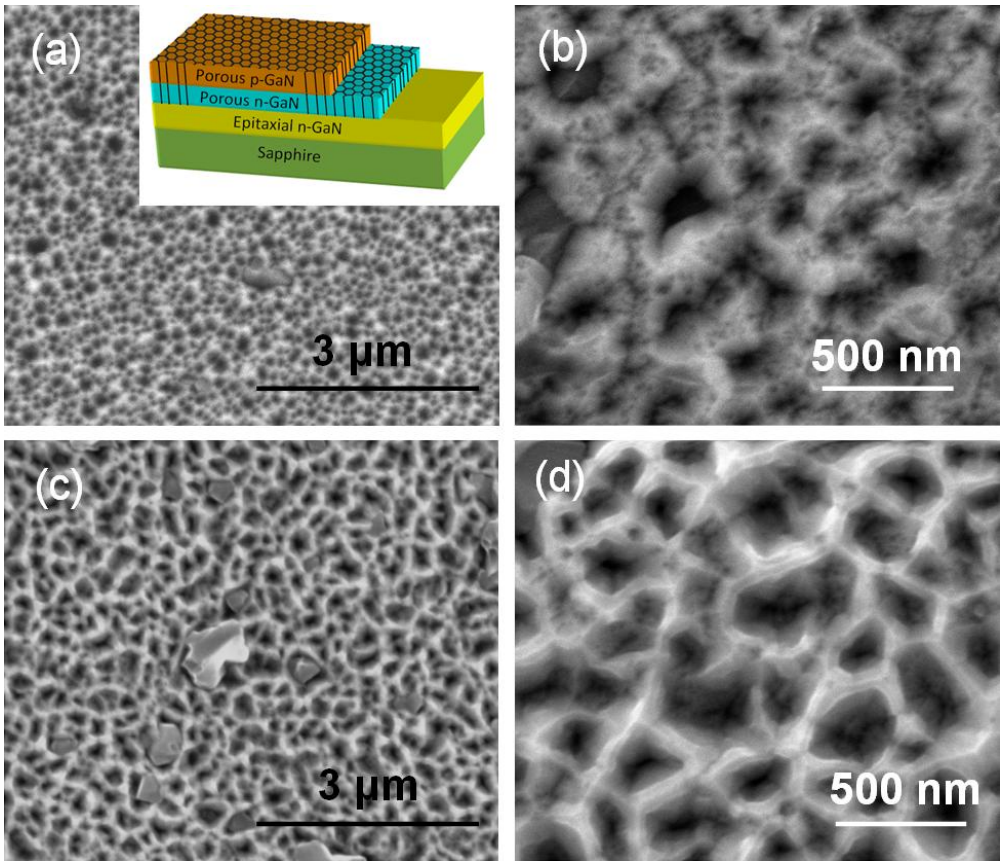

Figure 5.8. SEM top-view images of the fully porous GaN diode: (a) and (b) porous *n*-type GaN layer and (c) and (d) porous *p*-type GaN layer (partial reproduction of Figure 2 from Paper IX).

After growth *p*-type conductivity in Mg-doped porous GaN layers was activated by performing a thermal annealing at 973 K in a N_2 atmosphere for 20 min in order to break the Mg-H complexes.

5.3 Structural characterization of porous GaN *p-n* junctions

To analyze the influence of structural strain on our porous diodes, the rocking curves of partially and fully porous GaN *p-n* junctions were recorded, as reported in Paper IX. The rocking curves corresponding to the (0004) reflection of the three diodes are shown in Figure 5.9. Figure 5.9a shows the rocking curves corresponding to the porous *n-p* diode. In the figure, we can see the rocking curve corresponding to the non-porous *p*-type GaN substrate and the rocking curve corresponding to the porous *n*-type GaN layer. From the figure we can compare the position and the full width at half-maximum (FWHM) of the diffraction peak of each layer in the ω scan. For the non-porous *p*-type GaN substrate FWHM is 0.428º, while for the porous *n*-type GaN layer is slightly narrower 0.419º, indicating that the crystalline quality of the porous film is comparable to that of the non-porous substrate, or even a little better. The position of the peak for the non-porous *p*-type GaN layer is centered at 72.902º, while that of the porous *n*-type GaN layer is centered at 73.082º. This indicates a slight relaxation of

the porous layer when compared to the non-porous film grown on a sapphire substrate. The magnitude of the relaxation can be estimated according to the following expression [201]:

$$\Delta\in_{\perp} = (\boldsymbol{c}_{\text{strained}} - \boldsymbol{c}_{\text{relaxed}})/\boldsymbol{c}_{\text{relaxed}} \qquad \text{(Eq. 5.3)}$$

were $\boldsymbol{c}_{\text{strained}}$ accounts for the ***c*** crystallographic parameter of the non-porous *p*-type GaN grown on sapphire, and $\boldsymbol{c}_{\text{relaxed}}$ for the ***c*** crystallographic parameter of the porous *n*-type GaN layer, calculated both from the analysis of the rocking curves. According to that, a reduction of the strain perpendicular to the (0001) plane of 0.24% can be estimated. This strain reduction stems from the benefit of internal porosity and the fact that the porous GaN is grown on a native substrate, while the non-porous film was obtained on sapphire.

Table 5.2. Position and FWHM of the diffraction peaks extracted from the rocking curves recorded for the (0004) reflection of the different diodes fabricated, and relaxation of the different porous layers calculated according to Equation 5.3.

		Peak position (º)	**FWHM (º)**	**Relaxation (%)**
Porous *n*-*p* diode	porous *n*	73.082	0.419	0.24
	non-porous *p*	72.902	0.428	---
Porous *p*-*n* diode	porous *p*	73.204	0.420	0.46
	non-porous *n*	72.867	0.412	---
Fully porous *p*-*n* diode	porous *p*	72.938	0.392	0.07
	porous *n*	72.910	0.392	0.04
	non-porous *n*	72.883	0.388	---
Porous *n*-type on non-porous *n*-type layer	porous *n*	72.995	0.451	0.04
	non-porous *n*	72.969	0.427	---

Figure 5.9b shows the rocking curves recorded for the porous *p*-*n* diode, with the rocking curve corresponding to the non-porous *n*-type GaN substrate and the rocking curve of the porous *p*-type GaN layer. The values of the FWHM and the position of the peak for these rocking curves are listed in Table 5.2. From these data, and using equation 5.3, the relaxation of the *p*-type porous layer is 0.46 %, almost double than that achieved in the porous *n*-*p* diode. In that case, FWHM is slightly higher for the porous layer, but of the same order of that

obtained for the non-porous substrate, indicating that the crystalline quality of these two films is similar. The relaxation of the porous *p*-type layer is larger than that obtained for the porous *n*-type layer. This might be related with the wider size of the pores observed in the SEM figures for this *p*-type layer (see Figure 5.7b), that gives additional flexibility to the layer to accommodate on the substrate.

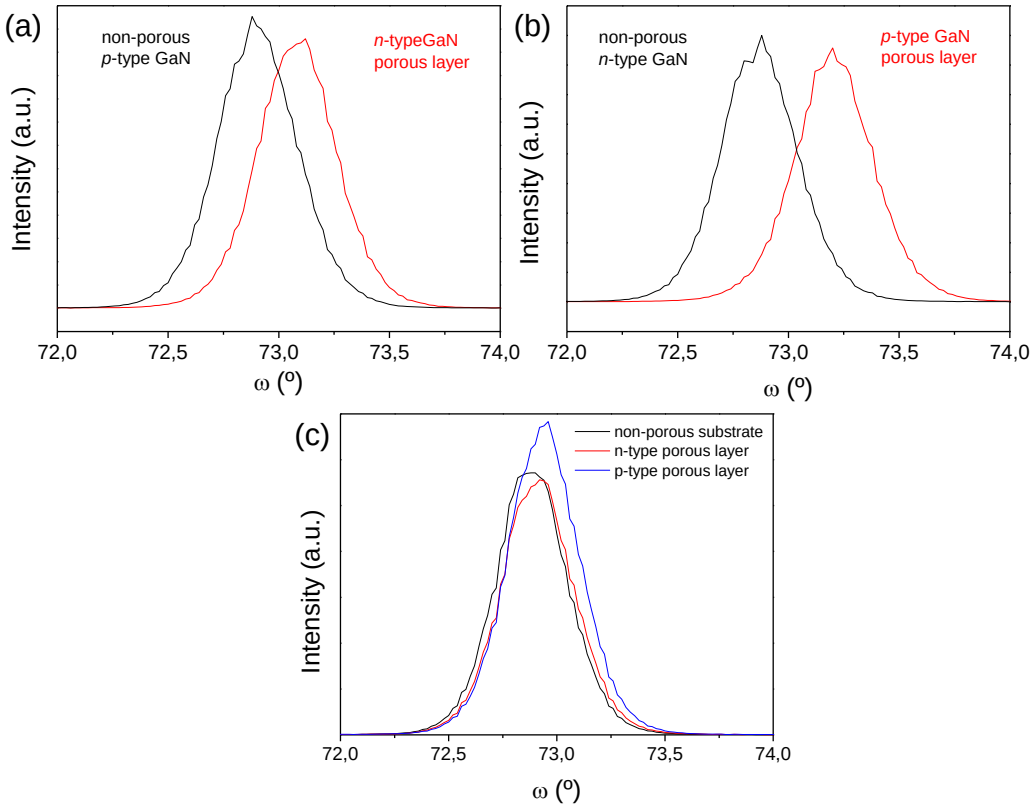

Figure 5.9. Rocking curves of (a) porous *n*-type GaN layer grown on non-porous *p*-type GaN substrates, (b) porous *p*-type GaN layer grown on non-porous *n*-type GaN and (c) fully porous GaN diode grown on non-porous *n*-type GaN layer on sapphire (partial reproduction of Figure 3 from Paper IX).

Finally, the fully porous GaN diode was also analyzed (see Figure 5.9c). In that case the FWHM for the two porous layers is equal and of the same order of that recorded for the non-porous *n*-type GaN substrate, as can be seen in Table 5.2. Thus, the crystalline quality of the three films is similar. From the position of the reflection peaks, we can estimate the relaxation of the porous layers. In that case, we can see from Figure 5.9c that the shift of the diffraction peak is substantially smaller than in the previous cases, which would mean that the relaxation of the porous films is smaller in that case. In fact, the relaxation calculated for these porous layers is 0.04 % for the *n*-type porous layer grown on the non-porous *n*-type GaN substrate, while that of the *p*-type porous layer grown on the porous *n*-type layer is 0.07 %. Again, the *p*-type porous layer is more relaxed than the *n*-type one, almost double, as in the previous case. To explain these differences there are different aspects to take into account. First, the substrate on which the first *n*-type porous layer has been grown is different than that used in the porous *n-p* diode. Here we used a non-porous *n*-type GaN film, while in the case of the porous *n-p* diode was a non-porous *p*-type GaN film. Thus, the stress of these two films

grown on sapphire must be different. Second, it might be possible that growing an additional porous GaN layer on the top of the one previously obtained by the CVD process induces a new stress to the porous film grown in the first step, which make it to appear less relaxed, and this influences in the amount of stress that the second porous layer can achieve. The differences between the relaxation of these porous layers to respect the previous diodes fabricated is related to the non-porous GaN substrate used in this case (*n*-type), which induces a lower relaxation towards the *n*-type porous GaN layer grown directly on this substrate (0.04 %), as it reveals the rocking curve recorded for this epitaxy, without an additional *p*-type porous layer on its top (see Figure 5.10).

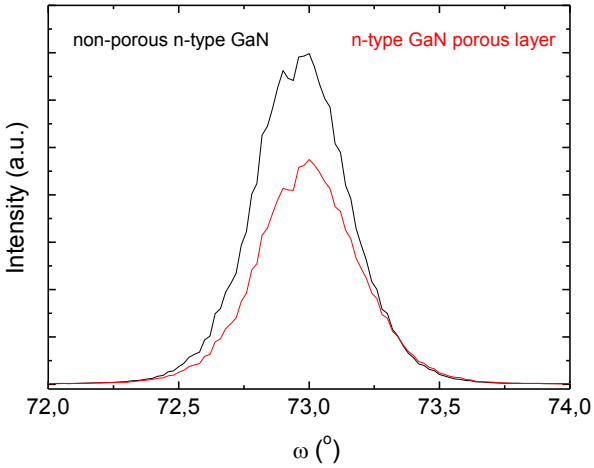

Figure 5.10. Rocking curves of porous *n*-type GaN layer grown on non-porous *n*-type GaN substrates

5.4 Luminescence characterization of porous GaN *p-n* junctions

5.4.1 Photoluminescence

PL measurements were performed on both Mg-doped porous GaN and undoped porous GaN, as described in Paper IX. Figure 5.11a shows the PL spectra for the undoped GaN taken in the range of temperatures from 11 K to 300 K at a constant laser power density. Undoped GaN forming the porous layer exhibits the expected band-edge luminescence with a blue shift from 3.43 eV (361 nm) at 300 K to 3.46 eV (358 nm) at 11 K and a narrow FWHM of ~12 meV at this temperature. Broad emission near the band gap typically results from tailing of the density of states due to randomly distributed impurities [202]. This broad emission near-band gap and band-edge emission equilibrate in intensity at 100 K and the broad emission near-band gap slightly dominates at around 120 K. However, the band-edge emission dominates at the rest of the studied temperatures.

Figure 5.11b shows the PL spectra for the Mg-doped GaN layer taken in the range of temperatures from 11 K to 300 K at a constant laser power density. The room temperature band-edge emission appears at a lower energy of 3.41 eV (363 nm) when compared to the *n*-type porous GaN in Figure 5.11a. At temperatures down to 11 K, however, this emission is blue-shifted and located at a value of 3.46 eV (358 nm) with a narrow FWHM of ~5 meV.

The band gap emission in both, undoped and Mg-doped GaN, is over an order of magnitude more intense at 11 K as compared to room temperature. We do observe some emission at very high super-bandgap energies of ~3.5 eV (354 nm), consistent with a bound exciton. As the GaN is Mg-doped and no Si nor shallow O donor-bound excitons are likely, we attribute this weak emission to acceptor bound excitons linked to Mg incorporation. The band-edge luminescence is followed by the donor-acceptor pair (DAP) luminescence at 3.27 and 3.28 eV (379 and 378 nm) at 11 K. This DAP emission is not found at 300 K for the *p*-type porous GaN, but it becomes more evident as temperature is going down. Also, the broad blue band clearly observed at 300 K disappears as temperature decreases and at 200 K is practically not observed. This type of emission has been previously observed and attributed to the formation of a Mg complex or some native defect level. As expected from Mg acceptors in doped GaN, we find the longitudinal optical (LO) phonon replicas at 3.18 and 3.19 eV (390 and 389 nm) at 150 and 11 K respectively, with several harmonics observable at 11 K. Thus, the PL spectrum of the porous GaN demonstrates Mg incorporation as an acceptor state in the GaN lattice, resulting in the *p*-type character (see Figure 5.11b).

Yellow luminescence (YL) is also present in both materials having similar characteristics in undoped [203] porous GaN and Mg-doped *p*-type porous GaN [204]. The YL has a weak temperature dependence and is not found to vary considerably due to Mg incorporation into the lattice.

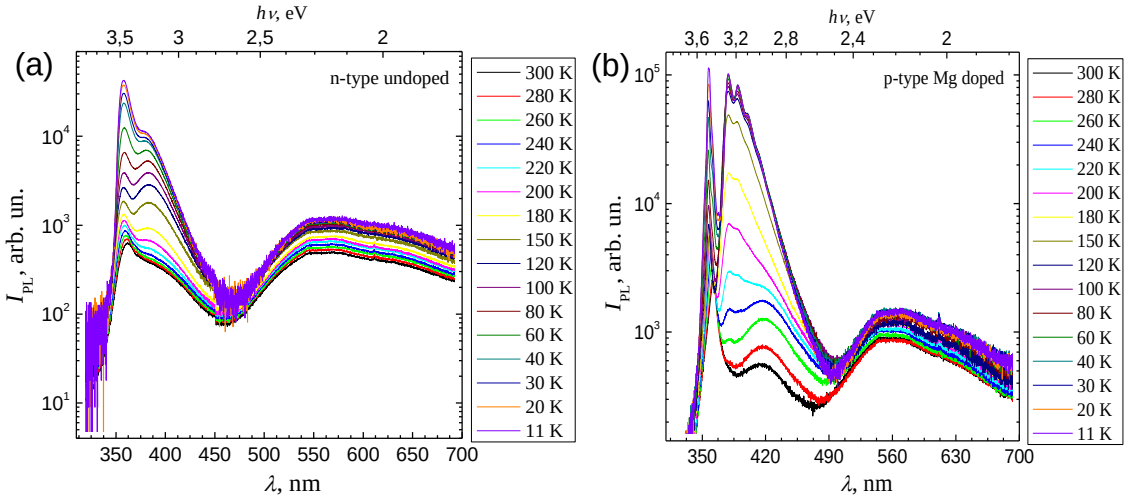

Figure 5.11. Temperature-dependent PL spectra of (a) undoped and (b) Mg-doped porous GaN, acquired after excitation at 325 nm (3.8 eV) (reproduction of Figure 6 from Paper IX).

5.4.2 Cathodoluminescence

Figure 5.12 shows SEM and the corresponding panchromatic CL images recorded for the *p*-type non-porous and *n*-type porous GaN films, as described in Paper 8. The panCL image of the non-porous sample, Figure 5.12a, shows the typical granular luminescence pattern of GaN [205], due to the distribution of clusters of dislocations in the material. In the corresponding SEM image, some porosity is apparent, likely related to the high temperature

to which the substrate has been exposed during the growth process. The panchromatic CL image of the *n*-type GaN layer, Figure 5.12b, shows a more uniform distribution of the luminescence. It is also important to note that the presence of the pores does not quench the luminescence arising from the porous GaN layer. In fact, when we compare this image with the corresponding SEM image, the pores (that can be clearly seen in the SEM image) are not visible in the CL image, with the exception of the larger pores, for which a dark contrast can be observed in the CL image.

Figure 5.12c shows the panchromatic CL image recorded at the border between the *p*-type non-porous and the *n*-type porous GaN films. From this image it is clear that the extraction of light from porous GaN is more efficient than from the non-porous substrate, related to the high quality of the porous GaN epitaxial layer. Also, one can consider the beneficial effect of multiple reflections that the light generated by the sample suffers at the walls of the pores, which allows overcoming the limit of total reflection imposed by the refractive index contrast between GaN and air. The CL spectra recorded in both regions are also shown in Figure 5.12c. The spectrum recorded for the non-porous substrate corresponds to the typical CL spectrum of *p*-type GaN, with the donor-acceptor pair (DAP) luminescence located at 3.28 eV (378 nm), and a LO phonon replica at 3.19 eV (388 nm). The spectrum recorded for the porous GaN epitaxial layer exhibits the expected band-edge luminescence of *n*-type GaN, located at 3.40 eV (364 nm), with a FWHM of ~52 meV. Apart from this, the YL band, normally attributed to point defects (Ga vacancies) and impurities such as oxygen and carbon [203] was also observed. It can be attributed to transitions between the conduction band or shallow donors and deep acceptor levels caused by crystallographic point defects in the GaN layer, since it is almost independent of temperature [206]. In the present case, we also observed a variation in the intensity of the band-edge and YL bands, depending on the probed point along the sample. This can be attributed to different effects, such as an inhomogeneity in the distribution of impurities or defects in the GaN structure.

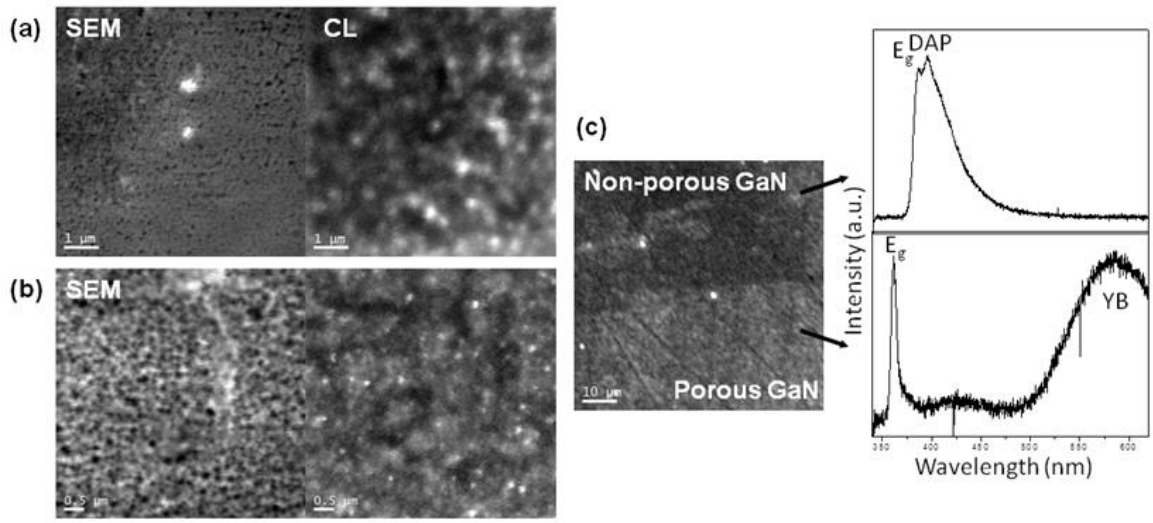

Figure 5.12. SEM and panchromatic CL images of (a) *p*-type non-porous GaN on sapphire and (b) *n*-type porous GaN grown on non-porous *p*-type GaN. (c) Panchromatic CL image recorded at the border between *n*-type porous and *p*-type non-porous GaN, and CL spectra recorded at these two layers (reproduction of Figure 5 from Paper VII).

Figure 5.13 shows SEM and panchromatic CL images and CL spectra recorded for the non-porous Si doped *n*-type GaN film and the porous undoped *n*-type GaN layer, corresponding to the fully porous *p*-*n* diode, as described in Paper IX. In Figure 5.13a, SEM and the panchromatic CL image with the corresponding CL spectrum of the non-porous *n*-type GaN substrate are shown. The panchromatic CL image shows the typical granular luminescence pattern of GaN, due to the distribution of clusters of dislocations in the material [205]. The spectrum recorded for the non-porous *n*-type GaN substrate shows the band gap emission located at 3.49 eV (~355.6 nm) and the DAP luminescence at 3.29 eV (~377 nm). The panchromatic CL image of the porous *n*-type GaN layer shows a quite uniform distribution of luminescence (see Figure 5.13b). However, the pores, that can be clearly seen in the SEM image, are not visible in the CL image, except the larger pores, where a dark contrast can be observed in the CL image. Thus, again the presence of the pores does not quench the luminescence arising from the porous GaN. The spectrum recorded for the porous *n*-type GaN layer exhibits a quite broad near-band edge luminescence, located at 3.42 eV (~362 nm). YL band is also present. Here, again, depending on the place on the sample a variation in the intensity of the band-edge and YL bands is observed, what can be attributed to an inhomogeneity in the distribution of impurities or defects in the GaN.

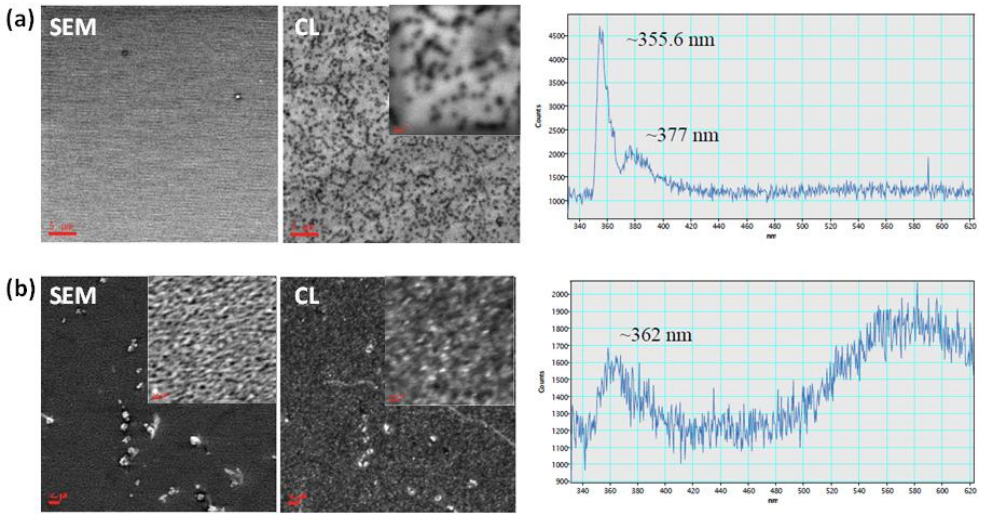

Figure 5.13. SEM and CL images taken in the same region of the sample, and CL spectra of the (a) non-porous *n*-type GaN substrate and (b) porous *n*-type GaN layer, corresponding to the fully porous *p*-*n* diode. Insets show magnified areas of the pictures.

Figure 5.14a shows the SEM and panchromatic CL images of the porous *p*-type GaN layer taken in the same region of the sample. In the panchromatic CL image, where the bright spots in the image represent high emission intensity regions and dark spots represent low emission intensity regions, the pores are not visible as compared to the SEM image. High intensity regions correspond to porous GaN particles that also grow on the top of the porous layer, but with a different crystallographic orientation. Figure 5.13b shows a closer view of the panchromatic CL image of the *p*-type GaN sample from which a reconstructed image (see Figure 5.14c) based on the intensity of the 358 nm emission peak was made (marked with a green square on Figure 5.14b). The CL spectra were taken in two different points shown on

this monochromatic CL image, representing the high intensity and low intensity emission regions observed (see Figure 5.14d). The spectrum recorded for the Mg-doped porous film (point 2) correspond to the typical CL spectrum of a *p*-type GaN, with the band gap emission at 3.46 eV (~358 nm), the DAP luminescence at 3.27 eV (~379 nm) and a LO phonon replica at 3.20 eV (~388 nm). The inset of Figure 5.14d shows the two spectra with higher resolution, from where it can be concluded that both spectra have the same features belonging to the Mg-doped *p*-type GaN. However, in the spectrum recorded in the point 1, that corresponds to the porous GaN particle grown on the top of porous layer, the intensity of the DAP emission is much lower than the intensity of the near-band gap emission. It might be related to an inhomogeneity of doping of the porous GaN layer and it would indicate that a higher doping level is achieved in the porous GaN layer. YL, which is commonly observed in the PL spectrum of *n*- and *p*-type GaN is quite weak here, what indicates the high electronic quality of the porous *p*-type GaN film.

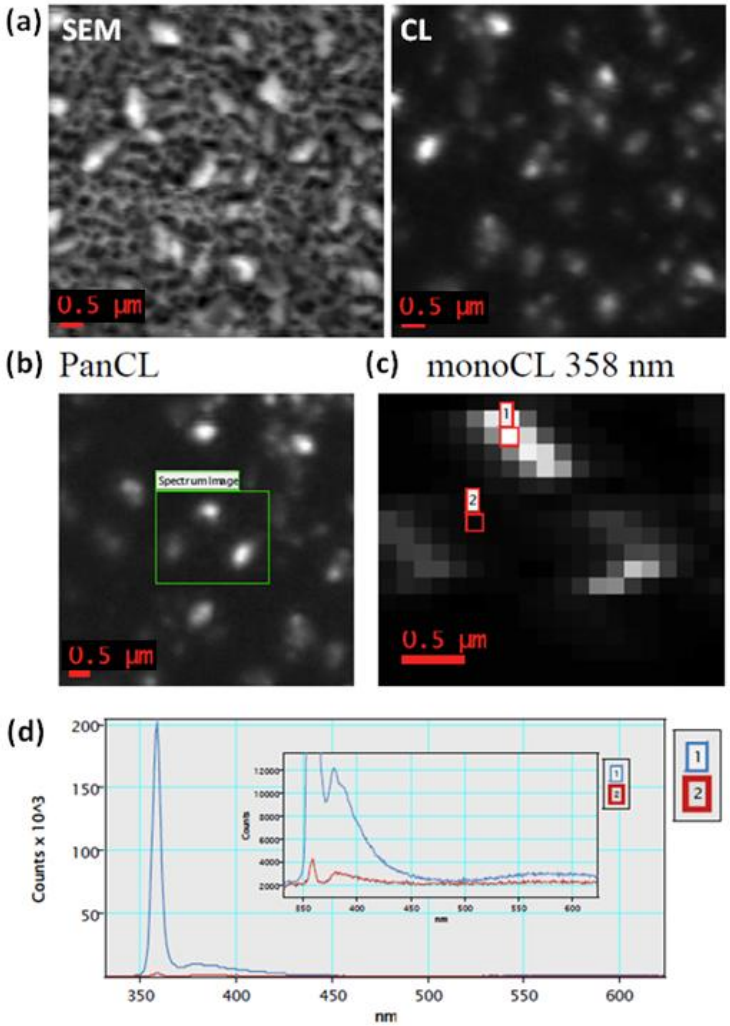

Figure 5.14. (a) SEM and CL image of porous *p*-type GaN taken in the same region of the sample. (b) Panchromatic CL image of the same sample from which a reconstructed image based on the intensity of the 358 nm emission peak was made in the region marked with a green square, as shown in (c). (d) CL spectra recorded for points 1 and 2 marked in pannel (c). Inset in the graph is a magnification of the same spectra to show the features observed in the two spectra (reproduction of Figure 4 from Paper IX).

SEM and panchromatic CL cross-sectional images of the fully porous GaN diode were recorded (see Figure 5.15). The cross-sectional SEM micrograph clearly shows the non-porous GaN film and the porous GaN layer, consisting of Mg-doped porous *p*-type GaN and undoped porous *n*-type GaN layers. The interface between the non-porous GaN film and the porous GaN layer are well defined and abrupt. The thickness of the porous GaN layer is ~ 2.1 μm, what corresponds to the growth of two layers of Mg-doped porous *p*-type GaN layer and undoped porous *n*-type GaN layer with a thickness of ~1 μm for each one. In the panchromatic CL image shown in Figure 5.15b a clear difference between the porous *p*-type GaN and porous *n*-type GaN layers can be seen. The porous *n*-type GaN layer on the image appears dark while the porous *p*-type GaN layer appears bright, what indicates the generation of a much higher intensity of emission from the porous *p*-type GaN layer than from the porous *n*-type GaN layer. This can be related to the higher concentration of charge carriers in the Mg-doped porous *p*-type GaN layer (~10^{18} cm^{-3}) when compared to the charge carriers concentration determined in the porous *n*-type GaN particles (~10^{16} cm^{-3}). Figure 5.15c shows the CL spectra recorded from the cross-section images for *p*-type porous GaN and *n*-type non-porous GaN. Here, the emission from DAP in the Mg-doped porous *p*-type GaN is observed, while the emission from band gap does not appear. In the case of the non-porous *n*-type GaN substrate, a strong emission at 3.49 eV (~355 nm) is observed. The spectra corresponding to the undoped porous *n*-type GaN layer could not be recorded due to its low intensity.

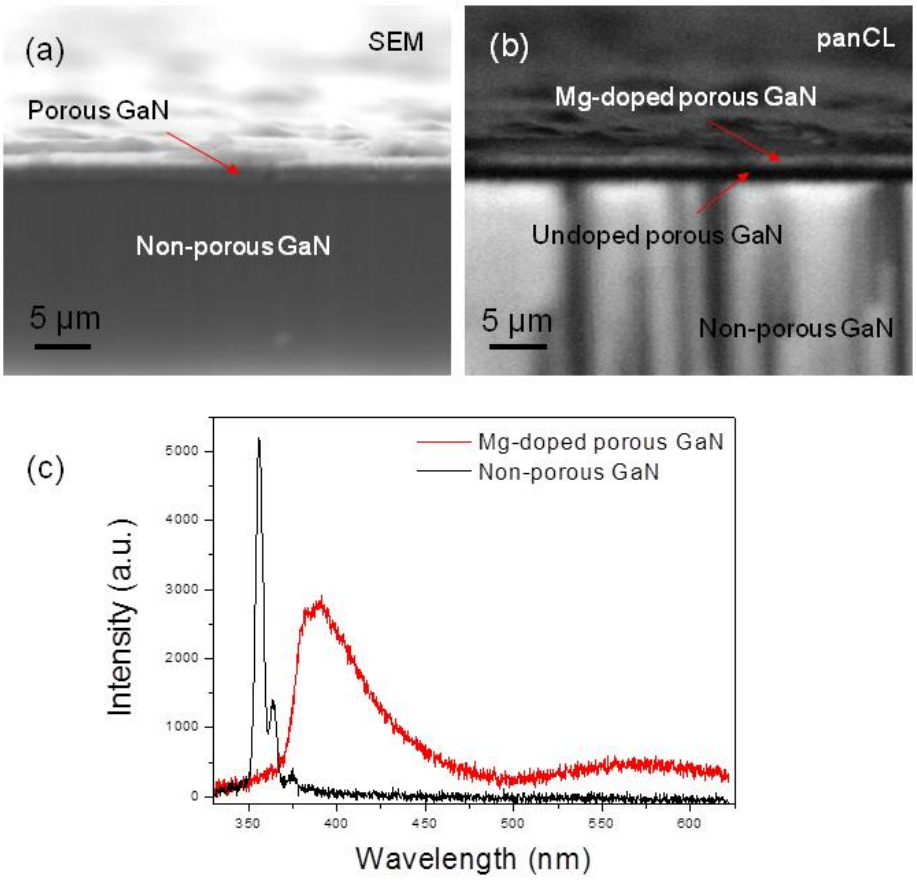

Figure 5.15. (a) SEM and (b) panchromatic CL cross-sectional images of the fully porous GaN diode fabricated. (c) CL spectra recorded for points 1 and 2 marked in pannel (c) (reproduction of Figure 5 from Paper IX).

5.5 Electrical characterization of porous GaN *p-n* junctions

To investigate the behavior of the three types of porous GaN diodes obtained, electrical characterization was conducted, as described in Paper IX. Figure 5.16 shows the non-linear typical I-V curves characteristics of a diode behaviour acquired for these porous GaN *p-n* junctions. The clear *p-n* junction response confirms the formation of high quality rectifying porous GaN diodes. Figure 5.16a shows the I-V curve recorded between the porous *n*-type GaN layer and the non-porous *p*-type GaN substrate. The high bias resistance turn-over of this porous *p-n* diode occurs just above 1 V. When the *p*-type GaN is positively biased, current flow through the *p-n* junction varies exponentially. The barrier to the exponential current increase is found to be much lower than the expected GaN diode response, i.e. E_g/q. The turn-on voltage for this *p-n* junction is $\sim E_g/4q - E_g/2q$, i.e. 0.5 – 0.68 V. In case of the porous *p-n* diode and the totally porous GaN diode the turn-on voltage is found to be even lower, in the range $E_g/6q - E_g/4q$, i.e. 0.36 – 0.54 V (see Figure 5.16b and 5.16c). This response has several features that have been seen in InN and GaN nanowires arrays [207]. However, in all cases the diode nature is confirmed and low reverse bias leakage currents are found for the porous GaN structures.

The electron density for porous unintentionaly doped *n*-type GaN is estimated as 1.6×10^{16} cm^3, as shown in Chapter 3. The effective hole density for porous *p*-type GaN is estimated, at 300 K using the effective hole and electron masses for wurzite GaN, to be $\sim 9 \times 10^{18}$ cm^{-3}, as shown in Chapter 4. Assuming an abrupt, one-side junction for comparative analysis to coherent GaN films, the barrier potential V_B can be estimated as:

$$V_B = \frac{kT}{q} \ln\left(\frac{N_D N_A}{n_i^2} \right) \qquad \text{(Eq. 5.4)}$$

where N_D and N_A are the donor and acceptor densities of *n*-type GaN and *p*-type GaN forming the *p-n* junction, respectively, n_i^2 is the intrinsic doping density of GaN. Taking into account the values of donor and acceptor densities of non-porous *n*-type GaN and non-porous *p*-type GaN of $N_D = 10^{19}$ cm^{-3} and $N_A = 10^{18}$ cm^{-3}, respectively, and the corresponding values mentioned above for porous *n*-type GaN and porous *p*-type GaN, we can estimate the barrier potential V_B for the porous *n-p* diode as 0.72 V, for the porous *p-n* diode as 0.9 V and for the fully porous diode as 0.71 V. Also, the current at an equal value of the forward voltage in the fully porous *p-n* diode is found to be three orders of magnitude higher than that in partially porous diodes, what indicates the low resistivity of the porous GaN layers and this is a promising characteristic for future LED applications.

Based on this measurement we should mention some important aspects for the porous GaN *p-n* junctions. Microscopic characterization confirms a well-defined interface between the porous and the non-porous GaN layers, and thus, no significant tunnelling barrier exists either at the GaN-GaN interface or on the surface of the GaN with the Ohmic contact. Also, microscopic characterization excludes any interfacial contaminants that would alter the effective barrier. The measurements were repeated from different points on several separate *p-n* junction diodes and they exhibited similar I-V responses.

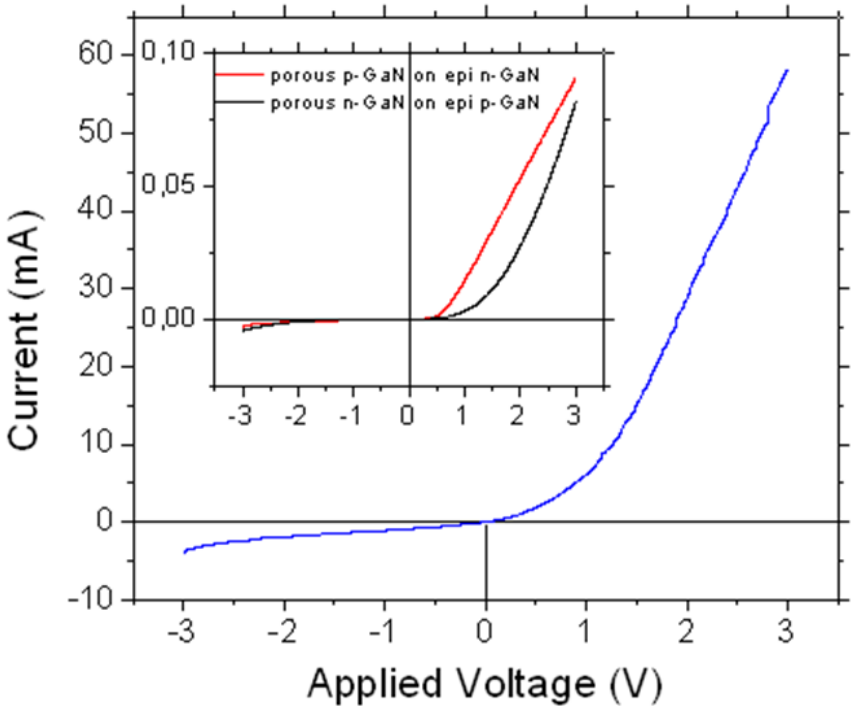

Figure 5.16. I-V curves of the fully porous diode. Inset shows the I-V curves recorded for the porous *n-p* and porous *p-n* diodes (partial reproduction of Figure 7 from Paper IX).

5.6. Applications of porous GaN *p-n* junctions

5.6.1 Application of porous GaN *p-n* junctions to high temperature electronics

Figure 5.17 shows the I-V curves recorded for the porous *n-p* diode at different temperatures ranging from 298 K to 673 K and in the range of voltages between -10 V and 10 V, as described in Paper IX. The forward and reverse bias currents of the diode increase when the temperature increased due to the increase in the number of carrier charges across the barrier height. This suggests that the carrier charges are effectively generated in the junction with the increase of temperature. The turn-on voltage for this *p-n* junction is ~ $E_g/4q - E_g/2q$ at room temperature, as explained before. With the increase of temperature, the value of the turn-on voltage decreases. At high temperatures the high bias resistance turn-over of the porous GaN *n-p* diode occurs just above 0 V. The forward bias I–V curve is exponential at low bias voltages and linear at higher voltages, but with the increase of temperature the forward bias I–V curve is found to increase linearly at lower voltages and practically no exponential characteristic is observed at 673 K. At high temperatures the current increases, what can improve the performance of the porous *p-n* diode in forward bias. At each studied temperature the porous *n-p* diode shows quite good rectification properties. Also, the breakdown voltage was not observed in the studied range of voltages and temperatures.

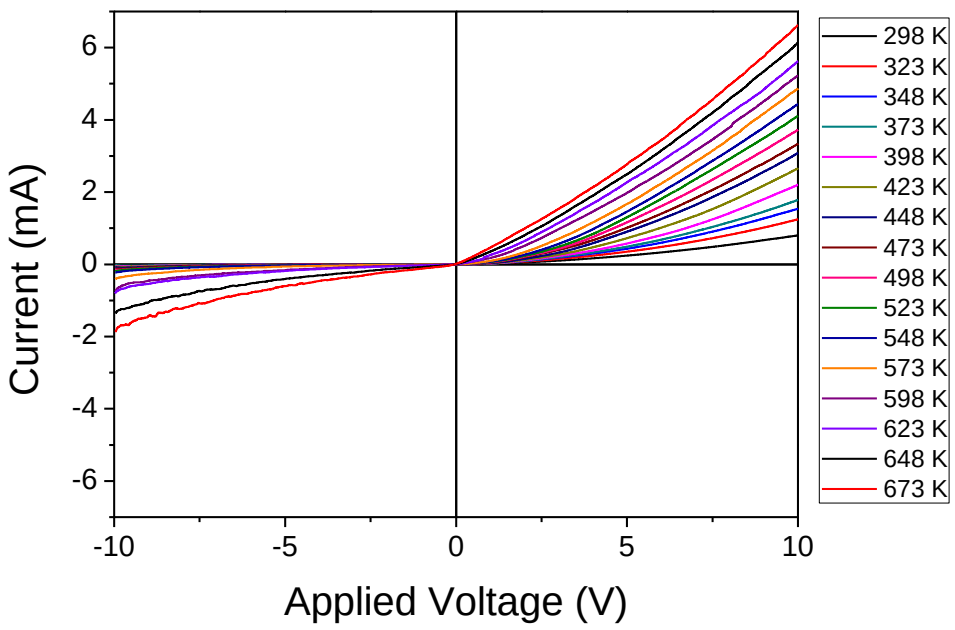

Figure 5.17. I-V curves of the porous *n-p* diode recorded at different temperatures in the range between 298 K and 673 K (partial reproduction of Figure 7 from Paper IX).

5.6.2 Use of porous GaN *p-n* junctions as current rectifiers

An important property of a *p-n* junction is the rectifying effect, which means that it only allows the electric current to flow in one direction. As expected, by applying both reverse and forward bias to the porous GaN diode, a distinct rectifying behaviour is observed. Figure 5.18 shows current vs. time plots recorded at different constant voltages for each of three porous GaN diodes, after changing the polarity of diode bias with a frequency of 0.1 Hz. The fully porous GaN *p-n* junction diodes, and those comprising porous *n*- or *p*-type GaN on non-porous epilayers, all exhibited stable rectification. The I-t characteristics recorded at ±0.4 V does not show clear rectification behavior, since this voltage is below or on the limit of the turn-on voltage of the porous GaN diodes. At ±1 V, ±2 V, ±3 V and ±5 V voltages all diodes demonstrate rectifying behavior. The highest leakage voltage and the lowest rectification ratio is observed at ±5 V. Also, porous GaN diodes demonstrate very stable values of current with time at both, forward and reverse bias. The stability confirms that for porous *p-n* junctions using a single porous layer deposited on an epitaxial continuous GaN film, or from a porous layer grown on another porous layer, a remarkable stability in rectification is maintained. Porous GaN films can exhibit random porosity (compared to arrays of nanostructures), but their ease of deposition over large areas without dominating leakage currents is promising for wideband gap applications, including sensors.

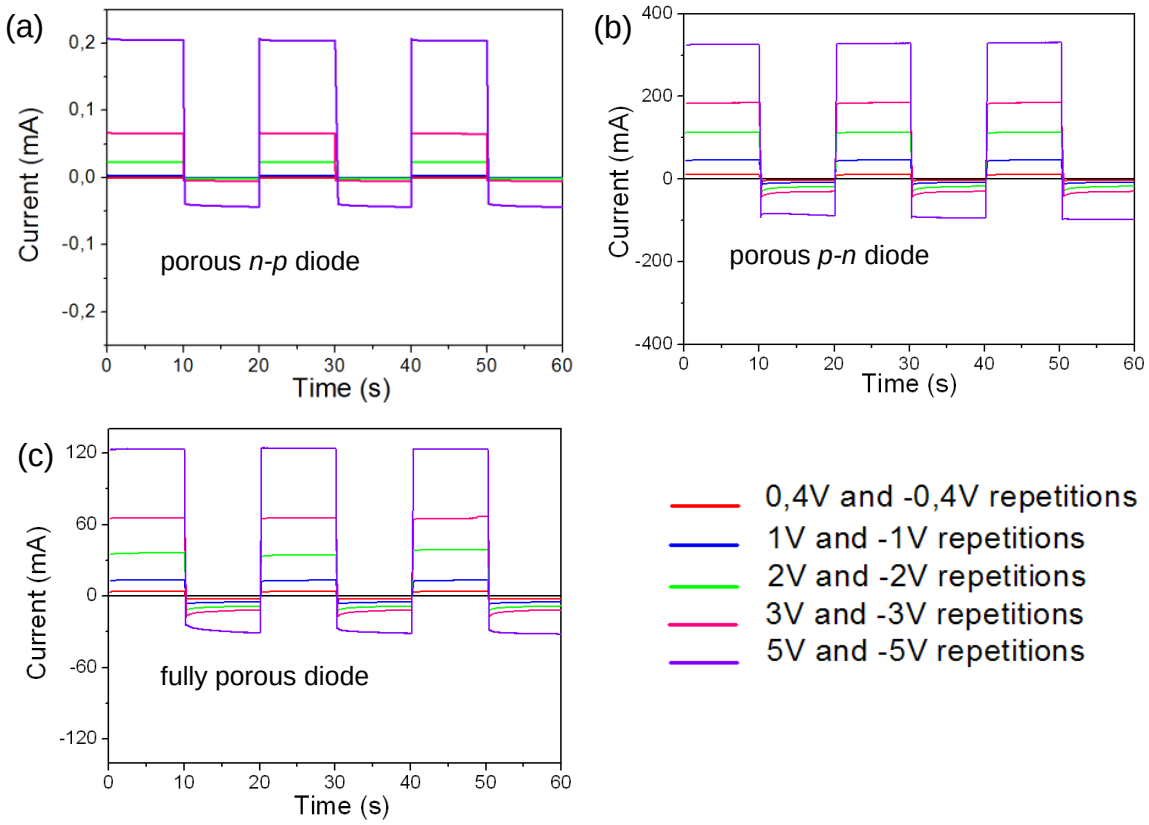

Figure 5.18. Rectification properties of the (a) porous *n-p* diode, (b) porous *p-n* diode and (c) fully porous diode, recorded at different voltages.

Chapter 6

Synthesis and characterization of red phosphors pumped by the GaN emission: an approach towards tuning the emission of the potential LEDs

White LEDs have got much attention because of their wide applications and advantages over conventional light sources. Their benefits include long operating life, high colour rendering index, compact size, vibration resistance, low-voltage operation, minimal maintenance cost and minimal environmental impact [208, 209]. There are several approaches to develop white LEDs. One approach is to produce white light by the combination of a blue InGaN chip (450–470 nm) with Ce:YAG yellow phosphors [210]. Another approach of achieving white light, which is a quite promising method, is to use a UV LED (350–410 nm) to pump red, green, and blue phosphors [211]. Among the different red phosphors that can be used for this purpose, Eu:Y_2O_3 and (Eu,Bi):Y_2O_3 nanoparticles are specially attractive due to its high efficiency, stability, and appropriate excitation wavelengths for UV LEDs [212, 213].

6.1 Synthesis of (Eu, Bi) doped Y_2O_3 nanocrystals

We synthesized luminescent Eu:Y_2O_3 and (Eu,Bi):Y_2O_3 nanoparticles on porous GaN with the intention to introduce them inside the pores of the GaN particles through a sol-gel technique. Phosphor nanoparticles deposited inside the pores of porous GaN structures, apart from giving the required emission that we need to mix to generate one of the colours to produce warm white light, will also offer a medium with an intermediate refractive index that might enhance the light extraction efficiency from the LED. This would be the preliminary step towards developing a procedure that might allow controlling the characteristics of the white light generated by the LED, allowing developing LEDs that emit white light with different colour index renderings by controlling the concentration of phosphor nanoparticles emitting in each colour.

7 mol % Eu and 1.5 mol % Bi doped Y_2O_3 and 7 mol % Eu doped Y_2O_3 nanocrystals were synthesized by a sol-gel technique, the so called modified Pechini method [214]. The scheme of the synthesis process of Y_2O_3 nanocrystals is shown in Figure 6.1. The starting materials were powders of Y_2O_3, Eu_2O_3 and Bi_2O_3 depending on the particles to be prepared. A stoichiometric amount of each reagent was first mixed in concentrated HNO_3 (65 wt %). The excess of HNO_3 was removed to obtain nitrate precipitates by slowly stirring and heating the solution. Next, a chelating agent, ethylenediaminetetraacetic acid (EDTA), was added with a molar ratio of EDTA to the total metal content (CM =[EDTA]/[METAL]) equal to 1 to get the metal complexes. Ethylene glycol (EG) was then added into the solution as the sterification agent, that was slowly heated, producing the precursor resin. The amount of EG added was calculated on the basis of a molar ratio of EDTA to EG (CE = [EDTA]/[EG]) equal to 2 according to the optimized procedure developed in our research group [214]. The precursor resin was then calcined at 573 K for 3 h to obtain the precursor powder, which was calcined again for several hours at different temperatures to obtain the Y_2O_3 nanocrystals.

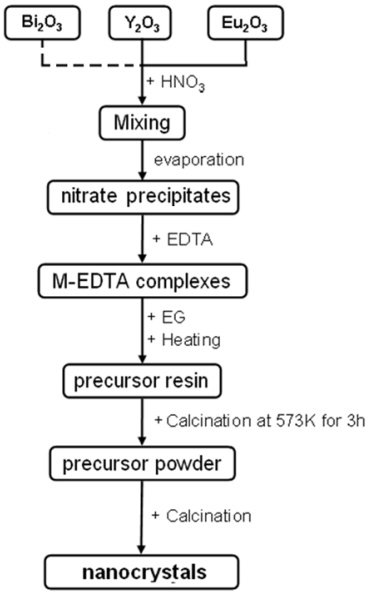

Figure 6.1. Scheme of the synthesis procces of Eu:Y_2O_3 and (Eu,Bi):Y_2O_3 nanocrystals by the modified Pechini method.

6.2 Characterization of Eu:Y_2O_3 and (Eu,Bi):Y_2O_3 nanocrystals

6.2.1 Morphological and structural characterization

We analyzed the conditions for the synthesis of luminescent nanoparticles to optimize the morphology, crystallinity and the strongest red luminescence after excitation in the UV at the GaN band-edge emission around 365 nm.

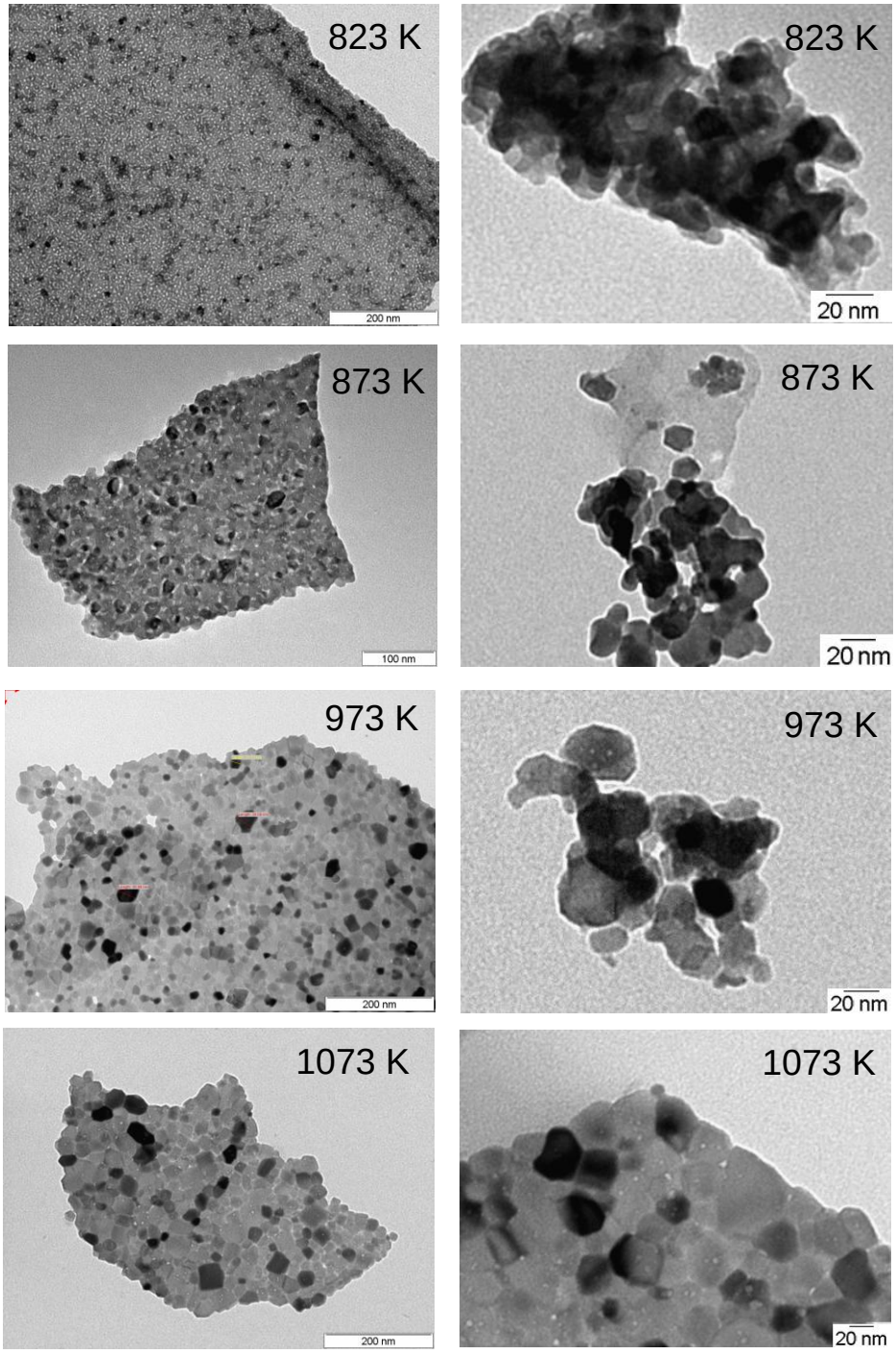

Figures 6.2. TEM images of the Eu:Y_2O_3 nanoparticles obtained after calcination for 3 h at different temperatures.

We studied the influence of calcinations temperature on the morphology and particle size. For this, the precursor powder of 7 mol % Eu:Y_2O_3 was calcined for different times at different temperatures. This concentration was chosen, because the emission from Eu:Y_2O_3 reaches its maximum at 7 mol % [212]. Figure 6.2 shows the TEM images of the Eu:Y_2O_3 nanoparticles obtained at different temperatures after calcination for 3 hours. We can observe a similar level of aggregation of nanoparticles synthesized at different temperatures. Also, with the increase of temperature the size of the particles seem to increase. The sizes of the particles are in ranges between 10 and 30 nm.

As can be seen from the images, the particles tend to form a bidimensional layers (see Figure 6.3a), although these layers tend to aggregate to form three-dimensional structures, as can be seen in Figure 6.3b.

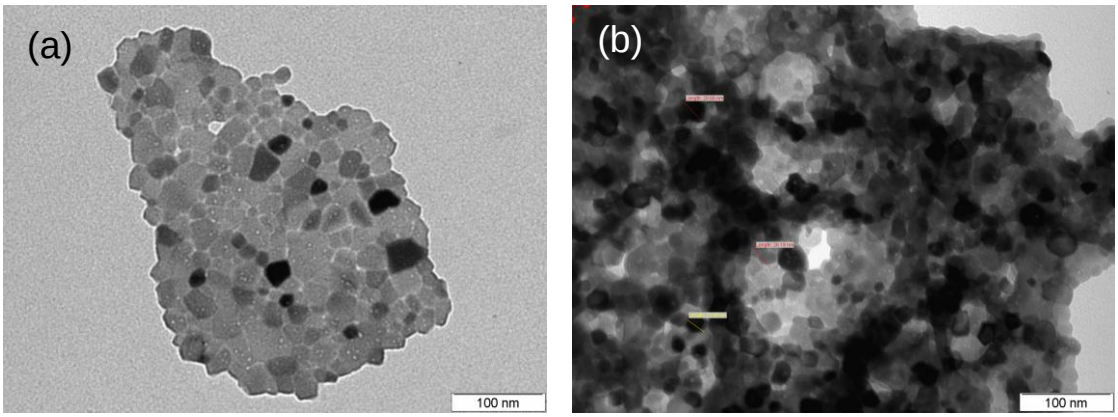

Figure 6.3. (a) TEM image of Eu:Y_2O_3, where bidimensional layers and single particles can be observed and (b) TEM images of the nanoparticles forming a three-dimensional structure, obtained after calcination at 973 K.

We studied the possibility to destroy, by ultrasonication, this three-dimensional aggregates, in order to release single nanoparticles. To do this an ultrasonic finger with powers of 600 W was used. Figure 6.4 shows the nanoparticles prepared at 873 K after ultrasonication for 60 min. We observed that this procedure did not allow to split the three-dimensional aggregates, that were only broken in pieces with smaller sizes.

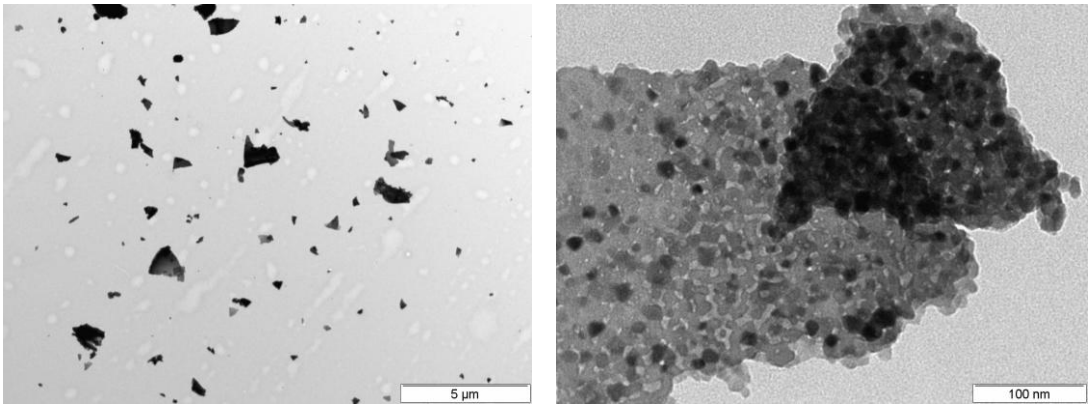

Figure 6.4. TEM images of Eu:Y_2O_3 nanoparticles after ultrasonication for 60 min.

X-ray diffraction analysis of the particles calcined at different temperatures was performed in order to determine the crystalline phase of the material and the degree of crystallinity. Figure 6.5a shows the array of XRD patterns of the Eu:Y_2O_3 nanoparticles obtained after calcination between 723 K and 998 K. We observe that in all cases we have only one crystalline phase which corresponds to the cubic Y_2O_3 crystal structure, with the Ia3 space group. Also we can see that the particles obtained at 723 K are quite amorphous, and that relatively good crystalinity appears above 798 K. Figure 6.5b shows the XRD patterns of the (Eu,Bi):Y_2O_3 nanoparticles obtained after calcination between 723 K and 998 K. The results of XRD analysis of (Eu,Bi):Y_2O_3 nanoparticles are very similar to those obtained for Eu:Y_2O_3, which proves that the presence of Bi did not affect to the appearance of any additional crystalline phase or the crystallinity of the structure.

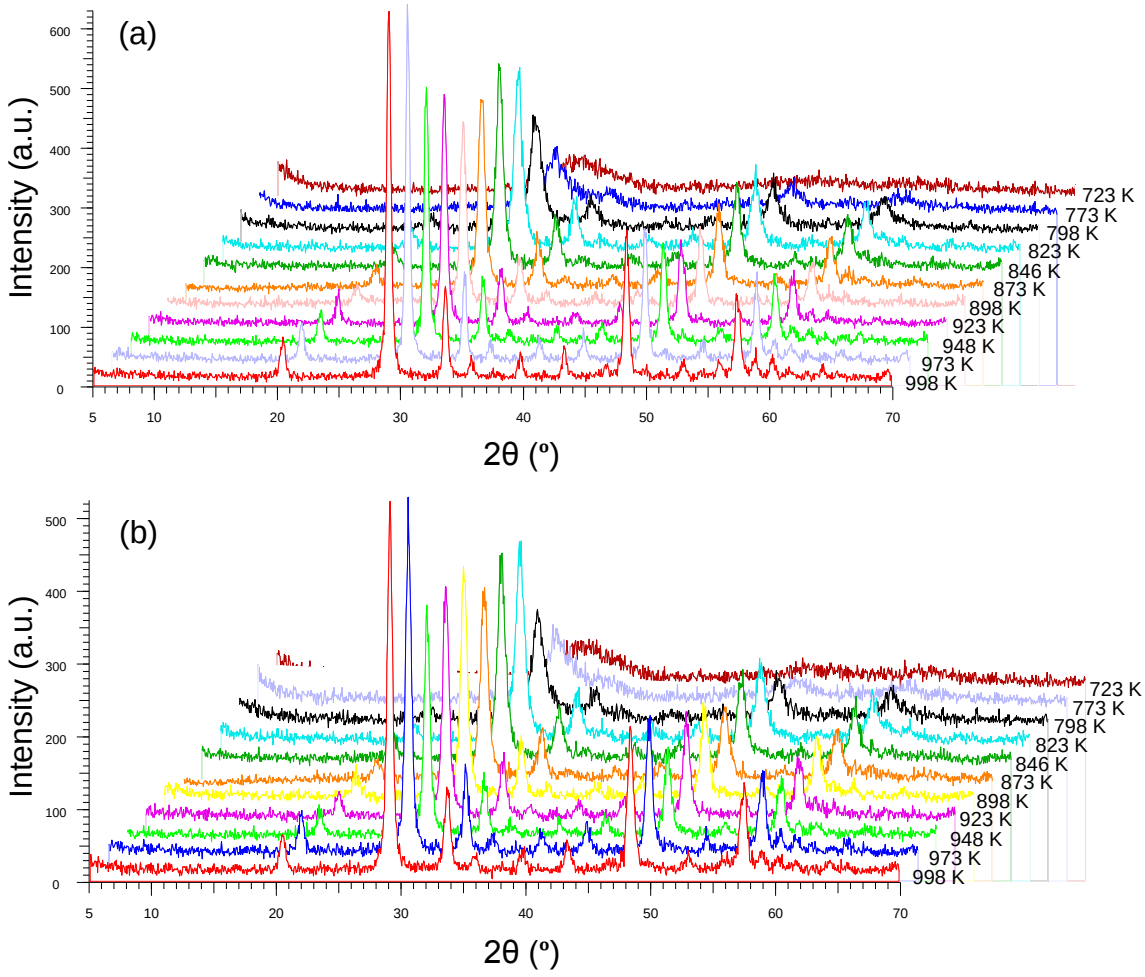

Figure 6.5. XRD patterns of (a) Eu:Y_2O_3 and (b) (Eu,Bi):Y_2O_3 obtained after calcination between 723 K and 998 K.

To determine the size of the particles by XRD, we used Scherrer equation [215]:

$$\tau = \frac{k\lambda}{\beta \cos\theta} \qquad \text{(Eq. 6.1)}$$

where τ is the mean size of the crystalline domains, k is a dimensionless shape factor (the shape factor that has a value of 0.9), λ is the X-ray wavelength (0.154056 nm in our case), β is the line broadening at half the maximum intensity (FWHM) of the XRD peak and θ is the Bragg angle. Table 6.1 summarize the calculated mean sizes of nanoparticles of Eu:Y_2O_3 and (Eu,Bi):Y_2O_3 obtained at different calcination temperatures using the (222) diffraction peak located at 29º. We can see that the mean size of the nanoparticles is increasing with the increase of temperature, but it is still below 20 nm at the maximum calcination temperature we used. These data are consistent with the TEM measurements.

Table 6.1. Mean sizes of Eu:Y_2O_3 and (Eu,Bi):Y_2O_3 nanoparticles determined from the Scherrer equation at different calcination temperature.

Calcinations temperature (K)	**Eu:Y_2O_3**		**(Eu,Bi):Y_2O_3**	
	FWHM (º)	**τ (nm)**	**FWHM (º)**	**τ (nm)**
798	1.1752	6.98	1.2847	6.39
823	0.8627	9.51	0.9217	8.90
846	0.7416	11.06	0.8282	9.91
873	0.6707	12.23	0.7754	10.58
898	0.6034	13.60	0.6714	12.22
923	0.5360	15.31	0.6524	12.58
948	0.4711	17.42	0.5913	13.88
973	0.4266	19.23	0.5796	14.16
998	0.4380	18.74	0.5324	15.41

In order to study the effect of calcinations time in the synthesis of the nanoparticles, the precursors of Eu:Y_2O_3 and (Eu,Bi):Y_2O_3 were calcined during 3, 6 and 10 hours at 798 K, since at this temperature and for a calcination time of 3 h, the degree of crystallinity of the nanoparticles was still low. So we expect that by extending the calcinations time we might obtain nanoparticles with a higher crystallinity but with a lower degree of aggregation. Figure 6.6 shows the TEM images corresponding to these particles calcined at different times. As can be seen from the images, however, and there is no significant differences in the morphology and aggregation degree of the particles obtained.

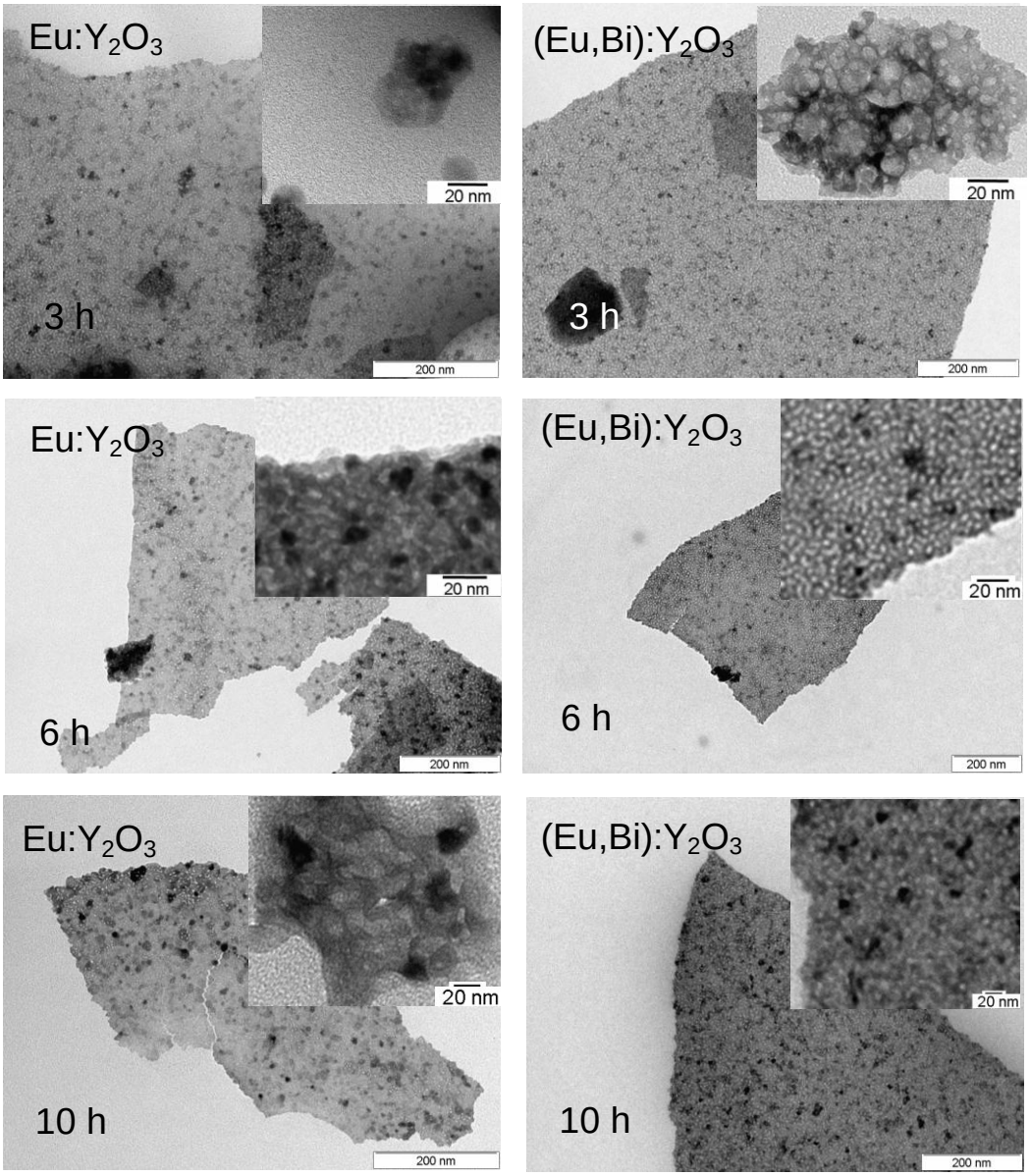

Figure 6.6. TEM images of Eu:Y_2O_3 and (Eu,Bi):Y_2O_3 nanoparticles calcined for 3, 6 and 10 h at 798 K.

To analyze the crystallinity of these particles, again an XRD analysis was conducted. Figure 6.7a and 6.7b shows the XRD patterns corresponding to Eu:Y_2O_3 and (Eu,Bi):Y_2O_3 nanoparticles, respectively. We analyzed the FWHM of the peak located at ~ 29°, corresponding to the (222) reflection, to asset the crystallinity degree of the particles. In the case of Eu:Y_2O_3 the FWHMs are 1.1752°, 0.8278° and 0.8128° for nanoparticles prepared during 3, 6 and 10 h respectively. And in the case of (Eu,Bi):Y_2O_3 FWHMs are 1.2847°, 0.8937° and 0.8052° for nanoparticles prepared during 3, 6 and 10 h respectively. As can be seen, the FWHM decreases with the increase of calcination time in both cases indicating that the size of te particles will increase, but at the same time that the crystallinity degree is higher. To determine the size of the particles by XRD, we used the Scherrer equation. As can be seen from the Table 6.2, with the increase of calcination time, the size of particles is increasing. For calcination during 3 h we obtained a good crystallinity degree and smaller sizes of the particles, thus, we decided that the optimal calcination time is 3 h.

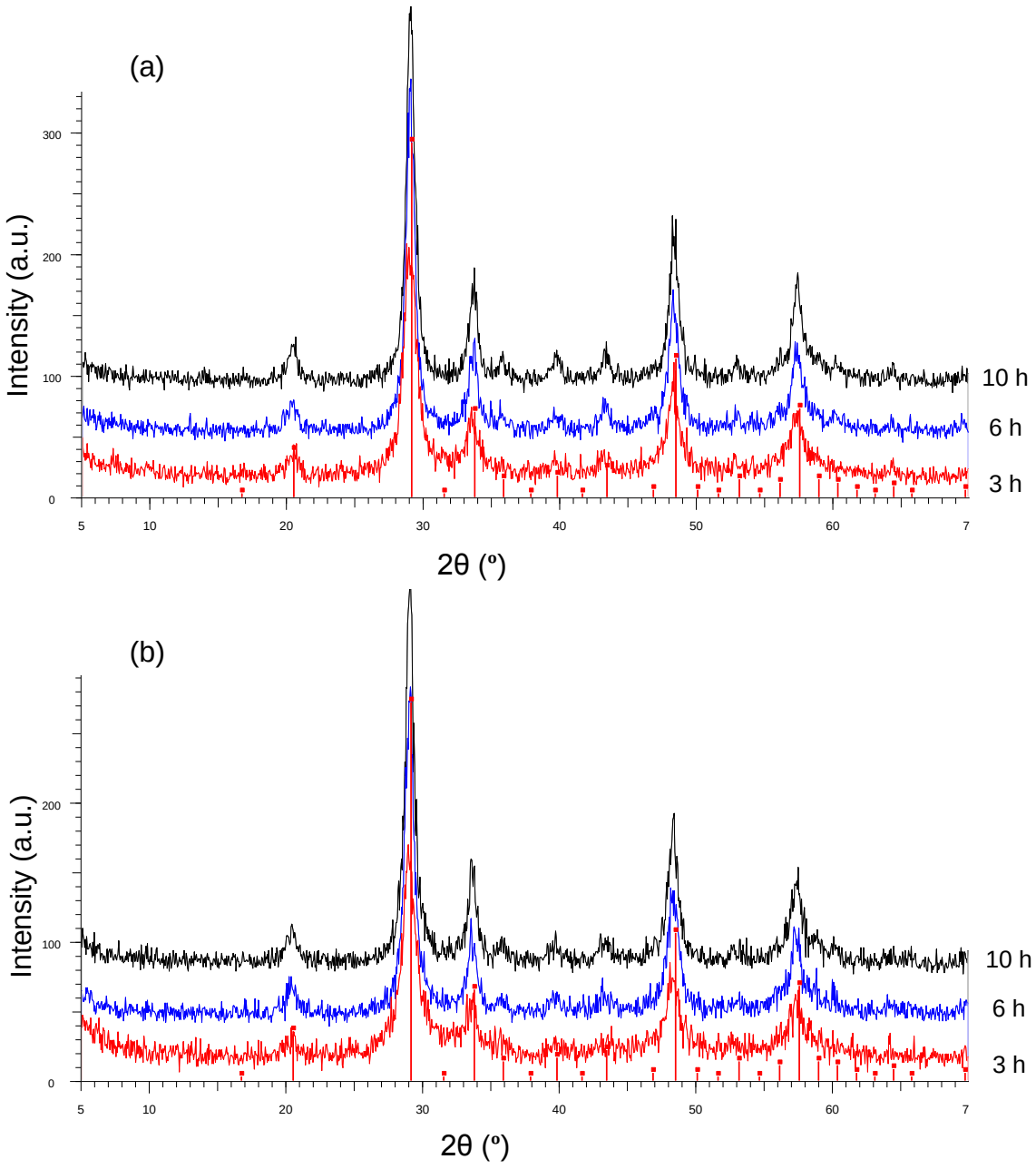

Figure 6.7. XRD patterns corresponding to (a) Eu:Y_2O_3 and (b) (Eu, Bi):Y_2O_3 nanoparticles calcined at 798 K for 3 h, 6 h and 10 h.

Table 6.2. Mean sizes of Eu:Y_2O_3 and (Eu,Bi):Y_2O_3 nanoparticles obtained at 798 K for different calcination times calculated using the Scherrer equation.

Calcinations time (h)	Eu:Y_2O_3		(Eu,Bi):Y_2O_3	
	FWHM (º)	τ (nm)	FWHM (º)	τ (nm)
3	1.1752	6.98	1.2847	6.38
6	0.8278	9.91	0.8937	9.18
10	0.8128	10.09	0.8052	10.19

6.2.2 Spectroscopic characterization

The emission generated by the Eu:Y_2O_3 and (Eu,Bi):Y_2O_3 nanoparticles was analyzed by photoluminescence. Figure 6.8a shows the excitation spectrum of the Eu:Y_2O_3 nanoparticles monitored at λ = 610 nm. The wide band observed from 230 nm to 280 nm, and centered at 254 nm, corresponds to the Eu^{3+}-O^{2-} charge-transfer state (CTS) band. Also, two bands corresponding to the $f \rightarrow f$ transitions $^7F_{0,1} \rightarrow {}^5L_6$ and $^7F_{0,1} \rightarrow {}^5D_2$ of Eu^{3+} can be observed in the figure [216]. As can be concluded from the spectra, normalized in intensity for the $^7F_{0,1} \rightarrow {}^5D_2$ transition, the maximum intensity of the Eu^{3+}-O^{2-} CTS band was found for the particles calcined at 998 K.

Figure 6.8b shows the emission spectra of Eu:Y_2O_3 nanoparticles normalized in intensity to the band located at 610 nm, corresponding to the red emission generated by these nanoparticles after excitation at 254 nm, coinciding with the CTS band of these nanoparticles. The emission spectra represent five groups of sharp peaks from 575 to 710 nm, which are attributed to $^5D_0 \rightarrow {}^7F_J$ (J = 0, 1, 2, 3, and 4) transitions of Eu^{3+} ions [213]. The dominant peak at 610 nm is ascribed to the forced electron dipole $^5D_0 \rightarrow {}^7F_2$ transition of Eu^{3+} ions when Eu^{3+} occupies a low symmetry site with no inversion center in the structure [217]. The emission at 610 nm with the strongest intensity was obtained for the nanoparticles calcined at 998 K.

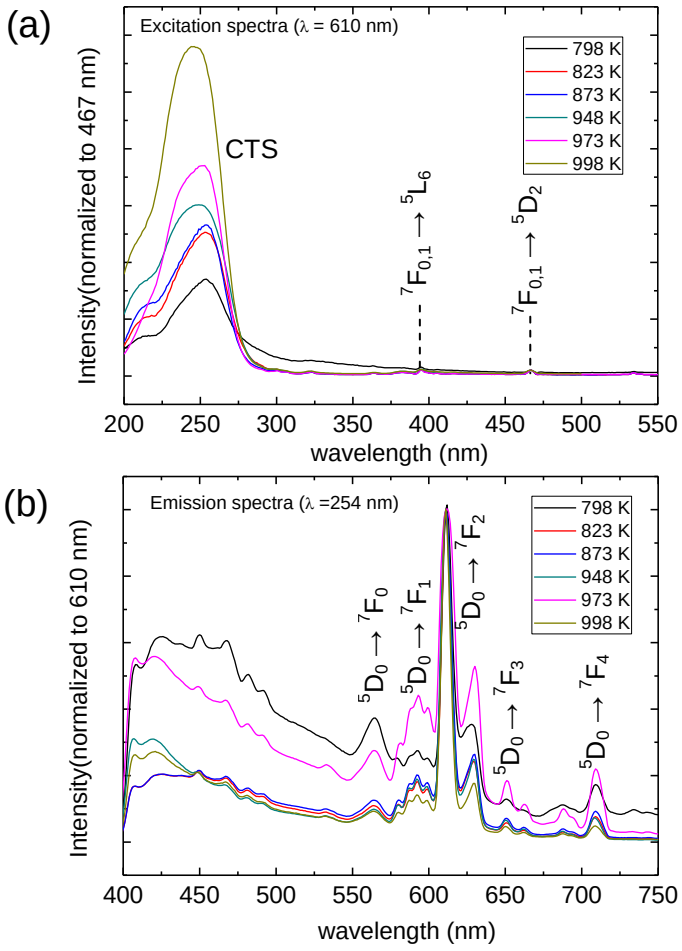

Figure 6.8. (a) Excitation and (b) emission spectra of the Eu:Y_2O_3 nanoparticles synthesized at different temperatures.

Figure 6.9a shows the excitation spectrum of (Eu,Bi):Y_2O_3 nanoparticles monitored at λ=610 nm. Apart from a the Eu^{3+}-O^{2-} CTS wide band from 230 nm to 280 nm and centered at 254 nm, there is a strong broad band in the range of 300-400 nm with a maximum at 338 nm. Bi^{3+} ions have a $6s^2$ electronic configuration with $^1S_0$ ground state level and a 6s6p configuration where the excited states split into $^3P_0$, $^3P_1$, $^3P_2$, and $^1P_1$ levels in order of increasing energy. However, the $^3P_1$ level undergoes mixing with the $^1P_1$ level by spin-orbit coupling, allowing the $^1S_0 \rightarrow {}^3P_1$ transition [216, 218]. This transition corresponds to the band observed in the spectrum with maximum at 338 nm. Also, two weak absorptions bands corresponding to the $^7F_{0,1} \rightarrow {}^5L_6$ and $^7F_{0,1} \rightarrow {}^5D_2$ transitions of Eu^{3+} can be seen in the figure. The excitation spectrum recorded for the nanoparticles prepared at 773 K has a different shape in comparison to the rest of the spectra. This might be related to the low degree of crystallinity of the nanoparticles obtained (see Figure 6.5b). As concluded from the normalized spectra presented in the figure, the maximum intensity was found for the nanoparticles calcined at 998 K.

Figures 6.9b and 6.9c show the emission spectra collected after excitation at 254 nm and 365 nm, respectively, coinciding with the CTS band of Eu^{3+} and the band-edge emission of GaN, where we can see, among others, the emission of red light from the nanoparticles. As in the previous case the emission spectra represent five groups of sharp peaks, which are attributed to $^5D_0 \rightarrow {}^7F_J$ (J = 0, 1, 2, 3, and 4) transitions of Eu^{3+} ions, being that at 610 nm the dominant one. The emission at 610 nm with the strongest intensity in both cases is observed for the nanoparticles obtained at 998 K. However, the intensity of the red light at 610 nm is stronger after excitation at 365 nm, which indicates that the emission generated by GaN effectively excites these particles though the $^1S_0 \rightarrow {}^3P_1$ transition of Bi^{3+}, that then efficiently transfers the energy to Eu^{3+}.

From the analysis above we can conclude that the most suitable material for deposition on porous GaN is (Eu,Bi):Y_2O_3 calcined at 998 K for 3 h, since the maximum of the Bi^{3+} absorption band is located at 338 nm, close to the band edge emission of GaN (~365 nm), which would allow pumping the red phosphor efficiently.

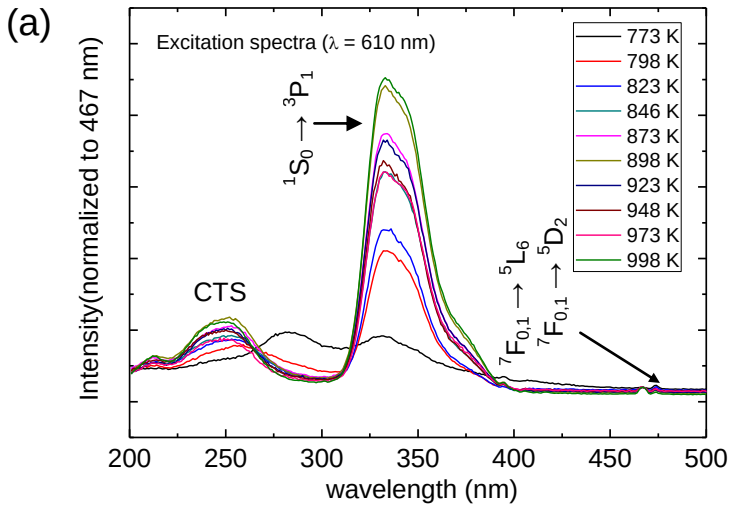

Figure 6.9. (a) Excitation spectra of (Eu,Bi):Y_2O_3 nanoparticles monitored at λ = 610 nm and emission spectra of (Eu,Bi):Y_2O_3 nanoparticles after excitation at (b) λ = 254 nm and (c) λ = 365 nm (continuation next page).

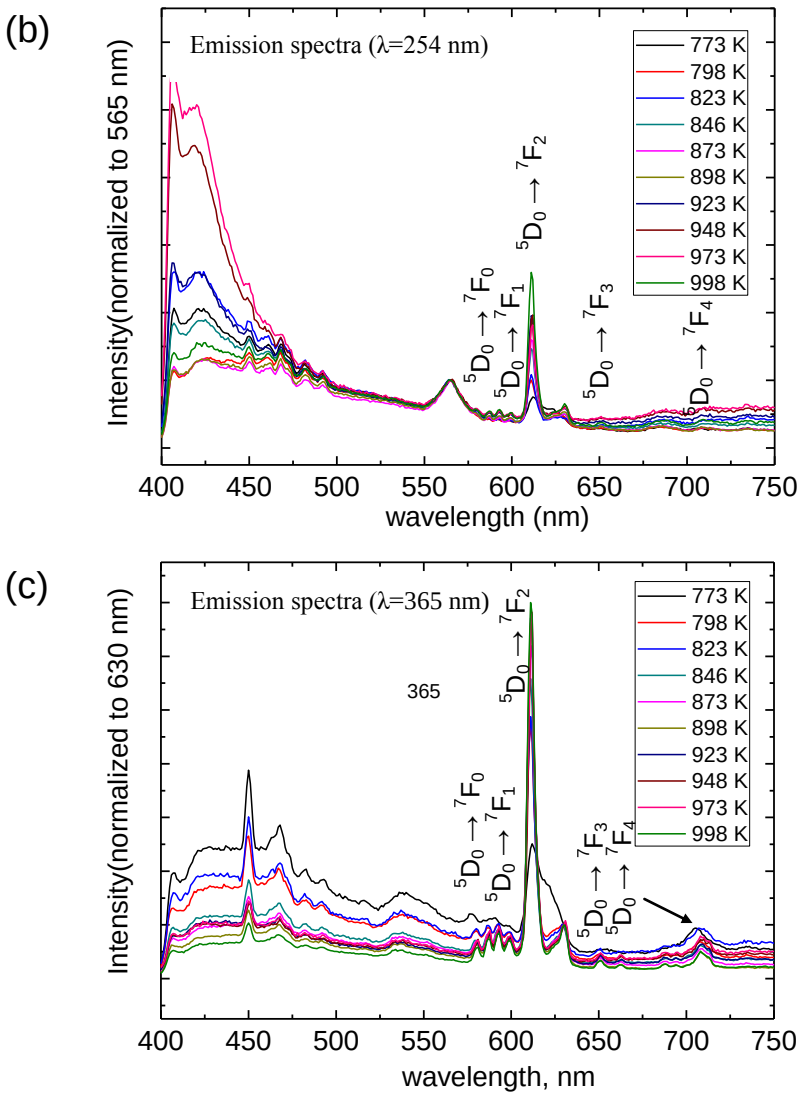

Figure 6.9. (a) Excitation spectra of (Eu,Bi):Y_2O_3 nanoparticles monitored at λ = 610 nm and emission spectra of (Eu,Bi):Y_2O_3 nanoparticles after excitation at (b) λ = 254 nm and (c) λ = 365 nm.

6.3 Formation of (Eu,Bi):Y_2O_3 nanocrystals/porous GaN composites

We proceeded forming (Eu,Bi):Y_2O_3 nanocrystals/porous GaN composites. To do this, we used two approaches. In the first case, we placed the powder of luminescent nanoparticles obtained before the last calcination step onto a porous GaN layer previously grown on a Si (100) substrate and calcined the composite at 998 K for 3 h. In the second case, we introduced a porous GaN layer grown on a Si (100) substrate into the liquid reaction media during the synthesis of (Eu,Bi):Y_2O_3 nanocrystals by the modified Pechini method when the precursor resin is formed. Afterwards, two calcination steps were performed to form the composites.

6.3.1 Formation of (Eu,Bi):Y_2O_3 nanocrystals/porous GaN composites by placing the precursor on the top of the porous GaN layer

The precursor of (Eu,Bi):Y_2O_3 was placed on the top of a porous GaN layer previously grown on a Si(100) substrate and then was calcined at 998 K. Figure 6.10 shows the SEM images of the porous GaN layer together with the (Eu,Bi):Y_2O_3 nanoparticles after calcination. We can clearly observe white flakes of (Eu,Bi):Y_2O_3 nanoparticles randomly distributed on the surface of the porous GaN layer. Higher magnification images demonstrate that (Eu,Bi):Y_2O_3 nanoparticles did not penetrate in the pores of the GaN microparticles. PL characterization revealed that the samples did not show any significant emission.

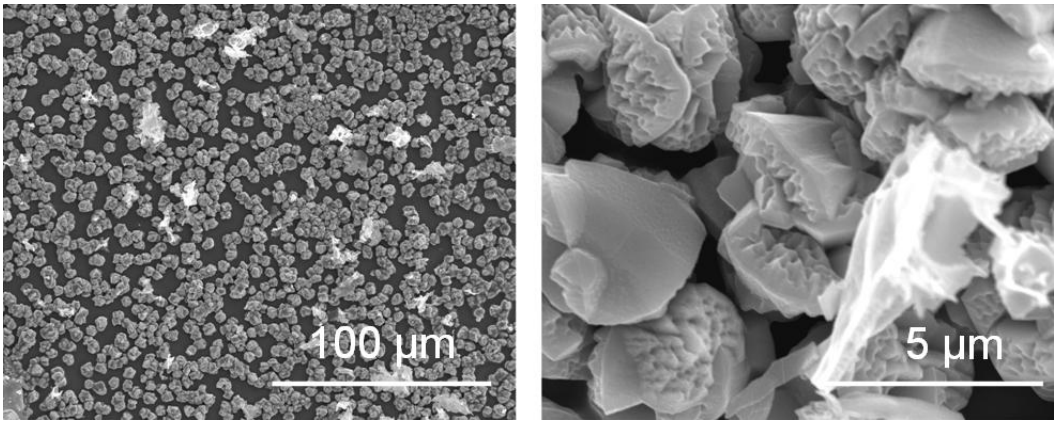

Figure 6.10. SEM images of the (Eu,Bi):Y_2O_3 nanocrystals/porous GaN composites formed after placing the nanoparticles precursor on the top of the porous GaN layer followed by a calcination process at 998 K.

X-Ray diffraction analysis of these composites is shown in Figure 6.11. As can be seen from the XRD pattern, the crystalline phase of Y_2O_3 is not detected.

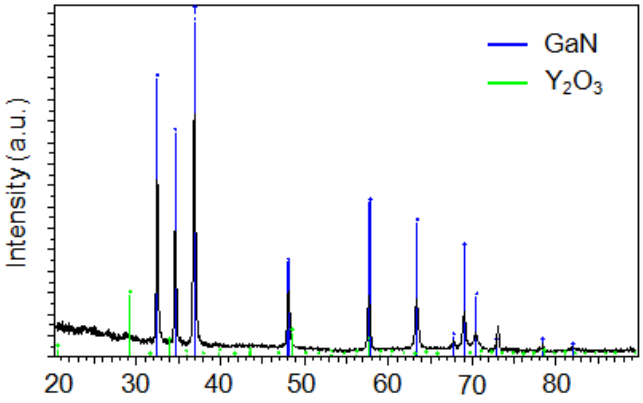

Figure 6.11. XRD pattern of the (Eu,Bi):Y_2O_3 nanocrystals/porous GaN composites formed after placing the nanoparticles precursor on the top of the porous GaN layer followed by a calcination process at 998 K. The reference XRD patterns corresponding to GaN (00-050-0792) and Y_2O_3 (00-041-1105) have been included to help reader to assign the different XRD peaks appearing in the experimental pattern.

6.3.2 Formation of (Eu,Bi):Y_2O_3 nanocrystals/porous GaN composites by introducing the porous GaN layer into the liquid reaction media of synthesis of the nanoparticles

In the second approach we explored to form (Eu,Bi):Y_2O_3 nanocrystals/porous GaN composites, the sample of porous GaN grown on a Si (100) substrate was introduced into the liquid reaction media during the synthesis of the (Eu,Bi):Y_2O_3 nanocrystals when the precursor resin is formed. Afterwards the sample was calcined first at 573 K for 3 hours and then at 998 K for 3 hours. Figure 6.12 shows the SEM images of the surface of the porous GaN layer together with the (Eu,Bi):Y_2O_3 nanoparticles after the two calcination processes. (Eu,Bi):Y_2O_3 nanoparticles cover the porous GaN layer and penetrate between the porous GaN microparticles. However, further characterization is needed to know if (Eu,Bi):Y_2O_3 nanoparticles have been introduced inside the pores of GaN.

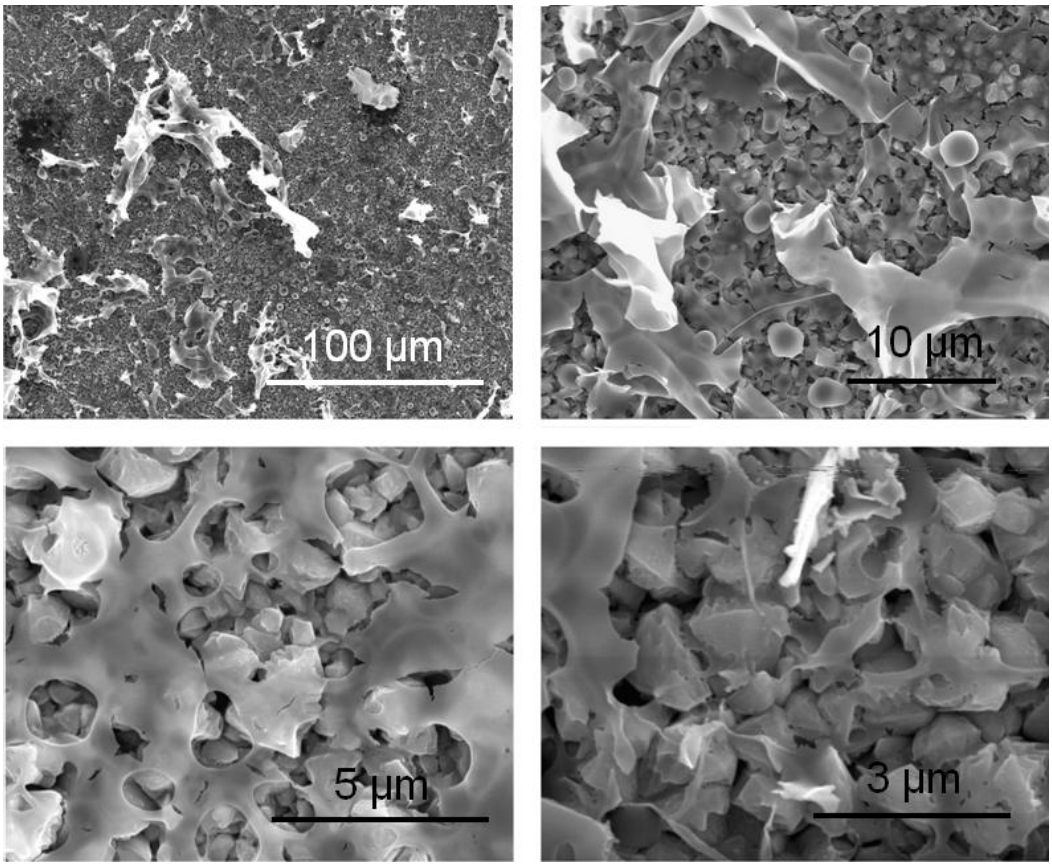

Figure 6.12. SEM images of the surface of the (Eu,Bi):Y_2O_3 nanocrystals/porous GaN composites formed after introducing the porous GaN layer into the liquid reaction media of synthesis of the nanoparticles and followed by calcination at 998 K.

The XRD analysis of these composites is shown in Figure 6.13. Figure 6.13a shows an optical picture of the sample after calcination, where a relatively uniform layer of (Eu,Bi):Y_2O_3 nanoparticles covering porous GaN can be observed. Figure 6.13b shows the XRD pattern, where the crystalline phase of Y_2O_3 can be observed. The reference patterns of GaN (00-050-0792) and Y_2O_3 (00-041-1105) have been included for a better identification of the crystalline phases present in the sample. Additionally, we recorded the XRD pattern of the

sample at a grazing incidence angle of 1º to increase the intensity of the diffraction peaks corresponding to the Y_2O_3 phase and disregard the presence of other crystalline phases. The XRD pattern shown in Figure 6.13c confirms the presence of only two crystalline phases in the sample, corresponding to GaN and Y_2O_3.

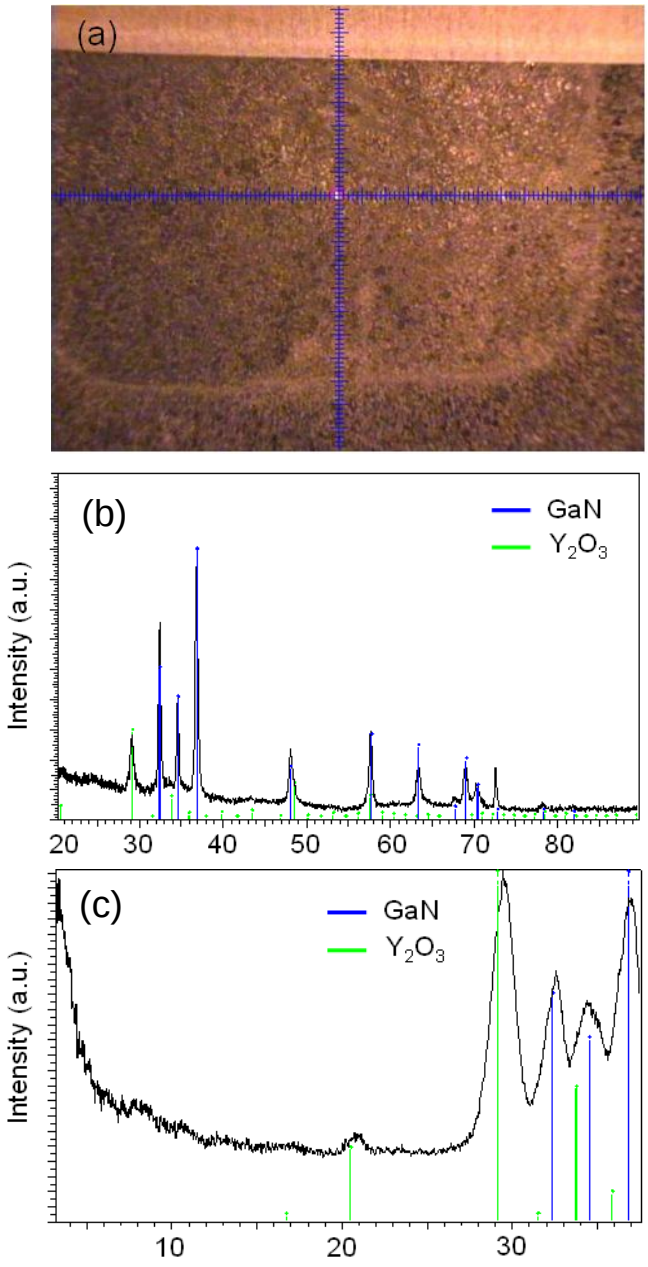

Figure 6.13. (a) Optical image and (b) XRD pattern of the sample formed after introducing the porous GaN layer into the liquid reaction media of synthesis of the nanoparticles followed by calcination at 998 K, (c) XRD pattern corrresponding to the same sample recorded at a glazing incidence angle of 1°. The reference XRD patterns corresponding to GaN (00-050-0792) and Y_2O_3 (00-041-1105) have been included for a better identification of the crystalline phases present in the sample.

Finally, we recorded the excitation and emission spectra of the (Eu,Bi):Y_2O_3 nanoparticles deposited onto porous GaN (see Figure 6.14). The excitation spectrum was

monitored at 610 nm, while the emission spectrum was recorded after excitation at 365 nm, corresponding to the band-edge emission of porous GaN. No significant differences could be observed on these spectra to respect those recorded for the (Eu,Bi):Y_2O_3 nanoparticles synthesized without the presence of GaN (see Figure 6.9), indicating that these composites would be useful to transfer the UV emission of porous GaN onto visible light. However, the efficiency of the process, as well as electrical activation of the system, have to be still analyzed.

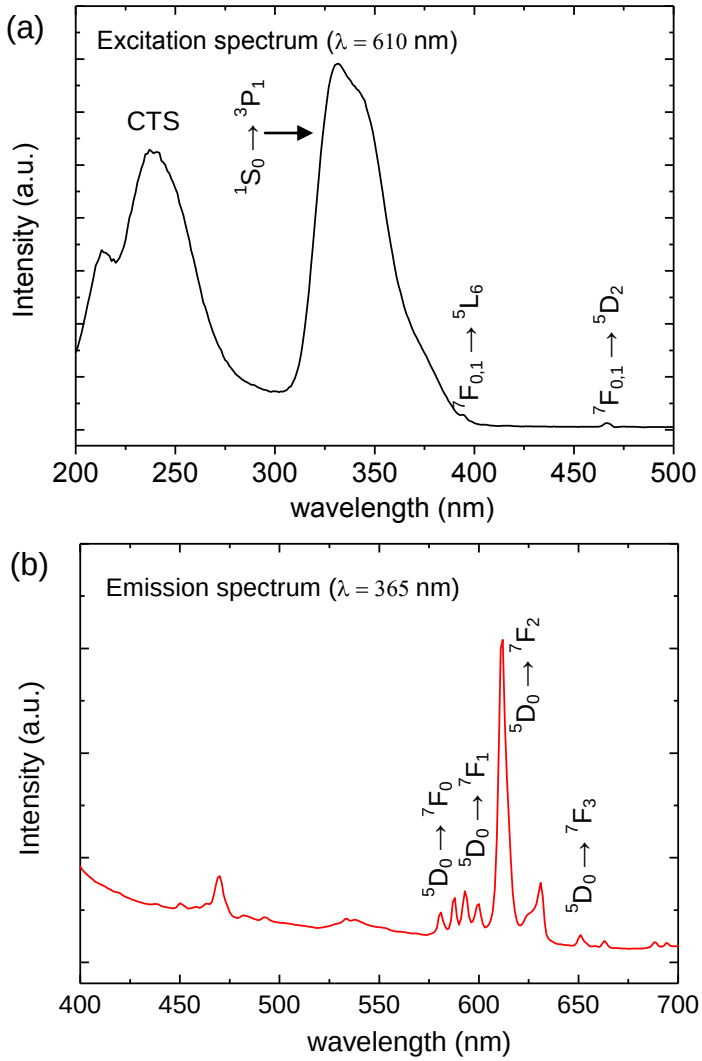

Figure 6.14. (a) Excitation and (b) emission spectra of the (Eu,Bi):Y_2O_3 nanocrystals/porous GaN composites formed after introducing the porous GaN layer into the liquid reaction media of synthesis of the nanoparticles followed by calcination at 998 K.

Chapter 7

Graphene for transparent electrodes in porous GaN-based LEDs: a preliminar approach

Graphene is a promising material for optoelectronic devices because it has very good electrical conductivity and high transparency over a wide range of the optical spectrum [219]. Graphene, which is a two-dimensional hexagonal array monolayer of sp^2-bonded carbon atoms [220], has been considered for applications as transparent conductive electrode for GaN-based LEDs [68] due to its superior properties such as high electrical and thermal conductivity, good chemical and mechanical stability, excellent mobility and high transmittance from the UV to the near-infrared spectral regions [220].

In this chapter, the synthesis of graphene by reducing it from graphite oxide is presented. The last part of the chapter is devoted to the research towards the achievement of graphene monolayers using graphene flakes by the Electrospray Ion-Assisted technique on silicon and amorphous quartz substrates and the corresponding characterization of the layers obtained.

7.1 Synthesis and characterization of graphene

Graphene has been prepared by several approaches, such as micromechanical exfoliation of graphite [221], chemical vapor deposition (CVD) [222, 223], epitaxial growth [224], and chemical reduction of graphite oxide (GO) [225]. Chemical reduction of GO is one of the established methods to produce graphene flakes in large scale. The chemical reduction of GO is often fulfilled by using poisonous and explosive reducing agents. Here, we used liquid-phase exfoliation of graphite via employing iron (Fe) as a reducing agent [226]. Fe can be naturally used as a reducing agent due to its mild reductive ability and nontoxicity providing a green and facile approach for mass production of graphene flakes.

7.1.1 Synthesis of graphite oxide and graphene

GO was synthesized from graphite using the Staudenmaier method [227]. 5 g of graphite were mixed with concentrated sulfuric acid (98 wt %, 87.5 ml) and concentrated nitric acid (65 wt %, 45 ml) and stirred. After the dispersion of graphite we added, carefully and slowly, potassium chlorate (55 g) and stirred for more than 96 h. Afterwards, the mixture was poured into distilled water and filtered. GO was washed and redispersed in a 5 wt % solution of HCl three times, to eliminate potassium chlorate. Finally, GO was washed with distilled water until a neutral pH value was obtained for the filtrate. Filtered GO was dried in a oven at 323 K and pulverized in a mortar.

Following the synthesis, we prepared a 0.5 mg/ml GO suspension in water. Ultrasonication was used in order to exfoliate GO. Fe acted as the reduction agent of exfoliated GO. According to this method [226], 1 g of Fe powder and 20 mL of HCl (35 wt %) were added into 100 ml of GO suspension at room temperature, stirred for 30 min and then maintained for 6 hours. After reduction, in order to remove the excess of Fe powders, 15 ml of HCl (35 wt %) were added into the solution. Finally, the graphene nanosheets were filtered, washed with distilled water and ethanol, and dried at 373 K for over 12 h in a vacuum oven (see Figure 7.1).

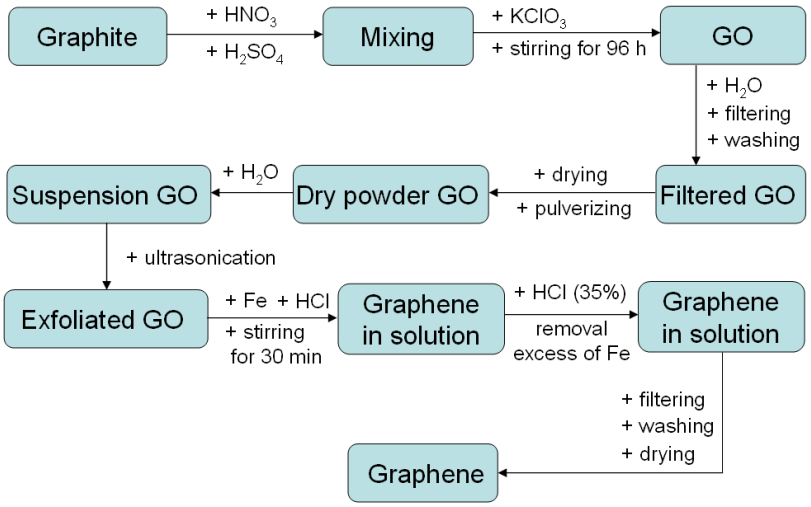

Figure 7.1. Scheme of the synthesis procces of graphene used in this thesis.

7.1.2 Morphological characterization of graphite oxide and graphene flakes

Figure 7.2 shows SEM images of multi-layered GO particles after drying and pulverization. Single layers can not be observed here. However, the nanosheets of GO exfoliate individually when suspended in ethanol, as can be seen by TEM after depositing several drops of this suspension on a Cu TEM grid (see Figure 7.3). The sizes of the layers are of a few micrometers. Some of the GO layers are wrinkled, as can be seen in Figure 7.3c, what might be related to the fast evaporation of the solvent during the preparation of the sample for TEM observation.

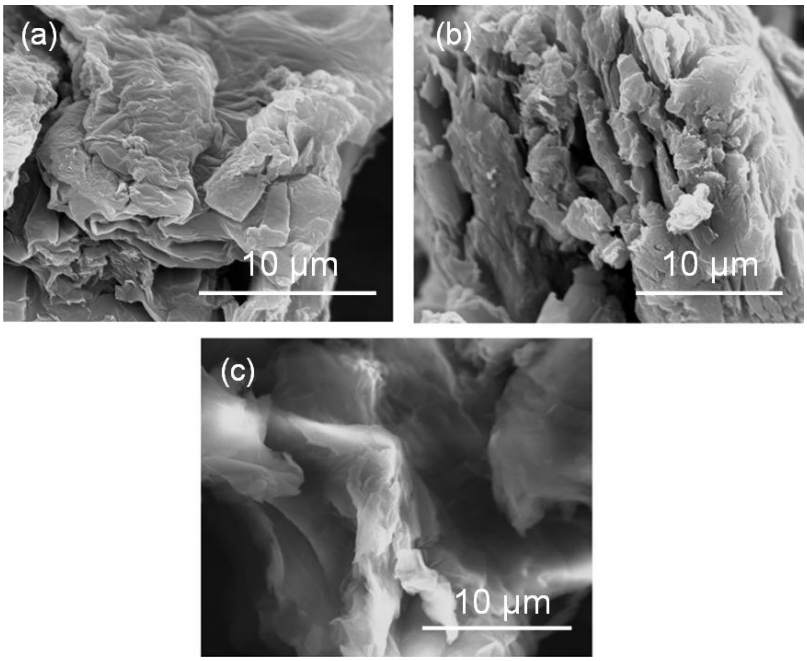

Figure 7.2. SEM images of multi-layered GO particles after drying and pulverization.

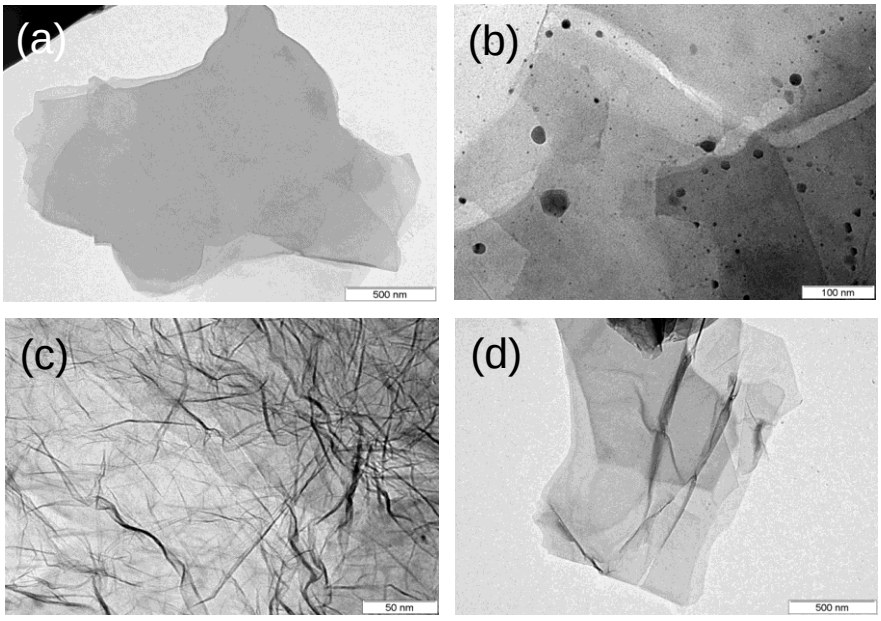

Figure 7.3. TEM images of the GO layers obtained.

Figure 7.4 shows SEM images of the multi-layered graphene particles after drying them. Each particle is formed by many graphene nanosheets, which cannot be observed by SEM. However, the layered structure can be clearly observed in Figure 7.4b. The nanosheets exfoliate individually when suspended in ethanol, as can be seen by TEM after depositing several drops of this suspension on a Cu TEM grid (see Figure 7.5). Here, wrinkles are also observed.

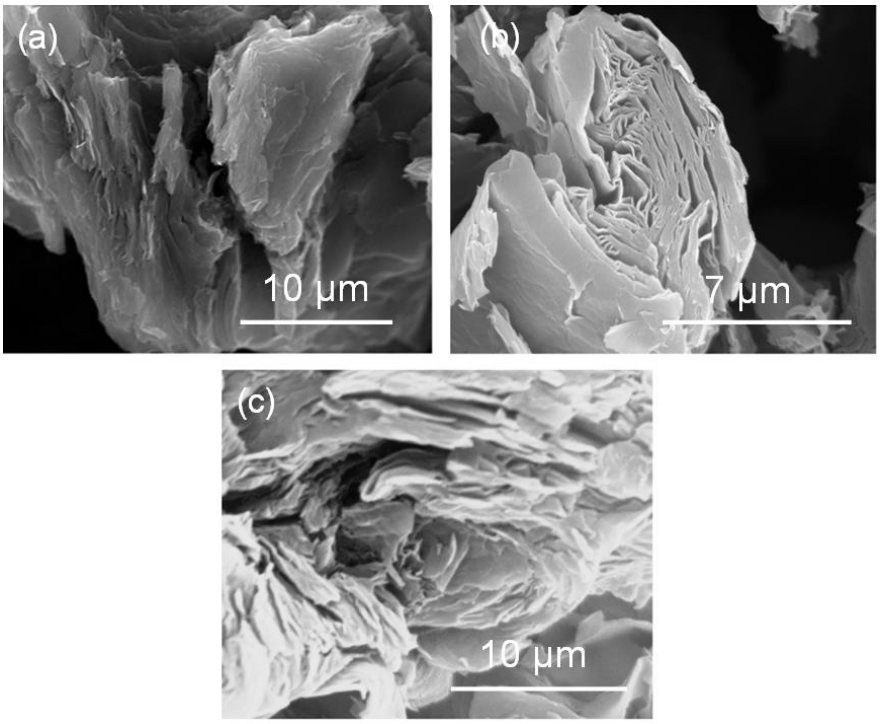

Figure 7.4. SEM images of dry multi-layered graphene particles.

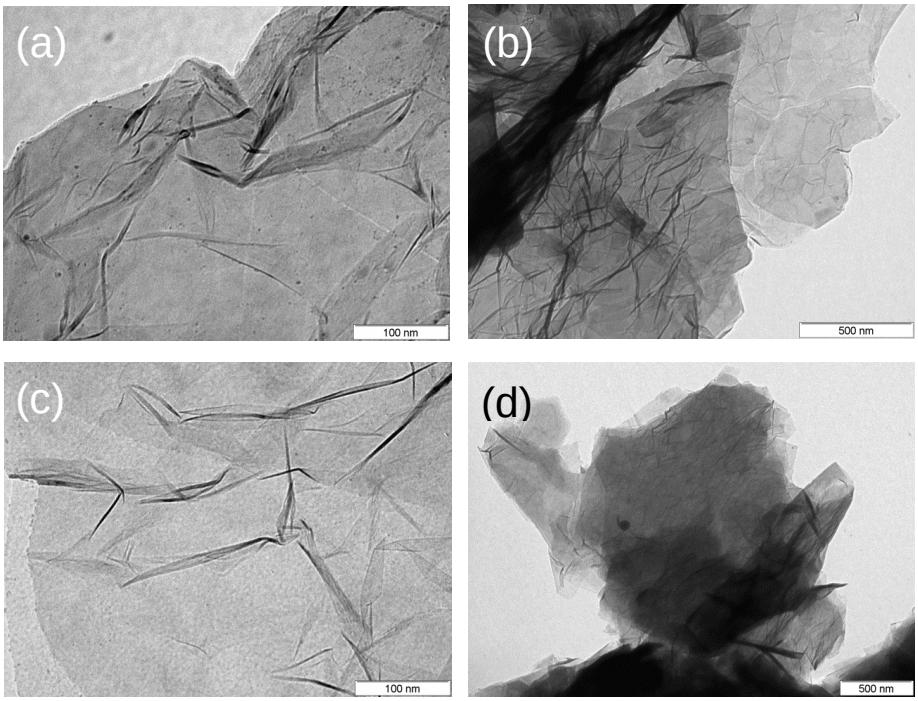

Figure 7.5. TEM images of the graphene layers obtained in this thesis..

7.1.3 Structural characterization of graphite oxide and graphene

GO and graphene were also characterized by Raman scattering and XRD. Raman scattering is strongly sensitive to the electronic structure and probes to be an essential tool to characterize graphite and graphene materials [228, 229]. Usually the Raman spectrum of graphene is characterized by two main features, the G mode arising from the first order scattering of the E_{2g} phonon of sp^2 carbon atoms (usually observed at ~1575 cm^{-1}) and the D mode arising from a mode of κ-point photons of A_{1g} symmetry (~1350 cm^{-1}) [230, 231]. The D and the G bands of Raman spectrum of graphite are usually observed at ~1350 cm^{-1} and at ~1575 cm^{-1} and the intensity of the G band is much higher in comparison to that of the D band (see Figure 7.6a). Also, the second order of the D peak (the 2D peak) is observed at ~ 2700 cm^{-1}, and is caused by the double resonant Raman scattering with two-phonon emissions [232]. The 2D band can be decomposed into two lorentzians of different intensities, marked as $(2D)_l$ and $(2D)_h$, where l an h stands for the low and high energy side of 2D band, respectively [233].

In the Raman spectrum of GO (see Figure 7.6b), the D and G bands broaden and shift to ~ 1340 cm^{-1} and ~ 1585 cm^{-1}, respectively. Additionally, the intensity of the D band is rising significantly, indicating a reduction in size of the in-plane sp^2 domains, what is possibly related to the oxidation [234].

Figure 7.6c shows the Raman spectrum of graphene after reduction from GO. The D and G bands appear quite narrow and almost equal in intensity. The high intensity of the D band is related to the presence of unrepaired defects that remain after the removal of partial oxygen moieties [226].

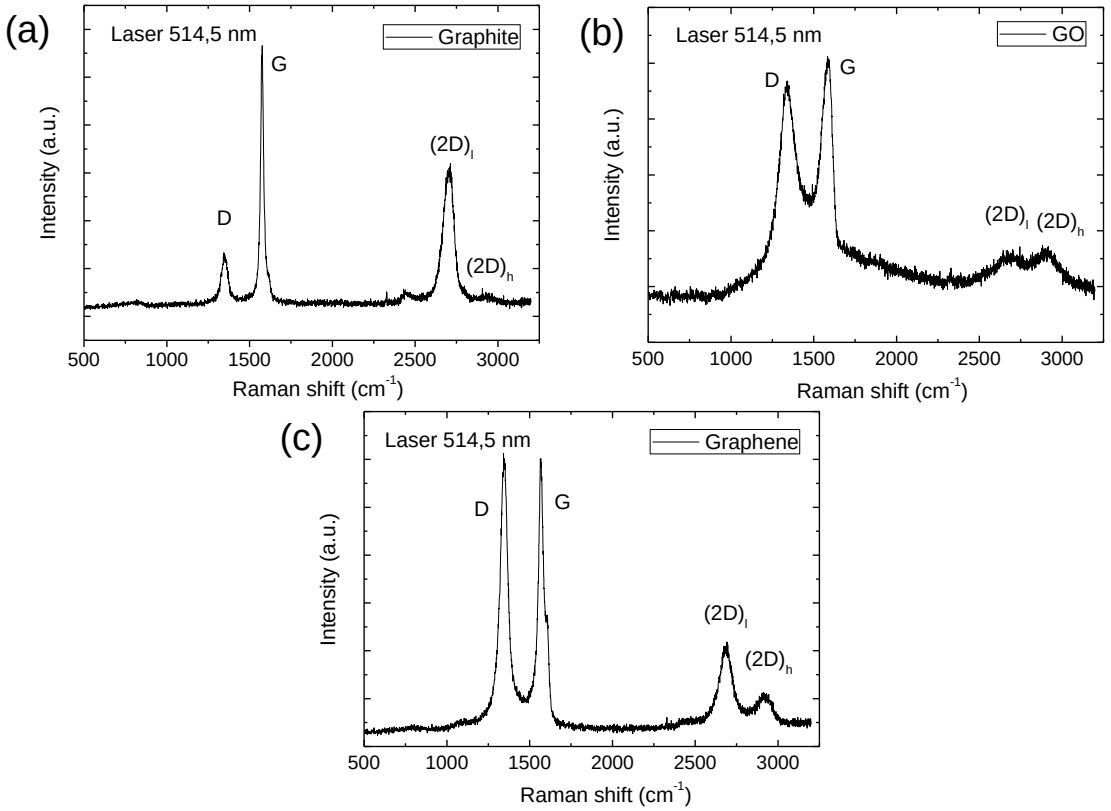

Figure 7.6. Raman spectra recorded for (a) graphite, (b) GO and (c) graphene.

In addition, we further characterized the crystal structure of graphite, GO and graphene by XRD (see Figure 7.7). Because of the introduction of oxygenated functional groups on carbon sheets, the basal distance of GO obtained from the (001) peak is large compared to that of graphite [235]. When GO is reduced by Fe, the peak at 11.8° disappears completely and a broad peak at 24.3° appears, what is attributed to the removal of some oxygen-containing functional groups. This indicates the reduction of GO and the exfoliation of the layered graphene [236].

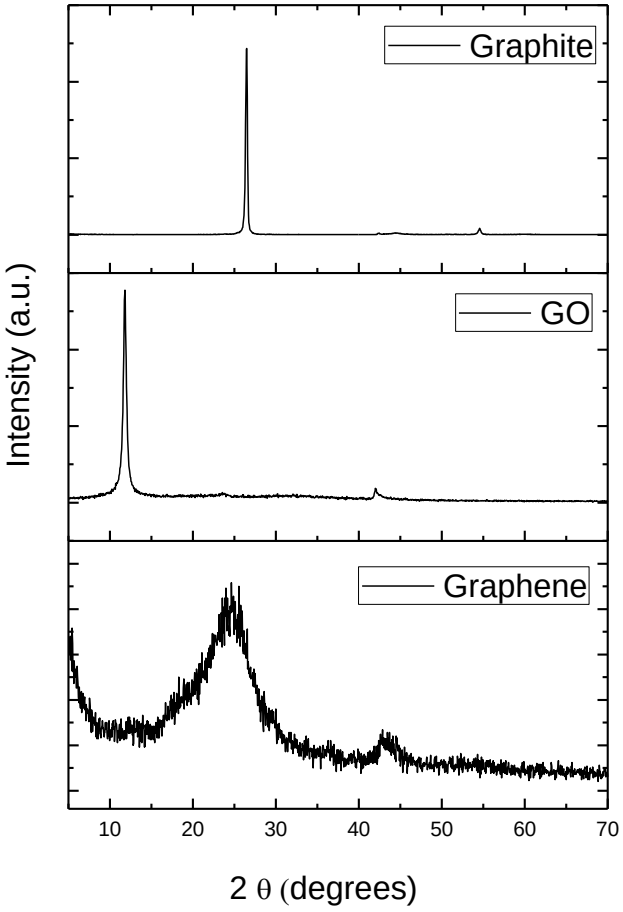

Figure 7.7. XRD patterns recorded for graphite, GO and graphene.

7.2 Deposition of graphene by the electrospray method

In the electrospray-deposition experiments, graphene nanosheet powder suspensions in dimethylformamide (DMF) were used to form graphene layers on silicon and quartz substrates. DMF was selected as solvent because it prevents agglomeration of the graphene flakes. For the depositions we used two types of graphene: the graphene prepared from GO by the above described method and commercial graphene from GRAnPH nanotech with a suspension of 99 % dimethylformamide (DMF) and 1 % graphene. Graphene from GRAnPH nanotech had more uniform graphene flakes in size, as can be seen in Figure 7.8.

The suspensions of graphene in DMF were stable over many hours, allowing for sufficient time to undertake depositions on the substrates. A stable spray was obtained at a liquid flow rate of 0.06 ml/h and an applied voltage of 4.4 kV for suspensions of < 0.5 wt % graphene prepared by reduction with Fe and 0.005 wt % commercial graphene. The distance between the needle and the substrate was 8 cm, the cylinder was rotated at 1400 RPM, and the voltage of the ions field was -7 kV. As substrates for the deposition we used Si(100) and amorphous quartz. Prior to deposition, the substrates were cleaned by immersing them in acetone inside an ultrasonic bath for 2 min, and after by immersing them in methanol also in the ultrasonic bath for 2 min. To finish the cleaning process, the substrates were rinsed with deionised water for 2 min in the ultrasonic bath.

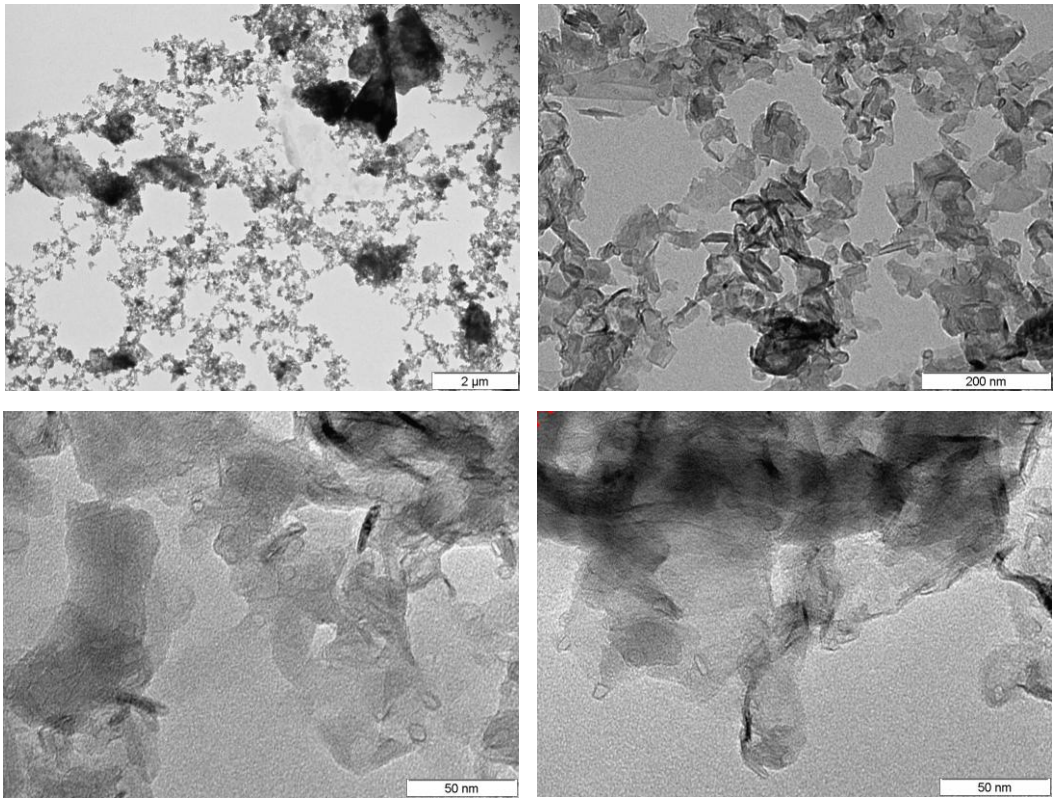

Figure 7.8. TEM images of commercial graphene from GRAnPH nanotech.

The conditions used for the different graphene depositions we analyzed are summarized in Table 7.1. In our study we mainly focused on the deposition time of graphene.

Figure 7.9 shows the AFM images with the corresponding profiles in the marked lines, corresponding to samples prepared using the graphene synthesized by reduction with Fe. We can observe that graphene layers are overlapping each other, forming multilayered structures on both, Si and amorphous quartz substrates (see Figures 7.9a and 7.9c). Also, the corresponding topography profiles show steps of ~6 nm, what may indicate that graphene deposits as multilayers, since a single layer would have a thickness of 0.34 nm. Thus, long time deposition conditions seem not to be optimal for getting a single graphene layer.

Table 7.1. Conditions of graphene depositions used in this thesis. Electrospray distance and liquid flow rate were kept constant for all the experiments at 8 cm and 0.06 ml/h, respectively.

Sample ID	Susp. conc. (wt %)	Deposition time (min)	Type of graphene	Substrate	Comments
A	< 0.5	60	Prepared from GO	Silicon	
ATA	< 0.5	60	Prepared from GO	Silicon	Annealed in N_2 at 673 K
B	< 0.5	60	Prepared from GO	Amorphous Quartz	
BTA	< 0.5	60	Prepared from GO	Amorphous Quartz	Annealed in N_2 at 673 K
C	0.005	3	GRAnPH nanotech	Silicon	
D	0.005	5	GRAnPH nanotech	Silicon	
E	0.005	7	GRAnPH nanotech	Silicon	
F	0.005	10	GRAnPH nanotech	Silicon	
G	0.005	15	GRAnPH nanotech	Silicon	
H	0.005	7	GRAnPH nanotech	Amorphous Quartz	
I	0.005	10	GRAnPH nanotech	Amorphous Quartz	
J	0.005	15	GRAnPH nanotech	Amorphous Quartz	

Thermal annealing of the samples was performed in an inert atmosphere of N_2 at 673 K for 240 min. The thermal annealing may improve the quality of deposited graphene layers [237], by eliminating the oxygen-containing groups. However, the analysis of topography of the graphene depositions after the annealing process shows that most of the graphene layers were removed from the surface of the substrate (see Figures 7.9b and 7.9d), since we can observe a reduced number of graphene flakes on the surface of the samples.

Raman spectra were recorded for samples B and BTA (before and after thermal annealing), as shown in Figure 7.10. Apparently, the quality of the Raman spectrum of sample B is better than that of sample BTA. The D and the G peaks in the BTA sample appear broader and noisy, what does not prove a good quality of the graphene layer (see Figure 7.10b). Also, in the BTA sample, the quality and intensity of the Raman spectra depended on the place of the surface on which the spectra were recorded, what indicates an inhomogeneous distribution of graphene flakes and layers. Thus, it seems that thermal anealing in N_2 does not improve the quality, but instead removes most of the graphene flakes previously deposited.

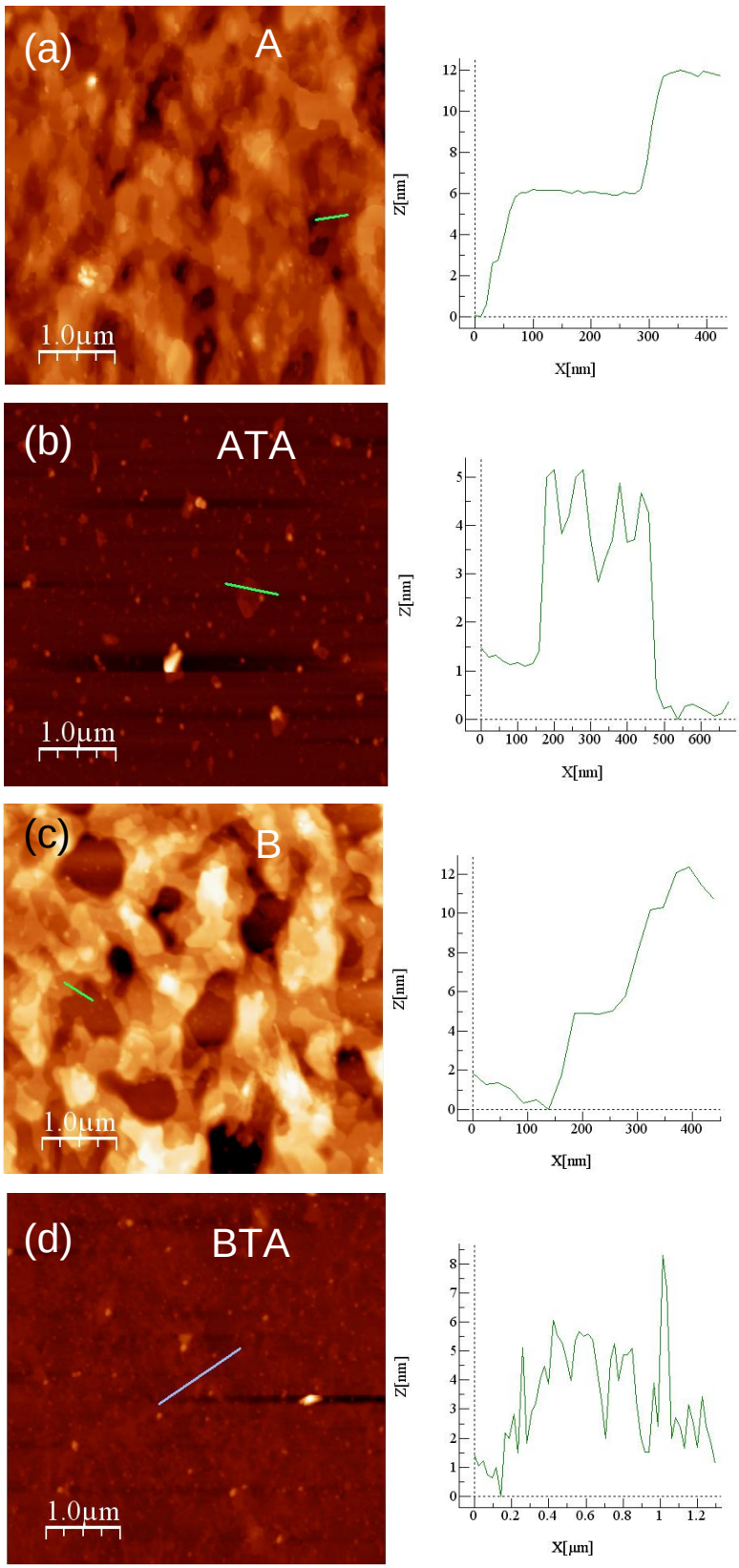

Figure 7.9. AFM images and topographic profiles of the samples prepared during (a) 60 min on a Si substrate (sample A); (b) sample shown in (a) after thermal treatment at 673 K for 240 min in N_2 atmosphere (sample ATA); (c) 60 min on a quartz substrate (sample B); and (d) sample shown in (c) after a thermal treatment at 673 K for 240 min in N_2 (sample BTA).

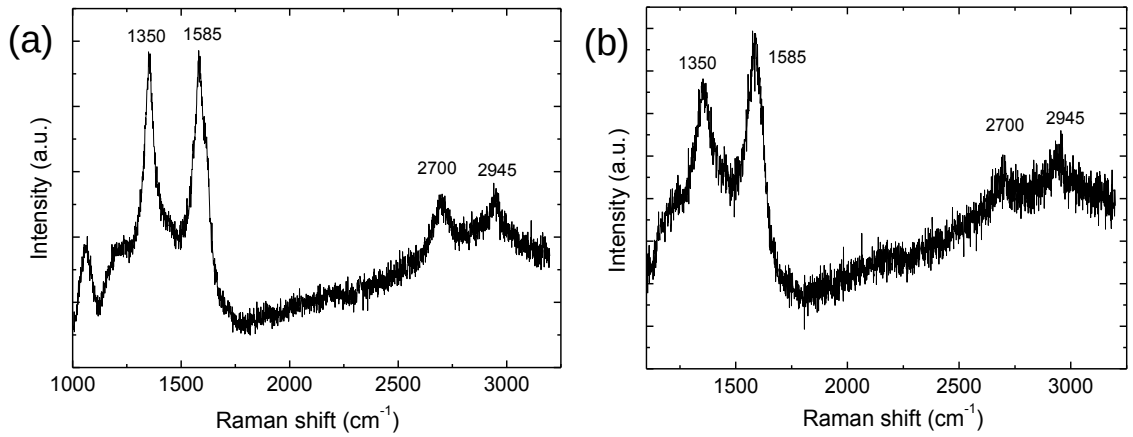

Figure 7.10. Raman spectra recorded for (a) B and (b) BTA samples.

To continue the investigation, the deposition time was reduced to the range from 3 min to 15 min. Figure 7.11 shows the topography AFM images, the phase AFM images (where contrast in color indicates differences in material composition), and the topological profiles of the graphene layers on a Si substrate with different deposition times. Phase images have been included to give more contrast to the topographic images, where sometimes it is difficult to distinguish graphene from the substrate. For a deposition time of 3 minutes (see Figure 7.11a) we observe independent graphene flakes on the Si surface that do not form a continuous single layer of graphene. Also, the heights measured for these flakes, of several nm, indicate that the flakes are not constituted by a single layer of graphene. As the deposition time increases, we observe a more complete coverage of the substrate with graphene. Another effect observed is the reconnection of the graphene flakes, tending to form a more continuous layer with a significantly reduced height around 1-1.5 nm.

A possible explanation for this phenomenon is that when the sample contains a small portion of graphene, seemingly graphene does not have enough energy and material for the reconstruction of the surface. The graphene flakes start to reconnect in samples prepared after 5 min of deposition time (see Figures 7.11b and 7.11c). For 10 min (see Figure 7.11d), we observe a quite homogenous layer of graphene covering most of the surface of the substrate. Finally, for 15 minutes of deposition time we start to observe multilayers of graphene that overlap each other (see Figure 7.11e), what indicates that we exceeded the limit of time for a single layer deposition. While surface without graphene still exists on the substrate, it seems that the graphene flakes are arranging on the substrate as a single monolayer, tending to occupy the whole surface. When the empty surface of the substrate decreases to a certain limit, the graphene has no preference on the location of deposition and it is deposited randomly on the surface of the substrate, forming multilayers, and this is reflected in the increase of the heights observed on the topographic profiles. These samples were prepared using commercial graphene from GRAnPH nanotech, unlike the previous cases analyzed. The morphology of the graphene flakes in both cases is similar, although in the case of the commercial graphene the flakes deposited on the surface of the substrate seem to be smaller.

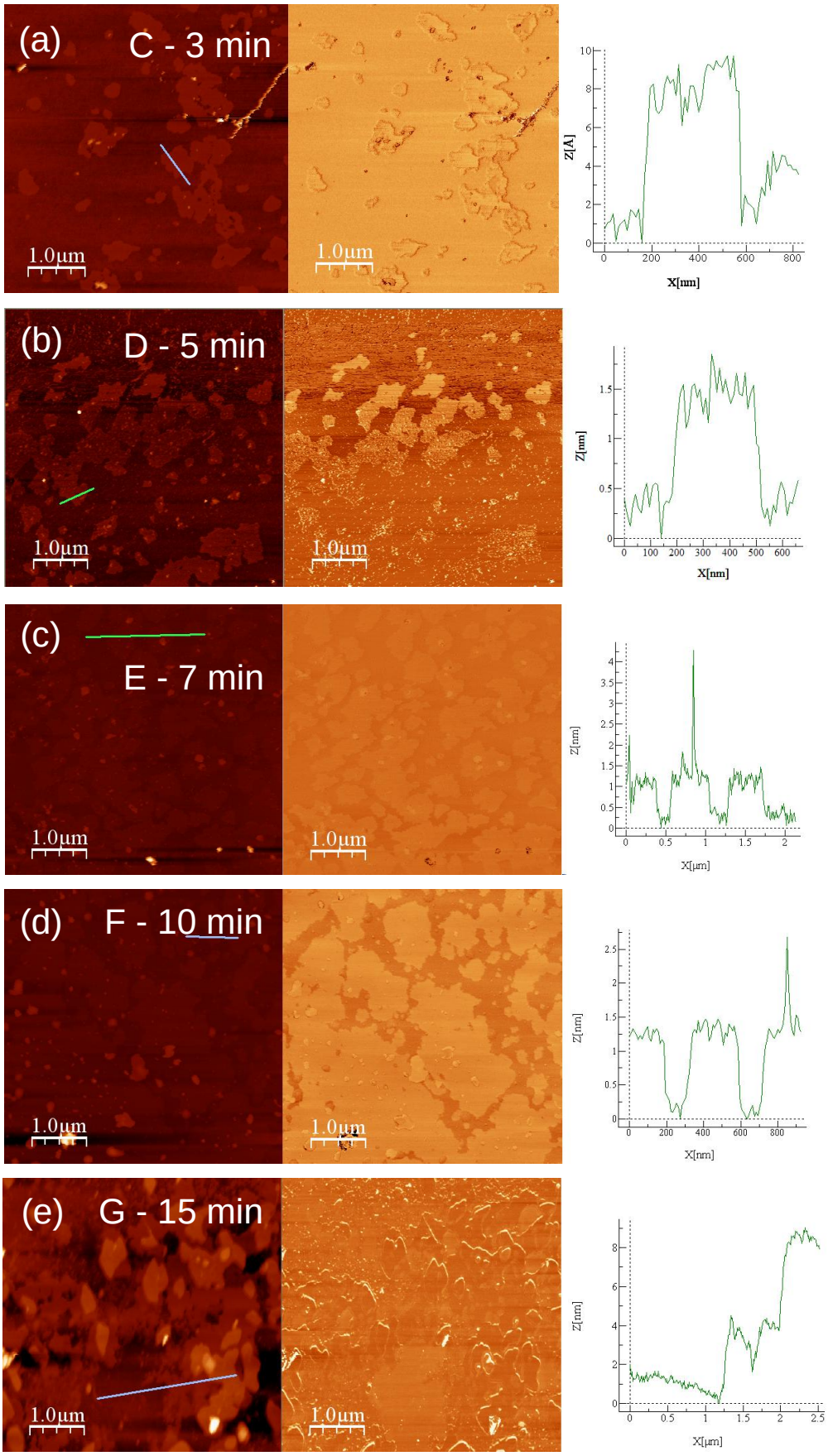

Figure 7.11. AFM images (topography and phase) and topographic profiles of graphene samples prepared on a Si substrate at deposition times of (a) 3 min (sample C), (b) 5 min (sample D), (c) 7 min (sample E), (d) 10 min (sample F) and (e) 15 min (sample G).

Figure 7.12 shows the AFM (topography and phase) images and the topographical profiles of the graphene layers deposited on amorphous quartz substrates at different deposition times between 7 and 15 min. The results obtained on amorphous quartz substrates are quite similar to those obtained on Si substrates. However, the AFM images of the samples prepared on quartz present a higher noise that we believe is due to the flatness of the amorphous quartz that creates difficulties in characterization by AFM of graphene layers deposited on this substrate.

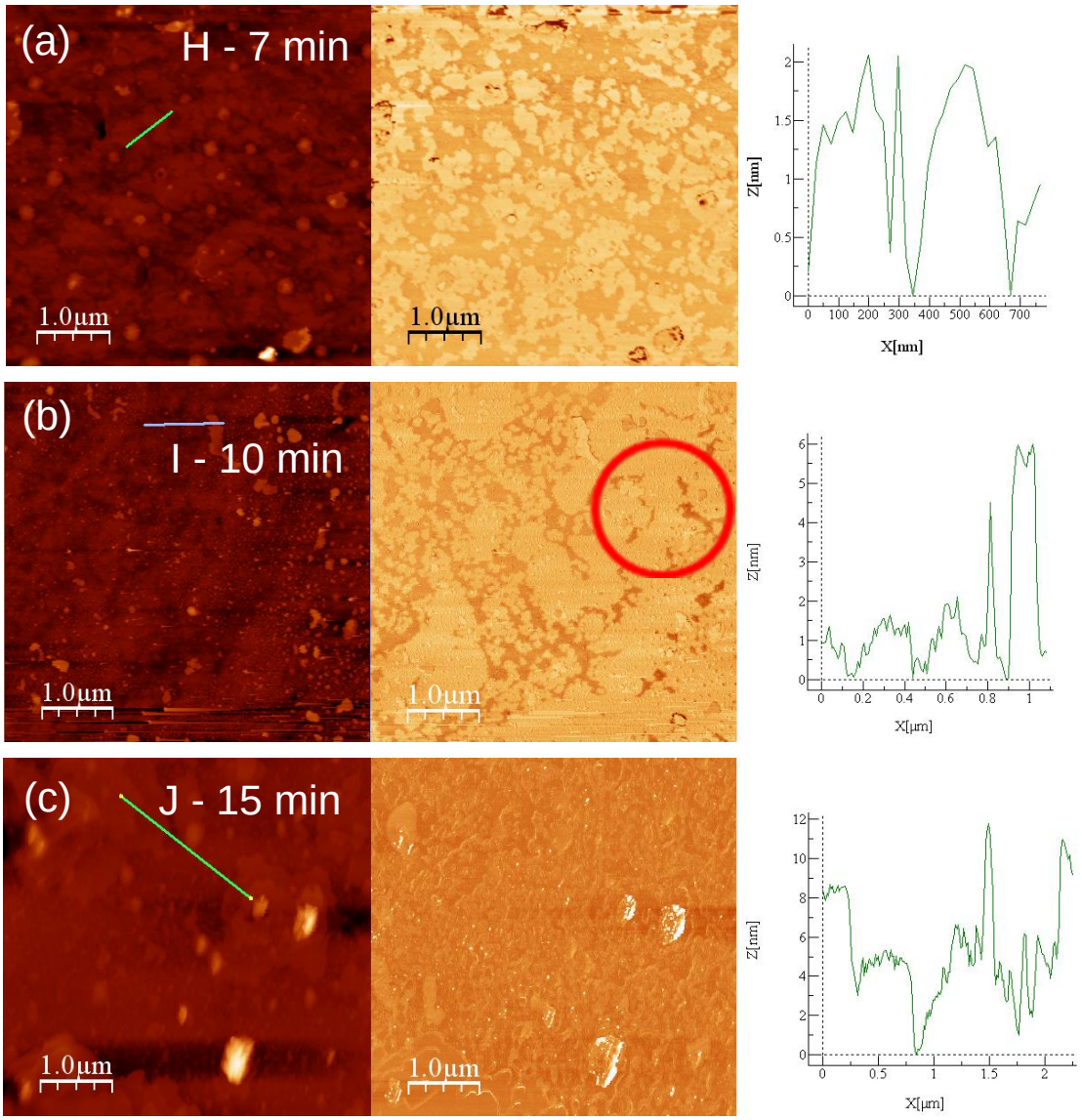

Figure 7.12. AFM images (topography and phase) and topographic profiles of graphene samples prepared at deposition times of (a) 7 min (sample H), (b) 10 min (sample I) and (c) 15 min (sample J) on amorphous quartz substrates.

It has been reported that graphene has the ability to self-reconstruct a damaged structure and build a uniform layer [238]. Nanoholes in single layer graphene sheets are shown to heal spontaneously by filling up with either nonhexagon, graphene-like, or perfect hexagon 2D

structures, as a result of their interaction with metal impurities. Since we observe a similar effect for deposition times between 7 and 10 min, we wanted to analyze more in detail this effect, and we retook AFM images of sample E 2.5 months after it was prepared, to analyze the evolution of the structure with time. However, from AFM images, shown in Figure 7.13 there is no apparent evolution of the sample with time.

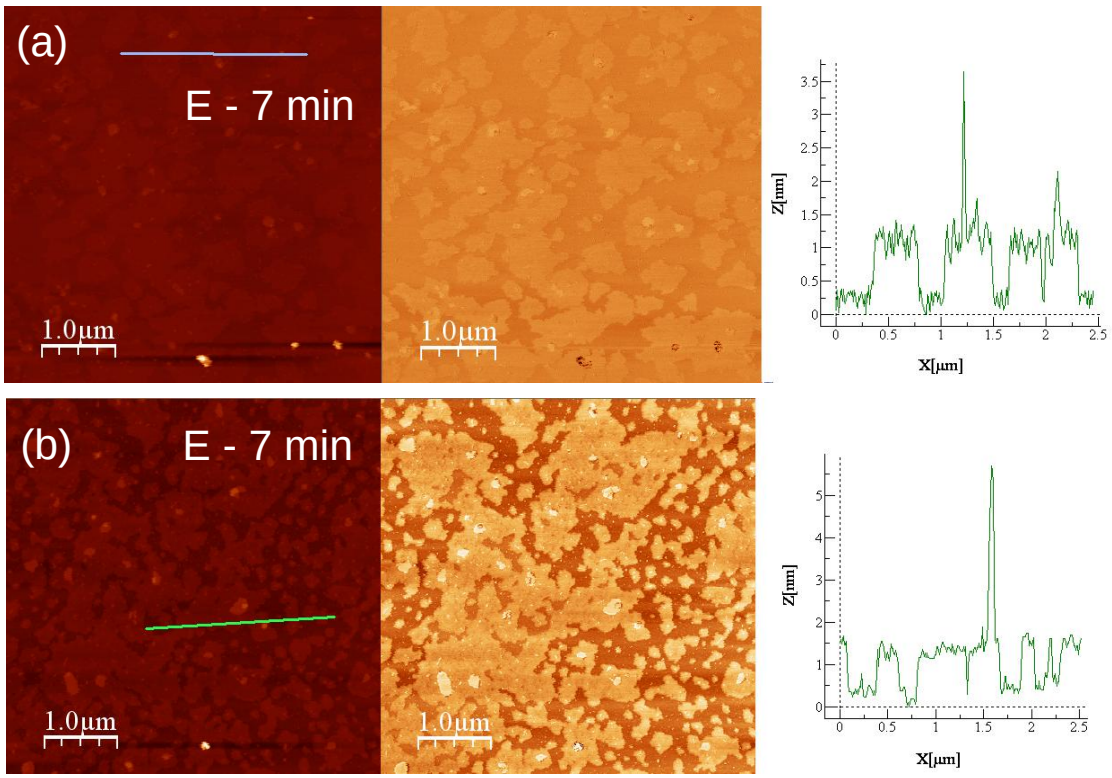

Figure 7.13. AFM images (topography and phase) and topographic profiles recorded for sample E taken (a) directly after deposition and (b) 2.5 months after deposition.

We also used Raman spectroscopy to analyze the quality of the graphene layers deposited on amorphous quartz substrates. Figure 7.14 shows the Raman spectrum of sample J. The D and G peaks appear quite broad and noisy in this sample. The intensity of the D peak is lower than that of the G peak. From this spectrum it is difficult to conclude about the approximate quality of the graphene layers.

However, the samples with graphene deposited on amorphous quartz appear to be transparent to the visible light. Figure 7.15 shows the transmittance spectrum for samples H and I deposited on amorphous quartz. These spectra show two characteristics about our graphene layers. First, the transparency is ~95-96 %, which indicates that our graphene deposits as multilayers. Second, transparency is almost constant in the whole range of spectra analyzed, from 870 to 2200 nm. This indicates that our deposits are constituted by graphene, with apparently no defects, such as oxygen-containing groups that would absorb in this region of the electromagnetic spectrum.

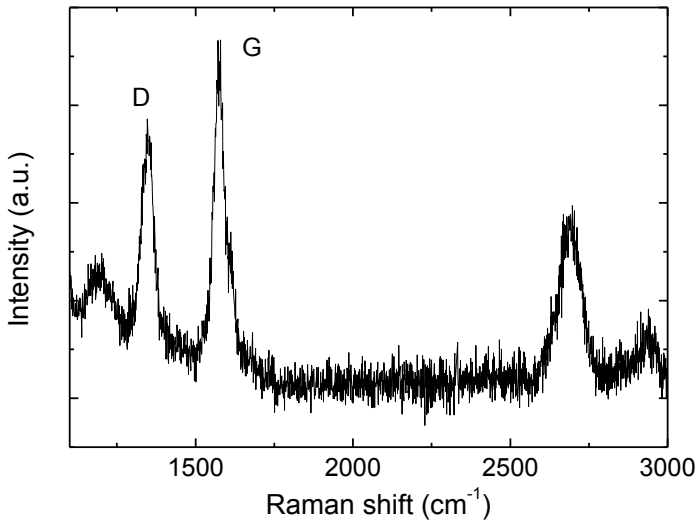

Figure 7.14. Raman spectrum recorded for sample J.

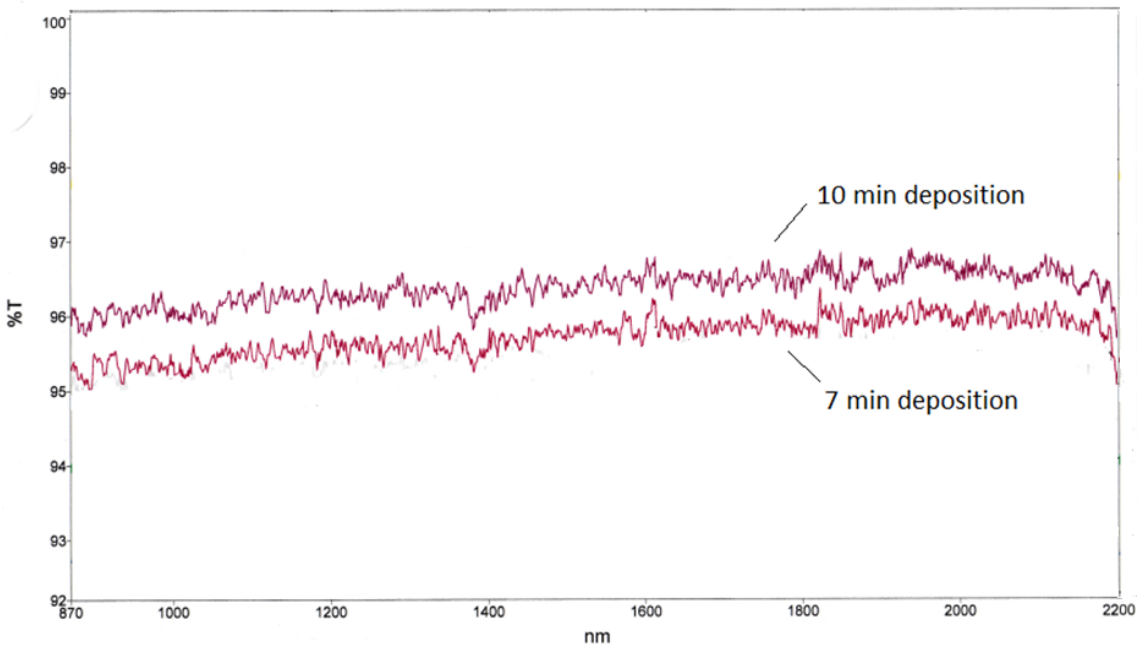

Figure 7.15. Transmittance spectra of samples I and H recorded in the 870-2200 nm region.

Finally, two-probe electrical measurements for F and I samples, deposited at 10 min on silicon and amorphous quartz substrates, respectively, were conducted using In/Ga liquid eutectic contacts. In/Ga eutectic droplets were placed on top of the sample. Linear voltage sweeps were obtained in the -3 V – 3 V range with a 50 mV/s sweep rate, as can be seen in Figure 7.16. The measurements were repeated with contacts on various points of each sample to ensure reproducibility. However, the samples do not show a good conductivity, what is probably related to a not complete percolation of graphene flake on the substrate.

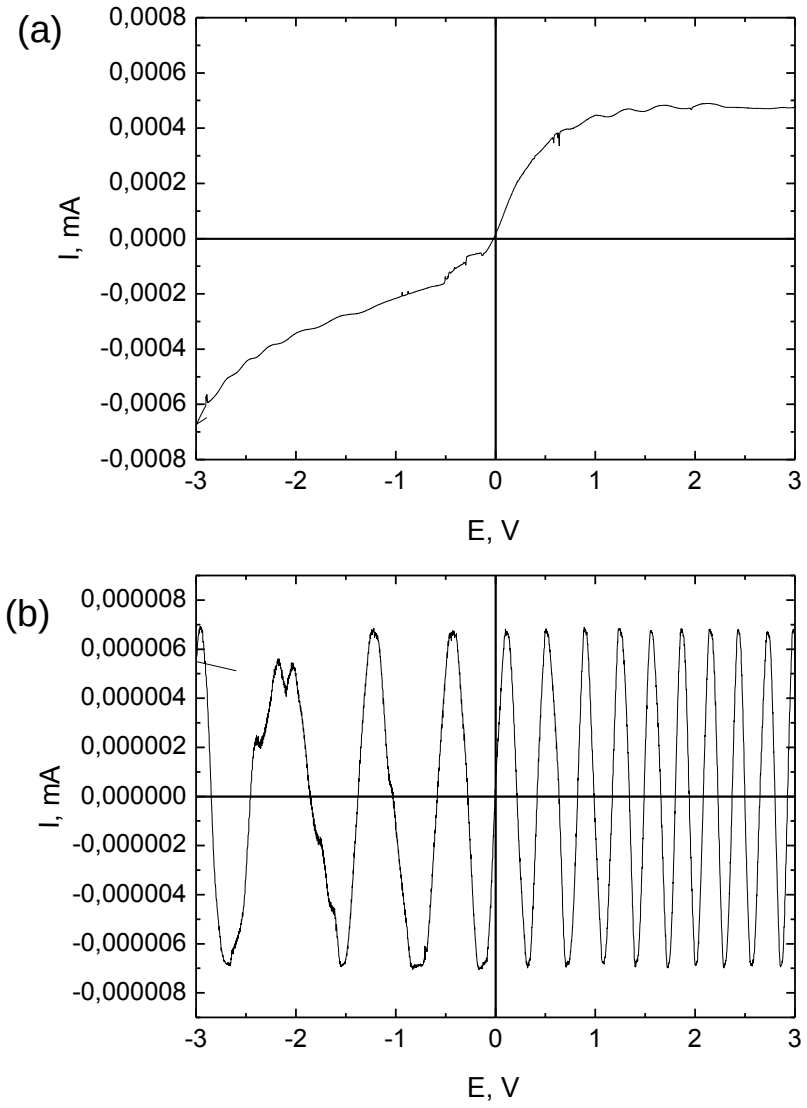

Figure 7.16. I-V curves recorded for (a) F and (b) I samples, deposited during 10 min on silicon and amorphous quartz substrates, respectively.

Conclusions

The potential of porous GaN for applications in electronics and optoelectronics has been demonstrated successfully during the realization of this thesis by the fabrication of low Ohmic resistivity contacts, efficient doping, MOS diodes and partially and fully porous *p-n* junctions based on porous GaN produced by the CVD method, based on the direct reaction of Ga with NH_3.

We obtained nanoporous GaN particles and epitaxial layers on different substrates by this technique at relatively high temperatures. The advantage of this technique, compared to other approaches used in the fabrication of porous GaN, is that it does not require any post-growth treatment, such as etching techniques that can damage the semiconductor structure and modify its properties. This technique simplifies previous methodologies used to generate porous GaN, and at the same time reduces the costs of these processes. Here, porosity is generated during the crystal growth process. The obtained porous GaN had straight nanopores, and their diameters, ranging between 50 and 100 nm, were constant all along the length of the pores. The porous GaN particles formed as a layer of single-crystal particles with interparticle and intraparticle porosity.

We studied how different reaction parameters such as the Ga holder, the Ga quantity, the deposition time, the catalyst and the substrate influence on the morphology, size and porosity degree of the nanoporous GaN particles. The geometry of the holder in which the Ga is contained affects to the first stages of its evaporation and deposition rate on the substrate. The Ga quantity has an influence on the coverage of the substrate with GaN particles. The deposition time also controls the coating of the substrate with nanoporous GaN particles. The catalyst plays two different roles: one is the control on the particle size and the other is the crystallographic orientation of the as-grown particles. The influence on the particle size is due to the metal alloy formed between the catalyst used and Ga and the size of the initial

nucleuses that can be formed. A second role is observed in the case of Ti, which leads to a texturation of the layer deposited on the substrate.

The substrate also plays an important role in the morphology and distribution of the nanoporous GaN particles on its surface. We have investigated the growth of porous GaN epitaxial layers on Al_2O_3, SiC, AlN and GaN substrates, among others. The results show that the lattice mismatch between the substrate and the porous GaN layer plays an important role in achieving a continuous porous layer.

With these data analyzed we have more tools to control and manipulate the deposition conditions of porous GaN in order to obtain the desired morphology, density, and porosity of the nanoporous GaN particles produced by CVD towards the required application.

The mechanism of crystal growth through a vapour-solid-solid process was confirmed by the formation, for instance, of a Au−Ga crystalline intermetallic alloy of cubic Ga_2Au that seeds the GaN formation by reaction with NH_3. Electrical characterization of porous GaN particles grown as high surface area layers from Pt- and Au-coated silicon showed *n*-type behavior of unintentiously doped porous GaN and at the same time confirmed near-Ohmic transport through polycrystalline porous *n*-type GaN. Metal−Ga intermetallic alloy formation during VSS growth promotes thermionic emission-based low-resistance Ohmic transport through the porous layer, and very low contact resistivities are possible to the faceted, rough *n*-type GaN surface. The ability of contacting the GaN using such metals gives opportunities for superior diode-based optoelectronics and sensing. The overall method of using intermetallic as Ohmic contacts could also be applied to simultaneously grow and contact nanoscale III-N compounds for optoelectronic devices.

We have shown that high structural and electronic quality, confirmed by CL and PL characterization, *p*-type GaN with a high density of charge carriers (~10^{18} cm^{-3}) can be grown on Si and also on epitaxial GaN substrates as a porous layer using magnesium nitride and magnesium acetylacetonate as precursors.

By depositing porous GaN in a manner similar to deterministic *p*-type porous GaN and incresing the concentration of Mg_3N_2, we formed GaN/MgO MOS diode in a single fabrication step. The Mg film formed initially is subsequently oxidized to polycrystalline MgO underneath the porous *n*-type GaN layer, resulting in a high-κ dielectric MgO. This method, promising for the development of porous GaN, augers well for new electronic and optoelectronic devices with improved external quantum efficiencies and large surface area biosensing based on capacitor or transistor functions.

We successfully fabricated partially porous *p*-*n* junctions using the same methodology, in which only the *n*-type or *p*-type GaN layers are porous and oriented along ***c***-crystalographic axis. Moreover, we produced by CVD fully porous GaN *p*-*n* junctions and compared their performance with partially porous *p*-*n* junctions. Fully porous *p*-*n* junctions were fabricated in a two crystal growth step process. First, an undoped *n*-type porous GaN layer was grown on non-porous GaN. Second, another porous *p*-type GaN layer was grown on the top of the porous *n*-type GaN layer. To prove the potentiality of these porous *p*-*n* junctions for diode applications, we characterized their diode behavior at high temperatures, and demonstrate their ability as current rectifiers. The electrical and optical characteristics confirm high electronic quality GaN growth for porous layers when compared with non-porous epitaxially

grown GaN, even when overgrown with opposite conduction type porous layers. we believe this investigation can be extended to other III-V materials, such as InN and AlN to span the visible spectrum, and as a route towards porous graded index III-V materials as a basis for unencapsulated white light LEDs incorporating other color centers, or for reducing refraction losses and narrowing the output light cone for improved LED external quantum efficiencies. Furthermore, high surface area diodes fabricated by this route do not require complicated core-shell architectures and may be viable routes to chemically stable wide bandgap (bio)sensors.

We developed an approach towards tuning the emission of a potential LED fabricated with this technology based on the introduction of luminescent Eu:Y_2O_3 and (Eu,Bi):Y_2O_3 nanoparticles directly inside the pores of GaN through a sol-gel technique, the so called modified Pechini method. The emission and excitation spectra of the deposited nanoparticles onto GaN were recorded and the emission of red light after excitation at the band edge emission of GaN was observed. However, further analysis will be required to study the possible energy transfer mechanism between GaN and (Eu,Bi):Y_2O_3 nanoparticles. Phosphor nanoparticles deposited inside the pores of GaN structures, apart from giving the required emissions to produce warm white light, will also offer a medium with an intermediate refractive index that might enhance the light extraction efficiency of the LED.

Finally, we performed preliminary research towards the achievement of graphene monolayers with good coverage of the substrate by the Electrospray Ion-Assisted technique on silicon and amorphous quartz substrates. The results obtained show that we were able to deposit a few/single layers of graphene covering most of the area of the substrate by using a suspension of graphene flakes on DMF. However, further research is needed to obtain a homogenous and percolated monolayer of graphene that can be considered for applications as transparent conductive electrode for GaN-based LEDs.

Overall, this thesis confirms porous GaN as a promising material for further development of advanced optoelectronic devices.

References

1. Nakamura, S., and Krames, M.R. (2013). *History of gallium-nitride-based light-emitting diodes for illumination*. Proc. IEEE *101*, 2211–2220.

2. Jordan, E.C. (1985). *Reference data for engineers: radio, electronics, computer, and communications* (H.W. Sams).

3. Jain, S.C., Willander, M., Narayan, J., and Overstraeten, R.V. (2000). *III–nitrides: Growth, characterization, and properties*. J. Appl. Phys. *87*, 965–1006.

4. Strite, S., and Morkoç, H. (1992). *GaN, AlN, and InN: A review*. J. Vac. Sci. Technol. B *10*, 1237–1266.

5. Shi, B.M., Xie, M.H., Wu, H.S., Wang, N., and Tong, S.Y. (2006). *Transition between wurtzite and zinc-blende GaN: An effect of deposition condition of molecular-beam epitaxy*. Appl. Phys. Lett. *89*, 151921.

6. Ehrentraut, D., Meissner, E., and Bockowski, M. (2010). *Technology of Gallium Nitride Crystal Growth* (Heidelberg; New York: Springer).

7. Shibata, H., Waseda, Y., Ohta, H., Kiyomi, K., Shimoyama, K., Fujito, K., Nagaoka, H., Kagamitani, Y., Simura, R., and Fukuda, T. (2007). *High thermal conductivity of gallium nitride (GaN) crystals grown by HVPE process*. Mater. Trans. *48*, 2782–2786.

8. Palacios, T., Chakraborty, A., Rajan, S., Poblenz, C., Keller, S., DenBaars, S.P., Speck, J.S., and Mishra, U.K. (2005). *High-power AlGaN/GaN HEMTs for Ka-band applications*. IEEE Electron Device Lett. *26*, 781–783.

9. Leszczynski, M., Teisseyre, H., Suski, T., Grzegory, I., Bockowski, M., Jun, J., Porowski, S., Pakula, K., Baranowski, J.M., Foxon, C.T., et al. (1996). *Lattice parameters of gallium nitride*. Appl. Phys. Lett. *69*, 73–75.

10. Dahal, R., Pantha, B., Li, J., Lin, J.Y., and Jiang, H.X. (2009). *InGaN/GaN multiple quantum well solar cells with long operating wavelengths*. Appl. Phys. Lett. *94*, 063505.

11. Neufeld, C.J., Toledo, N.G., Cruz, S.C., Iza, M., DenBaars, S.P., and Mishra, U.K. (2008). *High quantum efficiency InGaN/GaN solar cells with 2.95 eV band gap*. Appl. Phys. Lett. *93*, 143502.

12. Cros, A., Dimitrov, R., Angerer, H., Ambacher, O., Stutzmann, M., Christiansen, S., Albrecht, M., and Strunk, H.P. (1997). *Influence of magnesium doping on the structural properties of GaN layers*. J. Cryst. Growth *181*, 197–203.

13. Cremades, A., Görgens, L., Ambacher, O., Stutzmann, M., and Scholz, F. (2000). *Structural and optical properties of Si-doped GaN*. Phys. Rev. B *61*, 2812–2818.

14. Götz, W., Johnson, N.M., Walker, J., Bour, D.P., Amano, H., and Akasaki, I. (1995). *Hydrogen passivation of Mg acceptors in GaN grown by metalorganic chemical vapor deposition*. Appl. Phys. Lett. *67*, 2666–2668.

15. Amano, H., Kito, M., Hiramatsu, K., and Akasaki, I. (1989). *P-Type Conduction in Mg-Doped GaN Treated with Low-Energy Electron Beam Irradiation (LEEBI).* Jpn. J. Appl. Phys. *28*, L2112–L2114.

16. Nakamura, S., Mukai, T., Senoh, M., and Iwasa, N. (1992). *Thermal Annealing Effects on P-Type Mg-Doped GaN Films.* Jpn. J. Appl. Phys. *31*, L139–L142.

17. Glaser, E.R., Murthy, M., Freitas Jr, J.A., Storm, D.F., Zhou, L., and Smith, D.J. (2007). *Optical and magnetic resonance studies of Mg-doped GaN homoepitaxial layers grown by molecular beam epitaxy*. Phys. B Condens. Matter *401–402*, 327–330.

18. Pearton, S.J., Vartuli, C.B., Zolper, J.C., Yuan, C., and Stall, R.A. (1995). *Ion implantation doping and isolation of GaN*. Appl. Phys. Lett. *67*, 1435–1437.

19. Nakamura, S., Mukai, T., and Senoh, M. (1991). *High-Power GaN P-N Junction Blue-Light-Emitting Diodes*. Jpn. J. Appl. Phys. *30*, L1998.

20. Tolbert, L. M., Ozpineci, B., Islam, S. K., and Chinthavali, M. S. (2003) *Wide bandgap semiconductors for utility applications*. in Proc. Power and Energy Systems. ACTA Press, USA.

21. Kemerley, R.T., Wallace, H.B., and Yoder, M.N. (2002). *Impact of wide bandgap microwave devices on DoD systems*. Proc. IEEE *90*, 1059–1064.

22. Jagadish, C., and Pearton, S.J. (2011). *Zinc Oxide Bulk, Thin Films and Nanostructures: Processing, Properties, and Applications* (Elsevier).

23. Ozpineci, B., and Tolbert, L. M. (2003). *Comparision of wide band gap semiconductors for power electronics applications.* OAK Ridge National Laboratory Oak Ridge, Tennessee 37831.

24. Wang, T., Lei, G., Chen, X., Guido, L., Ngo, K., and Lu, G.-Q. (2009). *Improved thermal performance of high-power LED by using low-temperature sintered chip attachment.* In International Conference on Electronic Packaging Technology High Density Packaging, ICEPT-HDP '09, pp. 581–584.

25. Redwing, J.M., Tischler, M.A., Flynn, J.S., Elhamri, S., Ahoujja, M., Newrock, R.S., and Mitchel, W.C. (1996). *Two-dimensional electron gas properties of AlGaN/GaN heterostructures grown on 6H–SiC and sapphire substrates*. Appl. Phys. Lett. *69*, 963–965.

26. Zhang, Y., Smorchkova, I.P., Elsass, C.R., Keller, S., Ibbetson, J.P., Denbaars, S., Mishra, U.K., and Singh, J. (2000). *Charge control and mobility in AlGaN/GaN transistors: Experimental and theoretical studies*. J. Appl. Phys. *87*, 7981–7987.

27. Shibata, N. (2005). *Fabrication of LED based on III-V nitride and its applications*. In Materials Research Society Symposium Proceedings, pp. 27–35.

28. Dorsaz, J., Castiglia, A., Cosendey, G., Feltin, E., Rossetti, M., Duelk, M., Velez, C., Carlin, J.-F., and Grandjean, N. (2010). *AlGaN-free blue III-nitride laser diodes grown on c-plane GaN substrates*. Appl. Phys. Express *3*.

29. Tripathi, N., Bell, L.D., Grandusky, J.R., Jindal, V., and Shahedipour-Sandvik, F. (2008). *Growth and characterization of a novel hyperspectral detector using the III-nitrides.* Phys. Status Solidi C Curr. Top. Solid State Phys. *5*, 2228–2230.

30. Jewett, S.A., Makowski, M.S., Andrews, B., Manfra, M.J., and Ivanisevic, A. (2012). *Gallium nitride is biocompatible and non-toxic before and after functionalization with peptides*. Acta Biomater. *8*, 728–733.

31. Boshitskaya, N.V., Lavrenko, V.A., Bartnitskaya, T.S., Makarenko, G.N., Shkurko, G.A., and Danilenko, N.V. (2000). *Reaction of aluminum nitride powder with biochemical media*. Powder Metall. Met. Ceram. *39*, 157–162.

32. Tanaka, A. (2004). *Toxicity of indium arsenide, gallium arsenide, and aluminium gallium arsenide*. Toxicol. Appl. Pharmacol. *198*, 405–411.

33. Ulm University. From http://www-opto.e-technik.uniulm.de/lehre/cs/index.html

34. Grzegory, I., Jun, J., Boćkowski, M., Krukowski, S., Wróblewski, M., Łucznik, B., and Porowski, S. (1995). *III–V Nitrides—thermodynamics and crystal growth at high N_2 pressure.* J. Phys. Chem. Solids *56*, 639–647.

35. Yamane, H., Shimada, M., Clarke, S.J., and DiSalvo, F.J. (1997). *Preparation of GaN Single Crystals Using a Na Flux*. Chem. Mater. *9*, 413–416.

36. Dwiliński, R., Doradziński, R., Garczyński, J., Sierzputowski, L.P., Puchalski, A., Kanbara, Y., Yagi, K., Minakuchi, H., and Hayashi, H. (2009). *Bulk ammonothermal GaN*. J. Cryst. Growth *311*, 3015–3018.

37. Dwiliński, R., Doradziński, R., Garczyński, J., Sierzputowski, L.P., Puchalski, A., Kanbara, Y., Yagi, K., Minakuchi, H., and Hayashi, H. (2008). *Excellent crystallinity of truly bulk ammonothermal GaN*. J. Cryst. Growth *310*, 3911–3916.

38. Dwiliński, R., Doradziński, R., Garczyński, J., Sierzputowski, L., Kucharski, R., Zając, M., Rudziński, M., Kudrawiec, R., Serafińczuk, J., and Strupiński, W. (2010). *Recent achievements in AMMONO-bulk method*. J. Cryst. Growth *312*, 2499–2502.

39. Grandjean, N., Massies, J., Martinez, Y., Vennéguès, P., Leroux, M., and Laügt, M. (1997). *GaN epitaxial growth on sapphire (0001): the role of the substrate nitridation*. J. Cryst. Growth *178*, 220–228.

40. Ager, J.W., Suski, T., Ruvimov, S., Kruger, J., Conti, G., Weber, E.R., Bremser, M.D., Davis, R., and Kuo, C.P. (1997). *Intrinsic and thermal stress in gallium nitride epitaxial films.* In Materials Research Society Symposium - Proceedings, pp. 775–780.

41. Motoki, K. (2010). *Development of Gallium Nitride Substrates*. In SEI technical review. Englsh addition. *70*, 28–35.

42. Kung, P., Saxler, A., Zhang, X., Walker, D., Lavado, R., and Razeghi, M. (1996). *Metalorganic chemical vapor deposition of monocrystalline GaN thin films on β-$LiGaO_2$ substrates.* Appl. Phys. Lett. *69*, 2116–2118.

43. Maruska, H.P., and Tietjen, J.J. (1969). *The preparation and properties of vapor-deposited single-crystal-line GaN.* Appl. Phys. Lett. *15*, 327–329.

44. Dmitriev, V., and Usikov, A. (2006). *Chapter 1: Hydride Vapor Phase Epitaxy of Group III Nitride Materials.* From III-Nitride Semiconductor Materials (Imperial College Press, Technologies and Devices International, Inc., USA).

45. Vodakov, Y.A., Mokhov, E.N., Roenkov, A.D., Boiko, M.E., and Baranov, P.G. (1998). *High rate GaN epitaxial growth by sublimation sandwich method*. J. Cryst. Growth *183*, 10–14.

46. Hitchman, M.L., and Jensen, K.F. (1993). *Chemical Vapor Deposition: Principles and Applications*. (Academic Press).

47. Keller, S., Keller, B.P., Wu, Y.-F., Heying, B., Kapolnek, D., Speck, J.S., Mishra, U.K., and DenBaars, S.P. (1996). *Influence of sapphire nitridation on properties of gallium nitride grown by metalorganic chemical vapor deposition*. Appl. Phys. Lett. *68*, 1525–1527.

48. Kato, Y., Kitamura, S., Hiramatsu, K., and Sawaki, N. (1994). *Selective growth of wurtzite GaN and AlxGa1-xN on GaN/sapphire substrates by metalorganic vapor phase epitaxy*. J. Cryst. Growth *144*, 133–140.

49. Choy, K.L. (2003). *Chemical vapour deposition of coatings*. Prog. Mater. Sci. *48*, 57–170.

50. Davey, J.E., and Pankey, T. (1968). *Epitaxial GaAs Films Deposited by Vacuum Evaporation*. J. Appl. Phys. *39*, 1941–1948.

51. Shelton, H., and Cho, A.Y.H. (1966). *Evaporative Lifetimes of Copper, Chromium, Beryllium, Nickel, Iron, and Titanium on Tungsten and Oxygenated Tungsten*. J. Appl. Phys. *37*, 3544–3548.

52. Arthur Jr., J.R. (1968). *Interaction of Ga and As_2 Molecular Beams with GaAs Surfaces.* J. Appl. Phys. *39*, 4032–4034.

53. Balakrishnan, K., Okumura, H., and Yoshida, S. (1998). *Study on the initial stages of heteroepitaxial growth of hexagonal GaN on sapphire by plasma assisted MBE*. J. Cryst. Growth *189-190*, 244–249.

54. Sobanska, M., Klosek, K., Zytkiewicz, Z.R., Borysiuk, J., Witkowski, B.S., Lusakowska, E., Reszka, A., and Jakiela, R. (2012). *Plasma-assisted MBE growth of GaN on Si(111) substrates*. Cryst. Res. Technol. *47*, 307–312.

55. From the website of berkeley
http://www.mse.berkeley.edu/groups/weber/research/ganmbe.html

56. Hou, W.-C., Tang, W.-C., Tsai, C.-H., and Hong, F.C.-N. (2012). *Low temperature growth of GaN nanowires by plasma-enhanced chemical vapor deposition*. J. Technol. *27*, 91–96.

57. Yasui, K., Morimoto, K., and Akahane, T. (2003). *Growth of GaN films on nitrided GaAs substrates using hot-wire CVD*. Thin Solid Films *430*, 174–177.

58. Weisbuch, C., and Vinter, B. (1991). *Quantum Semiconductor Structures: Fundamentals and Applications.* (Elsevier).

59. Schubert, E.F. (2002). *Light-Emitting Diodes.* (Cambridge University Press).

60. Morkoç, H. (2008). *Light-Emitting Diodes and Lighting*. In Handbook of Nitride Semiconductors and Devices, (Wiley-VCH Verlag GmbH & Co. KGaA), pp. 1–168.

61. Chen, Z.Z., Qin, Z.X., Hu, C.Y., Hu, X.D., Yu, T.J., Tong, Y.Z., Ding, X.M., and Zhang, G.Y. (2004). *Ohmic contact formation of Ti/Al/Ni/Au to n-GaN by two-step annealing method*. Mater. Sci. Eng. B *111*, 36–39.

62. Zellweger, C. *Realization of GaN-based light emitting devices.* (2003). Thesis, EPFL Lausanne, Switzerland.

63. Lee, C.-S., Lin, Y.-J., and Lee, C.-T. (2001). *Investigation of oxidation mechanism for ohmic formation in Ni/Au contacts to p-type GaN layers*. Appl. Phys. Lett. *79*, 3815–3817.

64. Horng, R.-H., Wuu, D.-S., Lien, Y.-C., and Lan, W.-H. (2001). *Low-resistance and high-transparency Ni/indium tin oxide ohmic contacts to p-type GaN*. Appl. Phys. Lett. *79*, 2925–2927.

65. Bogart, K.H.A., and Crofton, J. (2006). *Calculations and measurements of contact resistance of semi-transparent Ni/Pd contacts to p-GaN*. J. Electron. Mater. *35*, 605–612.

66. Lin, Y.C., Chang, S.J., Su, Y.K., Tsai, T.Y., Chang, C.S., Shei, S.C., Kuo, C.W., and Chen, S.C. (2003). *InGaN/GaN light emitting diodes with Ni/Au, Ni/ITO and ITO p-type contacts*. Solid-State Electron. *47*, 849–853.

67.Jang, H.W., and Lee, J.-L. (2004). *Mechanism for ohmic contact formation of Ni/Ag contacts on p-type GaN*. Appl. Phys. Lett. *85*, 5920–5922.

68. Kim, B.-J., Lee, C., Jung, Y., Baik, K.H., Mastro, M.A., Hite, J.K., Jr, C.R.E., and Kim, J. (2011). *Large-area transparent conductive few-layer graphene electrode in GaN-based ultra-violet light-emitting diodes*. Appl. Phys. Lett. *99*, 143101.

69. Youn, D.-H., Yu, Y.-J., Choi, H., Kim, S.-H., Choi, S.-Y., and Choi, C.-G. (2013). *Graphene transparent electrode for enhanced optical power and thermal stability in GaN light-emitting diodes.* Nanotechnology *24*, 075202.

70. Nakamura, S., Pearton, S., and Fasol, G. (2000). *The Blue Laser Diode: The Complete Story*. (Springer).

71. Mukai, T., Nagahama, S., Iwasa, N., Senoh, M., and Yamada, T. (2001). *Nitride light-emitting diodes*. J. Phys. Condens. Matter *13*, 7089.

72. Nakamura, S., Senoh, M., Iwasa, N., and Nagahama, S. (1995). *High-Brightness InGaN Blue, Green and Yellow Light-Emitting Diodes with Quantum Well Structures*. Jpn. J. Appl. Phys. *34*, L797–L799.

73. Nakamura, S., Senoh, M., Iwasa, N., and Nagahama, S. (1995). *High-power InGaN single-quantum-well-structure blue and violet light-emitting diodes.* Appl. Phys. Lett. *67*, 1868–1870.

74. Mottier, P. (2010). *LEDs for Lighting Applications.* (John Wiley & Sons).

75. Kim, S.H., Park, H.H., Song, Y.H., Park, H.J., Kim, J.B., Jeon, S.R., Jeong, H., Jeong, M.S., and Yang, G.M. (2013). *An improvement of light extraction efficiency for GaN-based light emitting diodes by selective etched nanorods in periodic microholes*. Opt. Express *21*, 7125–7130.

76. Gardner, N.F., Müller, G.O., Shen, Y.C., Chen, G., Watanabe, S., Götz, W., and Krames, M.R. (2007). *Blue-emitting InGaN–GaN double-heterostructure light-emitting diodes reaching maximum quantum efficiency above 200A/cm^2*. Appl. Phys. Lett. *91*, 243506

77. Wang, P., Cao, B., Gan, Z., and Liu, S. (2011). *Analysis of light extraction efficiency of GaN-based light-emitting diodes.* J. Phys. Conf. Ser. *276*.

78. Krames, M.R., Shchekin, O.B., Mueller-Mach, R., Mueller, G., Zhou, L., Harbers, G., and Craford, M.G. (2007). *Status and Future of High-Power Light-Emitting Diodes for Solid-State Lighting.* J. Disp. Technol. *3*, 160–175.

79. Zhou, L., An, B., Wu, Y., and Liul, S. (2009). *Analysis of delamination and darkening in high power LED packaging.* In Proceedings of the International Symposium on the Physical and Failure Analysis of Integrated Circuits, IPFA, pp. 656–660.

80. OSRAM. *Optosemiconductors. Projection with LED Light Sources*. (2014). Application note.

81. Liu, D.-S., Lin, T.-W., Huang, B.-W., Juang, F.-S., Lei, P.-H., and Hu, C.-Z. (2009). *Light-extraction enhancement in GaN-based light-emitting diodes using grade-refractive-index amorphous titanium oxide films with porous structures*. Appl. Phys. Lett. *94*, 143502.

82. Kim, T.K., Kim, S.H., Yang, S.S., Son, J.K., Lee, K.H., Hong, Y.G., Shim, K.H., Yang, J.W., Lim, K.Y., Bae, S.J., et al. (2009). *GaN-based light-emitting diode with textured indium tin oxide transparent layer coated with Al_2O_3 powder*. Appl. Phys. Lett. *94*, 161107.

83. Yeh, D.-M., Huang, C.-F., Chen, C.-Y., Lu, Y.-C., and Yang, C.C. (2007). *Surface plasmon coupling effect in an InGaN/GaN single-quantum-well light-emitting diode*. Appl. Phys. Lett. *91*, 171103.

84. Lu, Y.-C., Chen, Y.-S., Tsai, F.-J., Wang, J.-Y., Lin, C.-H., Chen, C.-Y., Kiang, Y.-W., and Yang, C.C. (2009). *Improving emission enhancement in surface plasmon coupling with an InGaN/GaN quantum well by inserting a dielectric layer of low refractive index between metal and semiconductor*. Appl. Phys. Lett. *94*, 233113.

85. Song, Y.M., Choi, E.S., Park, G.C., Park, C.Y., Jang, S.J., and Lee, Y.T. (2010). *Disordered antireflective nanostructures on GaN-based light-emitting diodes using Ag nanoparticles for improved light extraction efficiency*. Appl. Phys. Lett. *97*, 093110.

86. Okamoto, K., Niki, I., Scherer, A., Narukawa, Y., Mukai, T., and Kawakami, Y. (2005). *Surface plasmon enhanced spontaneous emission rate of InGaN/GaN quantum wells probed by time-resolved photoluminescence spectroscopy*. Appl. Phys. Lett. *87*, 071102.

87. Bao, K., Zhang, B., Wang, Z., Dai, T., Kang, X., Chen, Z., Xu, K., Ji, H., Chen, Y., and Gan, Z. (2007). *Improvement of surface light extraction from flip-chip GaN-based LED by embossing of thermosetting polymers*. Phys. Status Solidi C Curr. Top. Solid State Phys. *4*, 33–36.

88. Shchekin, O.B., Epler, J.E., Trottier, T.A., Margalith, T., Steigerwald, D.A., Holcomb, M.O., Martin, P.S., and Krames, M.R. (2006). *High performance thin-film flip-chip InGaN-GaN light-emitting diodes*. Appl. Phys. Lett. *89*, 071109.

89. Fujii, T., Gao, Y., Sharma, R., Hu, E.L., DenBaars, S.P., and Nakamura, S. (2004). *Increase in the extraction efficiency of GaN-based light-emitting diodes via surface roughening*. Appl. Phys. Lett. *84*, 855–857.

90. Wang, P., Cao, B., Gan, Z., and Liu, S. (2011). *Analysis of light extraction efficiency of GaN-based light-emitting diodes.* J. Phys. Conf. Ser. *276*.

91. Fujita, M., Takahashi, S., Tanaka, Y., Asano, T., and Noda, S. (2005). *Simultaneous Inhibition and Redistribution of Spontaneous Light Emission in Photonic Crystals.* Science *308*, 1296–1298.

92. Yablonovitch, E. (1987). *Inhibited Spontaneous Emission in Solid-State Physics and Electronics*. Phys. Rev. Lett. *58*, 2059–2062.

93. Oder, T.N., Shakya, J., Lin, J.Y., and Jiang, H.X. (2003). *III-nitride photonic crystals.* Appl. Phys. Lett. *83*, 1231–1233.

94. Wierer, J.J., Krames, M.R., Epler, J.E., Gardner, N.F., Craford, M.G., Wendt, J.R., Simmons, J.A., and Sigalas, M.M. (2004). *InGaN/GaN quantum-well heterostructure light-emitting diodes employing photonic crystal structures*. Appl. Phys. Lett. *84*, 3885–3887.

95. Cho, H.K., Kim, S.-K., Bae, D.K., Kang, B.-C., Lee, J.S., and Lee, Y.-H. (2008). *Laser Liftoff GaN Thin-Film Photonic Crystal GaN-Based Light-Emitting Diodes*. IEEE Photonics Technol. Lett. *20*, 2096–2098.

96. Cho, C.-Y., Kang, S.-E., Kim, K.S., Lee, S.-J., Choi, Y.-S., Han, S.-H., Jung, G.-Y., and Park, S.-J. (2010). *Enhanced light extraction in light-emitting diodes with photonic crystal structure selectively grown on p-GaN*. Appl. Phys. Lett. *96*, 181110.

97. Wierer, J.J., David, A., and Megens, M.M. (2009). *III-nitride photonic-crystal light-emitting diodes with high extraction efficiency.* Nat. Photonics *3*, 163–169.

98. Ryu, S.-W., Park, J., Oh, J.-K., Long, D.H., Kwon, K.-W., Kim, Y.-H., Lee, J.K., and Kim, J.H. (2009). *Analysis of Improved Efficiency of InGaN Light-Emitting Diode With Bottom Photonic Crystal Fabricated by Anodized Aluminum Oxidxe*. Adv. Funct. Mater. *19*, 1650–1655.

99. Omar, K., Hassan, Z., Goh, K., Teh, H., and Hassan, H.A. (2009). *Synthesis Porous GaN by Using UV-assisted Electrochemical Etching and Its Optical Studies*. Mod. Appl. Sci. *3*, p132.

100. Nie, B., Duan, B.K., and Bohn, P.W. (2013). *Nanoporous GaN-Ag composite materials prepared by metal-assisted electroless etching for direct laser desorption-ionization mass spectrometry*. ACS Appl. Mater. Interfaces *5*, 6208–6215.

101. Lehmann, V., and Gösele, U. (1991). *Porous silicon formation: A quantum wire effect.* Appl. Phys. Lett. *58*, 856–858.

102. Tiginyanu, I.M., Ursaki, V.V., Monaico, E., Foca, E., and Föll, H. (2007). *Pore Etching in III-V and II-VI Semiconductor Compounds in Neutral Electrolyte*. Electrochem. Solid-State Lett. *10*, D127–D129.

103. O'Dwyer, C., Buckley, D.N., Sutton, D., Serantoni, M., and Newcomb, S.B. (2007). *An Investigation by AFM and TEM of the Mechanism of Anodic Formation of Nanoporosity in n-InP in KOH.* J. Electrochem. Soc. *154*, H78–H85.

104. Stevens-Kalceff, M.A., Tiginyanu, I.M., Langa, S., Föll, H., and Hartnagel, H.L. (2001). *Correlation between morphology and cathodoluminescence in porous GaP*. J. Appl. Phys. *89*, 2560–2565.

105. Kovalev, D., Timoshenko, V.Y., Künzner, N., Gross, E., and Koch, F. (2001). *Strong Explosive Interaction of Hydrogenated Porous Silicon with Oxygen at Cryogenic Temperatures.* Phys. Rev. Lett. *87*, 068301.

106. Kochergin, V. *Omnidirectional Optical Filters*. (2003). Kluwer Academic, Boston, Mass, USA.

107. Kovalev, D., Polisski, G., Diener, J., Heckler, H., Künzner, N., Timoshenko, V.Y., and Koch, F. (2001). *Strong in-plane birefringence of spatially nanostructured silicon.* Appl. Phys. Lett. *78*, 916–918.

108. Kochergin, V., Christophersen, M., and Swinehart, P.R. (2004). *Macroporous silicon UV filters for space and terrestrial environments*. pp. 223–234.

109. Kaltsas, G., and Nassiopoulou, A.G. (1999). *Novel C-MOS compatible monolithic silicon gas flow sensor with porous silicon thermal isolation.* Sens. Actuators Phys. *76*, 133–138.

110. Oton, C.J., Pancheri, L., Gaburro, Z., Pavesi, L., Baratto, C., Faglia, G., and Sberveglieri, G. (2003). *Multiparametric porous silicon gas sensors with improved quality and sensitivity.* Phys. Status Solidi A *197*, 523–527.

111. Huang, Y., Duan, X., Cui, Y., and Lieber, C.M. (2002). *Gallium Nitride Nanowire Nanodevices.* Nano Lett. *2*, 101–104.

112. Mynbaeva, M., Bazhenov, N., Mynbaev, K., Evstropov, V., Saddow, S. e., Koshka, Y., and Melnik, Y. (2001). *Photoconductivity in Porous GaN Layers*. Phys. Status Solidi B *228*, 589–592.

113. Mynbaeva, M., Titkov, A., Kryganovskii, A., Ratnikov, V., Mynbaev, K., Huhtinen, H., Laiho, R., and Dmitriev, V. (2000). *Structural characterization and strain relaxation in porous GaN layers.* Appl. Phys. Lett. *76*, 1113–1115.

114. Li, X., Kim, Y.-W., Bohn, P.W., and Adesida, I. (2002). *In-plane bandgap control in porous GaN through electroless wet chemical etching.* Appl. Phys. Lett. *80*, 980–982.

115. Vajpeyi, A.P., Chua, S.J., Tripathy, S., Fitzgerald, E.A., Liu, W., Chen, P., and Wang, L.S. (2005). *High Optical Quality Nanoporous GaN Prepared by Photoelectrochemical Etching. Electrochem*. Solid-State Lett. *8*, G85–G88.

116. Zhuang, D., and Edgar, J.H. (2005). *Wet etching of GaN, AlN, and SiC: a review*. Mater. Sci. Eng. R Rep. *48*, 1–46.

117. Ohkubo, M. (1998). *Anodic etching of n-type GaN films in NaOH electrolyte with Cl ions.* J. Cryst. Growth *189-190*, 734–737.

118. Díaz, D.J., Williamson, T.L., Adesida, I., Bohn, P.W., and Molnar, R.J. (2003). *Morphology evolution and luminescence properties of porous GaN generated via Pt-assisted electroless etching of hydride vapor phase epitaxy GaN on sapphire*. J. Appl. Phys. *94*, 7526–7534.

119. Kohl, P.A., and Harris, D.B. (1993). *Photoelectrochemical methods for semiconductor device processing*. Electrochimica Acta *38*, 101–106.

120. Vajpeyi, A.P., Chua, S.J., Tripathy, S., Fitzgerald, E.A., Liu, W., Chen, P., and Wang, L.S. (2005). *High optical quality nanoporous GaN prepared by photoelectrochemical etching*. Electrochem. Solid-State Lett. *8*, G85–G88.

121. Youtsey, C., Adesida, I., and Bulman, G. (1997). *Highly anisotropic photoenhanced wet etching of n-type GaN.* Appl. Phys. Lett. *71*, 2151–2153.

122. Ainorkhilah, M., Naser Mahmoud, A., Yuhamdan, Y., Yam, F.K., Chuah, L.S., Husnen R., A., and Zainuriah, H. (2013). *A Novel AC technique for high quality porous GaN.* International Journal of Electrochemical Science 8 (4): 5801-5809.

123. Soh, C.B., Hartono, H., Chow, S.Y., Chua, S.J., and Fitzgerald, E.A. (2007). *Dislocation annihilation in regrown GaN on nanoporous GaN template with optimization of buffer layer growth.* Appl. Phys. Lett. *90*, 053112.

124. Zhang, Y., Leung, B., and Han, J. (2012). *A liftoff process of GaN layers and devices through nanoporous transformation.* Appl. Phys. Lett. *100*, 181908.

125. Ramizy, A., Hassan, Z., and Omar, K. (2011). *Porous GaN on Si (111) and its application to hydrogen gas sensor*. Sens. Actuators B Chem. *155*, 699–708.

126. Yam, F.K., and Hassan, Z. (2007). *Schottky diode based on porous GaN for hydrogen gas sensing application.* Appl. Surf. Sci. *253*, 9525–9528.

127. Vial, J.C., Bsiesy, A., Gaspard, F., Herino, R., Ligeon, M., Müller, F., Romestain, R., and Macfarlane, R.M. (1992). *Mechanisms of visible-light emission from electro-oxidized porous silicon.* Phys. Rev. B *45*, 14171–14176.

128. Hwang, J.M., Hung, W.H., and Hwang, H.L. (2008). *Efficiency Enhancement of Light Extraction in LED With a Nano-Porous GaP Surface*. IEEE Photonics Technol. Lett. *20*, 608–610.

129. Wang, R., Liu, D., Zuo, Z., Yu, Q., Feng, Z., and Xu, X. (2012). *Metal-assisted electroless fabrication of nanoporous p-GaN for increasing the light extraction efficiency of light emitting diodes*. AIP Adv. *2*, 012109.

130. Kim, K., Choi, J., Bae, T.S., Jung, M., and Woo, D.H. (2007). *Enhanced Light Extraction from Nanoporous Surfaces of InGaN/GaN-Based Light Emitting Diodes*. Jpn. J. Appl. Phys. *46*, 6682.

131. Ryu, S.-W., Park, J., Oh, J.-K., Long, D.H., Kwon, K.-W., Kim, Y.-H., Lee, J.K., and Kim, J.H. (2009). *Analysis of Improved Efficiency of InGaN Light-Emitting Diode With Bottom Photonic Crystal Fabricated by Anodized Aluminum Oxide*. Adv. Funct. Mater. *19*, 1650–1655.

132. Cho, C.-Y., Kang, S.-E., Kim, K.S., Lee, S.-J., Choi, Y.-S., Han, S.-H., Jung, G.-Y., and Park, S.-J. (2010). *Enhanced light extraction in light-emitting diodes with photonic crystal structure selectively grown on p-GaN*. Appl. Phys. Lett. *96*, 181110.

133. Chhajed, S., Lee, W., Cho, J., Schubert, E.F., and Kim, J.K. (2011). *Strong light extraction enhancement in GaInN light-emitting diodes by using self-organized nanoscale patterning of p-type GaN*. Appl. Phys. Lett. *98*, 071102.

134. Fu, X., Zhang, B., Kang, X., Deng, J., Xiong, C., Dai, T., Jiang, X., Yu, T., Chen, Z., and Zhang, G.Y. (2011). *GaN-based light-emitting diodes with photonic crystals structures fabricated by porous anodic alumina template*. Opt. Express *19*, A1104–A1108.

135. Carvajal, J.J., and Rojo, J.C. (2009). *Morphology Control in As-Grown GaN Nanoporous Particles.* Cryst. Growth Des. *9*, 320–326.

136. Sudarshan, E. by J.-H.P. and T.S. (2000). *Surface Engineering Series Volume 2: Chemical Vapor Deposition*. (ASM International).

137. Sato, M. (1997). *Nitrogen radical densities during GaN growth by molecular beam epitaxy, plasma-assisted metalorganic chemical vapor deposition, and conventional metalorganic chemical vapor deposition*. Solid-State Electron. *41*, 223–226.

138. Mackenzie, J.D. (2003). *Sol-Gel Research — Achievements Since 1981 and Prospects for the Future.* J. Sol-Gel Sci. Technol. *26*, 23–27.

139. Jaworek, A. (2010). *Electrospray Technology for Thin Film Devices Deposition.* (Nova Science Publishers, Incorporated).

140. Zhou, W., Apkarian, R., Wang, Z.L., and Joy, D. (2007). *Fundamentals of Scanning Electron Microscopy (SEM).* In Scanning Microscopy for Nanotechnology, W. Zhou, and Z.L. Wang, eds. (Springer New York), pp. 1–40.

141. Williams, D.B., and Carter, C.B. (1996). *Transmission Electron Microscopy: A Textbook for Materials Science*. (Springer).

142. Wirth, R. (2009). *Focused Ion Beam (FIB) combined with SEM and TEM: Advanced analytical tools for studies of chemical composition, microstructure and crystal structure in geomaterials on a nanometre scale*. Chem. Geol. *261*, 217–229.

143. Eaton, P., and West, P. (2010). *Atomic Force Microscopy* (OUP Oxford).

144. From http://analyticalprofessional.blogspot.com.es/2013/05/atomic-force-microscopy.html

145. Haugstad, G. (2012). *Atomic Force Microscopy: Understanding Basic Modes and Advanced Applications*. (John Wiley & Sons).

146. Suryanarayana, C., and Norton, M.G. (1998). *X-Ray Diffraction: A Practical Approach.* (Springer).

147. Ferraro, J.R. (2003). *Introductory Raman Spectroscopy.* (Academic Press).

148. Seshan, K. (2002). *Handbook of thin-film deposition processes and techiques. Principles, Methods, Equipment and Applications. Second Edition*. Noyes Publications/William Andrew Publishing, New York (USA).

149. Franssila, S. (2004). *Introduction to Microfabrication*. (Wiley).

150. Madou, M.J. (2002). *Fundamentals of Microfabrication: The Science of Miniaturization.* Second Edition (CRC Press).

151. Schroder, D.K. (2006). *Semiconductor Material and Device Characterization.* (John Wiley & Sons).

152. Van der Pauw, L. (1958). *A method of measuring specific resistivity and Hall effect of discs of arbitrary shape*. Philips ResRep *13*.

153. Tang, Z., and Wie, C.R. (2010). *Capacitance–voltage characteristics and device simulation of bias temperature stressed a-Si:H TFTs*. Solid-State Electron. *54*, 259–267.

154. Hurni, C.A., Kroemer, H., Mishra, U.K., and Speck, J.S. (2012). *Capacitance-voltage profiling on polar III-nitride heterostructures*. J. Appl. Phys. *112*, 083704.

155. Kim, K., Choi, P., Kim, H., Park, H., and Choi, B. (2013). *Determination of the Drain Saturation Voltage of a Metal–Oxide–Semiconductor Field-Effect Transistor by the Capacitance–Voltage Method*. Jpn. J. Appl. Phys. *52*, 068005.

156. Levinshtein, M.E., Rumyantsev, S.L., and Shur, M.S. (2001). *Properties of Advanced Semiconductor Materials: GaN, AIN, InN, BN, SiC, SiGe.* (John Wiley & Sons).

157. Ozawa, L. (2010). *Cathodoluminescence and Photoluminescence: Theories and Practical Applications.* (CRC Press).

158. Boggs/Krinsley (2006). *Application of Cathodoluminescence Imaging to the Study of Sedimentary Rocks*. (Cambridge University Press).

159. Sung, M.M., Kim, C., Yoo, S.H., Kim, C.G., and Kim, Y. (2002). *CVD of GaN Films on Si(111). Chemically Clean Decomposition of* $Et_2Ga(N_3)\cdot MeHNNH_2$. Chem. Vap. Depos. *8*, 50–52.

160. He, M., and Mohammad, S.N. (2007). *Structural characteristics of single-crystal nanowires grown by self-catalytic chemical vapor deposition method*. J. Vac. Sci. Technol. B *25*, 1909–1915.

161. Gottschalch, V., Wagner, G., Bauer, J., Paetzelt, H., and Shirnow, M. (2008). *VLS growth of GaN nanowires on various substrates*. J. Cryst. Growth *310*, 5123–5128.

162. Hou, W.-C., Chen, L.-Y., Tang, W.-C., and Hong, F.C.N. (2011). *Control of Seed Detachment in Au-Assisted GaN Nanowire Growths.* Cryst. Growth Des. *11*, 990–994.

163. Kim, T.Y., Lee, S.H., Mo, Y.H., Nahm, K.S., Shim, H.W., Suh, E.-K., Lee, S.H., and Park, G.S. (2003). *Growth of GaN nanowires on Si substrate using Ni catalyst in vertical chemical vapor deposition reactor*. In 2003 Third IEEE Conference on Nanotechnology, 2003. IEEE-NANO 2003, pp. 815–818 vol. 2.

164. Tracy, K.M., Hartlieb, P.J., Einfeldt, S., Davis, R.F., Hurt, E.H., and Nemanich, R.J. (2003). *Electrical and chemical characterization of the Schottky barrier formed between clean n-GaN(0001) surfaces and Pt, Au, and Ag.* J. Appl. Phys. *94*, 3939–3948.

165. Lin, M.E., Ma, Z., Huang, F.Y., Fan, Z.F., Allen, L.H., and Morkoç, H. (1994). *Low resistance ohmic contacts on wide band-gap GaN*. Appl. Phys. Lett. *64*, 1003–1005.

166. Schmitzy, A. C., Pingy, A. T., Khanz, M. Asif, Chenz, Q., Yangz, J. W., and Adesiday, I. (1996). *Schottky barrier properties of various metals on n-type GaN*. Semicond. Sci. Technol. *11*:464–1467.

167. Sporken, R., Silien, C., Malengreau, F., Grigorov, K., Caudano, R., Sanchez, F. J., Calleja E., Munoz, E., Beaumont, B. and Gibart, P. (1997). *XPS study of Au/GaN and Pt/GaN contacts.* MRS Internet J. Nitride Semicond. Res. *2*:23.

168. Glaser, E.R., Kennedy, T.A., Doverspike, K., Rowland, L.B., Gaskill, D.K., Freitas, J.A., Asif Khan, M., Olson, D.T., Kuznia, J.N., and Wickenden, D.K. (1995). *Optically detected magnetic resonance of GaN films grown by organometallic chemical-vapor deposition.* Phys. Rev. B *51*, 13326–13336.

169. Aoki, M., Yamane, H., Shimada, M., Sekiguchi, T., Hanada, T., Yao, T., Sarayama, S., and Di Salvo, F. J. (2000). *Growth of GaN single crystals from a Na-Ga melt at 750 ^{o}C and 5MPa of N_2.* J. Cryst. Growth. *218*:7-12.

170. Toth, M., Fleischer, K., and Phillips, M.R. (1999). *Direct experimental evidence for the role of oxygen in the luminescent properties of GaN*. Phys. Rev. B *59*, 1575–1578.

171. Fleischer, K., Toth, M., Phillips, M.R., Zou, J., Li, G., and Chua, S.J. (1999). *Depth profiling of GaN by cathodoluminescence microanalysis*. Appl. Phys. Lett. *74*, 1114–1116.

172. Reshchikov, M.A., Morkoç, H., Park, S.S., and Lee, K.Y. (2001). *Yellow and green luminescence in a freestanding GaN template*. Appl. Phys. Lett. *78*, 3041–3043.

173. Kim, S.J., Kim, J.E., and Yang, Y.S. (2004). *Directional growth by low electric-field-controlled crystallization of bulk amorphous lithium tetraborate*. Appl. Phys. Lett. *85*, 5956–5958.

174. Choi, J.H., Zoulkarneev, A., Kim, S.I., Baik, C.W., Yang, M.H., Park, S.S., Suh, H., Kim, U.J., Bin Son, H., Lee, J.S., et al. (2011). *Nearly single-crystalline GaN light-emitting diodes on amorphous glass substrates*. Nat. Photonics *5*, 763–769.

175. Nakamura, S., Senoh, M., and Mukai, T. (1993). *High-power InGaN/GaN double-heterostructure violet light emitting diodes.* Appl. Phys. Lett. *62*, 2390–2392.

176. Strite, S., and Morkoç, H. (1992). *GaN, AlN, and InN: A review*. J. Vac. Sci. Technol. B *10*, 1237–1266.

177. Akasaki, I., and Amano, H. (1994). *Widegap column-III nitride semiconductors for UV/blue light emitting devices*. J. Electrochem. Soc. *141*, 2266–2271.

178. Götz, W., Johnson, N.M., Walker, J., Bour, D.P., and Street, R.A. (1996). *Activation of acceptors in Mg-doped GaN grown by metalorganic chemical vapor deposition*. Appl. Phys. Lett. *68*, 667–669.

179. Nakamura, S., Iwasa, N., Senoh, M., and Mukai, T. (1992). *Hole Compensation Mechanism of P-Type GaN Films*. Jpn. J. Appl. Phys. *31*, 1258-1266.

180. Nakagawa, Y., Haraguchi, M., Fukui, M., Tanaka, S., Sakaki, A., Kususe, K., Hosokawa, N., Takehara, T., Morioka, Y., Iijima, H., et al. (2004). *Hydrogen Dissociation from Mg-doped GaN*. Jpn. J. Appl. Phys. *43*, 23-29.

181. Kaufmann, U., Kunzer, M., Maier, M., Obloh, H., Ramakrishnan, A., Santic, B., and Schlotter, P. (1998). *Nature of the 2.8 eV photoluminescence band in Mg doped GaN*. Appl. Phys. Lett. *72*, 1326–1328.

182. Nakamura, S., Mukai, T., Senoh, M., and Iwasa, N. (1992). *Thermal Annealing Effects on P-Type Mg-Doped GaN Films*. Jpn. J. Appl. Phys. *31*, L139-L142.

183. Harima, H., Inoue, T., Nakashima, S., Ishida, M., and Taneya, M. (1999). *Local vibrational modes as a probe of activation process in p-type GaN*. Appl. Phys. Lett. *75*, 1383–1385.

184. Myers, S.M., Seager, C.H., Wright, A.F., Vaandrager, B.L., and Nelson, J.S. (2002). *Electron-beam dissociation of the MgH complex in p-type GaN*. J. Appl. Phys. *92*, 6630–6635.

185. http://www.alfa.com/de/GP100w.pgm?DSSTK=41946

186. http://www.sigmaaldrich.com/catalog/product/aldrich/129577?lang=es&region=ES

187. Zhong, Z., Qian, F., Wang, D., and Lieber, C.M. (2003). *Synthesis of p-Type Gallium Nitride Nanowires for Electronic and Photonic Nanodevices.* Nano Lett. *3*, 343–346.

188. Hoene, J.V., Charles, R.G., and Hickam, W.M. (1958). *Thermal Decomposition of Metal Acetylacetonates: Mass Spectrometer Studies*. J. Phys. Chem. *62*, 1098–1101.

189. Ponce, F.A., Bour, D.P., Götz, W., and Wright, P.J. (1996). *Spatial distribution of the luminescence in GaN thin films*. Appl. Phys. Lett. *68*, 57–59.

190. Koide, Y., Jr, D.E.W., White, B.D., Brillson, L.J., Murakami, M., Kamiyama, S., Amano, H., and Akasaki, I. (2002). *Simultaneous observation of luminescence and dissociation processes of Mg–H complex for Mg-doped GaN*. J. Appl. Phys. *92*, 3657–3661.

191. Franssen, G., Litwin-Staszewska, E., Piotrzkowski, R., Suski, T., and Perlin, P. (2003). *Optical and electrical properties of homoepitaxially grown multiquantum well InGaN/GaN light-emitting diodes*. J. Appl. Phys. *94*, 6122–6128.

192. Tsao, H.-Y., Lin, Y.-J., Chen, Y.-H., and Chang, H.-C. (2011). *Leakage currents through In/MgO/n-type Si/In structures*. Solid State Commun. *151*, 693–696.

193. http://www.sigmaaldrich.com/catalog/product/aldrich/465755?lang=es&region=ES

194. Huang, T., Parrish, W., Masciocchi, N., Wang, P. (1990). Adv. X-ray Anal. *33*, 295.

195. Hannam, A. L., and Shaffer P. T. B. *Revised X-ray diffraction line intensities for silicon carbide polytypes*. (1969). J. Appl. Cryst. *2*, 45-48.

196. Schulz, H., and Thiemann, K.H. (1977). *Crystal structure refinement of AlN and GaN*. Solid State Commun. *23*, 815–819.

197. Balkas, C.M., Basceri, C., and Davis, R.F. (1995). *Synthesis and characterization of high purity, single phase GaN powder*. Powder Diffr. *10*, 266–268.

198. Pernot, J., Bustarret, E., Rudzinski, M., Hageman, P.R., and Larsen, P.K. (2007). *Strain relaxation in GaN grown on vicinal 4H-SiC(0001) substrates*. J. Appl. Phys. *101*, 033536.

199. Moon, Y.T., Fu, Y., Yun, F., Dogan, S., Mikkelson, M., Johnstone, D., and Morkoç, H. (2005). *A study of GaN regrowth on the micro-facetted GaN template formed by in-situ thermal etching*. Phys. Status Solidi A *202*, 718–721.

200. Pearton, S.J., Wilson, R.G., Zavada, J.M., Han, J., and Shul, R.J. (1998). *Thermal stability of 2H-implanted n- and p-type GaN*. Appl. Phys. Lett. *73*, 1877–1879.

201. Görgens, L., Ambacher, O., Stutzmann, M., Miskys, C., Scholz, F., and Off, J. (2000). *Characterization of InGaN thin films using high-resolution x-ray diffraction*. Appl. Phys. Lett. *76*, 577–579.

202. Shan, W., Ager, J.W., Walukiewicz, W., Haller, E.E., Little, B.D., Song, J.-J., Schurman, M., Feng, Z.C., Stall, R.A., and Goldenberg, B. (1998). *Near-band-edge photoluminescence emission in AlxGa1-xN under high pressure.* Appl. Phys. Lett. *72*, 2274–2276.

203. Neugebauer, J., and Walle, C.G.V. de (1996). *Gallium vacancies and the yellow luminescence in GaN*. Appl. Phys. Lett. *69*, 503–505.

204. Gelhausen, O., Klein, H.N., Phillips, M.R., and Goldys, E.M. (2003). *Low-energy electron-beam irradiation and yellow luminescence in activated Mg-doped GaN*. Appl. Phys. Lett. *83*, 3293–3295.

205. Dassonneville, S., Amokrane, A., Sieber, B., Farvacque, J.-L., Beaumont, B., and Gibart, P. (2001). *Luminescence of epitaxial GaN laterally overgrown on (0001) sapphire substrate: Spectroscopic characterization and dislocation contrasts*. J. Appl. Phys. *89*, 3736–3743.

206. Song, J.-O., Ha, J.-S., and Seong, T.-Y. (2010). *Ohmic-Contact Technology for GaN-Based Light-Emitting Diodes: Role of P-Type Contact*. IEEE Trans. Electron Devices *57*, 42–59.

207. Yang, Y., Ling, Y., Wang, G., Lu, X., Tong, Y., and Li, Y. (2013). *Growth of gallium nitride and indium nitride nanowires on conductive and flexible carbon cloth substrates*. Nanoscale *5*, 1820–1824.

208. Hu, Y., Zhuang, W., Ye, H., Zhang, S., Fang, Y., and Huang, X. (2005). *Preparation and luminescent properties of (Ca1-x,Srx)S:Eu^{2+} red-emitting phosphor for white LED*. J. Lumin. *111*, 139–145.

209. Yan, S., Zhang, J., Zhang, X., Lu, S., Ren, X., Nie, Z., and Wang, X. (2007). *Enhanced Red Emission in CaMoO4:Bi^{3+},Eu^{3+}*. J. Phys. Chem. C *111*, 13256–13260.

210. Wang, Y., Sun, Y., Zhang, J., Ci, Z., Zhang, Z., and Wang, L. (2008). *New red $Y_{0.85}Bi_{0.1}Eu_{0.05}V_{1-y}M_yO_4$ (M=Nb, P) phosphors for light-emitting diodes.* Phys. B Condens. Matter *403*, 2071–2075.

211. Thomas, M., Prabhakar Rao, P., Deepa, M., Chandran, M.R., and Koshy, P. (2009). *Novel powellite-based red-emitting phosphors: $CaLa_{1-x}NbMoO_8$:xEu^{3+} for white light emitting diodes*. J. Solid State Chem. *182*, 203–207.

212. Strel'tsov, A.V., Dmitrienko, V.P., Akmaeva, T.A., Kudryavtsev, S.V., Dmitrienko, A.O., Razumov, K.A. (2009). *The influence of activation of Y_2O_3polycrystalline matrices by Bi^{3+} ions on the luminescence of Y_2O_3:Eu^{3+}*. Inorg. Mater. *45*, 889.

213. Chi, L.S., Liu, R.S., and Lee, B.J. (2005). *Synthesis of Y2O3 : Eu , Bi Red Phosphors by Homogeneous Coprecipitation and Their Photoluminescence Behaviors*. J. Electrochem. Soc. *152*, J93–J98.

214. Galceran, M., Pujol, M.C., Aguiló, M., and Díaz, F. (2007). *Sol-gel modified Pechini method for obtaining nanocrystalline KRE(WO4)2 (RE = Gd and Yb).* J. Sol-Gel Sci. Technol. *42*, 79–88.

215. Koch, C., Ovid'ko, I., Seal, S., and Veprek, S. (2007). *Structural Nanocrystalline Materials: Fundamentals and Applications* (Cambridge University Press).

216. Sun, L., Liao, C., and Yan, C. (2003). *Structure transition and enhanced photoluminescence of $Gd_{2-x}YxO_3$:Eu nanocrystals*. J. Solid State Chem. *171*, 304–307.

217. Méndez, M., Carvajal, J.J., Cesteros, Y., Marsal, L.F., Martínez-Ferrero, E., Giguere, A., Drouin, D., Salagre, P., Formentín, P., Pallarès, J., et al. (2010). *Photoluminescence and cathodoluminescence of Eu: La_2O_3 nanoparticles synthesized by several methods*. Phys. Procedia *8*, 114–120.

218. Porter-Chapman, Y., Bourret-Courchesne, E., and Derenzo, S.E. (2008). *Bi^{3+} luminescence in $ABiO_2Cl$ (A=Sr, Ba) and $BaBiO_2Br$*. J. Lumin. *128*, 87–91.

219. Castro Neto, A.H., Guinea, F., Peres, N.M.R., Novoselov, K.S., and Geim, A.K. (2009). *The electronic properties of graphene*. Rev. Mod. Phys. *81*, 109–162.

220. Soldano, C., Mahmood, A., and Dujardin, E. (2010). *Production, properties and potential of graphene*. Carbon *48*, 2127–2150.

221. Novoselov, K.S., Geim, A.K., Morozov, S.V., Jiang, D., Zhang, Y., Dubonos, S.V., Grigorieva, I.V., and Firsov, A.A. (2004). *Electric Field Effect in Atomically Thin Carbon Films.* Science *306*, 666–669.

222. Kim, K.S., Zhao, Y., Jang, H., Lee, S.Y., Kim, J.M., Kim, K.S., Ahn, J.-H., Kim, P., Choi, J.-Y., and Hong, B.H. (2009). *Large-scale pattern growth of graphene films for stretchable transparent electrodes.* Nature *457*, 706–710.

223. Sutter, P.W., Flege, J.-I., and Sutter, E.A. (2008). *Epitaxial graphene on ruthenium*. Nat. Mater. *7*, 406–411.

224. Berger, C., Song, Z., Li, T., Li, X., Ogbazghi, A.Y., Feng, R., Dai, Z., Marchenkov, A.N., Conrad, E.H., First, P.N., et al. (2004). *Ultrathin Epitaxial Graphite: 2D Electron Gas Properties and a Route toward Graphene-based Nanoelectronics*. J. Phys. Chem. B *108*, 19912–19916.

225. Park, S., and Ruoff, R.S. (2009). *Chemical methods for the production of graphenes*. Nat. Nanotechnol. *4*, 217–224.

226. Fan, Z.-J., Kai, W., Yan, J., Wei, T., Zhi, L.-J., Feng, J., Ren, Y., Song, L.-P., and Wei, F. (2011). *Facile Synthesis of Graphene Nanosheets via Fe Reduction of Exfoliated Graphite Oxide*. ACS Nano *5*, 191–198.

227. Staudenmaier, L. (1898). Ber. Dtsch. Chem. Ges. *31*, 1481–1487.

228. Ferrari, A.C., Meyer, J.C., Scardaci, V., Casiraghi, C., Lazzeri, M., Mauri, F., Piscanec, S., Jiang, D., Novoselov, K.S., Roth, S., et al. (2006). *Raman Spectrum of Graphene and Graphene Layers.* Phys. Rev. Lett. *97*, 187401.

229. Dresselhaus, M.S., Jorio, A., and Saito, R. (2010). *Characterizing Graphene, Graphite, and Carbon Nanotubes by Raman Spectroscopy*. Annu. Rev. Condens. Matter Phys. *1*, 89–108.

230. Kudin, K.N., Ozbas, B., Schniepp, H.C., Prud'homme, R.K., Aksay, I.A., and Car, R. (2008). *Raman Spectra of Graphite Oxide and Functionalized Graphene Sheets*. Nano Lett. *8*, 36–41.

231. Reich, S., and Thomsen, C. (2004). *Raman spectroscopy of graphite.* Philos. Trans. R. Soc. Lond. Ser. Math. Phys. Eng. Sci. *362*, 2271–2288.

232. Basko, D.M., Piscanec, S., and Ferrari, A.C. (2009). *Electron-electron interactions and doping dependence of the two-phonon Raman intensity in graphene*. Phys. Rev. B *80*, 165413.

233. Baibarac, M., Baltog, I., Mihut, L., Pasuk, I., and Lefrant, S. (2013). *Casimir effect demonstrated by Raman spectroscopy on trilayer graphene intercalated into stiff layered structures of surfactant*. Carbon *51*, 134–142.

234. Ferrari, A.C., and Robertson, J. (2000). *Interpretation of Raman spectra of disordered and amorphous carbon*. Phys. Rev. B *61*, 14095–14107.

235. Gray, D., McCaughan, A., and Mookerji, B. (2009). *Crystal Structure of Graphite, Graphene and Silicon*. Physics for Solid State Applications *6*, 730.

236. Hassan, H.M.A., Abdelsayed, V., Khder, A.E.R.S., AbouZeid, K.M., Terner, J., El-Shall, M.S., Al-Resayes, S.I., and El-Azhary, A.A. (2009). *Microwave synthesis of graphene sheets supporting metal nanocrystals in aqueous and organic media*. J. Mater. Chem. *19*, 3832–3837.

237. Jang, S.-Y., Kim, Y.-G., Kim, D.Y., Kim, H.-G., and Jo, S.M. (2012). *Electrodynamically sprayed thin films of aqueous dispersible graphene nanosheets: highly efficient cathodes for dye-sensitized solar cells*. ACS Appl. Mater. Interfaces *4*, 3500–3507.

238. Zan, R., Ramasse, Q.M., Bangert, U., and Novoselov, K.S. (2012). *Graphene Reknits Its Holes*. Nano Lett. *12*, 3936–3940.

Paper I

Mena, J.; Carvajal, J.J.; Bilousov, O.V.; Díaz, F. and M. Aguiló. *Optimization of the growth conditions of nanoporous GaN particles by Chemical Vapor Deposition.* Submitted to CrystEngComm.

Optimization of the growth conditions of nanoporous GaN particles by Chemical Vapor Deposition

J. Mena, J.J. Carvajal*, O. Bilousov, F. Díaz, M. Aguiló
Física i Cristal·lografía de Materials i Nanomaterials (FiCMA-FiCNA) and EMaS, Universitat Rovira i Virgili (URV), Marcel·lí Domingo, s/n, Tarragona, E-43007 Spain.

Abstract: With this paper we go beyond the analysis performed in previous works based on the influence of different parameters in the production of as-grown nanoporous GaN particles by the direct reaction of Ga and NH_3 in a chemical vapour deposition (CVD) system, without requiring any post-growth treatment to induce porosity. The parameters analyzed previously were temperature that influences the porosity and coalescence of pores, NH_3 flow rate which influences the degree of nanoporosity of the GaN particles and the pressure of the CVD system which controls the external shape of the particles. Now we analyze the effect of other reaction parameters such as the Ga holder shape, Ga quantity, the deposition time, the influence of the catalyst and the substrate, on the porous particles obtained at a morphological and structural level, as well as in terms of porosity. The Ga holder shape effects to the size of the pores, the Ga quantity as well as the deposition time have an effect on the coverage of the substrate by nanoporous GaN particles, and both the catalyst and substrate play a role in the morphology and crystallographic orientation of the particles.

INTRODUCTION

GaN is a III-V wide band-gap semiconductor crystallizing in the hexagonal system with wurtzite crystal structure ($P6_3mc$ space group). Its direct band-gap is 3.4 eV, which is an intrinsic characteristic to all III-nitride semiconductors, including AlN (6.2eV)[1] and InN (0.9eV)[2]. Owing to their similar structural and physical properties III-nitrides can combine producing AlGaInN heterostructures with band-gaps that can cover ranges from the near infrared (NIR) to the deep ultraviolet (UV). As a result III-nitrides revolutionized the LED technology[3]. That is what makes GaN a promising material for developing applications in optoelectronic devices in the UV-visible range. GaN is also suitable for high temperature optoelectronic applications owing to its high bond strength[4].

One of the disadvantages of GaN for optoelectronics applications, especially for thje development of LEDs, is the big refractive index contrast between GaN (n=2.5)[5] and air (n=1) that confines light inside the material and only photons below the critical angle θ_c=23° can escape the material[5]. The classical approach used to solve this problem has been the coverage of the material with a polymeric capsule with an intermediate refraction index[6]. Nevertheless, this approach is no longer valid in high power applications since the polymer coverage can be easily damaged by the emitted intensity of the LED, becoming opaque, and reducing the light emitting properties of the device. An alternative approach to increase the light extraction efficiency of GaN based unencapsulated LEDs is the use of porous GaN[7]. The induced porosity in the material increases the reflection probabilities of emitted photons, and provides additional surfaces through which photons can escape[8].

Many attempts have been done in order to improve light extraction efficiency from GaN LEDs from surface roughening as a first approach[8], until the formation of porous structures of GaN by different techniques ranging from electrochemical etching[9], photoelectrochemical etching[10], metal-assisted electroless[11], use of anodic porous alumina templates[12], all of them with a successful result in the enhancement of the light extraction efficiency.

Classical methods to produce porous GaN are based on corrosive and etching techniques[13]. However, these techniques can damage the GaN surface, leading to crystal defects and rough surfaces that might affect the electrical and optical properties of the material. Based on the studies developed by ourselves[14] we use a non etching approximation to produce porous GaN using the direct reaction between metallic Ga

and NH_3 in a Chemical Vapor Deposition (CVD) system, in one single step without requiring any post-growth treatment to induce the porosity.

Despite all the potential applications of nanoporous GaN for LED applications its integration on Si technology on which microelectronic industry is based, is very challenging[15]. In 2012 we presented the possibility of an easy integration of nanoporous GaN on Si substrates coated with a metallic catalyst[16]. Furthermore, the addition of this metallic catalyst allows the formation of a metallic contact that can be used for further electrical characterization of porous GaN and device fabrication. In this context, low resistivity Ohmic contacts have been demonstrated on porous GaN grown on Si substrates coated with high workfunction metals such as Au and Pt[17].

In the present work we analyze morphologically and structurally the nanoporous GaN particles obtained by the direct reaction between Ga and NH_3 in a CVD system by exploring the effect of different experimental conditions, such as the gallium holder shape, deposition time, the amount of Ga, the metallic catalyst and the substrate used in order to optimize the crystal growth conditions to obtain single crystal porous GaN micron-size particles. The control of morphology, nanoporous density, and crystallographic orientation of the GaN particles are important parameters for advanced light emitting applications.

EXPERIMENTAL SECTION

Crystal growth. Nanoporous GaN particles were grown on different substrates by the direct reaction of metallic Ga (Alfa Aesar 99.999%) and NH_3 (Carburos Metalicos >99.98%) as Ga and N sources, respectively, in a CVD horizontal tubular furnace. An scheme of the CVD set up is shown in Figure 1.

Metallic Ga was introduced into the system in the form of a droplet onto a quartz crucible. The quartz crucibles or Ga holders were made in three different shapes: flat plate (the spreading of the Ga drop on the surface of the crucible was not limited), half of a cylindrical tube (spreading of Ga was limited from two sides) and concave crucible (the spreading of Ga is limited from all sides).

As substrates we used silicon wafers with (100) and (111) crystallographic orientations, pyrolitic-boron nitride (BN) and tungsten wire. The substrate was placed above the Ga source at a vertical distance of 2 cm onto a BN support. Previous to their introduction in the furnace, the silicon substrates were cleaned with piranha solution and then with ethanol while, the rest of the substrates were cleaned only with ethanol.

In our experiments as catalysts we used $Ni(NO_3)_2$, where the catalyst was deposited on the surface of the substrate by spreading several drops of an ethanolic solution of $Ni(NO_3)_2$, and continuous films, 20 nm thick, of Au, Pt, Ti, Ni and W deposited on the substrates by RF sputtering (AJA International) at a power of 150 W and a pressure of 3 mTorr.

In a typical experiment of crystal growth the quartz reactor, 5 cm in diameter and 1 m long, was degassed to a vacuum pressure of 1×10^{-2} Torr. Ammonia was then introduced through a mass-flow controller at 75 sccm from one end of the quartz reactor and the furnace was heated up to the reaction temperature of 1200K. Then, the furnace was kept at this temperature during the reaction time, that we have changed between 30-120 min, under a constant flow of NH_3, keeping the pressure of the system constant at 15 torr while the chemical reaction was taking place. When the reaction was finished, we cooled down the furnace to room temperature while we stopped the ammonia flow.

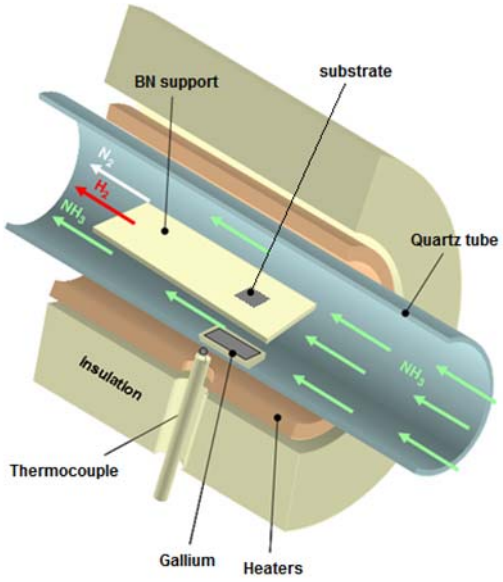

Figure 1. Schematic representation of the CVD system used for the crystal growth of nanoporous GaN micron-size particles.

Morphological and structural characterization. The nanoporous GaN microparticles deposited on the Si substrates were characterized morphologically using a JEOL
JSM 6400 scanning electron microscope (SEM). Before observation, samples were Au coated in a Bal-Tec SCD004 sputterer.

The thickness of the nanoporous GaN particles layers were measured with a PLμ2300 SENSOFAR optical imaging profiler that combines confocal and interferometric techniques to measure the surface topography. The thickness of the porous layer was determined by comparing the height measured in the non-coated substrate, and the part of the substrate coated by the porous layer.

X-ray diffraction (XRD) patterns of the samples were recorded in a Bruker-AXS D8-Discover diffractometer equipped with parallel incident beam (Göbel mirror), a vertical θ-θ goniometer, and a General Area Diffraction Detection System (GADDS) HI-STAR detector with a multiwire proportional counter with an area of 30 × 30 cm and 1024 × 1024 pixel density. The X-ray diffractometer was operated at 40 kV and 40 mA to generate Cu Kα radiation. Data were recorded from 20-90° in 2θ range. The incident beam and the detector were at a distance of 15 cm of the sample. Identification of the crystalline phases obtained was achieved by comparing the XRD diffractogram with the Joint Committee on Powder Diffraction Standards (JCPDS) database using Diffrac^{plus} Evaluation software.

RESULTS AND DISCUSION

Effect of the shape of the gallium holder. A set of experiments with several holders for Ga with different shapes were carried out to analyze how the shape of the crucible affected the spreading of the Ga droplet, and how this affected to the final shape and porosity of the particles obtained.

Figure 2 shows the evolution of the spreading of the Ga droplet as the temperature increased for the different Ga holders analyzed. Through the optical window, located at one end of the CVD reactor, we recorded the evolution of the Ga droplet during the growth process with a CCD camera to which we coupled a telescope.

Figure 2(a) shows the evolution of the Ga droplet on the flat plate holder. Up to 1177 K the GaN droplet remained unaffected.

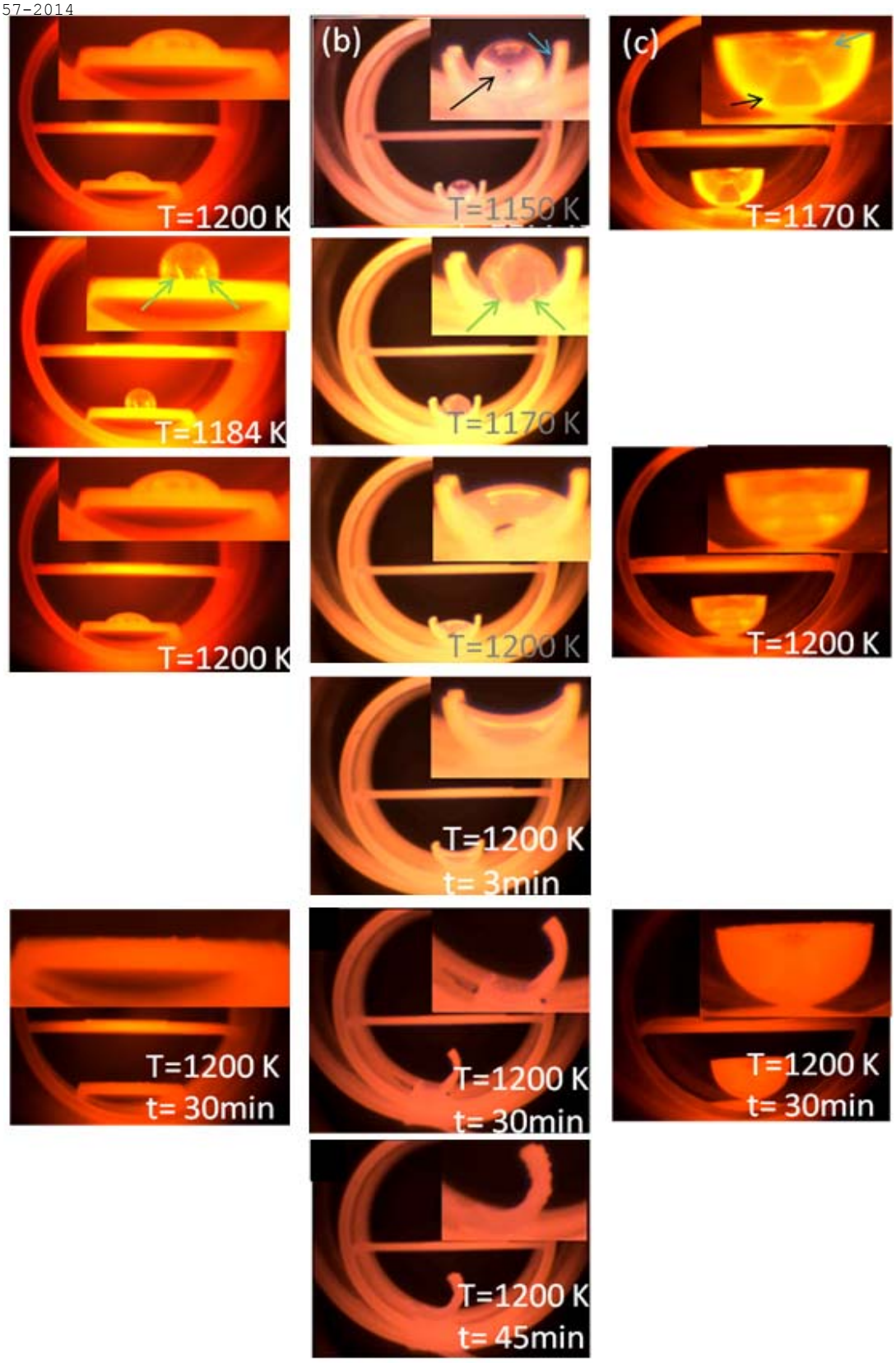

Figure 2. Optical images in front-side view taken inside the horizontal tube furnace showing the evolution (cracks are pointed with a green arrow) of the Ga droplet (pointed with a black arrow in the first row of images) with the different Ga holders (pointed with a blue arrow) used in these experiments: (a) flat plate, (b) half cylindrical tube and (c) concave crucible.

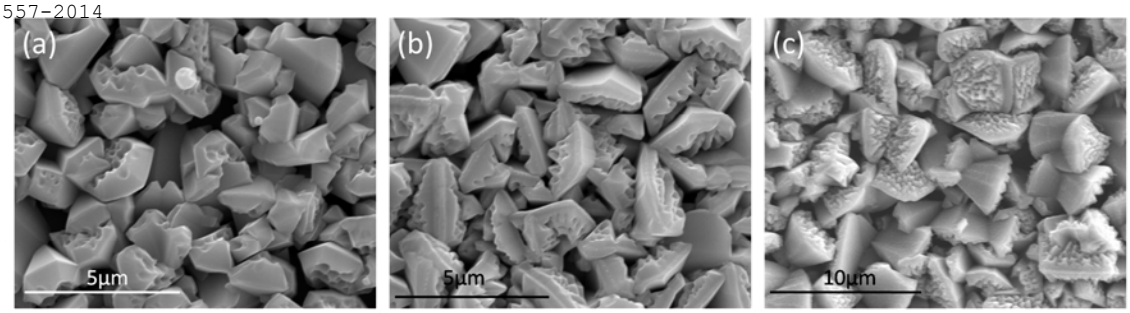

Figure 3. SEM pictures of the nanoporous GaN particles obtained using different Ga holders: (a) flat plate, (b) half cylindrical tube, and (c) concave crucible.

From that moment some cracks appeared at the bottom part of the Ga droplet, the part in contact with the Ga holder, marked with green arrows in Figure 2. It is from these cracks that the surface tension of the liquid Ga is broken and the Ga droplet started to spread out. 2 min after the formation of the cracks the furnace reached a temperature of 1200 K, and the Ga droplet totally spread. Finally, at around 30 min after the furnace reached 1200 K we observed a scalation of the material covering the crucible, identified later as GaN by XRD.

Figure 2(b) shows the evolution of the Ga droplet on the half of a cylindrical tube holder, similar to that observed in the flat plate holder. However, the temperatures at which each step of the spreading out process of the Ga dropplet happened were different. The cracks at the bottom of the Ga droplet started to appear at 1170 K, earlier than when the flat holder was used. After 3 min the furnace reached 1200 K, the meniscus of the Ga droplet passed from a convex shape towards a concave shape, indicating that the surface tension was reduced. From that moment, the liquid Ga climbed through the holder walls and spread also on the quartz liner tube. This caused the leaning of the Ga holder at around 30 min after the furnace reached 1200 K. Finally, the scalation of the material covering of the crucible occurred at around 45 min after the furnace reached 1200 K, later than in the previous case.

When using the concave holder (see Figure 2(c)), the Ga droplet followed a similar behaviour as in the previous cases. However, it was impossible to see clearly what was happening inside the concave holder. Thus, we could not establish very well at which temperature each phenomena occurred. What we could clearly see was that when the Ga droplet reached a temperature of 1200 K it started to climb through the walls of the holder until it spread over the quartz liner. In this case nor lean of the Ga holder, neither scalation of material was observed.

SEM pictures of the GaN samples synthesized using different Ga holders on (100) silicon substrates covered with Ni are shown in Figure 3. In all cases, the temperature of reaction was chosen to ensure the total spread out of the Ga droplet, generating the maximum extension of the surface of metallic Ga to favour the evaporation of this precursor. The GaN particles obtained when using a flat plate or a half cylindrical tube as Ga holders we similar, with sizes between 2-3µm, and a similar degree of porosity (see Figures 3(a) and 3(b)). The particles obtained using the concave crucible (see Figure 3(c)) show bigger sizes (around 4 µm), and the pores seem to be smaller in diameter and do not form ridges, giving a more rough aspect to the surface of the particles.

Topological profiles were recorded with a confocal-interferometric microscope to analyze the thickness of the layer of nanoporous GaN particles along the substrate. Depending on the shape of the Ga holder used, the thickness of the layer seems not to be uniform along the substrate. The sample grown using a flat plate had the maximum ununiformity in thickness with an average value of 2.53 ±1.73 µm. The sample grown using a half cylindrical tube has the smallest thickness, 1.1 ±0.14 µm, but with a higher uniformity. Finally, the highest thickness value was obtained in the sample grown using the concave crucible, with a mean value of 3.61 ± 0.87 µm. According to these measurements, despite the thickness of the layer obtained using a half cylindrical tube was the smallest, it was very uniform, what is a necessary condition for the fabrication of functional devices based on these nanoporous GaN particles. Thus, in the rest of the experiments, we used this kind of Ga holder.

Effect of the Ga quantity. Three sets of experiments with the introduction of different amounts of Ga at the beginning of the experiment (0.2 g (N/Ga: 70.04) , 0.4 g (N/Ga: 53.02) and 0.6 g (N/Ga: 23.35)) were

carried out to analyze its effect on the coverage of the substrate with nanoporous GaN particles, while keeping constant the other reaction parameters. Figure 4 shows SEM pictures of the GaN particles grown using different amounts of Ga. In the three cases hexagonal nanoporous particles were obtained with different particle diameter, but more importantly, with different substrate coverage.

When 0.2 g of Ga were used (see Figure 4(a)) a low degree of substrate coverage can be observed. This is attributed to the low Ga evaporated and deposited on the substrate forming a small number of nucleuses along the substrate. This is confirmed by the fact that particles are bigger in diameter than in the other cases, around 5-6 μm. A higher coverage of nanoporous GaN particles can be seen when 0.4 g of Ga were used (see Figure 4(b)). In contrast with the previous case, the particle diameter is lower of around 2μm. This is attributed to the higher evaporation of Ga and the formation of a higher number of Ga-metallic catalyst nucleuses which leads to a higher coverage of the substrate with smaller nanoporous GaN particles. Finally in Figure 4(c) we can see a SEM image of GaN particles grown using 0.6 g of Ga. A similar particles density and size is observed when compared to the experiment using 0.4 g of Ga. This would indicate that it exist a quantity of Ga above which no more GaN particles are formed, probably related to the Ga/N ratio used. Interferometric microscope measurements of the thickness of the nanoporous GaN layer of the sample grown using 0.2 g of Ga confirmed the presence of isolated nucleuses of nanoporous GaN particles with heights around 4 μm, similar to the size of the particles observed by the SEM images. A quite uniform layer is seen when 0.4 g of Ga were used with a mean thickness of the nanoporous film of 1.10 ± 0.15 μm. Finally, in the sample grown using 0.6 g of Ga, we observed a tendency to have higher heights of the porous film towards the centre of the sample. The mean thickness value is similar to that obtained with 0.4 g of Ga, 1.19 ± 0.35 μm. This would confirm that, above 0.4 g of Ga the deposition of GaN is limited.

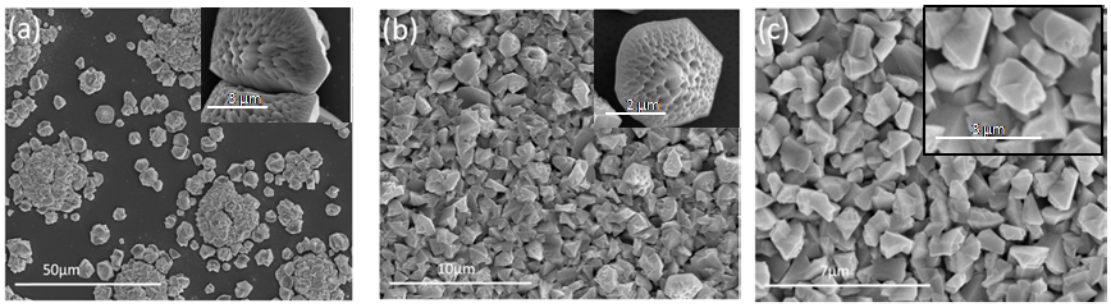

Figure 4. SEM pictures of the nanoporous particles obtained using different Ga quantities at the beginning of the experiment: (a) 0.2 g, (b) 0.4 g, and (c) 0.6 g.

Effect of the deposition time. We performed additional experiments to analyze the influence of the deposition time in the shape and porosity of the GaN particles. The deposition times selected were 30, 45, 60 and 120 min. The first two times were chosen because we observed two particular moments during the development of the growth process, highlighted in Figure 2. The first one is related to the leaning of the crucible when a half cylindrical tube was used, due to the wetting of both, the crucible and the liner because of the spreading of Ga at 30 min after the reactor reached 1200 K. The second one is the time when we observed the scalation of the material covering the crucible, identified later as GaN by X-ray diffraction, 45 min after the reactor reached 1200 K. We also have explored one additional deposition time above 60 min, which is the time used up to now to produce these nanoporous GaN particles[14] , to analyze if the chemical reaction continued after we observed the scalation of GaN on the crucible.

The deposition time has an important effect in the coverage of the substrate with nanoporous GaN particles, as can be seen in Figure 5, while the particle size is more or less constant. Figure 5(a) shows the evolution of the thickness of the nanoporous GaN film with deposition time. Even though the sample grown during 30 min shows an average thickness value of 1.61 ± 0.11 μm it is mainly due to isolated nucleuses that are encountered along the substrate. Similar fact occurs with the sample grown at 45 min, which shows a mean thickness of 2.08 ± 0.28 μm but the layer is not covering the full substrate. When the deposition time is set for 60 min we have a uniform layer 1.1 ± 0.14 μm thick. Finally, the interferometric measurements of the sample grown at 120 min show a decrease of the layer thickness.

Figure 5 also shows SEM images of the samples. In these images we can see that the density of GaN particles on the surface of the substrate increases with increasing the deposition time until 60 min. From there, it seems that no additional particles nucleate and the particles density remains constant. Hexagonal pyramidal porous particles were obtained in all cases; however, as we increased the deposition time, the morphology of the particles seems to fade away. Also, at long times, smaller particles can be seen covering the substrate, which might form by decomposition and further nucleation at expenses of the big particles, which would explain the deformation observed. This hypothesis would be confirmed by the reduction of the thickness of the sample at long deposition time, due to the high temperature and low pressure at which the sample is exposed during the growth experiment. Particles follow the same porous pattern observed up to now: nanopores located only on the (0002) face, with wider holes in the central part of the particles. It seems that the particles obtained after 30 min reaction time (Figure 5 (a,b)) have a larger amount of pores, and those seem to be more superficial. These particles tend to show a smaller number of ridges; this would mean that ridges are formed by the coalescence of the neighbouring pores at long enough deposition times, since these ridges are more apparent at the central part of the particles as the deposition time is extended. Also, the bigger contrast observed in the SEM images for the pores, would indicate that the particles obtained at longer times show deeper pores. When the deposition time is 120 min the porosity is less evident (see Figure 5(g,h)), which would corroborate the evaporation of the material to form the smaller particles observed in the background and would be more pronounced at the rough faces, i.e. those that contain the pores.

Dipòsit Legal: T 1557-2014

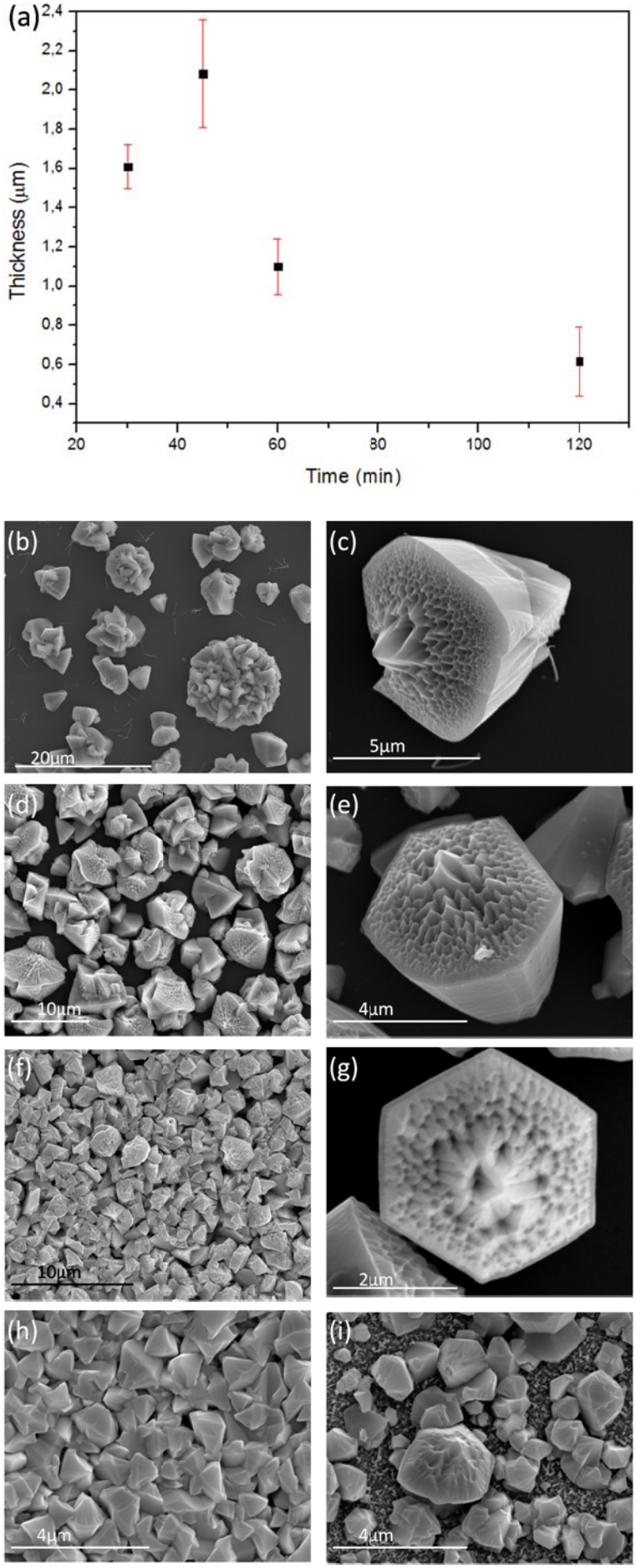

Figure 5. Evolution of the thickness of the porous GaN layers with deposition time. In frame (a) the errors graph showing the evolution of the thickness with the deposition time. SEM pictures of the particles obtained at (b,c) 30 min, (d,e) 45,(f,g) 60, and (h,i) 120 min deposition times.

Effect of Catalyst. To synthesize porous GaN on Si substrates, it is necessary to coat the substrate with a metallic catalyst[11]. Here, we tested different catalysts with which we coated (100) Si substrates: Ni, introduced as $Ni(NO_3)_2$ dissolved in ethanol, and 20 nm thick films of Ni, Au, Pt, and Ti deposited by RF sputtering.

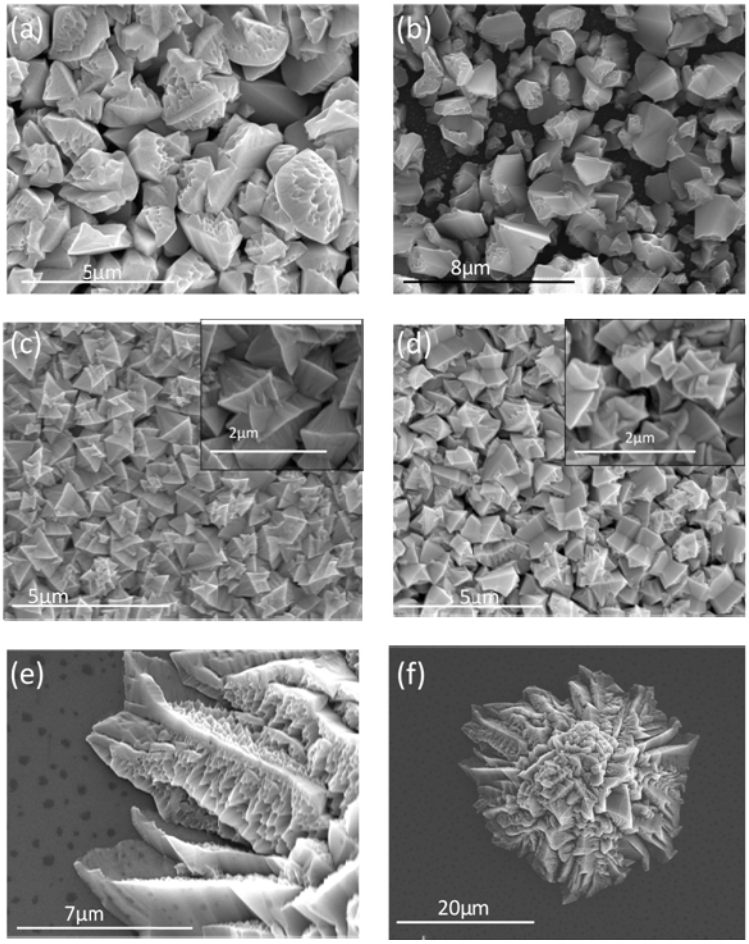

Figure 6. SEM pictures of nanoporous GaN grown on (100) Si with the use of different catalysts: (a) $Ni(NO_3)_2$, (b) Ni, (c) Au, (d) Pt, (e) and (f) Ti. The insets in figures (c) and (d) show a magnificated image of the interparticles porosity.

SEM pictures of as-grown GaN on (100) Si substrates shown in Figure 6 demonstrates that by using all catalysts, GaN appears in the form of microsized nanoporous particles. The bigger particles were obtained using $Ni(NO_3)_2$ as catalyst, while using Pt and Au we obtain smaller particles very homogenous in size. The highest level of porosity was obtained, however, in the GaN particles synthesized using $Ni(NO_3)_2$. It is curious to notice that Ni, introduced as $Ni(NO_3)_2$ or directly as metallic Ni has a different effect on the morphology and porosity degree of the particles, despite $Ni(NO_3)_2$ is reduced to Ni under the reaction conditions[11]. This different effect on obtaining porous GaN might be attributed to the distribution of the catalyst on the surface of the substrate. Agglomeration of big particles with high porosity were obtained using $Ni(NO_3)_2$ as can be seen in Figure 6(a). However, as can be seen in Figure 6(b) the particles grown on a continuous Ni film have an irregular shape and a lower degree of porosity. Porous GaN layers grown using Pt and Au catalysts show a uniform coverage of the substrate with GaN particles (see Figure 6(c) and 6(d). These polycrystalline films show an interesting dual porosity since they present interparticle and intraparticle pororosity, as defined in a previous publication [17]. The level of intraparticle porosity is higher when Pt is used (see insets in Figure 6(c) and (d)).

Porous GaN particles grown on Ti thin films have a totally different morphology, remembering the shape of a sea star with a high level of

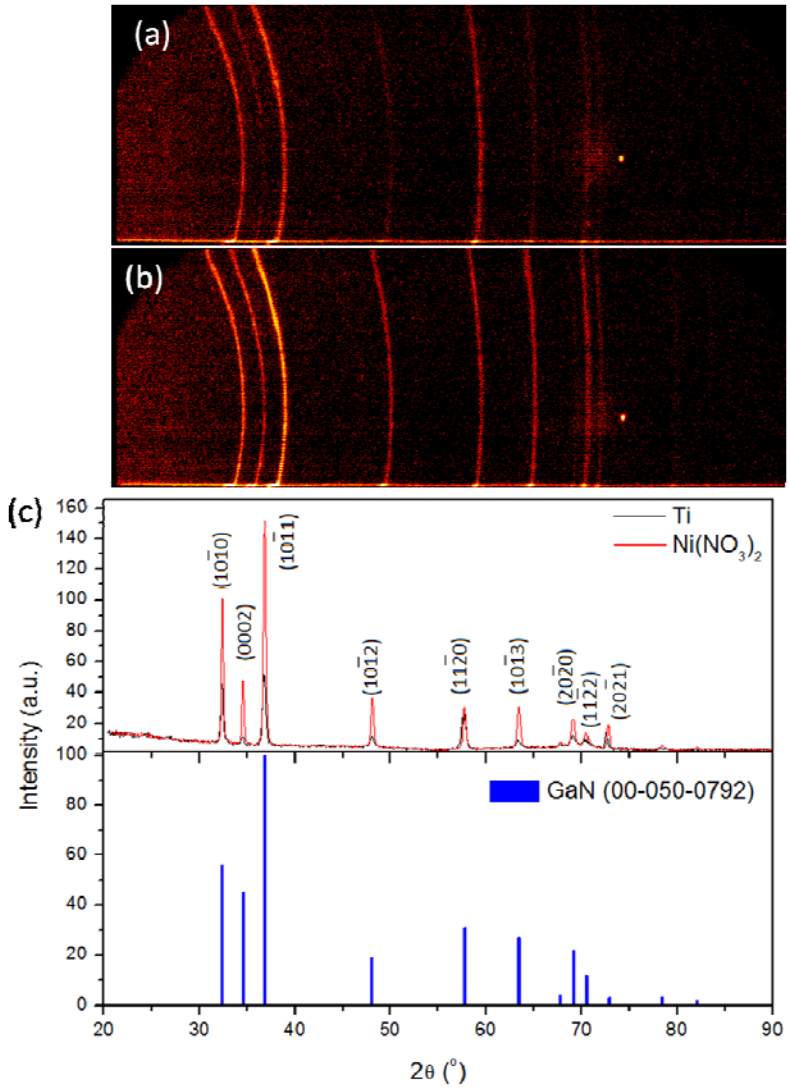

Figure 7. X-ray diffraction patterns of nanoporous GaN obtained on (100) Si substrates coated with Ti and Ni(NO3)2. (a,b) Debye rings recorded for both samples, respectively, and (c) diffraction patterns. The pattern of the GaN standard for JCPDS (00-050-0792) has been included for comparison.

porosity. In this case it seems that GaN starts growing as an epitaxial layer on the substrate with a further growth of nanoporous GaN particles on the top of it (see Figure 6(f)). This texturation of the film induced by the catalyst is confirmed by the XRD pattern recorded for this sample shown in Figure 7. The non-uniform distribution of intensity in the Debye rings observed with the GADDS detector (see Figure 7(a)) and the different intensity of the diffraction peaks when compared to the reference XRD pattern for GaN (00-050-0792) included in Figure 7(b) for comparison, reveal a texturation of the sample, although it is not trivial to establish which is the preferential orientation of the particles, from the data obtained. This is more evident when we compare this XRD pattern with any of those recorded for the porous GaN particles obtained using other catalysts, corresponding to porous GaN particles obtained using $Ni(NO_3)_2$ as catalyst, that can be seen in Figures 7(b) and (c).

Effect of the substrate. We have tested different substrates to ascertain if it might play a role in the crystallographic orientation of the GaN particles. For this purpose we used amorphous SiO_2 (fused silica), tungsten wire (W), (111) Silicon, and pyrolitic boron nitride (p-BN) as substrates. We have chosen these substrates with the criterion of using an amorphous substrate (fused silica), a cubic substrate different than Si and without a particular crystallographic orientation (W wire), and a substrate with hexagonal structure (p-BN). We also tested (111) Si since it has been reported that (0001) GaN films can be deposited on these substrates[18]. Since this is the direction along which the pores are aligned, if can provide a way to orient the porous GaN particles, the pores will be oriented at the same time, being perpendicular to the surface. In all cases, with the exception of (111) Si, we sprayed an ethanolic solution of $Ni(NO_3)_2$ on the surface of the

Dipòsit Legal: T 1557-2014

substrates to facilitate the nucleation of GaN. (111) Si substrates were coated with 20nm thick films of Au, Pt, Ti, and W.

SEM pictures of the nanoporous GaN particles grown on these substrates reveal in all cases that GaN appears in the form of hexagonal micron-sized nanoporous particles (see Figure 8). When using fused silica, the level of porosity in the particles is low, with the pores more concentrated at the central part of the particles, and with an elongated shape towards the external parts of the particles, instead of exhibiting the round shapes observed up to now (see Figure 8(a)).

On the W wire, the density of particles is very high, which might induce to think that GaN particles grow with a plate shape instead of the pyramids observed before (see Figure 8(b)). However, in the inset included in this figure, it can be clearly seen that the individual particles have a similar morphology than those obtained up to now.

GaN grown on (111) Si substrates coated with different catalyst appears in the form of microsized nanoporous particles with a mean size particle of 2-5 μm (see Figures 8 (c-f). The lowest level of porosity was obtained when W was used as catalyst (see Figure 8(f)). In most of the cases, nanowires were also observed together with the porous particles specially when Au and Pt where used as catalyst (see insets of Figures 8 (c-d). When Ti and W were used as catalyst it is observed at the edges of the sample the earlier stages of epitaxial growth, but it fades away as we shift to the centre of the sample (see insets of Figures 8 (e-f). If we compare the particles obtained on (100) Si and (111) Si substrates coated with the same catalyst, we observe that the GaN particles obtained on (111) Si substrates tend to be more irregular in shape. According to these images, it seems that the combination of the substrate and the catalyst play a big role in the morphology of the particles.

In the case of p-BN, a certain degree of alignment of the GaN particles can be observed since a bigger number of pores perpendicular to the surface can be seen (see Figure 8(g)), however, and due to the misalignment of the BN flakes that form p-BN, there are also particles with different crystallographic orientations. Also the porosity degree in these particles is lower than in the other cases.

Despite these observations, XRD characterization of these samples did not reveal any preferential growth along any particular direction in any of these samples, probably related to the fact that the interlayer formed by the catalyst, and located between the substrate and the GaN layer, hampers the influence of the structure of the substrate on the growing GaN layer.

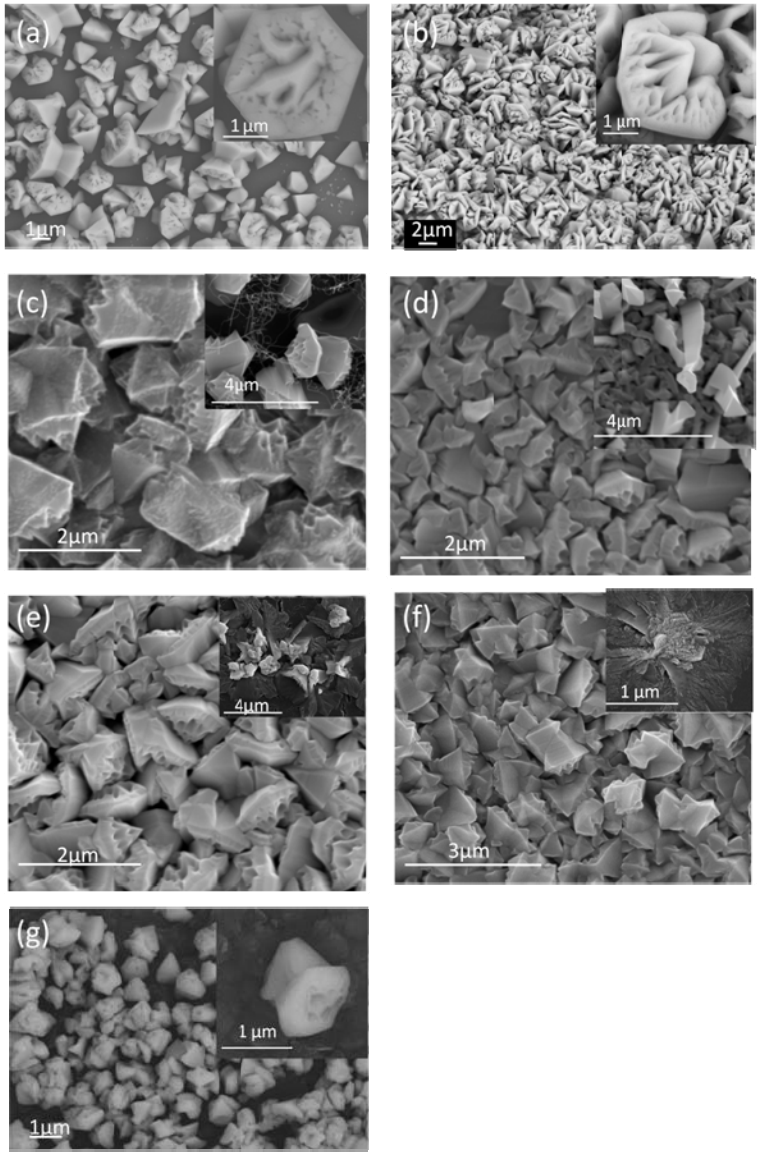

Figure 8. SEM images of the nanoporous GaN particles grown on different substrates: (a) SiO_2- fused silica, (b) W, (c-f) (111) Si coated with different catalysts (c) Au, (d) Pt, (e) Ti and (f) W and (g) pyrolitic BN.

Conclusions

We presented how different reaction parameters such as Ga holder, Ga quantity, deposition time, catalyst and substrate influence on the nanoporous Ga particles morphology, size and porosity degree grown by the direct reaction of metallic Ga and NH_3 in a CVD system. The Ga holder seems to have some influence on the size of the pores and the formation of ridges on the nanoporous GaN particles, since it has an influence on the earlier stages of evaporation and deposition of Ga on the substrate. Therefore the geometry in which the Ga is contained affects to the first stages of its evaporation and deposition rate on the substrate. The Ga quantity has an influence on coverage of the substrate with GaN particles. Nevertheless, an excess of Ga is undesired since this excess of Ga is not evaporated and the formation of additional nanoporous GaN particles is limited. The deposition time also controls the coating of the substrate with nanoporous GaN particles. However, long deposition times lead to a decomposition of the GaN particles previously formed, that disfigure their morphology with a later deposition of small nucleus of GaN on the substrate. The catalyst plays two different roles: one is the control on the particle size and the other is the crystallographic orientation of the as-grown particles. The influence on the particle size is due to the metal alloy formed between the catalyst used and Ga and the size of the initial nucleuses that can be formed. The second role is observed in the case of Ti, which leads to a texturation of the layer deposited on the substrate. Finally, the substrate also plays an important role in the morphology and distribution of the nanoporous GaN particles on its surface, although the interlayer formed by the catalyst hampers the replication of the structure of the substrate by the porous GaN growing layer. With all these data analyzed

we have more tools to control and manipulate the deposition conditions of porous GaN in order to obtain the desired morphology, density, and porosity of the nanoporous GaN particles produced by CVD towards the required application.

Acknowledgements

This work was supported by the Spanish Government under projects No. MAT2011-29255-C02-02 and TEC2010-21574-C02-02, the Catalan Government under project No. 2009SGR235, and the European Commission within the Seventh Framework Program under project No. FP7-SPA-2010-263044.

References

(1) S. Nakamura, S. Pearton and G. Fasol. Introduction. *The blue laser diode: the complete story.* 2º Edition; Springer: Germany, 2000, pp 3.
(2) V. Y. Davydov, A. A. Klochikhin, R. P. Seisyan, V. V. Emtsev, S. V. Ivanov, F. Bechstedt, J. Furthmuller, H. Harima, A. V. Mudryi, J. Aderhold, O. Semchinova and J. Graul, *Phys. Stat. Sol.,* 2002, **229**, R1-R3.
(3) S. Nakamura, M. Senoh, N. Iwasa and S. Nagahama, *Appl. Phys. Lett.,* 1995, **67**, 1868-1870.
(4) R. C. Schoonmaker, A. Buhl and J. Lemley, *J. Phys. Chem.,* 1965, **69**, 3455-3460.
(5) T. Kim, S. H. Kim, S. S. Yang, J. K. Son, K. H. Lee, Y. G. Hong, K. H. Shim, J. W. Yang, K. Y. Lim, S. J. Bae and G. M. Yang, *Appl. Phys. Lett.,* 2009, **94**, 161107-1 – 161107-3.
(6) F. Hide, P. Kozodoy, S. P. DenBaars and A. J. Heeger, *Appl. Phys. Lett.,* 1997, **70**, 2664-2666
(7) T. Fuji, Y. Gao, R. Sharma, E. L. Hu, S. P. DenBaars and S. Nakamura, *Appl. Phys. Lett.,* 2004, *84*, 855-857.
(8) J. J. Wierer, A. David and M. M. Megens, *Nat. Photonics.,* 2009, **3**, 163-169.
(9) C. B. Soh, C. B. Tay, R. J. N. Tan, A. P. Vajpeyi, I. P. Seetoh, K. K. Ansah-Antwi and S. J. Chua, *J. of Phys. D: Appl. Phys.,* 2013, **46**, 365102.
(10) H.-P. Shiao, C.-Y. Wang, M.-L. Wu and C.-H. Chiu, *IEEE Photon. Technol. Lett.,* 2010, **22**, 1653-1655.
(11) R. Wang, D. Liu, Z. Zuo, Q. Yu, Z. Feng and X. Xu, *AIP Advances,* 2012, **2**, 012109.
(12) T. Dai, B. Zhang, X. N. Kang, K. Bao, W. Z. Zhao, D. S. Xu, G. Y. Zhang and Z. Z. Gan, *IEEE Photon. Technol. Lett.,* 2008, **20**, 1974-1976.
(13) M. S. Minsky, M. White and E. L. Hu, *Appl. Phys. Lett.,* 1996, **68**, 1531-1533.
(14) J. J. Carvajal and J. C. Rojo, *Cryst. Growth Des.,* 2009, **9**, 320-326.
(15) A. Strittmatter, A.Krost, M. Strassburg, V. Turck, D. Bimberg, J. Blasing and J. Christen, *App. Phys. Lett.,* 1999, **74**, 1242-1244.
(16) J. J. Carvajal, O. V. Bilousov; D. Drouin, M. Aguiló, F. Díaz and J. C. Rojo, *Microsc. Microanal.,* 2012, **18**, 905-911.
(17) O. V. Bilousov, J. J. Carvajal, D. Drouin, X. Mateos, F. Díaz, M. Aguilo and C. O'Dwyer, *ACS Appl. Mater. Interfaces.,* 2012, **4**, 6927-6934.
(18) M. M. Sung, C. Kim, S. H. Yoo, C. G. Kim and Y. Kim, *Chem. Vap. Deposition.,* 2002, **8**, 50-52.

Paper II

Bilousov, O.V.; Carvajal, J.J.; Drouin, D.; Mateos, X.; Díaz, F.; Aguiló, M. and O'Dwyer, C. *Reduced workfunction intermetallic seed layers allow growth of porous n-GaN and low resistivity, ohmic electron transport* **(2012)** ACS Applied Materials and Interfaces, 4 (12), pp. 6927-6934.

ACS APPLIED MATERIALS & INTERFACES

Research Article

www.acsami.org

Reduced Workfunction Intermetallic Seed Layers Allow Growth of Porous *n*-GaN and Low Resistivity, Ohmic Electron Transport

Oleksandr V. Bilousov,[†] Joan J. Carvajal,*[,†] Dominique Drouin,[‡] Xavier Mateos,[†] Francesc Díaz,[†] Magdalena. Aguiló,[†] and Colm O'Dwyer*[,§,∥,⊥]

[†]Física i Cristallografia de Materials i Nanomaterials (FiCMA-FiCNA) and EMaS, Universitat Rovira i Virgili (URV), Marcellí Domingo s/n, E-43007 Spain

[‡]Department of Electrical and Computer Engineering, Université de Sherbrooke, Sherbrooke, PQ, J1K 2R1, Canada

[§]Applied Nanoscience Group, Department of Chemistry, University College Cork, Cork, Ireland

[∥]Materials and Surface Science Institute, University of Limerick, Limerick, Ireland

[⊥]Micro & Nanoelectronics Centre, Tyndall National Institute, Dyke Parade, Cork, Ireland

Supporting Information

ABSTRACT: Porous GaN crystals have been successfully grown and electrically contacted simultaneously on Pt- and Au-coated silicon substrates as porous crystals and as porous layers. By the direct reaction of metallic Ga and NH_3 gas through chemical vapor deposition, intermetallic metal-Ga alloys form at the GaN–metal interface, allowing vapor–solid–solid seeding and subsequent growth of porous GaN. Current–voltage and capacitance–voltage measurements confirm that the intermetallic seed layers prevent interface oxidation and give a high-quality reduced workfunction contact that allows exceptionally low contact resistivities. Additionally, the simultaneous formation of a lower workfunction intermetallic permits ohmic electron transport to n-type GaN grown using high workfunction metals that best catalyze the formation of porous GaN layers and may be employed to seed and ohmically contact a range of III-N compounds and alloys for broadband absorption and emission.

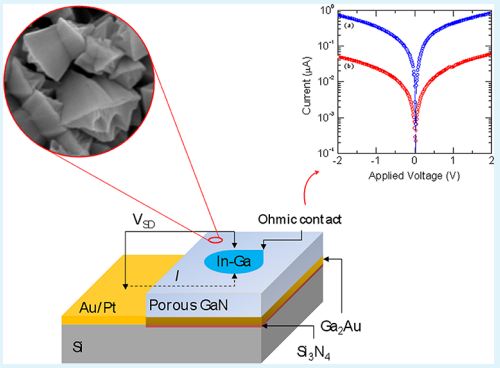

KEYWORDS: *porous GaN, ohmic electron transport*

1. INTRODUCTION

GaN and its related alloys such as InN and AlN that span the UV–vis–NIR spectrum have received much attention in the realization of new devices for electronics, microwave, and optoelectronics/photonics applications. With large bandgap energies, high breakdown fields, large carrier velocities, and a tolerance to high junction temperatures, the nitrides have a myriad of possibilities, including LEDs,[1] lasers for reading or storing data on high density optical media, solar blind detectors, biological monitoring, gas sensing,[2] and high temperature/high power electronics.[3]

The discovery of light-emitting nanoporous Si[4] propelled investigations of porosity formation in III–V and Group IV semiconductors.[5−7] Their unique properties compared to their bulk counterparts[8] have advanced their use in sensors, interfacial structures, and biomedical and catalysis applications.[9−11] Generally, pore formation in semiconductors can be obtained by anodizing them in a suitable electrolyte, under proper conditions;[12] however, the ability to form relatively uniform, crystalline porous GaN layers over large areas through complex etching without photolithographic masking or processing is challenging. For GaN, both wet and dry etching techniques have been unsuccessful in forming unique structures of the material, and these methods can infer unwanted interface states and surface contamination that can affect transport properties by rendering the GaN surface more resistive. The double issue of dry etching techniques increasing GaN resistivity and wet etching techniques not as crystallographically controllable for GaN as it is for other III–V semiconductors, for example, can be alleviated by other growth methods involving seeding processes, some of which, as will be shown here, allow crystallographically delineated porous layers with improved contact resistivities.

Until now, nanoporous GaN thin films have received particular interest as buffer layers or templates for hetero-epitaxial growth of lattice-mismatched materials with low defect density.[13−15] The porous material decreases the number of defects in the epitaxial layer, even when the lattice mismatch between the substrate and the GaN epitaxial layer is large, and it furthermore allows the growth of stress-realized epitaxies.[1] Extensions to wider and narrow gap InN and AlN, respectively, would allow the possibility of operation from the UV to IR

Received: September 21, 2012
Accepted: November 20, 2012
Published: November 20, 2012

wavelengths, and these materials are beginning to be investigated on the nanoscale.[16−18]

Porous GaN has been typically fabricated by (photo)-electrochemical and chemical etching methods,[19−22] giving textured surfaces as a result of pore coalescence and variations in etch rates for extended etching times. Metal catalysts are also used to initiate growth through either a vapor−liquid−solid (VLS)[23,24] or vapor−solid−solid (VSS)[25,26] mechanism when using molecular beam epitaxy (MBE) and chemical vapor deposition (CVD), where the catalyst can influence the growth; e.g., colloidal gold nanoparticles can initiate the growth of GaN nanowires. Additionally, as the ohmic contact technology to many III-N compounds is now well established[27] the marriage of seeded growth methods that infer alternative transport properties is an approach that could allow for new contacts to ternary and quaternary III-nitrides. Alternative techniques that allow band structure modification while also facilitating the direct growth of GaN, AlN, or InN, for example, with resulting low resistivity, ohmic contacts are thus of significant fundamental and commercial interest.

We produced porous GaN through the direct reaction of metallic Ga with NH_3 in a simple chemical vapor deposition (CVD) system.[28] Micrometer sized nanoporous GaN particles were grown directly onto boron nitride (BN) and silicon[29] substrates using this technique without necessitating any secondary electrochemical or electroless etching or subsequent chemical treatment after growth to induce porosity. Furthermore, it is possible to deposit porous GaN directly onto Si substrates in a single growth step. The development of porous GaN augers well for new electronic and optoelectronic devices with improved external quantum efficiencies, the incorporation of phosphors for LEDs, and high surface area sensing.[30,31]

Here, we report the successful growth and simultaneous electrical contacting of nanoporous GaN grown using high workfunction Au- and Pt-coated silicon substrates, through the direct reaction of Ga and NH_3 in the CVD system. Au and Pt both acted as a catalyst for the synthesis of porous GaN and result in the formation of an intermetallic compound at the GaN−metal interface that prevents oxidation of the GaN, promotes vapor−solid−solid growth of porous, single crystals, and in parallel allows for high-quality ohmic electrical contacts to the porous layers facilitated by a significantly reduced Schottky barrier height.

2. EXPERIMENTAL SECTION

2.1. Synthesis of GaN Particles. Nanoporous GaN microparticles were deposited using a Chemical Vapor Deposition (CVD) system on Au- and Pt-coated silicon (100) substrates with an area of 1 cm^2, using a horizontal single-zone split tubular furnace Thermolyne 79300. Figure S1, Supporting Information, shows a schematic of the experimental setup. The system consists of a quartz tube inside of which a BN support is placed that holds the Si substrates during the growth experiments. The BN support has a hole in its center that allows exposure of the Si substrate to the Ga source. Gallium metal (99.99%) and ammonia (>99.98%) were used as the Ga and N sources, respectively. An excess amount of Ga was placed at the bottom of the quartz tube, in close contact with the temperature-controlling thermocouple. A 20 nm layer of Au or Pt was deposited on Si substrates using an RF sputtering process (AJA International) at a power of 150 W and a pressure of 3 mTorr. The coated substrate was placed 2 cm above the Ga source as can be seen in the schematic of the experimental setup shown in Figure S1 (Supporting Information). The quartz tube of the furnace was degassed to a vacuum pressure of 1×10^{-2} Torr, after which NH_3 was introduced through a mass-flow controller at a flow rate of 75 sccm and the furnace heated to the reaction temperature of 1203 K at a rate of 100 K min^{-1}, while the pressure was kept at 15 Torr. The reaction was continued at this temperature and pressure for 60 min under a constant flow of NH_3. Growth was halted by cooling to room temperature without NH_3 flow, reducing the pressure to 1×10^{-2} Torr.

2.2. Characterization. The nanoporous GaN microparticles deposited on the Si substrates as a porous layer were characterized morphologically using a JEOL JSM 6400 scanning electron microscope (SEM). Before observation, samples were coated with a thin layer of gold with a Bal-Tec SCD004 sputterer.

Pore shapes, lengths, and propagation directions were analyzed by focused ion beam (FIB)-based tomography, i.e., time-resolved serial slicing and imaging with a Zeiss 1540 Cross Beam microscope (see Supporting Information). This dual beam system is equipped with a FIB column with a Ga source and a high-resolution field emission electron column. The FIB column stands at 52° to the electron column, and the sample surface is perpendicular to the ion column. The ion milling was performed using a 5 pA beam current to minimize surface damage and material redeposition.

X-ray diffraction (XRD) spectra and imaging in $\theta-2\theta$ geometry of the as-grown sample were made using Cu Kα radiation in a Bruker-AXS D8-Discover diffractometer equipped with parallel incident beam (Göbel mirror), vertical $\theta-\theta$ goniometer, XYZ motorized stage, and a General Area Diffraction Detection System (GADDS) HI-STAR detector with a multiwire proportional counter of 30 × 30 cm^2 area and 1024 × 1024 pixel density. Samples were placed directly on the sample holder, and the area of interest was selected with the aid of a video-laser focusing system. An X-ray collimator system allows the analysis of 500 μm^2 surface areas. The X-ray diffractometer was operated at 40 kV and 40 mA to generate Cu Kα radiation. We collected 2D XRD patterns covering a range of 2θ between 20 and 85° at a distance of 15 cm from the sample. The exposure time was 120 s per frame. Identification of the crystalline phases was achieved by comparison of the XRD diffractogram with the ICDD database using Diffrac^{plus} Evaluation software (Bruker 2007).

High-resolution transmission electron microscopy (HRTEM) and convergent beam electron diffraction (CBED) were conducted on a JEOL 2100F FEGTEM operating at 200 kV and on a JEOL FEM 3000F TEM. Lattice resolution energy-dispersive X-ray analysis (EDAX) was acquired using the EDX Genesis XM 4 system 60 detector.

Charge transport measurements through the porous GaN films were conducted using two- and four-probe measurements using a dc-voltage and an Agilent 34401A Digital Multimeter in a Peltier cell, thermostatted to 295 K in a Faraday cage. Liquid metal contacts were made using In−Ga eutectic blown into a sphere from a gold metallized short borosilicate capillary tube, ensuring good wetting (several μm^2) to the rough top-surface morphology of the porous GaN and avoiding electrical shorting to the underlying metallized silicon. Measurements were made in two-probe, four-probe, and van der Pauw[32] geometry. Resistivity values were extracted from $I-V$ curves in the high bias regime (series resistance) and also from four-point probe measurements. Capacitance−voltage analysis using gold Schottky contacts to porous GaN was performed by scanning the applied potential at a rate of 10 mV s^{-1} with a superimposed AC signal with an amplitude of 15 mV at a frequency of 1 MHz.

3. RESULTS AND DISCUSSION

3.1. Morphological Characterization of Porous GaN. The resulting nanoporous GaN structures, deposited on the surfaces of Si substrates coated with Au and Pt, were characterized morphologically by SEM. Figures 1(a) and (b) show the typical porous GaN layer morphologies grown using this approach, and in Figures 1(c) and (d) we observe that the porous GaN particles have a characteristic morphology consisting of faceted hourglass crystals with a mean size of ~1.5 μm end-to-end. The GaN crystals have smooth lateral faces, while pores are observed on their basal planes, similar to

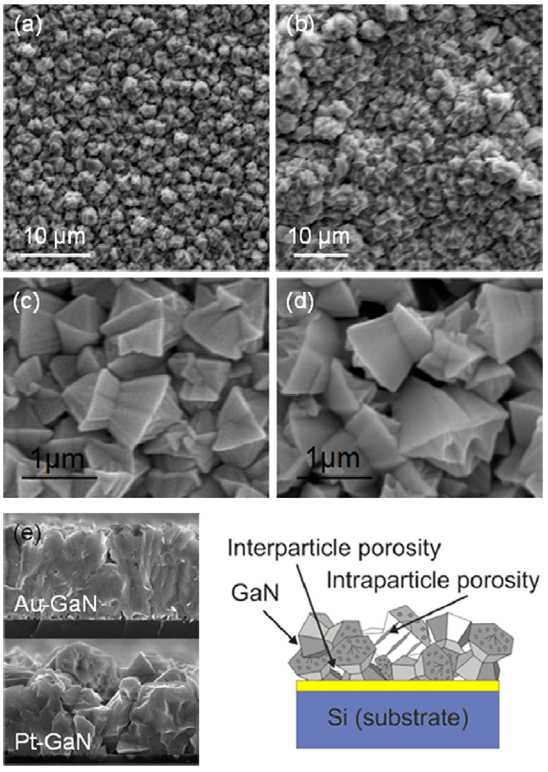

Figure 1. SEM images of porous GaN particles grown on Si(100) substrates coated with (a,c) 20 nm film of Au and (b,d) 20 nm film of Pt. (e) Cross-sectional SEM images of the GaN layers for each system (bottom left) and schematic representation of a sample of GaN nanoporous particles grown on a Si substrate coated with Au showing the interparticle and intraparticle porosity of the GaN layers (bottom right).

those we observed on BN substrates[28] or Si substrates coated with $Ni(NO_3)_2$.[29] Crystal growth occurs progressively on the surface with individual crystals ripening until a layer of porous GaN microparticles covers the surface as a porous layer. The particles obtained on the Si substrates coated with Pt showed a higher degree of internal porosity, with the pores aligned along the [0001] direction, than those grown from Au-coated Si substrates. Figure S2 (Supporting Information) shows the energy dispersive X-ray (EDX) spectra for these two samples, showing the contents of Ga and N in these porous particles. The concentration of N is lower than expected due to the low atomic weight of this atom, which is difficult to detect by using this technique.

The GaN layers are both microporous and mesoporous. The microporosity stems from the free space between particles (see Figures 1(c) and (d)), whereas the nanoscale mesoporosity comes from internal pore features within the particles, confirmed with time-resolved FIB-based tomography, shown in Figure 2(a,b,c) together with the simulation of the external morphology of the particle, shown in Figure 2(d). With this technique, we analyzed the shape and length of the pores, as well as their direction of propagation inside of the GaN particles by removing the material, slice-by-slice, using ion-milling, closer to the lateral surfaces of the GaN nanoporous particle. The secondary electron images recorded concurrently revealed straight pores with lengths similar to the dimension of the GaN particles. These pores are parallel to the facet direction and do not intersect nor branch, as can be seen in the video milling sequence in the Supporting Information. In some cases,

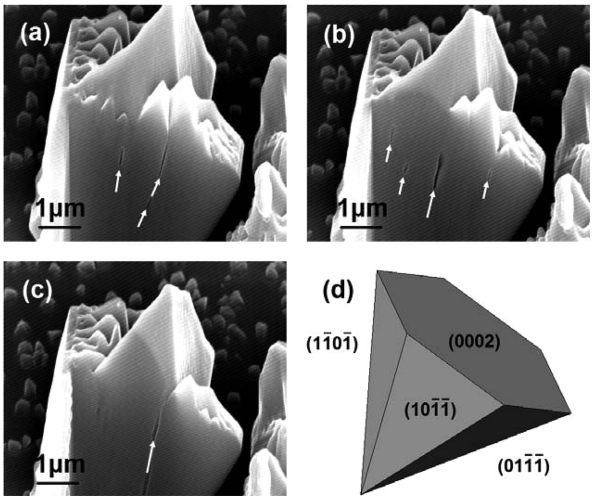

Figure 2. FIB tomography acquired with a milling current of 5 pA for a duration of 160 s revealing the GaN intraparticle porosity (a,b,c) and simulation of the morphology of the GaN crystal with terminating crystal planes identified (d).

the initiation of epitaxial polycrystalline segments within an hourglass crystal is also found as shown in Figure 2c. The diameters of the pores ranged from 50 to 100 nm, with negligible variation in diameter with length (nontapered). From these images and the video recorded during the tomography (see Supporting Information) performed on different GaN particles, we conclude that the nanopores in the central part of the GaN particles follow an orientation parallel to the [0001] crystallographic direction. However, the nanopores found in the outer portions of the GaN particles are parallel to the lateral faces of these particles.

3.2. Structural Characterization of VSS Porous GaN. The crystalline structure of the porous GaN particles deposited on Si substrates coated with Au and Pt was analyzed using X-ray diffraction. The XRD pattern shown in Figure 3(b) for GaN grown on Au-coated Si substrates confirms crystalline wurtzite GaN growth with a predominant diffraction intensity from low-index crystal facets. The regions at which the (400) diffraction peak of Si appears at 69.131° 2θ have been excluded from the measurement to avoid intensity saturation. This allows observation of lower intensity reflections that are attributed to crystalline Si_3N_4 and a crystalline Au−Ga intermetallic alloy of cubic Ga_2Au. We believe that the Si_3N_4 formation is most likely due to reaction between NH_3 and silicon accelerated by the metallic catalyst.

The formation of the Au−Ga crystalline alloy, which occurs here above the solid-solution formation temperature of 923 K, confirms intermetallic seeding to form GaN by reaction with NH_3 through a vapor−solid−solid process. The uniform intensity of the Debye rings (along the curved ring portions in Figure 3(c)) collected for porous GaN confirms that there is no texturing in the layer of porous crystals (see Figure 3(c)).

HRTEM measurements were carried out to confirm the crystallinity of the nanoporous GaN crystals. Figure 3(d) shows low- and high-magnification HRTEM images of a typical porous GaN particle. Pores are not directly observable here due to the thickness of the crystal. In the high-magnification image, the two-dimensional atomic structure of the GaN crystal is resolved. In this figure we identified two different *d*-spacings of 0.52 and 0.28 nm corresponding to the (0001) and (10−10)

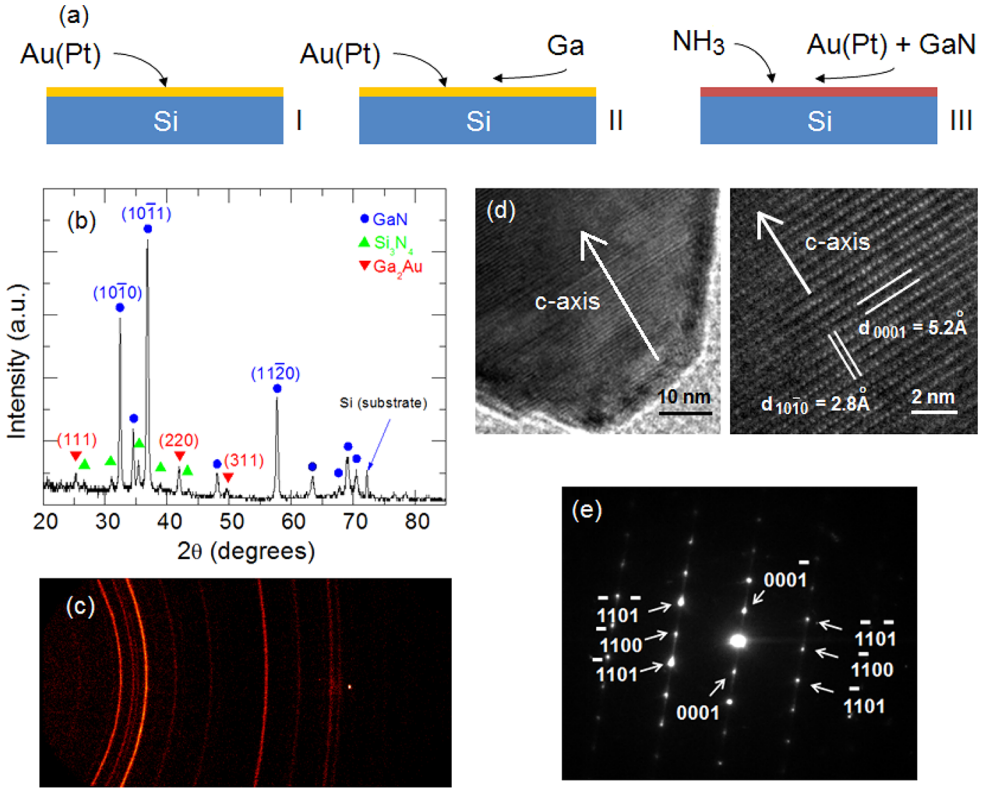

Figure 3. (a) Mechanism of growth of the GaN nanoporous particles through the VSS process. (b) XRD pattern for porous GaN deposited on Au-coated Si(100) showing the formation of crystalline GaN (ICDD 01−073−7289), Si_3N_4 (ICDD 03−065−8613), and Ga_2Au alloy (ICDD 01−071−6479). (c) Debye rings recorded with a GADDS detector indicating no texturation of the porous GaN layer. (d) HRTEM image shows the presence of a few stacking faults and the two-dimensional atomic structure with *d*-spacings for the (0001) and (10−10) planes. (e) SAED zone [11−20] axis pattern.

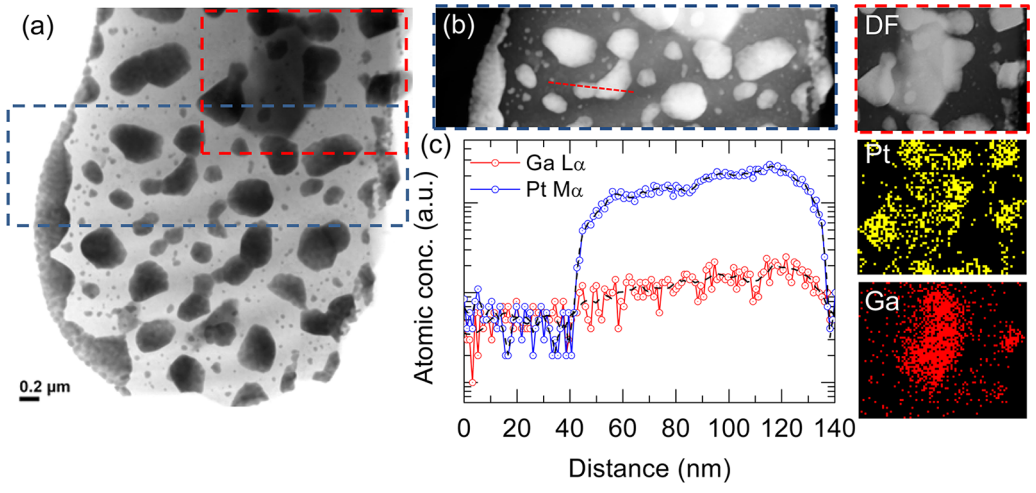

Figure 4. (a) Bright-field TEM image of the Pt−Ga intermetallic islands formed at the GaN interface and (b) corresponding dark-field STEM image with (c) corresponding line profiles of atomic concentration for the Ga L*α* and Pt M*α* X-rays. (Right) EDX maps confirming the presence of Pt and Ga in most metallic islands on the silicon surface.

planes of the GaN structure. Figure 3(e) shows a selected area electron diffraction (SAED) pattern taken from one of the corners of the GaN porous particle. This diffraction pattern corresponds to the wurtzite structure of GaN, confirming that the nanoporous GaN particle is a single crystal. The existence of some (0001) diffraction streaks that generated a splitting of the diffraction intensity in the SAED patterns suggests the existence of thin lamellar defects lying parallel to the (0001) plane;[28] stacking faults along the crystallographic *c*-axis can be seen in the HRTEM image in Figure 3(d). The growth of these GaN nanoporous particles is assisted by a solid particle through the vapor−solid−solid (VSS) mechanism, the main stages of which are: the Ga incorporation into the Au or Pt solid phase eutectic, the formation of a Ga−Au or Ga−Pt alloy, the solubilization of nitrogen in the Ga−Au(Pt) alloy, and finally the nucleation and growth of GaN (see Figure 3(a)).

For Pt-seeded VSS grown porous GaN, we examined the surface of the silicon substrate directly underneath the GaN

crystals. Figure 4(a) shows a bright-field TEM image of a portion of the silicon substrate where the Pt−Ga seed crystals (dark regions) are found. The seeds have characteristic faceted morphology and shape, and the deposit comprises fused grains. EDX analysis in Figure 4(b) confirms the presence of both Pt and Ga, and while the intensity of Pt is greater as would be expected, the atomic concentration of Ga follows that of Pt, where the variation stems from increasing seed crystal volume along the line scan. Corresponding mapping of the intermetallic Pt−Ga seeds in Figure 4 confirms that not all of the Pt particles contain Ga, i.e., that a proportion of the metallic seeds take up Ga to form the intermetallic, but it should be noted that the site of interest examined is taken from a region of the substrate between fully grown GaN crystals. As with the Ga_2Au seeds, the Pt−Ga seeds are where VSS GaN growth starts, but a crystalline diffraction pattern is not found for this phase as readily as for Au-seeded GaN.

3.3. Electrical Characterization of Pt- and Au-Contacted Porous GaN. An important consideration for porous layers is that electrically they are sensitive to grain boundary density, and when rough, the sheet and contact resistances (ρ_c) are influenced not only by the physical state of the interface at the contact but also by the geometry. In all cases, the ability to accurately evaluate the contacts is critical. The standard techniques of linear transmission line measurements (TLMs) and circular TLM (c-TLM) have been established.[12] For porous GaN specifically, the thickness is determined by the size of the crystals and their assembly on the surface, which results in a "rough" topology, with a high density of grain boundary scattering centers. For thin GaN layers with higher (than thick smooth epi-layers) sheet resistance (R_s), the accuracy of the TLM-type approaches becomes an issue. Here, although the layers are quite thick compared to epi-layers of GaN on LED structures for example, their R_s values are expected to be close to that of thin epi-layers. Thus, both TLM and less geometrically sensitive van der Pauw measurements were acquired to probe the transport mechanism but also the contact resistivity and its contribution to the overall resistance, a contribution that decreases with improving ρ_c.

Figure 5 shows the $I-V$ curves from the porous GaN catalyzed by Pt (Figure 5(a)) and also by Au (Figure 5(b)), with the second contact placed on the underlying metal, as shown schematically in Figure 5. The $\ln(I)-V$ curves show only slight asymmetry indicative of near-ohmic, weak Schottky barriers to Pt and Au. Consistently, the conductivity of porous GaN grown from Pt is higher than that grown from Au. In such cases, there is no detectable presence of any remaining Ga−Pt phases between the catalyzed GaN and the contact metal. The $I-V$ curve of porous GaN−Pt in Figure 5c shows the low-bias nonlinearity consistent with such a weak Schottky barrier. Both contacts fit with thermionic emission theory, acknowledging a near potential-independent high ideality factor for near-ohmic barriers. In any diode, a number of transport mechanisms play a role, including diffusion and tunneling currents in addition to thermionic emission. At room temperature, the effective linearity of the $I-V$ response measured for porous GaN to high work function metals, with an intermetallic seed layer between the metal and GaN, is maintained at high bias. Since the ideality factor does not change due to near-ohmic response, the differential resistance and series resistance values are quite similar, as will be shown below. The Schottky barrier height (SBH) can still be estimated from

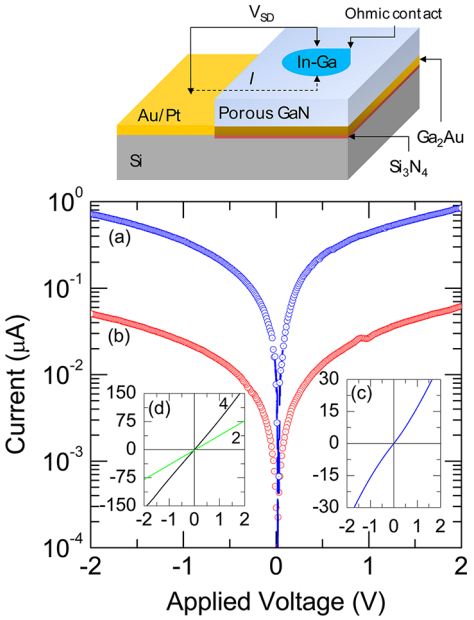

Figure 5. (Top) Schematic representation of the contacted porous GaN layer. (Bottom) $\ln(I)-V$ curves for porous GaN grown from (a) Pt and (b) Au. (c) $I-V$ curve for the porous GaN grown directly from Pt and (d) $I-V$ curves from two- and four-probe measurements using In−Ga ohmic contacts to porous GaN.

$$I = I_0\left[\exp\left(\frac{qV - IR_S}{kT}\right) - 1\right] \quad (1)$$

where $I_0 = AA^{**}T^2 \exp(-q\varphi^{\circ}_{B,n}/kT)$[33] where A^{**} is the effective Richardson constant. The estimated SBHs using the theoretical value for the effective Richardson constant (26.4 A cm^{-2} K^{-2}) for Pt and Au contacted porous GaN are 0.66 and 0.53 eV, respectively.

Effective ohmic contacts can form with n-type GaN suggesting that the grain boundary scattering or resistivity dominates transport through an alloyed interface that promotes ohmic transport in a far from ideal diode arrangement where current flow is through the contact. Two terminal transport measurements (Figure 5d) acquired between the In−Ga ohmic contacts showed perfect ohmicity. Corresponding four-probe analysis gives sheet resistances for porous GaN films in the range 4.3−4.9 kΩ/□. The van der Pauw measurements confirm these values independent of contact area and effective geometry on rough surfaces. Additionally, it is important to note that deposited Pt (and Au) forms coarsened NP distributions after the growth of GaN, due primarily to temperature-mediated coalescence and ripening. For electrical measurements, particle distributions confirm that both nearest-neighbor distances and overall distribution of various non-spherical particles prevent the formation of a percolating conduction layer beneath the GaN; the electrical characterization is of the porous GaN polycrystalline layer.

Contact resistivities were determined with variable inter-contact separation using the transmission line measurement (TLM) approach. For the contact resistivity of the rough, faceted top surface, we assume that the semiconductor sheet resistance underneath the contacts remains unchanged. This is reasonable since no alloyed contacts (referring to the drain contact, not the interfacial metal−Ga layer) are used which is known to affect sheet resistance.[34] In spite of higher porosity from Pt-grown porous GaN, low contact resistivities between

2.2−4.1 × 10^{-4} Ω cm^2 for Pt-catalyzed *n*-GaN and 5.9−8.8 × 10^{-4} Ω cm^2 from Au-mediated porous *n*-GaN layers are found. Current flow from the porous GaN to the metal is assumed to flow horizontally through the intermetallic seed layer at the GaN interface and collected at the Au or Pt metallized silicon. Leakage currents from the slightly more resistive intermetallic seed layers are prevented by the formation of a crystalline dielectric Si_3N_4 layer. This approach is valid as long as the injection of current across the contact is uniform. The current spreading length, which is a measure of the effective length over which current is injected into the porous GaN layer, is given by $L_S = \sqrt{(\rho_c/R_S)}$ and holds for epi-layer systems with two ohmic contacts. From a TLM measurement, we find that the contribution from the contacts to the overall series resistance between them scales with $\sqrt{\rho_c}$ as would be expected from a double ohmic contact system, in spite of high workfunction metals contacting a rough, n-type GaN layer. The accuracy of ρ_c is limited by its relative value compared to the total intercontact resistance; lower ρ_c relates to smaller contributions and increased errors in its determination from TLM measurements and the geometry of wetting liquid metal contacts to a rough, faceted porous GaN layer, which is unavoidable. Definitive nonlinearity in the *I*−*V* response and also variations in site-to-site measurement can also contribute to these errors. Here, as the GaN is unintentionally n-type and consequently has a more uniform doping profile as a function of distance than corresponding p-type layers which require temperature-mediated activation, site-to-site variations were found to be minimal and varied by ∼0.6%.

Compared to the R_S values, it is clear that an effective ohmic contact is formed, and sheet and series resistances through the GaN layer are dominated by the layer structure. The overall series resistance, *R*, to which the sheet and contact resistivities contribute can also be determined from the thermionic emission theory described above. In the presence of the intermetallic contact, the transport is effective ohmic. The series resistance can also be obtained from the differential conductance through its proportionality to the current according to

$$\frac{dI}{dV} = \left(R_S + \frac{kT}{q}\left[\frac{1/I_0}{I/I_0 - 1}\right]\right)^{-1} \quad (2)$$

For the thermionic emission-based transport through the porous *n*-GaN layer, the reciprocal of dI/dV approaches R_S at the higher currents, provided that the ideality factor remains unchanged, which is the case here. The differential resistance is plotted in Figure 6b. As observable from the *I*−*V* curves in Figure 6a, the response from Pt contact porous GaN is slightly less symmetric and thus has a slightly higher Schottky barrier, giving very weak rectification with a reverse bias current that is potential dependent. From Figure 6b, we find that the differential conductance curves confirm this variation in contact type, where porous GaN grown from a seed layer of Ga_2Au exhibits an essentially horizontal response indicative of a linear *I*−*V* curve; the slope varies for Pt-seeded contacts consistent with a slight nonlinearity in the *I*−*V* response and also a higher overall (by a factor of 10−13) conductance compared to Au-seeded porous *n*-GaN.

It is worth noting that the n-type contacts were effectively ohmic as deposited and did not need any postdeposition annealing to induce this effective ohmicity; such linear *I*−*V* behavior is not found with Au contacts, and the intermetallic

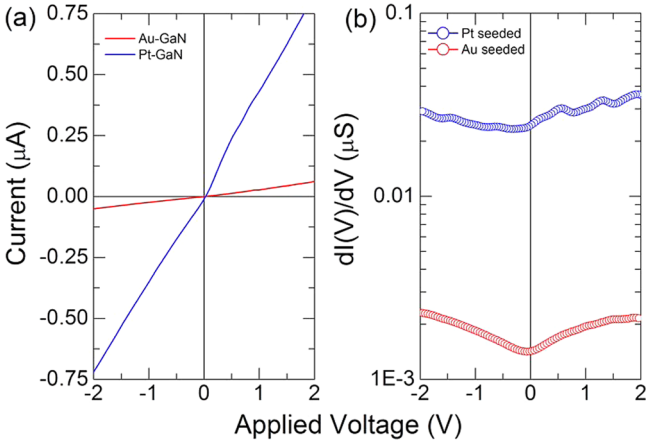

Figure 6. Room temperature (a) *I*−*V* and (b) differential conductance ($dI(V)/dV$) for Au- and Pt-seeded porous GaN layers.

seed layer interface is critical for removing the transport Schottky barrier. The values match those of MBE grown GaN thin films with Ti/Au alloy contacts after annealing to 973 K[35] and are caused by the efficient interface between the metal and the growing porous GaN. Additionally, since annealing at 1173 K is known to initially improve contact resistivities down to 10^{-6} Ω cm^2 with ohmic Ti/Al contacts, continued heating at this temperature for more than 40 s has been shown to result in a drastic increase in ρ_c.[35] The present method avoids this by the use of noble metal contacts as catalysts and solid seed layers for the GaN growth and as electrodes for transport measurements.

Capacitance−voltage analysis was performed by scanning the applied potential at a rate of 10 mV s^{-1} with a superimposed AC signal with an amplitude of 15 mV at a frequency of 1 MHz to determine the capacitance of the porous GaN under depletion conditions. For these porous GaN layers, this frequency was sufficient to sinusoidally vary the depletion region width without unwanted contributions to capacitance from the dielectric Si_3N_4 present at the Ga_2Au interface. Gold contacts were made to the porous GaN and formed a Schottky contact for the measurement. The $1/C^2$−*V* analysis in the framework of the Mott−Schottky model, shown in Figure 7(a), confirms an unintentional n-type GaN with a donor concentration N_D given by the slope $N_D = 2C^2V/q\varepsilon\varepsilon_0$ corresponding to a net impurity concentration[36] in porous GaN of $n = 1.6 \times 10^{16}$ cm^3 using a dielectric constant $\varepsilon = 8.9$ for GaN. These low values for unintentionally doped *n*-GaN give a corresponding SBH from

$$\varphi^0_{B,n} = eV_{bi} + eV_n + kT \quad (3)$$

where eV_{bi} is the barrier height from the voltage intercept and $eV_n = E_{C,n} - E_F$, of 0.78 ± 0.1 eV and 0.62 ± 0.1 eV for Pt-GaN and Au-GaN, respectively. Minima in differential capacitance indicating transition beyond depletion conditions are also found close to the respective values for the built-in potential of these Schottky junctions. These values are lower than standard epi-layer of *n*-GaN, even when accounting for image force lowering of the barrier height in this case. The Fermi level energy with respect to the Pt and Au workfunction is markedly reduced compared to standard values owing to the interfacial alloy[37] whose work function is less than the respective noble metal, giving lower Schottky barriers to carrier transport through the high grain-boundary density GaN layer. This is also reflected in the carrier mobilities, which for a doping density of

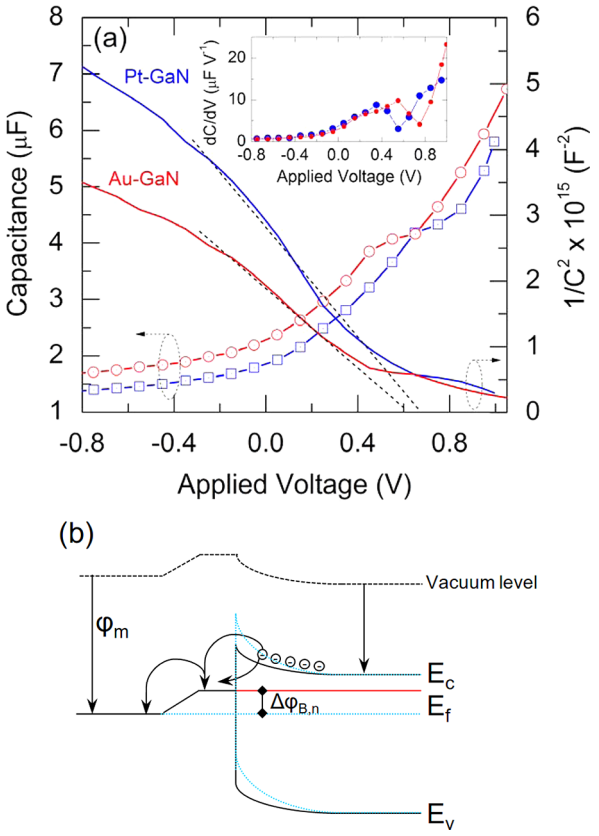

Figure 7. (a) Interface capacitance and Mott–Schottky ($1/C^2 - V$) profile for Pt- and Au-catalyzed porous GaN layers. (b) Proposed band structure model for intermetallic interface phase formation acting as the effective ohmic contact. The barrier with (solid line) and without (dashed line) the presence of the intermetallic is shown.

effectively ~10^{16} cm^{-3} an average electronic mobility of ~208 cm^2 V^{-1} s^{-1} is determined.

A plausible band structure for the interfacial intermetallic contact is also shown in Figure 7(b), which shows the presence of the Ga_2Au interface, with its lower workfunction, between the Au and GaN (a similar situation can be drawn when using Pt rather than Au). With forward bias, electrons can easily overcome the significantly reduced barriers, by thermionic-field emission to inject into the Au or Pt from the intermetallic. When the bias becomes negative, holes can tunnel through the Au/intermetallic interface barrier and inject into the notch to recombine with electrons. The contact resistance is markedly reduced as it provides a recombination center for carriers giving a linear $I-V$ response.

For the low resistance contacts to a porous GaN layer, either a low barrier Schottky contact forms with a graded band gap interface or a tunnel contact is formed. From XRD analysis, a crystalline Si_3N_4 dielectric layer forms when deposition is performed on silicon, just prior to continued VSS porous GaN growth, and is not likely from N out-diffusion from the GaN. The GaN, too, is not expected to decompose at 1203 K in NH_3,[38] but the Au and Pt melting points are close to this temperature. These metals solidify once the crystalline Ga_2Au solid phase is formed as the GaN interface. Oxide growth that would increase the resistivity of the contact is also prevented at this growth interface. To examine the reduction in effective barrier height, we considered the possibility of the influence of Ga_2O_3 formation between the intermetallic and the GaN, as is widely known for metal contacts to GaN. The reduction in $\varphi^0_{B,n}$ is thus correlated with the absence of an insulating oxide and is detailed in the Supporting Information. The variance in V_{fb} from the $C-V$ measurements, as observed in many metal/GaN systems, suggests Fermi-level pinning is not prevalent, and thus we do not consider surface state-mediated conduction or gap states to play a major role in effective ohmicity.

On Pt and Au, however, we confirm an intermetallic Ga_2Au phase typical of a VSS growth process which suggests a band structure that promotes transport by lowering the Schottky barrier by acting as a low barrier, ohmic contact to the GaN, rather than forming a definitive tunnel contact which shows ohmicity over a small potential range. In such a case, negative differential resistance caused by carrier effective mass increases, and reduction in mobility is prevented. The intermetallic formation at the interface that allows the growth of the GaN effectively acts as an intermetallic ohmic contact at the semiconductor interface, and the method may be extended to growing nanoscale III-N materials and alloys using metals that are not typically employed for contacting, to give ohmic response.

4. CONCLUSIONS

Porous GaN particles have been successfully grown as high surface area layers from Pt- and Au-coated silicon substrates by a vapor–solid–solid process. The particles form as a layer of single-crystal particles with interparticle and intraparticle porosity. Current–voltage and capacitance–voltage measurements show near-ohmic transport through low-doped, polycrystalline (as a layer), porous *n*-GaN without alloy contacts or low work function metals. Metal–Ga intermetallic alloy formation during vapor–solid–solid growth promotes thermionic emission-based low-resistance ohmic transport through the porous layer, and very low contact resistivities are possible to the faceted, rough *n*-GaN surface. The ability of contacting the GaN using such metals while at the same time facilitating the growth in a high surface area, crystalline porous network, including intraparticle pores, gives opportunities for superior diode-based optoelectronics and sensing and also metallic or colloidal quantum dot inclusions to tune broad-band light emission characteristics. The overall method of using intermetallic as ohmic contacts could also be applied to simultaneously grow and contact nanoscale III-N compounds for optoelectronic devices.

■ ASSOCIATED CONTENT

Supporting Information

A document with further details on the crystal growth setup (Figure S1) and energy dispersive X-ray (EDX) spectra for GaN samples grown on Si(100) substrates and coated with Pt and Au catalysts (Figure S2) is provided. The document also includes a short discussion about the effect that an interfacial oxide between the intermetallic layer and porous GaN would have on the electrical performance of the samples. Finally, a video showing the results obtained in time-resolved FIB tomography of a single porous GaN particle is also included to illustrate the intraporosity of the samples. This material is available free of charge via the Internet at http://pubs.acs.org.

■ AUTHOR INFORMATION

Corresponding Author

*E-mail: joanjosep.carvajal@urv.cat; c.odwyer@ucc.ie.

Notes

The authors declare no competing financial interest.

■ ACKNOWLEDGMENTS

This work was supported by the EU Framework 7 under Project No. FP7-SPA-2010-263044, the Spanish Government under Projects No. MAT2011-29255-C02-02, TEC2010-21574-C02-02, PI09/90527, and by Catalan Authority under Project No. 2009SGR235. This work was also supported by Science Foundation Ireland under contract No. 07/SK/B1232a and under the framework of the INSPIRE programme, funded by the Irish Government's Programme for Research in Third Level Institutions, Cycle 4, National Development Plan 2007-2013. The authors are also grateful to V. Mogili and D. Tanner for STEM imaging.

■ REFERENCES

(1) Lin, C. F.; Chen, K. T.; Lin, C. M.; Yang, C. C. *IEEE Electron Device Lett.* **2009**, *30*, 1057−1059.
(2) Ramizy, A.; Hassan, Z.; Omar, K. *Sens. Actuators, B* **2011**, *155*, 699−708.
(3) Nakamura, S.; Pearton, S.; Fasol, G. In *The Blue Diode Laser. The Complete Story*; Springer: Berlin, 2000; p 7.
(4) Lehmann, V.; Gösele, U. *Appl. Phys. Lett.* **1991**, *58*, 856−858.
(5) Tiginyanu, I. M.; Ursaki, V. V.; Monaico, E.; Foca, E.; Foll, H. *Electrochem. Solid-State Lett.* **2007**, *10*, D127−D129.
(6) O'Dwyer, C.; Buckley, D. N.; Sutton, D.; Serantoni, M.; Newcomb, S. B. *J. Electrochem. Soc.* **2007**, *154*, H78−H85.
(7) Stevens-Kalceff, M. A.; Tiginyanu, I. M.; Langa, S.; Foll, H.; Hartnagel, H. L. *J. Appl. Phys.* **2001**, *89*, 2560−2565.
(8) Bressets, P. M. M. C.; Knappen, J. W. J.; Meulenkamp, E. A.; Kelly, J. J. *Appl. Phys. Lett.* **1992**, *61*, 108−110.
(9) Huang, Y.; Duan, X.; Cui, Y.; Lieber, C. M. *Nano Lett.* **2002**, *2*, 101−104.
(10) Zhou, T.; Cheng, D.; Zheng, M.; Ma, L.; Shen, W. *Nanoscale Res. Lett.* **2011**, *6*, 276.
(11) Huang, J.; Ding, K.; Wang, X.; Fu, X. *Langmuir* **2009**, *25* (14), 8313−8319.
(12) O'Dwyer, C.; Buckley, D. N.; Sutton, D.; Newcomb, S. B. *J. Electrochem. Soc.* **2006**, *153*, G1039−G1046.
(13) Ghosh, B. K.; Tanikawa, T.; Hashimoto, A.; Yamamoto, A.; Ito, Y. *J. Cryst. Growth* **2003**, *249*, 422−428.
(14) Mynbaeva, M.; Totkov, A.; Kryzhanovski, A.; Kotousova, I.; Zubrilov, A. S.; Ratnikov, V. V.; Davidov, V. Y.; Kuznetsov, N. I.; Mynbaev., K.; Tsvetkov., D.; et al. *MRS Internet J. Nitride Semicond. Res.* **1999**, *4*, 14.
(15) Qhalid Fareed, R. S.; Adivarahan, V.; Chen, C. Q.; Rai, S.; Kuokstis, E.; Yang, J. W.; Khan, M. A.; Caissie, J.; Molnar, R. J. *Appl. Phys. Lett.* **2004**, *84*, 696−698.
(16) Cui, K.; Fathololoumi, S.; Kibria, M. G.; Botton, G. A.; Mi, Z. *Nanotechnology* **2012**, *23*, 085205.
(17) Wang, D.; Pierre, A.; Kibria, M. G.; Cui, K.; Han, X.; Bevan, K. H.; Guo, H.; Paradis, S.; Hakima, A.-R.; Mi, Z. *Nano Lett.* **2011**, *11*, 2353−2357.
(18) Chang, Y.-L.; Li, F.; Fatehi, A.; Mi, Z. *Nanotechnology* **2009**, *20*, 345203.
(19) Mynbaeva, M.; Titkov, A.; Kryganovskii, A.; Ratnikov, V.; Mynbaev, K.; Huhtinen, H.; Laiho, R.; Dmitriev, V. *Appl. Phys. Lett.* **2000**, *76*, 1113−1115.
(20) Wang, Y. D.; Chua, S. J.; Sander, M. S.; Chen., P.; Tripathy, S.; Fonstad, C. G. *Appl. Phys. Lett.* **2004**, *85*, 816−818.
(21) Bae, S. Y.; Seo, H. W.; Park, J.; Yang, H.; Kim, B. *Chem. Phys. Lett.* **2003**, *376*, 445−451.
(22) Diaz, D. J.; Williamson, T. L.; Adesida, I.; Bohn, P. W.; Molnar, R. J. *J. Appl. Phys.* **2003**, *94*, 7526−7534.
(23) Wagner, R. S.; Ellis, W. C. *Appl. Phys. Lett.* **1964**, *4*, 89−90.
(24) Gottschalch, V.; Wagner, G.; Bauer, J.; Paetzelt, H.; Shirnow, M. *J. Cryst. Growth* **2008**, *310*, 5123−5128.
(25) Persson, A. I.; Larsson, M. W.; Stenstron, S.; Ohlsson, B. J.; Samuelson, L.; Wallenberg, L. R. *Nat. Mater.* **2004**, *3*, 677−681.
(26) Hou, W.-C.; Chen, L.-Y.; Tang, W.-C.; Hong, F. C. N. *Cryst. Growth Des.* **2011**, *11*, 990−994.
(27) Song, J. O.; Ha, J.-S.; Seong, T.-Y. *IEEE Trans. Electron Devices* **2010**, *57*, 42−59.
(28) Carvajal, J. J.; Rojo, J. C. *Cryst. Growth Des.* **2009**, *9*, 320−326.
(29) Carvajal, J. J.; Bilousov, O. V.; Drouin., D.; Aguiló, M.; Díaz, F.; Rojo, J. C. *Microsc. Microanal.* **2012**, *18*, 1−7.
(30) Mei, Y.; Thurmer, D. J.; Deneke, C.; Kiravittaya, S.; Chen, Y.-F.; Dadgar, A.; Bertram, F.; Bastek, B.; Krost, A.; Christen, J.; et al. *ACS Nano* **2009**, *3*, 1663−1668.
(31) Liang, Z.; Wildeson, I. H.; Colby, R.; Ewoldt, D. A.; Zhang, T.; Sands, T. D.; Stach, E. A.; Benes, B.; García, R. E. *Nano Lett.* **2011**, *11*, 4515−4519.
(32) O'Dwyer, C.; Szachowicz, M.; Visimberga, G.; Lavayen, V.; Newcomb, S. B.; Sotomayor Torres, C. M. *Nat. Nanotechnol.* **2009**, *4*, 239−244.
(33) Fan, Z.; Mohammad, S. N.; Kim, W.; Aktas, O.; Botchkarev, A. E.; Morkoç, H. *Appl. Phys. Lett.* **1996**, *68*, 1672−1674.
(34) Tracy, K. M.; Hartlieb, P. J.; Einfeldt, S.; Davis, R. F.; Hurt, E. H.; Nemanich, R. J. J. *J. Appl. Phys.* **2003**, *94*, 3939−3948.
(35) Lin, M. E.; Ma, Z.; Huang, F. Y.; Fan, Z. F.; Allen, L. H.; Morkoç, H. *Appl. Phys. Lett.* **1994**, *64*, 1003−1005.
(36) Schroder, D. K. In *Semiconductor Material and Device Characterization*; Wiley: New York, 1998; p 156.
(37) Sporken, R.; Silien, C.; Malengreau, F.; Grigorov, K.; Caudano, R.; Sanchez, F. J.; Calleja, E.; Munoz, E.; Beaumont, B.; Gibart, P. *MRS Internet J. Nitride Semicond. Res.* **1997**, *2*, 23.
(38) Goldberg, Yu. A.; Posse, E. A. *Semiconductors* **1998**, *32*, 181−183.

Paper III

Bilousov, O.V.; Carvajal, J.J.; O'Dwyer, C.; Mateos, X.; Díaz, F. and Aguiló, M. *Low resistivity electrical contacting of porous n-type GaN layers due to reduced workfunction intermetallic seed layers* **(2013)** Proceedings of SPIE - The International Society for Optical Engineering, 8625.

Low resistivity electrical contacting of porous n-type GaN layers due to reduced workfunction intermetallic seed layers

Oleksandr V. Bilousov[a], Joan J. Carvajal[a]*, Colm O'Dwyer[b,c], Xavier Mateos[a], Francesc Díaz[a], Magdalena Aguiló[a]

[a]Física i Cristallografia de Materials i Nanomaterials (FiCMA-FiCNA) and EmaS Universitat Rovira i Virgili (URV), Marcellí Domingo s/n, E-43007 Spain
[b]Applied Nanosicence Group, Department of Chemistry, Univeristy College Cork, Cork, Ireland
[c]Micro & Nanoelectronics Centre, Tyndall National Institute, Dyke Parade, Cork, Ireland

ABSTRACT

Porous GaN crystals have been grown on Pt- and Au- coated silicon substrates as porous crystals and as porous layers. By the direct reaction of metallic Ga and NH_3 gas in a CVD system, intermetallic metal-Ga alloys formed at the interface allow the seeding and growth of porous GaN by vapor-solid-solid processes. Current-voltage and capacitance-voltage measurements confirm that the intermetallic seed layers result in near-ohmic contacts to porous n-GaN with low contact resistivities.

Keywords: Porous GaN, ohmic electron transport

1. INTRODUCTION

Gallium nitride (GaN) is considered one of the most important wide band-gap semiconductors for a number of applications in electronics and optoelectronics[1]. In its porous form, GaN has received particular interest in the last decade due to beneficial optical and electronic properties for gas sensors with high sensitivity[2], and light-emitting diodes (LEDs) with high light extraction efficiency[3]. Porous GaN has been typically fabricated by (photo)electrochemical and chemical etching methods[4-7], giving textured surfaces as a result of pore coalescence and variations in etch rates for extended etching times.

We produced porous GaN through the direct reaction of metallic Ga with NH_3 in a simple chemical vapor deposition (CVD) system[8]. Using this procedure we have been able to deposit micrometer size nanoporous GaN particles directly onto boron nitride (BN)[8] and silicon[9] substrates without necessitating any secondary etching or chemical treatment after growth to induce porosity. Furthermore, by using this technique we have demonstrated that it is possible to deposit porous GaN directly onto Si substrates in a single growth step. The only requirement, when depositing such porous particles on silicon substrates is that it is necessary to use a metal catalyst to induce the crystal growth of GaN. Metal catalysts are typically used to initiate growth through either a vapour-liquid-solid (VLS)[10] or vapor-solid-solid (VSS)[11] mechanism when using molecular beam epitaxy (MBE) and chemical vapor deposition (CVD), where the catalyst can influence the growth, e.g. colloidal gold nanoparticles can initiate the growth of GaN nanowires.

The development of porous GaN augers well for new electronic and optoelectronic devices with improved external quantum efficiencies, the incorporation of phosphors for LEDs, and high surface area sensing. However, the electrical properties of porous GaN and their correlation to its growth, have been scarcely reported in the literature.

Gallium Nitride Materials and Devices VIII, edited by Jen-Inn Chyi, Yasushi Nanishi, Hadis Morkoç, Joachim Piprek, Euijoon Yoon, Hiroshi Fujioka, Proc. of SPIE Vol. 8625, 86250T · © 2013 SPIE
CCC code: 0277-786X/13/$18 · doi: 10.1117/12.2003949

In this paper, we report the successful growth and simultaneous electrical contacting of nanoporous GaN grown using high workfunction Au- and Pt-coated silicon substrates, through the direct reaction of Ga and NH_3 in the CVD system. Au and Pt acted both as catalyst for the synthesis of porous GaN and as electrodes for the electrical characterization of the porous layers. The electrical measurements demonstrate the influence of the growth mechanism so that near-ohmic contacts can be made to n-type porous GaN layers using high workfunction metals (Au and Pt) which also form intermetallic seed layers to support vapor-solid-solid (VSS) growth of the porous GaN crystals.

2. EXPERIMENTAL

2.1 Synthesis of GaN particles

Nanoporous GaN microparticles were deposited on Au- and Pt-coated silicon (100) substrates with an area of 1 cm^2, using a horizontal single zone split tubular furnace Thermolyne 79300. Gallium metal (99.99%) and ammonia (>99.98%) were used as the Ga and N sources, respectively. A 20 nm layer of Au or Pt was deposited on the Si substrates using a RF sputtering process (AJA International) at a power of 150 W and a pressure of 3 mTorr. The coated substrate was then placed 2 cm above the Ga source. The quartz tube of the furnace was degassed to a vacuum pressure of 1×10^{-2} Torr, after which NH_3 was introduced through a mass-flow controller at a flow rate of 75 sccm and the furnace heated to the reaction temperature of 1203 K at a rate of 100 K min^{-1}, while the pressure was kept at 15 Torr. The reaction was continued at this temperature and pressure for 60 min under a constant flow of NH_3. Growth was halted by cooling to room temperature without NH_3 flow, reducing the pressure to 1×10^{-2} Torr. Figure 1 shows a schematic representation of the growth set-up used.

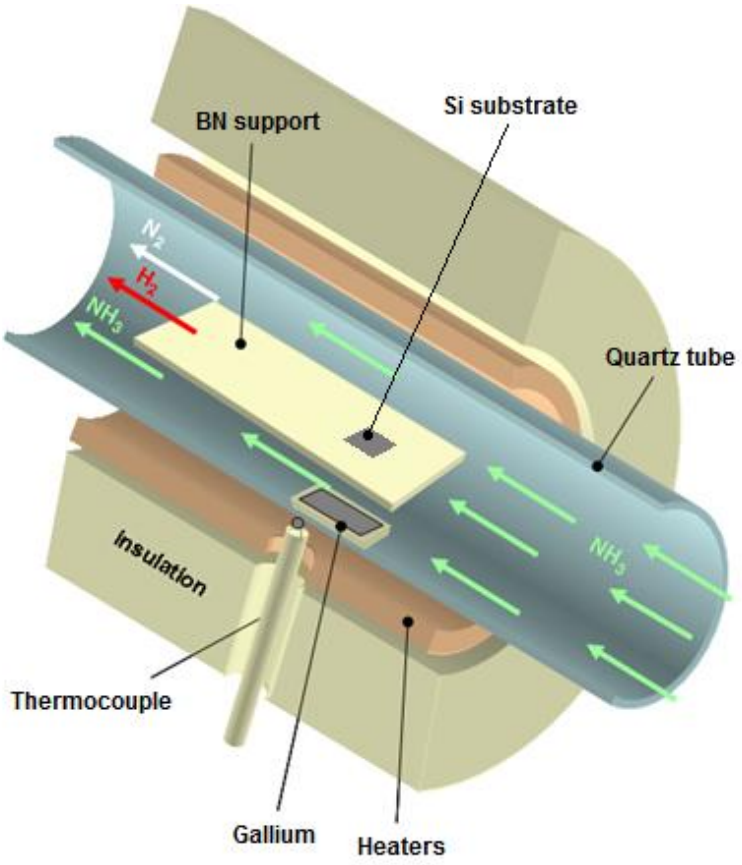

Figure 1. Growth set-up used to produce porous GaN layers on catalyst metal coated Si (100) substrates.

2.2 Structural and morphological characterization

X-ray diffraction (XRD) spectra and imaging in θ-2θ geometry of the as-grown sample were made using Cu Kα radiation in a Bruker-AXS D8-Discover diffractometer equipped with parallel incident beam (Göbel mirror), vertical θ-θ goniometer, XYZ motorized stage and a General Area Diffraction Detection System (GADDS) HI-STAR detector with a multiwire proportional counter of area 30 × 30 cm and 1024 × 1024 pixel density. Samples were placed directly on the sample holder and the area of interest was selected with the aid of a video-laser focusing system. An X-ray collimator system allows to analyze areas of 500μm. The X-ray diffractometer was operated at 40 kV and 40 mA to generate Cu Kα radiation. We collected 2D XRD patterns covering a range of 2θ between 20 - 85º at a distance of 15 cm from the sample. The exposure time was 120 s per frame. Identification of the crystalline phases was achieved by comparison of the XRD diffractogram with the ICDD database using Diffrac^{plus} Evaluation software (Bruker 2007).

The nanoporous GaN microparticles deposited on the Si substrates as a porous layer were characterized morphologically using a JEOL JSM 6400 scanning electron microscope (SEM). Before observation samples were coated with a thin layer of gold with a Bal-Tec SCD004 sputterer.

2.3 Electrical characterization

Charge transport measurements through the porous GaN films were conducted using 2- and 4-probe measurements using a dc-voltage course and an Agilent 34401A Digital Multimeter in a Peltier cell, thermostated to 295 K in a Faraday cage. Liquid metal contacts were made using In-Ga eutectic blown into a sphere from a gold metallized short borosilicate capillary tube ensuring good wetting (several μm^2) to the rough top-surface morphology of the porous GaN and avoid electrical shorting to the underlying metallized silicon. Measurements were made in 2 probe, 4-probe and van der Pauw[12] geometry. Resistivity values were extracted from I-V curves in the high bias regime (series resistance) and also from 4-point probe measurements.

3. RESULS AND DISCUSSIONS

3.1 Morphological characterization

Figures 2 (a) and (b) confirm that the porous GaN particles have a characteristic morphology consisting of faceted hourglass crystals with a mean size of ~1.5 μm. Crystal growth occurs progressively on the surface with individual crystals ripening until a layer of porous GaN microparticles covers the surface as a porous layer. The GaN layers are both microporous and mesoporous. The microporosity stems from the free space between particles (see Figure 2 (c)), whereas the nanoscale mesoporosity comes from internal pore features within the particles, confirmed with time-resolved focused ion beam (FIB) based tomography[11]. The particles obtained on the Si substrates coated with Pt showed a higher degree of internal porosity than those grown from Au-coated Si substrates.

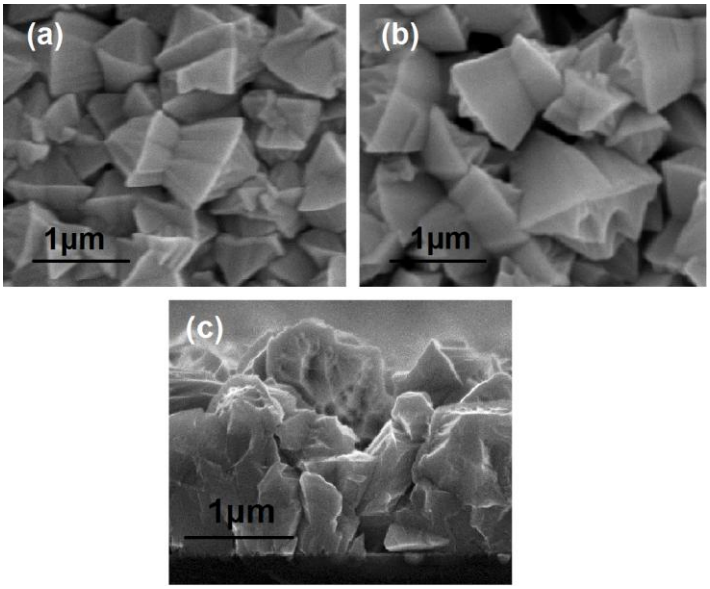

Figure 2. SEM image of porous GaN particles grown on Si (100) substrates coated with (a) 20 nm film of Au and (b) 20 nm film of Pt. (c) SEM cross sections showing interparticle porosity of the GaN layer.

We believe that the growth of these GaN nanoporous particles is assisted by a solid particle through the vapour–solid–solid (VSS) mechanism, the main stages of which are: the Ga incorporation into the Au or Pt solid phase eutectic, the formation of a Ga-Au or Ga-Pt alloy, the solubilisation of nitrogen on the Ga-Au(Pt) alloy, and finally the nucleation and growth of GaN.

3.2 Structural characterization

The crystalline structure of the porous GaN particles deposited on Si substrates coated with Au and Pt was analysed using X-ray diffraction. The XRD pattern shown in Figure 3 (a) for GaN grown on Au-coated Si substrates, confirms crystalline wurtzite GaN growth with a predominant diffraction intensity from low-index crystal facets. The regions at which the (400) diffraction peak of Si should appear (69.131º) has been excluded from the measurement to avoid problems of intensity saturation. This allows observation of lower intensity reflections that are attributed to crystalline Si_3N_4 and a crystalline Au-Ga intermetallic alloy of cubic Ga_2Au. We believe that the Si_3N_4 formation is most likely due to the reaction between NH_3 and silicon accelerated by the metallic catalyst. The formation of the Au-Ga crystalline alloy, which occurs here above the solid-solution formation temperature of 923 K, confirms intermetallic seeding to form GaN by reaction with NH_3 through a vapor-solid-solid process. The uniform intensity of the Debye rings (along the curved ring portions in Fig. 3b) collected for porous GaN confirms that there is no texturation of the layer of porous crystals (see Figure 3 (b)). For porous GaN grown on Pt-coated substrates, similar results were obtained, although we could not identify the formation of any specific crystalline Pt-Ga alloy, as can be seen in Figure 3(c) and (d).

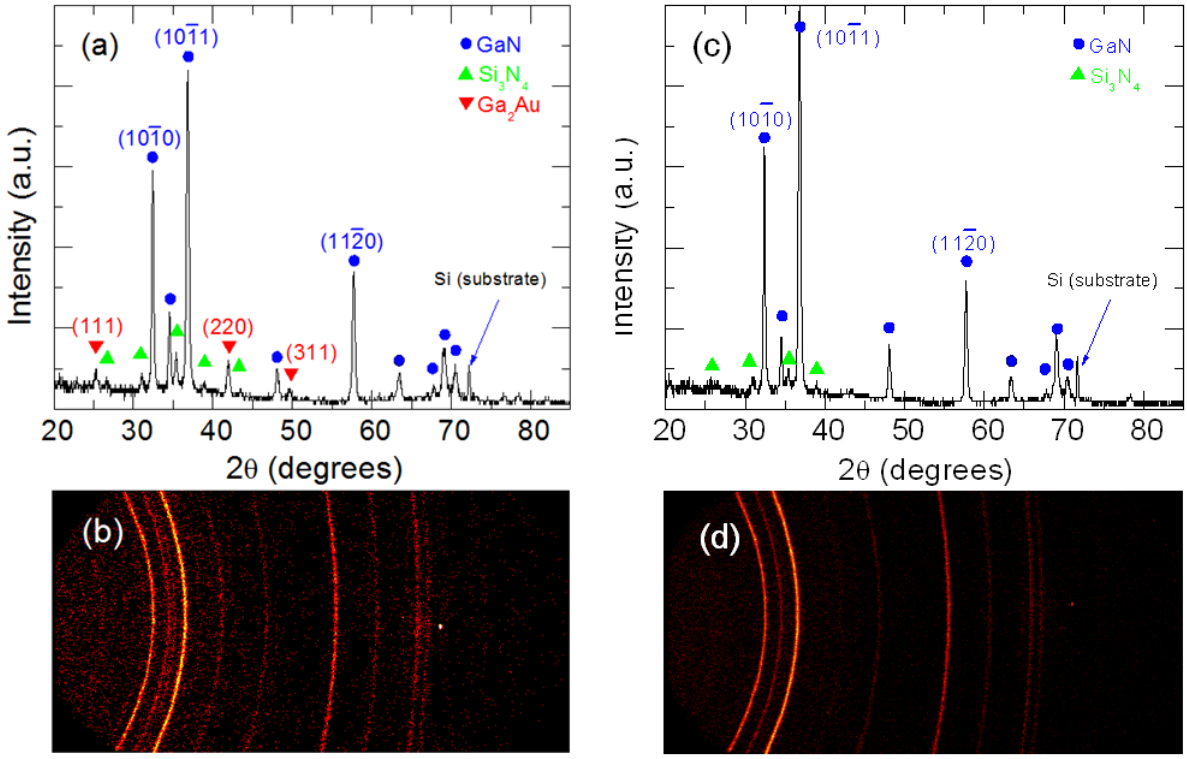

Figure 3. (a) XRD pattern for porous GaN deposited on Au-coated Si(100) showing the formation of crystalline GaN (ICDD 01-073-7289), Si_3N_4 (ICDD 03-065-8613) and Ga_2Au alloy (ICDD 01-071-6479). (b) Debye rings recorded with GADDS detector indicating no texturation of the porous GaN layer. (c) XRD pattern for porous GaN deposited on Pt-coated Si(100) showing the formation of crystalline GaN (ICDD 01-073-7289) and Si_3N_4 (ICDD 03-065-8613). (d) Debye rings recorded with GADDS detector indicating no texturation of the porous GaN layer.

3.3 Electrical characterization of Pt- and Au-contacted porous GaN

Figure 4 shows the *I-V* curves from the porous GaN catalyzed by Pt (Figure 4a) and also by Au (Figure 4b), with the second contact placed on the underlying metal which was under heating to 1203K in NH_3. The ln(*I*)-*V* curves show only slight asymmetry indicative of near ohmic, weak Schottky barriers of Pt and Au. Consistently, the conductivity of porous GaN grown from Pt is higher than that grown from Au, in spite of the higher workfunction. The *I-V* curve of porous GaN-Pt in Figure 5(a) shows the low-bias non-linearity consistent with a weak Schottky barrier. Both contacts are described using the thermionic emission theory, acknowledging a high ideality factor for weak barriers. The Schottly barrier height can still be estimated from:

$$I = I_0\left[\exp\left(\frac{qV - IR_S}{kT}\right) - 1\right] \quad (1)$$

where $I_0 = AA^{**}T^2\exp(-q\varphi^o_{B,n}/kT)$[13] where A^{**} is the effective Richardson constant. The estimated Schottky barrier heights using the theoretical value for the effective Richardson constant (26.4 A cm^{-2} K^{-2}) for Pt and Au contacted porous GaN are 0.66 eV and 0.53 eV, respectively.

In spite of the higher porosity from Pt-grown porous GaN, the contact resistivity of the Pt contact is $2 - 4 \times 10^{-4}$ Ω cm^2 while that of the gold contact is $6 - 9 \times 10^{-4}$ Ω cm^2. Thus the interface dominated the transport more than the crystallinity or morphology of the porous microstructure, and effective ohmic contacts can form with n-type GaN. Two terminal transport measurements (Figure 5b) acquired between the In-Ga ohmic contacts showed perfect ohmicity from

which low contact resistivities were determined with variable intercontact separation using the TLM approach and found to be in the range 1.7 – 4.4 × 10^{-4} Ω cm^2, in spite of the multifaceted, porous morphology. Corresponding 4-probe analysis gives sheet resistances for porous GaN films in the range 43-49 kΩ/□, which is higher than compact thin film forms as expected from a layer comprising microcrystals in intimate contact. The van der Pauw geometry measurements confirm these values with an average of 43 kΩ, independent of contact area on rough surfaces. The values, that match those of MBE grown GaN thin films with Ti/Au alloy contacts after annealing to 973 K[14], are caused by the efficient interface between the metal and the growing porous GaN[9]. Additionally, although annealing at 1173 K is known to initial improve contact resistivities down to the 10^{-6} Ω cm^2 with Ti/Al contacts, continued heating at this temperature for more than 40 seconds results in a drastic increase in contact resistance[14]. The present method avoids this by the use of noble metal contacts as catalysts for the GaN growth.

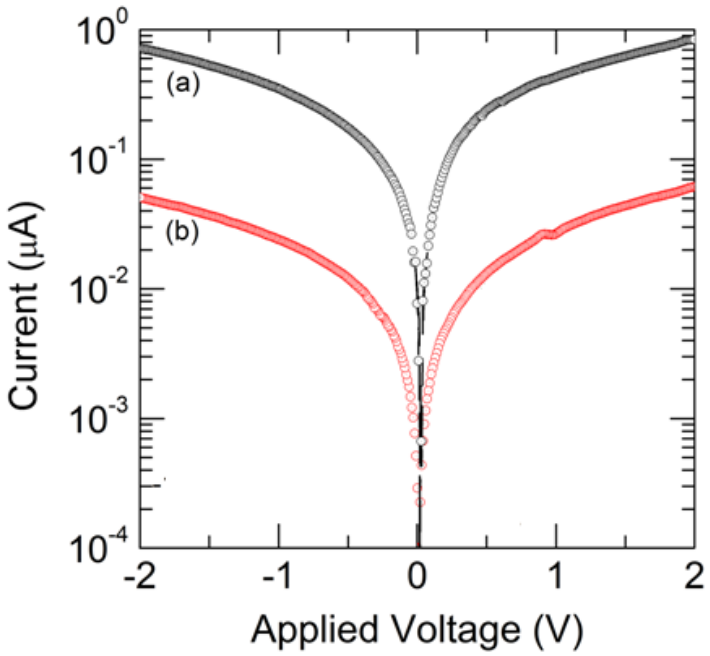

Figure 4. ln(*I*)-*V* curves for porous GaN grown from (a) Pt and (b) Au.

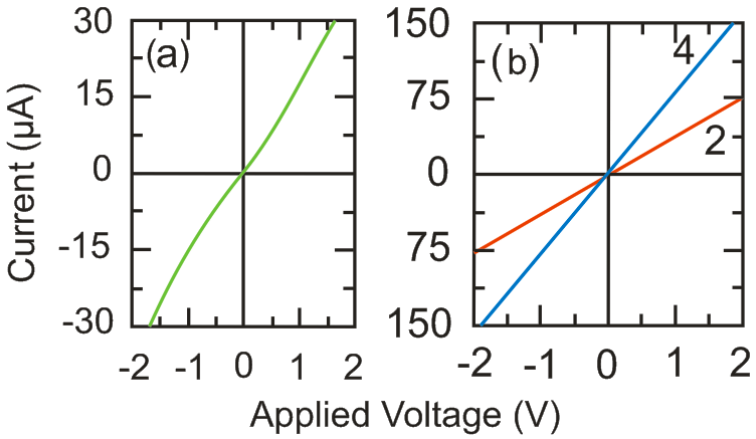

Figure 5. (a) *I-V* curve for the porous GaN grown directly from Pt and (b) *I-V* curves from 2- and 4-probe measurements using In-Ga ohmic contacts to porous GaN.

Capacitance-voltage analysis was performed by scanning the applied potential at a rate of 10 mV s^{-1} with a superimposed AC signal with an amplitude of 15 mV at a frequency of 1 MHz to determine the capacitance of the porous GaN under depletion conditions. For these porous GaN layers, this frequency was sufficient to sinusoidally vary the depletion region width without unwanted contributions to capacitance from the dielectric Si_3N_4 present on the Ga_2Au interface. Gold contacts made to the porous GaN formed a Schottky contact for the measurement. The $1/C^2$-V analysis in the framework of the Mott-Schottky model, shown in Figure 6, confirms an n-type semiconductor with a donor concentration N_D given by the slope $N_D = 2C^2V/q\varepsilon\varepsilon_0$ corresponding to a net impurity concentration[15] in porous GaN of $n = 1.6 \times 10^{16}$ cm^3 using a dielectric constant $\varepsilon = 8.9$ for GaN. These low values for unintentionally doped n-GaN give a corresponding Schottky barrier height from:

$$\varphi^0{}_{B,n} = eV_{bi} + eV_n + kT \tag{2}$$

where eV_{bi} is the barrier height from the voltage intercept and $eV_n = E_{C,n} - E_F$, of 0.78 ± 0.1 eV and 0.62 ± 0.1 eV for Pt-GaN and Au-GaN respectively. The Fermi level energy with respect to the Pt and Au workfunction is markedly reduced compared to standard values due to the formation of an interfacial alloy[16] between Ga and those metals, whose work function is less than the respective noble metal, giving lower Schottky barriers to carrier transport through the high grain-boundary density GaN layer. This is also reflected in the carrier mobilities, which for a doping density of effectively ~10^{16} cm^{-3}, the mobilities are only ~208 cm^2 V^{-1} s^{-1}.

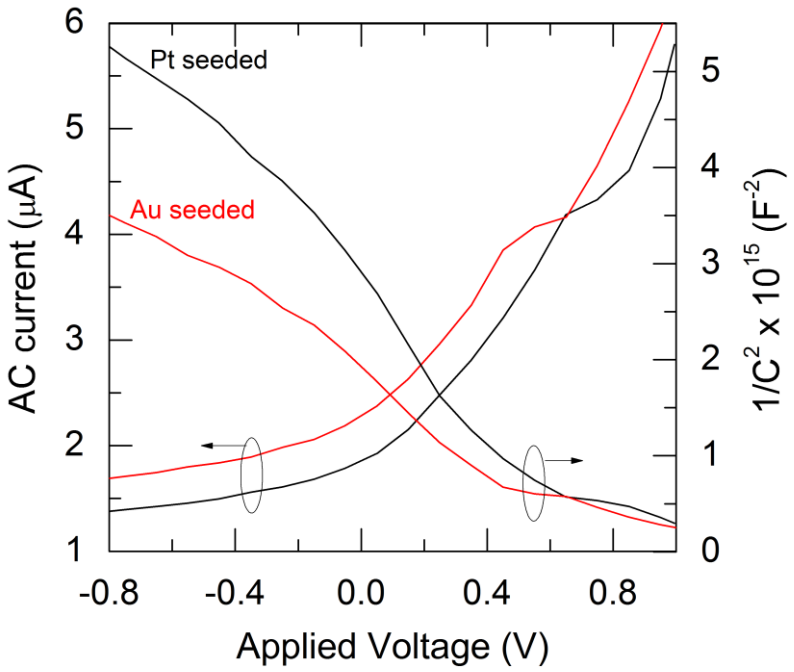

Figure 6. AC current and corresponding depletion layer capacitance plotted as $1/C^2 - V$ for Pt and Au catalyzed porous GaN layers.

For the low resistance contacts to a porous GaN layer either a low barrier Schottky contact forms with a graded band-gap interface or a tunnel contact is formed. From XRD analysis, a crystalline Si_3N_4 dielectric layer forms when deposition is performed on silicon, just prior to continued VSS porous GaN growth and is not likely from N out-diffusion from the GaN. The GaN too, is not expected to decompose at 1203 K in NH_3 (it would at a slightly higher temperature in vacuum)[17], but the Au and Pt melting points are close to this temperature. These metals solidify once the crystalline intermetallic Ga_2Au solid phase is formed. Oxide growth that would increase the resistivity of the contact is also prevented. The intermetallic Ga_2Au phase suggests a band structure that promotes transport by lowering the Schottky barrier such as metal-induced gap states, rather than forming a definitive tunnel contact which shows ohmicity over a

small potential range, so that a negative differential resistance regime caused by carrier effective mass increases and reduction in mobility, is prevented. If tunnelling currents were to play a role and give high ideality factor consistent with a very poorly rectifying contact, the multiple heterojunctions through which tunnelling currents can flow would be required, and this is not the case for the ohmic and near-ohmic contacts to porous GaN.

4. CONCLUSIONS

In summary, porous GaN particles have been successfully grown as high surface area layers from Pt- and Au- coated silicon substrates by a vapor-solid-solid process. The particles form as a layer of single-crystal particles with interparticle and intraparticle porosity. Current-voltage and capacitance-voltage measurements show near-ohmic transport through low-doped, polycrystalline (as a layer), porous n-GaN without alloy contacts or low work function metals. Metal-Ga intermetallic alloy formation during vapor-solid-solid growth promotes thermionic emission-based low-resistance ohmic transport through the porous layer and very low contact resistivities are possible to the faceted, rough n-GaN surface.

ACKNOWLEDGMENT

This work was supported by the EU Framework 7 under Project No. FP7-SPA-2010-263044, the Spanish Government under Projects No. MAT2011-29255-C02-02, TEC2010-21574-C02-02, PI09/90527, and by Catalan Authority under Project No. 2009SGR235. This work was also supported by Science Foundation Ireland under contract No. 07/SK/B1232a and under the framework of the INSPIRE programme, funded by the Irish Government's Programme for Research in Third Level Institutions, Cycle 4, National Development Plan 2007-2013.

REFERENCES

[1] Nakamura, S., Pearton, S. and Fasol, G., [The Blue Diode Laser. The Complete Story], Springer, Berlin, 7 (2000).
[2] Ramizy, A., Hassan, Z. and Omar, K., "Porous GaN on Si (111) and its application to hydrogen gas sensor, " Sens. Actuators, B 155, 699-708 (2011).
[3] Lin, C. F., Chen, K. T., Lin, C. M. and Yang, C. C., "InGaN-Based Light-Emitting Diodes With Nanoporous Microhole Structures, " IEEE Electron Device Lett. 30, 1057-1059 (2009).
[4] Mynbaeva, M., Titkov, A., Kryganovskii, A., Ratnikov, V., Mynbaev, K., Huhtinen, H., Laiho, R. and Dmitriev, V., "Structural characterization and strain relaxation in porous GaN layers," Appl. Phys. Lett. 76**,** 1113-1115 (2000).
[5] Wang, Y. D., Chua, S. J., Sander, M. S., Chen. P., Tripathy, S. and Fonstad, C. G., "Fabrication and properties of nanoporous GaN films, " Appl. Phys. Lett. 85**,** 816-818 (2004).
[6] Bae, S. Y., Seo, H. W., Park, J., Yang, H. and Kim, B., "Porous GaN nanowires synthesized using thermal chemical vapor deposition, " Chem. Phys. Lett. 376**,** 445-451 (2003).
[7] Diaz, D. J., Williamson, T. L., Adesida, I., Bohn, P. W. and Molnar, R. J., "Morphology evolution and luminescence properties of porous GaN generated via Pt-assisted electroless etching of hydride vapor phase epitaxy GaN on sapphire, " J. Appl. Phys. 94, 7526-7534 (2003).
[8] Carvajal, J. J. and Rojo, J. C., "Morphology Control in As-Grown GaN Nanoporous Particles," Cryst. Growth Des. 9, 320-326 (2009).
[9] Carvajal, J. J., Bilousov, O. V., Drouin. D., Aguiló, M., Díaz, F. and Rojo, J. C., "Chemical Vapor Deposition of Porous GaN Particles on Silicon," Microsc. Microanal. 18, 1-7 (2012).
[10] Wagner, R. S. and Ellis, W. C., "Vapour-Liquid-Solid mechanism of single crystal growth," Appl. Phys. Lett. 4, 89-90 (1964).
[11] Persson, A. I., Larsson, M. W., Stenstron, S., Ohlsson, B. J., Samuelson, L. and Wallenberg, L. R., "Solid-phase diffusion mechanism for GaAs nanowire growth, " Nat. Mater., 3, 677-681 (2004).

[12] O'Dwyer, C., Szachowicz, M., Visimberga, G., Lavayen, V., Newcomb, S. B. and Sotomayor Torres, C. M. "Bottom-up growth of fully transparent contact layers of indium tin oxide nanowires for light-emitting devices," Nat. Nanotech. 4, 239-244 (2009).
[13] Tracy, K. M., Hartlieb, P. J., Einfeldt, S., Davis, R. F., Hurt, E. H. and Nemanich R. J. "Electrical and chemical characterization of the Schottky barrier formed between clean n-GaN(0001) surfaces and Pt, Au, and Ag," J. Appl. Phys. 94, 3939-3948 (2003).
[14] Lin, M. E., Ma, Z., Huang, F. Y., Fan, Z. F., Allen, L. H. and Morkoç, H., "Low resistance ohmic contacts on wide band-gap GaN," Appl. Phys. Lett. 64, 1003-1005 (1994).
[15] Schroder, D. K., [Semiconductor Material and Device Characterization], Wiley, New York, 156 (1998).
[16] Sporken, R., Silien, C., Malengreau, F., Grigorov, K., Caudano, R., Sanchez, F. J., Calleja E., Munoz, E., Beaumont, B., and Gibart, P., "XPS study of Au/GaN and Pt/GaN contacts," MRS Internet J. Nitride Semicond. Res. 2, 23 (1997).
[17] Goldberg, Yu. A. and Posse, E. A., "Ohmic contact formation during continuous heating of GaAs and GaP Shottky diodes," Semiconductors 32, 181-183 (1998).

Paper IV

Carvajal, J.J.; Bilousov, O.V.; Drouin, D.; Aguiló, M.; Díaz, F. and Rojo, J.C. *Chemical vapor deposition of porous GaN particles on silicon* **(2012)** Microscopy and Microanalysis, 18 (4), pp. 905-911.

Microsc. Microanal. 18, 905–911, 2012
doi:10.1017/S1431927612001134

Microscopy AND Microanalysis

Chemical Vapor Deposition of Porous GaN Particles on Silicon

Joan J. Carvajal,[1,2,*] Oleksandr V. Bilousov,[1] Dominique Drouin,[2] Magdalena Aguiló,[1] Francesc Díaz,[1] and J. Carlos Rojo[3,†]

[1]*Física i Cristallografia de Materials i Nanomaterials (FiCMA-FiCNA), Universitat Rovira i Virgili, Campus Sescelades, c/Marcel·lí Domingo s/n, 43007 Tarragona, Spain*
[2]*Department of Electrical and Computer Engineering, Université de Sherbrooke, Sherbrooke, Québec J1K 2R1, Canada*
[3]*Department of Materials Science and Engineering, State University of New York, Stony Brook, NY 11794, USA*

Abstract: We present a technique for the direct deposition of nanoporous GaN particles on Si substrates without requiring any post-growth treatment. The internal morphology of the nanoporous GaN particles deposited on Si substrates by using a simple chemical vapor deposition approach was investigated, and straight nanopores with diameters ranging between 50 and 100 nm were observed. Cathodoluminescence characterization revealed a sharp and well-defined near band-edge emission at ~365 nm. This approach simplifies other methods used for this purpose, such as etching and corrosion techniques that can damage the semiconductor structure and modify its properties.

Key words: III-nitrides, chemical vapor deposition, nanoporous semiconductors, cathodoluminescence, focused ion beam, silicon technology

Introduction

The unique properties that porous semiconductor materials exhibit compared to their bulk counterparts (Bressets et al., 1992) have propelled the utilization of these materials in the fabrication of enhanced devices for advanced microelectronics, sensors, interfacial structures, and catalysis. The actual application of these materials does, however, critically hinge on the development of processing methods able to precisely control the optical and electrical properties of the resulting porous materials.

Porosification in semiconductors can be obtained by anodization in a suitable electrolyte (Föll et al., 2006), which depends on many parameters that require complex equipment for their control. This, together with the fact that many electrolytes are highly toxic and/or corrosive, provides the motivation to develop new approaches to produce porous semiconductors that overcome these limitations and provide a "greener" technology. Chemical vapor deposition (CVD) technology has also been used, in some cases, to produce porous semiconductors. For instance, noncrystalline porous Si (Stöger et al., 1999), porous boron carbonitride nanotubular fibers (Yin et al., 2005), and more recently porous SiC (Zangooie et al., 2000) were fabricated by this technique, but in any case these structures were deposited on Si substrates.

Among all of these materials, wide band-gap semiconductors, and especially GaN, are expected to potentially contribute to the advancement of novel technologies in magnetism, catalysis, and biotechnology (Föll et al., 2006). Preexisting technologies for the fabrication of porous GaN involve several costly post-growth treatments based mainly in corrosion methods to induce the porosity in the samples, such as electrolytic etching (Li et al., 2002), electroless direct- and metal-assisted chemical etching (Diaz et al., 2003; Qhalid Fareed et al., 2004), dry etching (Mynbaeva et al., 2000), anodization processes (Pakes et al., 2003), and inductively plasma etching through anodic alumina films (Wang et al., 2004). Other methods used to produce porous GaN include the thermal treatment of GaAs layers in H_2 ambient (Ghosh et al., 2003), the transamination of $Ga_2(NMe_2)_6$ in an aprotic solvent or its pyrolysis under an ammonia atmosphere (Chaplais et al., 2003; Chaplais & Kaskel, 2004), and the bombardment of GaN layers by heavy ions (Kucheyev et al., 2000). Metal-organic CVD has also been used to produce porous columnar GaN on Al_2O_3 substrates (Wohlfart et al., 2001). More recently, we also produced porous GaN on BN substrates by a simple CVD technique (Carvajal & Rojo, 2009).

Up to now, nanoporous GaN thin films have found application as buffer layers or templates for heteroepitaxial growth of lattice-mismatched materials with a low density of defects (Mynbaeva et al., 1999; Ghosh et al., 2003; Qhalid Fareed et al., 2004). Furthermore, the strong photoresponse that this porous semiconductor exhibits (Mynbaeva et al., 2001) makes it attractive for the development of sensors and detectors operating in the visible and the ultraviolet (UV) wavelengths of the electromagnetic spectrum.

Despite its interest, an additional major difficulty for the practical application of porous GaN appears with the lack of simple routes for its integration on the most common semiconductor technologies, based on silicon.

Here we present a new process of integrating nanoporous GaN particles on Si substrates by using only a simple chemical vapor deposition approach based on the direct

Received September 9, 2010; accepted April 15, 2012
*Corresponding author. E-mail: joanjosep.carvajal@urv.cat
†Currently at GE Global Research, Niskayuna, NY 12309, USA

reaction of gallium and ammonia catalyzed by Ni that does not require any post-growth treatment to induce the porosity. This is the first time that a nanoporous semiconductor has been obtained on Si substrates using this technique. This approach is simpler and less costly than preexisting technologies. Also, it does not use corrosive electrolytes or toxic metallorganic compounds, allowing for the generation of a green technology for the production of porous GaN. In addition, this is the first time that integration of nanoporous GaN on silicon substrates has been reported, to the best of our knowledge, facilitating the application of this porous semiconductor to the general optoelectronics industry.

Materials and Methods

Crystal Growth of the Nanoporous GaN Particles

We grew nanoporous GaN micron-sized particles by the direct reaction of metallic Ga with ammonia in a tubular CVD system (Carvajal & Rojo, 2009). We placed an excess amount of pure metal Ga (99.99999%, metal basis) at the bottom of the quartz tube of the furnace. One and two inch (111)- and (001)-oriented silicon wafers were placed above the Ga source at a vertical distance of 2.2 cm. Prior to their introduction in the furnace, the substrates were cleaned for 5 min in boiling acetone, followed by 5 min in boiling ethanol. In all these experiments we used $Ni(NO_3)_2$ as catalyst that was crucial for the nucleation of the nanoporous GaN micron-sized particles of Si substrates because we observed that without the use of a catalyst GaN did not form on the surface of the Si substrates. With temperature and under a reducing atmosphere, $Ni(NO_3)_2$ reduces to Ni and form droplets on the surface of the substrate. Ni has been used as catalyst for the nucleation of GaN nanowires on Si substrates through the vapor-liquid-solid mechanism (Chen et al., 2001). The catalyst was deposited on the surface of the substrate by dipping it in an ethanolic solution of $Ni(NO_3)_2$. After that, ethanol was evaporated in air, prior to the introduction of the substrates into the furnace. Ammonia (99.999%, Spec Gas Inc., Ivyland, PA, USA) was then introduced through a mass-flow controller at a rate of 75 sccm, and the furnace was heated up to the reaction temperature (1073–1173 K) at a heating rate of 100 K/min. Then, the furnace was kept at this temperature for 60 min under a constant flow of NH_3. The total pressure of the system was kept at 15 Torr (2 kPa) during the experiments. Finally, we cooled down the furnace to room temperature while we stopped the ammonia flow.

The samples have been identified by indicating the substrate on which they have been grown and the temperature at which the reaction was developed. The flow of NH_3, the time of reaction, and the pressure of the system were kept constant for all experiments, thus no information about these parameters was necessary in the identification of the samples. So, a sample labeled as Si-111-1123 corresponds to a sample grown on a Si (111) substrate at 1123 K.

Characterization

θ-2θ X-ray diffraction scans and imaging of the as-grown samples were performed in a Bruker-AXS D8-Discover diffractometer (Bruker, Karlsruhe, Germany) with parallel incident beam (Göbel mirror) and vertical goniometer, equipped with a collimator for the X-ray beam of 500 μm and a General Area Detector Diffraction System (GADDS) detector.[a] Cu radiation was obtained from a copper X-ray tube operated at 40 kV and 40 mA. Data were recorded in three different steps with area detector by performing a ω-scan with a frame width of 15° in the 2θ range 33–63° with an integration time of 120 s/frame.

To analyze the pore shapes, lengths, and propagation directions, we used focused ion beam (FIB)-based tomography, i.e., serial slicing and imaging, with a Zeiss 1540 Cross Beam microscope (Carl Zeiss, Oberkochen, Germany). This dual beam system is equipped with a FIB column with a Ga source and a high-resolution field emission electron column. The FIB column is standing at 52° of the electron column, and the sample surface is perpendicular to the ion column. The ion milling was performed using a 5 pA beam current to minimize surface damaging and materials redeposition.

Room temperature cathodoluminescence (CL) imaging and spectroscopy were performed in a field emission scanning electron microscope (Zeiss Supra 55) operating at 4 keV and 200 pA using a Gatan (Pleasanton, CA, USA) MonoCL 2 system and a Hamamatsu (Hamamatsu City, Japan) photomultiplier tube (R2228) over a scanned area of 4,000 μm^2. All spectra were corrected for the monochromator and detector response and normalized to maximum intensity.

Results and Discussion

Crystal Growth of the Nanoporous GaN Particles

The resulting nanoporous GaN structures, deposited on the surfaces of the Si substrates facing to the Ga source, were characterized morphologically by scanning electron microscopy (SEM). The particles, with diameters between 200 nm and 10 μm depending on the temperature of growth, showed in all cases a prismatic shape resembling a hexagonal pyramid with smooth lateral faces, but with pores from 30 nm up to 1.5 μm in diameter in their basal planes, in a similar way to those obtained previously on nanoporous GaN deposited on boron nitride substrates (Carvajal & Rojo, 2009). The walls between the smallest pores had thicknesses $<$50 nm.

In general, the external morphology of the GaN nanoporous particles indicates that the growth orientation is parallel to the $\langle 0001 \rangle$ direction, with their basal (0002) planes perpendicular to this direction, and their lateral faces constituted by planes of the $\{10\bar{1}\bar{1}\}$ family.

[a]The GADDS detector was 30 $\times$ 30 cm^2 with a 1024 $\times$ 1024 pixel charge-coupled device sensor.

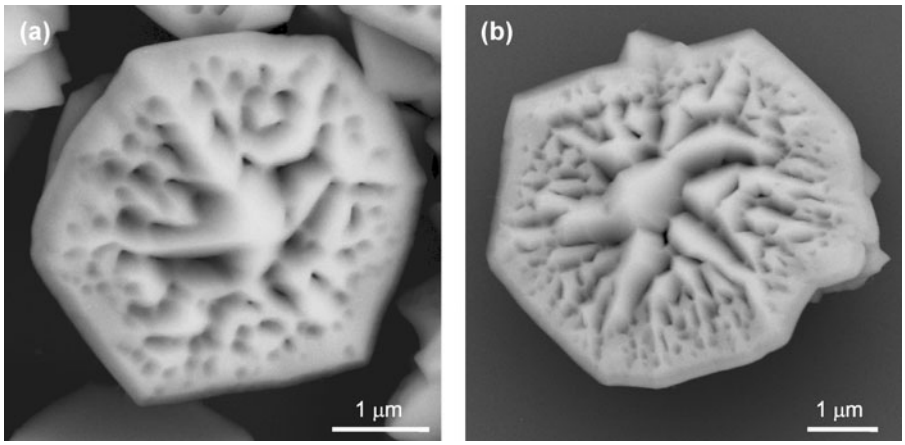

Figure 1. SEM pictures of GaN nanoporous particles deposited on (**a**) Si-100-1143 and (**b**) Si-111-1143 samples, showing the results obtained on two Si substrates with different crystallographic orientation, (100) and (111), respectively. The SEM pictures show the plane of the samples on which porosity has been observed.

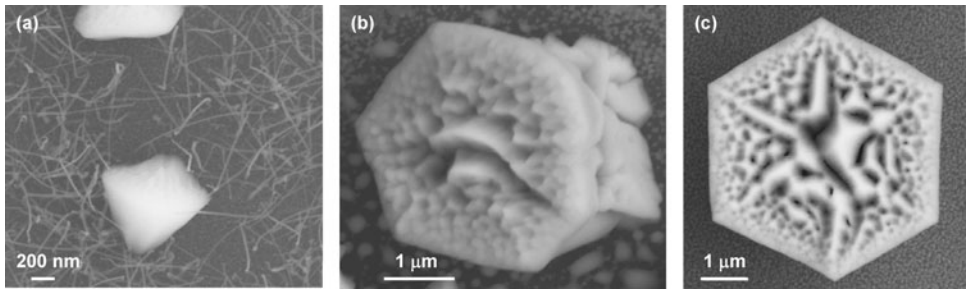

Figure 2. SEM pictures of GaN nanoporous particles obtained on samples (**a**) Si-111-1073, (**b**) Si-111-1143, and (**c**) Si-111-1173, grown on Si (111) substrates at three different temperatures, ranging from 1,073 to 1,173 K.

Nanoporous GaN particles obtained on Si (100) and Si (111) substrates showed similar features, with nanopores only found on the basal (0002) planes, as can be seen in Figure 1 for samples Si-100-1143 and Si-111-1143. In the central parts of the basal planes, nanopores seem to coalesce to form ridges. The degree of porosity in both cases is very similar, although the diameters of the smallest pores observed seem to be smaller in the particles obtained in Si (111) substrates, especially in the areas near the edges of the basal planes.

The size of the GaN particles and the induced porosity seem to be highly dependent on the temperature used in the growth process. Figure 2 shows scanning electron micrographs of GaN nanoporous particles obtained on samples Si-111-1073, Si-111-1143, and Si-111-1173. Although in these samples we always obtained GaN nanoporous particles with a similar morphology, their sizes and the diameters of the pores changed.

For instance, in sample Si-111-1073, small nanoporous particles with sizes around 200 nm are obtained (see Fig. 2a). These particles show the smallest nanopores observed in the GaN particles analyzed. A large quantity of GaN nanowires was obtained together with the nanoparticles.

In samples Si-111-1143 and Si-111-1173, GaN nanoporous particles with sizes around 3 μm were obtained. These particles are shown in Figures 2b and 2c. In these particles we observed a tendency to the coalescence of the pores as the temperature increased. Particles obtained in sample Si-111-1143 show a large number of discrete pores (see Fig. 2b), and only some pores in the center of the basal plane of the particle started to coalesce forming ridges. The tendency to the formation of these ridges increased with increasing the temperature, and the particles obtained in sample Si-111-1173 show several ridges originating from the central part of the basal planes of the particles and extending to the edges of these basal planes, distributed in a star configuration (see Fig. 2c).

By X-ray diffraction we examined the crystalline structure of these nanoporous GaN particles deposited on Si (100) and (111) substrates. Figures 3a and 3b show the X-ray powder diffraction patterns obtained on these nanoporous particles obtained on samples Si-100-1143 and Si-111-1143, respectively. The regions at which the (111) and (400) diffraction peaks of Si should appear (28.443° and 69.131°, respectively) have been excluded to avoid problems of intensity saturation in the detector. In the two cases the hexagonal wurtzite GaN phase was identified (JCPDS 00-050-0792). While in the sample Si-100-1143 we obtained only hexagonal GaN, in Si-111-1143, a second phase, corresponding to Ga_3Ni_2 alloy (JCPDS 01-071-8623), was also identified. This alloy is formed by the reaction of the excess of Ga with the Ni catalyst. However, the low intensity of the

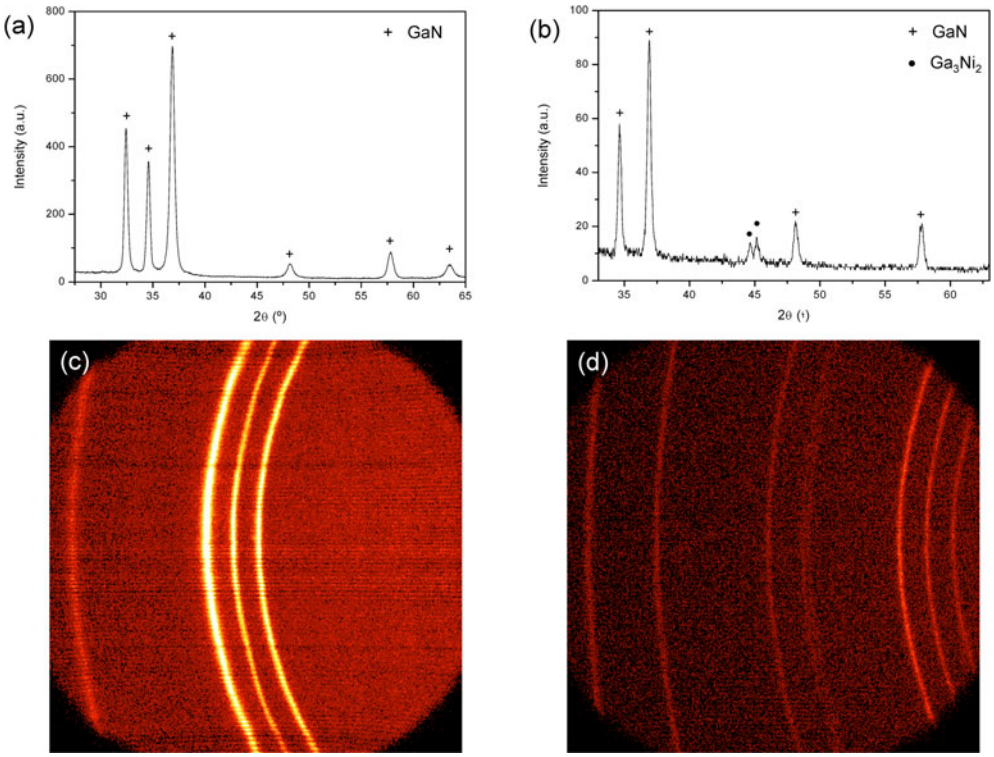

Figure 3. X-ray powder diffraction patterns of the obtained nanoporous GaN particles in (**a**) Si-100-1143 and (**b**) Si-111-1143 samples obtained on two silicon substrates with different crystallographic orientation, (100) and (111), respectively. X-ray diffraction images obtained with the area detector showing a partial view of the Debye rings detected for nanoporous GaN particles in (**c**) Si-100-1143 and (**d**) Si-111-1143 samples obtained on the same two silicon substrates with different crystallographic orientation presented in panels **a** and **b**.

peaks corresponding to this phase in comparison with the intensity of the peaks of the wurtzite GaN phase indicate that most of the Ga has reacted with ammonia to form the nanoporous GaN structures. The identification of this Ga_3Ni_2 alloy in the samples indicates that $Ni(NO_3)_2$ decomposes with temperature and is reduced under the experimental conditions of the crystal growth process to form metallic nickel, thus the catalyst under the reaction conditions is metallic nickel and not $Ni(NO_3)_2$. Figures 3c and 3d show a partial view of the Debye rings for the Si-100-1143 and Si-111-1143 samples, respectively, as have been observed in the GADDS detector. These images show that for the analyzed area (50 $\times$ 50 μm) in each sample, the deposited nanoporous GaN particles are not textured.

With a FIB attached to a scanning electron microscope, we performed a cross-section analysis of the discrete nanoporous GaN particles obtained in Si-111-1143. In this way we analyzed the shape and the length of the pores, as well as their direction of propagation inside of the GaN particles by removing layer by layer the material closer to the lateral surfaces of the GaN nanoporous particles. Nanopores were always observed on the (0002) faces of these GaN particles. The images recorded with the SEM revealed straight pores with lengths as long as 3 μm, similar to the sizes of the GaN particles, not interconnected among them, and not branched. The diameters of the pores ranged from 50 to 100 nm, with almost no variations in diameter with length. Figure 4 shows different images taken at different times on two different GaN nanoporous particles, showing different steps of the FIB milling and revealing different nanopores in the particles. A schematic sketch of the morphology of these particles has been included for a better understanding of their crystallographic orientation. As can be seen in Figure 4a, the nanopores in the central part of the GaN particles seem to follow an orientation parallel to the [0001] crystallographic direction. However, the nanopores found in the most external parts of the GaN particles (see Figs. 4b, 4e) seem to be parallel to the lateral faces of these particles, following the $[10\bar{1}1]$ crystallographic direction.

By comparing the images of the nanopores observed in these GaN particles with those pores obtained previously in GaN by other methods, we could find only two other approaches in which straight nanopores in GaN could be obtained: by Pt-assisted electroless etching (Diaz et al., 2003) and by inductively plasma etching using anodic aluminum oxide films as etch masks (Wang et al., 2004). However, these two techniques used different post-growth approaches to induce the porosity and also presented several drawbacks, such as the tendency of the pores to coalesce and form ridges (Diaz et al., 2003) or the generation of short-length pores of the order of their diameters (Wang et al., 2004).

The chemical composition of the as grown nanoporous GaN particles was analyzed qualitatively by energy-dispersive

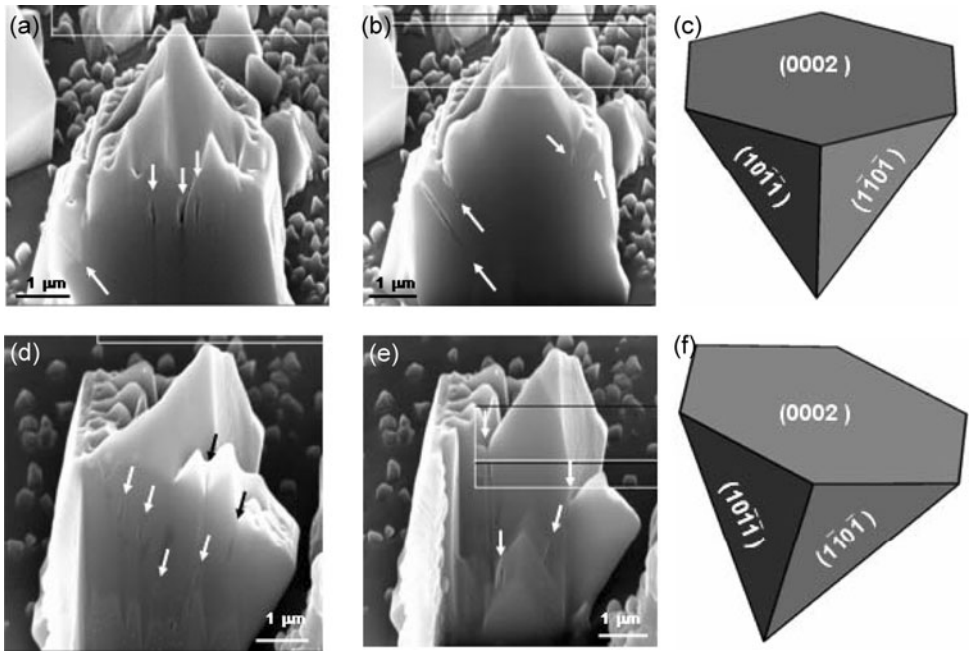

Figure 4. Tomography images of two different GaN nanoporous particles obtained in Si-111-1143 by slicing them with a FIB, and schematic sketches of the morphology of these GaN nanoporous particles obtained with the Shape software, version 7.2, for a better understanding of the crystallographic orientation of the nanopores. Arrows indicate the position of the pores observed on the samples.

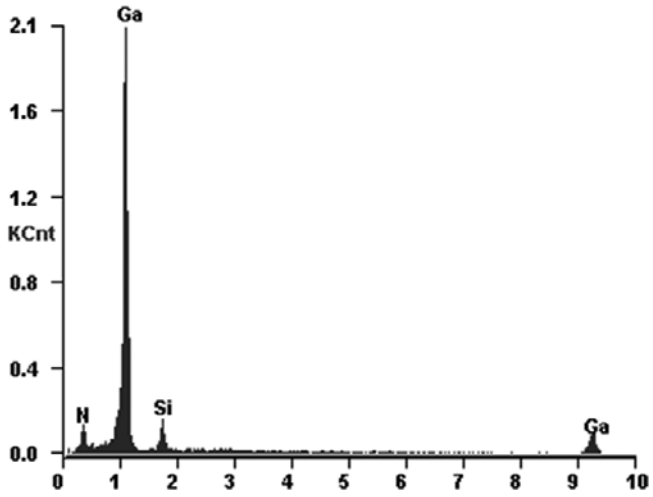

Figure 5. Energy-dispersive X-ray fluorescence spectrum of the GaN nanoporous particles obtained in Si-111-1143 showing only peaks corresponding to Ga and N, that arise from nonporous GaN, and Si, that arises from the silicon substrate.

X-ray spectrometry, revealing Si, Ga, and N, as shown in Figure 5 for the Si-111-1143 sample. At the level of detection used in these experiments (1.0 wt%), nickel, used as a catalyst, seems not to be incorporated in the GaN nanoporous particles, although further analyses and characterization will be required to confirm our hypothesis.

Figure 6 shows the results obtained in the characterization of the nanoporous GaN particles obtained in Si-111-1143 by CL. Figure 6a shows the CL spectra taken at room temperature. Near band-edge emission was observed at room temperature at around 365 nm (3.4 eV). CL studies revealed a sharp and well-defined band-gap emission with a full-width at half-maximum (FWHM) of 0.16 eV.

The band-gap emission observed in our nanoporous GaN structures was located at a similar position to those observed in nonporous GaN, and the bandwidth measured at FWHM was also similar to those measured for nonporous GaN by CL (Ponce et al., 1996; Yamane et al., 1998; Yano et al., 1999; Aoki et al., 2000). When compared with CL studies performed on porous GaN obtained by other methods (Diaz et al., 2002, 2003), the band-gap emission we observed is blueshifted by ~4 nm.

These results show that the porosity we are inducing on these nanoparticles does not affect the near band-edge emission of GaN and other possible emission at lower energies because defects and vacancies are not present in our structures.

The images recorded by CL show the parts of the sample that contribute most to the emission of light detected in the spectra. Figure 6b shows the CL image taken at $\lambda = 364$ nm, corresponding to the band-edge emission region in the ultraviolet range of the spectrum, for the Si-111-1143 sample. The bright spots in the image represent high emission intensity regions, while dark spots represent low emission intensity regions. The smallest features observed in these images are of the order of 50 nm in diameter. Since these samples are not flat, they are not limited by diffusion length and interaction volume (50 nm at 4 keV for GaN) and topography should be the major factor modulating the CL intensity. CL images revealed that luminescence is not spatially homogeneous. A higher intensity of light

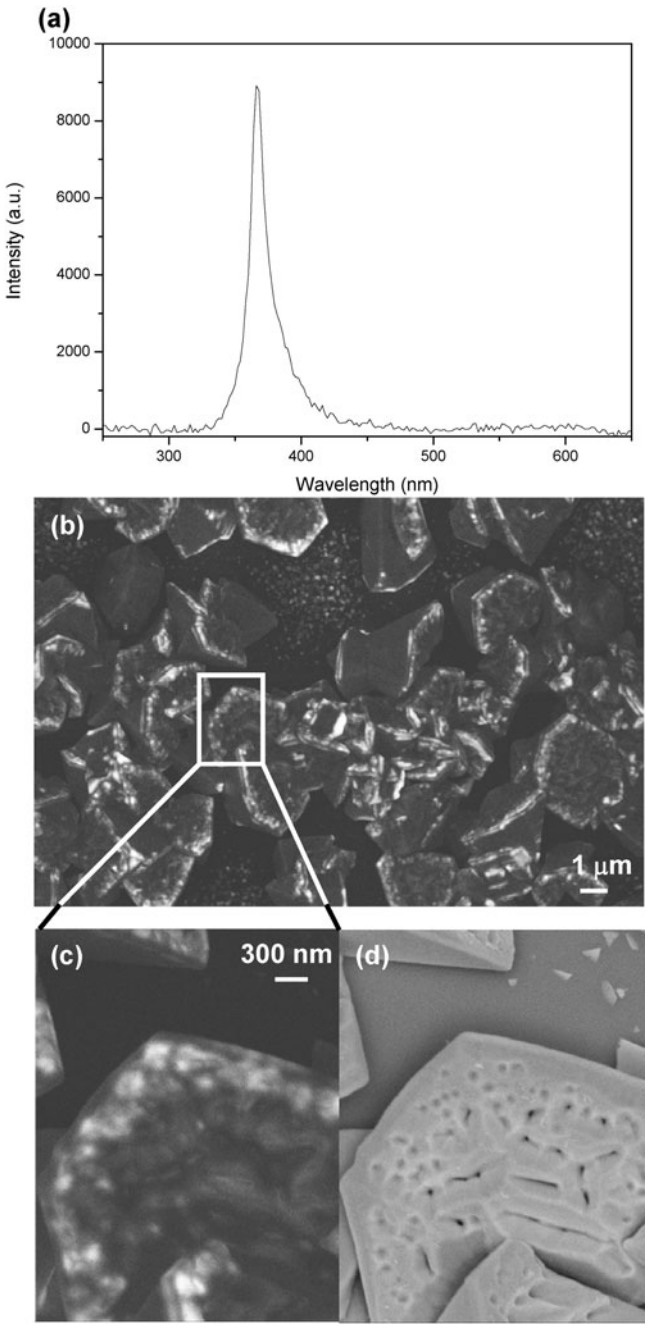

Figure 6. Room temperature CL (**a**) spectra and (**b**) monochromatic image (l = 364 nm) of nanoporous GaN particles obtained in Si-111-1143 recorded at 4 keV and 200 pA. An enlarged image of the selected region in panel **b** can be seen in panel **c**. The same region under secondary electrons can be seen in panel **d**.

from edges of the rough basal plane that contains the nanopores in the particles, when compared to their smooth lateral surfaces, is observed. The secondary electron image together with the CL image than can be seen in Figures 6c and 6d, respectively, in which the rough porous structure of the basal plane of one of the nanoporous GaN particles can be clearly seen, reveal that strong UV emission comes from areas surrounding the pores of the structure, while the pores coincide with dark spots in the images. The observed CL contrast is most likely due to the presence of nonradiative recombination channels around the pores, although topography can also play a role (Cherns et al., 2001; Miyajima et al., 2001).

Conclusions

We present results obtained for the direct deposition of nanoporous GaN particles on Si substrates through the direct reaction of Ga with NH_3 at relatively high temperatures. The advantage of this technique, compared to other approaches used in the fabrication of porous GaN, is that it does not require any post-growth treatment, such as etching techniques that can damage the semiconductor structure and modify its properties. The characterization performed on these nanoporous GaN particles shows that the main emission arising from these particles originates near the band-edge at 365 nm with a sharp and well-defined peak. This indicates that the nanoporosity induced in these particles during the growth process did not alter the emission expected for nonporous GaN. The nanopores were straight, and their diameters, ranging between 50 and 100 nm, were constant all along the length of the pores.

With this approach we demonstrated that it is possible to obtain porous GaN on Si substrates without applying any post-growth treatment. This technique simplifies previous methodologies used to generate porous GaN, and at the same time reduces the costs of these processes. In this technique porosity is generated during the crystal growth process. The enhancement of emission we obtained from the areas of the GaN particles surrounding the pores when compared to nonporous areas encourages us to keep developing these structures for optoelectronic applications.

Acknowledgments

This work was partially supported by the Spanish government under projects MAT2008-04046-E/MAT, MAT2008-06729-C02-02/NAN, and PI09/90527, by the Catalan authority under project 2009SGR235, and by the College of Engineering Dean's Office of the SUNY Stony Brook and the Center for Advanced Technology in Diagnostic Tools and Sensor Systems. J.J.C. is supported by the Education and Science Ministry of Spain and European Social Fund under the Ramón y Cajal program, RYC2006-858.

References

Aoki, M., Yamane, H., Shimada, M., Sekiguchi, T., Hanada, T., Yao, T., Sarayama, S. & Di Salvo, F.J. (2000). Growth of GaN single crystals from a Na-Ga melt at 750°C and 5Mpa of N_2. *J Crystal Growth* **218**, 7–12.

Bressets, P.M.M.C., Knappen, J.W.J., Meulenkamp, E.A. & Kelly, J.J. (1992). Visible light emission from a porous silicon/solution diode. *Appl Phys Lett* **61**, 108–110.

Carvajal, J.J. & Rojo, J.C. (2009). Morphology control in as-grown GaN nanoporous particles. *Crystal Growth Design* **9**, 320–326.

Chaplais, G. & Kaskel, S. (2004). Porosity control in pre-ceramic molecular precursor-derived GaN based materials. *J Mater Chem* **14**, 1017–1025.

Chaplais, G., Schlichte, K., Stark, O., Fischer, R.A. & Kaskel, S. (2003). Template assisted design of microporous gallium nitride materials. *Chem Commun* 730–731.

Chen, C.C., Yeh, C.C., Chen, C.H., Yu, M.Y., Li, H.L., Wu, J.J., Chen, K.H., Chen, L.C., Peng, J.Y. & Chen, Y.F. (2001). Catalytic growth and characterization of gallium nitride nanowires. *J Am Chem Soc* **123**, 2791–2798.

Cherns, D., Henley, S.J. & Ponce, F.A. (2001). Edge and screw dislocations as nonradiative centers in InGaN/GaN quantum well luminescence. *Appl Phys Lett* **78**, 2691–2693.

Diaz, D.J., Williamson, T.L., Adesida, I., Bohn, P.W. & Molnar, R.J. (2002). Morphology and luminescence of porous GaN generated via Pt-assisted electroless etching. *J Vac Sci Technol B* **20**, 2375–2383.

Diaz, D.J., Williamson, T.L., Adesida, I., Bohn, P.W. & Molnar, R.J. (2003). Morphology evolution and luminescence properties of porous GaN generated via Pt-assisted electroless etching of hydride vapor phaser epitaxy GaN on sapphire. *J Appl Phys* **94**, 7526–7534.

Föll, H., Carstensen, J. & Frey, S. (2006). Porous and nanoporous semiconductors and emerging applications. *J Nanomater* **2006**(1), 91635-1–10.

Ghosh, B.K., Tanikawa, T., Hashimoto, A., Yamamoto, A. & Ito, Y. (2003). Reduced-stress GaN epitaxial layers grown on Si(111) by using a porous GaN interlayer converted from GaAs. *J Crystal Growth* **249**, 422–428.

Kucheyev, S.O., Williams, J.S., Jagadish, C., Zou, J., Craig, V.S.J. & Li, G. (2000). Ion-beam-induced porosity of GaN. *Appl Phys Lett* **77**, 1455–1457.

Li, X., Kim, Y.W., Bohn, P.W. & Adesida, I. (2002). In-plane bandgap control in porous GaN through electroless wet chemical etching. *Appl Phys Lett* **80**, 980–982.

Miyajima, T., Hino, T., Tomiya, S., Yanashima, K., Nakajima, H., Araki, T., Nanishi, Y., Satake, A., Masumato, Y., Akimoto, K., Kobayashi, T. & Ikeda, M. (2001). Threading dislocations and optical properties of GaN and GaInN. *Phys Status Solidi B* **228**, 395–402.

Mynbaeva, M., Bazhenov, N., Evstropov, K.M., Saddow, S.E., Koshka, Y. & Melnik, Y. (2001). Photoconductivity in porous GaN layers. *Phys Stat Sol B* **228**, 589–592.

Mynbaeva, M., Titkov, A., Kryzhanovski, A., Ratnikov, V.V., Mynbaev, K., Huhtinen, H., Laiho, R. & Dmitriev, V.A. (2000). Structural characterization and strain relaxation in porous GaN layers. *Appl Phys Lett* **84**, 1113–1115.

Mynbaeva, M., Titkov, A., Kryzhanovski, A., Kotousova, I., Zubrilov, A.S., Ratnikov, V.V., Davidov, V.Y., Kuznetsov, N.I., Mynbaev, K., Tsvetkov, D.V., Stepanov, S., Cherenkov, A. & Dmitriev, D.A. (1999). Strain relaxation in GaN layers grown on porous GaN sublayers. *MRS Internet J Nitride Semicond Res* **4**, 14(1–5).

Pakes, A., Skeldon, P., Thompson, G.E., Fraser, J.W., Moisa, S., Sproule, G.I., Graham, M.J. & Newcomb, S.B. (2003). Anodic oxidation of gallium nitride. *J Mater Sci* **38**, 343–349.

Ponce, F.A., Bour, D.P., Götz, W. & Wright, P.J. (1996). Spatial distribution of the luminescence in GaN thin films. *Appl Phys Lett* **68**, 57–59.

Qhalid Fareed, R.S., Adivarahan, V., Chen, C.Q., Rai, S., Kuokstis, E., Yang, J.W., Khan, M.A., Caissie, J. & Molnar, R.J. (2004). Air-bridged lateral growth of crack-free $Al_{0.24}Ga_{0.76}N$ on highly relaxed porous GaN. *Appl Phys Lett* **84**, 696–698.

Stöger, M., Breymesser, A., Schlosser, V., Ramadori, M., Plunger, V., Peiró, D., Voz, C., Bertomeu, J., Nelhiebel, M., Schattschneider, P. & Andreu, J. (1999). Investigation of defect formation and electronic transport in microcrystalline silicon deposited by hot-wire CVD. *Physica B* **273–274**, 540–543.

Wang, Y.D., Chua, S.J., Sander, M.S., Chen, P., Tripathy, S. & Fonstad, C.G. (2004). Fabrication and properties of nanoporous GaN films. *Appl Phys Lett* **85**, 816–818.

Wohlfart, A., Devi, A., Hipler, F., Becker, H.W. & Fischer, R.A. (2001). Growth of porous columnar alpha-GaN layers on c-plane Al_2O_3 by MOCVD using bisazido dimethylaminopropyl gallium as single source precursor. *J Phys IV* **11**, 683–687.

Yamane, H., Shimada, M., Sekiguchi, T. & Di Salvo, F.J. (1998). Morphology and characterization of GaN single crystals grown in a Na flux. *J Crystal Growth* **186**, 8–12.

Yano, M., Okamoto, M., Yap, Y.K., Yoshimura, M., Mori, Y. & Sasaki, T. (1999). Control of nucleation site and growth orientation of bulk GaN crystals. *Jpn J Appl Phys* **38**, L1121–L1123.

Yin, L.W., Bando, Y., Golberg, D., Gloter, A., Li, M.S., Yuan, X. & Sekiguchi, T. (2005). Porous BCN nanotubular fibers: Growth and spatially resolved cathodoluminescence. *J Am Chem Soc* **127**, 16354–16355.

Zangooie, S., Woollam, J.A. & Arwin, H. (2000). Self-organization in porous 6H-SiC. *J Mater Res* **15**, 1860–1863.

Paper V

Bilousov, O.V.; Geaney, H.; Carvajal, J.J.; Zubialevich, V.Z.; Parbrook, P.J.; Giguère, A.; Drouin, D.; Díaz, F.; Aguiló, M. and O'Dwyer, C. *Fabrication of p-type porous GaN on silicon and epitaxial GaN* **(2013)** Applied Physics Letters, 103 (11), art. no. 112103.

Fabrication of p-type porous GaN on silicon and epitaxial GaN

O. V. Bilousov, H. Geaney, J. J. Carvajal, V. Z. Zubialevich, P. J. Parbrook, A. Giguère, D. Drouin, F. Díaz, M. Aguiló, and C. O'Dwyer

Citation: Applied Physics Letters **103**, 112103 (2013); doi: 10.1063/1.4821191
View online: http://dx.doi.org/10.1063/1.4821191
View Table of Contents: http://scitation.aip.org/content/aip/journal/apl/103/11?ver=pdfcov
Published by the AIP Publishing

APPLIED PHYSICS LETTERS **103**, 112103 (2013)

Fabrication of p-type porous GaN on silicon and epitaxial GaN

O. V. Bilousov,[1] H. Geaney,[2,3] J. J. Carvajal,[1,a)] V. Z. Zubialevich,[3] P. J. Parbrook,[3,4] A. Giguère,[5] D. Drouin,[5] F. Díaz,[1] M. Aguiló,[1] and C. O'Dwyer[2,3,b)]
[1]*Física i Cristallografia de Materials i Nanomaterials (FiCMA-FiCNA) and EMaS, Universitat Rovira i Virgili (URV), Marcellí Domingo s/n, E-43007 Spain*
[2]*Department of Chemistry, University College Cork, Cork, Ireland*
[3]*Tyndall National Institute, Lee Maltings, Cork, Ireland*
[4]*Department of Electrical & Electronic Engineering, University College Cork, Cork, Ireland*
[5]*Interdisciplinary Institute for Technical Innovation, Université de Sherbrooke, Sherbrooke, Quebec J1K 2R1, Canada*

(Received 31 July 2013; accepted 29 August 2013; published online 11 September 2013)

Porous GaN layers are grown on silicon from gold or platinum catalyst seed layers, and self-catalyzed on epitaxial GaN films on sapphire. Using a Mg-based precursor, we demonstrate p-type doping of the porous GaN. Electrical measurements for p-type GaN on Si show Ohmic and Schottky behavior from gold and platinum seeded GaN, respectively. Ohmicity is attributed to the formation of a Ga_2Au intermetallic. Porous p-type GaN was also achieved on epitaxial n-GaN on sapphire, and transport measurements confirm a p-n junction commensurate with a doping density of $\sim 10^{18}\,cm^{-3}$. Photoluminescence and cathodoluminescence confirm emission from Mg-acceptors in porous p-type GaN. © *2013 AIP Publishing LLC*. [http://dx.doi.org/10.1063/1.4821191]

Gallium nitride (GaN) is considered one of the most important wide band-gap semiconductors for a number of applications in electronics and optoelectronics.[1] In its porous form, GaN has received particular interest due to beneficial optical and electronic properties for gas sensors with high sensitivity[2] and light-emitting diodes (LEDs) with high light extraction efficiency.[3] The formation of p-type porous GaN is particularly relevant[4] for the fabrication of junctions and active regions for GaN-based LEDs with improved light extraction efficiency and external quantum efficiencies by gradation of the effective refractive index.[5] Porous GaN has been typically fabricated by (photo)electrochemical and chemical etching methods,[6–9] predominantly a top-down etching of epitaxial GaN, giving textured surfaces as a result of pore coalescence and variations in etch rates for extended etching times. A range of nanoscale III-N materials[10,11] in arrays and assemblies spanning emission from the blue to red regions of the visible spectrum,[12] and white light emitting light emitting devices and multi quantum wells have also been realized.[13] The ability to form relatively uniform, crystalline porous GaN layers over large areas without unwanted surface damage through complex etching without photolithographic masking or processing is challenging. Previously, we reported the bottom-up growth of low-resistivity, Ohmically contacted porous n-GaN in a single growth step[14] without the need for any secondary etching or chemical treatment after growth to induce porosity.[15,16]

Mg is the dopant most commonly used to generate p-type conductivity in GaN. Mg substitution of Ga in the GaN lattice is the shallowest acceptor which can be introduced in sufficient concentrations to enable p-type conduction.

In this letter, we detail the growth of porous GaN on Si and epitaxial GaN substrates on sapphire and evidence the introduction of p-type character by Mg-doping. Porous GaN formation was conducted within a chemical vapor deposition (CVD) system with growth on Si proceeding *via* the use of either a Pt or Au catalyst layer. Electrical transport measurements for the porous p-type GaN grown on Si from Au and Pt show Ohmic and Schottky behavior, respectively, with the former attributed to the formation of an Au/Ga intermetallic. Porous p-type GaN growth was also achieved on non-porous n-type epitaxial GaN and electrical transport measurements were used to confirm the formation of a p-n junction commensurate with the formation of p-type GaN. Additional evidence for the formation of p-type GaN was also obtained from low temperature photoluminescence (PL) data which showed clear differences for the undoped and Mg-doped samples.

GaN doped with Mg was produced through the direct reaction of metallic Ga with NH_3 in a simple CVD system. Nanoporous GaN microparticles were deposited on silicon (100) substrates with an area of $1\,cm^2$ coated with 20 nm thick films of Au or Pt used as the growth catalyst in a horizontal tubular furnace Thermolyne 79300 (see schematics in Figure 1). Further details can be found elsewhere.[14,15] Mg doped samples were annealed in atmosphere of N_2 for 20 min in order to break Mg-H complexes and activate the p-type conductivity of porous GaN. The epitaxial GaN substrates had n-type (doped with Si) conductivity. Mg-doped porous GaN was also grown on epitaxial n-type GaN substrates on sapphire. Gallium metal (99.99%), ammonia (>99.98%), and magnesium nitride (99.95%) were used as the Ga, N, and Mg sources, respectively, with the magnesium source placed 4 cm up-stream of the Ga source. The porous GaN layers were imaged using a JEOL JSM 6400 scanning electron microscope (SEM). PL was excited by 244 nm emission (second harmonic of 488 nm line) from a cw Ar-ion laser with power density of $2\,W/cm^2$. PL spectra were acquired using a Horiba iHR320 spectrometer equipped with a Synapse CCD matrix. Samples were placed in an evacuated chamber of a Janis closed-cycle helium cryostat

a)joanjosep.carvajal@urv.cat
b)c.odwyer@ucc.ie

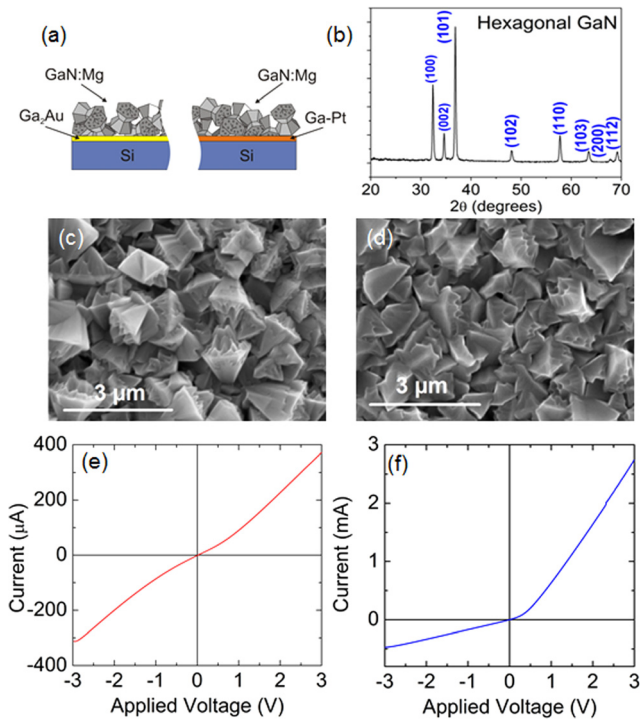

FIG. 1. (a) Schematic presentation of porous Mg-doped GaN on Si with Ga_2Au and Pt-Ga intermetallic layer, (b) X-ray diffraction pattern of porous Mg doped GaN on Si; SEM images of porous Mg-doped GaN grown on Si substrates coated with (c) Au and (d) Pt and corresponding I-V curves for (e) Au- and for (f) Pt-seeded GaN.

for PL measurements at different temperatures. Room temperature cathodoluminescence (CL) imaging and spectroscopy were performed in a field emission scanning electron microscope (Zeiss Supra 55) operating at 5–10 keV and 200 pA using a Gatan MonoCL 2 system and a Hamamatsu photomultiplier tube (R2228) over a scanned area of 4000 μm^2. All spectra were corrected for the monochromator and detector response and normalized to maximum intensity. X-ray diffraction (XRD) measurements were made using Cu Kα radiation in a Bruker-AXS D8-Discover diffractometer operated at 40 kV and 40 mA, equipped with parallel incident beam (Göbel mirror), a General Area Diffraction Detector System (GADDS), and a 500 μm^2 X-ray collimator system.

Figure 1(a) shows schematic presentation of porous GaN on Si with Ga_2Au and Pt-Ga intermetallic layers. The XRD pattern shown in Figure 1(b) for Mg doped GaN confirms crystalline wurtzite GaN. Figures 1(c) and 1(d) confirm that the porous GaN particles have a characteristic morphology consisting of faceted crystals with a mean size of $\sim$1.5 μm, similar to that observed in undoped samples.[14] In both cases, crystal growth occurs progressively on the surface with individual crystals until a layer of porous GaN microcrystals covers the surface as a porous layer.

Two-probe electrical measurements of the various Mg-doped GaN samples were conducted using In/Ga liquid eutectic contacts and a Biologic SP-50 potentiostat. An In/Ga eutectic droplet was used as the Ohmic contact. Linear voltage sweeps were obtained between the range of −3 V and 3 V with a 50 mV/s sweep rate. Figures 1(e) and 1(f) show I-V curves taken from Mg-doped porous GaN grown from Au- and Pt-coated Si (100) substrates, respectively. For samples grown using an Au catalyst, a near Ohmic contact behavior was repeatedly observed which is consistent with the formation of a Ga_2Au intermetallic between the underlying substrate and GaN material[9] in a similar way observed for undoped porous GaN particles.[14] However, for the GaN samples grown using Pt as catalyst, the response was markedly different with the profile indicating the formation of a Schottky contact. For porous GaN specifically, the thickness is determined by the size of the crystals and their assembly on the surface, which results in a "rough" topology, with a high density of grain boundary scattering centers. For electrical measurements, particle distributions[14] confirm that both nearest neighbour distances and overall distribution of various nonspherical catalyst material prevent the formation of a percolating conduction layer beneath the GaN; the electrical characterization is of the porous GaN polycrystalline layer. At room temperature, the effective linearity of the I−V response measured for porous GaN to high work function metals, with an intermetallic seed layer between the metal and GaN, is maintained at high bias. As stated earlier, the Pt-Ga alloy results in a Schottky contact to the porous p-type GaN. The Schottky barrier height $\varphi^o_{B,p}$ (SBH) can be estimated from $I = I_0\exp[(qV - IR_s)/kT - 1]$ with $I_0 = AA^{**}T^2\exp(-q\varphi^o_{B,p}/kT)$, where A^{**} is the effective Richardson constant ($26.4\,A\,cm^{-2}\,K^{-2}$).[17] The estimated SBHs for Pt contacted porous p-GaN is 0.57 eV. While a small in-built potential also exists for the Au-contacted sample, the symmetry in the response at negative bias confirms that the presence of the intermetallic Ga_2Au at the GaN-Si interface prevents a rectifying barrier. Also, as with unintentionally n-type GaN growth we investigated previously,[14] the Pt-Ga contact to the GaN at the silicon interface results in an order of magnitude higher current, but in the case of p-GaN, the transport mechanism gives a non-linear, Schottky-type response.

To further investigate the nature of the Mg-doped porous GaN, it was grown on epitaxial n-type GaN substrates (without the presence of catalyst layer) under the same conditions. In this case, the porous crystals of GaN have a different morphology as the porous GaN was found to be grown oriented along the c-axis direction with respect to the epitaxial GaN on the substrate (Figures 2(a) and 2(c)). Figure 2(b) shows I-V measurements taken between the underlying epitaxial n-type GaN substrate and the porous p-type GaN of porous contacts; the clear p-n junction response confirms the formation of p-type porous GaN confirmed by the asymmetric diode response in Fig. 2(d) where a clear exponential I-V relationship is found. The high bias resistance turn-over of the porous p-type GaN occurs at $\sim$1 V. At this voltage, the exponential current increase results in high level carrier injection across the junction as the voltage is increased, and then follows a linear dependency on applied voltage above 1 V (and is found to remain so up to $\sim$5 V in all cases), consistent with an effective series resistance which is believed to arise from the high density of inter-crystal contacts within the porous GaN layer. These values are consistent with corresponding characteristic voltages found in uniform epitaxially grown GaN.[18]

The barrier to the exponential current increase is found to be much lower than the expected GaN diode response, i.e., $E_g/q \sim 2.16$ V. The knee voltage where significant

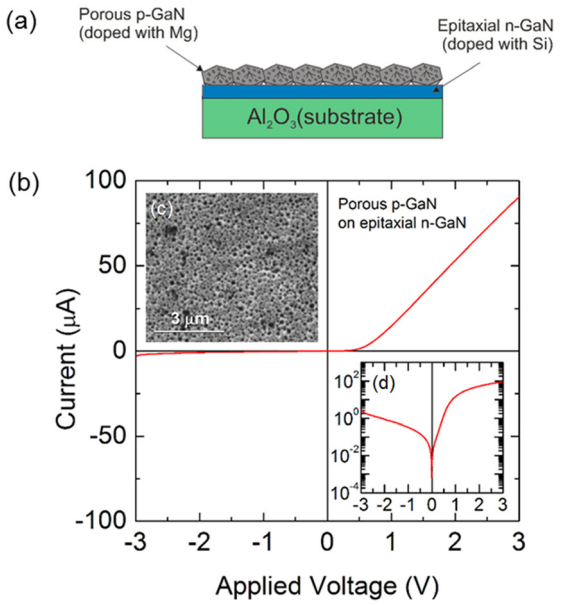

FIG. 2. (a) Schematic presentation of porous GaN on epitaxial GaN substrate. (b) I-V curve of the p-n junction formed between porous GaN doped with Mg and n-type epitaxial GaN. (c) Top-view SEM image of the porous GaN layer. (d) ln $I(V)$ curve of the porous p-GaN corresponding to the I-V curve in (b).

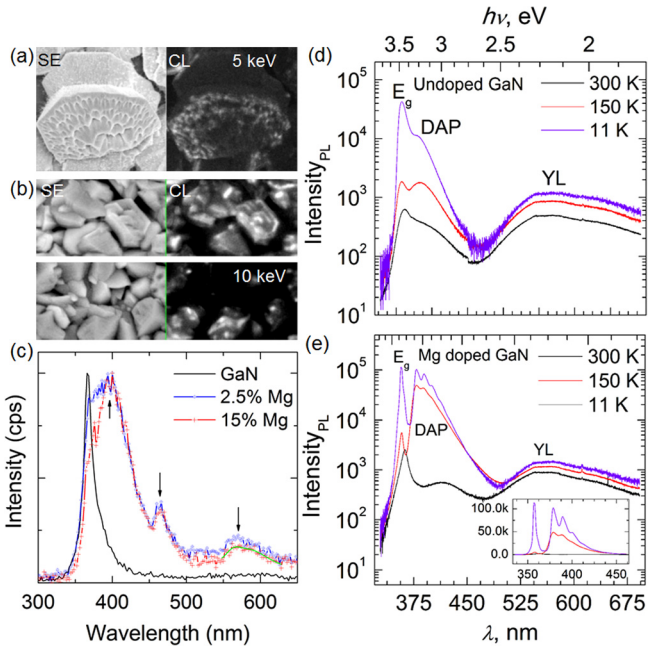

FIG. 3. (a) Secondary electron (SE) and CL images of n-GaN crystals at 5 kV. (b) SE and CL images of porous GaN with 2.5% and 15% Mg-precursor at 10 kV. (c) Cathodoluminescence spectra from Mg-doped porous GaN crystals before and after Mg-doping. (d) Temperature-dependent PL spectra of undoped and (e) Mg-doped GaN acquired after excitation at 325 nm (3.8 eV). The inset shows the PL emission on a linear scale.

current is seen is found to be in the range of $E_g/6q$–$E_g/4q$, i.e., 0.36–0.54 V. This response has several features that have been seen in InN and GaN nanowires arrays but not in bulk or thin film GaN.[19] However, the p-type nature of the porous GaN is confirmed and in both cases, low reverse bias leakage current are found for the porous assembly of GaN crystals in the layer.

The effective hole density is estimated at 300 K for the porous GaN layer from $np = N_C N_V \exp(-E_g/kT)$, where $N_C = 4.3 \times 10^{14} \cdot T^{3/2}\,\mathrm{cm}^{-3}$ and $N_V = 8.9 \times 10^{15} \cdot T^{3/2}\,\mathrm{cm}^{-3}$ are the effective densities of states of the conduction and valence bands, using the effective hole and electron masses for wurtzite GaN at 300 K.[20] Using $n = 10^{19}\,\mathrm{cm}^{-3}$ for the epitaxial n-GaN, we estimate the hole density for the porous p-GaN to be $\sim 9 \times 10^{18}\,\mathrm{cm}^{-3}$. From the Poisson distribution of space charge distribution leading to the dependence of majority and minority carrier densities across an abrupt, one-side junction, the barrier potential V_B across the depletion region for the porous GaN junction is estimated as $V_B = kT/q \ln(N_D N_A / n_i^2) = 0.9$ V, where N_D and N_A are the donor and acceptor densities, respectively, determined for the charge neutrality condition $p + N_D^+ = n + N_A^-$, and $n_i^2 = 2.8 \times 10^{11}\,\mathrm{cm}^{-3}$ is the intrinsic doping density of GaN estimated by the e–h product above. The value (at zero applied bias) is greater ($E_g/2.5q$) than the knee voltage, although typically found for epitaxial GaN with knee voltages in p-n junctions >2 V. This discrepancy is likely due to a graded junction and similar to other nanoscale III-Ns that show similar behaviour but for porous GaN does not seem to be a dominant size effect (micron sizes crystals).

Cathodoluminescence investigations of the Mg-doping of porous GaN was performed using two different quantities of dopant precursor. Figure 3(a) shows SEM and CL images of porous n-GaN crystals within the porous layer. Porous GaN allows a considerable signal to be observed for the band-edge emission compared with that at $V_{acc} = 20$ kV.[21] Typically, epitaxial or MBE grown GaN films suffer from low intensities due to e-h pair formation at low voltages which increases surface recombination that is non-radiative. In this case of porous GaN, the emission is enhanced at the high density of sharp edge surfaces found on the crystal and thus throughout the porous film. Figure 3(b) shows a pair of SEM and CL images of porous GaN doped with 2.5% and 15% Mg and their corresponding CL spectra (Fig. 3(c)) recorded at room temperature. In the spectra acquired at an accelerating voltage, $V_{acc} = 10$ kV, a shift of the CL peak is found in comparison to undoped GaN. The yellow-luminescence (YL) seen from CL shows two contributions, typically ascribed to pair recombination and deep level emission characteristic of doped p-type GaN. The near-band edge emission is similar in both doped samples and not found in undoped GaN, but lower in energy (397 nm) than the bandgap emission from GaN (the monochromator edge was 368 nm for Mg-doped CL).

PL measurements were performed on both Mg-doped samples and undoped porous GaN to conclusively define the p-type character of the crystals. Figures 3(d) and 3(e) show PL spectra taken at 11, 150, and 300 K at a constant laser power density. We observe that the undoped GaN crystal forming the porous layer exhibit expected band-edge luminescence, blue-shifting from 3.43 eV at 300 K to 3.46 eV at 11 K with a narrow FWHM of ~12 meV. Emission from high energy bound excitons sometimes observed in epitaxially grown GaN (of any conduction type) is not found in these samples. The capture of excitons by deep energy centers often from localized states accompanying defects in epitaxial GaN films drastically limit the radiative recombination near the band gap, which is detrimental for device function. The near band-gap

luminescence in Figure 3(d) is quite broad for undoped GaN crystal forming the porous layer.[22] None of the constituent phases at the silicon interface (Pt, Au, their alloys, etc.) contribute to the luminescence. The blue luminescence is often attributed to recombination between a deep donor and a Mg acceptor.[23,24] Broad emission near the band gap typically results from tailing of the density of states due to randomly distributed impurities, but the emission bandwidth reduces at high doping densities. We find that the near-band gap emission and band-edge emission equilibrate in intensity at 150 K, but the band-edge emission dominates at higher and lower temperatures.

The PL spectrum of the porous GaN crystals after activation of Mg conclusively demonstrates Mg incorporation as an acceptor state in the GaN lattice, resulting in the p-type character confirmed through I-V measurements in p-n junctions. The room temperature band-edge emission is marginally lower energy at 3.41 eV compared with the n-type material, but this emission is located at a consistent value of 3.46 eV at temperatures down to 11 K with a narrow FWHM of ~5 meV. The band gap emission in both materials is over an order of magnitude more intense at 11 K compared with 150 K. We do observe some emission at very high superbandgap energies of ~3.5 eV, consistent with a free or shallow-bound exciton. As the GaN is Mg doped and neither Si nor shallow O donor-bound excitons are likely, we attribute this weak emission to acceptor bound excitons linked to Mg incorporation. Deeply bound-exciton emission is not observed from the substrate-GaN interface and no reduction in band-edge energy is found due to bound excitons linked to atomic vacancies.

The band-edge luminescence is followed by the donor-acceptor pair (DAP) luminescence at 3.27 and 3.28 eV at 150 and 11 K, respectively. This DAP emission is not found at 300 K for the p-type porous GaN. This type of emission has been previously observed and attributed to the formation of a Mg complex or some native defect level. As expected from Mg acceptors in doped GaN, we find the longitudinal optical (LO) phonon replicas at 3.18 and 3.19 eV at 150 and 11 K, respectively, with several harmonics observable at 11 K, indicating that the electronic quality of the doped GaN crystals directly on Si matches that of epitaxially grown p-doped GaN.[25]

Yellow luminescence (YL) in n-GaN is normally attributed to point defect Ga vacancies, impurities, such as oxygen and carbon.[26] YL is also present in Mg-doped GaN, as observed in Figure 3(e). The marked intensity variation in band-edge and YL as a function of temperature is seen on a linear scale in the inset. Most probably, the YL arises from a transition between the conduction band or shallow donors[27] and deep acceptor levels caused by crystallographic point defects in the GaN crystals[28] since we find that the YL emission profile and temperature-dependence is similar and characteristic of both undoped and p-type GaN crystals comprising the porous GaN layer. The YL is weakly temperature-dependent and is not found to vary considerably due to Mg incorporation into the lattice.

In summary, we have shown that high structural and electronic quality p-type GaN can be grown as single crystals directly on Si and also on epitaxial GaN substrates on sapphire as a porous layer. On Si, vapor-solid-solid growth catalyzed by either Au or Pt allows GaN growth with the direct formation (in the case of Au) of an Ohmic intermetallic contact, without unwanted effects of interfacial resistive oxide formation nor the need for post-deposition annealing steps to introduce Ohmicity. Self-catalyzed growth of porous p-type GaN is also demonstrated to be possible on sapphire and grows with a similar porous morphology. P-n junction measurements of porous GaN and epitaxial GaN show that Mg incorporation from the precursor results in p-type conduction character. The overall method of using intermetallic as Ohmic contacts could also be applied to simultaneously grow and contact nanoscale III-N compounds and nanoscale arrays of p-n junctions for optoelectronic devices, and on epitaxial GaN, this extends to p-n junctions of porous crystalline assemblies that are strongly c-axis aligned with the underlying opposite conduction type GaN substrate. Porous III-N materials with rational doping also have great potential for wide band-gap biosensors.

This work was supported by the EU Framework 7 under Project No. FP7-SPA-2010-263044, the Spanish Government under Projects No. MAT2011-29255-C02-02, TEC2010-21574-C02-02, and by Catalan Authority under Project No. 2009SGR235. This work was also supported by the UCC Strategic Research Fund, by Science Foundation Ireland under Award No. 07.SK.B1232a-STTF11, and through the Irish Research Council New Foundations Award 2012.

[1]S. Nakamura, S. Pearton, and G. Fasol, *The Blue Laser Diode: The Complete Story* (Springer-Verlag, Berlin Heidelberg, 2000).
[2]A. Ramizy, Z. Hassan, and K. Omar, Sens. Actuators B **155**(2), 699–708 (2011).
[3]C.-F. Lin, C. Kuei-Ting, L. Chun-Min, and Y. Chung-Chieh, IEEE Electron Device Lett. **30**(10), 1057–1059 (2009).
[4]S. J. Pearton and F. Ren, Adv. Mater. **12**, 1571 (2000).
[5]C.-C. Yang, C. F. Lin, C.-M. Lin, C. C. Chang, K.-T. Chen, J.-F. Chien, and C.-Y. Chang, Appl. Phys. Lett. **93**(20), 203103-203103-203103 (2008).
[6]Y. D. Wang, S. J. Chua, M. S. Sander, P. Chen, S. Tripathy, and C. G. Fonstad, Appl. Phys. Lett. **85**(5), 816–818 (2004).
[7]S. Y. Bae, H. W. Seo, J. Park, H. Yang, and B. Kim, Chem. Phys. Lett. **376**(3), 445–451 (2003).
[8]D. J. Diaz, T. L. Williamson, I. Adesida, P. W. Bohn, and R. J. Molnar, J. Appl. Phys. **94**(12), 7526–7534 (2003).
[9]J. A. Bardwell, I. G. Foulds, J. B. Webb, H. Tang, J. Fraser, S. Moisa, and S. Rolfe, J. Electron. Mater. **28**(10), L24–L26 (1999).
[10]K. Cui, S. Fathololoumi, M. G. Kibria, G. A. Botton, and Z. Mi, Nanotechnology **23**, 085205 (2012).
[11]Y.-L. Chang, F. Li, A. Fatehi, and Z. Mi, Nanotechnology **20**, 345203 (2009).
[12]D. Wang, A. Pierre, M. G. Kibria, K. Cui, X. Han, K. H. Bevan, H. Guo, S. Paradis, A.-R. Hakima, and Z. Mi, Nano Lett. **11**, 2353–2357 (2011).
[13]Y. Huang, X. Duan, Y. Cui, and C. M. Lieber, Nano Lett. **2**, 101–104 (2002).
[14]O. V. Bilousov, J. J. Carvajal, D. Drouin, X. Mateos, F. Díaz, M. Aguiló, and C. O'Dwyer, ACS Appl. Mater. Interfaces **4**(12), 6927–6934 (2012).
[15]J. J. Carvajal, O. Bilousov, D. Drouin, M. Aguiló, F. Díaz, and J. C. Rojo, Microsc. Microanal. **18**, 905 (2012).
[16]J. J. Carvajal and J. C. Rojo, Cryst. Growth Des. **9**, 320 (2009).
[17]D. K. Schroder, *Semiconductor Material and Device Characterization* (Wiley, New York, 1998).
[18]J. O. Song, J.-S. Ha, and T.-Y. Seong, IEEE Electron Device Lett. **57**(1), 42 (2010).
[19]Y. Yang, Y. Ling, G. Wang, X. Lu, Y. Tong, and Y. Li, Nanoscale **5**(5), 1820–1824 (2013).

[20]B. Santic, Semicond. Sci. Technol. **18**, 219 (2003).
[21]F. A. Ponce, D. P. Bour, W. Gatz, and P. J. Wright, Appl. Phys. Lett. **68**, 57 (1996).
[22]B. Qu, Q. Zhu, X. Sun, S. Wan, Z. Wang, H. Nagai, Y. Kawaguchi, K. Hiramatsu, and N. Sawaki, J. Vac. Sci. Technol. A **21**(4), 838–841 (2003).
[23]M. A. Reshchikov and H. Morkoç, J. Appl. Phys. **97**(6), 061301-061301–061395 (2005).
[24]U. Kaufmann, M. Kunzer, M. Maier, H. Obloh, A. Ramakrishnan, B. Santic, and P. Schlotter, Appl. Phys. Lett. **72**(11), 1326–1328 (1998).
[25]L. Eckey, J. C. Holst, P. Maxim, R. Heitz, A. Hoffmann, I. Broser, B. Meyer, C. Wetzel, E. Mokhov, and P. Baranov, Appl. Phys. Lett. **68**(3), 415–417 (1996).
[26]J. Neugebauer and C. G. Van de Walle, Appl. Phys. Lett. **69**(4), 503–505 (1996).
[27]O. Gelhausen, H. Klein, M. Phillips, and E. Goldys, Appl. Phys. Lett. **83**(16), 3293–3295 (2003).
[28]K. Saarinen, T. Laine, S. Kuisma, J. Nissilä, P. Hautojärvi, L. Dobrzynski, J. M. Baranowski, K. Pakula, R. Stepniewski, M. Wojdak, A. Wysmolek, T. Suski, M. Leszczynski, I. Grzegory, and S. Porowski, Phys. Rev. Lett. **79**(16), 3030–3033 (1997).

Paper VI

Bilousov, O.V.; Carvajal, J.J.; Vilalta-Clemente, A.; Ruterana, P.; Diaz, F.; Aguilo, M. and O'Dwyer, C. *Porous GaN and high-k MgO-GaN MOS diode layers grown in a single step on silicon*. **(2014)** Chemistry of Materials, *26* (2), pp 1243-1249.

CHEMISTRY OF MATERIALS

Article

pubs.acs.org/cm

Porous GaN and High-κ MgO–GaN MOS Diode Layers Grown in a Single Step on Silicon

O. V. Bilousov,[†] J. J. Carvajal,*[,†] A. Vilalta-Clemente,[§] P. Ruterana,[§] F. Díaz,[†] M. Aguiló,[†] and C. O'Dwyer*[,‡,∥]

[†]Física i Cristallografia de Materials i Nanomaterials (FiCMA-FiCNA) and EMaS, Universitat Rovira i Virgili (URV), Marcellí Domingo s/n, E-43007 Tarragona, Spain

[‡]Department of Chemistry, University College Cork, Cork, Ireland

[§]CIMAP, UMR 6252 CNRS-ENSICAEN-CEA-UCBN, 6 Boulevard du Maréchal Juin, 14050 Caen Cedex, France

[∥]Micro & Nanoelectronics Centre, Tyndall National Institute, Lee Maltings, Cork, Ireland

ABSTRACT: Porous GaN polycrystalline layers with n-type conduction characteristics were catalytically grown from Mg films formed by decomposition of a Mg_2N_3 precursor typically employed for activating p-type conduction in GaN. After being exposed to oxygen, the Mg film oxidized to a polycrystalline high-κ oxide between the ohmic alloy interlayer contact and the porous GaN, while maintaining a clean interface. Electrical measurements on devices coupled to composition analysis and electron microscopy of the component layers confirm that a MOS-type porous GaN diode on silicon can be formed by chemical vapor deposition in a single growth regime.

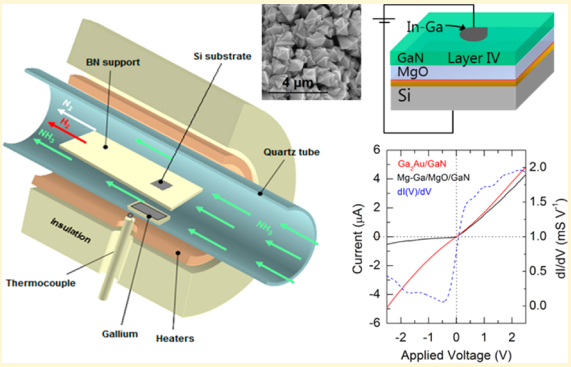

INTRODUCTION

Gallium nitride (GaN) and its alloys have proven to be important as wide band gap semiconductors for a number of applications in electronics and optoelectronics.[1] In their porous and nanostructured forms, GaN,[2] InGaN,[3] and InN[4] have attracted particular interest in the past decade because of beneficial optical and electronic properties for optoelectronics, gas sensors with high sensitivity, light-emitting diodes (LEDs) with high light extraction efficiency,[5] wide-band gap biosensors,[6,7] and high-electron mobility transistors for high-frequency and high-power devices. Nanoscale analogues of III–N materials have been investigated to probe exotic optical and high-mobility transport[8] effects particularly for photonics applications.[9,10] The wide band gap of GaN can minimize the generation of charge carriers because of undesirable background optical or thermal excitations but also allow for electroluminescent color-tuning from the ultraviolet to the infrared in multiple-quantum well (MQW)[11] or nanowire[12] heterostructures.

Porous semiconductor materials such as Si,[13−15] III-Vs,[16] and GaN[17,18] have been typically fabricated by (photo)-electrochemical and chemical etching[19] methods, giving textured surfaces as a result of pore coalescence and variations in etch rates for extended etching times. Controlling the degree of porosity in a functional layer of GaN is more difficult to use than top-down etching in relieving an array of nanostructures, for example. Alternative methods for introducing porosity into high-quality, doped GaN are advantageous for several high-surface area, chemically stable applications requiring wide band gaps, such as biosensors with optically active regions. Because of the wide band gap nature of the material (3.5 eV for GaN compared to 1.12 eV for Si), it is extremely stable to a temperature increase, and electronic devices can be operated at temperatures up to 500 °C. Usefully, there is no effective uniform wet chemical etchant for GaN, making it chemically stable in almost any liquid environment.

In recent years, considerable research and development effort into chemical and biosensors[20] was driven by a high demand for biosensors[21] that can be used in glucose monitoring, infectious disease biomarking, and cancer diagnosis, which use capacitance and electrical properties of semiconductors.[22] Wide band gap sensors are being developed for point-of-care applications, and in particular,[6] transistor-based sensors hold great promise for application in medical science in addition to optoelectronics.[23] In transistor geometry, device physics can be married to sensor requirements to offer improvements in precision and stability and faster response times and, with large surface areas such as those provided by porous semiconductors, can be made sensitive to minute quantities of analyte.[7,24−26] To do this, the transistors use variations in the effective barrier height caused by the material or liquid being analyzed on the surface of the device. These devices are typically high-electron mobility transistors (HEMTs) and benefit from a high two-

Received: November 7, 2013
Published: January 7, 2014

   dx.doi.org/10.1021/cm4037023 | Chem. Mater. 2014, 26, 1243−1249

dimensional electron gas (2DEG) mobility and saturation velocity.[27] The conducting 2DEG channel of AlGaN/GaN HEMTs, for example, is extremely sensitive to charge alteration from adsorption of analytes or species as it is designed close to the surface of the device.

Such sensors can also benefit from the large surface areas of high-quality GaN and related materials, but mass production would also benefit from lower-cost routes to upscaled device manufacture. We previously produced porous GaN through the direct reaction of metallic Ga with NH_3 in a simple chemical vapor deposition (CVD) system on sapphire and Si substrates.[28,29] Metal catalysts are typically used to initiate growth through either a vapor−liquid−solid (VLS) or vapor−solid−solid (VSS) mechanism[30] when using molecular beam epitaxy (MBE) and chemical vapor deposition (CVD), where the catalyst can influence the growth without necessitating any secondary etching or chemical treatment after GaN growth to induce porosity.

Reports of Schottky diodes based on porous GaN have shown good performance for hydrogen gas sensing applications,[31,32] and this can be extended to three-terminal devices. In larger surface area GaN-based devices, electrochemical etching techniques were used, some of which can provoke surface damage or electronic surface state variations that can lead to changes in barrier heights in some cases.

For thin-film transitors (TFTs) and metal oxide semiconductor (MOS) HEMTs, high-κ dielectrics can help reduce the operating voltage and increase drain current density and transconductance using a high-mobility 2DEG. High-κ growth with porous III−N systems has not been investigated, and the route for channel dielectric magnesium oxide (MgO) is a candidate of high-k gate dielectrics (κ = 9.4−9.8)[33] because of its good isolation[34] and chemical inertness. Additionally, using bottom-up catalytic growth processes for III−Ns, Mg precursors are typically used to create p-type conduction characteristics after lattice incorporation and thermal activation of these acceptors.

In this paper, we present a new method of fabrication of MOS diodes based on metal-catalyzed large surface area porous GaN layers with a MgO high-κ dielectric layer located between the metallic electrode (Ga−Pt or Ga_2Au-based intermetallic Ohmic contacts) in a single bottom-up catalytic growth step. Electrical measurements demonstrate the influence of the growth mechanism, so that near-ohmic contacts can be made to n-type porous GaN layers using alloyed interlayer contacts. Mg-based precursors were deposited in such a way as to seed a Mg film under the porous GaN, which was oxidatively crystallized to MgO without affecting the conduction type or composition of the GaN layer. Charge transport measurements allowed us to demonstrate the fabrication of a Ga_2Au/MgO/GaN/In−Ga large surface area MOS diode.

EXPERIMENTAL SECTION

Synthesis and Catalyzed Growth of the Porous GaN Layer. For the synthesis of porous GaN nanostructures by chemical vapor deposition (CVD), a horizontal single-zone split tubular furnace (Thermolyne 79300, Thermo Fisher Scientific Inc.) with a built-in temperature controller was used. Nanoporous GaN doped with Mg was grown as micrometer-sized particles by the direct reaction of metallic Ga with ammonia in a tubular CVD system, using gallium metal (99.99%), ammonia (>99.98%), and Mg_3N_2 (99.5%) as the sources of Ga, N, and Mg, respectively. These particles were deposited on Si(100) wafers. A 20 nm layer of Au or Pt, acting as a catalyst in the reaction, was deposited on the Si substrates using a RF sputtering process (AJA International) at a power of 150 W and a pressure of 3 mTorr. The coated substrate was then placed 2 cm above the Ga source. The Mg_3N_2 powder, with a 0.025:1 weight ratio respect to Ga, was placed 4 cm upstream of the Ga source. The quartz tube of the furnace was degassed to a vacuum pressure of 1×10^{-2} Torr. Afterward, ammonia was introduced through a mass-flow controller, and the furnace was heated to the reaction temperature at a flow rate of 75 sccm and the furnace heated to the reaction temperature of 1203 K at a rate of 100 K/min. The reaction was continued at this temperature for 60 min under a constant flow of NH_3. Growth was halted by cooling the samples to room temperature without NH_3 flow, reducing the pressure to 1×10^{-2} Torr.

Structural, Morphological, and Compositional Characterization. X-ray diffraction (XRD) patterns in the $\theta-2\theta$ geometry of the as-grown sample were made using Cu Kα radiation in a Bruker-AXS D8-Discover diffractometer equipped with a parallel incident beam (Göbel mirror), a vertical $\theta-\theta$ goniometer, an XYZ motorized stage, and a General Area Diffraction Detection System (GADDS) HI-STAR detector with a multiwire proportional counter with a 30 cm × 30 cm area and 1024 × 1024 pixel density. Samples were placed directly on the sample holder, and the area of interest was selected with the aid of a video-laser focusing system. An X-ray collimator system allows analysis of 500 μm areas. The X-ray diffractometer was operated at 40 kV and 40 mA to generate Cu Kα radiation. We collected 2D XRD patterns covering a range of 2θ between 20° and 85°. Identification of the crystalline phases was achieved by comparison of the XRD diffractogram with the ICDD database using Diffrac^{plus} Evaluation (Bruker, 2007).

The nanoporous GaN microparticles deposited on the Si substrates as a porous layer were characterized morphologically using a JEOL JSM 6400 scanning electron microscope (SEM). Before being observed, samples were coated with a thin layer of gold with a Bal-Tec SCD004 sputterer.

The transmission electron microscopy (TEM) specimens were prepared in the conventional way via mechanical polishing and dimpling down to a few micrometers followed; the electron transparency was next obtained using Ar^+ ion milling at 5 keV. The accelerating voltage was systematically decreased to 0.7 keV in the final stage to reduce the ion beam damage. The observations were made with a JEOL-2010FEG TEM instrument operating at 200 keV, and simultaneously, energy dispersive X-ray spectroscopy (EDS) has been used to determine the local composition in GaN(Mg).

Electrical Characterization. Charge transport measurements through the porous GaN films were conducted using two- and four-probe measurements using a dc voltage course and an Agilent 34401A Digital Multimeter in a Peltier cell, thermostated to 295 K in a Faraday cage. Liquid metal contacts were made using In−Ga eutectic blown into a sphere from a gold metallized short borosilicate capillary tube ensuring good wetting (several square micrometers) to the rough top-surface morphology of the porous GaN and avoid electrical shorting to the underlying metallized silicon. Resistivity values were extracted from $I-V$ curves in the high-bias regime (series resistance) and also from four-point probe measurements. Diode measurements of the GaN/MgO system were made in symmetrical vertical two-probe measurements.

RESULTS AND DISCUSSION

Vapor−Solid−Solid Growth of Porous GaN on Silicon. The growth of the GaN nanoporous particles was assisted by a solid particle through the vapor−solid−solid (VSS) mechanism, the main stages of which are the incorporation of Ga into the Au or Pt solid phase eutectic, the formation of a Ga−Au or Ga−Pt alloy, the solubilization of nitrogen in the Ga−Au(Pt) alloy, and finally the nucleation and growth of GaN.[28] Panels a and b of Figure 1 confirm that the porous GaN particles grown without additional Mg vapor have a characteristic morphology consisting of faceted hourglass crystals with a mean size of ~1.5 μm. Crystal growth occurs progressively on the surface, with

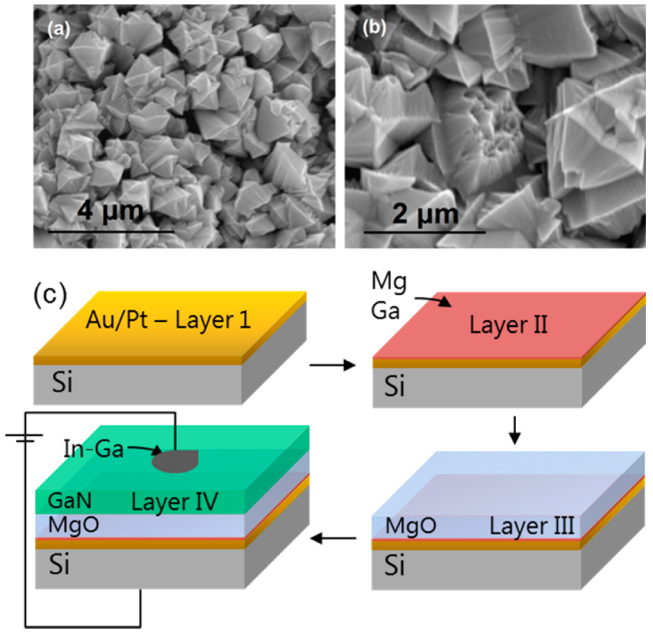

Figure 1. SEM image of porous GaN particles grown on Si(100) substrates coated with (a) a 20 nm film of Au and (b) a 20 nm film of Pt. (c) Mechanism of the creation of MgO/GaN layers of the MOS diode by subsequent catalytic VSS growth during CVD.

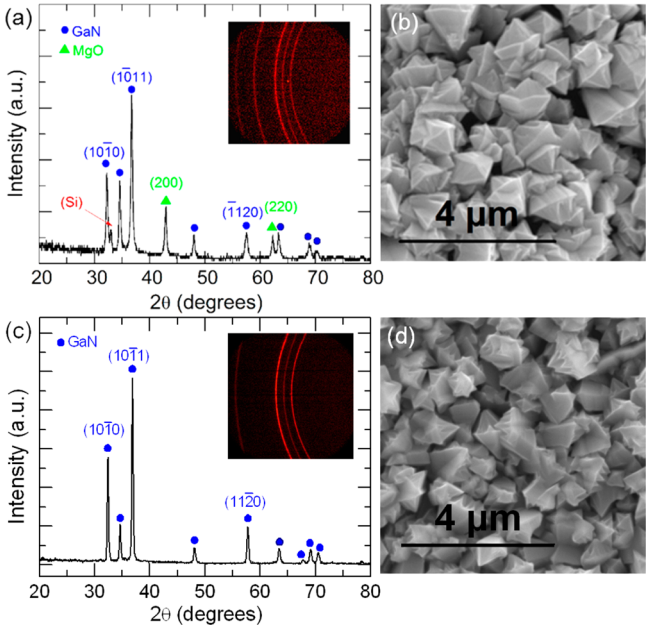

Figure 2. (a) XRD pattern for porous crystalline wurtzite GaN (*P*63*mc*) grown on Si(100) using a high concentration of Mg_3N_2 (the inset shows Debye rings). The Si(400) diffraction peak has been excluded to avoid intensity saturation. (b) SEM image of the Mg-catalyzed porous GaN grown on Si. (c) XRD pattern for porous crystalline wurtzite GaN (*P*63*mc*) grown on Si(100) using a low concentration of Mg_3N_2 (the inset shows Debye rings). (d) SEM image of the Au-catalyzed Mg-doped porous GaN grown on Si.

individual crystals ripening until a layer of porous GaN microparticles in the form of single-crystal truncated bipyramids[35] covers the surface as a connected porous layer, which was confirmed with time-resolved focused ion beam (FIB)-based tomography.[36]

Using Mg_3N_2, typically used for Mg doping of GaN, a layer of crystalline MgO is formed between the silicon surface and the porous GaN, depending on the initial concentration of the Mg precursor. Two different Mg_3N_2 concentrations, 0.015 and 0.025 weight ratios with respect to Ga, were used. When a concentration of 0.015 was used, Mg-doped porous GaN was formed.[29] On the other hand, for a concentration of Mg_3N of 0.025, Figure 2 shows the XRD pattern for the resulting multilayer deposition. The XRD pattern shown in Figure 2a for the MgO/GaN layer grown on Au-coated Si substrates confirms crystalline wurtzite GaN growth with a predominant diffraction intensity from low-index crystal facets. The uniform intensity of the Debye rings (along the curved ring portions in Figure 2a) confirms that there is no texturation of the layer of porous crystals, as confirmed by the SEM images shown in panels b and d of Figure 2.

We find that the deposit formed with a higher concentration of Mg_3N_2 also contains crystalline MgO, oxidatively crystallized because of the presence of Mg during incorporation at the growth stage of the porous GaN. The porous GaN single crystals formed in both cases are identical to those grown in the absence of the Mg precursor, and they also retain their unintentionally n-doped conduction because we did not anneal this sample to activate the p-type conduction.

In GaN nitride thin films, TEM investigations have pointed out that they can contain numerous crystallographic defects such as dislocations,[37,38] inversion domains,[39] and basal[40] and/or prismatic stacking faults.[41] These defects form because of the large lattice and thermal mismatches that exist between GaN and the most used substrates such as sapphire,[42] silicon carbide,[37] or silicon,[43] when the growth is conducted by MBE or metalorganic vapor phase epitaxy (MOVPE). In such instances, the layers are almost monocrystalline with very highly textured domains and XRD shows in-plane or out-of-plane full width half-maxima in the range of 200−300″, but they also may exhibit large angle grain boundaries.[44] In our case, the aim was to fabricate porous films, and this was confirmed by the TEM analysis, which showed that the polycrystalline MgO is located under the porous GaN, despite being present at initial stages of the seeding-mediated growth of the GaN itself. The large quantities of the Mg-containing precursors preferentially form this layer rather than doping the GaN lattice. This is in contrast with what has been observed when a smaller amount of Mg_3N_2 is used, in which case, only the polycrystalline layer of porous GaN is observed. Mg is detected in those GaN microcrystals with a tendency to have a higher Mg concentration in the crystals deposited in the latter stages that are located at the top of the polycrystalline layer. As shown in Figure 3a, the porous GaN layer doped with Mg grown on a Si(100) substrate and obtained with a high concentration of Mg_3N_2 typically exhibits four different regions. EDS analysis was used to estimate the Mg content as indicated in Figure 3a for 12 positions and Table 1. The four regions are characterized by changes in contrast that may be related to the variable Mg content (and thus scattering) in each of the marked regions. Region I corresponds to the Si substrate. In Region II, around point 1, there is good adhesion to the Si, and the layer has a dark contrast, with a Ga content of 26.7% and a Mg content of 73.3%. However, the phase formed in this region does not exhibit diffraction as an intermetallic crystal, and therefore, it likely corresponds to a Mg−Ga alloy as is the case with Ga−Pt reactions during GaN growth.[28] In region III (points 2−4), the contrast is very light, agreeing with the low (~1.5−3%) measured content of Ga and

dx.doi.org/10.1021/cm4037023 | *Chem. Mater.* 2014, 26, 1243−1249

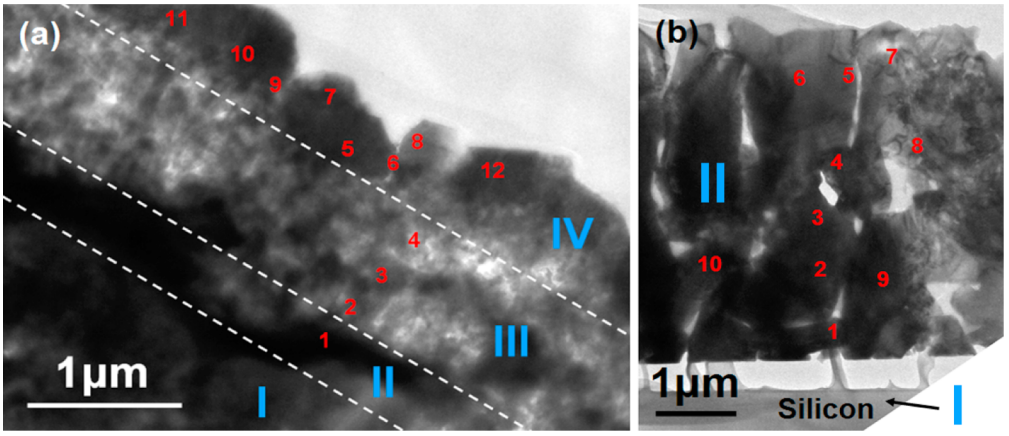

Figure 3. (a) TEM micrograph of the porous GaN layer doped with Mg grown on a Si(100) substrate obtained when a high concentration of Mg_3N_2 was used. Each of the four layers indicated in Figure 1 is marked. (b) TEM micrograph of the porous GaN layer doped with Mg on a Si(100) substrate obtained using a low concentration of Mg_3N_2.

Table 1. EDS Content of Mg and Ga in the Final MOS Diode Layers and Mg-Doped GaN[a]

position	Mg (%)	Ga (%)	position	Mg (%)	Ga (%)
EDS Content of Mg and Ga in the MOS Diode Layers					
1	73.3	26.7	7	11.7	97.8
2	98.5	1.5	8	7.9	92.1
3	97.0	3	9	9.5	90.5
4	97.3	2.7	10	8.9	91.1
5	7.9	92.1	11	7.9	92.1
6	11	89	12	8.1	91.9
EDS Content of Mg and Ga in Mg-Doped GaN					
1	1.3	98.7	6	2.2	97.8
2	1.5	98.5	7	2.5	97.6
3	1.9	98.1	8	1.8	98.2
4	3.9	96.1	9	1.8	98.2
5	2.6	97.4	10	1.4	98.6

[a]The measurement points relate to those numbered in Figure 3.

the Mg content of ~97−98%, which indicates that a new phase rich in Mg is formed, and as oxygen was also detected in our EDS analysis, this phase most probably corresponds to a Mg−O oxide. The area exhibits a very poor crystalline state as well as high porosity, which is in agreement with the light contrast in this bright field micrograph; its thickness is ~1 μm, although with a large roughness at the top and at the bottom. Toward the surface, region IV (points 5−12) consists of a polycrystalline phase that is rich in Ga (90.5−97.8%), while the Mg content remains ~7.9−11.7% from grain to grain. This area corresponds to Mg-doped GaN made of individual grains with a mean thickness of ~0.5 μm for each of them. A close examination shows that the crystallographic relationships between these grains are very random, with no specific orientation connection, and even spacing as can be seen in positions 6 and 9 in Figure 3a. Therefore, this doped GaN top layer is also porous. TEM energy dispersive X-ray analysis, shown in Figure 3a, confirms the interfacial location of the MgO between the silicon substrate and intermetallic seed layer, and the porous GaN at the surface.

When the GaN layer was grown using a low concentration of Mg_3N_2 (Figure 3b), only two regions were observed. Region I corresponds to the Si substrate, and region II, totally detached from the Si substrate, corresponds to Mg-doped GaN, with a thickness of ~4.5 μm, a value substantially larger than that obtained when a high concentration of Mg_3N_2 was used. As one can see, this layer is also porous, with more or less elongated and good quality crystallites throughout the layer thickness. The EDS analysis corresponding to 10 separate locations of this sample, also listed in Table 1, indicates that the content of Mg presents a slight increase toward the layer surface.

The following mechanism is proposed for the uninterrupted CVD growth of the interfacial high-κ MgO layer on an Ohmic intermetallic with catalytic growth of GaN as a MOS diode, summarized in Figure 1. First, an intermetallic layer of Ga, Mg, and the metallic catalyst (Au or Pt) used for a solid eutectic phase identified in region I in Figure 2 forms layer II. At higher temperatures, a second layer formed almost entirely by Mg is deposited on the intermetallic layer. This layer quickly oxidizes to polycrystalline MgO by reaction with O_2 when the furnace is opened, forming layer III. Finally, the growth of nanoporous GaN particles doped with Mg (layer IV) should proceed on the top of this Mg layer, Mg acting as a catalyst for the formation of this porous layer, because it appears not to be in contact with the catalyst with which we coated the substrate. Because no residual Mg or MgO is found on the unintentionally n-doped GaN after it had been heated and exposed to oxygen when the furnace was opened, the growth of the porous GaN particles proceeds through the vapor−solid−solid (VSS) mechanism, consistent with that observed without the deposition of the Mg-containing material.[28]

Figure 4 shows the $I-V$ curves from the porous GaN catalyzed by Au (forming Ga_2Au). The $I-V$ curves show only slight asymmetry indicative of nearly ohmic, weak Schottky barriers. Consistently, the conductivity of porous GaN grown from Pt was separately shown to be higher than that grown from Au.[28] The intermetallic layer contacts are described using the thermionic emission theory, taking into account a high ideality factor for weak barriers. The Schottky barrier height $\varphi^{\circ}_{B,n}$ (SBH) is estimated from the equation $I = I_0 \exp[(qV - IR_S)/kT - 1]$, where $I_0 = AA^{**}T^2 \exp[(-q\varphi^{\circ}_{B,n})/(kT)]$, where A^{**} is the effective Richardson constant (26.4 A cm^{-2} K^{-2}).[45] The SBH for Au-catalyzed porous n-GaN is estimated to be 0.66 eV. It is worth noting that the n-type contacts were effectively ohmic as deposited and did not need any postdeposition annealing to induce this effective ohmicity. For porous GaN, and also for GaN grown on Mg-based films, the effect of an interfacial oxide was considered. The barrier height of an untreated metal/GaN diode can be altered by a

dx.doi.org/10.1021/cm4037023 | Chem. Mater. 2014, 26, 1243−1249

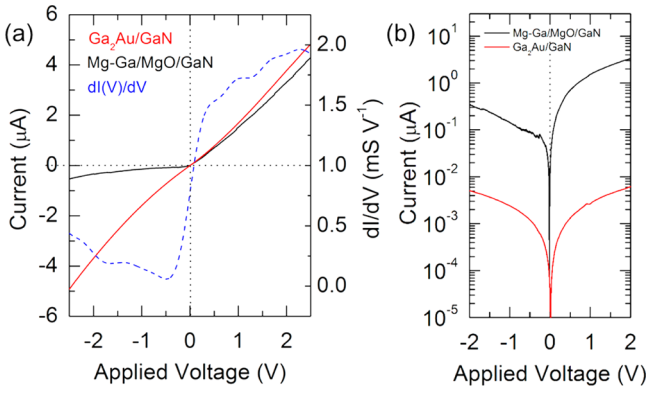

Figure 4. (a) $I-V$ and dI/dV curves for porous n-GaN with a MgO dielectric layer, and from a Au-seeded porous GaN layer on silicon. (b) Ln(I)$-V$ curve for the ohmic Au-seeded GaN contact and the MgO/GaN diode.

(photo)electrochemical etching treatment that yields defective GaN surface and interfaces and is described by the equation $\varphi_{B,n} = \varphi^{o}_{B,n} + \Delta\varphi$, where $\varphi^{o}_{B,n}$ represents the barrier height without the interfacial layer and $\Delta\varphi$ is the additional barrier due to the oxide. $\Delta\varphi$ is considered to be a tunneling barrier of the form $\Delta\varphi = [(2kT)/\hbar](2m\chi)^{1/2}\delta$, where $\hbar$ is Planck's constant, m is the tunneling effective mass, χ is the mean tunneling barrier, and δ is the thickness of the interfacial oxide. $\Delta\varphi$ was found to be in the range of 0.18−0.25 eV for Pt- and Au-based intermetallic contacts with n-GaN.[28] This corresponds to a maximal native oxide thickness of ∼2.7 nm on untreated GaN and would increase the overall effective barrier height. Microscopy and transport measurements thus confirm the growth of porous catalyzed GaN is mostly free of influential surface contaminants.

The MgO/GaN porous layers formed on silicon exhibit diode behavior consistent with a MOS system. Figure 4 shows $I-V$ curves across the device using an In−Ga euctectic to ohmically contact both the silicon substrate and the porous GaN. A rectifying diode response is found in the presence of the MgO, compared to the ohmic response between the intermetallic termination porous n-GaN and the substrate. We assumed that the net current is due to the thermionic emission current because the metal−semiconductor−metal contact now contains a dielectric at one interface, mimicking a Schottky contact with series resistance and an interfacial layer. Additionally, this is confirmed by forward bias voltages of $V > 3kT/q$, which is the case for this MOS diode. The downturn to linearity in the current after ∼0.25 V confirms a series resistance, R_S, that most likely originates from the MgO and porous n-GaN, as opposed to either of the metal contacts that are confirmed to be ohmic in nature. At a higher bias (>0.25 V), R_S dominates, which can be seen from the differential conductance dI/dV curve in Figure 4a.

Effective ohmic contacts can form with n-type GaN, suggesting that the resistivity dominates transport through an alloyed interface that promotes ohmic transport.[28] When a high-κ MgO layer is introduced, the series resistance markedly increases at much lower voltages. The MgO/n-GaN sandwich effectively has an altered electron affinity with respect to the In−Ga top contact. The overall series resistance, R_S, to which the sheet and contact resistivities contribute can also be determined from diffusion and thermionic emission theory summarized for a barrier-dominated diode. For the Ga_2Au intermetallic contact, the response in Figure 4b is symmetric (ohmic). The current system behaves as a diode but utilizing an ohmic contact formed by the intermetallic under the MgO layer, biased by the underlying silicon substrate. In the presence of the intermetallic bottom contact, the transport is effectively ohmic at the MgO interface. As the top contact with n-GaN is also ohmic, the diodic response in Figure 4b is dominated by differences in affinity between the MgO and the n-GaN (doped at $\sim 10^{16}$ cm^{-3}). The series resistance can also be obtained from the differential resistance through its proportionality to the current according to

$$\frac{dV}{dI} = \left[R_S + \frac{kT}{q}\left(\frac{1/I_0}{I/I_0 - 1}\right)\right] \approx R_S + \frac{nkT}{qI} \quad (1)$$

Figure 5a shows the differential resistance dV/dI as a function of the inverse of the current, plotted according to eq 1.

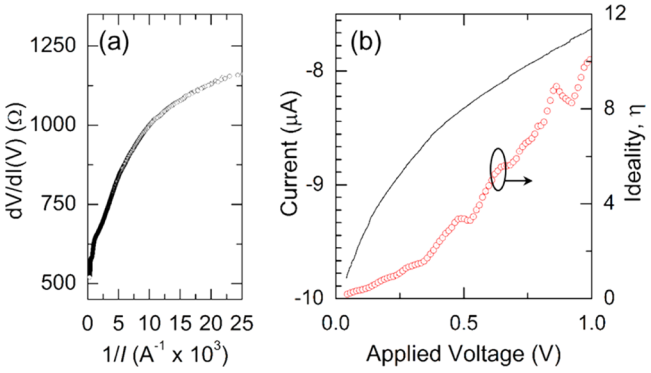

Figure 5. (a) Differential resistance (dV/dI) as a function of current for the MgO/porous GaN diode. (b) Ln(I)$-V$ curve and voltage dependence of the ideality factor for the diode.

Although it does not allow deconvolution of the contribution of the specific grain boundary resistance to the flow of current through the porous layers, the series resistance is estimated to be in the range of 5−6 kΩ for the MgO/porous GaN sandwich; dV/dI approaches R_S at the higher currents, but as seen in Figure 5b, the series resistance also includes likely tunnelling effects as the ideality factor is strongly voltage dependent and quite high in the higher-current and higher-bias regions. Further work is underway to identify the mechanism contributing to such high ideality factors, which are indicative of several mechanisms, including tunnelling current through multiple heterojunctions. Porosity complicates the transport mechanism, increasing shunt and series resistances.[46] One possibility is a strong contribution by Poole−Frenkel (P−F) tunneling, and surface leakage. In the former, electron−hole transport processes are accommodated by lowering of the barrier when the carriers interact with the trap states in the MgO layer, especially because electron microscopy confirms that its morphology is not continuous. These recombinative states are likely to have a high density in a thick MgO film with a graded MgO composition at the interface with GaN (lower) and also with the silicon substrate (higher Mg concentration), as determined by elemental concentrations within the MgO layer at either interface. Variations in the interfacial composition are known to strongly affect Schottky and P−F leakage current in MOS structures.[47]

Thus, charge transport measurements through this system conducted using two- and four-probe measurements and

dx.doi.org/10.1021/cm4037023 | Chem. Mater. 2014, 26, 1243−1249

confirm the fabrication of a porous GaN diode, catalyzed by Mg that subsequently undergoes oxidative crystallization to form a MgO high-κ dielectric layer. The MOS diode-like response was confirmed via composition, microscopy, and electrical transport analyses. Ohmic transport is found in the absence of a second oxide semiconducting layer between the intermetallic and the porous n-GaN. The porous GaN layer retains a morphology and conduction type similar to those of porous GaN catalyzed using Au or Pt on silicon. The method may be extended to growing nanoscale III−N materials and alloys using metals that are not typically employed for contacting, to give the ohmic response and MOS-based systems on silicon substrates for chemically inert, large surface area electrically continuous transistors and diodes for capacitive (bio)sensing.

■ CONCLUSIONS

In summary, porous GaN crystals have been successfully grown as large surface area layers from Pt- and Au-coated silicon substrates by a vapor−solid−solid process. The particles form as a layer of single-crystal particles with interparticle and intraparticle porosity. Current−voltage and capacitance−voltage measurements show nearly ohmic transport through weakly doped, polycrystalline (as a layer), porous n-GaN without alloy contacts or low-work function metals. Metal/Ga intermetallic alloy formation during vapor−solid−solid growth promotes thermionic emission-based low-resistance ohmic transport through the porous layer, and a very low contact resistivity is possible with the faceted, rough n-GaN surface. By depositing Mg in a manner similar to deterministic p-type doping of GaN, we formed a similar porous GaN. The Mg film is subsequently oxidized to polycrystalline MgO underneath the porous n-GaN layer, resulting in a high-κ dielectric oxide that allows the single-step formation of a porous GaN/MgO MOS diode. The development of porous GaN augers well for new electronic and optoelectronic devices with improved external quantum efficiencies, the incorporation of phosphors for LEDs, and large surface area biosensing based on capacitor or transistor function.

■ AUTHOR INFORMATION

Corresponding Authors

*E-mail: c.odwyer@ucc.ie.
*E-mail: joanjosep.carvajal@urv.cat.

Notes

The authors declare no competing financial interest.

■ ACKNOWLEDGMENTS

This project was supported by EU Framework 7 under Project FP7-SPA-2010-263044, the Spanish Government under Projects MAT2011-29255-C02-02 and TEC2010-21574-C02-02, and the Catalan Authority under Project 2009SGR235. This work was also supported by the UCC Strategic Research Fund and through the Irish Research Council New Foundations Award. A.V.-C. and P.R. acknowledge the EU for Grant PITN-GA-2008-213238 and the Initial Training Network RAINBOW of the 7th RTD Framework.

■ REFERENCES

(1) Nakamura, S.; Pearton, S.; Fasol, G. *The blue laser diode: The complete story*; Springer-Verlag: Berlin, 2000.
(2) Huang, Y.; Duan, X.; Cui, Y.; Lieber, C. M. *Nano Lett.* **2002**, *2*, 101−104.
(3) Song, J. O.; Ha, J.-S.; Seong, T.-Y. *IEEE Electron Device Lett.* **2010**, *57*, 42.
(4) Yang, Y.; Ling, Y.; Wang, G.; Lu, X.; Tong, Y.; Li, Y. *Nanoscale* **2013**, *5*, 1820−1824.
(5) Yang, C.-C.; Lin, C. F.; Lin, C.-M.; Chang, C. C.; Chen, K.-T.; Chien, J.-F.; Chang, C.-Y. *Appl. Phys. Lett.* **2008**, *93*, 203103−203103-3.
(6) Pearton, S. J.; Lele, T.; Tseng, Y.; Ren, F. *Trends Biotechnol.* **2007**, *25*, 481.
(7) Lo, C.-F.; Xia, Y.; Liu, L.; Pearton, S. J.; Doré, S.; Hsu, C.-H.; Dabiran, A. M.; Chow, P. P.; Ren, F. *Sens. Actuators, B* **2013**, *176*, 708.
(8) Li, Y.; Xiang, J.; Qian, F.; Gradecak, S.; Wu, Y.; Yan, H.; Lieber, C. M. *Nano Lett.* **2006**, *6*, 1468.
(9) Zhong, Z.; Qian, F.; Wang, D.; Lieber, C. M. *Nano Lett.* **2003**, *3*, 343.
(10) Li, Y.; Qian, F.; Xiang, J.; Lieber, C. M. *Mater. Today* **2006**, *9*, 18.
(11) Qian, F.; Li, Y.; Gradecak, S.; Park, H.-G.; Dong, Y.; Ding, Y.; Wang, Z. L.; Lieber, C. M. *Nat. Mater.* **2008**, *7*, 701.
(12) Qian, F.; Li, Y.; Gradecak, S.; Wang, D.; Barrelet, C. J.; Lieber, C. M. *Nano Lett.* **2004**, *4*, 1975.
(13) Cullis, A. G.; Canham, L. T. *Nature* **1991**, *353*, 335.
(14) McSweeney, W.; Lotty, O.; Mogili, N. V. V.; Glynn, C.; Geaney, H.; Tanner, D.; Holmes, J. D.; O'Dwyer, C. *J. Appl. Phys.* **2013**, *114*, 034309.
(15) Hochbaum, A. I.; Gargas, D.; Hwang, Y. J.; Yang, P. *Nano Lett.* **2009**, *9*, 3550.
(16) Lynch, R.; O'Dwyer, C.; Quill, N.; Nakahara, S.; Newcomb, S. B.; Buckley, D. N. *J. Electrochem. Soc.* **2013**, *160*, D260−D270.
(17) Wang, Y. D.; Chua, S. J.; Sander, M. S.; Chen, P.; Tripathy, S.; Fonstad, C. G. *Appl. Phys. Lett.* **2004**, *85*, 816−818.
(18) Diaz, D. J.; Williamson, T. L.; Adesida, I.; Bohn, P. W.; Molnar, R. J. *J. Appl. Phys.* **2003**, *94*, 7526−7534.
(19) Bardwell, J. A.; Foulds, I. G.; Webb, J. B.; Tang, H.; Fraser, J.; Moisa, S.; Rolfe, S. *J. Electron. Mater.* **1999**, *28*, L24−L26.
(20) Huber, F.; Lang, H. P.; Gerber, C. *Nat. Nanotechnol.* **2008**, *3*, 645−646.
(21) Chen, R. J.; Bangsaruntip, S.; Drouvalakis, K. A.; Kam, N. W. S.; Shim, M.; Li, Y.; Kim, W.; Utz, P. J.; Dai, H. *Proc. Natl. Acad. Sci. U.S.A.* **2003**, *100*, 4984.
(22) Sandhu, A. *Nat. Nanotechnol.* **2007**, *2*, 746−748.
(23) Pearton, S. J.; Norton, D. P.; Ren, F. *Small* **2007**, *3*, 1144.
(24) Lo, C.-F.; Liu, L.; Chu, B.-H.; Ren, F.; Pearton, S. J.; Dore, S.; Hsu, C.-H.; Kim, J.; Dabiran, A. M.; Chow, P. P. *J. Vac. Sci. Technol., A* **2012**, *B30*, 010606-1-4.
(25) Wang, Y.-L.; Chu, B. H.; Chang, C. Y.; Lo, C. F.; Pearton, S. J.; Dabiran, A.; Chow, P. P.; Ren, F. *Sens. Actuators, B* **2010**, *146*, 349.
(26) Lo, C.-F.; Chu, B. Y.; Pearton, S. J.; Dabiran, A.; Chow, P. P.; Dore, S.; Hung, S. C.; Chen, C. W.; Ren, F. *Appl. Phys. Lett.* **2011**, *99*, 142107.
(27) Pearton, S. J.; Ren, F. *Adv. Mater.* **2000**, *12*, 1571.
(28) Bilousov, O. V.; Carvajal, J. J.; Drouin, D.; Mateos, X.; Díaz, F.; Aguiló, M.; O'Dwyer, C. *ACS Appl. Mater. Interfaces* **2012**, *4*, 6927−6934.
(29) Bilousov, O. V.; Geaney, H.; Carvajal, J. J.; Zubialevich, V. Z.; Parbrook, P. J.; Giguère, A.; Drouin, D.; Díaz, F.; Aguiló, M.; O'Dwyer, C. *Appl. Phys. Lett.* **2013**, *103*, 112103.
(30) Persson, A. I.; Larsson, M. W.; Stenstron, S.; Ohlsson, B. J.; Samuelson, L.; Wallenberg, L. R. *Nat. Mater.* **2004**, *3*, 677.
(31) Ramizy, A.; Hassan, Z.; Omar, K. *Sens. Actuators, B* **2011**, *155*, 699−708.
(32) Duan, B. K.; Bohn, P. W. *Analyst* **2010**, *135*, 902−907.
(33) Yan, L.; Lopez, C. M.; Shrestha, R. P.; Irene, E. A.; Suvorova, A. A.; Saunders, M. *Appl. Phys. Lett.* **2006**, *88*, 142901.
(34) Gila, B. P.; Kim, J.; Luo, B.; Onstine, A.; Johnson, W.; Ren, F.; Abernathy, C. R.; Pearton, S. J. *Solid-State Electron.* **2003**, *47*, 2139.
(35) Carvajal, J. J.; Rojo, J. C. *Cryst. Growth Des.* **2009**, *9*, 320.
(36) Carvajal, J. J.; Bilousov, O.; Drouin, D.; Aguiló, M.; Díaz, F.; Rojo, J. C. *Microsc. Microanal.* **2012**, *18*, 1.

(37) Vermaut, P.; Ruterana, P.; Nouet, G.; Morkoç, H. *Inst. Phys. Conf. Ser.* **1995**, *146*, 289.
(38) Ning, X. J.; Chien, F. R.; Pirouz, P.; Wang, J. W.; Khan, M. A. *J. Mater. Res.* **1996**, *3*, 580.
(39) Potin, V.; Nouet, G.; Ruterana, P. *Philos. Mag. A* **1999**, *79*, 2899.
(40) Ruterana, P.; Barbaray, B.; Béré, A.; Vermaut, P.; Hairie, A.; Paumier, E.; Nouet, G.; Salvador, A.; Botchkarev, A.; Morkoc, H. *Phys. Rev. B* **1999**, *59*, 1591.
(41) Potin, V.; Ruterana, P.; Nouet, G. *J. Phys.: Condens. Matter* **2000**, *12*, 10301.
(42) Ruterana, P.; Potin, V.; Barbaray, B.; Nouet, G. *Philos. Mag. A* **2000**, *80*, 937.
(43) Sánchez, A. M.; Ruterana, P.; Benamara, M.; Strunk, H. P. *Appl. Phys. Lett.* **2003**, *82*, 4471.
(44) Potin, V.; Ruterana, P.; Nouet, G.; Pond, R. C.; Morkoç, H. *Phys. Rev. B* **2000**, *61*, 5587.
(45) Schroder, D. K. *Semiconductor Material and Device Characterization*; Wiley: New York, 1998.
(46) Franssen, G.; Litwin-Staszewska, E.; Piotrzkowski, R.; Suski, T.; Perlin, P. *J. Appl. Phys.* **2003**, *9*, 6122.
(47) Tsao, H.-Y.; Lin, Y.-J.; Chen, Y.-H.; Chang, H.-C. *Solid State Commun.* **2011**, *151*, 693−696.

Paper VII

Bilousov, O.V.; Carvajal, J.J.; Drouin, D.; Vilalta, A.; Ruterana, P.; Pujol, M.C.; Mateos, X.; Díaz, F., Aguiló, M. and O'Dwyer, C. *Metal catalyzed porous N-type GaN layers: Low resistivity ohmic contacting and single-step MgO/GaN diode formation* **(2013)** ECS Transactions, 53 (2), pp. 17-27.

ECS Transactions, 53 (2) 17-27 (2013)
10.1149/05302.0017ecst ©The Electrochemical Society

Metal catalyzed porous n-type GaN layers: low resistivity ohmic contacting and single-step MgO/GaN diode formation

O. V. Bilousov[1], J. J. Carvajal[1], D. Drouin[2], A. Vilalta[3], P. Ruterana[3], M. C. Pujol[1], X. Mateos[1], F. Díaz[1], M. Aguiló[1], C. O'Dwyer[4,5]

[1] *Physics and Crystallography of Materials and Nanomaterials (FiCMA-FiCNA), Universitat Rovira i Virgili (URV), Tarragona, Spain*
[2] *Department of Electrical and Computer Engineering, Université de Sherbrooke, Sherbrooke, Québec J1K 2R1, Canada*
[3] *CIMAP, UMR 6252, CNRS-ENSICAEN-CEA-UCBN, 6, Boulevard du Maréchal Juin, 14050 Caen Cedex, France*
[4] *Department of Chemistry, University College Cork, Cork, Ireland*
[5] *Micro- and Nanoelectronics Centre, Tyndall National Institute, Lee Maltings, Cork, Ireland*

Porous GaN crystals have been successfully grown and electrically contacted simultaneously on Pt- and Au-coated silicon substrates as porous crystals and as porous layers. By the direct reaction of metallic Ga and NH_3 gas through chemical vapor deposition, intermetallic metal-Ga alloys form at the GaN-metal interface, allowing vapour-solid-solid seeding and subsequent growth of porous GaN. Current-voltage and capacitance-voltage measurements confirm that the intermetallic seed layers prevent interface oxidation and give a high-quality reduced workfunction contact that allows exceptionally low contact resistivity. Additionally, the simultaneous formation of a lower workfunction intermetallic permits ohmic electron transport to n-type GaN grown using high workfunction metals that best catalyze the formation of porous GaN layers and may be employed to seed and ohmically contact a range of III-N compounds and alloys for broadband absorption and emission. Additionally, we show how a porous GaN rectifying diode can be formed by oxidatively crystallizing Mg typically employed for p-doping GaN, as a layer formed under porous structure resulting in a high-k polycrystalline MgO dielectric.

Introduction

Gallium nitride (GaN) is considered one of the most important wide band-gap semiconductors for a number of applications in electronics and optoelectronics (1). In its porous form, GaN has received particular interest in the last decade due to beneficial optical and electronic properties for gas sensors with high sensitivity (2), and light-emitting diodes (LEDs) with high light extraction efficiency (3). Porous GaN has been typically fabricated by (photo)electrochemical and chemical etching methods (4-7), giving textured surfaces as a result of pore coalescence and variations in etch rates for extended etching times.

We produced porous GaN through the direct reaction of metallic Ga with NH_3 in a simple chemical vapor deposition (CVD) system. Metal catalysts are typically used

to initiate growth through either a vapour-liquid-solid (VLS) (8) or vapor-solid-solid (VSS) (9) mechanism when using molecular beam epitaxy (MBE) and chemical vapor deposition (CVD), where the catalyst can influence the growth, e.g. colloidal gold nanoparticles can initiate the growth of GaN nanowires. Using this procedure we have been able to deposit micrometer size nanoporous GaN particles directly onto boron nitride (BN) (10) and silicon (11) substrates without necessitating any secondary etching or chemical treatment after growth to induce porosity. Furthermore, by using this technique we have demonstrated that it is possible to deposit porous GaN directly onto Si substrates in a single growth step (12). The only requirement, when depositing such porous particles on silicon substrates is that it is necessary to use a metal catalyst to induce the crystal growth of GaN.

The development of porous GaN augers well for new electronic and optoelectronic devices with improved external quantum efficiencies, the incorporation of phosphors for LEDs, and high surface area sensing. However, the electrical properties of porous GaN and their correlation to its growth, have been scarcely reported in the literature.

In this paper, we report the successful growth and simultaneous electrical contacting of nanoporous GaN grown using high work-function Au- and Pt-coated silicon substrates, through the direct reaction of Ga and NH_3 in the CVD system. Au and Pt acted both as catalyst for the synthesis of porous GaN and as electrodes for the electrical characterization of the porous layers. The electrical measurements demonstrate the influence of the growth mechanism so that near-ohmic contacts can be made to n-type porous GaN layers using high work-function metals (Au and Pt) which also form intermetallic seed layers to support vapor-solid-solid (VSS) growth of the porous GaN crystals. Lastly, p-type Mg dopants were deposited in such a way as to seed a Mg film under the porous GaN, which was oxidatively crystallized without changing the dopant type from n- to p-type, resulting in a single step top-down n-GaN/high-k poly-MgO diode.

Experimental

Synthesis of porous GaN particles

Nanoporous GaN microparticles were deposited on Au- and Pt-coated silicon (100) substrates with an area of 1 cm^2, using a horizontal single zone split tubular furnace Thermolyne 79300. Gallium metal (99.99%) and ammonia (>99.98%) were used as the Ga and N sources, respectively. A 20 nm layer of Au or Pt was deposited on the Si substrates using a RF sputtering process (AJA International) at a power of 150 W and a pressure of 3 mTorr. The coated substrate was then placed 2 cm above the Ga source. The quartz tube of the furnace was degassed to a vacuum pressure of 1×10^{-2} Torr, after which NH_3 was introduced through a mass-flow controller at a flow rate of 75 sccm and the furnace heated to the reaction temperature of 1203 K at a rate of 100 K min^{-1}, while the pressure was kept at 15 Torr. The reaction was continued at this temperature and pressure for 60 min under a constant flow of NH_3. Growth was halted by cooling to room temperature without NH_3 flow, reducing the pressure to 1×10^{-2} Torr.

Nanoporous GaN doped with Mg was grown as micron-sized particles by the direct reaction of metallic Ga with ammonia in a tubular CVD system, using gallium metal (99.99%), ammonia (>99.98%) and Mg_3N_2 (99.5%) as the Ga, N and Mg sources, respectively. The Mg_3N_2 powder, with a 0.025 to 1 weight ratio respect to Ga, was placed 5 cm up-stream of the Ga source.

Structural and morphological characterization

X-ray diffraction (XRD) spectra and imaging in θ-2θ geometry of the as-grown sample were made using Cu Kα radiation in a Bruker-AXS D8-Discover diffractometer equipped with parallel incident beam (Göbel mirror), vertical θ-θ goniometer, XYZ motorized stage and a General Area Diffraction Detection System (GADDS) HI-STAR detector with a multiwire proportional counter of area 30 × 30 cm and 1024 × 1024 pixel density. Samples were placed directly on the sample holder and the area of interest was selected with the aid of a video-laser focusing system. An X-ray collimator system allows to analyze areas of 500μm. The X-ray diffractometer was operated at 40 kV and 40 mA to generate Cu Kα radiation. We collected 2D XRD patterns covering a range of 2θ between 20 - 85º at a distance of 15 cm from the sample. The exposure time was 120 s per frame. Identification of the crystalline phases was achieved by comparison of the XRD diffractogram with the ICDD database using Diffrac^{plus} Evaluation software (Bruker 2007).

The nanoporous GaN microparticles deposited on the Si substrates as a porous layer were characterized morphologically using a JEOL JSM 6400 scanning electron microscope (SEM). Before observation samples were coated with a thin layer of gold with a Bal-Tec SCD004 sputterer.

Electrical characterization

Charge transport measurements through the porous GaN films were conducted using 2- and 4-probe measurements using a dc-voltage course and an Agilent 34401A Digital Multimeter in a Peltier cell, thermostated to 295 K in a Faraday cage. Liquid metal contacts were made using In-Ga eutectic blown into a sphere from a gold metallized short borosilicate capillary tube ensuring good wetting (several μm^2) to the rough top-surface morphology of the porous GaN and avoid electrical shorting to the underlying metallized silicon. Measurements were made in 2- and 4-probe arrangements. Resistivity values were extracted from *I-V* curves in the high bias regime (series resistance) and also from 4-point probe measurements. Diode measurements of the GaN/MgO system were made in vertical 2-probe measurements.

Results and Discussion

Vapor-solid-solid growth of porous GaN

Figures 1(a) and (b) confirm that the porous GaN particles have a characteristic morphology consisting of faceted hourglass crystals with a mean size of ~1.5 μm. Crystal growth occurs progressively on the surface with individual crystals ripening until a layer of porous GaN microparticles covers the surface as a porous layer. The GaN layers are both microporous and mesoporous. The microporosity stems from the free space between particles (see Figure 2 (c)), whereas the nanoscale mesoporosity comes from internal pore features within the particles, confirmed with time-resolved focused ion beam (FIB) based tomography (11). The particles obtained on the Si substrates coated with Pt showed a higher degree of internal porosity than those grown from Au-coated Si substrates.

The growth of these GaN nanoporous particles is assisted by a solid particle through the vapour-solid-solid (VSS) mechanism, the main stages of which are: the Ga incorporation into the Au or Pt solid phase eutectic, the formation of a Ga-Au or Ga-Pt alloy, the solubilization of nitrogen in the Ga-Au(Pt) alloy, and finally the nucleation

and growth of GaN (see Fig. 1). HRETM analysis of such structure shows that they are single crystal in nature, with structure defect comprising internal pores within the crystals.

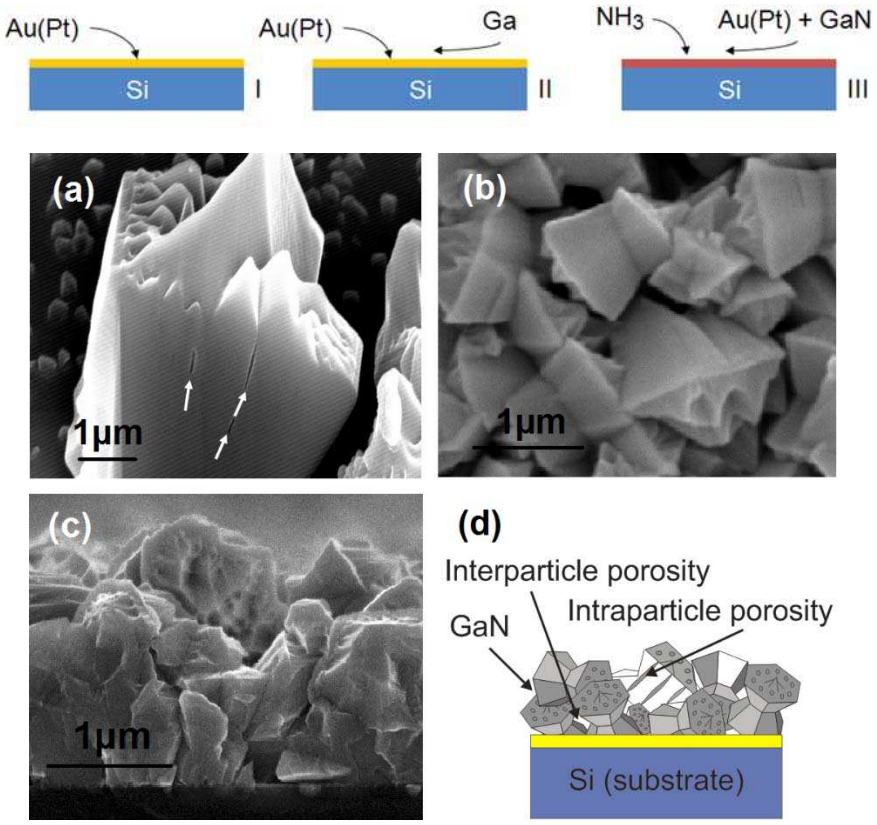

Figure 1. (Top) Mechanism of growth of the GaN nanoporous particles through the VSS process. SEM image of porous GaN particles grown on Si (100) substrates coated with (a) 20 nm film of Au and (b) 20 nm film of Pt. (c) SEM cross sections showing interparticle porosity of the GaN layer. (d) Schematic of the porosity inherent in the GaN film.

The crystalline structure of the porous GaN particles deposited on Si substrates coated with Au and Pt was analysed using X-ray diffraction. The XRD pattern shown in Fig. 2(a) for GaN grown on Au-coated Si substrates, confirms crystalline wurtzite GaN growth with a predominant diffraction intensity from low-index crystal facets. The regions at which the (400) diffraction peak of Si should appear (69.131º) has been excluded from the measurement to avoid problems of intensity saturation. This allows observation of lower intensity reflections that are attributed to crystalline Si_3N_4 and a crystalline Au-Ga intermetallic alloy of cubic Ga_2Au. We believe that the Si_3N_4 formation is most likely due to the reaction between NH_3 and silicon accelerated by the metallic catalyst.

The formation of the Au-Ga crystalline alloy, which occurs here above the solid-solution formation temperature of 923 K, confirms intermetallic seeding to form GaN by reaction with NH_3 through a vapor-solid-solid process. The uniform intensity of the Debye rings (along the curved ring portions in Fig. 2b) collected for porous GaN confirms that there is no texturation of the layer of porous crystals (see Figure 2 (b)). For porous GaN grown on Pt-coated substrates, similar results were obtained, although we could not identify the formation of any specific crystalline Pt-Ga alloy.

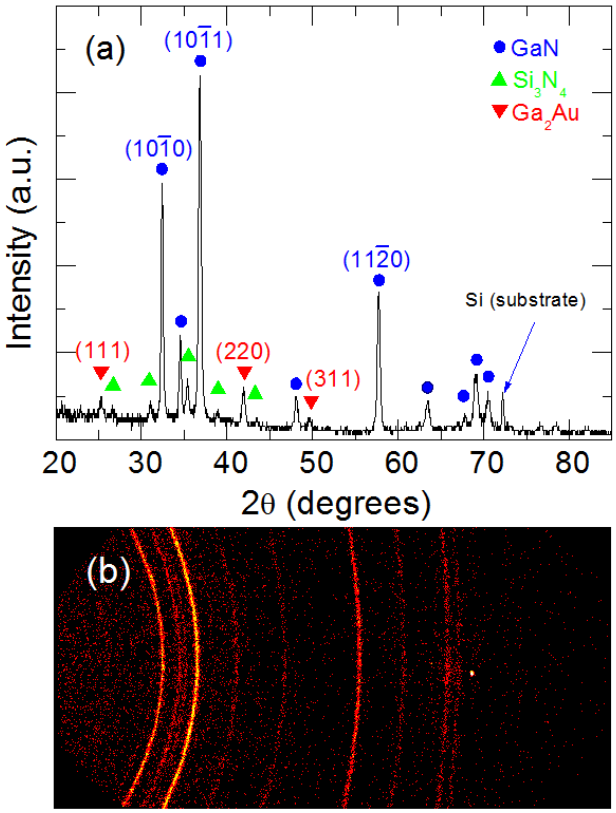

Figure 2. (a) XRD pattern for porous GaN deposited on Au-coated Si(100) showing the formation of crystalline GaN (ICDD 01-073-7289), Si_3N_4 (ICDD 03-065-8613) and Ga_2Au alloy (ICDD 01-071-6479). (b) Debye rings recorded with GADDS detector indicating no texturation of the porous GaN layer.

Electrical characterization of Pt- and Au-contacted porous GaN

Figure 3 shows the *I-V* curves from the porous GaN catalyzed by Pt (Figure 3a) and also by Au (Fig. 4b), with the second contact placed on the underlying metal which was under heating to 1203 K in NH_3. The *I-V* curves show only slight asymmetry indicative of near ohmic, weak Schottky barriers of Pt and Au. Consistently, the conductivity of porous GaN grown from Pt is higher than that grown from Au, in spite of the higher workfunction. The *I-V* curve of porous GaN-Pt in Fig. 4(b) shows the low-bias non-linearity consistent with a weak Schottky barrier. Both contacts are described using the thermionic emission theory, acknowledging a high ideality factor for weak barriers. The Schottky barrier height can still be estimated from:

$$I = I_0\left[\exp\left(\frac{qV - IR_S}{kT}\right) - 1\right] \quad (1)$$

where $I_0 = AA^{**}T^2\exp(-q\varphi^{o}_{B,n}/kT)$[15] where A** is the effective Richardson constant. The estimated Schottky barrier heights using the theoretical value for the effective Richardson constant (26.4 A cm^{-2} K^{-2}) for Pt and Au contacted porous GaN are 0.66 eV and 0.53 eV, respectively.

In spite of the higher porosity from Pt-grown porous GaN, the contact resistivity of the Pt contact is $2 - 4 \times 10^{-4}$ Ω cm^2 while that of the gold contact is $6 - 9 \times 10^{-4}$ Ω cm^2. Thus the interface dominated the transport more than the crystallinity or

morphology of the porous microstructure, and effective ohmic contacts can form with n-type GaN.

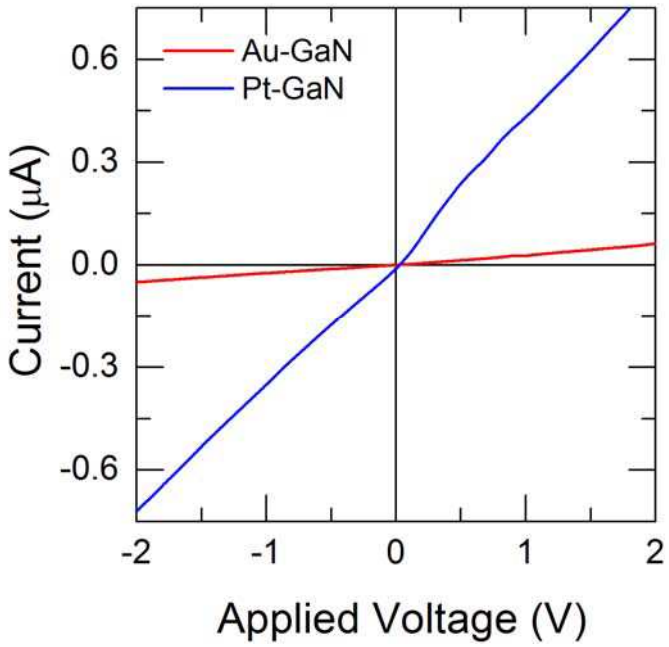

Figure 3. *I–V* curves for porous GaN grown from (a) Pt and (b) Au.

Two terminal transport measurements (Fig. 4a) acquired between the In-Ga ohmic contacts showed perfect ohmicity for transport through the porous GaN layer only, from which low contact resistivities were determined with variable intercontact separation using the TLM approach and found to be in the range $1.7 – 4.4 \times 10^{-4}$ Ω cm^2, in spite of the multifaceted, porous morphology. Corresponding 4-probe analysis gives sheet resistances for porous GaN films in the range 43-49 kΩ/□, which is higher than compact thin film forms as expected from a layer comprising microcrystals in intimate contact. The values, that match those of MBE grown GaN thin films with Ti/Au alloy contacts after annealing to 973 K (16), are caused by the efficient interface between the metal and the growing porous GaN (10). Additionally, although annealing at 1173 K is known to initial improve contact resistivities down to the 10^{-6} Ω cm^2 with Ti/Al contacts, continued heating at this temperature for more than 40 seconds results in a drastic increase in contact resistance (16). The present method avoids this by the use of noble metal contacts as catalysts for the GaN growth. It is worth noting that the n-type contacts were effectively ohmic as deposited and did not need any post-deposition annealing to induce this effective ohmicity; such linear I−V behavior is not found with Au contacts, and the intermetallic seed layer interface is critical for removing the transport Schottky barrier (17).

For the low resistance contacts to a porous GaN layer either a low barrier Schottky contact forms with a graded band-gap interface or a tunnel contact is formed. From XRD analysis, a crystalline Si_3N_4 dielectric layer forms when deposition is performed on silicon, just prior to continued VSS porous GaN growth and is not likely from N out-diffusion from the GaN. The GaN too, is not expected to decompose at 1203 K in NH_3 (it would at a slightly higher temperature in vacuum)[17], but the Au and Pt melting points are close to this temperature. These metals solidify once the crystalline intermetallic Ga_2Au solid phase is formed. Oxide growth that would increase the resistivity of the contact is also prevented.

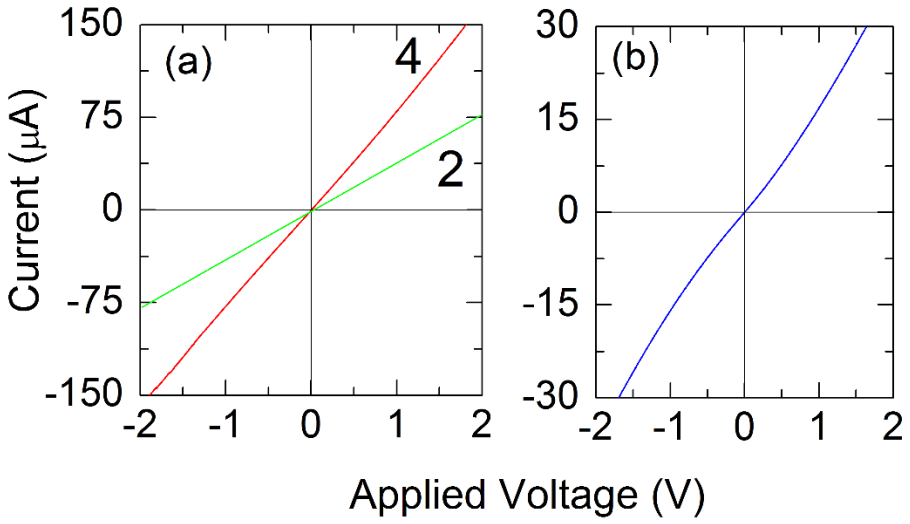

Figure 4. (a) *I–V* curve for the porous GaN grown directly from Pt and (c) I–V curves from two- and four-probe measurements using In–Ga ohmic contacts to porous GaN.

The intermetallic Ga_2Au phase suggests a band structure that promotes transport by lowering the Schottky barrier, rather than forming a definitive tunnel contact which shows ohmicity over a small potential range. The intermetallic formation at the interface that allows the growth of the GaN effectively acts as an intermetallic ohmic contact at the semiconductor interface, and the method may be extended to growing nanoscale III-N materials and alloys using metals that are not typically employed for contacting, to give ohmic response.

Single step high-k MgO/porous n-GaN diode formation

When doping these nanoporous GaN with a high concentration of Mg using Mg_3N_2 as precursor, a layer of crystalline MgO is formed in between the Au- or Pt-electrode and nanoporous GaN. Fig. 5 shows the XRD pattern for the resulting deposition.

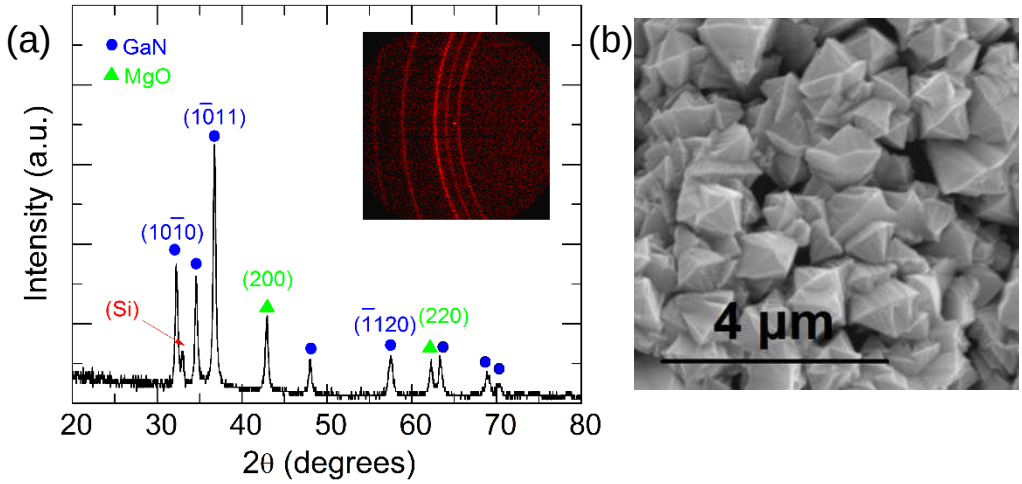

Figure 5. (a) XRD pattern for porous crystalline wurtzite GaN (P63*mc*) doped with Mg grown on a Si(100) substrate using $Ni(NO_3)_2$ as catalyst, with inset of Debye rings. (b) SEM images of the Mg-GaN particles deposited on Si.

We find that deposit also contains crystalline MgO, oxidatively crystallized from the Mg presence during incorporation at the growth stage of the porous GaN. From Fig. 5b, that the single crystals remain nearly identical those grown in the absence of the Mg precursor, and separate data shows that they also retain their unintentionally n-doped character.

TEM analysis confirms that the polycrystalline MgO is located under the porous GaN, in spite of being present at initial stages of the seeding mediated growth of the GaN itself. The high quantities of the Mg-containing precursors preferentially forms this layer rather than doping the GaN lattice. The Mg concentration from TEM energy dispersive X-ray analysis, shown in Fig. 6, confirms the interfacial location of the MgO between the silicon substrate/intermetallic seed layer, and the porous GaN.

# (b)	Mg %	G %	#	Mg %	Ga %
1	73.3	26.7	7	11.7	97.8
2	98.5	1.5	8	7.9	92.1
3	97.0	3	9	9.5	90.5
4	97.3	2.7	10	8.9	91.1
5	7.9	92.1	11	7.9	92.1
6	11	89	12	8.1	91.9

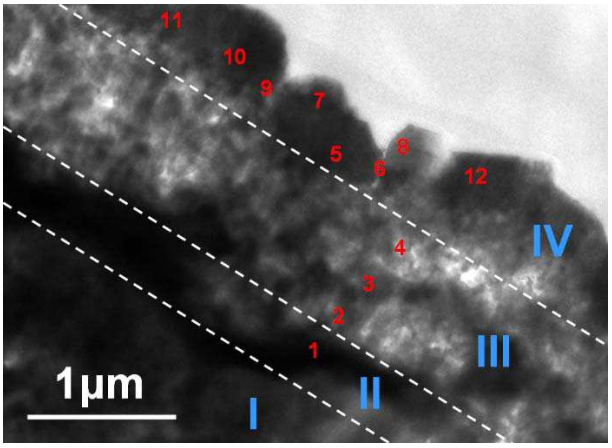

Figure 6. (a) TEM image of porous GaN layer doped with Mg grown on a Si(100) substrate. (b) EDX content of Mg and Ga in the pores particles. The measurement points (#) relate to those numbered in (a).

Figure 7 shows *I-V* curves across the device using an In-Ga euctectic to ohmically contact both the substrate and the porous GaN. The GaN layer in this case was grown using a Au seed layer. A rectifying diode response is found in the presence of the MgO, compared to ohmic response between the intermetallic termination porous n-GaN and the substrate (18,19). We assumed that the net current is due to thermionic emission current since the metal-semiconductor-metal contact now contains a dielectric at one interface, mimicking a Schottky contact with series resistance and an interfacial layer. Additionally, this is confirmed by forward bias voltages of $V > 3kT/q$, which is the case here. The downturn to linearity in the current after ~0.25 V confirms a series resistance, R_S most likely originates from the MgO and porous n-GaN, as opposed to either of the metal contacts which are confirms to be ohmic in nature. At higher bias

(>0.25 V), the *R*s dominates, as can be seen from the differential conductance d*I*/d*V* curve in Fig. 7a.

Effective ohmic contacts can form with n-type GaN, as shown earlier, suggesting that the resistivity dominates transport through an alloyed interface that promotes ohmic transport. When and high-k MgO layer is introduced, the series resistance markedly increases at much lower voltages. The MgO/n-GaN sandwich effectively has an altered electron affinity with respect to the contact In-Ga top contact.

The overall series resistance, *R*s, to which the sheet and contact resistivities contribute can also be determined from diffusion and thermionic emission theory summarised for a Schottky type diode in Eq. (1). In the presence of the intermetallic bottom contact, the transport is effectively ohmic. As the top contact to n-GaN is also Ohmic, the diodic response stems from affinity differences between the MgO high-k oxide and the GaN semiconductor. The series resistance can also be obtained from the differential resistance through its proportionality to the current according to

$$\frac{dV}{dI} = \left(R_s + \frac{kT}{q}\left[\frac{1/I_0}{I/I_0 - 1}\right]\right) \approx R_s + \frac{nkT}{qI} \qquad (2)$$

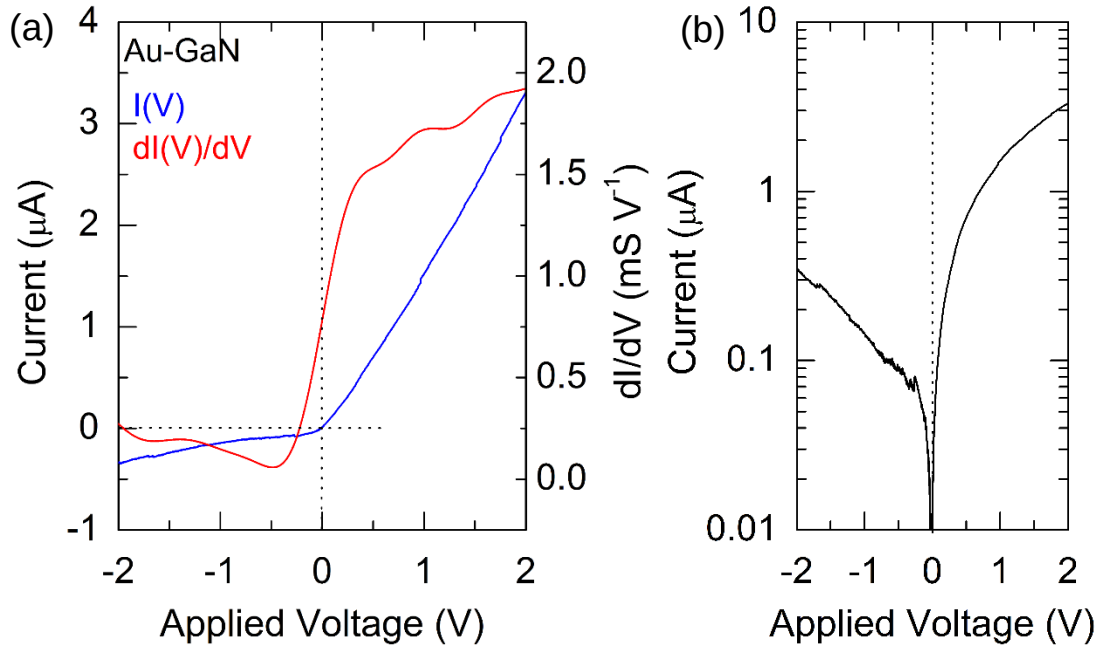

Figure 7. (a) *I*-*V* and d*I*/d*V* curves for Au-seeded porous n-GaN with a MgO dielectric layer. (b) ln(*I*)-*V* curve for the diode.

Figure 8a shows the differential resistance d*V*/d*I* as a function of applied of the inverse of the current in the high current region, plotted according to Eq. 2. Although it does not take account of specific grain boundary effects, the series resistance is estimated to be in the range 5-6 kΩ for the MgO/porous GaN sandwich. For the transport through the MgO/porous n-GaN stack, d*V*/d*I* approaches *R*S at the higher currents, but as seen in Fig. 8b, the series resistance also includes likely tunnelling effects as the ideality factor is strongly voltage dependent and quite high in the higher current and higher bias regions. Further work is underway to identify mechanism contributing to such high ideality factors which in Schottky junctions are indicative of several mechanisms including tunnelling current, through multiple heterojunctions. Porosity complicates the transport mechanism, increasing shunt and series resistances (21).

Charge transport measurements through this system were conducted using 2- and 4-probe measurements and confirm the fabrication of a porous GaN diode with an *in-situ* grown crystalline MgO high-k dielectric layer. For Au-seeded porous n-GaN, Ohmic transport is found in the absence of a second oxide semiconducting layer between the intermetallic and the porous n-GaN, as shown in Figs 3 and 4. Further work is in progress to determine the direct effect of porosity on the reverse bias current mechanisms, and optimization of the diode response from Pt-seeded intermetallic-mediated porous GaN growth based on detailed investigations of the influence of the porosity on contact and sheet resistivity, and performance as a chemically inert, high surface area field effect transistor for sensing.

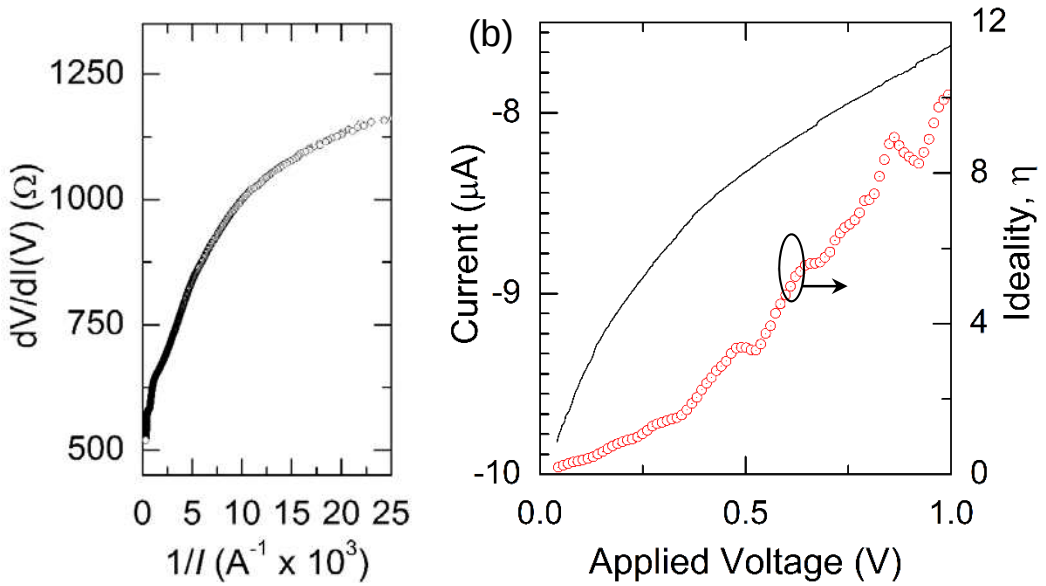

Figure 8. (a) Differential resistance (dV/dI) as a function of current for the MgO/porous GaN diode. (b) ln(I)-V curve and the voltage dependence of the ideality factor for the diode.

Conclusions

In summary, porous GaN particles have been successfully grown as high surface area layers from Pt- and Au-coated silicon substrates by a vapor-solid-solid process. The particles form as a layer of single-crystal particles with interparticle and intraparticle porosity. Current-voltage and capacitance-voltage measurements show near-ohmic transport through low-doped, polycrystalline (as a layer), porous n-GaN without alloy contacts or low work function metals. Metal-Ga intermetallic alloy formation during vapor-solid-solid growth promotes thermionic emission-based low-resistance ohmic transport through the porous layer and very low contact resistivity is possible to the faceted, rough n-GaN surface. By depositing Mg in a manner similar to deterministic p-type doping of GaN, a thin Mg films that is oxidized to polycrystalline MgO, is formed underneath the porous n-GaN layer, resulting in a high-k dielectric oxide that allows the single step formation of a porous GaN/MgO diode.

Acknowledgements

This work was supported by the EU Framework 7 under Project No. FP7-SPA-2010-263044, the Spanish Government under Projects No. MAT2011-29255-C02-02,

TEC2010-21574-C02-02, PI09/90527, and by Catalan Authority under Project No. 2009SGR235. This work was also supported by Science Foundation Ireland under contract No. 07/SK/B1232a.

References

[1] S. Nakamura, S. Pearton, G. Fasol, G., *The Blue Diode Laser - The Complete Story*, Springer, Berlin, 7 (2000).
[2] A. Ramizy, Z. Hassan, K. Omar, *Sens. Actuators, B* **155**, 699 (2011).
[3] C. F. Lin, K. T. Chen, C. M. Lin, C. C. Yang, *IEEE Electron Dev. Lett.* **30**, 1057 (2009).
[4] M. Mynbaeva, A. Titkov, A. Kryganovskii, V. Ratnikov, K. Mynbaev, H. Huhtinen, R. Laiho, V. Dmitriev, *Appl. Phys. Lett.* **76,** 1113 (2000).
[5] Y. D. Wang, S. J. Chua, M. S. Sander, P. Chen. S. Tripathy, C. G. Fonstad, *Appl. Phys. Lett.* **85,** 816 (2004).
[6] S. Y. Bae, H. W. Seo, J. Park, H. Yang, B. Kim, *Chem. Phys. Lett.* **376,** 445 (2003).
[7] D. J. Diaz, T. L. Williamson, I. Adesida, P. W. Bohn, R. J. Molnar, *J. Appl. Phys.* **94**, 7526 (2003).
[8] R. S. Wagner, W. C. Ellis, *Appl. Phys. Lett.* **4**, 89 (1964).
[9] A. I. Persson, M. W. Larsson, S. Stenstron, B. J. Ohlsson, L. Samuelson, L. R. Wallenberg, *Nat. Mater.* **3**, 677 (2004).
[10] J. J. Carvajal, J. C. Rojo, *Cryst. Growth Des.* **9**, 320 (2009).
[11] J. J. Carvajal, O. V. Bilousov, D. Drouin. M. Aguiló, F. Díaz, J. C. Rojo, *Microsc. Microanal.* **18**, 1 (2012).
[12] C. O'Dwyer, M. Szachowicz, G. V. Visimberga, V. Lavayen, S. B. Newcomb, C. M. Sotomayor Torres, *Nat. Nanotech.* **4**, 239 (2009).
[13] C. O'Dwyer, D. N. Buckley, D. Sutton, S. B. Newcomb, *J. Electrochem. Soc.* **153**, G1039 (2006).
[14] M. E. Lin, Z. Ma, F. Y. Huang, Z. F. Fan, L. H. Allen, H. Morkoç, *Appl. Phys. Lett.* **64**, 1003 (1994).
[15] D. K. Schroder, *Semiconductor Material and Device Characterization*, Wiley, New York, 156 (1998).
[16] R. Sporken, C. Silien, F. Malengreau, K. Grigorov, R. Caudano, F. J. Sanchez, E. Calleja, E. Munoz, B. Beaumont, P. Gibart, *MRS Internet J. Nitride Semicond. Res.* **2**, 23 (1997).
[17] Yu. A. Goldberg, E. A. Posse, *Semiconductors,* **32**, 181 (1998).
[18] O. V. Bilousov, J. J. Carvajal, D. Drouin, X. Mateos, F. Díaz, M. Aguiló and C. O'Dwyer, *ACS Appl. Mater. Interfaces*, **4**, 6927 (2012).
[19] R. H. Horng, D. S. Wuu, Y. C. Lien, W. H. Lan, *Appl. Phys. Lett* **79,** 2925 (2001).
[20] D. J. Dumin, G. L. Pearson, *J. Appl. Phys.* **36**, 3418 (1965).
[21] G. Franssen, E. Litwin-Staszewska, R. Piotrzkowski, T. Suski, P. Perlin, *J. Appl. Phys.* **9**, 6122 (2003).

Paper VIII

Bilousov, O.V.; Carvajal, J.J.; Martínez, O.; Jiménez, J.; Geaney, H.; Díaz, F.; Aguiló, M. and O'Dwyer, C. *Epitaxially grown (0001) oriented porous GaN p-n junctions by chemical vapour deposition*. Submitted to Advanced Functional Materials.

Epitaxial growth of (0001) oriented porous GaN layers by chemical vapour deposition

O.V. Bilousov[a], J.J. Carvajal[a,*], O. Martínez[b], J. Jiménez[b], H. Geaney[c,d] , F. Díaz[a], M. Aguiló[a], C. O'Dwyer[c,d]

[a] Física i Cristal·lografia de Materials i Nanomaterials (FiCMA-FiCNA) and EMaS, Universitat Rovira i Virigli (URV), Marcel·lí Domingo s/n, E-43007 Spain
[b]GdS-Optronlab, Departamento Física Materia Condensada, Univ. de Valladolid, Edificio I+D, Paseo de Belén, 11, 47011, Valladolid, Spain
[c] Department of Chemistry, University College Cork, Cork, Ireland
[d] Micro & Nanoelectronics Centre, Tyndall National Institute, Lee Maltings, Cork, Ireland

Abstract

LEDs with enhanced light extraction efficiency and sensors with improved sensitivity have been developed using porous semiconductors. Here, the growth of porous GaN epitaxial layers oriented along the [0001] crystallographic direction on Al_2O_3, SiC, AlN and GaN substrates is demonstrated. Lattice mismatch between the substrate and the porous GaN layer directly affects the structure and porosity of the porous GaN layer on each substrate. Deposition of unintentionally doped *n*-type porous GaN on non-porous *p*-type GaN layers allow for the fabrication of high quality rectifying *p*-*n* junctions, with potential application in high brightness unencapsulated GaN-based light emitting diodes and in high surface area wide bandgap sensor devices.

Introduction

III-N semiconductors, such as GaN, have a wide range of applications principally due to its wide direct band gap, being the most used materials for solid state lighting, both as LEDs and laser diodes , with emission in the UV and visible spectral ranges, being essential for the production of white light.[1] They present also interest for high temperature/high power electronics because of their large band gap, high thermal stability and excellent physical properties.[2]

In its porous form GaN is particularly interesting for developing optoelectronic devices with improved efficiency, such as LEDs with enhanced light extraction efficiency. This is due to the multiple reflections on the lateral walls of the pores and an "effective" reduced refractive index[3,4] that alleviates the high refraction index contrast between GaN, or other semiconductors, and air.[5,6] They are also interesting for their use in (bio)sensors, with improved sensitivity induced by the larger surface area of the porous structures.[7,8] Another attractive application of porous GaN is its use as a buffer layer to reduce the structural defects in non-porous GaN grown on foreign substrates, by reducing the stress due to the lattice mismatch.[9,10]

However, porous GaN has been typically fabricated by (photo)electrochemical and chemical etching methods.[11-13] These methods generally suffer from a lack of control over the size, morphology and distribution of the pores, making the fabrication of optoelectronic devices difficult. Furthermore, the use of these techniques might induce unwanted interface states and surface contamination and defects that can affect properties of the crystals, negatively affecting the performance of the systems based on

them. Also, one has to take into account that anodization processes, to generate the required porosity, demand complex equipment for their control, and in general many of the electrolytes are highly toxic and/or corrosive. In the specific case of porous GaN, the ability to form relatively uniform, crystalline porous GaN layers over large areas through complex etching processes without photolithographic masking is challenging.[11,14]

We have previously shown that it is possible to produce nanoporous GaN microparticles in a simple chemical vapor deposition (CVD) reactor,[15] without the need of additional etching or chemical treatments after growth for generating the porosity. The porosity in these particles is only present on the (0001) face. Recently, we demonstrated that these nanoporous GaN particles can be also grown on silicon substrates using a metallic catalyst, obtaining porous particles with a low density of defects.[16,17] However, the result is a polycrystalline porous GaN film with dual porosity (intraparticle and interparticle), where the porous particles, are not crystallographically oriented. In spite of this, electronically, GaN retains a clean surface with low presence of deep levels,[18] which is useful for applications requiring a high surface-to-volume ratio.

Here we show the possibilities of growing grains oriented along the [0001] crystallographic direction, so that all the pores would be aligned along the same direction through the directional effect provided by the substrate on which porous GaN is grown. The substrates for the oriented growth of nanoporous GaN were sapphire (which is the most widely used substrate for GaN deposition), SiC (also one of the most used substrates for GaN production), and commercial AlN and GaN epitaxial layers, since they have the same crystallographic structure and thus induce reduced lattice mismatches. The obtained porous films are characterized morphologically, structurally, electrically and optically. When growing on *p*-type non-porous GaN films, a clear *p*-*n* junction response was obtained, demonstrating the potential for functional devices based on epitaxial GaN and CVD grown porous GaN multilayers.

Materials and Methods

Nanoporous GaN thin layers were grown on different substrates by the direct reaction of metallic Ga with ammonia in a tubular CVD reactor, using gallium metal (99.999%) and ammonia (99.99%), as Ga and N sources, respectively. Metallic Ga was introduced into the system in the form of droplets in a quartz crucible.

The substrates used were Al_2O_3 (0001), SiC (0001), and commercial AlN (0001) and GaN (0001) thin films grown on sapphire (0001) substrates. The substrate was placed 1.7 cm above the Ga source. Prior to their introduction in the furnace, the substrates were cleaned with ethanol. No catalyst was used in this case, in contrast when nanoporous GaN polycrystalline films were obtained on Si substrates by the same method;[17] therefore, the reaction was self-catalyzed.

The quartz tube of the furnace was degassed to a vacuum pressure of 1×10^{-2} Torr. Ammonia was then introduced through a mass-flow controller at a flow rate of 75 sccm, while the pressure was set at 15 Torr and the furnace was heated up to the reaction temperature of 1203 K. Then, the furnace was kept at constant temperature for 60 min under constant NH_3 flow and pressure, while the chemical reaction took place. When the reaction was finished, the furnace was cooled down to room temperature while the ammonia flow was stopped, thus the pressure of the system dropped to 1×10^{-2} Torr.

The nanoporous GaN layers deposited on the different substrates were characterized using a JEOL JSM 6400 scanning electron microscope (SEM).

The (0001) surface morphology of the porous films was visualized by Atomic Force Microscopy (AFM) using an Agilent 5500 microscope in the tapping mode, using Si tips with a diameter of 10 nm and oscillating at a resonance frequency of 75 kHz.

Rocking curves of the thin films were recorded using a Bruker-AXS D8-Discover diffractometer equipped with parallel incident beam (Göbel mirror), vertical θ-θ goniometer, XYZ motorized stage and a General Area Diffraction Detection System (GADDS). Samples were placed directly on the sample holder and the area of interest was selected with the aid of a video-laser focusing system. The X-ray diffractometer was operated at 40 kV and 40 mA to generate Cu Kα radiation. The GADDS detector was a HI-STAR (multiwire proportional counter of 30 × 30 cm with a 1024 × 1024 pixel). The rocking curves covered an omega angle of 6º from 120 frames, and were recorded at a step size of 0.05^{o} and 15 s of exposition time per frame.

Two-probe electrical measurements of porous GaN samples were conducted using In/Ga liquid eutectic contacts and a Biologic SP-50 potentiostat. An In/Ga eutectic droplet was used as the Ohmic contact. Linear voltage sweeps were obtained between the range of -3 V and 3 V with a 50 mV/s sweep rate.

Cathodoluminescence (CL) imaging and spectra (at both room temperature and 80 K) and EBIC measurements at RT were carried out in a field emission scanning electron microscope (Carl Zeiss-LEO 1500) operating at 10 kV. For CL measurements, a XiCLOne mono-CL2 system from Gatan was used, the detection being done with a charge-coupled device camera.

For EBIC measurements, the electrical current generated by the electron beam was collected and amplified by a low noise current amplifier (MODEL DLPCA-200, FEMTO Messtechnik, Germany). These measurements conditions allowed spatial resolutions of the order of few hundred nanometers.

Results and discussion

Morphological characterization of the porous GaN films. Figure 1 shows the SEM top view images of the nanoporous GaN films obtained on the different substrates used in this work. Prior to the experiments, we expected porous GaN layers to grow oriented along the ***c***-crystallographic direction, since all our substrates belong to the hexagonal system and are oriented perpendicular to the [0001] direction. However, the morphology, grain structure and the crystallographic orientation of the films depends strongly on the lattice mismatch between the substrate and GaN.

We calculated the two-dimensional lattice mismatch from the expression to have an estimation of the biaxial stress of the samples:[19]

$$f_{(hkil)} = [(S^{L}_{(hkil)} - S^{S}_{(hkil)}) / S^{S}_{(hkil)}] \times 100 \qquad \text{Eq. 1}$$

where $S^{S}_{(hkil)}$ and $S^{L}_{(hkil)}$ are the areas calculated from the periodicity vectors of the substrate and the layer, respectively, for the (0001) plane. Table 1 summarizes the lattice parameters used to calculate the lattice mismatch and the obtained values for the different substrates. The sign of the lattice mismatch indicates if the films are under either compressive or tensile strain when grown on a particular substrate. A negative lattice mismatch means that the plane of the substrate is larger than that of GaN, in this case the porous layer should be under tensile strain. A positive lattice mismatch means that the surface area of the (0001) plane of the substrate is smaller than that of GaN, thus the porous films suffer from compressive stress.

As it can be seen in Table 1, sapphire offers a negative lattice mismatch with GaN, while SiC and AlN result in positive lattice mismatch. The lattice mismatch calculated for the films grown on GaN is zero.[20,21] Thus, the porous GaN layer grown on sapphire should be compressed, whereas those layers obtained on SiC and AlN should be stretched. Furthermore, the absolute value of the lattice mismatch calculated for GaN/Al_2O_3 is larger than for GaN/SiC and GaN/AlN, and can be arranged in the following order from bigger to smaller: $f^{Al_2O_3}_{(0001)} > f^{SiC}_{(0001)} > f^{AlN}_{(0001)} > f^{GaN}_{(0001)}$.

The lattice mismatch between GaN and the substrate can be also estimated by the difference between the c-axis parameters of the substrate and the thin film, according to the following equation, although it only takes into account the uniaxial stress:

$$f'_{[0001]} = \left[\left(c^L - c^s \right) / c^S \right]$$

where c^S and c^L are the c cell parameters of the substrate and the layer, respectively. If this methodology is used, the lattice mismatch between sapphire and GaN is reduced to -11%, while the rest of the calculated lattice mismatches do not change substantially.

Table 1. Lattice mismatch, calculated for the (0001) plane, between GaN and the different analyzed substrates

	Lattice parameters		**Lattice mismatch, %**	
Substrate	***a* (Å)**	***c* (Å)**	$f_{(hkl)}$	f'_c
Sapphire[22]	4.75	12.99	-55.1	-11.16
6H-SiC[23]	3.07	10.05	7.7	7.7
AlN[24]	3.11	4.98	5.1	5.1
GaN[25]	3.19	5.18	0	0

Porous GaN obtained on Al_2O_3 appears in the form of a continuous layer of randomly oriented GaN particles, with porosity present on the (0001) face (see Figure 1a), as observed previously on Si and BN substrates.[16] In spite of such porosity, an ordered coverage of the surface of the substrate is apparent at low magnifications (see inset in Figure 1a).

In the case of SiC (0001), the smaller lattice mismatch and the similar thermal expansion coefficients with GaN, results in porous GaN growing as a quasi-continuous layer with porous GaN particles aligned along the [0001] crystallographic direction and pores on the (0001) GaN face (see Figure 1b). However, crystal grains do not tend to coalesce during growth, and individual particles are still evident in the image.

On AlN, a ***c***-oriented continuous quasi-porous GaN layer similar to that on SiC is obtained, but with a different morphology. Individual particles are not evident; however, the pores have and higher dispersion of shapes. Interparticle porosity in this case is favoured, while negligible intraparticle porosity (within each crystal) is found, as is the case for other growth regimes (see Figure 1c).[17]

Similar results to those obtained on AlN were obtained on GaN (0001) thin films on sapphire (see Figure 1d).

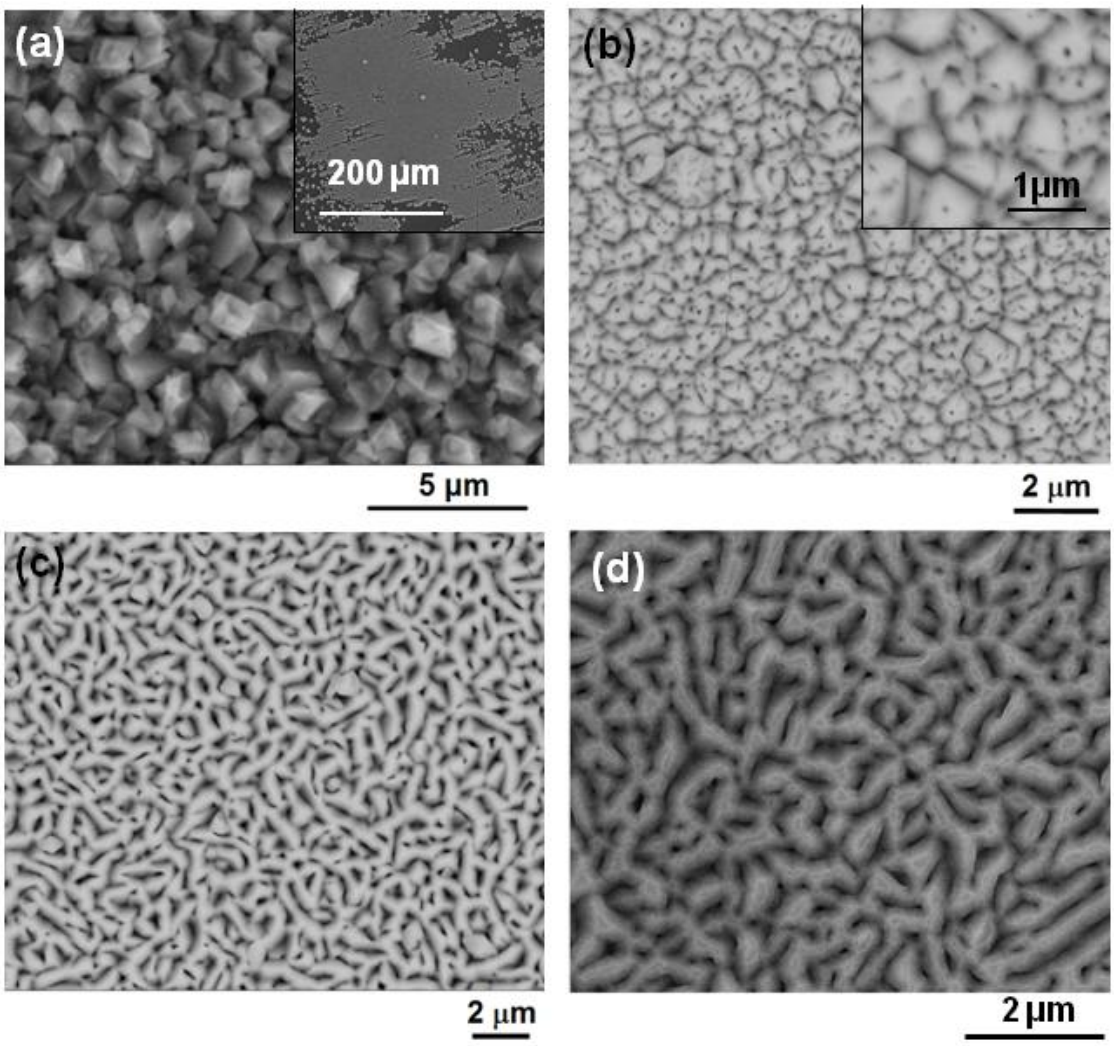

Figure 1. SEM images of porous GaN films obtained on (a) Al_2O_3 (0001), (b) SiC (0001), (c) AlN (0001) and (d) GaN (0001) thin films on sapphire.

The porous GaN epitaxial layers (grown via CVD) obtained on GaN (0001) coated sapphire (0001) substrates were further investigated to follow the evolution of the morphology of the pores and the growth rate with reaction times between 15 and 60 min. Figures 2(a-c) shows the top-down SEM images of porous GaN obtained. These micrographs show that by increasing the reaction times the diameters of the pores increases. The sample obtained at 15 min showed the highest degree of porosity, while the sample obtained after 60 min of reaction showed the lowest degree of porosity. This evolution of the pores with time seems to suggest that a coarsening of the pores is happening as the reaction time increases. Especially in the case of the CVD porous GaN obtained at 15 and 30 min, they have the appearance of a perfectly c-oriented continuous porous GaN layer, and the aspect of a true epitaxial porous layer. These results obtained on GaN (0001) coated sapphire (0001) substrates suggest that by decreasing the reaction time on the epitaxial growth of CVD porous GaN on AlN, also porous epitaxial layers would be obtained.

To know the thickness of the CVD porous GaN epitaxial layers obtained on GaN (0001) coated sapphire (0001) substrates, cross sectional-images of the samples were recorded by SEM, as shown in Figures 2(d-f), corresponding to 15, 30 and 60 min of

reaction time, respectively. These cross-sectional micrographs clearly show the sapphire substrate, the non-porous GaN film with a thickness of ~5 μm, and the CVD porous GaN layer. The interface between the non-porous GaN film, and the CVD porous GaN layer are well defined and abrupt, which is the consequence of the change in density (material quantity) of the two layers. The thickness of the CVD porous GaN layer increases with reaction time, from ~0.5 μm at 15 min to 1.7 μm at 60 min.

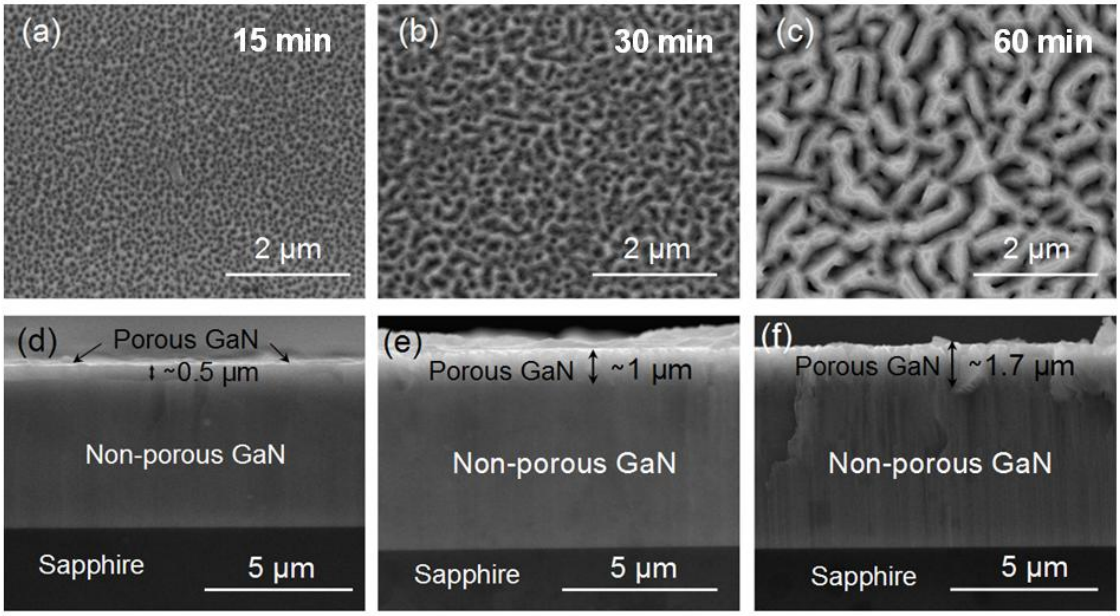

Figure 2. Top views and cross-sectional SEM images of the CVD porous GaN epitaxial layers obtained on GaN (0001) thin films coated sapphire (0001) substrates obtained after (a), (d) 15 min, (b), (e) 30 min, and (c), (f) 60 min reaction time.

AFM in tapping mode was used to visualize more in detail the CVD porous GaN layers, see Figure 3a. The porosity is evident in the image, and pores of different diameters are observed. Two profiles of the surface of the sample, corresponding to the lines indicated in Figure 3a, are shown in Figure 3b to describe the typical diameters of the pores, ranging from 200 to 300 nm.

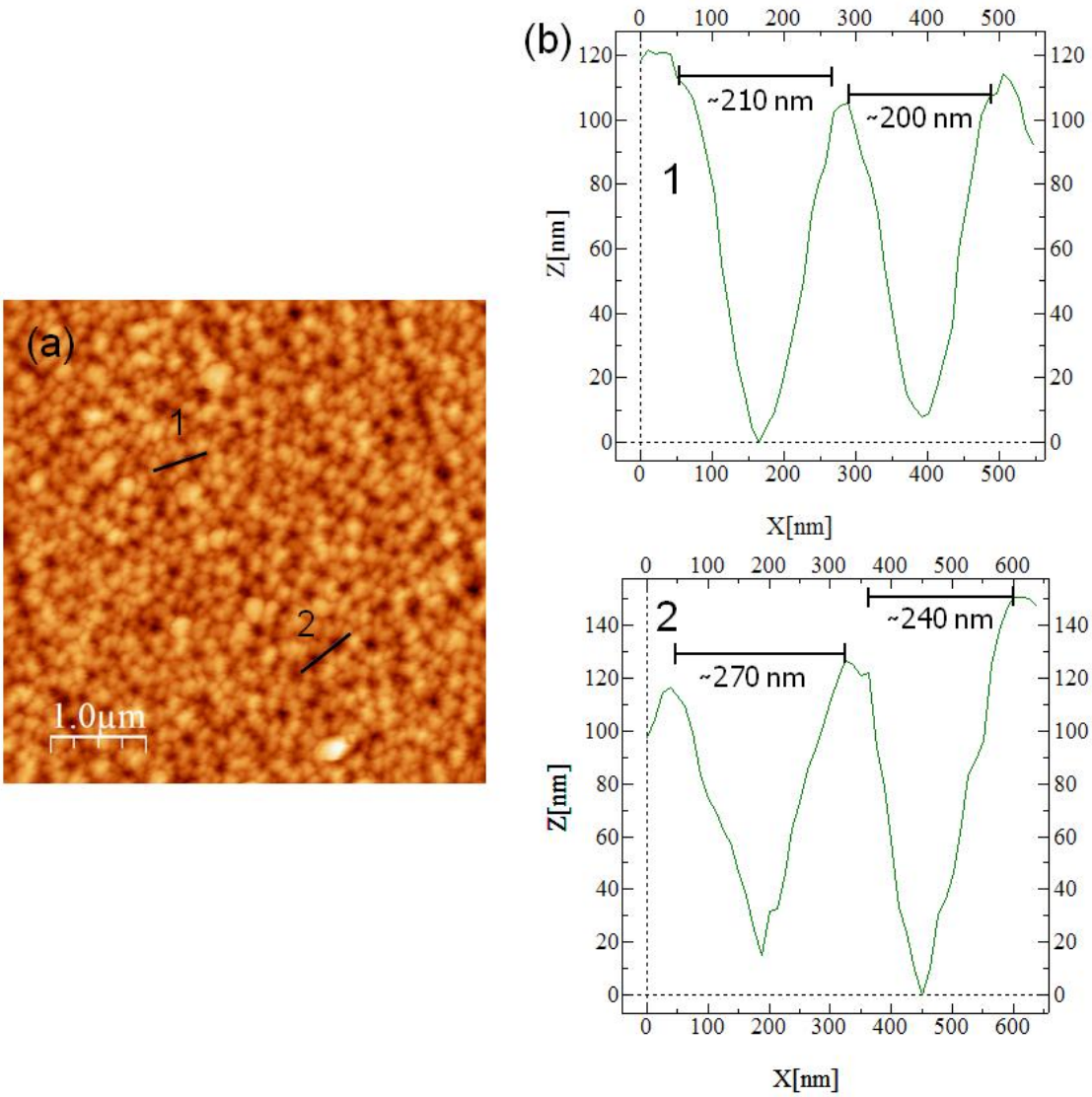

Figure 3. (a) AFM image and (b) profiles of the CVD porous GaN epitaxial layer grown for 30 min on non-porous GaN film coated sapphire (0001) substrates, taken at the locations highlighted in (a), showing the typical diameters of the pores.

Structural characterization of the CVD porous GaN epitaxial layer. The rocking curves corresponding to the (0004) XRD reflection of both the CVD porous GaN epitaxial layer and the non-porous GaN film are shown in Figure 4. For the non-porous GaN film the measured FWHM is 0.428º, while for the CVD porous GaN epitaxial layer the FWHM is 0.419º. The reduction in the FWHM for the porous layer indicates the good structural quality of the epitaxial porous layer compared to epitaxially grown non-porous GaN films.

Furthermore, the rocking curve maximum is centered at 72.902º for the non-porous GaN film, as shown in Figure 3, while that of the CVD porous GaN epitaxial layer is centered at 73.082º. This shift indicates a slight relaxation of the porous layer. The reduction of the structural strain in the direction perpendicular to the plane of the sample can be determined by using the following expression:[26]

$$\Delta\in_{\perp} = (c_{\text{strained}} - c_{\text{relaxed}})/c_{\text{relaxed}}$$

were $c_{strained}$ in our case accounts for the *c* parameter of the non-porous GaN grown on sapphire, and $c_{relaxed}$ for the *c* parameter of the CVD porous GaN layer, calculated both from the analysis of the rocking curves. Accordingly, a reduction of the strain perpendicular to the (0001) plane of 0.21% can be estimated. This strain reduction stems from the benefit of internal porosity and the fact that the CVD porous GaN is grown on a native substrate, while the non-porous film is obtained on sapphire.

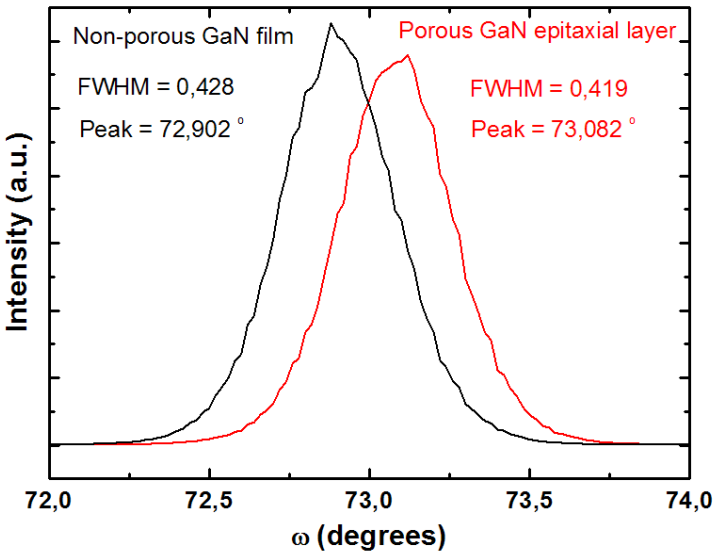

Figure 4. Rocking curves of porous GaN epitaxial layer grown on non-porous GaN films on sapphire.

Cathodoluminescence characterization. Figure 5 shows SEM and corresponding panCL images recorded for the non-porous and CVD porous GaN films. The panCL image of the non-porous sample, Figure 5a, shows the typical granular luminescence emission pattern of GaN,[27] due to the high concentration of dislocations (>10^9 cm^{-2}) in these layers. In the corresponding SEM image, some porosity is apparent, likely related to the thermal treatment to which the substrate has been exposed during the growth process. The panCL image of the CVD porous sample, Figure 5b, shows a more uniform distribution of the luminescence. It is also important to note that the presence of the pores does not quench the luminescence arising from the porous GaN. In fact, when we compare this image with the corresponding SEM image, the pores (that can be clearly seen in the SEM image) are not visible in the CL image, with the exception of the larger pores, for which a dark contrast can be observed in the CL image.

Figure 5c shows the panCL image recorded at the border between the non-porous and the CVD porous GaN films. From this image it is clear that the extraction of light from the porous GaN is more efficient than from the non-porous film, related to the high quality of the CVD porous GaN epitaxial layer. Also, one can consider the beneficial effect of multiple reflections that the light generated by the sample suffers at the walls of the pores, which allows limiting the total reflection imposed by the refractive index contrast between GaN (2.29)[28] and air to be overcome. The CL spectra recorded in both regions are also shown in Figure 5c. The spectrum recorded for the non-porous film corresponds to the typical CL spectrum of a *p*-type GaN, with the donor-acceptor pair (DAP) luminescence located at 3.28 eV (378 nm), and a longitudinal optical (LO) phonon replica at 3.19 eV (388 nm). The spectrum recorded for the CVD porous GaN epitaxial layer exhibits the expected band-edge luminescence

of *n*-type GaN, located at 3.40 eV (364 nm), with a FWHM of ~57 meV. Apart from this, a broad yellow luminescence (YL) band, normally attributed to point defects (Ga vacancies) and impurities such as oxygen and carbon[29] was also observed. For instance, in porous GaN deposited on Si by CVD, we observed the YL associated with a transition between the conduction band and a deep acceptor level, since its emission energy was independent of temperature.[30] In the present case, we also observed an spatial variation in the intensity of the band-edge and YL bands, depending on the probed point along the sample. This can be attributed to different effects, such as an inhomogeneity in the distribution of impurities or defects in the GaN structure, but also to changes in the light extraction associated with the geometrical features of the pores.

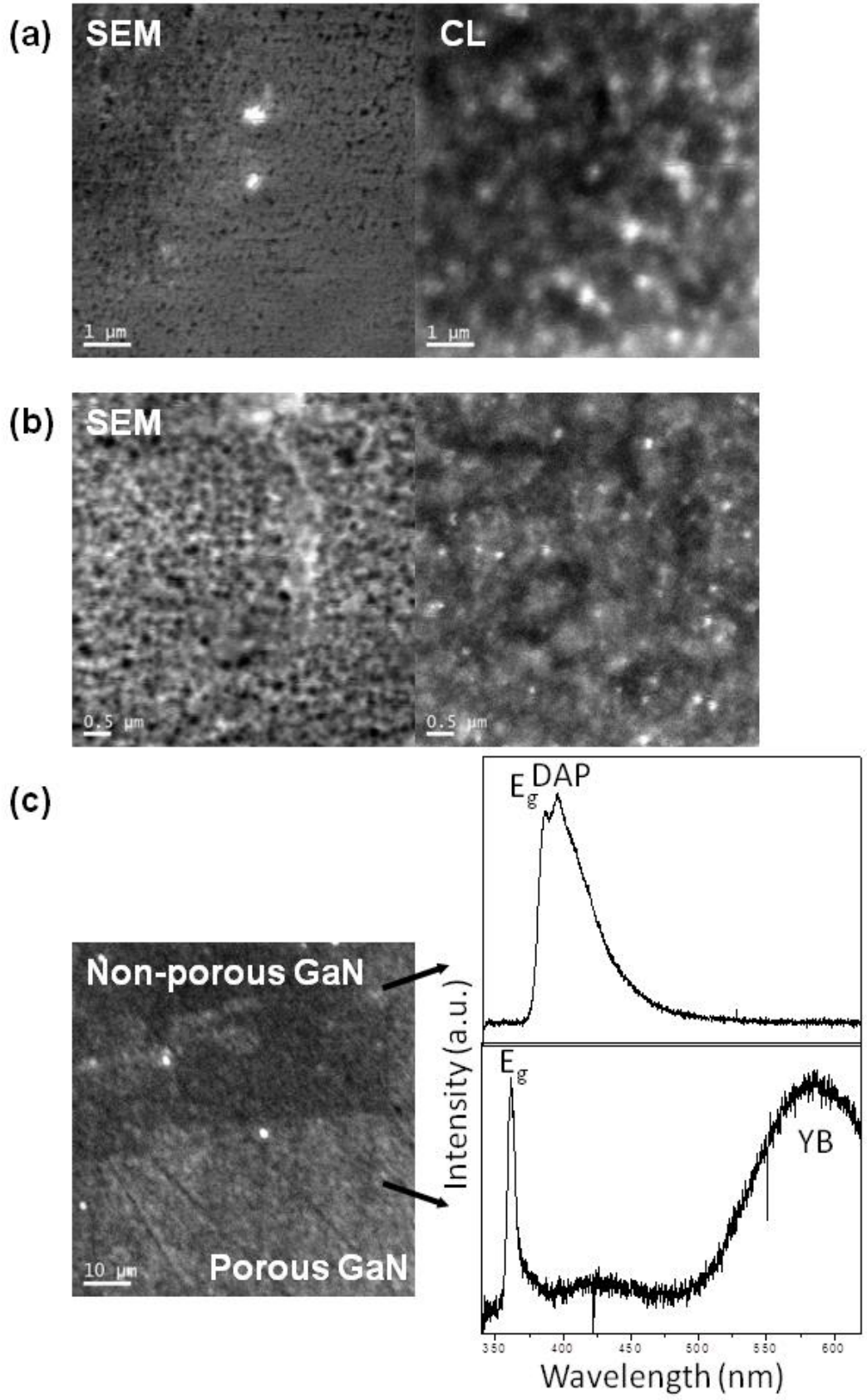

Figure 5. SEM and panchromatic CL images of (a) GaN on sapphire and (b) porous GaN. (c) Panchromatic CL image recorded at the border between porous and non-porous GaN, and CL spectra recorded at these two layers.

Electrical characterization. To further demonstrate the potential of the CVD porous GaN layers, we have grown them on a Mg-doped non-porous GaN film on sapphire. When such a structure is grown, a *p*-*n* junction is formed, as revealed by the non-linear I-V curve typical of a diode behaviour, as shown in Figure 6a. I-V curves were acquired between the underlying non-porous *p*-type GaN film and the porous GaN epitaxial layer. The clear *p*-*n* junction response confirms the formation of unintentionally doped *n*-type porous GaN. Microscopic examination (not shown here) confirms a clean interface without oxides or contaminants.

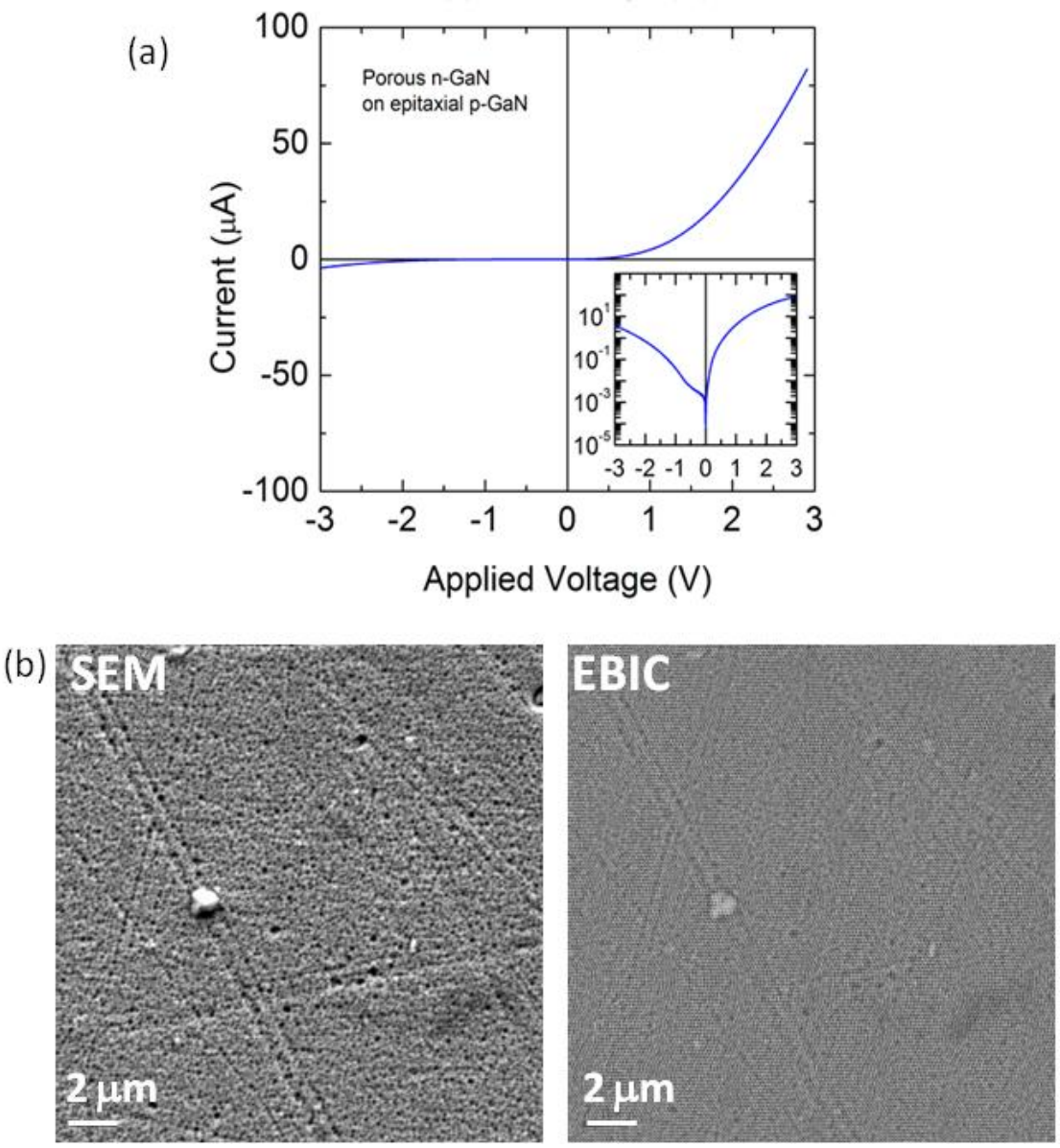

Figure 6. (a) I-V curve of the *p*-*n* junction formed from unintentionally doped CVD porous GaN epitaxial layers grown on non-porous *p*-type GaN films on sapphire. (b) SEM and (c) EBIC images of a CVD porous *n*-type GaN layer grown on a *p*-type non-porous GaN film on sapphire.

The high bias resistance turn-over of the porous *n*-type GaN occurs just above 1 V. At this voltage, high level carrier injection occurs across the *p*-*n* junction at higher applied bias, and is found to increase linearly with voltage above ~3V.[30,31] These values are consistent with the corresponding characteristic voltages found in uniform epitaxially grown GaN. In the case of CVD porous *n*-type GaN on non-porous *p*-type GaN films, current flow through the junction varies exponentially when the *p*-type material is positively biased. The turn-on (knee) voltage for the *p*-*n* junction is characteristically ~ $E_g/4q$ – $E_g/2q$, i.e. 0.5 – 0.68 V. This response presents several features already observed in InN, GaN and other *p*-*n* juction nanowires arrays. Low reverse bias leakage currents are found for the porous assembly of GaN crystals in the layer. Assuming an abrupt, one-side junction by comparative analysis to coherent GaN films, the barrier potential V_B is estimated as $V_B = \frac{kT}{q}\ln\left(\frac{N_D N_A}{n_i^2}\right)$ = 0.72 V, where N_D = 10^{16} cm^{-3} and N_A = 10^{18} cm^{-3} are the donor and acceptor densities of the porous *n*-type GaN and the epitaxial *p*-type GaN of the *p*-*n* junction, respectively.

The measurements allow us to infer several important aspects for non-porous and CVD porous GaN interfaces and *p*-*n* junctions. Firstly, microscopic characterization has ruled out oxide or interfacial contaminants that would alter the effective barrier. From Fig. 2, we can also conclude that the interface between the CVD porous and the non-porous GaN layers is well-defined and thus no significant tunnelling barrier exists either at the GaN-GaN interface or on the surface of the GaN with the Ohmic contact. Secondly, rectification arising from Schottky diodes contributions to transport are ruled out, since separate measurements[17] on the *n*-type GaN porous layer with In-Ga contact (that includes considerations of the transport mechanism variations facilitated by intermetallic interfaces) and those from *p*-type GaN contacts including measurement with epitaxial *n*- and *p*-type layers, conclusively show Ohmic behaviour. The porous *p*-*n* junction here dominates the I-V curve response. Finally, measurements from several separate *p*-*n* junction tests exhibited similar I-V response.

In order to corroborate the satisfactory *p*-*n* junction behaviour of the CVD porous *n*-type GaN layer grown on a *p*-type non-porous GaN film on sapphire, EBIC measurements were also performed. Figure 6(b,c) shows the SEM and corresponding EBIC image of a region of the sample. No dark features are observed in the EBIC image, which means homogeneous carrier recombination. In particular, the pores do not act as traps for the charge carriers generated by the electron beam. Only some contrast could be observed for the bigger pores. This demonstrates the good performance of the formed *p*-*n* junction, proving the possibilities of the (0001)-oriented porous GaN layers obtained by CVD for the development of practical electrical and optoelectronic devices.

Conclusion

We have investigated the growth of porous GaN epitaxial layers on Al_2O_3, SiC, AlN and GaN substrates. The results show that the lattice mismatch between the substrate and the porous GaN layer plays an important role in achieving a continuous layer formed by discrete porous microparticles. The lattice mismatch was found to influence the degree of porosity. The undoped porous GaN epitaxial layer grown on non-porous GaN films on sapphire probed to be *n*-type. When grown on a non-porous *p*-type GaN layer, it allows for the fabrication of a *p*-*n* junction of excellent junction characteristics,

with potential application in high brightness unencapsulated GaN-based light emitting diodes and in wide bandgap sensor devices.

Acknowledgments

This project was supported by the EU Framework 7 under Project No. FP7-SPA-2010-263044, the Spanish Government under Projects No. MAT2011-29255-C02-02, TEC2010-21574-C02-02, by the Catalan Authority under Project No. 2009SGR235 and by the "Conserjería de Educación de la Junta de Castilla y León" under Project No. VA166A11-2 . This work was also supported by the UCC Strategic Research Fund, and through the Irish Research Council New Foundations Award 2012. O.V. Bilousov is supported by Generalitat de Catalunya through the fellowship 2013FI-B2 00108.

References

(1) Nakamura, S.; Krames, M.R. *Proceedings of the IEEE* **2013**, 101 (10) , 2211.
(2) Jain, S. C.; Willander, M.; Narayan, J.; Van Overstraeten R. *Journal of Applied Physics* **2000,** 87, 965.
(3) O'Dwyer, C., Sotomayor Torres, C.M., *Front. Physics* **2013**, 1, 18.
(4) O'Dwyer, C., Szachowicz, M., Visimberga, G., Lavayen,V., Newcomb, S.B., Sotomayor Torres, C.M., *Nat. Nanotech.* **2009**, 4, 239.
(5) Lin, C. F.; Chen, K. T.; Lin, C. M.; Yang, C. C. *IEEE Electron Device Lett.* **2009**, 30, 1057.
(6) Lo, M.; H., Tu P. M., Wang,C. H.; Hung,C. W.; Hsu,S. C., Cheng,Y. J., Kuo H. C., Zan H. W.; Wang S. C.; Chang C. Y.;Huang S. C. ,*Appl. Phys. Lett*. **2009**, 95(4), 041109.
(7) Yam, F.K.; Hassan, Z., *Appl. Surf. Sci.* **2007**, 253, 9525.
(8) Ramizy, A.; Hassan, Z.; Omar, K. *Sens. Actuators, B* **2011**, 155**,** 699.
(9) Ghosh, B. K.; Tanikawa, T.; Hashimoto, A.; Yamamoto, A.; Ito, Y. *J. Cryst. Growth*, **2003**, 249**,** 422.
(10) Mynbaeva, M.; Savkina, N.; Tregubova, A.; Scheglov, M.; Lebedev, A. ; Zubrilov, A., Titkov, A.; Kryganovski, A.; Mynbaev, K.; Seredova, N.; Tsvetkov, D.; Stepanov, S., Cherenkov, A.; Kotousova, I.; Dimitriev, V.A. *Materials Science Forum*, **2000**, 338.
(11) Diaz, D. J.; Williamson, T. L.; Adesida, I.; Bohn, P. W.; Molnar, R. J. *J. Appl. Phys*. **2003**, 94**,** 7526.
(12) Nie, B.; Duan, B.K.; Bohn, P.W. *ACS Appl. Mater. Interfaces* **2013**, 5(13), 6208.
(13) Jang, L.-W.; Jeon, D.-W.; Polyakov, A.Y.; Cho, H.-S., Yun, J.-H., Jo, D.-S., Ju, J.-W., Baek, J.-H.; Lee, I.-H. *Applied Physics Express* **2013**, 6, 061001.
(14) Bardwell, J.A.; Foulds, I.G.; Webb, J.B.; Tang, H.; Fraser, J.; Moisa S.; Rolfe, S. *J. Electron. Mater.* **1999**, 28, L24-L26.
(15) Carvajal, J. J.; Rojo, J. C. *Cryst. Growth Des.* **2009**, 9, 320.
(16) Carvajal, J. J.; Bilousov, O. V.; Drouin, D.; Aguiló, M.; Díaz, F.; Rojo, J. C. *Microsc. Microanal*. **2012**, 18, 1.
(17) Bilousov O.V.; Carvajal J. J.; Drouin, D.; Mateos X .; Díaz, F.; Aguiló M.; O'Dwyer, C. *ACS Appl. Mater. Interfaces* **2012,** 4, 6927.
(18) Dhesi, S. S.; Satgarescu, C. B.; Smith, K. E. Phys. Rev. B **1997**, *56*, 10271

(19) Carvajal, J.J.; Raghothamachar, B.; Silvestre, O.; Chen, H.; Pujol, M.C.; Petrov, V.; Dudley, M.; Aguiló, M.; Díaz, F. *Cryst Growth Des.* **2009**, 9, 653
(20) Wang, H.Y.; Huang, S.C.; Yan T.Y.; Gong, J.R., Lin T.Y., Chen, Y.F. *Materials Science and Engineering B*, **1999,** 57, 218.
(21) Park, C.; Yeo, S.; Kim, J-ho, Yoon, D.; Anderson, T. J., *Thin Solid Films* **2006,** 498, 94.
(22) Huang, T.; Parrish, W.; Masciocchi, N.; Wang, P. *Adv. X-ray Anal*. **1990**, 33, 295.
(23) Hannam, Shaffer., *J. Appl. Crystallogr*. **1969**, 2, 45.
(24) Schulz, H.; Thiemann, K.H.; *Solid State Commun*. **1997**, 23, 815.
(25) Balkas, C.; Basceri, C.; Davis, R. *Powder Diffraction* **1995,** 10, 266.
(26) Görgens, L.; Ambacher, O.; Stutzmann, M.; Miskys, C.; Scholz, F.; Off, J. *Appl. Phys. Lett.* **2000**, 78, 577
(27) Dassonneville, S.; Amorkane, S.A.; Sieber, B.; Farvacque, J.L.; Beaumont, B.; Gibart, P., *J. Appl. Phys.* **2001**, *89*, 3736.
(28) Brunner, D.; Angerer, H.; Bustarret, E.; Freudenberg, F.; Höpler, R.; Dimitrov, R.; Ambacher, O.; Stutzmann, M. *J. Appl. Phys.* **1997**, 82, 5090
(29) Neugebauer, J.; Van de Walle, C.G. *Appl. Phys. Lett.* **1996**, 69, 503
(30) Song, J.O.; Ha, J.S.; Seong, T.Y. *IEEE Electron. Dev. Lett.* **2010**, 57, 42.
(31) Bilousov, O.V.; Geaney, H.; Carvajal, J.J.; Zubialevich, V.Z.; Parbrook, P.J.; Giguère, A.; Drouin, D.; Díaz, F.; Aguiló, M.; O'Dwyer, C. *Appl. Phys. Lett.* **2013**, 103, 112103.

Paper IX

Bilousov, O.V.; Carvajal, J.J.; Geaney, V. H.; Zubialevich, V.Z.; Parbrook, P.J.; Martínez, O.; Jiménez, J.; Díaz, F.; Aguiló, M. and O'Dwyer, C. *Fully porous GaN p-n junctions fabricated by chemical vapor deposition*. Submitted to Advanced Materials.

Fully porous GaN p-n junction diodes fabricated by chemical vapor deposition

O.V. Bilousov[a], J.J. Carvajal[a,*], H. Geaney[b,c], V. Z. Zubialevich[c], P.J. Parbrook[c,d], O. Martínez[e], J. Jiménez[e], F. Díaz[a], M. Aguiló[a], C. O'Dwyer[b,c,*]

[a] Física i Cristal·lografia de Materials i Nanomaterials (FiCMA-FiCNA) and EMaS, Universitat Rovira i Virigli (URV), Marcel·lí Domingo s/n, E-43007 Spain
[b] Department of Chemistry, University College Cork, Cork, Ireland
[c] Tyndall National Institute, Lee Maltings, Dyke Parade, Cork, Ireland
[d] School of Engineering, University College Cork, Cork, Ireland
[e] GdS-Optronlab, Departamento Física Materia Condensada, Univ. de Valladolid, Edificio I+D, Paseo de Belén, 11, 47011, Valladolid, Spain

*corresponding authors: joanjosep.carvajal@urv.cat, c.odwyer@ucc.ie

Abstract

Porous GaN based LEDs produced by corrosion etching techniques demonstrated enhanced light extraction efficiency in the pass. However, these fabrication techniques require further post-grown processing steps, which increases the price of the final system. Also, the penetration depth of these etching techniques is limited, and affects not only the semiconductor but also the other elements constituting the LED when applied to the final device. In this paper we present the fabrication of fully porous GaN *p-n* junctions only by growth means, using a sequential chemical vapor deposition (CVD) process to produce the different layers that will form the *p-n* junction. We characterized their diode behavior from room temperature to 673 K, and demonstrated their ability as current rectifiers, thus proving the potential of these fully porous *p-n* junctions for diode and LEDs applications. The electrical and luminescence characterization confirm that high electronic quality porous structures can be obtained by this method, and we believe this investigation can be extended to other III-N materials for the development of white light LEDs, or to reduce reflection losses and narrowing the output light cone for improved LED external quantum efficiencies.

Introduction

Modern society is experiencing an ever-increasing demand for energy to power a vast array of electrical and mechanical devices. A significant amount of the energy consumed is used for lighting purposes. For instance, this demand is ~17% of the total energy consumed in the USA in 2011.[1] Thus, any approach that can reduce energy consumption is important. In this context, the development of light emitting diodes (LEDs) incorporating at least one porous component, with improved light extraction efficiency, is being explored intensively.[2] However, up to now, only partially porous *p-n* junctions have been analyzed for this purpose.

Despite the wide interest of porous semiconductors in view to their peculiar electrical, optical, and mechanical properties for applications in many fields, from electronics to optoelectronics,[3] from photovoltaics[4] to biomedicine and environment monitoring,[5] fabrication of totally porous *p-n* junctions has been scarcely investigated and restricted almost exclusively to porous Si or III-Vs produced by anodization. The rectifying behavior of entirely porous *p-n* junctions is, from a theoretical point of view,

compatible with that of a high-density of randomly distributed elemental mesoscopic *p-n* crystalline junctions operating in parallel.[6] Also, it has been pointed out that conventional planar non-porous diode structures exhibit a number of inherent deficiencies that result in relatively low energy-conversion efficiencies, a problem that might be overcome by completely porous *p-n* junctions.[7] In fact, a ten-fold enhancement of efficiency compared to that of the usual planar non-porous devices has been demonstrated for totally porous Si *p-n* junctions in betavoltaics, and it has been postulated that significant efficiency gains might be expected also in photo detectors and solar cells fabricated using completely porous *p-n* junctions.[7]

The use of fully porous *p-n* junctions might be especially important for enhancing the light extraction of LEDs. It has been demonstrated that the induction of a porous structure in the LED device can lead to an enhancement of the light extraction efficiency of the device.[2a] In fact, the induction of partially porous *p-n* junctions in GaN-based LEDs has lead to different improvements of the light extraction efficiencies. For instance, an increase of 12% of the internal quantum efficiency and 23% higher optical power has been reported on a GaN diode including a photonic crystal structure in its *n*-type component,[2f] while an increase by 70% on the optical output power has been demonstrated for a LED with a photonic crystal structure selectively grown on *p*-type GaN.[2i] Using nanotextured *p*-type GaN, a 46% higher light output than in a standard LED with unpatterned *p*-type GaN has been reported.[2j] Furthermore, it has been postulated that if the porous structure, forming a photonic crystal structure, crosses the active region of the LED, i.e. the *p-n* junction thus forming an entirely porous *p-n* junction, the increase in light extraction efficiency could be enhanced even further.[2b] A light output power improvement as high as 94% has been demonstrated for such structures fabricated by chemical etching, in which porosity affected even the ITO electrode.[2k]

Recently, we have demonstrated that it is possible to produce nanoporous GaN by crystal growth methods during chemical vapor deposition (CVD), and without the need of any post-growth treatment to induce porosity.[8] We have also demonstrated that we can produce both *n*-type and *p*-type porous GaN by this methodology with a high density of charge carriers (~10^{18} cm^{-3}) and even forming low resistivity Ohmic contacts with high work function metals such as Au or Pt.[9]

In this paper, we present the fabrication of fully porous *p-n* junctions by using nanoporous GaN produced by CVD, and compare their performance with partially porous *p-n* junctions fabricated using the same methodology, in which only the *n*-type or *p*-type GaN layers are porous. We characterized their diode behavior at high temperatures, and demonstrated their ability as current rectifiers, thus proving the potential of these fully porous *p-n* junctions for diode and LEDs applications.

Epitaxial nanoporous GaN thin layers were grown by CVD through the direct reaction of metallic Ga with ammonia in a tubular reactor on non-porous GaN (0001) thin films (~ 3μm thick) grown by metalorganic vapour phase epitaxy (MOVPE) on sapphire (0001) substrates. After degassing the quartz reactor to a vacuum pressure of 1 $\times$ 10^{-2} Torr, ammonia was introduced through a mass-flow controller at a flow rate of 75 sccm, while the furnace was heated to 1200 K. The growth lasted for 30 min at the constant flow of NH_3 and temperature. After growth, the furnace was cooled down to room temperature and the NH_3 flow was stopped, reducing the pressure inside the reactor to 1 $\times$ 10^{-2} Torr. Figure 1 shows a schematic description of the process. We used either *n*-type or *p*-type non-porous GaN (0001) thin films deposited on sapphire (0001) as substrates, depending on the experiment and the *p-n* junction to be formed (Fig. 1a,b). Mg-doped samples were grown to produce *p*-type nanoporous GaN films (Fig.

1b). These samples after growth were annealed in a N_2 atmosphere at 973 K for 20 min in order to break the existing Mg-H complexes and activate the *p*-type conductivity of the porous GaN layers.[10] Fully porous *p*-*n* junctions were fabricated in a two crystal growth step process (Fig. 1c). First, an undoped *n*-type porous GaN layer was grown on non-porous GaN(0001). Second, another porous Mg-doped *p*-type GaN layer was grown on the top of the porous *n*-type GaN layer as represented in Figure 1, under the same reaction conditions.

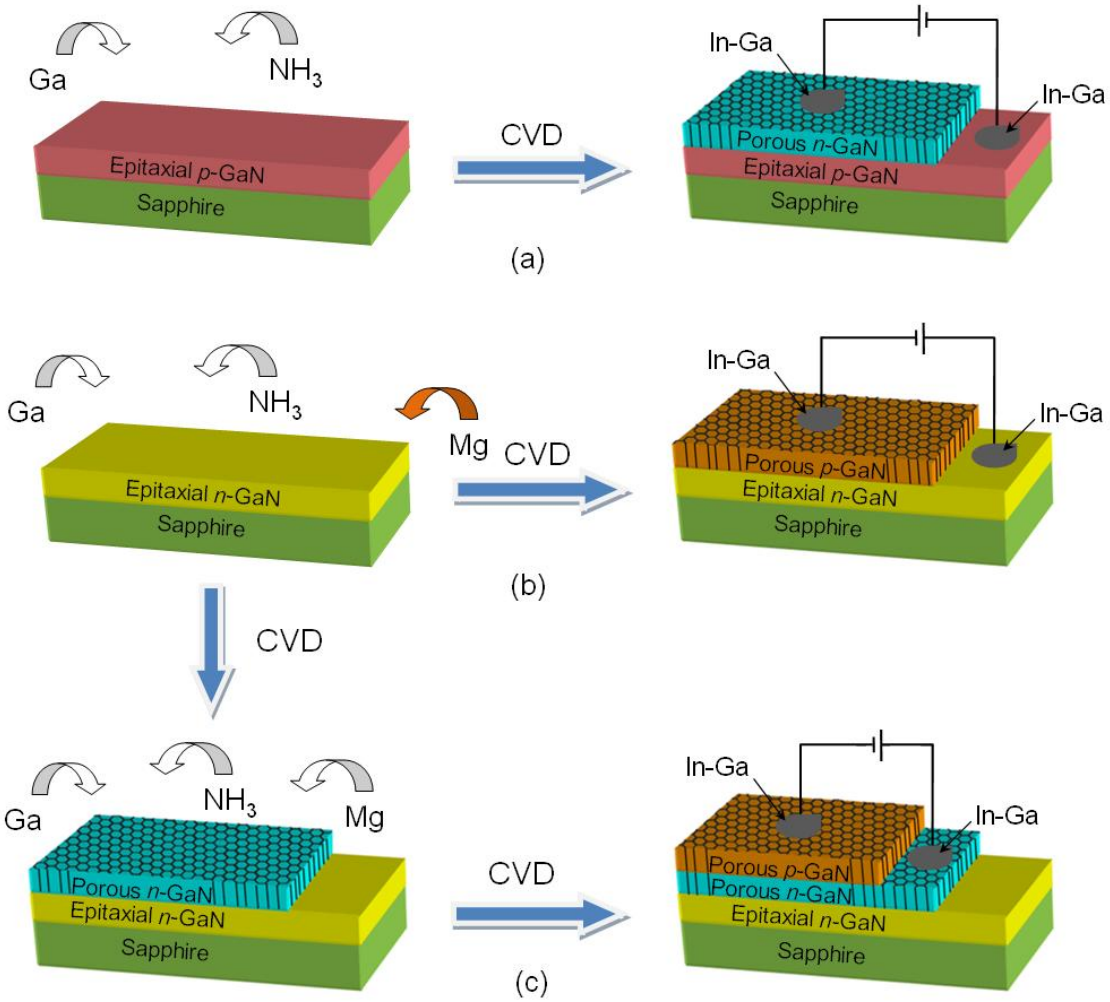

Figure 1. Schematic representation of the formation process of partially and fully porous GaN *p*-*n* junctions by CVD.

In this way, three types of porous GaN diodes were prepared: (i) undoped *n*-type porous GaN on non-porous *p*-type GaN (hereafter porous *n*-*p* diode), shown schematically in Figure 2(a); Mg-doped porous *p*-type GaN on non-porous *n*-type GaN (hereafter porous *p*-*n* diode), shown schematically in Figure 2(b); and Mg-doped porous GaN on undoped porous *n*-type GaN (hereafter fully porous *p*-*n* diode), shown schematically in Figure 2(c).

Figure 2 shows also top-view SEM images of the porous GaN layers. All porous GaN layers reveal a high degree of porosity with a large number of pores. Despite being grown under the same conditions, the porous *p*-type layers tend to show larger diameter pores when compared to those observed on the *n*-type porous layers. This is especially significant for fully porous GaN *p*-*n* diodes. The pores observed in the *p*-type layer are

significantly wider than those on the *n*-type layer prior to the second growth step that might be related to the corrugation of pores due to a lower decomposition temperature of Mg-doped GaN,[11] which would be accentuated by the presence of the pores. High magnification images of the porous structures for *n*-type and *p*-type GaN layers can be seen in Figure S1 in Supporting Information.

In all cases, however, the porous GaN layers are grown oriented along the ***c***-crystallographic direction, matching the crystallographic orientation of the non-porous epitaxial GaN thin-films used as substrates. Pore hollows are always parallel to this direction.

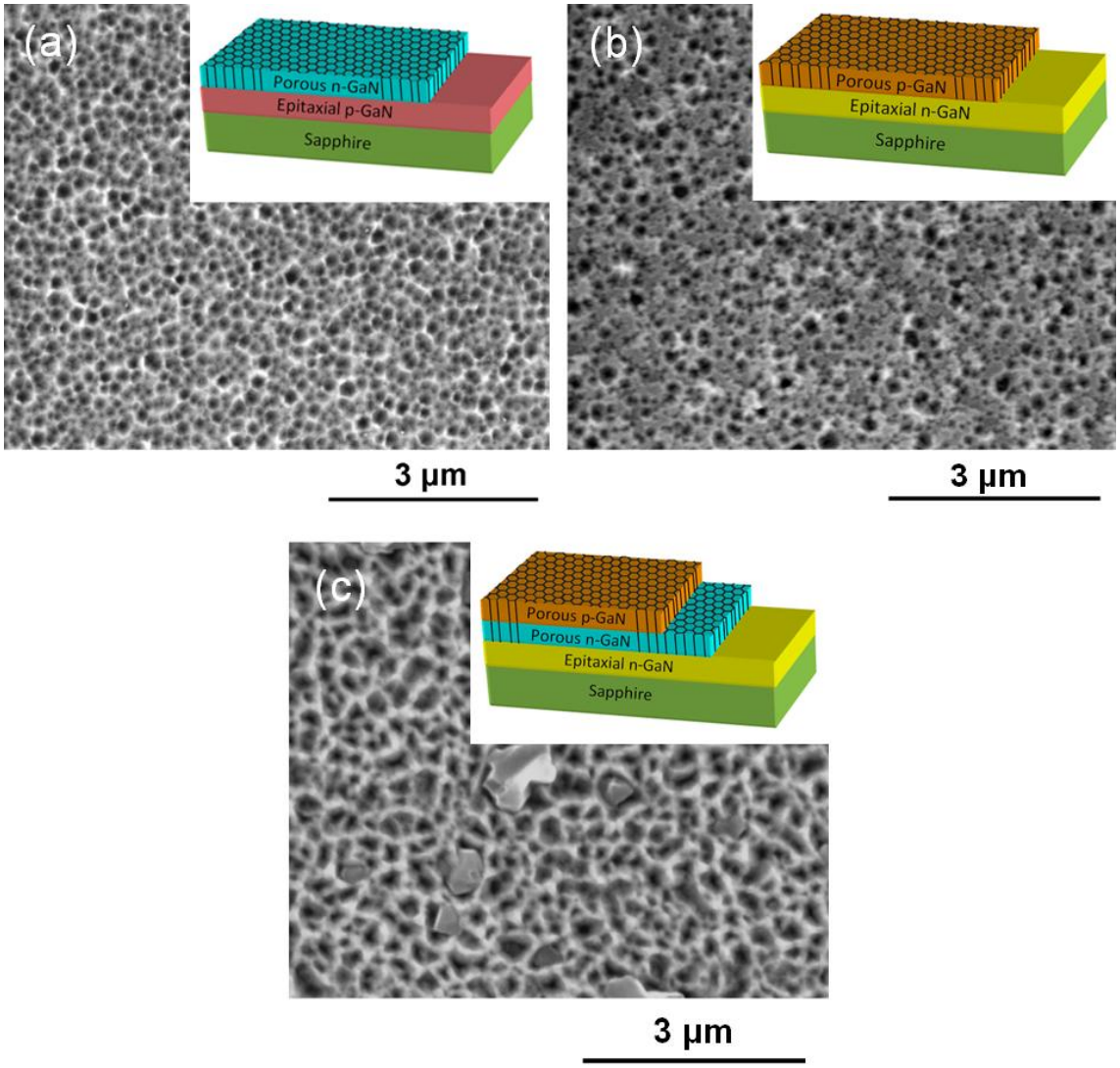

Figure 2. (a) Porous *n*-type GaN grown on non-porous epitaxial *p*-type GaN, (b) porous *p*-type GaN grown on non-porous epitaxial *n*-GaN, and (c) porous *p*-type GaN grown on porous *n*-type GaN corresponding to the fully porous diode. Insets show schemes of the structure of the partially and fully porous diodes.

X-ray rocking curves corresponding to the (0004) reflection were used to analyze the influence of structural strain on porous GaN *p*-*n* junction diodes, as shown in Figure 3. Figure 3(a) shows the rocking curves corresponding to the porous *n*-*p* diode, and

defines the response of the epitaxial *p*- and *n*-type GaN substrate for comparison, with FWHM of 0.428º and 0.419º for the non-porous and porous layers, respectively, indicating a good orientation of the porous material along the ***c***-crystallographic direction and that the crystalline quality of the porous layer is comparable to the non-porous film, or even better. The peak positions are 72.902º and 73.082º for the non-porous and porous layers, respectively, indicating a slight relaxation of the porous layer when compared to the non-porous one. The magnitude of the relaxation can be estimated according to the following expression:[12]

$$\Delta\in_{\perp} = (\boldsymbol{c}_{\text{strained}} - \boldsymbol{c}_{\text{relaxed}})/\boldsymbol{c}_{\text{relaxed}} \qquad \text{Eq. 1}$$

were $\boldsymbol{c}_{\text{strained}}$ and $\boldsymbol{c}_{\text{relaxed}}$ are the ***c*** crystallographic parameters of the non-porous *p*-type and porous *n*-type GaN layers, respectively, determined from the rocking curves. Accordingly, a reduction of the strain along the [0001] direction of 0.24% was estimated, which stems from the benefit of internal porosity (for details, see Table S1, Supporting Information).

Figure 3(b) shows the rocking curves corresponding to the porous *p*-*n* diode. The relaxation of the *p*-type porous layer is 0.46%, almost twice that achieved in the porous *n*-*p* diode, indicating the beneficial strain relief offered by the porous sub-surface.[13] In that case, FWHM is slightly higher for the porous layer, but of the same order of that obtained for the non-porous layer, indicating that the crystalline quality of these two films is similar. The relaxation of the porous *p*-type layer is larger than the one observed for the porous *n*-type layer, which might be related to the wider size of its pores (see Figure 2(b)), giving additional compliance to the layer to accommodate on the substrate.

Finally, the fully porous GaN diode exhibits equal FWHM in their rocking curves for the two porous layers and of the same order to that of the non-porous *n*-type GaN film (see Figure 3(c) and Table S1). Thus, the crystalline quality of the three films is closely similar. The relaxation calculated for these porous layers is 0.04 % for the *n*-type porous layer grown on the non-porous *n*-type GaN film, while that of the *p*-type porous layer grown on the porous *n*-type layer is 0.07%. In both homo and heterojunctions, relaxed porous layers are epitaxially grown on either porous or continuous thin films. The minimum strain is found between the non-porous and the porous *n*-type GaN layers.

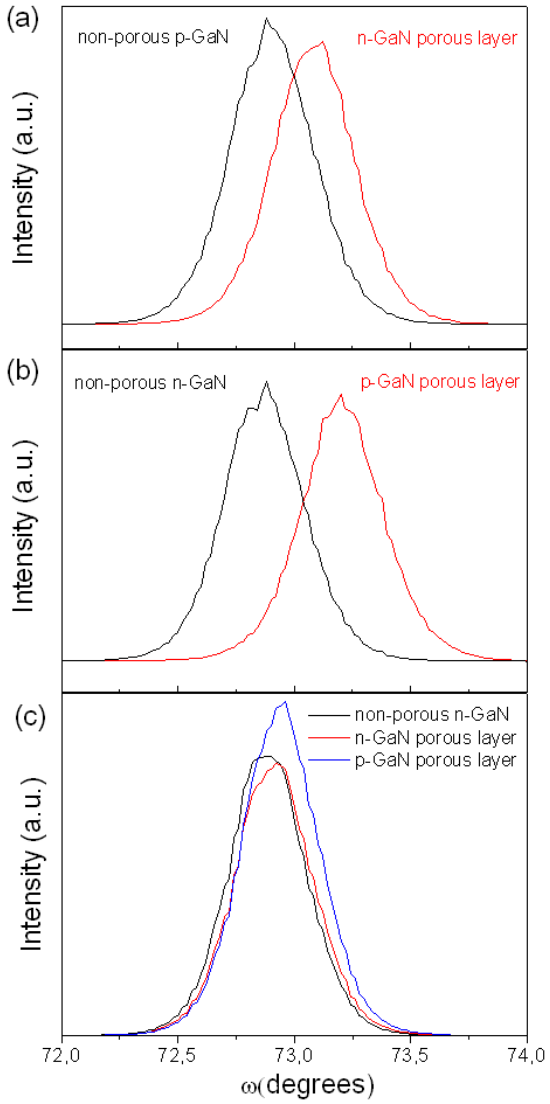

Figure 3. Rocking curves of (a) the porous *n-p*, (b) porous *p-n* and (c) fully porous diodes.

Figure 4 shows SEM and panchromatic cathodoluminescence (panCL) images, as well as CL spectra recorded for all the layers forming the fully porous *p-n* diode. The SEM image of the non-porous *n*-type GaN film shows a smooth surface, while the panCL image shows the typical granular luminescence pattern of GaN, due to the distribution of clusters of dislocations in the material.[14,15] The CL spectrum recorded for this layer shows the near-band gap emission (NBE) located at ~355.6 nm and a donor-acceptor pair (DAP) luminescence at ~377 nm, which characteristically results from point defects and/or impurities.[16]

The panCL image of the porous *n*-type GaN layer shows a different distribution of the luminescence emission, that could be related to the porous morphology, even if there is not a full correlation between the pores revealed in the SEM image and the panchromatic image contrast (see Figure 4b). The spectrum recorded for this layer exhibits quite a broad NBE luminescence, corresponding to *n*-type GaN, peaking at ~362 nm. A yellow luminescence (YL) band centered at ~580 nm, normally attributed to point defects (Ga vacancies) and/or impurities, such as oxygen and carbon[17] is also present.

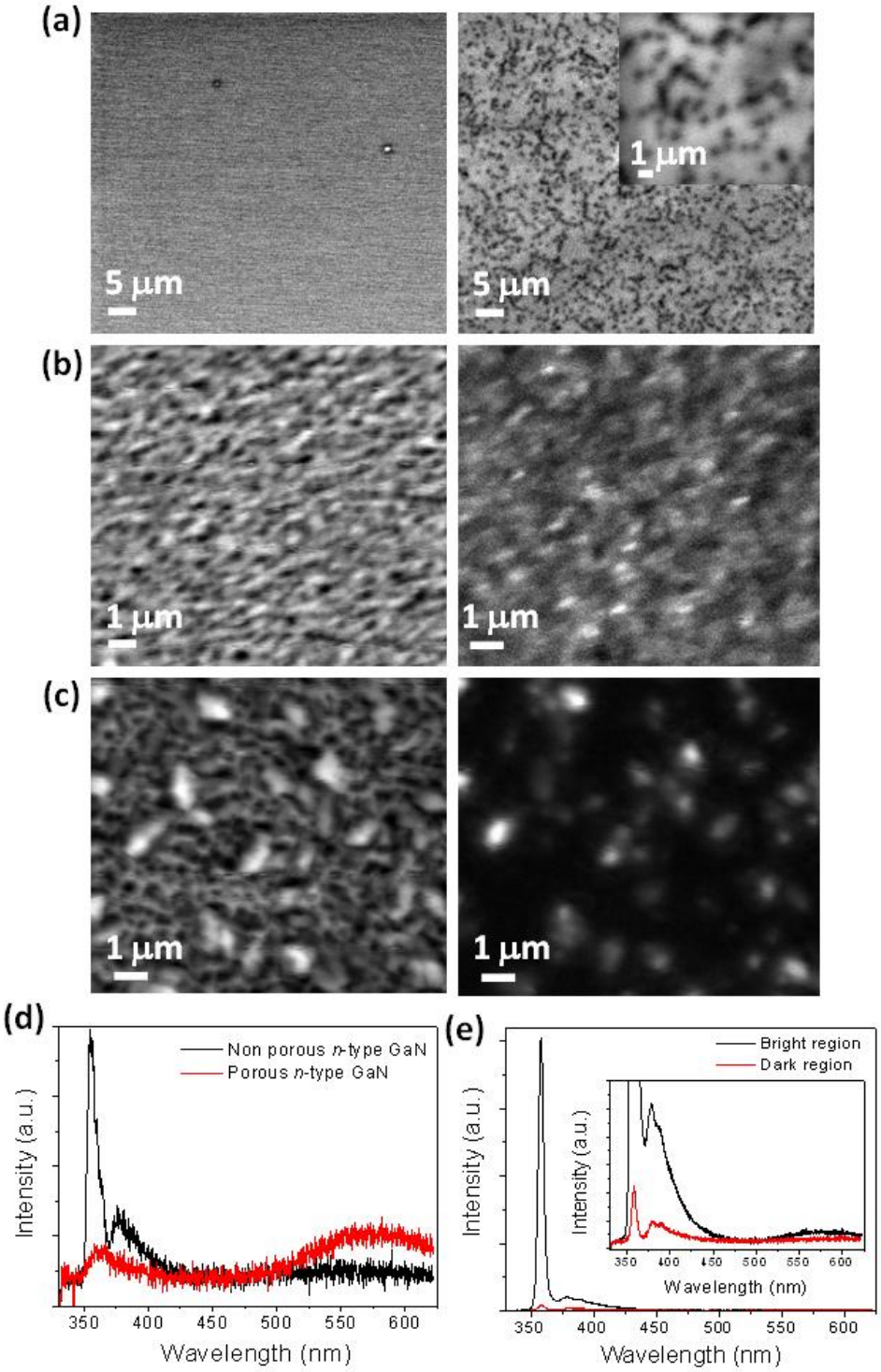

Figure 4: Top-view SEM and panCL images taken in the same region of the sample of (a) non-porous *n*-type GaN film, (b) porous *n*-type GaN layer and (c) porous *p*-type GaN, corresponding to the fully porous *p*-*n* diode. Insets show magnified areas of the pictures. CL spectra recorded for (d) non-porous and porous *n*-type GaN, and (e) bright and dark areas observed in the panCL image shown in (c). Inset in the graph is a magnification of the same spectra to show the features observed in the two spectra.

Figure 4c shows the SEM and the corresponding panCL image of the top layer of the fully porous *p*-*n* diode (porous *p*-type GaN). The pores are not visible in the panCL image, similar to what is observed in the porous *n*-type layer. High intensity regions correspond to porous GaN micron-size particles that grow on the top of porous layer, but with a different crystallographic orientation. The CL spectra shown in Figure 4e correspond to the high and low intensity emission regions observed in the panCL image, with the NBE of GaN at ~358 nm, the DAP band at ~379 nm and a longitudinal optical (LO) phonon replica at ~388 nm. These features correspond to the typical CL spectrum of *p*-type GaN. The spectrum recorded in the high intensity region, corresponding to a GaN micron-size particle grown on the porous layer, has a much lower DAP intensity emission relative to the NBE emission. This effect is likely related to a different Mg doping incorporation of the GaN porous layer and GaN micron-size particles[18] or to a different crystallographic orientation of the two regions,[19] which can also be responsible for changes in the incorporation of the Mg impurities.

SEM and corresponding panCL cross-section images of the totally porous *p*-*n* diode were recorded, as shown in Figure 5. The cross-sectional SEM micrograph clearly shows the non-porous GaN film and the porous GaN layers grown by CVD. In the panCL image, the dark lines observed in the non-porous GaN correspond to the threading dislocations crossing the substrate layer. The thickness of the porous GaN layers determined from SEM is ~2.1 μm, corresponding to the two porous layers, the Mg-doped porous *p*-type GaN and the undoped porous *n*-type GaN layer, each with a thickness of ~1 μm. Although the interface between these two porous layers is less discernible in the SEM image, it appears clear in the panCL image, where porous *n*-type GaN appears dark while porous *p*-type GaN appears bright. This can be related to a higher concentration of charge carriers in the Mg-doped porous *p*-type GaN layer (~10^{18} cm^{-3}) when compared to the undoped porous *n*-type GaN (~10^{16} cm^{-3}), as previously consigned.[9] The thickness of the two porous layers is proved to be similar in the panCL image. Figure 5c shows the CL spectra recorded for the different layers in the cross section view. In the case of the non-porous *n*-type GaN film, a strong emission at ~355 nm is observed similar to the one recorded in top-view (see Figure 4a). In the case of porous *p*-type GaN only the DAP emission related to the Mg doping is observed, with no emission from NBE, indicative of the incorporation of substitutional Mg for an efficient *p*-type doping of this layer. The difference with the CL spectrum recorded in top-view (see Figure 4e) indicates that in that case the NBE emission observed in the porous layer really arises from the non-porous GaN substrate. Concerning the porous *n*-type GaN layer, nearly no CL signal was detected, in agreement with the low intensity detected in the top-view configuration (see Figure 4d). The appearance of the yellow band, not observed for the non-porous substrate, confirms that the cross-sectional spectrum corresponds to the porous layer.

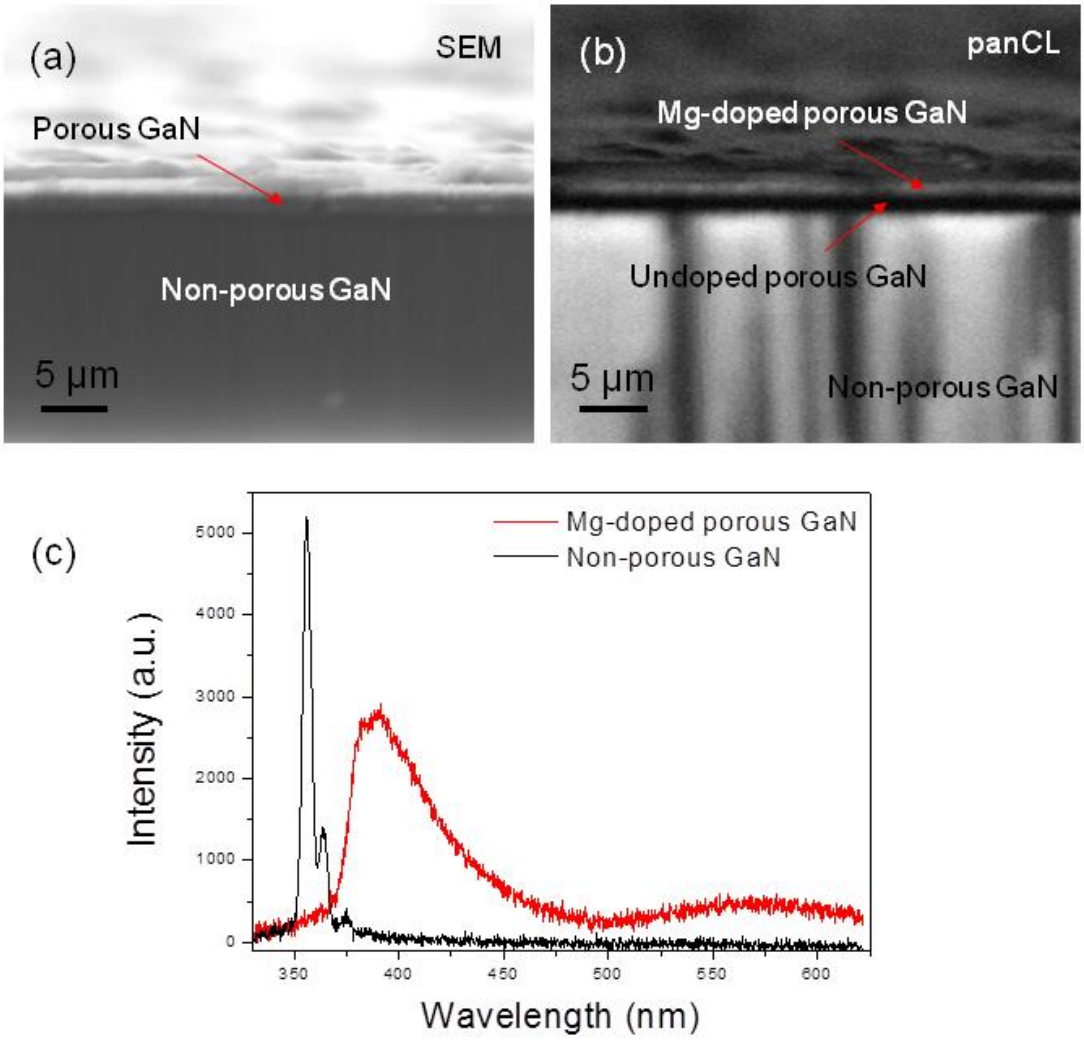

Figure 5: (a) Cross-sectional SEM and (b) corresponding panCL images of the fully porous GaN diode. (c) CL spectra recorded for non-porous GaN and Mg-doped porous GaN.

Photoluminescence (PL) measurements in top view were also performed on both Mg-doped porous GaN and undoped porous GaN layers corresponding to the totally porous GaN *p-n* junctions at different temperatures from 11 K to 300 K at a constant laser power density. Figure 6a shows PL spectra for undoped porous GaN. It exhibits the expected band-edge luminescence with a Varshni-like temperature redshift[20] from 3.43 eV at 300 K to 3.46 eV at 11 K and a narrow FWHM of ~12 meV at 11 K. Broad emission near the band gap typically results from the density of states tailing due to randomly distributed impurities. This broad emission near-band gap and band-edge emission equilibrate in intensity at 100 K and the broad emission near-band gap slightly dominates at 120 K. However, the band-edge emission dominates at other temperatures.

Figure 6b shows PL spectra for the Mg doped porous GaN. The room temperature band-edge emission appears at lower energy (3.41 eV) when compared to the undoped porous GaN. At temperatures down to 11 K, however, this emission is blue-shifted and located at a value of 3.46 eV with a narrow FWHM of ~5 meV. The band gap emission in both, undoped and Mg doped GaN, is over an order of magnitude more intense at 11

K as compared to room temperature. We observe some structure in the high energy side, at ~3.5 eV, probably associated with a bound exciton.[21] As the GaN is Mg doped and no Si nor shallow O donor-bound excitons are expected to be incorporated in the samples according to the synthesis conditions, we attribute this weak emission to excitons bound to Mg acceptors. The band-edge luminescence is followed by the DAP luminescence, located at 3.27 and 3.28 eV at 150 and 11 K, respectively. The DAP emission disappears at high temperatures. As expected from Mg acceptors in doped GaN, we find the LO phonon replicas at 3.18 and 3.19 eV at 150 and 11 K, respectively, with several harmonics observable at 11 K, indicating the good electronic quality of the *p*-type porous GaN layer obtained by CVD.[22] Another broad band at ~420 nm (blue band) is also clearly observed at 300 K, disappearing as the temperature decreases (~200 K). This type of emission has been previously observed[23] and attributed to the formation of a Mg complex or some native defect level.

YL in *n*-type GaN is often attributed to Ga vacancies and impurities, such as oxygen and carbon,[17] although it is not likely that these impurities are present in the samples through the growth process used. YL is also present in Mg-doped p-type porous GaN and can arise from a transition between the conduction band or shallow donors.[24] The YL has weak temperature dependence and is not found to vary considerably due to Mg incorporation into the lattice when compared to the undoped sample.

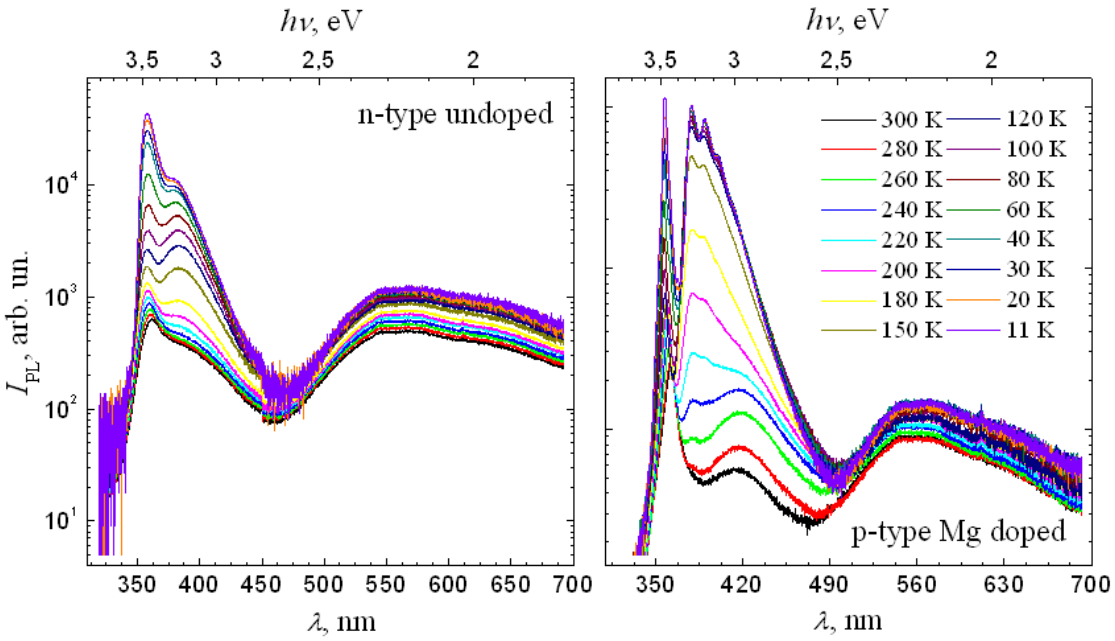

Figure 6. Temperature-dependent PL spectra of undoped (a) and Mg-doped GaN (b) porous layers corresponding to the fully porous GaN p-n junction (λ_{ex} = 325 nm).

Electrical characterization of the three types of porous GaN diodes is shown in Figure 7. Diodes comprising non-porous and porous GaN, and also fully porous *p-n* GaN junction exhibited characteristic I-V curves with strong rectification. Figure 7a shows the I-V curve corresponding to the porous *n-p* diode. The high bias resistance turn-over of the porous *n*-type GaN occurs just above 1 V. When the non-porous *p*-type GaN is positively biased, current flow through the *p-n* junction varies exponentially.

The barrier to the exponential current increase is found to be much lower than the expected GaN diode response, i.e. E_g/q. The turn-on voltage for this *p-n* junction lies in the range ~ $E_g/4q - E_g/2q$, i.e. 0.5 – 0.68 V. In the case of the porous *p-n* and the fully porous GaN diode the turn-on voltage is found to be even lower, in the range $E_g/4q - E_g/6q$ (see Figure 7b and 7c). In all cases the diode behavior is confirmed and low reverse bias leakage currents were found for these porous GaN structures. Moreover, the current at a fixed value of the forward voltage in the fully porous diode is found to be three orders of magnitude higher than that measured in the partially porous diodes, indicating a low resistivity for porous GaN layers and its promising perspectives for LEDs applications.

The electron density for unintentionally doped porous *n*-type GaN is estimated to be 1.6×10^{16} cm^3.[9a] The effective hole density for porous *p*-type GaN at 300 K is estimated using the effective hole and electron masses of wurzite GaN to be ~9×10^{18} cm^{-3}.[9b] Taking into account the values of donor and acceptor densities of non-porous *n*-type GaN and *p*-type GaN of $N_D = 10^{19}$ cm^{-3} and $N_A = 10^{18}$ cm^{-3}, respectively, and the corresponding values mentioned above for porous *n*-type GaN and *p*-type GaN, we can estimate V_B for the porous *n-p* diode as 0.72 V, for the porous *p-n* diode as 0.9 V, and for the totally porous diode as 0.71 V.

Based on these measurements we should mention some important aspects for porous GaN *p-n* junctions. Microscopic characterization confirms well-defined interface between the porous and the non-porous GaN layers (see Figure 5) and thus no significant tunnelling barrier exists either at the GaN-GaN interface or on the surface of the GaN / Ohmic contact. Also, microscopic characterization excludes any interfacial contaminants that would alter the effective barrier. The measurements were repeated from different points on several separate *p-n* junction diodes and they exhibited similar I-V response, which augers well for high surface area diodes and parallel arrays of devices from completely porous *p-n* junctions over large areas.[25]

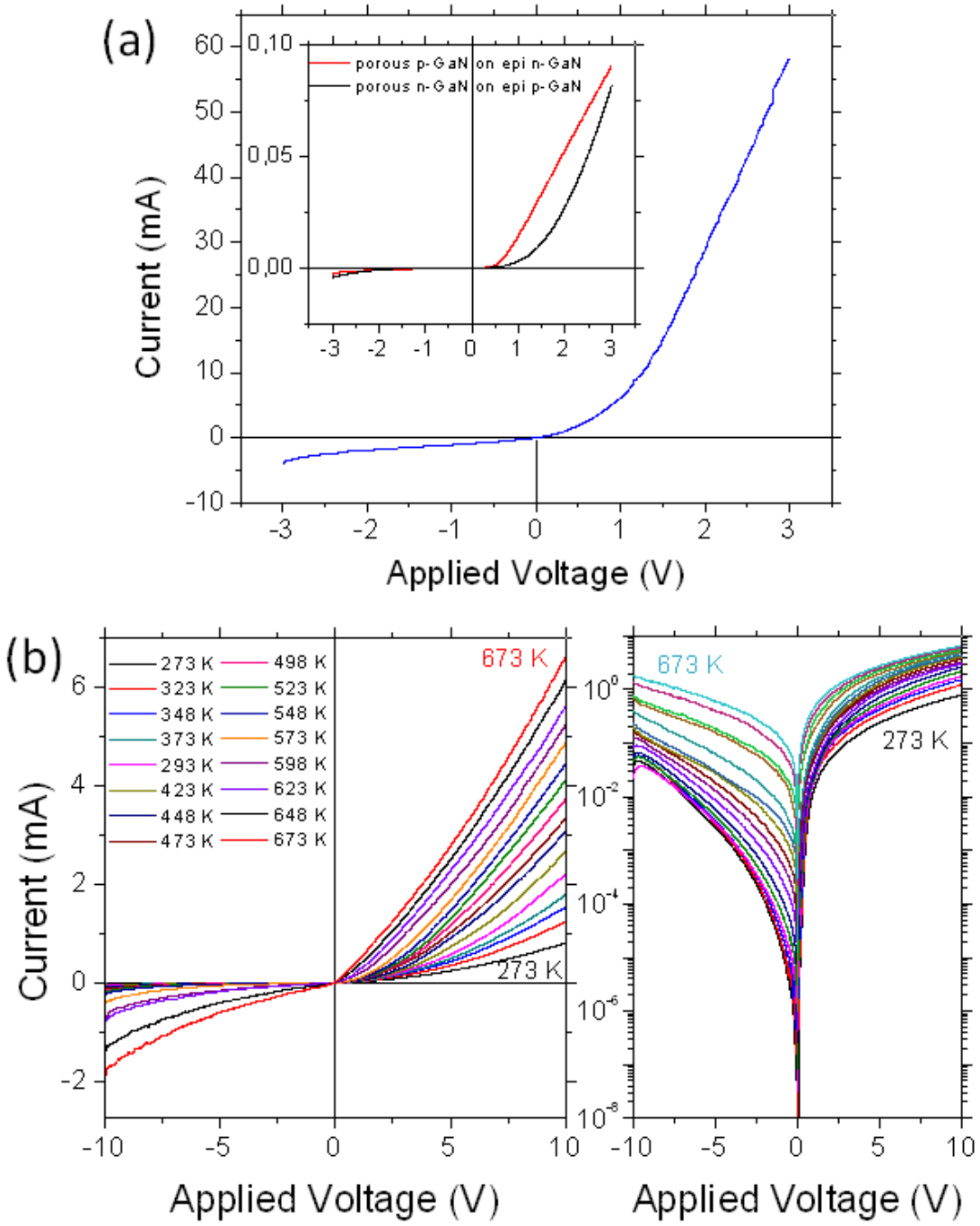

Figure 7. I-V curves of the fully porous diode. Inset shows the I-V curves recorded for the porous *n-p* and porous *p-n* diodes. (b) I-V curves of the porous *n-p* GaN diode recorded at T = 298 – 673 K.

Figure 7b shows the I-V curves recorded for the porous *n-p* diode at different temperatures ranging from 298 K to 673 K, confirming that we are dealing with a rectifying diode in all *p-n* junctions. The forward and reverse bias currents of the diode increase with the increase of temperature, thus accounting for an increase of the number of charge carriers across the barrier height. The turn-on voltage for this junction is characteristically ~$E_g/4q - E_g/2q$ at room temperature. With the increase of temperature,

this low knee voltage is reduced even further consistent with a thermionic process with greater carrier velocities at higher temperatures. At the highest temperatures the high bias resistance turn-over of the porous *n*-*p* diode occurs at very low potentials (~0.4 - 0.5 V), but the built-in potential $V_{bi} = (kT/q)\ln(N_A N_D/n_i^2)$ is overcome through tunneling. At all temperatures (at least to 673 K) the rectifying characteristics of the porous GaN diodes are preserved, and no breakdown voltage was observed even at 10 V at 673 K.

The fully porous GaN *p*-*n* junction diodes, and those comprising porous *n*- or *p*-type GaN on non-porous epilayers, all exhibited stable rectification. Figure 8 shows current rectification achieved at reverse bias and forward bias (> than knee voltage) recorded for the fully porous *p*-*n* diode (see Figure S2 in Supplementary Information for current rectification in partially porous diodes) at a bias polarity switch frequency of 0.1 Hz at room temperature. The I-t characteristics recorded at ±0.4 V does not show clear rectification behavior, since this voltage is below or on the limit of the turn-on voltage of the porous GaN diodes. At ±1 V, ±2 V, ±3 V and ±5 V voltages all diodes demonstrate rectifying behavior. The highest leakage voltage and the lowest rectification ratio is observed at ±5 V. Also, porous GaN diodes demonstrate very stable values of current with time at both, forward and reverse bias. The stability confirms that for porous *p*-*n* junctions using a single porous layer deposited on an epitaxial continuous GaN film, or from a porous layer grown on another porous layer, a remarkable stability in rectification is maintained. Porous GaN films can exhibit random porosity (compared to arrays of nanostructures), but their ease of deposition over large areas without dominating leakage currents is promising for wideband gap applications, including sensors.

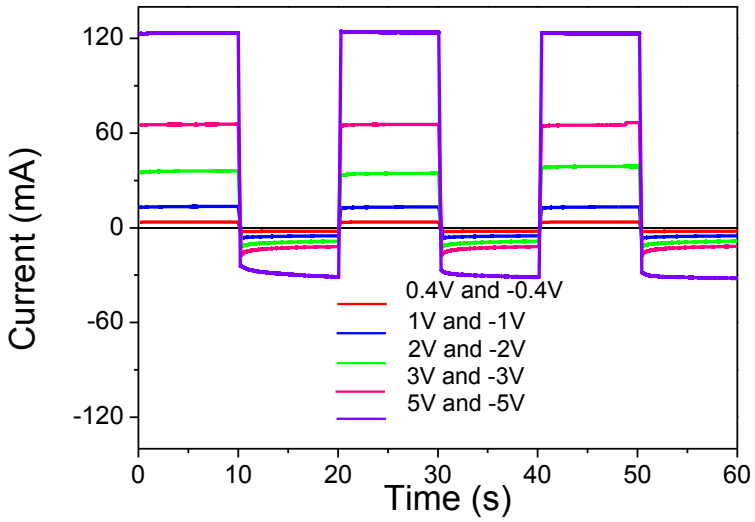

Figure 8. Rectifying characteristics of the fully porous diode at different voltages in the range 0.4 – 5 V.

Taken as a whole, the detailed investigation presented here demonstrates that completely porous high quality *p*-*n* junctions of porous *n*-type and porous *p*-type GaN can be grown over large areas by sequential chemical vapour deposition. The electrical and optical characteristics confirm high electronic quality GaN growth for porous layers

when compared with non-porous epitaxially grown GaN, even when overgrown with opposite conduction type porous layer to form porous/non-porous *p-n* junction diodes. We believe this investigation can be extended to other III-N materials such as InN and AlN to span the visible spectrum, and as a route towards porous, graded index III-N materials as a basis for white light LEDs incorporating other colour centers, or for reducing reflection losses and narrowing the output light cone for improved LED external quantum efficiencies. High surface area diodes by this route do not require complicated core-shell architectures in nanostructure arrays and may be viable routes to chemically stable wide bandgap (bio)sensors.

Experimental Section

Fabrication of partially and totally porous GaN diodes. Nanoporous GaN thin layers were grown on commercial non-porous GaN thin films with complementary electrical conductivity produced on sapphire (0001) substrates. The porous films were grown by the direct reaction of metallic Ga with ammonia in a tubular CVD system, using gallium metal (99.999%) and ammonia (99.99%), as Ga and N sources, respectively. To produce porous *p*-type GaN, Mg was introduced in the furnace in the form of magnesium nitride (99.95%), placing it 4 cm up-stream of the Ga source. The substrate was placed 1.7 cm above the Ga source. Prior to their introduction in the furnace, the substrates were cleaned with ethanol. When the substrate and the Ga and Mg precursors were introduced in the furnace, the quartz tube of the furnace was degassed to a vacuum pressure of 1×10^{-2} Torr. Ammonia was then introduced through a mass-flow controller at a flow rate of 75 sccm, while the pressure was set at 15 Torr and the furnace was heated up to the reaction temperature of 1203 K. Then, the furnace was kept at constant temperature for 60 min under constant NH_3 flow and pressure, while the chemical reaction took place. When the reaction was finished, the furnace was cooled down to room temperature while the ammonia flow was stopped, thus the pressure of the system dropped to 1×10^{-2} Torr. After growth, the samples containing porous Mg-doped GaN were annealed at 973 K in N_2 atmosphere for 20 min in order to break Mg-H complexes and activate the *p*-type conductivity in porous GaN.

Morphological and structural characterization of porous GaN. Nanoporous GaN layers deposited on GaN (0001) substrates were characterized morphologically using a JEOL JSM 6400 scanning electron microscope (SEM). Rocking curves were recorded using a Bruker-AXS D8-Discover diffractometer equipped with parallel incident beam (Göbel mirror), a vertical θ-θ goniometer, a XYZ motorized stage and a General Area Diffraction Detection System (GADDS). Samples were placed directly on the sample holder and the area of interest was selected with the aid of a video-laser focusing system. The X-ray diffractometer was operated at 40 kV and 40 mA to generate Cu Kα radiation. The GADDS detector was a HI-STAR (multiwire proportional counter of 30×30 cm^2 with 1024×1024 pixels). The rocking curves covered an omega angle of 6º, collected through 120 frames at a step size of 0.05^o and 15 s of exposition time per frame.

Cathodoluminescence and photoluminescence characterization. CL measurements were carried out in monoCL2 system from Gatan attached to a field emission scanning electron microscope (FESEM) (Carl Zeiss-LEO 1500) operating at 10 kV. The measurements were carried out at 80 K. The detection for panCL images was done with

a photomultiplier tube (PMT), and the CL spectra were recorded with a Peltier cooled charge coupled device (CCD) detector. PL was collected exciting the samples with the 244 nm line (second harmonic of 488 nm line) from a cw Ar-ion laser with a power density of 2 W/cm^2. PL spectra were acquired using a Horiba iHR320 spectrometer equipped with a Synapse CCD matrix. Samples were placed in an evacuated chamber of a Janis closed-cycle helium cryostat for temperature-dependent PL measurements.

Electrical characterization. Two point electrical measurements of partially and totally porous GaN diodes were conducted using In/Ga liquid eutectic contacts and a Biologic SP-50 potentiostat. An In/Ga eutectic droplet was placed on top of the porous GaN material with the other contact placed directly on the non-porous epitaxial *n*- or *p*-type GaN, in the case of the partially porous diodes, or on the porous n-type GaN layer in the case of the totally porous diode. Linear voltage sweeps were obtained in the range between -3 V and 3 V with a 50 mV/s sweep rate and of -10 V and 10 V with a 50 mV/s sweep rate for temperature-dependent measurements. Diode rectification measurements were conducted in the range between ±0.4V and ±5V voltages for forward and reverse bias. The measurements were repeated with contacts on various points of each sample to ensure repeatability.

Acknowledgements

This project was supported by the EU Framework 7 under Project No. FP7-SPA-2010-263044, the Spanish Government under Projects No. MAT2011-29255-C02-02, TEC2010-21574-C02-02, MAT2010-20441-C02-01-02, MAT-2010-16116 by the Catalan Authority under Project No. 2009SGR235 and by the "Conserjería de Educación de la Junta de Castilla y León" under Project No. VA166A11-2 and VA293U13. This work was also supported by the Irish Research Council New Foundations Award. O.V. Bilousov is supported by Generalitat de Catalunya through the fellowship 2013FI_B2 00108.

References

1. (a) Anual Energy Review 2011, U.S. Energy Information Administration, DOE/EIA-0384 (2011); (b) S. Nakamura, S. Pearton, G. Fasol, G. The blue laser diode: The complete story; Springer-Verlag: Berlin, 2000.
2. (a) M. Hwang, W. H. Hung, and H. L. Hwang, *IEEE Photon. Technol. Lett.* **2008**, *20*, 608; (b) J.J. Wierer, A. David, M.M. Megens, *Nature Photon.* **2009**, *3*, 163; (c) T.K. Kim, S.H. Kim, S.S. Yang, J.K. Son, K.H. Lee, Y.G. Hong, K.H. Shim, J.W. Yang, K.Y. Lim, S.J. Bae, G.M. Yang, *Appl. Phys. Lett.* **2009**, *94*, 161107; (d) C.H. Lee, J. Yoo, Y.J. Hong, J. Cho, Y.J. Kim, S.R. Jeon, J.H. Baek, G.C. Yi, *Appl. Phys. Lett.* **2009**, *94*, 213101; (e) D.S. Liu, T.W. Lin, B.W. Huang, F.S. Juang, P.H. Lei, C.Z. Hu, *Appl. Phys. Lett.* **2009**, *94*, 143502; (f) S.W. Ryu, J. Park, J.K. Oh, D.H. Long, K.W. Kwon, Y.H. Kim, J.K. Lee, J.H. Kim, *Adv. Funct. Mater.* **2009**, *19*, 1650; (g) M.H. Lo, P.M. Tu, C.H. Wang, C.W. Hung, S.C. Hsu, Y.J. Cheng, H.C. Kuo, H.W. Zan, S.C. Wang, C.Y. Chang, S.C. Huang, *Appl. Phys. Lett.* **2009**, *95*, 041109; (h) Y.M. Song, E.S. Choi, G.C. Park, C.Y. Park, S.J. Jang, Y.T. Lee, *Appl. Phys. Lett.* **2010**, *97*,

093110; (i) C.Y. Cho, S.E. Kang, K.S. Kim, S.J. Lee, Y.S. Choi, S.H. Han, G.Y. Jung, S.J. Park, *Appl. Phys. Lett.* **2010**, *96*, 181110; (j) S.Chhajed, W. Lee, J. Cho, E.F. Schubert, J.K. Kim, *Appl. Phys. Lett.* **2011**, *98*, 071102; (k) X.X. Fu, B. Zhang, X.N. Kang, J.J. Deng, C. Xiong, T. Dai, X.Z. Jiang, T.J. Yu, Z.Z. Chen, G.Y. Zhang, *Opt. Exp.* **2011**, *19*, A1104

3. (a) A.H.D. Graham, C.R. Bowen, J. Robbins, G. Lalev, F. Marken, J. Taylor, *Sens. Actuators B* **2010**, *147*, 697; (b) D. Valerini, A. Creti, A.P. Caricato, M. Lomascolo, R. Rella, M. Martino, *Sens. Actuators B* **2010**, *145*, 167; (c) S.J. Pearton, F. Ren, *Adv. Mater.* **2000**, *12*, 1571
4. Z. Fan, H. Razavi, J.W. Do, A. Moriwaki, O. Ergen, Y.L. Chueh, P.W. Leu, J.C. Ho, T. Takahashi, L.A. Reichertz, S. Neale, K. Yu, M. Wu, J.A. Ager, A. Javey, *Nat. Mater.* **2009**, *8*, 648
5. (a) E.J. Anglin, L. Cheng, W.R. Freeman, M.J. Sailor, *Adv. Drug Delivery Rev.* **2008**, *60*, 1266; (b) G. Jiménez-Cadena, J. Riu, F.X. Rius, *Analyst* **2007**, *132*, 1083
6. N. Bacci, A. Diligenti, G. Barillaro, *J. Appl. Phys.* **2011**, *110*, 036106
7. W. Sun, N.P. Kherani, K.D. Hirschmann, L.L. Gadeken, P.M. Fauchet, *Adv. Mater.* **2005**, *17*, 1230.
8. (a) J.J. Carvajal, J.C. Rojo, *Cryst. Growth Des.* **2009**, *9*, 320; (b) J.J. Carvajal, O.V. Bilousov, D. Drouin, M. Aguiló, F. Díaz, J.C. Rojo, *Microsc. Microanal.* **2012**, *18*, 905.
9. (a) O.V. Bilousov, J. J. Carvajal, D. Drouin, X. Mateos, F. Díaz, M. Aguiló and C. O'Dwyer. *ACS Appl. Mater. Interfaces* **2012,** *4*, 6927; (b) O. V. Bilousov, H. Geaney, J. J. Carvajal, V. Z. Zubialevich, P. J. Parbrook, A. Giguere, D. Drouin, F. Dıaz, M. Aguilo and C. O'Dwyer, *Appl. Phys. Lett.* **2013**, *103*, 112103
10. W. Götz, N.M. Johnson, J. Walker, D.P. Bour, R.A. Street, *Appl. Phys. Lett.* **1996**, *68*, 667
11. S.J. Pearton, R.G. Wilson, J.M. Zavada, J. Han, R.J. Shul, *Appl. Phys. Lett.* **1998**, *73*, 1877
12. J.O. Song, J.S. Ha, T.Y. Seong, *IEEE Electron. Dev. Lett.* **2010**, *57*, 42.
13. (a) M. Mynbaeva, A. Titkov, A. Kryganovskii, V. Ratnikov, K. Mynbaev, H. Huhtinen, R. Laiho, V. Dmitriev, *Appl. Phys. Lett.* **2000**, *76* 1113; (b) L. Liu, J.H. Edgar, *Mater. Sci. Eng. R* **2002**, *37*, 61
14. S. Dassonneville, S. A. Amorkane, B. Sieber, J.L. Farvacque, B. Beaumont, P. Gibart, *J. Appl. Phys.* **2001**, *89*, 3736
15. X.L. Sun, S.H. Goss, L.J. Brillson, D.C. Look, R.J. Molnar, *J. Appl. Phys.* **2002**, *91*, 6729
16. M. Herrera Zaldivar, P. Fernández, J. Piqueras, *J. Appl. Phys.* **1998**, *83***,** 462.
17. J. Neugebauer, C.G. Van de Walle, *Appl. Phys. Lett.* **1996**, *69*, 503
18. J.M. Myoung, K.H. Shim, S. Kim, *Jap. J. Appl. Phys. Part 1* **2001**, *40*, 476
19. F. Bertram, J. Christen, M. Schmidt, M. Topf, S. Koymov, S. Fischer, B. Meyer, *Mater. Sci. Eng. B* **1997**, *50*, 165.
20. W. Shan, T.J. Schmidt, X.H. Yang, S.J. Hwang, J.J. Song, B. Goldenberg, *Appl. Phys. Lett.* **1995**, *66*, 985

21. S.C. Jain, M. Willander, J. Narayan, R. Van Overstraeten, *J. Appl. Phys.* **2000**, *87*, 965
22. L. Eckey, J. C. Holst, P. Maxim, R. Heitz, A. Hoffmann, I. Broser, B.Meyer, C. Wetzel, E. Mokhov, P. Baranov, *Appl. Phys. Lett.* **1996**, *68*, 415.
23. M.A. Reshchikov, H. Morkoç, *J. Appl. Phys.* **2005**, *97*, 061301
24. O Gelhausen, HN Klein, MR Phillips, EM Goldys, *Appl. Phys. Lett.* **2003**, *83*, 3293.
25. (a) Y. Huang, X. Duan, Y. Cui, C,M, Lieber, *Nano Lett.* **2002**, *2*, 101−104; (b) X. Duan, C.M. Lieber, *J. Am. Chem. Soc.* **2000**, *122*, 188